HANDAI NANOPHOTONICS Volume 3

Nano Biophotonics

Science and Technology

Hiroshi Masuhara, Satoshi Kawata
and Fumio Tokunaga
Editors

NANO BIOPHOTONICS

Science and Technology

This page intentionally left blank

HANDAI NANOPHOTONICS Volume 3

NANO BIOPHOTONICS

Science and Technology

Proceedings of the 3rd International Nanophotonics Symposium Handai
July 6-8th 2006, Suita Campus of Osaka University, Osaka, Japan

Edited by

Hiroshi Masuhara, Satoshi Kawata** and **Fumio Tokunaga
Department of Applied Physics
Osaka University
Suita, Osaka, Japan

ELSEVIER

Amsterdam • Boston • Heidelberg • London • New York • Oxford • Paris
San Diego • San Francisco • Singapore • Sydney • Tokyo

Elsevier
Radarweg 29, PO Box 211, 1000 AE Amsterdam, The Netherlands
The Boulevard, Langford Lane, Kidlington, Oxford OX5 1GB, UK

First edition 2007

Library of Congress Cataloging-in-Publication Data
A catalog record for this book is available from the Library of Congress

British Library Cataloguing in Publication Data
A catalogue record for this book is available from the British Library

ISBN-13: 978-0-444-52878-0
ISBN-10: 0-444-52878-4
ISSN: 1574-0641

Printed and bound in Italy

07 08 09 10 11 10 9 8 7 6 5 4 3 2 1

Preface

Nanophotonics as the science to study the interaction between photons and nanostructures in the dimension smaller than the wavelength of light is both scientifically and technologically interesting and important. On the basis of our high activity on nanophotonics research in Osaka University, various projects and programs are being conducted, such as the Nanophotonics Research Initiative of Graduate School of Engineering, 21 Century COE Program on "Dynamics of Biological Systems" of Graduate School of Frontier Biosciences, Kawata Project on "Nonlinear Nanophotonics" of CREST-JST, Tokunaga Project on "Nanometer Assembling -μm Multiplication" of CREST-JST, and KAKENHI Project on "Molecular Nano Dynamics" of MEXT. One of their important topics is concerned with Nano Biophotonics and very interesting research is being developed on the same. Indeed Nano Biophotonics is an important hot topic in nanophotonics, integrating optics, photophysics and photochemistry, nanotechnology, and biosciences. In view of this interdisciplinary nature, an international forum involving physicists, chemists, spectroscopists, optical scientists, and electronics engineers is necessary and will contribute for growing this research field.

In July 2006, we had a two-day symposium with distinguished scientists to discuss the latest progress in this field and the excellent results presented there are summarized here as a book "Nano Biophotonics: Science and Technology". This is the 3rd volume on the Handai Nanophotonics Book Series, following the volumes of "Nanophonics: Integrating Photochemistry, Optics, and Nano/Bio Materials" and "Nanoplasmonics: From Fundamentals to Applications". The contents of this book are prepared by the invited lecturers, research members of the relevant projects/program, and some of general participants. The book has 27 chapters which are classified into 4 parts; nano bio spectroscopy, nano bio dynamics, nano bio processing, and nano bio devises. We believe this book reconstructs the excellent presentation and enthusiastic atmosphere of the symposium.

We would like to thank all the contributors, participants, and sponsors for the Handai Nanophotonics Book Series and the 3rd International Nanophonics Symposium Handai, and Dr. Prabhat Verma for his sincere support in editing this book.

Hiroshi Masuhara, Satoshi Kawata, and Fumio Tokunaga
at Handai, Suita, Japan

Organization of
The 3rd International Nanophotonics Symposium Handai on
Nano Biophotonics: Science and Technolgy

Sponsored by
Nanophotonics Research Initiative of Graduate School of Engineering,
21 Century COE Program on “Dynamics of Biological Systems” of Graduate School of Frontier Biosciences,
Kawata Project on “Nonlinear Nanophotonics” of CREST-JST,
Tokunaga Project on “Nanometer Assembling -μm Multiplication” of CREST-JST,
KAKENHI Project on “Molecular Nano Dynamics” (A01 Group) of MEXT
and
The Murata Science Foundation

Chairpersons
Hiroshi MASUHARA (Department of Applied Physics)
Satoshi KAWATA (Department of Applied Physics)
Fumio TOKUNAGA (Department of Earth and Space Science)

Organization Committee
Yasushi INOUE (Graduate School of Frontier Biosciences)
Satoshi KAWATA, Hiroshi MASUHARA, Zouheir SEKKAT (Department of Applied Physics)
Masanori OZAKI, Takatomo SASAKI, Toshiaki SUHARA (Division of Electric, Electronic, and Information Engineering)
Fumio TOKUNAGA (Department of Earth and Space Science)

Program Committee
Tsuyoshi ASAHI, Katsumasa FUJITA, Yoichiroh HOSOKAWA, Hiroyuki YOSHIKAWA (Department of Applied Physics)
Norio HAMADA, Ryosuke NAKAMURA (Center for Advanced Science and Innovation)
Nick Smith (Graduate School of Frontier Biosciences)

Participants list

Takuji Adachi	Osaka University
Yasuki Akisawa	Osaka University
Jun Ando	Osaka University
Mako Arakawa	Osaka University
Tsuyoshi Asahi	Osaka University
Harald Baumann	Osaka University
Edward Botchersby	Oxford University
Paul Campagnola	Connecticut University
Mark Cannell	University Auckland
Haik Chosrowjan	Institute for Laser Technology
Rajesh Dodla	Osaka University
Tokujiro Enatsu	Osaka University
Tetsuya Enoki	Osaka University
H'Dhili Fekhra	Riken
Shintaro Fujii	Osaka University
Junichi Fujikata	NEC
Masatoshi Fujimura	Osaka University
Akiko Fujita	Osaka University
Katsumasa Fujita	Osaka University
Akihiro Fujiwara	Osaka University
Masayuki Futamata	AIST
Keita Goto	Osaka University
Tatsushi Goto	Osaka University
Norio Hamada	Osaka University
Hiro-o Hamaguchi	The University of Tokyo
Tomoya Harada	FDK corporation
Akira Harata	Kyushu University
Daigo Hiraga	Osaka University
Tsunemi Hiramatsu	Osaka University
Osamu Hisatomi	Osaka University
Johan Hofkens	Katholieke Universiteit Leuven
Kanako Honda	Kinki University, Kyushu
Chie Hosokawa	AIST
Yoichiroh Hosokawa	Osaka University
Taro Ichimura	Osaka University
Seriya Iguchi	Osaka University
Yasushi Imamura	Osaka University
Yasushi Inouye	Osaka University

Katsuya Ishitani	Osaka University
Sawako Ishitobi	Osaka University
Syoji Ito	Osaka University
Shigeki Iwanaga	Sysmex Corporation
Hyeon-Gu Jeon	Osaka University
Takamasa Kai	Osaka University
Takahiro Kaji	Osaka University
Akari Kanazawa	Osaka University
Yasuo Kanematsu	Osaka University
Takanori Kanemitsu	Osaka University
Kunihito Katoh	Osaka University
Satoshi Kawaguchi	Osaka University
Fumio Kawamura	Osaka University
Shogo Kawano	Osaka University
Kenichiro Kawasaki	Osaka University
Satoshi Kawata	Osaka University
Tatsuo Kikuchi	Sumitomo Precision Products
Hiroshi Kimura	Taiyo Nippon Sanso
Kenji Kimura	MEXT
Masahiro Kishida	Kyushu University
Ryota Kito	Osaka University
Ai Kiyohara	AIST
Masahiro Kobayashi	Osaka University
Toshiyuki Koizumi	Osaka University
Hisato Kondoh	Osaka University
Karsten Konig	Fraunhofer Institute for Biomedical Engineering
Mari Kotoura	Osaka University
Yasuaki Kumamoto	Osaka University
Shanmugam Kumaran	Osaka University
Guillaume Louit	Osaka University
Lehui Lu	Kwansei Gakuin University
Hiroshi Masuhara	Osaka University
Kyoko Masui	Osaka University
Sadahiro Masuo	Kyoto Institute of Technology
Ryota Matsui	Osaka University
Hideaki Matsumoto	Osaka University
Sachihiro Matsunaga	Osaka University
Hideki Matsune	Kyushu University
Takeo Minamikawa	Osaka University

Hajime Mori	Kyoto Institute of Technology
Yusuke Mori	Osaka University
Hiroyuki Morita	Osaka University
Yu Nabetani	Osaka University
Kazuhiko Nakamura	Osaka University
Ryosuke Nakamura	Osaka University
Sana Nakanishi	Osaka University
Ryuichi Nakayama	Osaka University
Takayuki Negishi	Osaka University
Khanh Huy Nguyen	Osaka University
Niidome Niidome	Kyushu University
Hirohiko Niioka	Osaka University
Kenji Nishida	Osaka University
Hideki Noda	Osaka University
Tsutomu Ohmori	Tokyo Institute of Technology
Chikako Otori	Nihon Keizai Shimbun, Inc.
Masanori Ozaki	Osaka University
Yasuyuki Ozeki	Osaka University
Almar Palonpon	Osaka University
Lingyun Pan	Kwansei Gakuin University
Remo Proietti Zaccaria	Osaka University
Thomas Rodgers	Osaka University
Sukhdev Roy	Dayalbagh Education Institute
Senichi Ryou	Osaka University
Makoto Sakai	Tokyo Institute of Technology
Vahid Sandoghdar	ETH
Noriko Saruta	Cabinet Office, Government of Japan
Takatomo Sasaki	Osaka University
Markus Sauer	University of Bielefeld
Takeyuki Sekimoto	Osaka University
Zouheir Sekkat	Osaka University
Kunihiro Shibata	Osaka University
Satoru Shoji	Osaka University
Nicholas Smith	Osaka University
Yousuke Sora	Osaka University
Brahadeeswaran Srinivasan	Osaka University
Shohei Sugawa	Osaka University
Teruki Sugiyama	Osaka University
Toshiaki Suhara	Osaka University
Hidemasa Suzuki	Osaka University

Atsushi Taguchi	Osaka University
Yuuki Takao	Osaka University
Go Tanaka	Osaka University
Kazuo Tanaka	Gifu University
Masazumi Tanaka	Sumitomo Precision Products
Yoshito Tanaka	Osaka University
Naoki Tanimoto	Osaka University
Fumio Tokunaga	Osaka University
Masao Toyoda	Osaka University
Naoki Tsujimoto	Osaka University
Masahiro Uemukai	Osaka University
Kazumasa Uetsuki	Osaka University
Kiminori Ushida	Riken
Anwar Usman	Osaka University
Takayuki Uwada	Osaka University
Prabhat Verma	Osaka University
Alfred Vogel	Medical Laser Center Lubeck
Kiyoaki Wada	Osaka University
Wataru Watanabe	AIST
Shimon Weiss	UCLA
Qi Ya	Chinese Academy of Sciences
Vladislav Yakovlev	Osaka University
Atsushi Yamaguchi	Osaka University
Hideaki Yamaguchi	Osaka University
Mahito Yamamoto	Osaka University
Yusuke Yamamoto	Osaka University
Masahito Yamanaka	Osaka University
Yoshihisa Yamaoka	Kyoto Prefectural University of Medicine
Toshio Yanagida	Osaka University
Taka-aki Yano	Osaka University
Masakazu Yasuda	Osaka University
Shunsuke Yasugi	Osaka University
Ryohei Yasukuni	Osaka University
Kenichi Yoshida	Kwansei Gakuin University
Hirofumi Yoshikawa	Osaka University
Hiroshi Yoshikawa	Osaka University
Hiroyuki Yoshikawa	Osaka University
Jiang Yuqiang	Cybox Co.,Ltd

July 6-8th, 2006
Icho-Kaikan in Suita Campus, Osaka University, Osaka, Japan

This page intentionally left blank

TABLE OF CONTENTS

Part II: Nano Bio Dynamics

Part III: Nano Bio Processing

PART I: NANO BIO SPECTROSCOPY

This page intentionally left blank

Handai Nanophotonics, Volume 3
H. Masuhara, S. Kawata and F. Tokunaga (Editors)

Chapter 1

Single molecule nano-bioscience: Fluctuations and adaptive biological molecular machines

Toshio Yanagida[1,2], Jun Kozuka[1,2], Takuya Okada[1,2], Yuichi Taniguchi[1,2], Mitsuhiro Iwaki[1,2], and Yoshiharu Ishii[1]

[1]Soft nano-machine Project, CREST, JST

[2]Graduate School of Frontier Biosciences, Osaka University, 1-3 Yamadaoka, Suita, Osaka 565-0871 Japan

Biomolecules assemble to form molecular machines such as molecular motors, cell signal processors, DNA transcription processors and protein synthesizers. The molecular machines react and behave in response to their surroundings with great flexibility. This flexibility is essential for biological organisms and biological systems. The underlying mechanism of molecular machines is not as simple as that expected from an analogy with man-made machines. Given that molecular machines are only nanometers in size and have a flexible structure, they are very prone to thermal agitation. In addition, the input energy level is not much different from average thermal energy level, k_BT. Molecular machines can use this thermal noise with a high efficiency of energy conversion for their functions. This is sharp contrast to man-made machines that operate at energies much higher than thermal noise.

In recent years, single molecule detection techniques have attracted great deal of attention in the field of life science [1,2]. Observing and manipulating biomolecules allows their dynamic behaviors to be directly revealed as has been demonstrated for motor proteins. Reactions of biological molecules are generally stochastic. Therefore in ensemble measurements, dynamic behaviors of individual molecules are averaged and hidden. In biosystems such as live cells, biomolecules work in complicated heterogeneous systems, involving various types of molecules. It is difficult to qualitatively detect dynamic behaviors of proteins of interest in such systems using ensemble averaged measurements. The single molecule detection techniques are expected to overcome these difficulties and have already been successfully applied to study the dynamic properties of biological molecules such as motor proteins, enzymes, RNA polymerase and cell signaling proteins. The dynamic

behavior of biomolecules revealed using single molecule detection techniques will be a breakthrough for understanding the mechanism of function of biomolecules.

1. SINGLE MOLECULE IMAGING

The single molecule detection techniques are based on the two key techniques of single molecule imaging and single molecule manipulation. Light microscopy is a method that allows us to image biomolecules as they work in an active manner in biomolecular assemblies and cells. To visualize single molecules of nanometer size, fluorescent probes must be attached. In order to visualize faint fluorescence from single molecules, it is critical to increase S/N ratio by reducing the background. Local illumination is used to reduce the background noises contributed from fluorescent molecules in solution. We have developed total internal reflection fluorescence (TIRF) microscopy, in which only surface between solution and slide glass is illuminated (Figure 1A)[3]. The TIRF microscopy is advantageous for observation of behavior of biomolecules; that is, movement of individual molecules on the glass surface and the changes occurred in molecules immobilized on the glass surface are allowed to be visualized.

Fluorescence from single molecules is imaged as spots. Fluorescence signals are accumulation of photons emitted from single fluorescent molecules. Since photon detection is stochastic, the fluorescence intensity (total number of photons emitted) fluctuates. After emission of large number of photons, fluorescent molecules cease to emit photons all of sudden and do not emit them again (Figure 1B). This photobleaching is explained by irreversible photochemical reaction of the molecules. The number of photons that single molecules emit until the photobleaching characterizes the fluorophores. In the case of TMR or Cy3 which is used for single molecule measurements, the photobleaching occurs after a molecule emits approximately 100 thousand to 1 million photons. The sudden drop of the fluorescence due to the photobleaching is characteristic of single molecules and this is utilized as a test on whether the fluorescence spots observed come from single molecules or more. Fluorescent spots from single molecules of the order of nm in size spread to several hundreds nm due to diffraction of light (Figure 1C). It would be possible that several molecules exist in a small area 100 nm x 100 nm and that several molecules form an aggregate. It is difficult to distinguish overlapped spots in the images. From the observation of the photobleaching process it is possible to discriminate individual spots from an overlapped spot. The fluorescence from a single fluorophore drops in a single step and two molecules in two steps. Together with the fluorescence intensity, the number of fluorescent

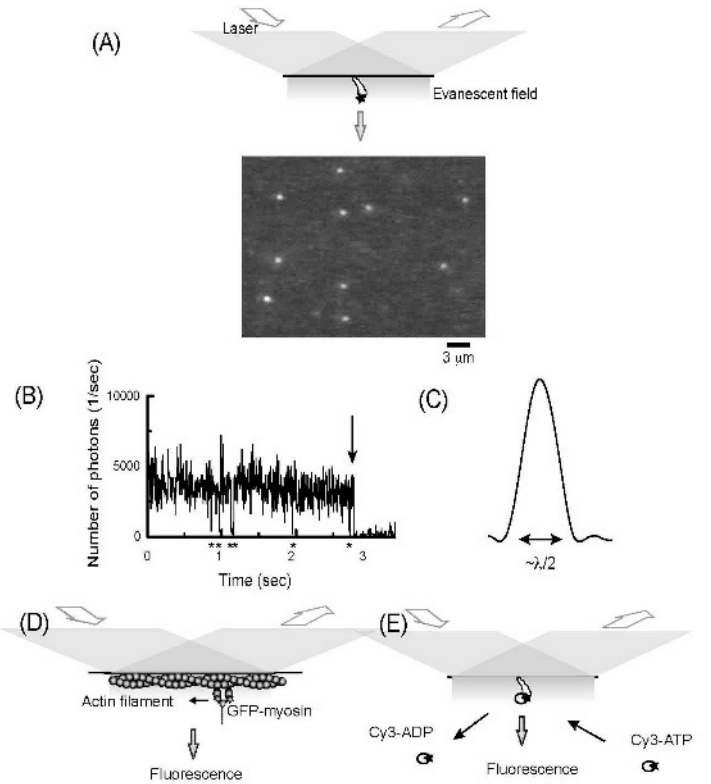

Fig. 1. Total internal reflection microscopy and single molecule imaging. (A) Evanescent field is generated near the surface between glass and water when a laser is total internally reflected. Individual spots arise from single fluorescence molecules attached to protein myosin. (B) Time trajectory of fluorescence intensity from single molecules. Arrow indicates photobleaching. The fluorescence intensity drops to a base line all of sudden. (C) Fluorescence intensity profile of a single spot in one-dimension. The fluorescence intensity distribute over a range of the wavelength of light. (D) Visualization of movement of single molecular motors myosin on actin filaments immobilized on the glass surface. The movement of single myosin molecules can be detected as movement of fluorescence spots. (E) Visualization of the turnover of the hydrolysis of ATP by detecting the association of Cy3-ATP and dissociation of Cy3-ADP. The turnover is seen as fluorescence turn-on and off at the position of myosin immobilized on the glass surface.

A single molecule fluorescence imaging microscope, which was first built based on an inverted microscope was prism type [3]. Epi- and prism type TIRF microscopy were switched by moving a mirror. For TIRF microscopy, a 60^{o} dispersion prism was placed on a quartz slide glass with a gap filled with fluorescence–less pure glycerol. Incident angle was adjusted in order for incident beam to be totally internally reflected on the interface between the

slide glass and buffer solution. Objective lens type TIRF microscopy is a method to generate evanescent field using an objective lens with large numerical aperture (NA) instead of a prism [4]. Epi- and TIRF fluorescence microscopy can be switched by shifting the position of the laser between the edge and center of the objective lens by moving the mirror. The illumination area does not change while the illumination method changes. The objective type TIRF microscopy allows us to change sample without changing the optical system. Also it provides large free space above the specimen where the prism is placed for a prism type TIRF microscope. It enables us to do other operations such as laser trap experiments at the same time [5]. Another advantage is the thickness between slide glass and cover glass. For objective TIRF microscopy, the illumination and detection is done on the same side, whereas, for prism type TIRF microscopy, the evanescent field is generated on the other side of the detection. The thickness of the specimens is limited for prism type TIRF microscopy. Thick sample space allows us to place bulky specimen such as cells [6].

2. IMAGING MOVEMENT AND CHEMICAL REACTION OF MOLECULAR MOTORS

The movement of molecular motors is visualized by tracing the position of fluorescently labeled protein molecules on the counterparts immobilized on the glass surface (Figure 1D). The movement of linear motors such as kinesin and unconventional myosin has been detected using fluorescently labeled or GFP tagged molecules [7]. The fluorescent spots arisen from single kinesin molecules move along fluorescent lines of microtubules immobilized on the surface in the presence of ATP. Kinesin moves processively or for long distance without dissociation. Unconventional myosin V and VI are also processive motors along actin filaments but the direction of the movement is opposite. The movement of both kinesin and unconventional myosin appears smooth with essentially constant velocity of several μm/sec. However, the movement no longer appears smooth when the spatial resolution is improved to a few nm. The stepwise movements of kinesin and unconventional myosin V and VI are clearly observed in the imaging under the condition where the movement is very slow at low concentration of ATP [8].

In addition to active movement, diffusive movement of molecular motors has been observed. In contrast to the stepwise movement of double-headed kinesin, single-headed kinesin such as unconventional KIF1A exhibits Brownian movement on microtubules in the presence of ATP [9]. Unconventional KIF1A is a naturally single headed motor protein in the kinesin family. The additional electrostatic interaction with microtubules is thought to prevent dissociation of kinesin from microtubules during

movement. Similar Brownian movement of single headed kinesin has been reported using truncated conventional kinesin [10]. In Brownian movement, the direction of the movement varies randomly and mean square displacement is in proportion to time, while mean displacement is in proportion to time in the case of active movement of molecular motors. Another example of Brownian movement is movement of a DNA-based molecular motor. RNA polymerase moves along a long DNA molecule in a stepwise manner while RNA grows according to the sequence of DNA. One step translocation of RNA polymerase is associated with the addition of one nucleotide to RNA with the energy released from the breakdown of pyrophosphate from nucleocide triphosphate. The movement is detected using manipulation techniques. Brownian movement of RNA polymerase is observed when it searches for a promotor region on the DNA molecules, where RNA polymerase starts transcription [11]. A DNA molecule is held taut by being trapped by a laser through beads at both ends. The movement of a single molecule of RNA polymerase along the DNA molecule trapped is visualized using fluorescently labeled RNA polymerase.

Single molecule detection allows us to measure a chain of reactions without breaking down the whole process and synchronizing the reaction. Among constituted steps some of steps can be monitored at the single molecule level. The steps that can be detected include mechanical movement of molecular motors and association and dissociation of ligands. Molecular motors are enzymes that hydrolyze ATP molecules to ADP and inorganic phosphate (Pi). The binding and dissociation of fluorescently labeled ATP to myosin immobilized on the glass surface can be measured (Figure 1E)[3,4]. Fluorescent spots appear at the position of the myosin molecules when ATP binds and disappears when ADP dissociates after hydrolyzed. When the fluorescent molecules are free in solution, they are outside the illumination area in most time in the case of TIRF microscopy or they are not observed as spots even when they are in the evanescent field. The duration time from the binding to the dissociation is fit to a single exponential decay and the average duration time gave turnover rime of ATP, which corresponds to the ATP hydrolysis rate at the limit of high concentration of ATP in the ensemble measurements.

3. SINGLE MOLECULE SPECTROSCOPY AND DYNAMIC STRUCTURES OF BIOMOLECULES

The conformational changes of single biomolecules are detected using fluorescence spectroscopic changes of fluorescent dyes attached. Fluorescence changes monitor spontaneous transitions between multiple conformational states corresponding to the multiple minimum states in the

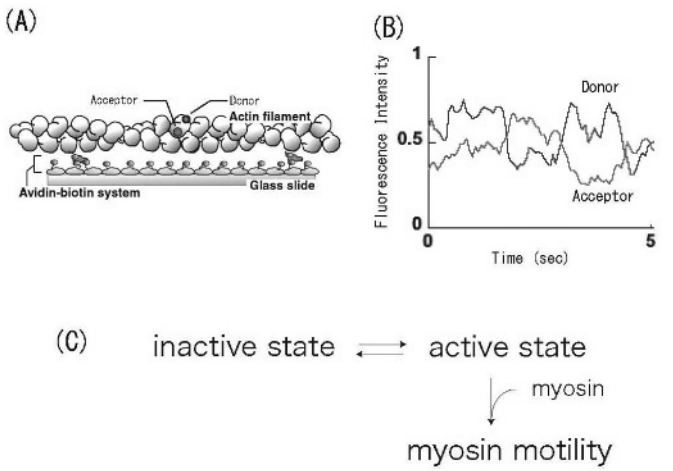

Fig 2. Spontaneous conformational transition of actin. (A) An actin molecule is labeled specifically with donor (dark) and acceptor (light) and polymerized with large excess of unlabeled actin. (B) The time trajectories of the donor (dark) and acceptor (light) fluorescence changed due to the changes in FRET; that is, the donor fluorescence increased when the acceptor fluorescence decreased and vice versa. (C) The structure of actin fluctuates between active state and inactive state. The binding of myosin to actin filaments shift the actin structure to the active state.

free energy landscape. Spontaneous fluctuation of the myosin structure is monitored by changes in fluorescence spectrum from the probes attached to the protein. The intensity and the peak position of the fluorescence of TMR attached to the most reactive cystein of muscle myosin fluctuates in the time scale of sec.

Fluorescence resonance energy transfer (FRET) is the technique that more directly monitors the conformational changes of biomolecules. Changes in the distance between two different types of fluorescent probes attached at two specific positions are monitored as changes in the efficiency of FRET (Figure 2A). Single molecule FRET from doubly labeled actin monomer in the filament has revealed that actin has multiple conformations and spontaneously changes the conformation between them with time (Figure 2B)[12]. The data showed that the myosin motility is activated through the conformational changes of actin. The multiple conformations are grouped into at least two states, a state in which myosin motility is activated and a state in which myosin motility is inhibited. In the presence of myosin, actin favorably takes the conformation in the state, in which the myosin motility is activated. The myosin motility inhibited state is attained when actin is crosslinked chemically with glutarardehide. In the crosslinked acrin filaments, the motility of myosin is inhibited, while the actin-ativated ATPase and the binding to actin is not affected. Thus actin spontaneously fluctuates between

the two conformational states that activate and inhibit the myosin motility and the binding of myosin activates the myosin motility by shifting the population of the conformational state of actin (Figure 2C). Thus, the observation of the conformational dynamics provides the mechanism that the myosin motility is activated through actin dynamics.

Similar conformational fluctuation has been observed for the signaling protein, Ras, a molecular switch in various signaling networks [13]. The cell signals triggered by the binding of signal molecules to the cell surface are transmitted through signal transduction processes to the nuclei inside the cell. Ras is a key player in signal transduction processes, involving in varieties of signal transduction processes. Ras can interact with various target proteins, triggering respective downstream signaling processes. Ras has multiple conformational states. Among them a low FRET inactivated state is distinguished from other high FRET activated states. The conformational transition between them occurred in the timescale of seconds. The binding of effectors Ras, Raf or RalGDS, preferentially binds to the activated state and shifts the population of the conformational states from the inactivated state to the activated states. The transition between conformational states within the activated states occurred on the time scale of 20 msec and in the presence of the effectors the transition was not observed, suggesting that Ras stays in one conformational state. Thus the binding of specific effecters may select a corresponding conformational state out of the multiple conformational states preexisting before binding. Thus the multiple conformation of Ras may be closely related to the fact that this protein can interact with varieties of target proteins to fulfill corresponding functions [14].

Thus, the single molecule measurements of protein structure has shown that the activated structures preexist before activation and the mechanism seems important for biological systems tin which biomolecules self-assemble and self-control.

4. IMAGING SINGLE MOLECULES IN LIVE CELLS

Cell is a system where various types of biomolecules are assembled, organized, net-worked to perform functions. Given that the system is so complicated, it is difficult to describe the behaviors of biomolecules and understand the mechanism. Many approaches have been attempted. Using cell biology techniques, various biomolecules involved have been identified and characterized using structural and biochemical studies. Fluorescence imaging has been used to study the localization of biomolecules of interest. Single molecule imaging technique is now applied to cells to monitor key events occurred in cells at the single molecule level. Several microscopy including TIRF, confocal and two-photon excitation microscopy can be used to

visualize single molecules on cell membranes and inside cells. In TIRF microscopy, cell plasma membranes of living cells placed close to the glass surface are illuminated by evanescent light generated on the surface of the glass and molecules on the membranes are monitored.

Cell functions in response to external signals. The binding of signal molecules to the surface of cells initiates a signaling process transmitted to cell nuclei. We demonstrated that the binding of single molecules of fluorescently labeled epidermal growth factor (EGF) to its receptor protein (EGFR) on the membranes can be observed in real time [6]. The EGFR molecules respond to the binding of EGF signals by dynamically dimerizing and clustering on the cell membranes, which was visualized using fluorescently labeled EGFR at the single molecule level. The dimerizaton of EGFR induces autophosphorylation on cytoplasmic Tyr residues. The autophosphorylation was also observed at the single molecule level using perforated cells. After stimulation with Cy5-EGF, cells were induced with Cy3-labeled antibody, Cy3-mAb74, that recognizes autophorphorylated EGFR. Using the same method the binding of fluorescently labeled cAMP to the cell surface of *dictyostelium* amoebae during chemotaxix were investigated [15]. The kinetic analysis of the binding of cAMP showed that the state of the cAMP receptor protein is not homogeneous but sensitive to the chemical gradient of cAMP outsides. The state of EGFR in the pseudopod region is activated to interact with downstream signaling G-proteins and not activated in the tail region. Thus single molecule imaging on the cell surface allows us to describe the initial step of the cell signaling processes.

To visualize single molecule inside the cells, confocal fluorescence microscopy and two-photon excitation fluorescence microscopy have been used. In a confocal microscope, a pinhole is placed in the front of a detector to block fluorescence light coming from section other than the conjugated focal plane. In two-photon microscopy, molecules are excited by simultaneous absorption of two photons of near-infrared light at wavelength twice as much as the wavelength of visible light. Images can be obtained using these microscopies by scanning in 2D or 3D with a Nipkow disk for example. Instead of scanning whole space, molecules coming in and going out in small areas where the detector is fixed are detected in fluorescence correlation spectroscopy (FCS). The optically observed volume generated by confocal or two photon excitation microscopy is about 1 femto liter. In such small volume only a few or even single molecules are present. Fluctuation of fluorescence due to the fluctuation of the number of molecules and due to the changes inside the molecules can be detected. Using these techniques, the behavior of proteins and RNA has been measured and new information on the flow of molecules and signals have been revealed.

5. Single molecule manipulation and mechanical properties of biomolecules

The function of biomolecules is performed through the interaction between them in a specific arrangement. Manipulation techniques of single biomolecules or assembly of biomolecules have been developed to allow the biomolecules to interact in appropriate arrangement under microscopy and the reaction of single molecules to be efficiently measured. Most primitive and basic way to manipulate biomolecules is to immobilize them to the surface of a slide glass. To control biomolecules more precisely, large probes such as a microneedle [16] and beads trapped optically [17] have been used. To attach biomolecules to glass surface and probes, several methods have been employed. Non-specific binding to large probes uses charge groups or hydrophobic areas distributed on the surface of biomolecules. Sometimes this method may damage biomolecules An avidin-biotin pair, antigen-hapten and His-tag system have recently been used because of high affinity and specificity. In any case biomolecules are tiny in the order of nanometer and fragile. The activities of biomolecules are readily damaged, when they are directly handled.

Various mechanical properties and function of biomolecules have been measured using these manipulation techniques. Actin filament is a polymer of actin molecules arranged in a double-stranded helix and the physical properties has been measured (Figure 3)[18]. One end of the filament is attached to a rigid microneedle to pull and the other end is to a flexible microneedle to measure the displacement of its tip. When actin filaments are pulled with large force, they are distorted and finally broken. The tensile strength of actin filaments measured as the maximum displacement of the microneedle immediately before the actin filament breaks is approximately 100 pN, which is not much greater than the force applied on the filament in a contracting muscle. Similarly, the force required for unfolding of single biomolecules has been measured when both ends of the biomolecules are pulled. The measurements of mechanically-induced unfolding at the single molecule level was first carried out with a gigantic protein called titin. Titin, which is responsible for the passive elasticity of the muscle, is composed of a repeating unit of immunoglobulin (Ig) domain. The mechanically induced unfolding of titin has been studied using a laser trap and atomic force microscopy [19-21]. In these measurements one end of the biomolecule is fixed to the surface and the other end is attached to a bead trapped by a laser or cantilever.

When two interacting biomolecules are pulled, unbinding force of the molecules can be measured. Myosin is a molecular motor that moves along actin filaments. Myosin interacts with actin strongly in the absence of

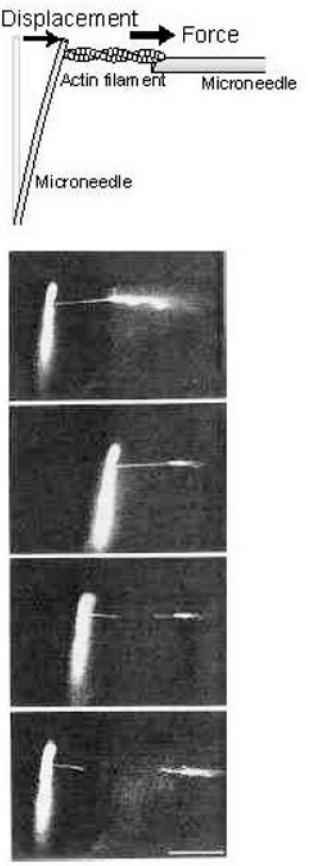

Fig. 3. Measurements of tensile force of single actin filament using a microneedle. Fluorescently labeled actin filaments are attached to stiff and flexible glass microneedle at both ends. The actin filament is pulled by the stiff microneedle, then the flexible microneedle is reflected until the filament is broken off.

nucleotides. To study the state of the binding of myosin to actin, an actin filament is pulled to break, when it interacts with myosin [22]. A bead trapped by a laser is attached to one end of an actin filament and the actin filament is brought into contact with myosin molecules immobilized on the glass surface. The unbinding force of myosin from actin filaments or the force required to break the binding is 7 pN, much less than the interaction force between actin molecules in the filament and only a little greater than the force that myosin generates. According to biochemical studies, in which the binding affinity is measured as amount of bound myosin on actin filaments on average, the interaction between myosin and actin is strong in the absence of nucleotides. The strong and weak interaction defined biochemically does not necessary

mean mechanical strong and weak, respectively. The single molecule mechanical approaches thus unveil different aspects of the interaction between biomolecules and deepen our understanding. The movement of molecular motors results from the dynamic changes in the interaction coupled with the ATP hydrolysis reactions. The molecular interaction in various nucleotide states has been measured using the same strategy with different molecular motor, kinesin [23]. The data of the load dependent-unbinding are useful to understand the mechanism of the movement of kinesin.

The stiffness of actin filaments is measured by monitoring the displacement of the tip of the microneedle, when the other end is moved with a piezo-actuator attached [18]. When a sinusoidal displacement is applied to one end of the actin filament, the displacement at the other end is damped and delayed because of the extensibility of the filament. The phase lag is measured and related to the stiffness of actin filaments (65 $pNnm^{-1}$). The value was donsistent with the stiffness obtained from the imaging of single actin filaments in which dynamic changes of the shape of single actin filaments have been imaged. The manipulation techniques have been refined and used for studies on the mechanism of molecular motors. Molecular motors move along protein tracks. Myosin moves on actin filaments and kinesin moves along microtubules. To monitor their movement under microscope, the movement of motors or track is visualized when the other is immobilized. The manipulation techniques make the motor and track molecules arranged to interact in a specific alignment and allow the measurements to be performed efficiently. These mechanical manipulation techniques are also used to impose forces on molecular motors while they are working. As they move, the restoring force against the movement increases thermal fluctuation and increase the spatial resolution, a system is required to be stiff. The stiffness of the system is determined by the shape of large probes and linkage between probes and proteins. For example, microneedles are less stiff than beads but in the case of nanometory with myosin motor attaching single myosin molecules to a tip of microneedle gives stiffer system than attaching actin filaments to beads because the linkage is stiffer for microneedle system.

6. NON-PROCESSIVE MYOSIN, MUSCLE MYOSIN

Muscle myosin (myosin II) is a non-processive motor. Myosin dissociates from actin filaments every cycle of the ATP hydrolysis. Actin filaments are manipulated using a microneedle and a laser trap and brought into contact with myosin molecules fixed on the surface of slide glasses. For laser trap experiments, both ends of actin filaments are attached to beads held by a laser trap [25]. Myosin or the head of myosin (S1 of HMM), which contains a

motor domain, is immobilized sparsely on a glass surface. To avoid the direct interaction of myosin with the glass surface that possibly interferes the motile activity, we incorporated a few myosin molecules into filaments by mixing myosin which contains the motor domain, together with large excess of myosin rod. The manipulation of single myosin molecules instead of actin filaments has been challenging. Single myosin S1 molecules are captured by a scanning probe [26]. It is proved by monitoring the photobleaching behavior of the fluorescence from the tip of the scanning probe that the molecules captured are single molecules. Single myosin S1 molecules are then brought into contact with the bundle of actin filaments on the glass surface. Use of the actin bundle is advantageous, because for the actin bundle systems, (i) the target for single myosin S1 molecules to interact is larger, and (ii) the system is tighter.

Whether actin filaments or myosin molecules are manipulated, the step movement is recorded with time. The average step size is 5 – 20 nm for

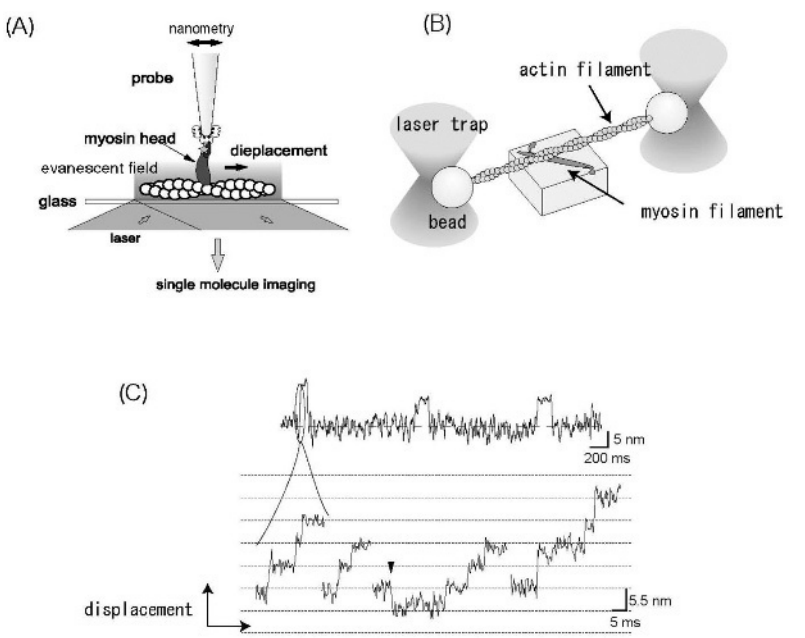

Fig. 4. Manipulation techniques for nanometory for the movement of muscle myosin. (A) manipulation of single myosin molecules by a cantilever. (B) manipulation of actin filament using a laser trap. (C) Non-processive movement of myosin II. (Top) The displacement of the microneedle attached to single myosin II head (S1) was measured as a function of time. (bottom) The rising phase of the displacement is expanded and the 5.5 nm substeps were measured within single rising steps.

muscle myosin The probes undergo thermal fluctuation, depending on the binding states of myosin to actin filaments. Myosin and actin (and the probes) undergo large thermal fluctuation when they are unbound, while the thermal motion is reduced when myosin is bound tightly to actin. The binding of myosin and the step movement are coupled; that is, the step movement occurs when myosin binds to actin and myosin steps back to the original position due to the restoring force when myosin dissociates from actin.

Large compliance existed in the linkage between the probes and proteins makes the space and time resolution low. In fact, when actin filaments are manipulated with laser trap, the fluctuation of the displacement is larger than when myosin is manipulated with a scanning probe. The root mean square displacement due to thermal motion (and corresponding stiffness) is 4.5 nm (< 0.2 $pNnm^{-1}$) for the manipulation of actin filaments with a laser trap system compared with 2.0 nm (1 $pNnm^{-1}$) for the manipulation of single myosin molecules with a scanning probe. The linkages between the probes and the actin filaments are compliant and also actin filaments themselves can be compliant. The direct attachment of probes to myosin improves the resolution of the measurements. In fact, the sub-steps within a step caused by the hydrolysis of a single ATP molecule are resolved using the probe microscopy (Figure 4C). The step generated by a single ATP molecule contains several sub-steps of 5.5 nm, coinciding with the interval between adjacent actin monomers on one strand of the filament. These sub-steps are not simply coupled to specific processes in the ATP hydrolysis cycle. The sub-steps rather occur stochastically and some of them (< 10% of the total) occur in the backward direction. One to five steps are observed in a single displacement, giving rise to a total displacement of ~5 to 30 nm with average of 13 nm. These data indicate that the movement of muscle myosin is driven by thermal Brownian movement and the random movement is biased.

7. MECHANISM OF MOLECULAR MOTORS: PROCESSIVE KINESIN MOTOR

Muscle myosin readily dissociates. In cells, muscle myosin molecules form filaments and function in a collective manner. Only small number out of large number of motors is sufficient to stay motors on the tracks, even though individual motor molecules are dissociated in most of time. Therefore it is difficult to track the behavior of single motors when they exist alone. For single molecule measurements of nonprocessive motors, it is essential to device to prevent proteins from diffusing away. Single myosin molecules are usually immobilized on the glass surface and actin filaments are manipulated. In contrast, processive motors such as kinesin and unconventional myosins move for long distance without dissociating from corresponding protein

tracks. In cells these molecular motors carry cargoes and the function is performed by only a small number of molecules. Processivity is suitable not only for this function but also for single molecule measurements. Single molecules of motor proteins are attached to beads and let them interact with protein tracks immobilized on the glass surface.

A processive motor, kinesin, on a bead trapped by a laser moves in a stepwise manner along microtubules immobilized on the glass surface (Figure 5A and B)[27]. In the optical trap measurements, the trapping force exerted on the bead increases as kinesin moves, slowing down the velocity and finally the movement ceases at stall force where the force generated by kinesin and

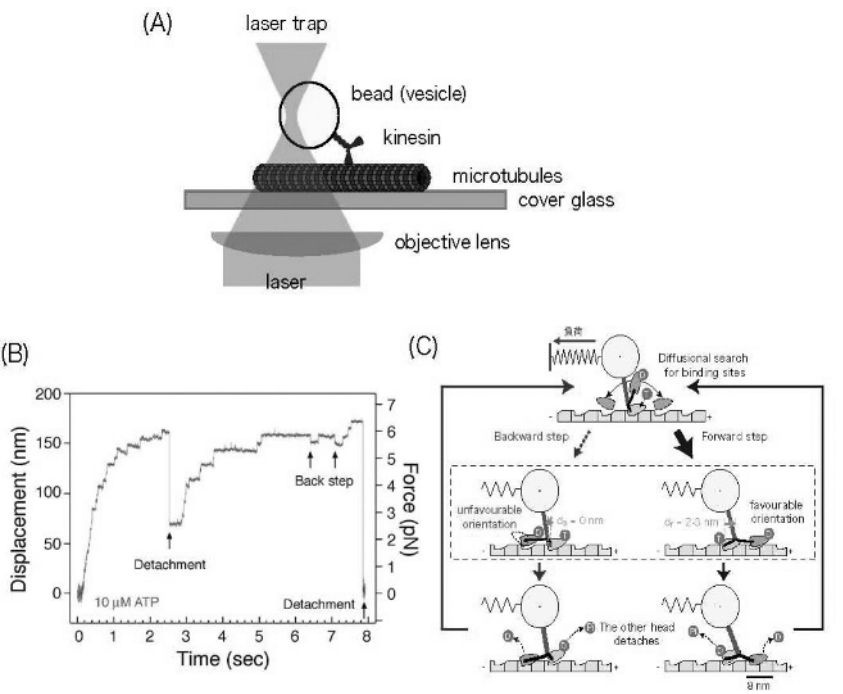

Fig. 5. Forward and backward step movement of kinesin. (A) A kinesin molecule is attached to a bead trapped by a focused laser as a cargo for measurements. (B) Time trajectory of displacement and force of kinesin. In the laser trap measurement, when kinesin moves the trapping force or external load increases indicated. (C) Forward and backward steps of kinesin are driven by Brownian movement of a detached head. Random steps are biased by preferential binding of the detached head to the forward binding site on mcrotubule, leading directional movement of kinesin. The preferential binding is entropic rather than enthalpic. In this model we proposed steric effects due to the asymmetric structure of kinesin and microtubules.

the trapping force are balanced. Kinesin moves several hundreds nm or 20 – 30 steps before it stops, although it moves several mm at no load. The dwell time between neighboring steps varies randomly at fixed load, reflecting stochastic nature of the kinetic reactions. The average dwell time is ATP concentration dependent and the dependence is explained by the Michaelis-Menten equation. Therefore it is concluded that the single step movements are coupled to the hydrolysis of single ATP molecules. Constant step size is 8 nm corresponding to the interval length of a unit structure of microtubules. The stall force for kinesin is ~7pN. The work done by single kinesin with single ATP molecules is ~56 nmpN, which corresponds to approximately 70% of the energy released from hydrolysis of single ATP molecules. Although kinesin moves primarily forward, backward steps coupled to the hydrolysis of single ATP molecules occur occasionally. At the superloaded condition, where the load is greater than the stall force, successive backward steps with a regular 8 nm have been reported [28]. Brownian movement is involved in forward and backward steps and the step is biased preferentially to one direction.

Kinesin moves using two head domains (motor domains including ATP and microtubule binding sites) connected at the tail domain. The two heads alternately step on the binding sites arranged regularly in an 8-nm interval on microtubules (hand-over-hand mechanism) [29,30]. Starting from the state that one head is attached to a binding site on microtubules and the other is detached, the detached head diffuses back and forth searching for the next binding sites in both directions. The detached head attaches to a neighboring binding site in either forward or backward directions, followed by the detachment of the other head to complete one cycle of the step movement. If the detached head attaches to the forward position, this step is a forward step. If the detached head is attached to the backward position, this step is a backward step. The preferential attachment of the head is described in the energy landscape of the forward and backward steps. The statistical analysis of the step movement showed that the activation free energy (energy barrier) for the forward step was ~ 6 k_BT lower than that for the backward step. The temperature dependence of the step movement of kinesin showed that the activation free energy G was break down to enthalpic contribution H and entropic contribution S, as $G = H - TS$ and the difference in the activation free energy between the forward and backward movement is mainly entropic rather than enthalpic [26]. One possible explanation for the entropic difference is sterically restricted geometry between the kinesin head and the binding sites on microtubules (Figure 5C). The kinesin head orients in the opposite direction relative to the orientation of the microtubule when it is located in the forward or backward positions. In the forward position, the most favorable orientation of the kinesin head coincides with the orientation

of the binding site on microtubules. In contrast, the favorable orientation of the kinesin head is incompatible to the orientation of the binding site on microtubules in the backward position. Thus the preferential binding to the forward sites can be explained by geometrical asymmetry of the orientation of the kinesin head and the kinesin binding site on microtubules.

8. PROCESSIVE MYOSIN MOTOR, MYOSIN V AND VI

Unconventional myosins which have been discovered recently have properties different from muscle myosin (myosin II). The movement of myosin V is processive like kinesin [31]. The stepsize of the movement is very large 36 nm. The large stepsize has been widely believed to occur by the rotation of a long and stiff neck domain, which is located between the head and tail domains.

Two-headed myosin VI is also a processive motor with a large stepsize[32,33]. However, the neck domain of myosin VI is too short to explain large step, suggesting the diffusion mechanism. Furthermore, it has been reported that wild-type myosin VI has only one head when it transports vesicles in cells. Generally, single headed motors must readily dissociate and diffuse away when it steps. In the case of single-headed kinesin, additional interaction with microtubules prevents kinesin from dissociating. In the case of myosin VI, in fact, single headed myosin VI did not move processively shown by fluorescence imaging. However, when it was attached to 200 nm polystyrene beads as cargoes, single headed myosin VI moved processively with a large step of 40 nm [34]. Thus, the cargoes make the movement of single headed myosin VI processive. This can be explained by slow diffusion of beads as compared with that of the head. The diffusion constant of the beads 200 nm is 60-fold lower than the myosin VI head in solution, because the size of the bead is much lager than the myosin VI head. The head of myosin VI is attached at its tail to the bead via flexible 30 nm a-helix connecting the tail and head. When the myosin VI head diffuses rapidly from one binding site to the next site on an actin filament, the bead diffuse slowly, preventing the complex of the myosin VI head and the bead from diffusing away from actin filament. The idea has been supported by experiments showing that the increase in the viscosity enhances the processivity of myosin VI through the decrease in the diffusion constant. In the measurements, the viscosity was decreased by meshwork structure of methylcellulose, which resembles the environment in cells. Thus diffusion-anchored mechanism makes a large contribution on long-distance transport of vesicles of single-headed myosin VI.

In a cycle of the ATP hydrolysis of myosin VI there are two reaction processes that diffusion is involved in; a process that the bead attached to the

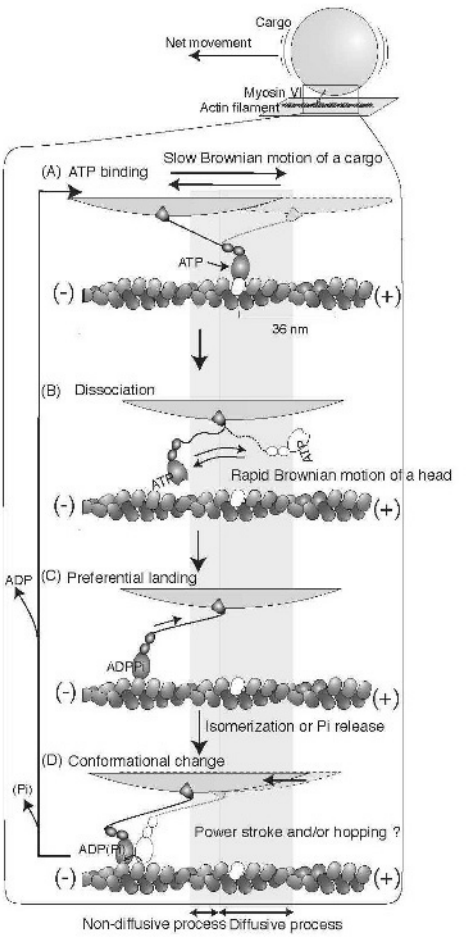

Fig. 6. Diffusion-anchored processive movement of single headed myosin VI. (A) Non-processive motion of single headed myosin VI becomes processive when it is attached to a bead as a cargo. The results can be explained by slow diffusion of beads as compared with myosin head. Preferential attachment of myosin to actin filament in direction makes the overall movement directional.

actin filament via myosin VI molecule diffuses and a process that the myosin head diffuses from one binding site to the next along actin filaments while the bead almost stays at the same position due to slow diffusion (Figure 6). Given that although the direction of the movement is opposite to other myosins, myosin VI moves in one direction, the diffusion must be biased to one direction. The preferential binding of the myosin head to the forward direction on the actin filament may cause the bias to directional movement. In the case

of myosin VI, we suppose that the myosin head senses the strain applied to it to accelerate the binding of ATP and the release of the products of the ATP hydrolysis.

9. CONCLUSIONS

The step movement of molecular motors is driven by thermal Brownian movement for muscle myosin. Recently similar Brownian movement was observed for myosin V and VI, suggesting that the substep is basic properties of many types of myosin. Random Brownian movement is preferentially directed to one direction as a result of interaction with a protein track, leading to directional movement of molecular motors. As seen in a track protein actin and a signaling protein Ras, protein molecules spontaneously fluctuate their structure and the fluctuation is shifted to active state by the interaction with ligands. The binding of myosin to actin activates its own motility through the structural changes of actin. The self-activation mechanism is suitable for the system in which molecules are self-assembled and self-controlled. The fluctuation may be sensitive to the surrounding environments. Molecular machines can function in response to environments through the environment-sensitive fluctuation. This fluctuation can be basis for the functions of cells. The fluctuation can provides the biosystems unique properties and makes the system behave in a flexible fashion. The single molecule detection is the unique tool that scrutinizes important dynamic information to understand such molecular machines.

REFERENCES

[1] Ishijima, A., Yanagida, T., (2001) Trends in Biochemical Sciences.26, 438-444.
[2] Ishii,Y., Ishijima, A., Yanagida: T., (2001) Trends in Biotechnology 19, 211-216.
[3] Funatsu,T. Harada, Y., Tokunaga, M., Saito, K.,Yanagida, T., (1995) nature 374, 555-5
[4] Tokunaga, M. Kitamura, K., Saito, K., Iwane, A.H., Yanagida, T., (1997) Biochem. Biophys. Res. Commum. 235, 47-53
[5] Ishijima A., Kojima, H., Harada, Y., Funatsu, T., Tokunaga, M., Higuchi, H. and Yanagida, T. (1998) cell 92, 161-171
[6] Sako, Y., Minoguchi, S., yanagida, T., (2000) nat. cell biol. 2, 168-17
[7] Vale, R.D. Funatsu, T., Pierce, D.W., Ronberg, L., Harada, Y., and Yanagida, T. (1996) nature 380, 451-453
[8] Yildiz, A., Firjey, J.N., McKinney, S.A., Ha, TJ., Goldman, Y.E., Selvin, P.R. (2003) science 300, 2061-2-65
[9] Okada,Y., Hirokawa : N. (1999) science 283, 1152
[10] Y. Inoue, Y., Iwane, A.H., Miyai, T., Muto, E., Yanagida, T. (2001) Biophys. J. 81, 2838
[11] Harada, Y., Funatsu, T., Murakami, K., Nonomura, Y., Ishihama, A., Yanagida, T., (1999) Biophys. J. 76, 709-715
[12] Kozuka J, Yokota H, Arai Y, Ishii Y, Yanagida T., (2006) nat chem biol. 2, 83-86.

[13] Arai, Y., Iwane, AH. Wazawa, T., Yokota, H., Ishii, Y., Kataoka, T., and Yanagida,T. (2006) Biochem Biophys Res Commun.343, 809-815
[14] Ito, Y., Yamasaki, K., Iwahara, J., Terada, T., Kamiya, A., Shirouzu, M., Muto, Y., Kawai, G., Yokoyama, S., Laue, E.D., Walchli, M., Shibata,T., Nishimura, S., Miyazawa, T., (1997) Biochemistry 36, 9109-9119.
[15] Ueda,M., Sako, Y., Tanaka, T., Devreotes, P.,Yanagida, T., (2001) science 294, 864-867.
[16] Kishino, A. and Yanagida, T. (1988) nature 334, 74-76
[17] Ashkin, A., Dziedzic, ,Yamane,,T. (1987) nature 330 769-771
[18] Yasuda, R., Akashi,K., Harada,Y., Miyata,Y., Kinosita,K.Jr, Itoh, H. (1999) nature 399, 446-448
[19] Kojima,H. Muto, E., Higuchi, H., and Yanagida, T. (1997) Biophys. J. 73, 2012-2022
[20] Tskhovrebova, L., Trinick, J., Sleep, J.A., Simmons, F.M.(1997) nature 387, 308-312
[21] Rief, M., Gautel, M., Oesterheilt, F., Ferrandez, J.M., Gaub, H.E (1997) science 276, 1109-1112
[22] Liphardt, D.J., Once,B., Smith, S.B., Tinoco, I.J., Bustamante, C. (2001) science 292, 733-737
[23] Nishizaka,T., Miyata, H., Yoshikawa,H., Ishhiwata, S., Kinosita Jr, K.(1995) nature 377 251-254
[24] Kawaguchi, K., Ishiwata, S. (2001) science 291, 667-669
[25] Svoboda, K., Schmidt, C.F., Schnapp, B.J., Block, S.M. (1993) nature 365, 721-727
[26] Carter, N.J., Cross, R.A. (2005) nature 435, 308-318
[27] Nishiyama, M., Higuchi, H, Yanagida, T., (2002) nat cell biol. 4, 790-797.
[28] Taniguchi, Y., Nishiyama, M., Ishii, Y., Yanagida, T. (2005) nat chem biol. 1, 346-351.
[29] Mehta, A.D., Rock, R.S., Rief, M., Spudich, J.M.,Mooseker, M.S., Cheney, R.E., (1999) nature 400, 590-593.
[30] Rock, R.S., Rice, S.E., Wells, A.L., Purcell, T.J., Spudich, J.A., Sweeney, H.L., (2001) Proc Natl Acad Sci U S A. 98:13655-13659.
[31] Nishikawa, S., Homma, K., Komori, Y., Iwaki, M., Wazawa, T., Iwane, A.H., Saito, J., Ikebe, R., Katayama, E., Yanagida, T., Ikebe, M. (2002) Biochem Biophys Res Commun. 290, 311-317.
[32] Iwaki M, Tanaka H, Iwane AH, Katayama E, Ikebe M, Yanagida T., (2006) Biophys J. 90, 3643-52.
[33] Finer, J.T. Simmons, R.M., and Spudich, J.A.(1994) nature 368;113-119
[34] Kitamura,K. Tokunaga, M., Iwane, A.H., and Yanagida, T.(1999) nature 397, 129-134

This page intentionally left blank

Handai Nanophotonics, Volume 3
H. Masuhara, S. Kawata and F. Tokunaga (Editors)

Chapter 2

Alternating laser excitation spectroscopy of freely diffusing single molecule: Applications to bimolecular structure, dynamics and interactions

E. Nir[a], M. Jäger[a], and S. Weiss[a,b,c]

[a]Department of Chemistry and Biochemistry, UCLA, Los Angeles, CA 90095

[b]Department of Physiology, UCLA, Los Angeles, CA 90095

[c]California NanoScience Institute, UCLA, Los Angeles, CA 90095

1. INTRODUCTION

Following the human genome project, there has been an increased interest in the detailed description of the structure and dynamics of biomolecules such as proteins, DNA and RNA and of the interactions between them. During the last decade, single molecule fluorescence resonance energy transfer (sm-FRET) has become an important method in the toolbox for studying those properties [1,2,3]. Unlike ensemble experiments, in which just an average of an observable is measured, single-molecule experiments directly reveal the distribution of the observable. This facilitates the ability to focus on part of the total population (subpopulation), which is otherwise concealed, refining our understanding of the complexity of biomolecules. Furthermore, since a single molecule can never really be in equilibrium, tracking of a time-dependent observable, e.g. intra-molecular distance, allows the direct measurement of molecular motions without the need of synchronizable non-equilibrium conditions. The first sm-FRET measurement of freely diffusing biomolecules was carried out in our lab in 1999 [1]. In this first experiment, FRET values of different lengths doubly labeled (TMR as a donor and CY5 as an acceptor) double-stranded DNA (dsDNA) molecules were measured.

We have recently introduced a major improvement to the sm-FRET method. Instead of using one continuous -wave (CW) laser that solely excites the donor, we instead employed two alternating lasers, one exciting the donor and the other directly exciting the acceptor, thus monitoring the presence (or absence) of

photo-active donor and acceptor, respectively. We dubbed this method Alternating Laser EXcitation (ALEX) spectroscopy. The first ALEX experiment was performed in 2004, on similar dsDNA molecules [4]. This ALEX improvement to the sm-FRET methodology has several advantages: (i) the ability to sort and resolve sub-populations; (ii) the ability to directly measure dye-labeling efficiency; (iii) the ability to directly measure molecular interactions and calculations of molecular affinity; (iv) the ability to reveal undesired photo-physical events, such as dyes bleaching and blinking, and to facilitate the removal of such events from the sm-FRET histogram. These advantages will be demonstrated and discussed in this chapter.

sm-FRET and ALEX experiments were made possible due to several important advances: introduction of bright, photo-stable dyes, and improvements in labeling and in purification techniques. Examples for improvements in proteins' sample preparation in our lab are reported in [5,6].

In terms of data acquisition, a cheaper and broader variety of lasers equipped with different wavelength and different pulse duration/repetition allowed for a better match to the dyes and to the specific experimental requirements. Faster and more sensitive photon detectors, better confocal microscopy (especially improvements in the objective technology), and improved optics (such as dichroic mirrors, filters and fibers) resulted in an increase in the photon collection efficiency. Faster and more powerful electronics allows for more accurate time-tagging, and faster computers with large memory allow for partial on-the-fly data analysis and longer data acquisition.

On the data analysis side, ALEX, together with other established techniques for burst-search [7] result in more reliable FRET (and other observables) histograms, an increase in information content and better understanding of the molecular system at hand that can be reliably extracted from the experiment.

Finally, the growing number of groups working in the field has resulted in the accumulation and sharing of knowledge. Naturally, this has helped establish single molecule techniques and led to new biological discoveries using these methods.

In the following we will review advances in the ALEX methodology: we will give a theoretical background, describe the burst-search algorithm, explain the histogram shape and possible experimental artifacts. We will then describe several biological ALEX studies performed in our laboratory:

1. We will demonstrate the power of ALEX for molecular sorting. One sorting example will demonstrate the ability to determine dye-labeling efficiencies of protein (CI2) at two sites (with a donor and an acceptor dyes). The other example will demonstrate the ability to detect and characterize protein-DNA interactions.

2. We will give two examples of structural dynamics studies in the field of protein folding. The first will demonstrate the use of microsecond ALEX (μsALEX) to determine the energy landscape along the reaction coordinate of protein folding-unfolding. The second will demonstrate the use of interleaved nanosecond pulsed lasers, dubbed nanosecond ALEX (nsALEX) to determine in even more details the energy landscape of the unfolded sub-population in conditions favoring the native-conformation, based on donor lifetime analysis.
3. We will demonstrate the use of ALEX to resolve which of three previously proposed mechanisms is in action during the initiation of transcription by the enzyme RNA Polymerase (the first step in gene expression).
4. Lastly, we will demonstrate the use of advanced FRET-histogram-shape-analysis to resolve the two-state energy landscape of a DNA-hairpin.

2. THEORETICAL AND THECHNICAL BACKGROUND

2.1. sm-FRET ALEX

Detailed theoretical background is given elsewhere [4, 8-13]. Here introduce the basics of Single Molecule Fluorescence Resonance Energy Transfer (sm-FRET) and of Alternating Laser EXcitation (ALEX).

Ideally, one would like to measure the FRET efficiency (E) of each detected molecule (or equivalently, burst), and study its distribution within the sampled population. To do this, one would have to use the standard definition of E:

$$E = \frac{{}^{D\to A}F_D^A}{{}^{D\to A}F_D^A + \gamma\,{}^{D}F_D^D} \tag{1}$$

Adopting the notations of Ref. 10, we denote by F_E^X the signal (number of photons) collected by channel E (donor: D or acceptor: A) during excitation of dye X (donor: D or acceptor: A). where the left upper index indicates the origin of the signal: D denotes the donor dye, A the acceptor dye, and D→A denotes acceptor signal originated by FRET. The factor γ is the ratio of the donor and acceptor detection efficiencies (η) and quantum yields (Φ):

$$\gamma = \frac{\eta_D \Phi_D}{\eta_A \Phi_A} \tag{2}$$

Although we will not directly discuss distance measurements in this article, it is worth recalling the relation between E and the distance R between donor and acceptor molecules:

$$E = \left(1 + \left(\frac{R}{R_0} \right)^6 \right)^{-1} \tag{3}$$

where R_0 is the Förster radius, a characteristic of the dye pair.

Extracting the quantities intervening in Eq. (1) from the raw detector data F_D^D and F_D^A (for the calculation of E) could be difficult and lead to unwanted uncertainties. It therefore has been a common practice to compute instead of the FRET efficiency E (Eq. (1)) the so-called proximity ratio PR, defined as:

$$PR = \frac{F_D^A}{F_D^A + F_D^D} \tag{4}$$

The proximity ratio PR reduces to the FRET efficiency E when there is no leakage, background and direct excitation of the acceptor, and $\gamma = 1$. Obviously this is rarely the case, so PR values cannot be used, in general, to extract real distances. However, qualitatively, PR follows the trend of E upon changes in donor-acceptor distance. In other words, a decrease of PR value can be interpreted as a decrease in E, or equivalently an increase in distance between donor and acceptor, and reciprocally. Moreover, in many experimental cases, even though there is leakage, background and direct excitation of the acceptor, their contribution is minimal on the calculated histogram. Since we assume in this chapter such minimal contribution, we will use E (= PR) to note the FRET efficiency. When $\gamma = 1$ the stochiometry ratio (S) is define as:

$$S = \frac{{}^D F_D^D + {}^{D\to A} F_D^A}{{}^D F_D^D + {}^{D\to A} F_D^A + {}^A F_A^A} \tag{5}$$

which is basically all photon detected during the donor laser excitation periods divided by all the photons detected. For discussion on $\gamma \neq 1$ see [10].

2.2. Experimental Setup

Detailed descriptions of the setups and the data analysis strategies used in the different experiments described below could be found in the cited references. Here we will introduce the basic configuration for ALEX analysis of freely diffusing molecules.

In an ALEX experiment, two modulated/pulsed lasers, preferably exciting at the donor and acceptor absorption maxima, are coupled into a single mode fiber (Fig. 1, (FI)). Laser alternation is achieved by several different methods. For

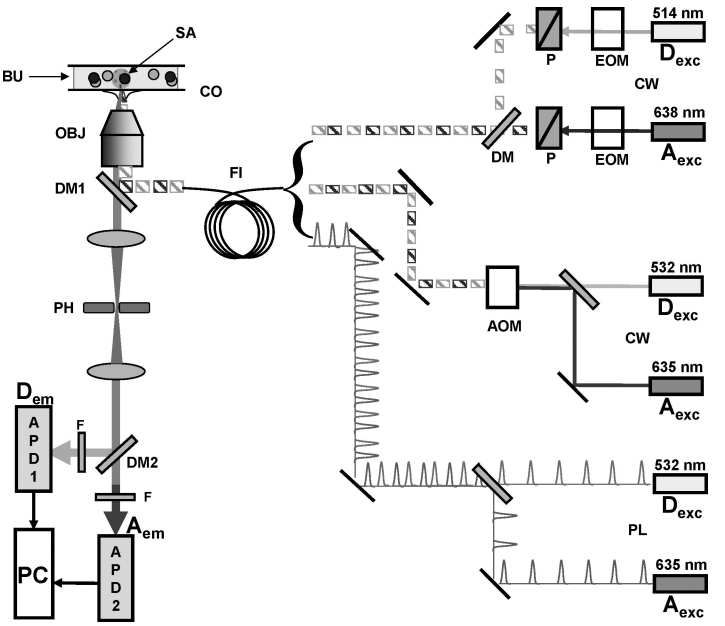

Fig. 1. Experimental Setup: CW laser are modulated by electro-optic modulators (EOM) or acousto-optic modulators (AOM). The modulated beams (in µsALEX) or the picoseconds pulsed beams (in nsALEX) are coupled into a fiber (FI). After the fiber, the beams are coupled into an inverted microscope. High NA objective (OBJ) focuses the beams 20-50 µm deep (from the water-coverslip glass interface) into buffer solution (BU). The emitted photons are collected with the same objective, separated from the excitation beam by a dichroic mirror (DM1), spatially filtered by a pinhole (PH), further separated to donor channel and acceptor channel by a second dichroic mirror (DM2), and focused onto Avalanche Photon Diodes (APD1, APD2).

µsALEX, two continuous wave lasers (CW) are externally modulated by two Electoro-Optical-Modulators (EOM) [4,9-11], or an Acousto-Optic Modulator (AOM) [12] , or directly modulated (in the case of solid-state lasers) [15]. For nsALEX [13], two short pulsed lasers (5-50 ps, typical repetition rate 20-80 MHz (PL)) are synchronized to the same clock frequency and their pulse trains are interleaved with a fixed delay on the order of 10-50 nanosecond between the two color pulses.

After the fiber, the beam (or beams) is expanded, collimated, coupled into an inverted microscope, and focused 20-50 µm deep into a sample solution held between two 170 µm thick coverslips (CO) and a gasket. Focus is achieved by a high numerical aperture (NA) water or oil immersion objective (OBJ).

The emitted florescence is collected by the same objective and separated from the excitation light by a dichroic mirror (DM1) and further, after spatially filtered by a pinhole (PH) to reject out-of-focus light, split by a second dichroic

mirror (DM2) into donor and acceptor channels. Each of the beams is focused onto an Avalanche Photo Diode (APD) after filtering by a band-pass (donor) or a long pass (acceptor) filters (F) which matches the donor/acceptor emission spectra. The APDs signals (TTL pulses for each detected photon) are recorded and stored as a function of time with ~10 nanoseconds accuracy in the case of μsALEX or with ~hundreds of picoseconds accuracy in the case of nsALEX. These detection channels could be further split and analyzed by polarization (not shown), providing additional information regarding the dyes' rotational freedom of motion.

2.3. Data analysis

The sample (SA) constitutes a low dilution of doubly-labeled macromolecules with two dyes (donor and acceptor). The macromolecules freely diffuse in the buffered solution (BU) surrounding the confocal spot. As the molecules stochastically diffuse and traverse the confocal spot (by Brownian motion), the donor and/or the acceptor (depend on the laser/s wavelength and on the absorption spectrum) absorb the excitation light and emit photons. In order to achieve single molecule resolution, a low concentration of labeled molecule must be maintained (~50-100 pM), resulting in a low occupancy of molecules in the observation volume (on the order of a few %). Higher concentrations will lead to too many coincident events, which will skew the measured E values (see Fig. 3c1) and eventually lose the 'singleness' of the measurement. When there is no labeled molecule in the confocal spot, only a constant background of photons is detected. The background count rate is usually on the order of 2-8 KHz. When a labeled molecule traverses the confocal spot, a burst of photons (with an instantaneous detected rate of up to 100 KHz) is detected. The first task in analyzing the data is to distinguish between the background and the bursts (signal).

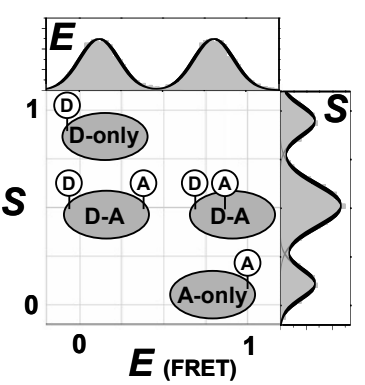

Fig. 2. Schematic presentation of ALEX 2D histogram: D-only; upper-left corner. A-only lower-right corner. D-A center (low E on the left and high E on the right).

Several different algorithms have been used to define a burst. The simplest is carried out by cutting the flux of photons into fixed time intervals called bins [1]. Typical bin duration used is on the order of 500-1000 μs. The disadvantage of such an approach stems from the lack of correlation between the bins and the stochastic appearance of bursts. This may result in a burst cut into two or more bins, or a bin predominantly containing background signal.

Contrary to the binning approach, *Seidel* and co-workers [7] have introduced an algorithm that detects the beginning and the end of a burst. In their approach, photons belonging to a burst of at least L successive photons have at least *M* neighboring photons within a time window of length T centered at their own arrival time. Typical parameters used are: L=50, M=10 and T=1ms. We dub this burst search the All-Photons-Burst-Search (APBS) [12].

The shortcoming of this approach is that if, for example, the acceptor is bleached during the transit time, a decrease in the acceptor photon flux and increase in the donor photon flux is resulted, biasing the calculated E towards a lower value, skewing the derived donor-acceptor distance (Fig. 3). In order to correct for this, we introduced an enhanced burst search algorithm that is based on ALEX [12]. Here, in addition to the search of the beginning and of the end of a burst, based on donor and acceptor photons emitted during the donor excitation periods, we perform a similar search on the acceptor photons emitted during the acceptor excitation periods. The first and the second burst searches confirm the photo-activity of the donor and the acceptor dyes, respectively. A burst is then defined for time periods during which both dyes are confirmed to be active. We dub this search Dual-Channel-Burst-Search (DCBS).

E (Eq. (4) and S (Eq. (5)) are calculated for each burst and binned in a 2D histogram. Fig. 2 shows a schematic presentation of such a 2D ALEX histogram (center) and the collapse of this histogram into FRET (upper) and into stochiometry (right) axes. The D-only sub-population is presented in the upper left, the A-only sub-population in the lower center-right and the doubly labeled sub-population in the center (low E in the left and high E in the right). It is easy to see that, by using ALEX, one can immediately distinguish between species containing D-only, A-only and D-A. This allows the detection of labeling efficiency and of biomolecular interactions (see below).

2.4. Artifacts

We have developed an ab-initio simulation that mimics the sm-FRET ALEX experiment [12]. The simulation contains many of the experimental features, and it contributes to the understanding of the correlation between physical/ experimental effects and the results as they appear in the final histogram. Here we will introduce several examples of simulated sm-FRET ALEX histogram resulted from undesired effects.

2.4.1. Bleaching and blinking

Due to a photophysical and/or photochemical reactions (usually while a dye is in the electronically excited state), a fluorophore might go to a permanent (bleaching) or a temporary (blinking) dark state, from which it will not emit.

Fig. 3 shows the compilation of simulation in an ALEX histogram of freely diffusing doubly labeled molecules of E=0.5. The acceptor stochastically bleaches (3a) or blinks (3b), on average once every 300 cycles of absorptions/emissions. In bursts in which the acceptor is bleached during the transit time, a decrease in the number of acceptor photons and an increase in the number of donor photons is detected. This result in E shifted towards a lower value and S shifted towards a higher value. The exact value depends on the timing of the bleaching relative to the burst duration. Since it is a stochastic process, it can happen anytime during the diffusion through the confocal spot, leading to a 'tail' of events bridging from E=0.5 and S=0.5 (for example) to D-only-like subpopulation (E=0 and S=1) in the ALEX histogram.

Fig. 3 shows histograms of the same simulated data using the APBS and DCBS burst filters. The DCBS clearly removes most of the blinking/bleaching events, leaving the ALEX histogram solely with the D-A photo-active subpopulation.

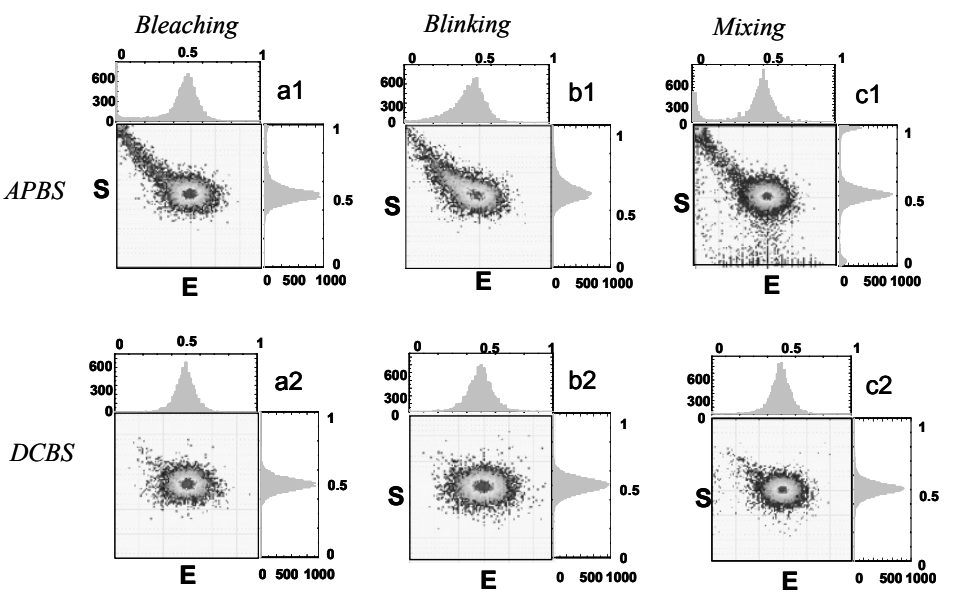

Fig. 3. Simulated sm-FRET ALEX histograms results using All-Photon-Burst-Search (APBS) and Dual-Channel-Burst-Search (DCBS) filters. Donor bleaching (a), donor blinking (b), D-only, A-only and D-A subpopulation mixing (c). Notice that the DCBS almost completely removes the unwanted events.

2.4.2. Mixing

In order to achieve single molecules resolution, the sample concentration has to bee kept low, such that there is a low probability for two different entities to be inside the confocal spot at the same time. If two different entities (for example, D-A molecule and D-only molecule) are in the confocal spot at the same time, the *E* and the *S* values will be altered. To prevent this, it is recommend to work with sample dilution <100 pM. If the concentration is higher (Fig. 3c, 300 pM), bridges between the D-A subpopulation and the D-only and the A-only are being formed, alternating the shape and the center of the FRET and ALEX histograms.

3. RESULTS AND DISCUSSION

3.1. Sorting

3.1.1. Labeling efficiency

Here we show how the ALEX methodology could be used to asses labeling efficiency. Fig. 4 shows the E-S histogram of the protein Chymotrypsin inhibitor 2 (CI2)-Cys40 labeled with a donor only (Alexa-488) (4a), CI2-Cys1 labeled with an acceptor only (Alexa-647) (4b) and CI2-Cys1/Cy40 labeled specifically with donor and acceptor (same dyes, respectively) (4c). In (4c) most of the bursts appear around *S*=0.5, which means that most of the CI2 is properly labeled with the two different dyes. Very few (less than 5%) of the bursts appear in the upper right and in the lower left, reflecting the minor presence of D-only and A-only subpopulations, respectively.

3.1.2. Biomolecular interaction

The independent excitation of two (or more) different dyes facilitates the possibility of detection and quantification of biomolecular interactions. The D-only and A-only species represents free interactants, and D-A represents a

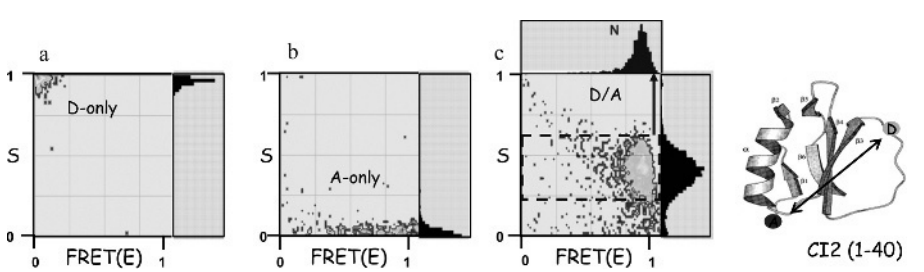

Fig. 4. sm-FRET-ALEX histogram of D-only labeled CI2 at position 40 (a), A-only labeled CI2 (b) at position 1 and doubly labeled CI2 (c).

complex (Fig. 5a); equilibrium binding and kinetic rate constants can be measured by simply counting molecules of the three major species. The interaction could be treated as a macromolecule-ligand interaction with dissociation constant K_d. the fraction of bound macromolecules (fractional occupancy θ) at ligand concentration $[L]$ is $\theta = [ML]/([ML]+[M]) = [L]/([L]+K_d)$. For macromolecule M^A and ligand L^D (Fig. 5a):

$$\theta = [D\text{-}A]/([D\text{-}A]+[A\text{-}only]) = [D\text{-}only]/([D\text{-}only]+K_d) \quad (6)$$

θ is extracted reliably from ALEX histograms. Measuring θ at several ligand concentrations $[L^D]$ allows calculation of equilibrium dissociation (K_d); θ can also be monitored as a function of time to evaluate association/dissociation kinetics.

3.1.3. Protein-DNA interaction

We studied the sequence-specific interaction of *E. coli* catabolite activator protein (CAP) with DNA as a model for protein-nucleic acid interactions [9]. The diffusion time of CAP-DNA (570 μs) is comparable to that of free DNA (540 μs), allowing sorting without detection-probability corrections. Specifically, we monitored the interaction of D-labeled CAP (as "ligand" CAP^D; Fig. 5e) with its consensus A-labeled DNA site (as "macromolecule" DNA^A), with or without allosteric effector cyclic AMP (cAMP). With 0.2 mM cAMP, CAP^D-DNA^A complexes were detected as D-A species (θ~0.50, Fig. 5c; cf. with DNAA in Fig. 5b). CAP^D-DNA^A complexes appeared as a wide and heterogeneous E distribution, with a main peak (65% of all D-A species) at E~0.63, a second peak (25%) at E~0.37, and a shoulder (10%) at E~0.84. High E values were consistent with a 60-100o overall DNA bend towards CAP, while the heterogeneity, apart from reflecting the two possible D-labeling sites on CAP (Fig. 5e), might reflect heterogeneity due to slow interconversion (slower than diffusion) between complexes with different magnitudes of DNA bending. CAPD-DNAA complexes also showed a wide, slightly asymmetric S distribution (0.50±0.15), possibly due to the small fraction of CAP^D with 2 donors (a D_2-A species, with S larger than for D-A species). Without cAMP, few complexes were formed (θ~0.03; Fig. 5d).

To assess equilibrium binding for the CAP-DNA interaction, we titrated 10 pM DNA^A with 0-300 pM active CAP^D, identified A-containing species, and calculated θ for each [CAPD] (Figs. 5a & 5f. With cAMP, the dependence of θ to $[CAP^D]$ resembles a rectangular hyperbola (Eq. 6 with [D-only]=$[CAP^D]$); upon fitting, Kd~32±3 pM, in good agreement with filter-binding-based values (24±2 pM). Without cAMP, CAP binds to DNA >150-fold weaker (Kd >5 nM).

We also monitored dissociation kinetics of CAP^D-DNA^A by forming the complex, diluting it in 50-fold molar excess unlabeled CAP (to sequester DNA^A formed due to dissociation), and observing the kinetics of θ decrease (Fig. 5g). The decrease of θ, fitted as a single exponential decay, k_d~(1.1±0.2)x10^{-4} s^{-1}, is in agreement with gel-based assay values (k_d~1.2x10^{-4} s^{-1}). However, θ decrease is clearly bi-exponential, with a fast (k_{d1}~[1.2±0.8]x10^{-3} s^{-1}) and a slow phase (k_{d2}~[0.7±0.1]x10^{-4} s^{-1}). This behavior has not been reported for CAP-DNA, but it has been reported for other protein-DNA complexes; it reflects equilibrium between stable and unstable complexes, with stable complexes converting slowly to the unstable complexes, which dissociate. It is possible that the small number of time points and partial dissociation of CAP-DNA during electrophoresis prevented observation of the fast phase by gel-based assays. ALEX can also monitor association kinetics, by fast mixing of low concentrations of CAP and DNA, and monitoring of the kinetics of θ increase.

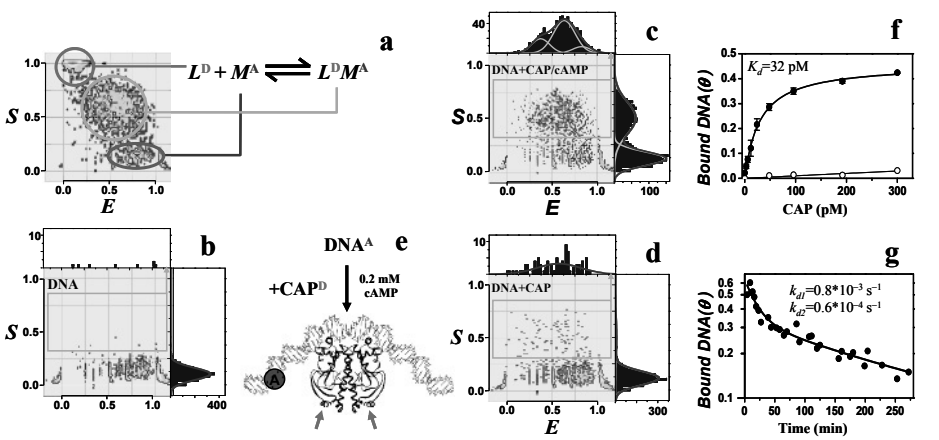

Fig. 5. Analysis of protein-DNA interactions using ALEX. (a) Using a labeled macromolecule (M^A; A-only species) and a labeled ligand (L^D; D-only species), we can monitor the formation of macromolecule-ligand complexes (M^AL^D; D-A species) on the E-S histogram by monitoring fractional occupancy θ at a ligand concentration [L^D]. Monitoring θ extracts equilibrium constants from histograms constructed at a single or multiple [L^D], and kinetic constants from histograms constructed at multiple time points. (b) ALEX histogram of 50 pM A-only DNA. (c) ALEX histogram of 50 pM A-only DNA, 200 pM D-only CAP, and 0.2 mM cAMP. (d) ALEX histogram of 50 pM A-only DNA and 200 pM D-only CAP (no cAMP). (e) Model of CAP-DNA complex and labeling scheme. The acceptor (Alexa647, in red) was placed on DNA, and the donor (TMR) was placed on 2 possible sites on CAP (green arrows); since labeling efficiency was kept low, most D-A species have a single donor. (f) ALEX-based titration of DNA with CAP in the presence (filled circles) or absence of cAMP (open circles). With cAMP, CAP binds DNA with high affinity (K_d~32 pM); without cAMP, CAP binds DNA weakly (K_d>5 nM). (g) Kinetics of CAP-DNA dissociation, reflecting distinct rates of dissociation.

3.2. Single molecule protein folding

3.2.1. Single molecule protein folding by μsALEX

In a series of initial experiments, the 64-residue CI2 was labeled site-specifically with A- and D-florophores at the N-terminus and at an internal position (residue 40), respectively. μsALEX histograms obtained at various concentrations of denaturant (Guanidine hydrochloride, GuCl) in solution are shown in Fig. 6a [1,5,6]. At or below 2 M GuCl, a single peak with $E \sim 0.90$ is observed. The high E suggests that the D- and A-fluorophores are in a close proximity, consistent with folded CI2. At very high denaturant concentrations (>5 M GuCl), again a single peak is detected. However, the mean-E is substantially lower ($E \sim 0.40$), indicating that the D-A distance increased due to unfolding of the protein. As intermediate denaturant concentrations are scanned between these extreme values (2.6 M < [GuCl] < 4.5 M), various ratios of the folded and unfolded peaks are observed. Further verification of the peak assignment to folded and unfolded conformers was possible by measurements of destabilized CI2 variants, which exhibited the same two peaks, but with different relative ratio (the area of one peak divided to the sum of the area of the two peaks), pointing to the dependence on denaturant concentration (data not shown).

The co-existence of the folded and unfolded macro-states at intermediate denaturant concentrations suggests that interconversion between these two states occurs on a time scale slower than the diffusion (~500 μs), and illustrates the existence of a free energy barrier separating the two macro-states (Fig. 6b). The existence of a barrier has also been inferred from ensemble kinetic studies which reported folding/unfolding rates on the order of tens of milliseconds to several tens of seconds, depending on denaturant concentration.

The ability to directly visualize and quantify conformational subpopulations that are populated during (un)folding at equilibrium is a unique property of single molecule resolution techniques, and enables one to directly confirm (or reject) folding models previously inferred from population averaging ensemble data. For example, as the areas of the peaks are an approximate measure of the occupation probabilities for the two states, a fractional occupation for the folded state can be extracted. A plot of this fraction versus denaturant concentration resulting from single-molecule denaturation experiment is shown in Fig. 6c. Similar curves, derived from ensemble data and the assumption of a particular unfolding model (2-state, 3-state etc.), are routinely used to quantify protein stability and map the mechanism of unfolding.

The single molecule denaturation curve (red square) obtained for CI2 is indistinguishable (within error) from the corresponding ensemble-FRET denaturation curve (blue circles), showing that sm-FRET faithfully reproduces

the equilibrium properties of CI2 and providing direct and model-independent evidence for a simple two-state equilibrium unfolding mechanism of CI2.

Additional information about the folding mechanism can be obtained by inspection of the mean transfer efficiencies of the various folding subpopulations. While E values for the folded subpopulation of CI2 does not change significantly ($\Delta E < 0.05$) as a function of denaturant, a small, but significant shift in the E value of the unfolded subpopulation is manifest when lowering the denaturant concentration from > 5 M ($E \sim 0.43$) to moderately destabilizing conditions (3.1 M, $E \sim 0.49$).

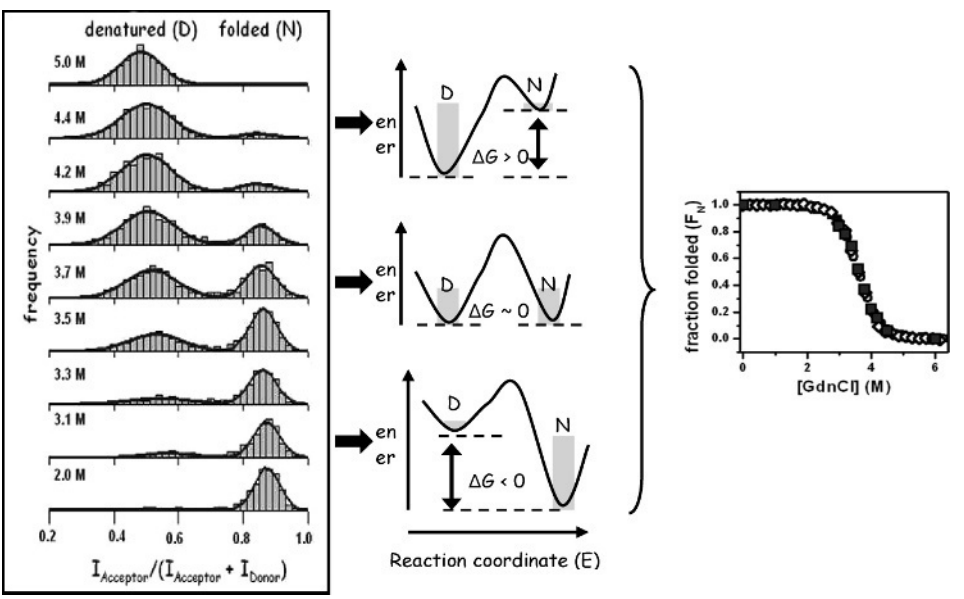

Fig. 6. Mapping of folding free energy landscapes of proteins using μsALEX. (a) FRET histograms of measured FRET efficiencies E at various GuCl concentrations for D-A labeled CI2. The solid red curves are the best fits to the data using single or double Gaussian functions. The black numbers indicate the concentration of denaturant (GuCl, in units of M). The high E peak (~ 0.9) represents the native subpopulation (N) of CI2 (D-A in close proximity), while the low E peak (~ 0.4) depicts the denatured subpopulation (D). CI2 remains folded at or below 2 M GuCl, and is completely unfolded at > 5 M GuCl. At intermediate concentrations, both N and D coexist. (b) Simplified free energy diagram using the D-A distance as a reaction coordinate. Folded and unfolded subpopulations adopt energy minima and are separated by a free energy barrier. Adding denaturant stabilizes D relative to N and leads to a population change of the folded and unfolded molecules. (c) Equilibrium unfolding denaturation curve (fractional occupancy of N (F_N) versus denaturant concentration) of CI2 constructed from ensemble-FRET data assuming the validity of a two-state unfolding model (open blue circles) and from sm-FRET data (filled red squares), calculated from the integrated areas of N and D of the sm-FRET- histograms.

Using various control measurements to rule out photophysics, it could be shown that this change in *E* value in the unfolded subpopulation must result from a change in D-A distance – a collapse of the polypeptide chain from a more expanded coil in the presence of high concentrations of denaturant to a more compact globule under more aqueous, and biologically relevant buffer conditions. Even though CI2 shows only moderate chain collapse, the experimental approach depicted here could be applied to other small single domain proteins or larger multidomain proteins, and in conjunction with site-directed mutagenesis, could reveal residues in the polypeptide chain that are required for chain collapse. The initiation of the folding process from an expanded random coil could be useful to benchmark the increasing number of atomic resolution scenarios of folding mechanisms from molecular dynamics simulations and/or rigorous theory.

3.2.2. Single molecule protein folding by nsALEX

Nanosecond ALEX (nsALEX) is the latest addition to the ALEX-based single molecule toolbox developed in our laboratory [13]. nsALEX differs from μsALEX in that the CW-excitation source is replaced by two interlaced pulsed lasers, affording alternating-laser-excitation and the direct measurement of D- and A-fluorescence lifetimes.

Lifetime measurements not only improve the accuracy of distance measurements, but also yield important information about fast polymer dynamics on a timescale down to the fluorescence lifetime (several ns). For a rigid molecule, say a double-stranded DNA or a folded protein labeled with a unique D-A FRET pair, FRET between the D and A shortens the D-lifetime [13] relative to the D-only labeled reference (Fig. 7). On the other hand, for a fluctuating molecule (say a polypeptide chain under denaturing conditions) one expects multiple donor lifetimes that will give rise to non-exponential D-lifetime

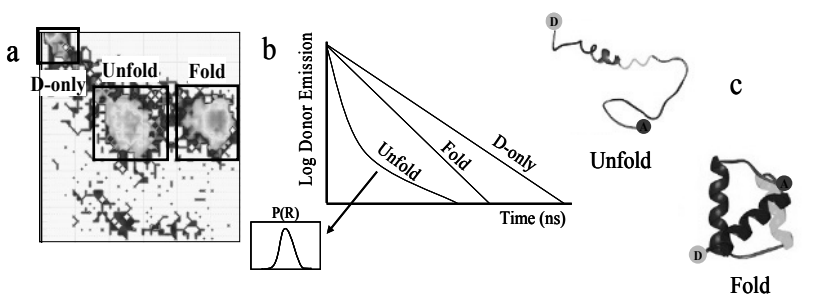

Fig. 7: nsALEX as a tool to investigate structural heterogeneities and fluctuations in biopolymers. For each of the subpopulatin (fold and unfold, (a)), donor lifetime is measured (b) and distance distribution (P(R)) is calculated. In the folded protein, a rigid molecule, the D-A distance remains constant yielded in single exponential decay of the donor lifetime, while in the unfolded protein, a flexible polymer, the D-A distance constantly change, yielded in multi-exponential decay.

decay curves. An unambiguous analysis of non-exponential lifetime decay curves in ensemble measurements is difficult due to the presence of multiple species (e.g. folded and unfolded conformers of a protein in the folding transition region), and/or contaminating D-only species resulting from A-bleaching or incomplete labeling.

NsALEX greatly facilitates such measurements as it allows the fluorescence-aided separation of subpopulations according to labeling stoichiometry and intra (or inter) dye distance in a 2D ALEX histogram.

This allows a detailed FRET-based analysis of distance distributions for a given protein for a particular subpopulation (say the unfolded subpopulation) even under conditions where this subpopulation coexists with the folded subpopulation. Since it is difficult to perform fluorescence-decay analysis on the small number of photons detected from a single molecule, such an analysis is typically performed for all photons from a subpopulation.

In a first study of its kind, we investigated the extent of structural heterogeneity in two small single domain proteins – the 64-residue CI2 and the 86-residue AcylCoA binding protein (ACBP), as a function of denaturant. The results show that under strongly denaturing conditions, both proteins can be modeled sufficiently accurate accurately by a random coil Gaussian chain. Lowering the denaturant concentration led to a progressive increase in the extent of D-A distance fluctuations, which are beyond the range accessible to a flexible Gaussian chain, pointing towards long-range tertiary interactions that are becoming increasingly favorable under mildly denaturing solvent conditions.

3.3. Initiation of transcription by RNA polymerase

Below we demonstrate how μsALEX was used to solve a long-standing puzzle with regard to the initiation of transcription by the enzyme RNA polemerase (RNAP) [14].

In the first steps of transcription initiation, RNAP binds to promoter DNA and unwinds ~14 bp surrounding the transcription start site to yield a catalytically competent RNAP-promoter open complex (RP_o) [see reference cited in 14]. In subsequent steps of transcription initiation, RNAP enters into initial synthesis of RNA as an RNAP-promoter initial transcribing complex (RP_{itc}), typically engaging in abortive cycles of synthesis and release of short RNA products, and, upon synthesis of an RNA product of ~9-11 nt, breaks its interactions with promoter DNA, breaks or weakens its interactions with initiation factors, leaves the promoter, and enters into processive synthesis of RNA as an RNAP-DNA elongation complex (RD_e).

The mechanism by which the RNAP active center translocates relative to DNA in initial transcription has remained controversial. DNA-footprinting results indicate that, surprisingly, the upstream boundary of the promoter DNA segment protected by RNAP is unchanged in RP_{itc} vs. in RP_o. To reconcile the

apparent absence of change in the upstream boundary of the promoter DNA segment protected by RNAP in RP_{itc} with the documented ability of RP_{itc} to synthesize RNA products up to ~8 nt in length, three models have been proposed (Fig. 8).

The first model, termed "transient excursions," invokes transient cycles of forward and reverse translocation of RNA. According to this model, in each cycle of abortive initiation, RNAP translocates forward as a unit, translocating 1 bp per phosphodiester bond formed; upon release of the abortive RNA, RNAP reverse translocates as a unit, regenerating the initial state. According to this model, the cycles of forward and reverse translocation are so short in duration and so infrequent in occurrence that, although they occur, they are not detected by a time-averaged, population-averaged method such as DNA footprinting.

The second model, termed "inchworming," invokes a flexible element in RNAP. Here, in each cycle of abortive initiation, a module of RNAP containing the active center detaches from the remainder of RNAP and translocates downstream, translocating 1 bp per phosphodiester bond formed; upon release of the abortive RNA, this module of RNAP retracts, regenerating the initial state.

The third model, termed "scrunching," invokes a flexible element in DNA. Here, in each cycle of abortive initiation, RNAP pulls downstream DNA into

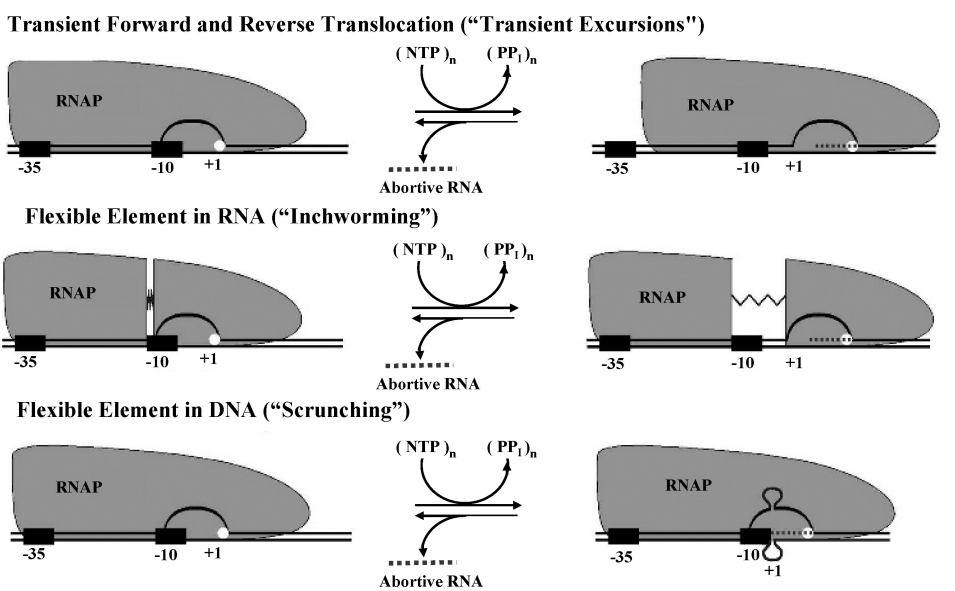

Fig. 8: Three models have been proposed for RNAP-active-center translocation during initial transcription: "Transient Excursions", "Inchworming", and "Scrunching". White circles: RNAP active center; red dashed lines: RNA; black rectangles: promoter -10 and -35 elements.

itself, pulling in 1 bp per phosphodiester bond formed and accommodating the accumulated DNA as single-stranded bulges within the unwound region; upon release of the abortive RNA, RNAP extrudes the accumulated DNA, regenerating the initial state.

We have directly tested the predictions of the three models by monitoring whether distance between RNAP and DNA change upon adding NTP (transition from RP_o to RP_{itc}). All models predict that there should be a decrease in the distance between RNAP leading edge relative to downstream DNA. Such a change upon adding NTP was recorded (data not shown), thus validating the experimental strategy. The transient excursions model predicts that there should be an increase in the distance between RNAP trailing edge and upstream DNA upon adding NTP. Such a change was not detected (data not shown), indicating that the first model is wrong. The inchworming model predicts that the distance between RNAP leading edge and upstream DNA should change. No such change was recorded (data not shown), indicating that the second model is also wrong. The scrunching model predicts that the DNA should condense, such that the distance between positions +15 and -15 on DNA will decrease upon adding NTP. As clearly shown in the FRET histogram (Fig. 9), such a shift towards higher *E* value is observed (notice that the non-shifted lower *E* peak is due to freely diffusing, unbound, doubly-labeled double-stranded DNA).

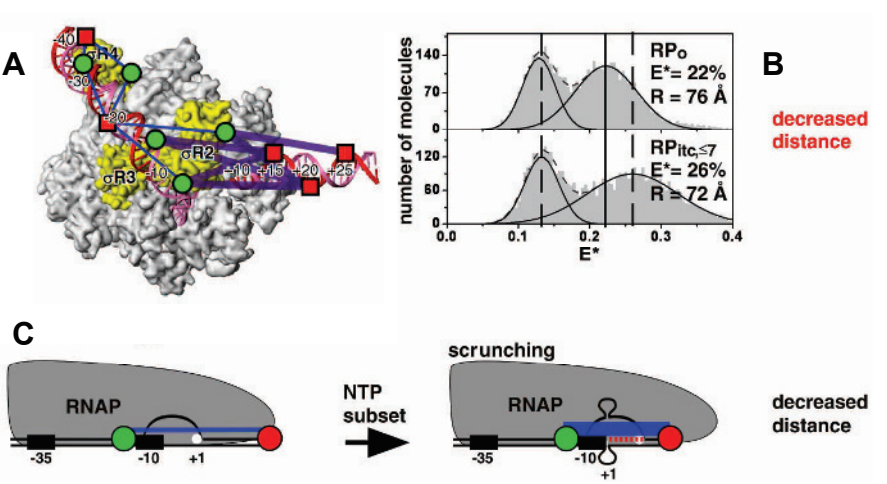

Fig. 9. "Scrunching" is the mechanism behind abortive initiation. (a) Crystal structure of RNAP-DNA complex with all the dyes' labeling position marked. Purple lines indicate donor-acceptor distances that decreased upon adding NTPs and blue lines indicate unchanged distances. (b) The FRET histogram clearly shows a shift towards higher *E* value (shorter distance) upon adding NTPs. The lower *E* peak (~*E*=0.13) is due to access free DNA. (c) and (d) show schematics before and after NTPs addition respectively.

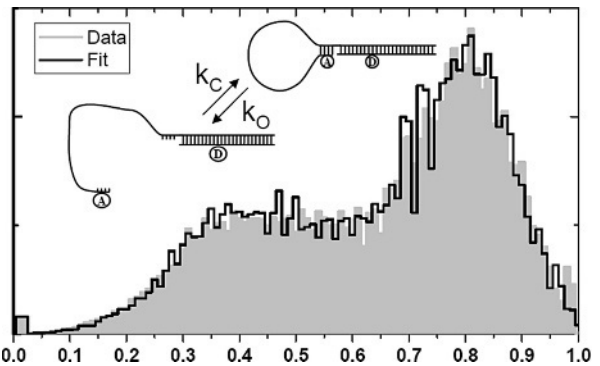

Fig. 10. ALEX histogram of DNA hairpin fitted with a two-state model. Experimental FRET histogram (gray bins) compared with the fit (black line). The best fit parameters are stated in the text.

3.4. DNA-Hairpin Structure and Dynamics

Except for the discussion on nsALEX, we have ignored so far the dynamic information content in the FRET histograms and considered them to represent static distributions of E values (and hence static distribution of distances). Here we introduce a FRET histogram of a two-state DNA-hairpin (having two configurations, of "open" and "close", with E_1 and E_2 respectively, see inset of Fig. 10). This hairpin has open/close rates comparable to the typical transit time through the observation volume. When the molecule changes its conformation while traversing the confocal spot (e.g. from E_1 to E_2), the recorded E value will reflect a superposition of E_1 and E_2 values. It is possible, in principle, to extract some of the thermodynamic and kinetic properties of the investigated system by analyzing the shape of the FRET histogram. We have developed a mathematical description and simulation of the FRET histogram for any given arbitrary energy landscape. Part of this mathematical development and the computer-based algorithm for the fitting was presented in a recent work [12]. Here we will only mention that the final FRET histogram shape is a combination of shot-noise, calculated based on empirical burst size distribution, and of the distribution of time periods the molecule spend in each of the possible states along it path on its energy landscape.

Fig. 10 shows a schematic of a DNA hairpin molecule (and the donor and acceptor labeling positions) studied by ALEX. The single strand part of the molecule contains a stem and a loop. One side of the stem contains the sequence 5'-AACCCA-3' and the other contains the complementary sequence 3'-TTGGGT-5'. These sequences and the loop cause the hairpin to transiently and stochastically close and open up. The FRET between the donor and acceptor therefore samples the two distances representing the two states. If the opening and closing rates are very slow compared to the transit time, one expects a

double-peaked FRET histogram (with the peaks centered at $\bar{E}_1$ and $\bar{E}_2$). If, however, the rates are very fast compared to the transit time, one expects a single, broad peak (centered in between $\bar{E}_1$ and $\bar{E}_2$). Using the model, the histogram shown in Fig. 10 was analyzed and fitted, yielding $\bar{E}_1$(close)=0.81 , $\bar{E}_2$(open)=0.36 and closing and opening rates of k_{Close} = 1425 s^{-1} and k_{Open} = 835 s^{-1} respectively.

4. SUMMERY

In this chapter, we showed that ALEX affords unparalleled insights into biomolecular structure and dynamics that are difficult to obtain with population-averaging ensemble techniques. They not only allow the visualization and enumeration of conformational subpopulations associated with biochemical reactions, but also enable the extraction of angstrom-resolution intra and/or intermolecular distances or distance distributions within and in between macromolecules with a time resolution down to nanoseconds. The past five years have shown that ALEX-based methodologies can accurately reproduce the ensemble thermodynamics of simple model systems. The next step will be the extension of these techniques to more complex systems and eventually to molecular machines inside the living cell.

ACKNOWLEDGEMENTS

We thank all past and present members of the Single Molecule Biophysics group at UCLA who contributed their intellect, hard work and dedication to the work described in this chapter. This work was funded by NIH grant GM069709-01 and DOE grants 02ER63339 and 04ER63938 to S.W. E.N. is supported by the Human Frontier Science Program (HFSP).

REFERENCES

[1] A.A Deniz, M. Daha, J.R. Grunwell, T Ha, A.E. Faulhaber, D.S. Chemla, S. Weiss and P.G. Schultz, Proc. Natl. Acad. Sci. USA, 96 (1999) 3670.
[2] S. Weiss SCIENCE, 283 (1999) 1676.
[3] T. Ha, T. Enderle, D.F. Oletree D.S. Chemla, P.R. Selvin and S. Weiss, Proc. Natl. Acad. Sci. 93 (1996) 6264.
[4] A.N. Kapanidis, T.A. Laurence, N.K. Lee, E. Margeat, X. Kong and S. Weiss, Acc. Chem. Res., 38 (2005) 523.
[5] M. Jäger, X. Michalet and S. Weiss, Protein Science, 14 (2005) 2059.
[6] M. Jäger, E. Nir, and S. Weiss, Protein Science, 15 (2006) 640.
[7] C. Eggeling, S. Berger, L. Brand, J.R. Fries, J. Schaffer A, Volkmer and C.A.M. Seidel, Biothechnolgy 86 (2001) 163.
[8] M. Dahan, A.A. Deniz, T. Ha, D.S. Chemla, P.G. Schultz and S. Weiss, Chemical Physics, 247 (1999) 85.

[9] A.N. Kapanidis, N.K. Lee, T.A. Laurence, S. Doose, E. Margeat and S. Weiss, PNAS, 101 (2004) 8936.
[10] N.K. Lee, A.N. Kapanidis, Y. Wang, X. Michalet, J. Mukhopadhyay, R.H. Ebright and S. Weiss, Biophysical Journal, 88 (2005) 2939.
[11] X. Michalet, S. Weiss and M. Jäger, Chem Rev, 106 (2006) 1785.
[12] E. Nir, X. Michalet, K. Hamadani. T.A. Laurence, D. Neuhauser, Y. Kovchegov, and S. Weiss, J. Phys. Chem B, (2006) in press.
[13] T.A. Laurence, X. Kong, M. Jäger, and S. Weiss, Proc. Natl. Acad. Sci. 102 (2005) 17348.
[14] A. N. Kapanidis, E. Margeat, S.O. Ho, E. Kortkhonjia, S. Weiss and R.H. Ebright, Science, (2006) in press.
[15] X. Kong, E. Nir, M. Jäger, K. Hamadani and S. Wiss, J. Phys. Chem B, (2006) submitted.

Handai Nanophotonics, Volume 3
H. Masuhara, S. Kawata and F. Tokunaga (Editors)

Chapter 3

Linear and non-linear Raman microspectroscopy and imaging of single living cells: Visualization of life and death at the cellular level

Hideaki Kano, Yu-San Huang, Yasuaki Naito, and Hiro-o Hamaguchi

Department of Chemistry, School of Science, The University of Tokyo,
Hongo 7-3-1, Bunkyo, Tokyo 113-0033, JAPAN
Tel: +81-3-5841-4329, FAX: +81-3-3818-4621
E-mail: hhama@chem.s.u-tokyo.ac.jp

1. INTRODUCTION

It is often said that "Spectra are letters from the molecule". Molecules send us various kinds of messages about themselves in the form of spectra. In particular, vibrational spectra such as Raman and infrared spectra embody many characteristic features that are specific to a molecule. By analyzing vibrational spectra, we can identify chemical species and elucidate in details their structure and dynamics. Thus, vibrational spectra are often called "molecular fingerprints". In the mid-infrared "fingerprint" region, we observe many vibrational bands that are attributable to skeletal modes characteristic to a molecule. Since biological materials are made up of molecules, vibrational spectroscopy should be useful in life sciences as much as it is in material sciences. Owing to its noninvasive and nondestructive nature, Raman spectroscopy is more suitable for biological applications than infrared. Thanks to recent technical developments, we can now investigate a living cell *in vivo* under a microscope. Thus, some number of Raman microspectroscopic studies have already been reported on living cells [1-11], though it was very difficult to confirm that the cells were really living. We recently found a strong Raman band in mitochondria of a living fission yeast cell, which sharply reflects the metabolic activity of mitochondria [8,9]. We call it the "Raman spectroscopic signature of life". By monitoring this signature, we can indeed confirm that the cell is living. In this chapter, we review our recent studies on the structure, transformation, and bioactivity of single living yeast cells by linear and non-linear microspectroscopy. We have successfully visualized not only the

distributions of molecular species but also the cell activity of the growing and dying yeast cells.

2. IN VIVO REAL-TIME PURSUIT OF THE CELL ACTIVITY OF SINGLE LIVING FISSION YEAST CELLS BY TIME- AND SPACE-RESOLVED RAMAN MICROSPECTROSCOPY

2.1. Experimental

We used a confocal Raman microspectrometer (Nanofinder, Tokyo Instrument Inc.). The 632.8 nm line of a He-Ne laser (Melles Griot 05-LHP-991) was used with a power of 1-4 mW at the sample. The spatial resolutions were 250 nm and 1.7 μm for the lateral and the axial directions, respectively. Each stage of the mitosis was confirmed by a yeast cell (*Schizosaccharomyces pombe*), whose nucleus was labeled by green fluorescent protein (GFP).

2.2. Space-resolved Raman spectra

Figure 1 shows the space-resolved Raman spectra of a single living fission yeast cell in the G1/S phase. These spectra were obtained under a low nutrition condition, so that the cell cycle was slowed down to allow a long exposure time of 300 s. Figs. 1(a), (b), and (d) correspond to the spectra for nucleus, mitochondria, and septum, respectively. The positions from where Raman spectra are measured are indicated by letters a, b, and d in the inset. Using a cell whose mitochondria are tagged by GFP, we have confirmed that the spectrum in Fig. 1(b) comes from mitochondria. The spectra from nuclei are dominated by known protein Raman bands. In particular, the bands in Fig. 1(a) shows the amide I mode of the main chain (1655-1660 cm^{-1}), the C-H bend of the aliphatic chain (1450 and 1340 cm^{-1}), the amide III mode of the main chain (1250-1300 cm^{-1}), and the breathing mode of the phenylalanine residue in proteins (1003 cm^{-1}). It is well known that the frequencies of the amide I and III bands are sensitive markers of the secondary structure of the protein main chain. In the present study, the amide I band is observed in the range of 1654-1659 cm^{-1}, which indicates the domination of α-helix structures [12]. Concerning the secondary structure, we need to investigate further in detail because this band is broad and thus we cannot neglect the contribution from other secondary structures. New insight into the secondary structure of proteins in a living cell is highly important in connection with the presence of natively unfolded proteins [12,13], which has been discussed intensively in the past few years. In addition to the protein bands, weak bands are observed at 781 and 1576 cm^{-1}, which can be assigned to nucleic acids. According to the result of a component analysis of isolated nuclei, the DNA/RNA/protein chemical composition ratio in a *S. pombe* nucleus is 1/9.4/115 [14]. This ratio means that proteins are about 10 times more

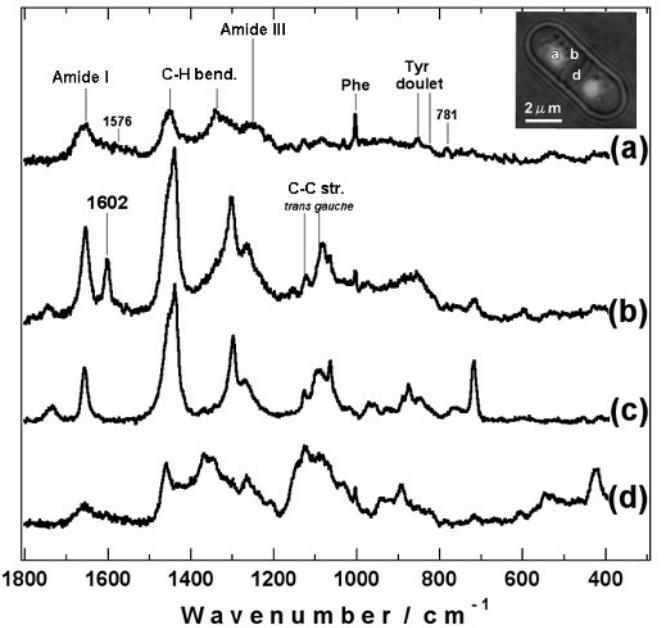

Fig. 1 Spatial-resolved Raman spectra of a single living fission yeast cell in the G1/S phase; (a) nucleus, (b) mitochondria, (c) phosphachidylcholine (model compound of lipid bilayer) and (d) septum.

abundant in the isolated nucleus than nucleic acids. This result is consistent with the result of the *in-vivo* Raman spectra observed in the present study. The intensity ratio of the band at 853 cm^{-1} to that at 825 cm^{-1} is known to be an indicator of the H-bonding strength of the phenolic hydroxyl group [15].

The Raman spectrum from mitochondria (Fig.1(b)) is similar to that of phosphatidylcholine (Fig. 1 (c)) except for an intense band at 1602 cm^{-1}. Apart from this 1602 cm^{-1} band, all prominent bands in Fig. 1(b) are ascribed to the known phospholipid vibrational modes with reference to the assignments of the spectrum of phosphatidylcholine [16,17]. The skeletal C-C stretch modes in the region of 1000-1150 cm^{-1} are known to be sensitive to the conformation of the hydrocarbon chains [18]. The bands at 1062 and 1122 cm^{-1} are assigned to the out-of-phase and in-phase modes of the all-trans chain. On the other hand, the band at 1082 cm^{-1} is attributed to the gauche conformation. The ratio of the intensity of the gauche band to that of the trans band is larger in the Raman spectrum from mitochondria (Fig. 1(b)) than in that from phosphatidylcholine (Fig. 1 (c)). This finding indicates that the hydrocarbon chains of the mitochondrial membrane are conformationally less ordered than that in pure phosphatidylcholine.

The Raman spectrum from septum is shown in Fig. 1(d). The bands are mostly assigned to polysaccharides. We found the change of the Raman spectrum of the septum in the course of the cell division process. Based on the normal-mode analysis of disaccharides [19,20], it is considered that this change reflects the gradual polymerization of the saccharide molecules.

2.3. Time- and space-resolved Raman spectra

As the cell division proceeds, the Raman spectrum is expected to change drastically, reflecting the changes in molecular composition of the organelles. Figure 2 shows the time- and space-resolved Raman spectra of a yeast cell dispersed in YE broth. We start the Raman measurement from the early M phase (a), in which a dividing nucleus is observed at the center of the cell. At 9 min (b), the two nuclei are put apart symmetrically toward the perimeter of the cell. At 1 h, 13 min (G1/S phase), the nuclei are completely separated and located at the two ends of the cell. In the following G1/S stage, a septum starts to form from the plasma membrane, as shown in (d). Finally, the septum becomes mature at 5 h, 54 min (e). In the course of the mitosis process, the Raman spectrum change significantly. The Raman bands at 0 min (a) are assigned to the proteins in the nucleus. The spectrum at 9 min is a superposition of those of the mitochondrion and cytoplasm. It means that the mitochondria started to be generated at the central part of the cell. At 1 h, 13 min (c), the phospholipid bands due to mitochondria are observed dominantly in the Raman spectrum. It should also be noticed that the intense band is found at the Raman shift of 1602 cm^{-1}. The intensity of this band relative to that of the 1654 cm^{-1} band is clearly higher than those observed in the space-resolved experiment in Fig. 1. This result is intriguing with regard to the relevance of the 1602 cm^{-1} band to the metabolic activity of mitochondria. The time- and space-resolved Raman spectra were obtained from the yeast cells dispersed in YE broth, while those for the space-resolved Raman spectra (Fig. 1) were measured under a low nutrition condition. It means that the band intensity at 1602 cm^{-1} depends on the nutrient condition. The stronger band at 1602 cm^{-1} in Fig. 2(c) is indicative of higher metabolic activities in a yeast cell in YE broth.

2.4. Discovery of the “Raman spectroscopic signature of life”

In order to investigate in further details the relationship between the band intensity at 1602 cm^{-1} and the metabolic activity of a mitochondrion, the following experiment has been carried out. We added a KCN aqueous solution to the yeast cell sample, in order to look at the effect of a respiration inhibitor on the intensity of the 1602 cm^{-1} band. The time- and space-resolved Raman spectra of a KCN-treated yeast cell are shown in Fig. 3. The temporal resolution is 100 sec. Five minutes before the addition of KCN, the Raman spectrum shows a

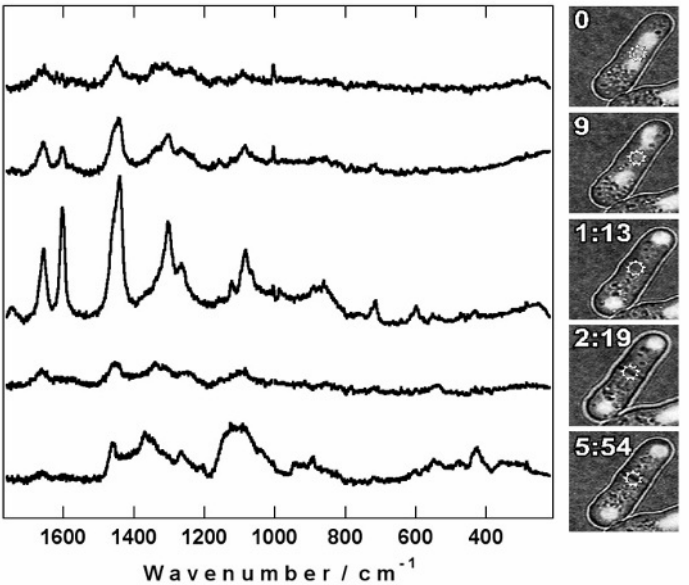

Fig. 2 Time- and space-resolved Raman spectra of the central part of a living yeast cell. The laser beam spot is denoted with a white broken circle.

strong band at 1602 cm^{-1} and the well known phospholipid bands at 1655, 1446, and 1300 cm^{-1}. Three minutes after the addition of KCN (b), the intensity of the band at 1602 cm^{-1} decreases considerably, while the other phospholipid bands remain unchanged. As time goes on, the 1602 cm^{-1} band becomes weaker ((c) and (d)), and finally disappears at 36 min (e). Concomitantly, the phospholipid bands gradually change from well-resolved peaks to diffuse broad bands. The protein band at 1003 cm^{-1} does not change, and no additional peaks appear throughout the time course of the experiment. We consider that the addition of KCN affects a mitochondrion of a living yeast cell in the following two steps. First, the cellular respiration is inhibited by the action of CN^-, and the metabolic activity of the mitochondrion is lowered. This process has been monitored by the drastic decrease in the intensity of the 1602 cm^{-1} band. Second, the double-membrane structure of the mitochondrion is degraded by the lowered metabolic activities, and it is eventually destroyed. This process has been probed by the changes in the phospholipid bands. It is highly likely that the 1602 cm^{-1} band probes the primary dying process of the KCN-treated yeast cell through the metabolic activity of a mitochondrion. Therefore, we call this band the "Raman spectroscopic signature of life".

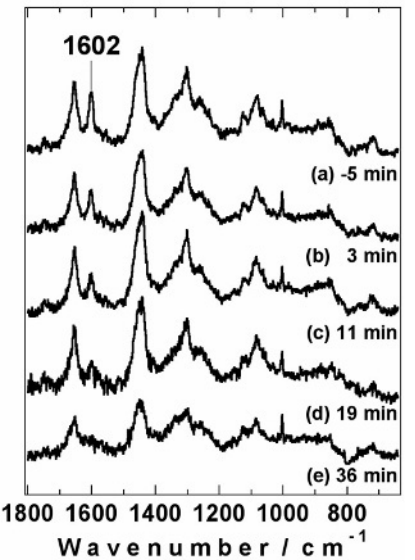

Fig. 3 Time- and space-resolved Raman spectra of a KCN-treated yeast cell.

3. *IN VIVO* TIME-RESOLVED RAMAN IMAGING OF A SPONTANEOUS DEATH PROCESS OF A SINGLE BUDDING YEAST CELL

3.1. Vacuole and dancing body in a budding yeast cell

Vacuole is one of the biggest organelles in a yeast cell. The function of vacuole includes amino acid storage and detoxification. Under a starvation condition, proteins are degraded in the vacuole. This process is known as autophagy. In a budding yeast (*S. cerevisiae*) vacuole, a particle called dancing body occasionally appears and moves actively for a while. Although a previous fluorescence study suggested that the main molecular component of the dancing body was polyphosphates [21], it was not clear. One of the difficulties for studying dancing body is that we cannot separate it from the vacuole. We have investigated the molecular component of a dancing body by time- and space-resolved Raman spectroscopy (data not shown), and have proved that the dancing body consists of crystal-like polyphosphate [10].

3.2. Spontaneous death process following the appearance of a dancing body

Figure 4 shows the time-resolved Raman images (a) and the optical microscope images (b) in a time span of about 20 hours of a single living *S. cerevisiae*. From the microscope images in Fig. 4(b), it is seen that a dancing body forms in a vacuole between 5 h, 50 min and 6 h. Then, the vacuole

disappears between 8 h, 41 min and 9 h, 31 min. Finally, the cell becomes totally destructed between 9 h, 31 min and 19 h, 37 min. It is obvious that these changes in the microscope images reflect a spontaneous cell death process of an *S. cerevisiae* cell. We have confirmed that this spontaneous death process observed in Fig. 4 also occurs for cells without laser irradiation. In fact, we have examined 642 cells to find that once a dancing body is formed in a vacuole, the cell eventually dies without any exception. In Fig. 4(b), we trace these changes at the molecular level by the Raman images at 1602 cm^{-1}, 1440 cm^{-1}, 1160 cm^{-1} and 1002 cm^{-1}. The 1602 cm^{-1} band, the Raman spectroscopic signature of life, reflects the metabolic activity of mitochondria. Therefore, the Raman image at 1602 cm^{-1} shows the distribution of active mitochondria in a cell. The band at 1445 cm^{-1} is due to the C-H bending modes of phospholipids. This band gives an image of phospholipid distribution, which corresponds to the location of mitochondria that contain high concentration of phospholipids. The polyphosphate band at 1160 cm^{-1} provides an image of phosphate distribution including the location of a dancing body. The band at 1002 cm^{-1} is assigned to the breathing mode of phenylalanine and shows the protein distribution in a cell. At 0 min, the cell has active mitochondria as shown by the1602 cm^{-1} image. The phospholipids (1440 cm^{-1}) and proteins (1002 cm^{-1}) are located only outside of a vacuole but some amount of polyphosphates do exist inside the vacuole as well as outside. At 6 h, when a dancing body becomes suddenly visible, the metabolic

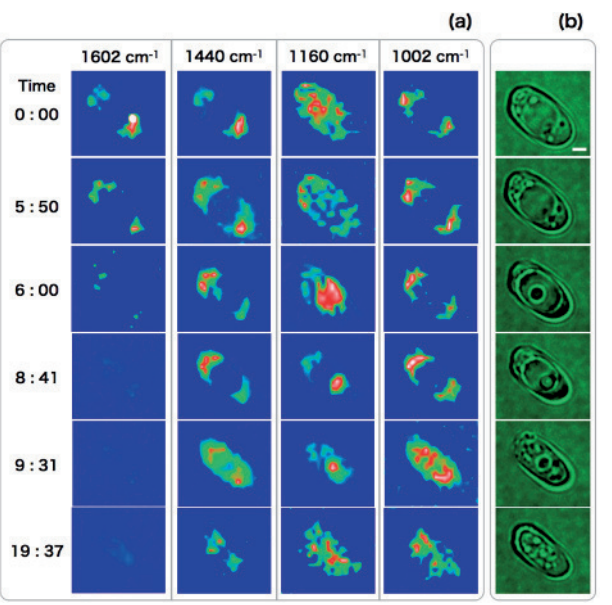

Figure 4. (a) Time-resolved Raman images and (b) corresponding optical microscope images of a dying *S. cerevisiae* cell.

activity in mitochondria is markedly lowered as seen from the 1602 cm^{-1} image, though the mitochondrial distribution (1440 cm^{-1}) does not change appreciably. The 1160 cm^{-1} band gives an image covering a large part of the vacuole, indicating that a dancing body is trapped by the laser field and that it moves with the scanning laser spot within the vacuole. There is no change in the protein distribution. At 8 h, 41 min, the dancing body stops moving and stays at the lower part of the vacuole. At this stage, the metabolic activity of mitochondria is completely lost, while the mitochondrial and protein distributions do not change much. The 1160 cm^{-1} band image corresponds to the remaining of the dancing body which does not move any more. At 9 h, 31 min, the vacuole is lost, while the black remaining of the dancing body still exists at the center of the cell. The Raman images show that the molecular distributions at this stage are highly randomized. It indicates the loss of structures in the cell. At 19h, 37min, the molecular distributions become totally random, showing that the cell is not alive any more. Thus, a spontaneous cell death process is visualized by *in vivo* time-resolved Raman imaging at the molecular level.

4. NON-LINEAR RAMAN MICROSPECTROSCOPY AND IMAGING OF SINGLE LIVING CELLS

4.1. Ultrabroadband multiplex coherent anti-Stokes Raman scattering (CARS) process

As shown above, spontaneous Raman microspectroscopy is powerful for elucidating intra-cellular structure *in vivo* with three-dimensional sectioning capability. However, it may not be suitable to trace a detailed dynamical behavior inside of the cell, because of its relatively low efficiency. Spontaneous Raman process often requires several minutes to obtain one spectrum. This low efficiency originates from the small scattering cross section of the spontaneous Raman process. An alternative approach to obtain vibrational images with high speed is coherent Raman microspectroscopy. Among them, coherent anti-Stokes Raman scattering (CARS) microscopy has been widely exploited [5,22-27]. In particular, multiplex CARS microspectroscopy is promising because of its capability to obtain vibrational spectra efficiently [24,28-31]. Figure 5 shows an energy diagram for the multiplex CARS process. The multiplex CARS process requires two laser sources, namely, a narrow band pump laser (ω_1) and a broadband Stokes laser (ω_2). The multiple vibrational coherences are created because of the wide spectral range of the frequency difference, ω_L-ω_2. If we can prepare ultrashort laser pulses, an impulsive Raman excitation and a subsequent narrow-band probe can also generate a multiplex CARS spectrum [32,33]. One of the most prominent features of multiplex CARS microspectroscopy lies in the fact that it can easily distinguish the concentration change of a particular molecule from the structural change through the spectral analysis [11]. It should

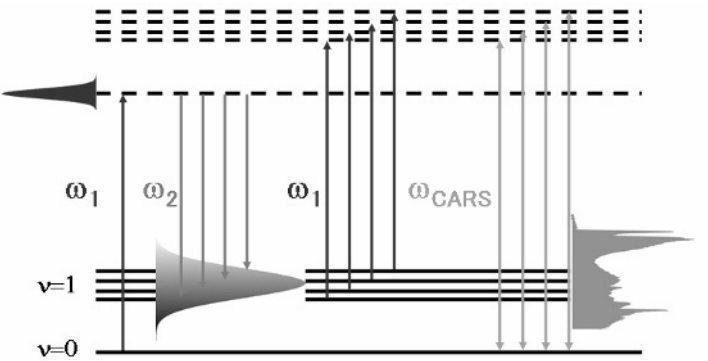

Fig. 5. Energy diagram for multiplex CARS process.

be emphasized that a single-wavenumber CARS detection, which is widely adopted in CARS microscopy, cannot discriminate these two phenomena. Although there were several restrictions on the spectral coverage of multiplex CARS microspectroscopy mainly due to the bandwidth of the laser emission [24,28-31], the spectral coverage has been significantly broadened using the supercontinuum light source generated from a photonic crystal fiber [11,34-36] or a tapered fiber[37]. Recently, the spectral coverage of the multiplex CARS microspectroscopy has been extended to be more than 2800 cm^{-1}[33], which is ranging from 360 nm to 3210 cm^{-1}.

4.2. Experimental setup for ultrabroadband multiplex CARS microspectroscopy

Figure 6 shows a schematic of the multiplex CARS microspectrometer. An unamplified mode-locked Ti:sapphire laser (Coherent, Vitesse-800) provides wavelength fixed radiation at 800 nm, which is used as the pump laser. Typical duration, pulse energy, and repetition rate are 100 fs, 12 nJ, and 80 MHz, respectively. A portion of the output from the oscillator is used as a seed for generating a supercontinuum in the PCF (Crystal Fibre, NL-PM-750). The input pulse energy for the supercontinuum generation is less than 2.3 nJ. As shown in Fig. 6, the fundamental of the Ti:sapphire laser and the supercontinuum are used for the pump (ω_1) and Stokes (ω_2) lasers, respectively. In order to obtain Raman spectrum with high frequency resolution, the pump laser pulses are spectrally filtered using a narrow band-pass filter. The bandwidth was measured to be about 20 cm^{-1}. Because the pump laser is in the near infra-red (NIR) region, the Stokes laser must also be in the NIR. The visible component in the supercontinuum is thus blocked by a long-wavelength pass filter. Thanks to the NIR excitation, we can expect several advantages such as low photodamage, suppression of the nonresonant background signal, and a deep penetration depth

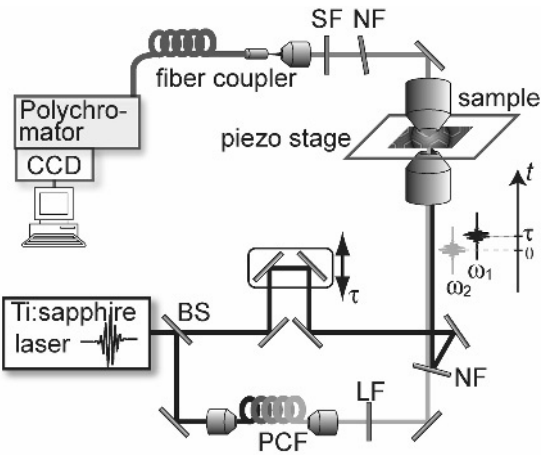

Fig. 6. Experimental setup for multiplex CARS microspectroscopy ; BS: beam splitter; NBF: narrow band-pass filter; LF: long-wavelength pass filter; NF: Notch filter; SF: short-wavelength pass filter.

for opaque samples. Two laser pulses are superimposed collinearly using an 800-nm Notch filter, and then tightly focused onto the sample with a $40\times$ 0.9 NA microscope objective. Under the tight focusing condition, the phase-matching conditions are relaxed due to the large angular dispersion and the small interaction volume [38,39]. The relaxation of the phase-matching condition is important especially for CARS spectroscopy, because a wide range of vibrational resonances can be accomplished simultaneously using the ultrabroadband Stokes laser. A $40\times$, 0.6-NA microscope objective is used to collect the forward-propagating CARS signal. Finally, the CARS signal is guided to a polychromator (Acton, SpectraPro-300i), and is detected by a CCD camera (Roper Scientific, Spec-10:400BR/XTE). The multiplex CARS images are measured by a point-by-point acquisition of the CARS spectrum. The sample is moved using piezo-driven xyz translators (MadCity, Nano-LP-100). We used fission yeast *S. pombe* as a sample [7-9]. The nuclei of yeast cells were labeled by GFP.

4.3. CARS imaging of single living cells

Figure 7(a) shows a typical spectral profile of the CARS signal of a living yeast cell. As clearly shown, a strong signal is observed at the Raman shift of 2840 cm^{-1}. This band originates from C-H stretch vibrational mode, which shows a slightly dispersive lineshape due to an interference with a nonresonant background. On the basis of our previous spontaneous Raman [7-9] and CARS [11] studies, the signal at the Raman shift of 2840 cm^{-1} is found particularly strong in mitochondria, because mitochondrion is an organelle containing a

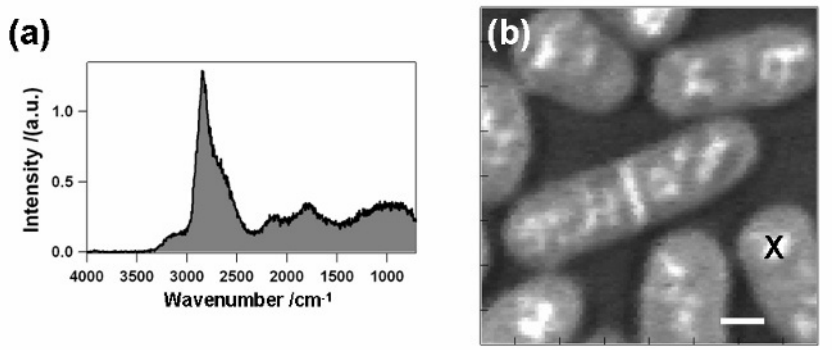

Fig. 7. Typical spectral profile of the CARS signal from a living yeast cell; (b) CARS image of living yeast cells at the Raman shift of C-H stretching vibrational mode. The short bar measures 2 μm.

high concentration of phospholipids. Figure 7(b) shows the vibrationally resonant CARS image at C-H stretching mode using a differentiation method [11]. The CARS spectrum of a yeast cell in Fig. 1(a) are obtained at (*x, y*)=(5.65 μm, -3.05 μm), which are indicated as a black cross in Fig. 1(b). In Figure 1(b) yeast cells at various cell-cycle stages are clearly imaged. Especially, a septum is visualized in the yeast cell around the center of Figure 1(b). The septum is composed of carbohydrates such as polysaccharide, which is also rich in C-H bonds.

Thanks to the three-dimensional sectioning capability, CARS microscopy enables us to obtain not only a lateral but also an axial slice of a living yeast cell. Figure 8 (a) shows a lateral CARS image of a yeast cell. Figure 8(b) corresponds

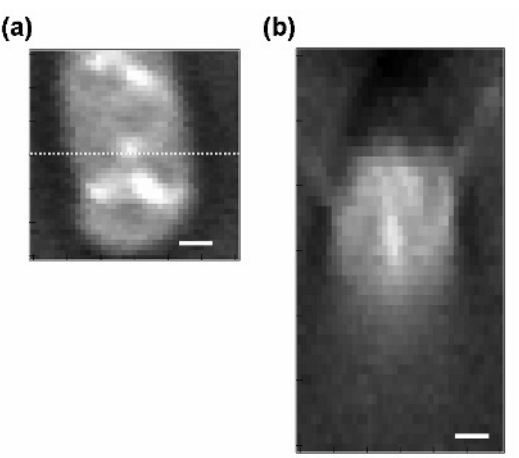

Fig. 8. Lateral(a) and axial(b) CARS images of a yeast cell at C-H stretching vibrational mode. The short bars correspond to 1 μm.

to the vertical slice of the yeast cell at the position of y=0. The CARS signal is weaker at the top part rather than the bottom part. It is due to the imperfect focusing of the two laser beams because of the spatially heterogeneous refractive index inside of the cell.

4.4. Multi-nonlinear optical image of single living cells

The supercontinuum light source can also be used as an excitation light source for the two-photon excitation fluorescence (TPEF) [40-42]. Owing to the broadband spectral profile of the supercontinuum, the two-photon allowed electronic state can be excited efficiently in comparison with conventional TPEF microscopy using a Ti:sapphire oscillator. Figure 9(a) shows the CARS and the TPEF spectra obtained in a 100 ms exposure time. The nuclei of the yeast cells in the present study are labeled by GFP. A broad but distinguishable peak is observed around 506 nm. Taking into account of the spectral profile of this signal, it is assigned to the TPEF signal due to GFP. Figures 9 (b) and (d) show CARS and TPEF images. It should be emphasized that both images of multiplex CARS and TPEF signals are obtained simultaneously in one single measurement. Since there is no overlap between the CARS and TPEF signals in spectral

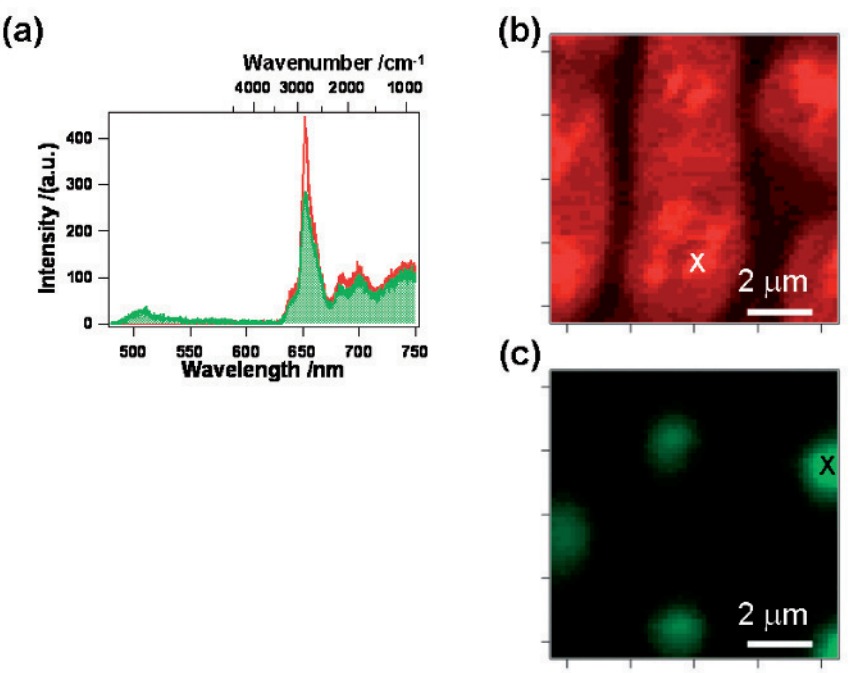

Fig. 9. (a) Spectral profile of the CARS and TPEF signals of a living yeast cell; (b) CARS lateral images of living yeast cells for C-H stretching mode; (c) TPEF lateral images of the same system at 506 nm. The red and green spectra in (a) are obtained at the white and the black crosses in (b) and (c), respectively.

domain, it can be easily differentiated using a spectrometer. Although dual imaging of the CARS and the TPEF signals have been reported using two synchronized Ti:sapphire oscillators [43], full spectral information is obtained for the first time in the present study.

As a result, we can obtain Raman spectrum and Raman image with high speed using ultrabroadband multiplex CARS microspectroscopy. At the moment, the exposure time is 30 ms, which is about 1/30 in comparison with that of the spontaneous Raman microscopy.

5. CONCLUSIONS

Owing to its inherent molecular specificity, Raman spectroscopy provides rich information on molecular composition, structure and dynamics in a living cell *in vivo*. In addition, the *Raman spectroscopic signature of life* enables us to visualize metabolically active mitochondria in a yeast cell, which cannot be obtained by any other biochemical methods. In the near future, we will be able to discuss the life and death at the molecular level quantitatively using time- and space-resolved linear and non-linear Raman spectroscopy.

ACKNOWLEDGEMENTS

This research is supported by a Grant-in-Aid for Creative Scientific Research (No. 15GS0204) from the Ministry of Education, Culture, Sports, Science, and Technology of Japan. H. K. is supported by a Grant-in-Aid for Young Scientists (B) (No. 15750005) from Japan Society for the Promotion of Science, and research grants from The Kurata Memorial Hitachi Science and Technology Foundation. The authors thank Dr. T. Karashima, Prof. M. Yamamoto and Prof. A. Toe for their collaboration.

REFERENCES

[1] G. J. Puppels, F. F. M. De Mul, C. Otto, J. Greve, M. Robert-Nicoud, D. J. Arndt-Jovin, T. M. Jovin, Nature, 347 (1990) 301.
[2] K. Maquelin, L. P. Choo-Smith, T. van Vreeswijk, H. P. Endtz, B. Smith, R. Bennett, H. A. Bruining, G. J. Puppels, Anal. Chem., 72 (2000) 12.
[3] K. C. Schuster, E. Urlaub, J. R. Gapes, J. Microbiol. Methods, 42 (2000) 29.
[4] V. Mohacek-Grosev, R. Bozac, G. J. Puppels, Spectrochimica Acta, 57A (2001) 2815.
[5] J.-X. Cheng, Y. K. Jia, G. Zheng, X. S. Xie, Biophys. J., 83 (2002) 502.
[6] C. Xie, Y.-q. Li, J. Appl. Phys., 94 (2003) 6138.
[7] Y.-S. Huang, T. Karashima, M. Yamamoto, H. Hamaguchi, J. Raman Spectrosc., 34 (2003) 1.
[8] Y.-S. Huang, T. Karashima, M. Yamamoto, T. Ogura, H. Hamaguchi, J. Raman Spectrosc., 35 (2004) 525.

[9] Y.-S. Huang, T. Karashima, M. Yamamoto, H. Hamaguchi, Biochemistry, 44 (2005) 10009.
[10] Y. Naito, A. Toh-e, H. Hamaguchi, J. Raman Spectrosc., 36 (2005) 837.
[11] H. Kano, H. Hamaguchi, Opt. Express, 13 (2005) 1322.
[12] N. C. Maiti, M. M. Apetri, M. G. Zagorski, P. R. Carey, V. E. Anderson, J. Am. Chem. Soc., 126 (2004) 2399.
[13] H. Jeong, S. P. Mason, A. L. Barabasi, Z. N. Oltvai, Nature, 411 (2001) 41.
[14] J. H. Duffus: Methods in Cell Biology, Academic press, New York, 1975.
[15] M. N. Siamwiza, R. C. Lord, M. C. Chen, T. Takamatsu, I. Harada, H. Matsuura, T. Shimanouchi, Biochemistry, 14 (1975) 4870.
[16] B. P. Gaber, W. L. Peticolas, Biochim. Biophys. Acta, 465 (1977) 260.
[17] Y. Takai, T. Masuko, H. Takeuchi, Biochim. Biophys. Acta, 465 (1977) 260.
[18] J. L. Lippert, W. L. Peticolas, Proc. Natl. Acad. Sci. U. S. A., 68 (1971) 1572.
[19] M. Dauchez, P. Derreumaux, P. Lagant, G. Vergoten, M. Sekkal, P. Legrand, Spectrochim. Acta, 50A (1994) 87.
[20] M. Dauchez, P. Lagant, P. Derreumaux, G. Vergoten, M. Sekkal, P. Legrand, B. Sombret, Spectrochim. Acta, 50A (1994) 105.
[21] R. A. Allan, J. J. Miller, Can. J. Microbiol., 26 (1980) 912.
[22] M. Hashimoto, T. Araki, S. Kawata, Opt. Lett., 25 (2000) 1768.
[23] A. Zumbusch, G. R. Holtom, X. S. Xie, Phys. Rev. Lett., 82 (1999) 4142.
[24] G. W. H. Wurpel, J. M. Schins, M. Mueller, Opt. Lett., 27 (2002) 1093.
[25] H. N. Paulsen, K. M. Hilligsoe, J. Thogersen, S. R. Keiding, J. J. Larsen, Opt. Lett., 28 (2003) 1123.
[26] R. D. Schaller, J. Ziegelbauer, L. F. Lee, L. H. Haber, R. J. Saykally, J. Phys. Chem. B, 106 (2002) 8489.
[27] T. Ichimura, N. Hayazawa, M. Hashimoto, Y. Inouye, S. Kawata, Phys. Rev. Lett., 92 (2004) 220801/1.
[28] C. Otto, A. Voroshilov, S. G. Kruglik, J. Greve, J. Raman Spectrosc., 32 (2001) 495.
[29] J.-X. Cheng, A. Volkmer, L. D. Book, X. S. Xie, J. Phys. Chem. B, 106 (2002) 8493.
[30] D. Oron, N. Dudovich, Y. Silberberg, Phys. Rev. Lett., 89 (2002) 273001.
[31] D. Oron, N. Dudovich, D. Yelin, Y. Silberberg, Phys. Rev. Lett., 88 (2002) 063004/1.
[32] S.-H. Lim, A. G. Caster, S. R. Leone, Phys. Rev. A, 30 (2005) 2805.
[33] H. Kano, H. Hamaguchi, J. Raman Spectrosc., 37 (2006) 411.
[34] S. O. Konorov, D. A. Akimov, E. E. Serebryannikov, A. A. Ivanov, M. V. Alfimov, A. M. Zheltikov, Phys. Rev. E, 70 (2004) 057601.
[35] H. Kano, H. Hamaguchi, Appl. Phys. Lett., 86 (2005) 121113/1.
[36] I. G. Petrov, V. V. Yakovlev, Opt. Express, 13 (2005) 1299.
[37] T. W. Kee, M. T. Cicerone, Opt. Lett., 29 (2004) 2701.
[38] B. N. Toleutaev, T. Tahara, H. Hamaguchi, Appl. Phys. B, 59 (1994) 369.
[39] J.-X. Cheng, A. Volkmer, X. S. Xie, J. Opt. Soc. Am. B, 19 (2002) 1363.
[40] C. McConnell, E. Riis, Phys. Med. Biol., 49 (2004) 4757.
[41] K. Isobe, W. Watanabe, S. Matsunaga, T. Higashi, K. Fukui, K. Itoh, Jpn. J. Appl. Phys. Part 2, 44 (2005) L167.
[42] J. A. Palero, V. O. Boer, J. C. Vijverberg, H. C. Gerritsen, H. J. C. M. Sterenborg, Opt. Express, 13 (2005) 5363.
[43] H. Wang, Y. Fu, P. Zickmund, R. Shi, J.-X. Cheng, Biophys. J., 89 (2005) 581.

Handai Nanophotonics, Volume 3
H. Masuhara, S. Kawata and F. Tokunaga (Editors)

Chapter 4

Raman, CARS and near-field Raman-CARS microscopy for cellular and molecular imaging

Prabhat Verma[a,b], Katsumasa Fujita[b], Taro Ichimura[a,b] and Satoshi Kawata[b,c]

[a]Graduate School of Frontier Biosciences, Osaka University, Osaka, Japan.

[b]Department of Applied Physics, Osaka University, Osaka, Japan

[c]RIKEN, Wako city, Saitama, Japan.

1. INTRODUCTION

When it comes to cellular and molecular imaging, in particular, biomolecular imaging, Raman spectroscopy always turns out to be advantageous over the other common techniques, because it is not only nondestructive, but also it does not need any staining of molecules, which guarantees preservation of the physiological activities of the sample molecules. When combined with microscopy, Raman spectroscopy takes advantage of the rich information available from the molecular vibrations, and helps providing a high quality image. However, there are several practical difficulties in obtaining Raman images, which limit the results in many ways. One problem is the long time involved in the imaging process, which is due to the inherent weak signal of Raman scattering. We have come over this problem by developing a technique of slit-scanning confocal Raman microscopy. Apart from an improved acquisition rate, this technique is based on collecting Raman signal from multiple points of the sample using a line-shaped illumination, which is scanned over the sample in the direction perpendicular to the illumination line, providing a two-dimensional *x*-*y*-image. At the same time, the sample can also be moved in the *z*-direction to construct a 3-D image. This method is particularly suitable for fast and high quality 3-D cellular imaging. The other important problem is the spatial resolution, which is limited by the diffraction limits of the probing light. The diffraction limit for a visible light is of the order of a few hundred nanometers, which is not small enough to investigate and image nano-sized bio-

materials and molecular systems. Also, Raman signal becomes tremendously weak for these extremely small samples due to small scattering volumes, often preventing us from obtaining any image from these samples. Both these problems have been overcome by involving the near-field techniques in Raman microscopy, which increases the spatial resolution far beyond the diffraction limits as well as enhances Raman signal from thousands to million folds, making it possible to detect even the weakest and otherwise undetectable signals. In addition, the image quality, such as the contrast and the resolution, can be further improved by combining the higher-order scattering effects in Raman scattering process, such as the coherent anti-Stokes Raman spectroscopy (CARS). With all these additions/improvements in the traditional Raman microscopy, we have achieved high quality imaging of several nanomaterials, including cellular and biomolecular samples.

2. SLIT-SCANNING RAMAN MICROSCOPY FOR CELLULAR IMAGING

Analytical techniques based on Raman spectroscopy has been utilized for cell observation, diagnosis and 3-D imaging [1,2]. Since Raman spectroscopy provides rich information from the direct detection of molecular vibration, unlike other conventional methods, it does not require staining samples before observation. This is an advantage in observation of living samples because fluorescence molecules, which are conventionally used for dyeing the biomolecules, sometimes interact with biomolecules and degrade their physiological activity. To apply Raman imaging technique for wide range of biological applications, we developed a high-speed Raman microscope by using the slit-scanning technique. High-speed detection of Raman spectra in each position of a sample allows us to observe biological activities that change with time under natural conditions. The possible applications of the imaging

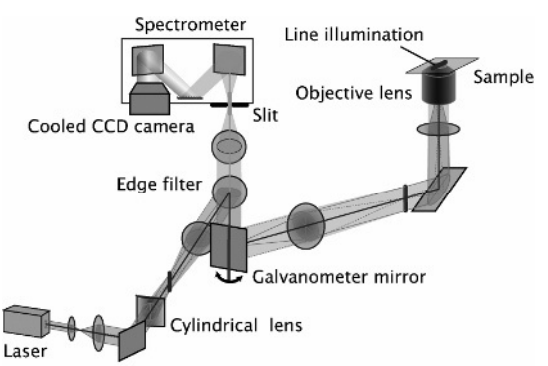

Fig.1. An optical setup of a slit-scanning Raman microscope.

technique are non-labelling cell imaging, diagnosis of diseases, investigation of drug distribution in cells, and material diagnosis in various fields.

Figure 1 shows the optical setup of the slit-scanning Raman microscope [3,4]. The line-shaped illumination was produced by a cylindrical lens, and the Raman spectra and their spatial distribution were detected by a cooled CCD camera with a spectrometer. The illumination light was scanned for the direction perpendicular to the illumination line to obtain the *x*-*y* distribution of Raman spectra of the sample. We used a galvanometer for scanning the illumination for *y*-direction. The sample was also scanned in *z*-direction by using a piezoelectric stage to construct a 3-D image of the sample. Since the slit at the entrance of the spectrometer does not allow the light from out-of-focus planes to enter the spectrometer, the slit works like a pinhole in a confocal microscope. This provides the spatial resolution in three dimensions, which enables us to obtain optically sliced images of the sample.

Figure 2 shows a volume image of living HeLa cells obtained by the slit-scanning Raman microscope. The laser intensity used for this observation was 5.8 mW/mm^2, and the exposure time was 10 sec/line. A total of 48 lines on the sample were illuminated to construct the image. Since the image is the spatial distribution of Raman spectra of the sample, one can observe the Raman spectrum of the position selected in the image. Since various components of the HeLa cell have their own fingerprint vibrations in Raman scattering, it is possible to select one particular Raman vibration, and construct an image for that particular vibration. The image thus constructed would be the image for the corresponding component of the HeLa cell, and hence it would show the 3-D distribution of that particular component. For example, the Adenine ring vibration at 785 cm^{-1}, the PO_2 symmetric-stretch vibration at 1095cm^{-1}, and the CH_2 symmetric-stretch vibration at 2835cm^{-1} correspond, respectively, to the nucleic acid, phosphoric acid, and lipid in HeLa cell. The spectrometer was set to these vibratioanal frequencies, and corresponding Raman images were obtained. Fig. 3 (a), (b) and (c) show the Raman images constructed at these Raman vibrations, which show the distribution of nucleic acid, phosphoric acid and lipid in the sample, respectively.

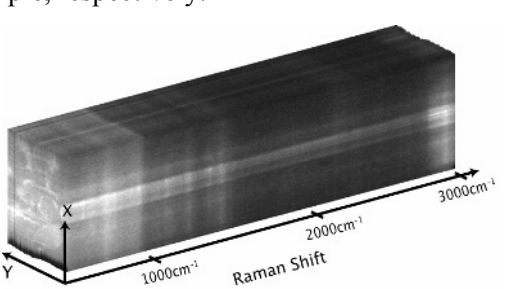

Fig.2. A 3-D image of living HeLa cell obtained by the slit-scanning Raman microscope.

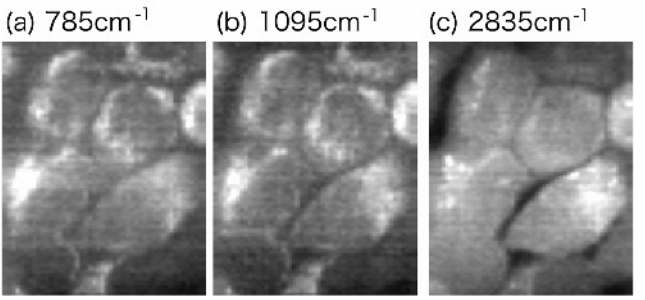

Fig.3. Raman images of HeLa cell constructed by Raman shifts of (a) 785cm^{-1} (Adenine ring vibration), (b) 1095cm^{-1}(PO_2 symmetric-stretch vibration) and (c) 2835cm^{-1} (CH_2 symmetric-stretch vibration), showing the distribution of nucleic acid, phosphoric acid and lipid, respectively, in the sample.

3. TIP-ENHANCED RAMAN SPECTROSCOPY

In order to deal with nano-sized samples, such as the biomolecules and other biomaterials, there are two important requirements that conventional Raman imaging fails to provide. One is high spatial resolution of the order of a few nanometers to a few tens of nanometers. Due to the wave nature of light, the minimum dimension that a light can image is limited to about half of the wavelength, which is about a few hundreds of nanometers for the visible light. The second important requirement is enhancement of scattered light, because due to the extremely small scattering volume of a nano-sized sample, the scattering intensity is often undetectably weak. Therefore, it is practically impossible to image many of biomaterials using conventional Raman microscopy. However, both these requirements can be fulfilled by combining the technique of near-field microscopy with Raman spectroscopy, *i.e*., by using tip-enhanced Raman spectroscopy (TERS) [5-8]. In our previous work [9,10], we have shown that the technique of TERS provides a super spatial resolution far beyond the diffraction limits of the probing light, along with an enhanced scattering efficiency, and hence it is suitable for the high quality imaging of biomaterials.

In this technique, a metal-coated nano-sized AFM-tip is brought close to the sample in the focal area of Raman microscope. When a metal-coated tip having a nano-sized apex is illuminated with light, it generates local surface plasmon polaritons (SPPs) in the vicinity of the tip apex. As the SPPs couple with incident photons resonantly, photons are densely confined in close vicinity of the nano-tip, which results in highly localized and strongly enhanced evanescent field near the tip apex. This enhanced field, which is of the same dimension as the tip apex, acts as a nano-light source for Raman scattering, and strong Raman scattering is generated from a small volume of the sample which is adsorbed in

this nano-sized evanescent field. Since Raman signal if selectively enhanced only from the molecules adsorbed in this evanescent field, TERS provided high resolution comparable to the size of the tip apex, along with strong enhancement, which ranges from a few thousand times to a million times. This technique of TERS was first proposed in 1999 [11] and was later used to analyze and image several nanomaterials [7-10]. Recently, we have added new dimensions to this technology by including, for example, nonlinear effects in Raman scattering [10], or the mechanical (pressure) effects in microscopy [8,12].

A typical schematics of the experimental setup used in TERS experiments can be found elsewhere [6]. The basic difference in the setup for TERS compared to that for conventional Raman scattering experiment is the addition of an AFM-head that controls and positions a metal-coated cantilever tip in the focal area. Far-field Raman spectra, which are basically the conventional Raman spectra, are obtained by moving the tip vertically away from the sample, and the near-filed spectra, which are TERS spectra, are obtained by bringing the tip close to the sample. The raw near-field signal contains a far-field contribution coming from the whole focal area, together with a near-field contribution coming from a small part of the sample within the focal area, which is adsorbed in the evanescent field. Thus, the true near-field component is obtained by subtracting a far-field Raman spectrum from the corresponding near-field Raman spectrum. The enhancement in Raman intensity for a particular Raman mode can be calculated by taking into account the ratio of the Raman intensities as well as the ratio of the scattering volumes involved in the two scattering configurations.

3. TERS ANALYSIS OF DNA-BASED ADENINE MOLECULES

In this section, we will first discuss the normal TERS results from a DNA based adenine molecule and demonstrate how the metallic tip enhances the weak Raman signal from a nanometer region, which cannot be detected by a conventional micro-Raman configuration. Next, we will show the effect of pressure that a tip can apply on the sample during the TERS experiments. For these experiments, the samples were prepared by casting adenine molecules dissolved in ethanol [7] on a glass coverslip. After drying, the samples crystallized in nanosize. The typical crystal size was laterally 7 nm by 20 nm wide and 15 nm high.

3.1. TERS from Adenine

Figure 4 shows a TERS spectrum of a single nanocrystal of adenine molecules. For a comparison, a far-field Raman spectrum of the same sample without a metallic tip is also shown. Figure 4 also schematically shows the tip position in the two cases. In TERS spectrum, several characteristic Raman peaks

of adenine molecules are enhanced and become visible, such as peaks at 736 cm^{-1} and 1330 cm^{-1}, while no Raman peak at these positions is observed when the tip is withdrawn from the near-field region (far-field Raman spectrum). The experimental condition was exactly the same for both experiments shown in Fig. 4 except for the tip-sample distance. The strong Raman peaks at 736 cm^{-1} and 1330 cm^{-1} are assigned to ring-breathing mode of a whole molecule and the ring-breathing mode of a diazole, respectively. Other Raman peaks are also assigned to the normal modes of adenine molecules [13-15]. The observed TERS peaks are shifted slightly from those obtained in the far-field. For example, the ring-breathing mode at 720 cm^{-1} in the far-field Raman spectrum of the bulk sample is shifted to 736 cm^{-1} in the TERS spectrum, while the ring-breathing mode of a diazole is not shifted. These phenomena in the spectral shifts are in good agreement with the SERS spectra of adenine molecules [16], and ensure that the metallic probe tip works as a surface enhancer for the SERS effect.

Assuming that the size of the enhanced electric field is 30 nm corresponding to the tip diameter and the size of the focused light spot is 400 nm, the enhancement factor for the ring-breathing mode of a whole molecule is estimated to be about 2700. The enhancement factor for the ring-breathing mode of a diazole is uncountable because the far-field Raman signal without a metallic probe tip is too weak to be detected.

3.2. TERS from Tip-Pressurized Adenine Molecules

When the metal-coated tip is in close proximity of a sample, it interacts with the sample electromagnetically to enhance the scattering signal. If the distance

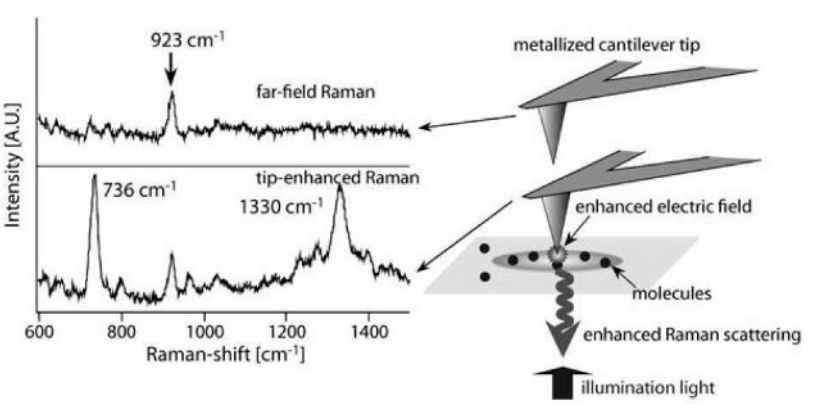

Fig. 4. Tip-enhanced near-field Raman (lower spectrum) and far-field Raman (upper spectrum) spectra of adenine nanocrystals. The peak at 923 cm^{-1} is from the glass substrate, and shows the same intensity in both TERS and the far-field Raman spectra. A schematic of the tip position in the two cases is also shown

between the tip and the sample is decreased, they can also interact chemically, which can enhance the scattered light as well as change the spectral shapes. If the distance is further decreased, then, in addition to the electromagnetic and chemical interactions, the tip starts to interact with the sample molecules mechanically. This happens when the metal molecules of the tip push against the sample molecules. This effect can be observed if the sample is pressurized, intentionally or unintentionally, by the tip [17]. Unlike the isotropic hydraulic pressure usually studied in high-pressure Raman scattering [18-20], the pressure applied by a tip is unidirectional, and hence it can change the bond lengths uniaxially, resulting in modifications of the molecular vibrations. The Raman modes tend to shift and get broadened. This phenomenon has been recently reported for carbon nanostructures [8,12]. Assuming that the atomic force is applied only to the contraction of the bond between the silver atom of the tip and the adjacent nitrogen of the adenine molecule, the bond distance for adenine sample would be expected to shrink and the vibrational frequencies may then shift upwards.

In our experiment, we used a cantilever with a spring constant of 0.03 N/m and a silver-coated tip apex diameter of this cantilever was 5 nm to 10 nm. The atomic force was kept constant at 0.3 nN by the feedback loop. As deduced from the unit-cell parameters of single-crystal 9-methyladenine [21], a couple of adenine molecules exist in a rectangle approximately 0.77 nm long by 0.85 nm wide. If we assume that the force is equally applied to all the molecules that are adjacent to the tip apex, the adenine molecules are subjected to a pressure of about 1 to 5 pN per molecule by the silver atom attached on the surface of the tip. As the metallic tip approaches the surface of the adenine nanocrystal, the tip is at first subject to a van der Waals attractive force and after passing through the equilibrium point, the tip receives a repulsive force. When the bond distance of the Ag–N linkage is reduced by 10%, the repulsive force of 7 pN per molecule is derived from a harmonic oscillation of the displacement by 0.025 nm and the energy difference by 1.7 kcal/mol in the case of the Ad–N3. The repulsive force coincides with the atomic force obtained with our system.

For the further understanding of the effect of tip-applied pressure in TERS, we theoretically investigated (using the density functional theory calculations) the transition states of both the Ad–N3 and the Ad–N7 isomers by changing the bond distance (in the model) between the nitrogen of the adenine molecule and the silver atom. The bond distances for the calculations were 2.502 (equilibrium), 2.75 (10% elongation), 2.25 (10% contraction), and 2.0Å (20% contraction). The binding energies, the vibrational frequencies of free adenine molecules, and the two complex isomers of three states were calculated. The partially optimized geometries exhibit imaginary frequencies, indicating transition states for the Ad–N3 and the Ad–N7. The ring–breathing mode of the Ad–N3 shows a significant shift towards a higher frequency as a function of the contracted bond

distance between the silver atom and the N3 nitrogen of adenine. The frequency of this mode is shifted upwards by 5 cm^{-1} when the bond distance is reduced by 10%. The frequency is shifted upwards by 17 cm^{-1} when the bond distance is reduced by 20%. The frequency shift of this band agrees well with those obtained in TERS experiments. On the other hand, the Ad–N7 shows only small frequency shifts. This difference in frequency shift suggests that interaction between an adenine molecule and the silver tip (*e.g.*, the Ad–N3) may be one of the possible reasons that we see large enhancement effects in TERS.

In addition to the higher-frequency shift, Raman-band broadening is also observed in TERS. The line broadening as well as the Raman frequency shift have also been reported in far-field high-pressure Raman scattering studies [18-20]. The line broadening occurs not only as a result of surface interaction, but also as a result of pressures caused by the silver tip.

4. TIP ENHANCED NONLINEAR OPTICAL SPECTROSCOPY

4.1. Photon confinement due to nonlinear optical effect

The nonlinear scattering process, such as the coherent anti-Stoke Raman scattering (CARS), provides better confinement of light field than the linear scattering due to the nonlinear effects, and provides better contrast due to the suppression of the luminescence background. Thus, a combination of CARS with near-field microscopy, *i.e.*, tip-enhanced CARS (TE-CARS), can further confine the light field to the very apex of the metallic tip, providing better spatial resolution along with high contrast due to the suppressed background. This technique has been applied to image adenine molecules [10], and a high quality image with a spatial resolution of 15 nm was obtained. This technique is proved to be successful for high quality imaging, particularly, of biomolecules.

Nonlinear optical effects contribute to spatial confinement of photons in a smaller volume than the size of the diffraction-limited focal spot. The intensity of the nonlinear effects is proportional to the high-order powers of the excitation

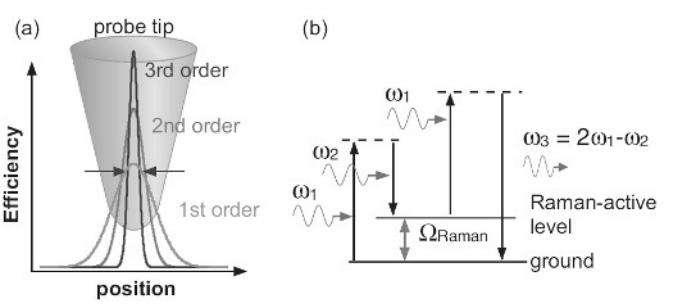

Fig. 5. (a) Illustration of spatial confinement of the excitation efficiency of high-order nonlinear effects. (b) Energy diagram of the CARS process.

light intensity. The spatial distribution of the signal emission (harmonic signal, two photon excited fluorescence, etc.) becomes narrower than the intensity distribution of the excitation field. This leads to the reduction of the effective volume of light-matter interaction beyond the diffraction limit. As illustrated in Fig. 5(a), higher-order optical effects give much finer spatial response. So far, many types of microscopies and fabrication methods using nonlinear optical effects have been reported [22,23]. The tip-enhanced near-field microscopy also gets benefited from the nonlinear effects. Because of the nonlinear responses, even a small enhancement of the excitation field could lead to a huge enhancement of the emitted signal, allowing a reduction of the far-field background.

4.2. Tip enhanced coherent anti-Stokes Raman scattering

In order to realize tip-enhanced nonlinear molecular-vibration spectroscopy, CARS spectroscopy is employed, which is one of the most widely used nonlinear Raman spectroscopies [24]. CARS is a four-wave mixing spectroscopic method, which includes a pump field (ω_1), a Stokes field (ω_2; $\omega_2 < \omega_1$), and a probe field ($\omega' = \omega_1$), and induces a non-linear polarization at the frequency of CARS, as shown in Fig. 5(b). When the frequency difference of ω_1 and ω_2, *i.e*, ($\omega_1 - \omega_2$), coincides with one of specific molecular vibrational frequencies of a given sample, the anti-Stokes Raman signal is resonantly generated. CARS spectroscopy is sensitive to molecular species and molecular conformation, resulting in a method of molecule identification without staining. As a CARS spectrum is obtained by scanning the frequency difference between two lasers, a high-resolution spectrometer is not required. Biological samples often have strong autofluorescence which overlaps with Stokes-shifted Raman scattering. Since the frequency of CARS is higher than those of the excitation lasers, CARS emission is separable from fluorescence. Although CARS

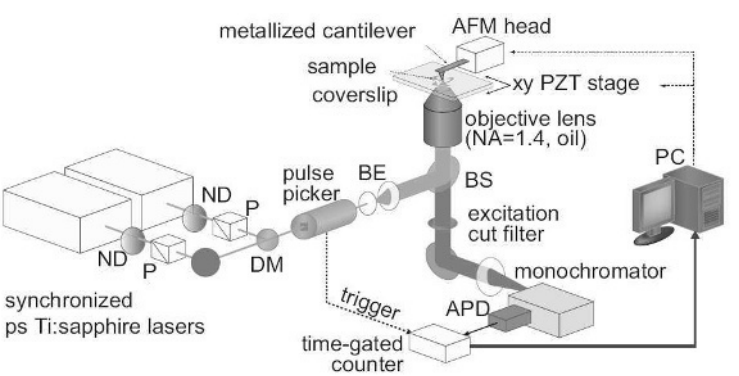

Fig. 6. A schematic for the experimental setup of TE-CARS microscopy.

spectroscopy has the above mentioned advantages, it has not been utilized for microscopy since the report of CARS microscopy by Duncan et al. in 1982 [25]. Phase matching is required for CARS, and consequently it was thought to be difficult that high spatial resolution consists with the phase matching condition.

Recently several scientists have reported that tight focusing of the excitation fields with a high-NA objective lens can achieve CARS microscopy with three-dimensional imaging capability at a submicron scale [26,27]. The phase matching condition can be satisfied automatically in the focused fields of multiple angles [28]. In other words, the phase matching condition is not necessary to be considered when the CARS polarizations are generated only in a volume smaller than the propagation wavelength of CARS light [29,30]. In our previous work, CARS was strongly amplified by isolated gold nanoparticles, which verified the possibility of the local enhancement of CARS by a metallic nano-structure [31]. Based on the concept mentioned above, one can observe CARS signals generated by the enhanced electric field at a metallic tip end of nanometric scale [32]. We have proposed a combination of the third-order nonlinear optical effect with the field enhancement effect of a metallic tip, that is, a technique for vibrational nano-imaging with TE-CARS. The alternative type of NSOM using an aperture-type probe was previously combined with CARS spectroscopy by Schaller et al. [26], where they employed a fiber probe for the signal collection of CARS excited by an external illumination and demonstrated chemical selective imaging of a biological sample. The use of tip-enhancement effect is, however, more advantageous with respect to spatial resolution, and is indispensable for observation of small number of molecules. The backscattered component of the enhanced scattered light can be efficiently collected with the high-NA focusing lens. By scanning the sample stage, while keeping the tip at the focused spot, one can acquire two-dimensional TE-CARS images of a specific vibratioanal mode with a high spatial resolution that is determined by the size of the tip end rather than the diffraction limited focused spot.

4.3. Experimental Setup for TE-CARS

Figure 6 shows the experimental system of TE-CARS microscopy [32]. The system mainly consists of an excitation laser, an inverted microscope, an AFM using a silver-coated probe, and a monochromator. Two mode-locked Ti:sapphire lasers (pulse duration: 5 ps, spectral band width: 4 cm^{-1}, repetition rate: 80 MHz) were used for the excitation of CARS. The ω_1 and ω_2 beams were collinearly combined in time and space, and introduced into the microscope with an oil-immersion objective lens (NA =1.4) focused onto the sample surface. The repetition rate of the excitation lasers was controlled by an electro-optically modulated pulse picker. The backscattered CARS emission enhanced by the metal-coated tip was collected with the objective lens and detected with an avalanche-photodiode based photon-counting module through an excitation-cut

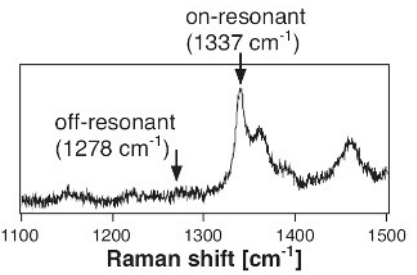

Fig. 7. A spontaneous Raman spectrum of DNA base. The two frequencies indicated by the arrows were selected for the off- and on-resonant TE-CARS imaging experiments

filter and a monochromator. The pulse signal from the APD was counted by a time-gated photon counter synchronously triggered with the pulse picker, which effectively reduces the dark counts down to almost 0 counts/sec.

4.4. TE-CARS Imaging of DNA Clusters

The DNA molecules of poly(dA-dT) aggregated into clusters were used as a model sample for CARS imaging. The poly(dA-dT) solution in water (250 μg/ml) was cast and dried on a glass substrate at the room temperature with the fixation time of 24 hours. The dimensions of the clusters were typically 20 nm in height and 100 nm in width. The frequency difference of the two excitation lasers for CARS imaging was set to 1337 cm^{-1}, corresponding to a Raman mode of adenine (ring-stretching mode of diazole) [17], by tuning the excitation frequencies ω_1 and ω_2 to be 12710 cm^{-1} (ω_1: 786.77 nm) and 11373 cm^{-1} (ω_2: 879.25 nm), respectively. After the imaging in this resonant condition, the frequency of ω_2 was changed such that the frequency difference corresponded to none of the Raman-active vibrations. Figure 7 shows a spontaneous Stokes Raman spectrum of a DNA sample in the fingerprint region. The solid arrows on the spectrum denote the frequencies adopted for the "on-resonant" and "off-resonant" conditions in TE-CARS imaging.

Figure 8 shows CARS images of the DNA clusters obtained by our experimental system. Figures 8(a) and (b) are the TE-CARS image in the on-resonant condition ($\omega_1 - \omega_2 = 1337$ cm^{-1}) and the simultaneously acquired topographic AFM image, respectively. The DNA clusters of about 100 nm diameter are visualized in Fig. 8(a). The two DNA clusters with separation of about 160 nm are clearly distinguished by the TE-CARS imaging. This indicates that the CARS imaging can successfully achieve the super-resolving capability beyond the diffraction limit of light. In the off-resonant condition ($\omega_1 - \omega_2 =$ 1278 cm^{-1}), CARS signals mostly vanished in Fig. 8(c). Figures 8(a) and (c) verify that vibrationally resonant CARS is emitted from the DNA molecules at a specific frequency. However, a slight trace of the clusters could be seen in the

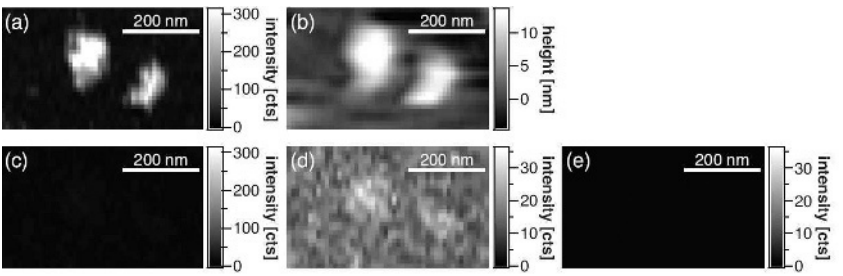

Fig. 8. CARS images of the DNA clusters. (a) Tip-enhanced CARS image at on-resonant frequency (1337 cm^{-1}), and (b) the simultaneously obtained topographic image. (c) TE-CARS image at the off-resonant frequency (1278 cm^{-1}). (d) The same image as (c) shown with a different gray scale. (e) CARS image of the corresponding area obtained without the silver tip. The scanned area was 500 nm by 300 nm. The number of photons counted in 100 ms was recorded for one pixel. The acquisition time for one image was 3 minutes. The average powers of the ω_1 and ω_2 beams were 30 μW and 15 μW at the 800 kHz repetition rate.

off-resonant condition in Fig. 8(d), which is the same as Fig. 8(c) but is shown with a different gray scale. This can be caused by both the frequency-invariant (non-resonant) component of the nonlinear susceptibility of DNA [24] and the topographic artifact [33]. Figure 8(e) is a CARS image at the on-resonant frequency which was obtained after retracting the tip off the sample. The CARS signal was not detected in the CARS image without the silver tip, which confirms that the CARS polarization in Fig. 8(a) is effectively induced by the tip-enhanced field. The background signal seen in Fig. 8(d) is attributed to both local four-wave-mixing emission of the silver probe due to its nonlinear susceptibility and to the white light continuum of silver due to electron-hole recombination [34,35]. These two components compete with the CARS process and degrade the image contrast and signal-to-noise ratio. Further, they subsequently limit the smallest number of molecules that can be observed. In this experiment, however, the TE-CARS signal intensity largely surpasses the background because the number of molecules in the excited volume is enough to induce the signal.

In order to assess the capability of the sensitivity of the TE-CARS microscopy, we prepared a DNA network of poly(dA-dT)-poly(dA-dT) [36]. DNA (poly(dA-dT)-poly(dA-dT)) dissolved in water (250 mg/ml) was mixed with MgCl2 (0.5 mM) solution, then the DNA solution was cast on a coverslip and blow-dried after the fixation time of 2 hours. Mg^{2+} has a role for the linkage between DNA and oxygen atoms of the glass surface. Figure 9(a) shows a typical topographic image of the DNA network sample. The DNA network consists of bundles of DNA double-helix filaments aligned parallel on the glass substrate. Since the diameter of single DNA double-helix filaments is about 2.5 nm, the height of the bundle structures is ~ 2.5 nm, and the width is from 2.5 nm

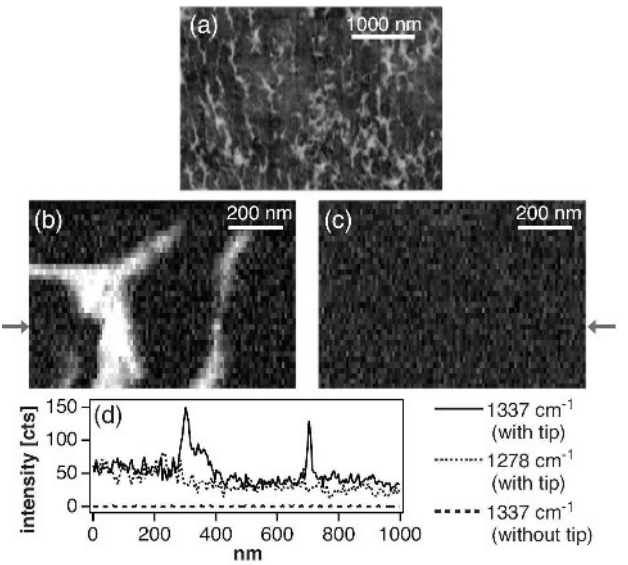

Fig. 9. TE-CARS images of the DNA network. (a) Topographic image of the DNA network. (b) TE-CARS image at on-resonant frequency (1337 cm^{-1}). (c) TE-CARS image at the off-resonant frequency (1278 cm^{-1}). (d) Cross sectional line profiles at y = 270 nm (indicated by the horizontal arrows). The scanned area is 1000 nm by 800 nm. The number of photons counted in 100 ms was recorded for one pixel. The acquisition time for one image was 12 minutes. The average powers of the ω_1 and ω_2 beams were 45 μW and 23 μW at the 800 kHz repetition rate.

(for single filaments) to a few tens of nanometers (for *ca*. 10 filaments). The TE-CARS images at the on- and off-resonant frequencies are shown in Figs. 9(b) and (c). The DNA bundles are observed at the resonant frequency in Fig. 9(b), while they cannot be visualized at the off-resonant frequency in Fig. 9(c). This indicates that the observed contrast is dominated by the vibrationally resonant CARS signals. Figure 9(d) shows one-dimensional line profiles at y = 270 nm (corresponding to the position marked by horizontal arrows in the figure), which were acquired with a step of ~ 5 nm. The line profile of far-field CARS acquired without the silver tip is also added for comparison. Only the TE-CARS in the on-resonant condition has peaks at the positions of x ~ 370 nm and x ~ 700 nm where adenine molecules exist in the DNA double helix, while the other line profiles do not sense the existence of the molecules. The full width at half maxima of the peak at x ~ 700 nm is 15 nm, which confirms that with the existing TE-CARS setup, we are able to obtain a special resolution down to 15 nm. This extremely high resolution is attributed to the combination of the near-field effects of TERS and the non-linearities of CARS. The intensity enhancement factor for each electric field is estimated to be about 100-fold. It

should be noted that this enhancement factor of the field intensity already includes the nonlinear effects of CARS. The estimated value of the enhancement factor (~100) is quite realistic and reasonable, as compared to previous numerical results [37,38], although this estimation is very much subject to the changes in each parameter with high-order dependency. If this value of field enhancement is used for the estimation of the enhancement factor for TERS intensity, it would be about 10000 times (second power of the intensity enhancement).

We also estimated the size of the locally excited volume of the DNA structure to be about 1 zeptoliter. The smallest detectable volume of DNA under the current experimental condition is estimated to be 1/4 zeptoliter, which is derived from the signal-to-noise ratio of 15:1 in Fig. 9(d) and the quadratic dependence of the CARS intensity on interaction volume. This indicates that our TE-CARS microscope is capable of sensing a vibrational-spectroscopic signal from an enormously small subzeptoliter volume.

REFERENCES

[1] H-J van Manen, Y. M. Kraan, D. Roos, and C. Otto, J. Phys. Chem. B, 108, (2004) 18762.
[2] H-J van Manen, Y. M. Kraan, D. Roos, and C. Otto, PNAS, 102 (2005) 10159.
[3] D. K. Veirs, J. W. Ager III, E. T. Loucks, and G. M. Rosenblatt, Appl. Opt., 29 (1990) 4969.
[4] K. Hamada, K. Fujita, M. Kobayashi, and S. Kawata, Extended Abstract of FOM 2006 (2006) 104.
[5] N. Hayazawa, Y. Inouye, Z. Sekkat, and S. Kawata, Opt. Commun., 183 (2000) 333.
[6] N. Hayazawa, Y. Inouye, Z. Sekkat, and S. Kawata, J. Chem. Phys., 117 (2002) 1296.
[7] N. Hayazawa, T. Yano, H. Watanabe, Y. Inouye, and S. Kawata, Chem. Phys. Lett., 376 (2003)174.
[8] P. Verma, K. Yamada, H. Watanabe, Y. Inouye and S. Kawata, Phys. Rev. B, 73 (2006) 045416.
[9] T. Yano, P. Verma, S. Kawata and Y. Inouye, Appl. Phys. Lett., 88 (2006) 093125.
[10] T. Ichimura, N. Hayazawa, M. Hashimoto, Y, Inouye and S. Kawata, Phys. Rev. Lett., 92 (2004) 220801.
[11] Y. Inouye, N. Hayazawa, K. Hayashi, Z. Sekkat, and S. Kawata, Proc. SPIE (1999) 40.
[12] T. Yano, Y. Inouye and S. Kawata, Nano Lett., 6 (2006) 1269.
[13] A. D. Becke, J. Chem. Phys., 98 (1993) 5648.
[14] C. Lee, W. Yang, and R. G. Parr, Phys. Rev. B, 37 (1988) 785.
[15] M. J. Frisch, G.W. Trucks, H. B. Schlegel, et al.: computer code GAUSSIAN98 Revision A.9 (1998)
[16] C. Otto, T. J. J. van den Tweel, F. F. M. de Mul, et al., J. Raman Spectrosc., 17 (1986) 289.
[17] H. Watanabe, Y. Ishida, N. Hayazawa, Y. Inouye and S. Kawata, Phys. Rev. B 69 (2004) 155418.
[18] J. R. Ferraro: *Vibrational Spectroscopy at High External Pressures* (Academic, New York 1984) p. 2

[19] R. A. Crowell and E. L. Chronister, Chem. Phys. Lett., 195 (1992) 602.
[20] S. A. Hambir, J. Franken, D. E. Hare, et al., J. Appl. Phys., 81 (1997) 2157.
[21] K. Hoogsten, Acta Crystallogr., 12 (1959) 822.
[22] W. Denk, J. H. Strickler, and W. W. Webb, Science, 248 (1990) 73.
[23] S. Kawata, H. B. Sun, T. Tanaka, and T. Takada, Nature, 412 (2001) 667.
[24] Y. R. Shen, '*Principles of Nonlinear Optics*', Wiley, New York, (1984).
[25] M. D. Duncan, J. Reintjes, and T. J. Manuccia, Opt. Lett., 7 (1982) 350.
[26] R. D. Schaller, J. Ziegelbauer, L. F. Lee, L. H. Haber, and R. J. Saykally, J. Phys. Chem. B, 106 (2002) 8489.
[27] A. Zumbusch, G. R. Holtom, and X. S. Xie, Phys. Rev. Lett., 82 (1999) 4142.
[28] M. Hashimoto, T. Araki, and S. Kawata, Opt. Lett., 25 (2000) 1768.
[29] M. Hashimoto and T. Araki, J. Opt. Soc. Am. A, 18 (2001) 771.
[30] J.-X. Cheng, A. Volkmer, and X. S. Xie, J. Opt. Soc. Am. B, 19 (2002) 1363.
[31] Z. Xiaolin and R. Kopelman, Ultramicroscopy, 61 (1995) 69.
[32] T. Ichimura, N. Hayazawa, M. Hashimoto, Y. Inouye, and S. Kawata, Appl. Phys. Lett., 84 (2004) 1768.
[33] B. Hecht, H. Bielefeldt, Y. Inouye, D. W. Pohl, and L. Novotny, J. Appl. Phys., 81 (1997) 2492.
[34] G. T. Boyd, Z. H. Yu, and Y. R. Shen, Phys. Rev. B, 33 (1986) 7923.
[35] J. P. Wilcoxon and J. E. Martin, J. Chem. Phys., 108 (1998) 9137.
[36] S. Tanaka, L. T. Cai, H. Tabata, and T. Kawai, Jpn. J. Appl. Phys., 40 (2001) L407.
[37] H. Furukawa and S. Kawata, Opt. Commun., 148 (1998) 221.
[38] J. T. Krug II, E. J. Sánchez, and X. S. Xie, J. Chem. Phys., 116 (2002) 10895.

This page intentionally left blank

Handai Nanophotonics, Volume 3
H. Masuhara, S. Kawata and F. Tokunaga (Editors)

Chapter 5

Enhanced photothermal spectroscopy for observing chemical reactions in biological cells

A. Harata

Department of Molecular and Material Sciences, Faculty of Engineering Sciences, Kyushu University, Kasugakoen 6-1, Kasuga-shi, Fukuoka 816-8580, JAPAN

1. SENSITIVE DETECTION OF NONFLUORESCENT BIOMOLECULES

1.1. Introduction

One of the ultimate goals of analytical biochemistry is to detect certain target molecules in a living cell and observe molecular behaviour *in-situ*. In the 1990s, it was demonstrated that target molecules flowing in a dilute liquid solution can be counted one by one [1-4]. Recently, techniques based on the single molecule detection of biological compounds have started to provide a variety of new and essential information on the way life works [5-6]. However, target molecules for single molecule detection are limited to exceptionally highly fluorescent compounds, even for molecule detection in a simple solution.

The majority of biologically important chemicals, such as amino acids, nucleotides, proteins, and hormones are natively nonfluorescent. As for nonfluorescent single molecule detection, electrochemical methods can detect single molecules in a liquid solution [7], and surface-enhanced Raman scattering may be applied if the adsorbed molecule on a silver nanoparticle is the target [8]. However, these methods have quite limited fields of applications. The development of a method for nonfluorescent single molecule detection in and around a living cell should be a great target for molecular biology. Photothermal spectroscopy-based techniques have great potential for the sensitive detection of nonfluorescent molecules.

1.2. Limit of detection in photothermal methods

Photothermal measurements are among the most sensitive methods for detecting chemical compounds, especially, non-luminescent substances, in both gas and condensed phases [9]. Photothermal methods (thermal lens spectroscopy,

photoacoustic spectroscopy, photothermal deflection spectroscopy, and others) are based on heat generation in a light-illuminated medium via optical absorption and subsequent nonradiative relaxation. The signal magnitude is directly related to the amount of generated heat and the increases in temperature. Better sensitivity can be achieved by stronger excitation, which causes a larger rate of heat-generation, and by allowing heat to accumulate for a longer period, which causes a larger increase in temperature. Thus, generally, the signal of photothermal measurements for a dilute solution linearly increases with the excitation light intensity. However, optical saturation of absorption easily occurs under a focused laser beam. The absorption saturation settles the upper limit of the photo-induced heat-generation rate per single target molecule and, thus, limits the detection sensitivity. For photothermal methods, it is generally recognized that some technical improvements are required to count certain target molecules, especially nonfluorescent molecules, even in a simple liquid solution.

1.3. Thermal lens observation of biological specimens

The thermal lens method, one of the photothermal methods, is suitable for observing substances in biological cells because it is based on the optical excitation and detection of photothermal effects and is easy to combine with an optical microscope. Using microscopic thermal lens methods, amino acid stained with a yellow dye of trinitrobenzensulfonate sodium salt in a single biological cell was determined [10]. The special distributions were observed of gold nanoparticles-labelled antibodies in cells [11] and an acid dye-stained surfactant in the cross-section of a human hair [12].

In the majority of biologically important chemicals, such as amino acids, nucleotides, proteins, and hormones, photo-absorption is limited to the ultraviolet wavelength, which presents a significant disadvantage to the application of the thermal lens method to *in situ* observations of molecules in and around biological cells. There is no high-performance ultraviolet laser light source, although a laser light source would strongly influence the entire performance of the thermal lens measurements. It was only in recent work that an ultraviolet laser light source of the fourth harmonics of pulsed Nd: YAG laser at 266 nm was used for quantitative analysis by thermal lens detection [13].

Regarding the sensitivity of thermal lens detection, a small volume of heat accumulation has a good effect because the spatial gradient of the refractive index, which is coupled to the temperature gradient by the thermooptic-coupling constant, is important. Crossed-beam and collinear configurations have been applied to probe molecules in small volumes. The detection limit of target molecules in a liquid solution at room temperature has been improved to the level of 100 molecules in 200 fL [14] and 1.3 fL [15], 0.5 molecules in 3 fL [16], and 0.34 molecules in 6 fL [17] of the probe volume. However, molecules in a liquid move around so fast that these values of the molecule numbers are

typically time-averaged over 4 s, while a single molecule can pass through the probe volume in several milliseconds. As for the one-by-one detection of nonfluorescent substances in a liquid, the counting of single colloidal silver particles with a diameter of 10 nm has been demonstrated by thermal lens measurements under a microscope [18]. The sensitivity of the thermal lens measurement is still insufficient for the detection of a single molecule.

1.4. Enhanced photothermal spectroscopy for biological cells

There are two points to be made regarding technical improvements in photothermal methods for the observation of biological cells. They involve, first, ultraviolet laser excitation and, secondly, improvement of the sensitivity beyond the limitation imposed by absorption saturation. A sensitivity improvement can be achieved with a signal enhancement by multi-colour excitation, as described in Section 2. An ultraviolet tunable coherent light source is obtained from the quasi-continuous wave emission of a femtosecond mode-locked Ti: sapphire laser as second, third, and fourth harmonics. Their combination is attractive to realize enhanced photothermal spectroscopy for the observation of chemical reactions in biological cells. Below are the descriptions of our trials involving enhanced photothermal spectroscopy.

2. PHOTOTHERMAL SIGNAL ENHANCEMENT

2.1. Saturation of photo-absorption and a photothermal signal

Absorption saturation occurs when populations of a compound are balanced between the ground state and an excited state, coupled together under a strong resonant light illumination. At that time, absorbance A is dependent on the light intensity I. In a simple two-level model, $A(I) = A_0 / (1 + I / I_{sat})$ where A_0 is the normal absorbance under a week light illumination condition and I_{sat} ($= h\nu / 2\sigma\tau$) is a measure of the light intensity when the absorption saturation becomes significant. $h\nu$ is the photon energy, σ is the absorption cross-section at the resonant wavelength, and τ is the mean lifetime of the excited state.

The photothermal signal intensity Q is proportional to the amount of heat generated by photoexcitation and relaxation; as a result, Q is proportional to $I(1 - 10^{-A})$. When A is small, as in the case of a low-concentration liquid solution, $Q \propto IA$. Generally, the signal Q increases by increasing I, which makes highly sensitive detection possible. However, the sensitivity improvement by increasing I alone presents an inevitable limitation because the absorption saturation limits IA to the maximum value, $I_{sat} A_0$. In a real molecular system, the situation is not simple, and the energy levels are complex. However, the absorption saturation does limit the photothermal signal intensity.

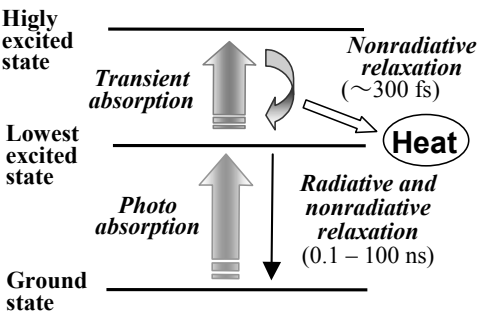

Fig. 1. Principle of photothermal signal enhancement. Transient absorption and successive relaxation are used.

2.2. Enhancement of the photothermal signal

To obtain a large photothermal signal beyond the absorption saturation limit, it is possible to implement chemical modifications and the enzyme-induced amplification of photo-absorbing chromophores; however, it is simpler to increase the number of photons absorbed per single target molecule. The use of transient absorption (optical absorption by molecules in photoexcited states) appears to be the best method. The scheme of the signal enhancement is shown in Fig. 1.

Heat generation via transient absorption has been observed and applied to investigate the dynamics of molecules in a dilute solution, in which sequential pulsed excitation was used in combination with photothermal detection [19-22]. Fortunately, a high efficiency of photon energy conversion into heat is expected for the transient absorption of visible light, because the highly photoexcited molecules in liquid generally relax with a small yield of photon emission, extremely rapidly to vibrationally and electronically lower excited states unless the photon energy is high enough to cause the molecules to ionize or dissociate into fragments.

Thermal lens signal enhancement using transient absorption has been demonstrated by two-colour sequential double-pulsed excitation [23] and by two-colour continuous-wave excitation [24] of solute molecules in liquid solutions. The signal intensity under certain conditions was one or two orders of magnitude larger than that expected from the ground-state absorption.

2.3. Experiment on thermal lens signal enhancement

The experimental setup used for the demonstration [24] is shown in Fig. 2. A continuous-wave diode laser emitting intensity-modulated violet light at 409 nm was used as a pump beam. A second harmonics of a Nd: YAG laser at 532 nm was used as the second pump beam. The thermal lens formed in a liquid solution flowing in a capillary cell was monitored with another diode laser

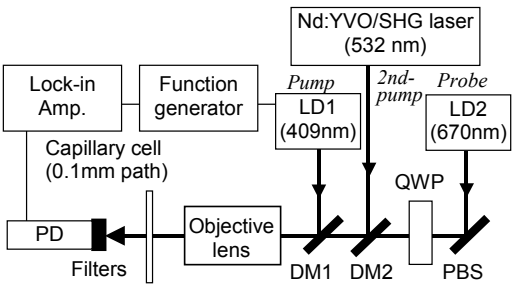

Fig. 2. Schematic illustration of the experimental setup for thermal lensing signal enhancement by two-colour continuous wave-laser excitation. DM1, dichroic mirror reflecting the 409 nm beam and transmitting the 532 nm and 670 nm beams; DM2, dichroic mirror reflecting the 532 nm beam and transmitting the 670 nm beam; LD1, laser diode emitting an intensity-modulated pump beam; LD2, laser diode emitting a continuous wave linearly polarized probe beam; PBS, polarizing beam splitter; PD, photodiode; and QWP, quarter-wave plate. A set of PBS and QWP was used for the reduction of the back scattering of the probe beam from the capillary cell and the optics.

emitting red light at 670 nm. The three-colour beam was focused by a microscopic objective lens (magnification, 40; numerical aperture, 0.65; working distance 0.5 mm) to the rectangular capillary cell with an optical path length of 0.1 mm and a width of 1 mm. A two-phase lock-in amplifier was used to measure the signal amplitude synchronized with the modulation of the pump beam at 409 nm. In this setup, no substantial signal was observed when the pump beam was turned off even under the second-pump beam illumination.

The samples used were iso-propanol solutions of naphthacene or 9,10-diphenylanthracene. These compounds have absorption at 409 nm, no significant absorption at 532 nm, and transient absorption at 532 nm.

Figure 3 illustrates the pump beam-power dependence of the thermal lens signal intensity under illumination of the second-pump beam with different powers. A linear increase of the signal intensity with the pump beam power increase was seen at each second-pump power. The larger the second-pump power from 0 to 3.6 W was, the larger the signal intensity obtained under a certain pump beam power condition was, which was noteworthy. The thermal lens signal was enhanced by the second-pump beam irradiation. It was experimentally confirmed that different chemical compounds have different degree of enhancement, a phenomenon that is thought to depend on a transient absorption cross-section.

2.4. Estimation of the transient absorption wavelength

In applying the enhanced thermal lens measurement to the analysis of a biological sample, it is important to know the absorption wavelength of the

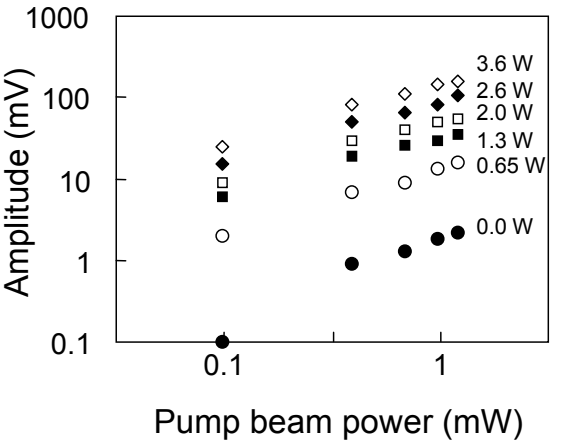

Fig. 3. Pump beam-power dependence of the modulation amplitude of thermal lensing signal under illumination of the continuous wave second-pump beam with different powers indicated (log-log plot). The sample was a 3.2 x 10^{-5} M solution of naphthacene in iso-propanol with 4.6 x 10^{-4} absorbance at 409 nm (optical path, 0.1 mm). The modulation frequency was 6.0 kHz.

target compound. It is easy to measure an absorption spectrum; a theoretical calculation on the basis of quantum chemistry can yield a good estimation at present. Unfortunately, the measurement of a transient absorption spectrum is not easy, especially when the ground-state absorption is in the ultraviolet region and the lifetime of an excited state is smaller than several nanoseconds. There are few reports on the transient absorption spectra of amino acids in a picosecond time regime. The theoretical calculation of a transient absorption spectrum is still unreliable. This seriously limits the application of enhanced thermal lens measurements.

Our research group has tried to determine whether or not biological compounds have transient absorption at a visible wavelength by using density function calculation [25]. Figure 4 contains the absorption spectra of serine and tryptophane. A fluorescence spectrum with a peak at 320 nm is shown for tryptophane. Serine is not fluorescent. The measured absorption spectra (curves) correspond well with the calculated results (bars). There are many energy levels for each molecule above the lowest excited state, and it is not unusual that a couple of states have an energy difference corresponding to the photon energy of visible light. Considering that the selection rule does not dominate the optical transition for a large molecule with low symmetry, it is not unreasonable to expect these molecules to have transient absorption at visible and near-infrared wavelengths.

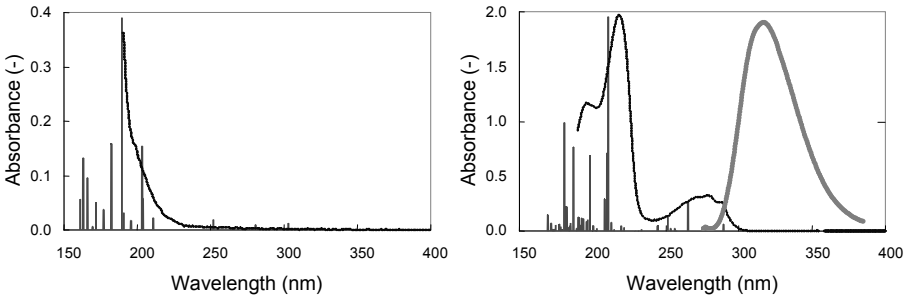

Fig. 4. Absorption spectra of serine (left) and tryptophane (right). The fluorescence spectrum having a peak at 320 nm is shown for tryptophane. The curves are the measured results for aqueous solutions. The bars are calculated with the density function method B3LYP with a base set of 6-31+G(d). For tryptophane, a solvent effect is taken into account [25].

3. ULTRAVIOLET-EXCITATION MICROSCOPIC THERMAL LENS MEASUREMENTS

3.1. Ultraviolet laser source and microscopic thermal lens measurements

As shown in Fig. 4, amino acids have optical absorption only in the ultraviolet wavelength. Biological compounds frequently have no substantial absorption at visible wavelengths. In analyzing a biological compound by photothermal measurements, an ultraviolet laser light source is important.

At the ultraviolet wavelength, a pulsed laser source with a repetition rate lower than 10 kHz is relatively easily available, whereas a continuous wave laser has greater limitations. Some pulsed lasers have wavelength tunability even at the ultraviolet region. However, the use of pulsed light is unsuitable for microscopic thermal lens detection because the pulsed laser easily damages the sample as well as the quartz glass holdings when high intensity light is applied to obtain a large thermal lens signal.

For practical reasons, it is important to use a small probe volume in order to achieve a high spatial resolution and minimize any background signal from surrounding materials and trace contaminants. A wide range of chemical and biological applications of microscopic thermal lens measurements with visible laser excitation have been demonstrated using a thermal-lens microscope [11-13, 26-29], in which microchip technology is sometimes combined with the thermal lens detection [27-29].

Excitation by continuous-wave lasers is strongly desirable for microscopic thermal lens detection. As for ultraviolet continuous-wave lasers, the second harmonics of an Argon ion laser at 244 and 257 nm and the forth harmonics of a Nd: YAG laser at 266 nm are available, although they have no wavelength

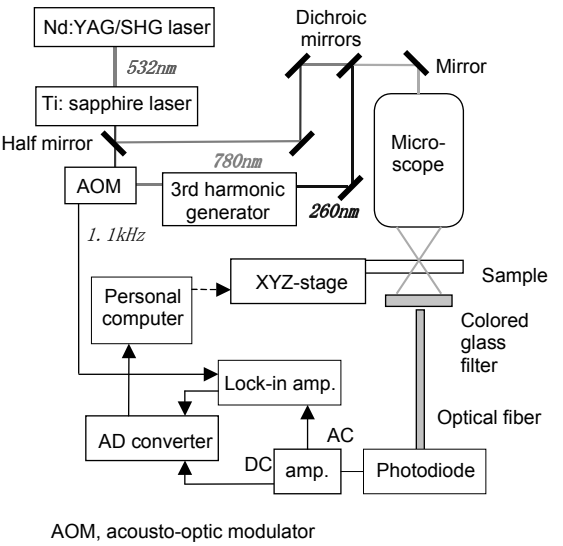

Fig. 5. Experimental setup for ultraviolet-laser excitation microscopic photothermal lens imaging. The thermal lens signal is obtained from the AC output of the photodiode, while the transmitted light intensity is monitored with the DC output.

tunability. The quasi-continuous wave of the third and fourth harmonics of a mode-locked Ti: sapphire laser seems to have the best performance.

3.2. Ultraviolet excitation microscopic thermal lens imaging

An ultraviolet-laser excitation microscopic photothermal lens imaging system has been designed and constructed for observing chemical compounds in biological cells [30].

A schematic illustration of the experimental setup is shown in Fig. 5. The third harmonics of a Ti: sapphire laser was used as the excitation light source. A thermal lens was generated in a sample on a slide glass by the third harmonics (260nm, <1mW). The thermal lens signal was probed with the fundamental emission (780nm, <3mW) of the Ti: sapphire laser. Both excitation and probe laser beams were focused with a reflection-objective lens (magnification x20, numerical aperture 0.38). The excitation beam was intensity-modulated at 1.1 kHz with an acousto-optic modulator. The probe beam passed through the sample. The light intensity at the probe beam center was monitored with a photodiode connected to an optical fibre. A coloured glass filter set between the sample and the optical fibre made the excitation beam block. The thermal lens signal monitored with a lock-in amplifier was obtained from the AC output. The DC output of the photodiode was used to monitor the transmitted light intensity.

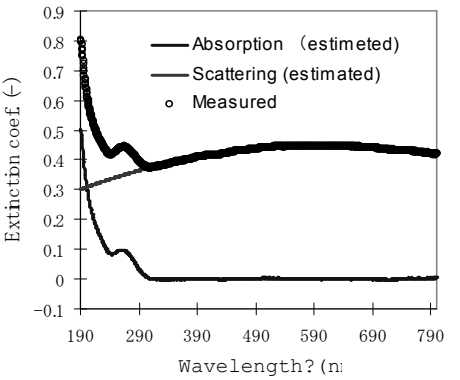

Fig. 6. Extinction spectrum of bulk yeast fungus cells.

The sample was set on an XYZ-mechanical stage that was compute-controlled using a laboratory-made software. Typically, a 20 μm x 20 μm area was observed with 0.5 μm of a scanning step. Three images, namely, those of the thermal lens amplitude and phase and transmitted probe beam intensity were simultaneously obtained.

The sample used was yeast fungus cells on a quartz plate under a quartz cover slip (0.7 mm thick). Commonly used slide glasses and cover slips generate a strong thermal lens signal, while the quartz glasses generate no substantial background signal.

3.3. Extinction spectrum of yeast fungus cells

The ultraviolet-visible absorption (extinction) spectrum of the yeast fungi in water showed optical absorption at a wavelength below 305 nm and a scattering peak at 600 nm (Fig. 6).). It is expected that the excitation light at 260 nm is absorbed and scattered by the yeast cells while the probe beam at 780 nm is simply scattered.

3.4. Photothermal images of cells

Photothermal images of the yeast cells were obtained using the quarts glasses for sample support. Figure 7 shows a photothermal in-phase image (a) and a photothermal out-of-phase image (b) of the yeast cells. The photothermal amplitude Q and phase P are calculated as $Q = \sqrt{S_{IP}{}^2 + S_{OP}{}^2}$ and $P = \arctan(S_{OP} / S_{IP})$, where S_{IP} and S_{OP} are the in-phase and out-of-phase signal intensities, respectively. Figure 8 shows a photothermal amplitude image (a) and a phase image (b) of the yeast cells along with a transmitted light intensity image (c) measured simultaneously for the 784 nm probe beam. For easy viewing, a birds' eye view plot of Fig. 8 (a) is given in Fig. 9.

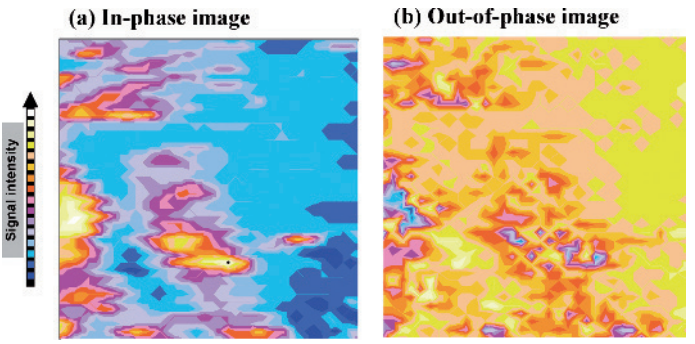

Fig. 7. Photothermal images of yeast fungus cells: (a), in-phase image; (b), out-of-phase image. The signal maxima and minima are 3.2 and –0.66 (arb. units) in (a) and 0.36 and –0.80 (arb. units) in (b), respectively. Excitation beam, 261 nm; probe beam, 784 nm; area size, 20 μm x 20 μm.

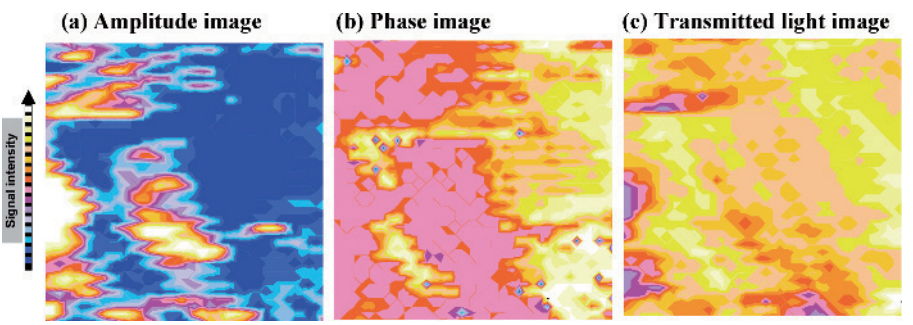

Fig. 8. Photothermal amplitude image (a), phase image (b), and transmitted light image (c) of yeast fungus cells. Excitation beam, 261 nm; probe beam, 784 nm; area size, 20 μm x 20 μm.

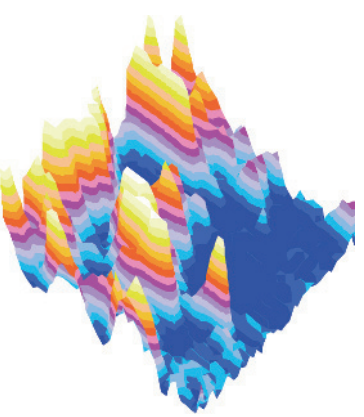

Fig. 9. Photothermal amplitude images of yeast fungus cells: a birds' eye view of Fig. 8 (a).

Features with the size of several micrometers are seen in these images, corresponding to the size of spherical yeast cells with diameters of approximately 5μm. Similar features have not been observed in samples that do not contain yeast cells. In a comparison of the images in Figs. 8(a) and 8(c), a tendency is observed that a position with a larger scattering at 784nm has a larger photothermal signal generated at 261 nm. This result is consistent with the extinction spectrum in Fig. 6 if the photo-absorption of yeast cells is monitored as a photothermal signal. The photothermal amplitude image is concluded to show the spatial distribution of yeast cells, although the position of each cell was not confirmed by conventional optical microscope observation in the present measurements.

The phase of the thermal lens signal measured under a microscopic focusing condition could depend on a variety of factors: refractive index inhomogeneity in the sample, causing a light path change and resulting in light intensity changes at the photo-detector; the dichroic property of the sample, causing a small change in the overlap of two beams; and the thickness between two quartz glasses, affecting the transmittance of the probe beam. However, in principle the phase shift reflects how photo-induced heat accumulates around the focal point of the pump beam so that it depends on local thermal properties such as heat capacity and thermal conductivity. It is considered that the image in Fig. 8(b) shows the distribution of the thermal properties. When compared with those in the position without cells (right-hand side), the small phase values around the positions of the yeast cells (left-hand side) are considered to indicate efficient heat accumulation around the yeast cells.

3.5. Limit of detection for a thermal lens probed with a quasi-continuous wave

The limit of detection has been reported [31] for thermal lens measurements using a quasi-continuous wave probe laser, in which a similar system to the microscopic thermal lens imaging described in Section 3.2. was used, except for the use of the second harmonics of a mode-locked femtosecond Ti: sapphire laser (repetition rate, 76 MHz) as the pump beam. The sample of an aqueous solution of auramine-O in a flow cell with an optical path length of 1 mm (detection volume, 100 pL) was excited with the 400 nm pump beam (10 mW), and the thermal lens was monitored with the 800nm fundamental emission (3 mW) of the laser. The modulation frequency was 1 kHz. The limit of detection (2σ) was 3×10^{-7} M as the concentration, 30 amol as the amount in the detection volume, and 3×10^{-4} as the absorbance. These values are comparable to the limit of detection of thermal lens measurements for aqueous solutions. It was concluded that a quasi-continuous wave probe of a thermal lens has similar performance to a continuous wave probe.

3.6. Light-induced damage to biological cells

It is generally believed that ultraviolet light irradiation easily damages biological cells, causing them to stop activity. Pump-beam intensity should be as week as possible, especially, in the ultraviolet excitation thermal lens imaging of biological cells. However, a larger signal-to-noise ratio under larger pump beam intensity makes rapid imaging possible. As a result, a quantitative evaluation of light irradiation damage is important to optimize the experimental conditions.

A trial has been started to evaluate ultraviolet irradiation damage to yeast cells [32]. Yeast cells spread over an agarose culture medium were irradiated with the third harmonics of a nanosecond pulsed Nd: YAG laser at 355 nm. Colony formation after 2 days of cultivation in a 30 ºC incubator was checked. It was found that the percentages of perishing yeast cells were linearly dependent on the irradiation time of the ultraviolet laser and that, at a fluence of 46 mJ/cm^2 per pulse, half of yeast cells survived after 6x10^3 pulses. Although it would appear experimentally that the yeast cells were able to withstand ultraviolet light irradiation at 355 nm, the wavelength dependence should be evaluated in the future.

3.7. Crossed-beam excitation and signal enhancement

In the thermal lens detection, the collinear configuration of the pump and probe beams sometimes presents a problem in the selection of a focusing lens because all optical glasses have a dichroic property, which results in chromatic aberration. A reflection objective lens without chromatic aberration has a low damage threshold to a laser. Transmittance of the focusing optics gives rise to another problem in the ultraviolet wavelength region. These problems become serious in enhanced photothermal measurements using three laser beams of different colours.

A crossed beam configuration of the pump and probe beams seems to be suitable for enhanced photothermal measurements because the degree of freedom in the optical setup is large. A crossed beam setup for thermal lens signal enhancement has been developed and tested [33]. A similar experimental setup to that shown in Fig. 2 was used, but the pump beam at 409 nm was not collinear with the second-pump and probe beams. It was focused on the capillary cell perpendicularly to the probe beam. A 20-fold enhancement has been demonstrated with the crossed beam configuration.

3.8. Combination to a micro-HPLC

Ultraviolet excitation thermal lens measurements have been applied to a separation analysis with a micro-HPLC, in which the crossed beam excitation configuration was used and signal enhancement was studied [34]. The drain of a micro-HPLC system (micro21, Jasco) equipped with a CrestpakC18 column

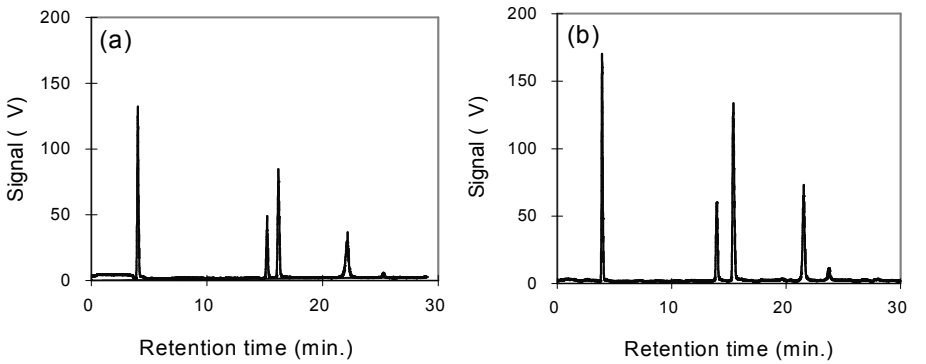

Fig. 10. Chromatograms of zolpidem and its metabolites, M-I and M-II, detected by thermal lens measurements; (a) without, and (b) with enhancement induced by a second-pump beam. The peaks at, 15, 16, and 22 min are attributed to M-I, M-II, and zorpidem, respectively. Pump wavelength, 266 nm; second-pump wavelength, 532 nm; probe wavelength, 672 nm.

(150 mm x 0.5 mm) was connected to the capillary detector of the crossed beam thermal lens system. Zolpidem, a sleep inducing drug, and its metabolites (M-I and M-II) were well-separated and detected at a pump wavelength of 266 nm and a probe wavelength of 672 nm, as shown in Fig. 10. The signal enhancement at the second-pump beam intensity of 2 W at 532 nm was only approximately 2 times for these compounds, as shown in Fig. 10(b). The small enhancement seemed to be due to the small cross-sections of the transient absorption at 532 nm for these compounds. Different degrees of signal enhancement for these compounds supported the supposition.

For the chromatographic separation, a gradient elution was used with two eluents: (eluent A) 10 mM ammonium acetate with pH 6.8 and (eluent B) acetonitrile. The program of the gradient elution was with 15% eluent B for 0-1 min; from 18% to 80% linear gradient of eluent B for 1-20 min; 80% eluent B for 20-30 min. Generally, thermal lens detection is unfit for gradient elution because a different refractive index of each elute causes a different optical path of the probe beam, resulting in a large background signal. It is notable that the background signal is small in Fig. 10. A good mixing of the eluents is achieved with the micro-HPLC. It is demonstrated that a combination of the micro-HPLC with the thermal lens detection is suitable for separation analysis.

4. MICROSCOPIC THERMAL LENS MEASUREMENTS WITH A MODE-LOCKED LASER

4.1. Additional features to a conventional thermal lens measurement

Microscopic thermal lens measurements, those obtained with a mode-locked laser, and those obtained with their combination have or may have additional

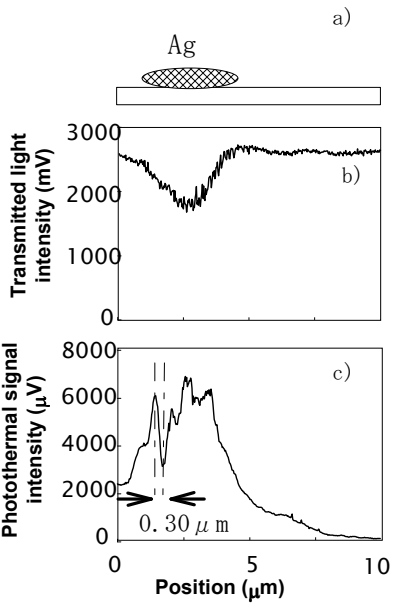

Fig. 11. One-dimensional scanning image of Ag aggregate vapor-deposited on a glass: a) a model of the sample; b) transmitted light intensity; c) thermal lens signal intensity measured with a modulation frequency of 2.93 kHz.

features to those of conventional thermal lens measurements. Some of these features, spatial and temporal resolutions and nonlinear optical excitation, are reviewed and discussed in this section to indicate the potential expansions of enhanced photothermal spectroscopy.

4.2. Spatial resolution

The spatial resolution of a thermal lens microscope has been reported [10, 12]. The spatial resolution is considered to be dominated by the overlap between the pump and probe beams, where thermal diffusion has some influence. The resolution in the depth direction appears to have the typical characteristics of thermal lens measurements [10], in which the position of the heat source in a sample with respect to the focal point of the probe beam dominates the polarity of the signal [9]. The signal of the cells can be discriminated from those from ultraviolet-absorbing glasses because of the depth resolution, although there have been no precise investigations.

For the resolution in a lateral direction, a structure that was smaller than the sizes of pump and probe beams was observed to be resolved [12], as shown in Fig. 11. Although such structures are sometimes observed in microscopic thermal lens measurements, the cause is not understood. It is possible that these structures are artifacts, but the reason for the contrast is still unknown.

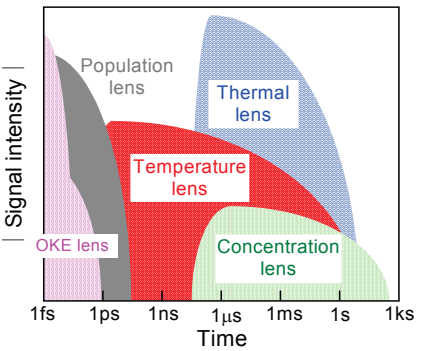

Fig. 12. Time dependent evolution of a variety of lensing effects. The axis of the ordinates indicates a measure of the absolute intensity of the lensing effects. A commonly used name for each lensing effect is given in the figure. The lenses of the optical Kerr effect (OKE) and population have an anisotropic character, and those of the temperature, thermal (mass density), and concentration have an isotropic character.

4.3. Temporal resolution

The use of two beams form a mode-locked femtosecond laser makes it possible to carry out a femtosecond time-resolved measurement with the pump-and-probe method [35, 36]. With a similar experimental setup to thermal lens measurements, except for an optical delay line controlling the timing between the pump and probe pulses, several of kinds of photo-induced lens (lensing effects) are observed.

The main cause of thermal lens formation is mass density variation around the photo-induced heat source generated via thermal expansion. However, a refractive index is a function of not only mass density but also the temperature of the solution and the concentration, population, and orientation of molecules. In a time-resolved measurement of the lensing effect, photo-induced refractive index changes have been observed to develop and diminish with time, depending on the causes of the refractive index change. A variety of lensing effects have been observed and named, as qualitatively shown in Fig. 12.

An experimental result of femtosecond time-resolved lensing measurements is shown in Fig. 13 [36]. These are ultrafast lensing responses of rhodamine B ($1x10^{-4}$ M) in methanol after some mathematical operations. The electronic and nuclear responses are calculated as 3/4 ($S_p + 2S_v$) and 2/5 ($S_p - 3S_v$), respectively, where S_p and $2S_v$ are the lensing signal intensities observed with polarizations of pump and probe beams being parallel and perpendicular, respectively [37]. The responses of pure methanol caused by the optical Kerr effect are subtracted before the calculation.

The measurement was carried out with a pump beam at 390 nm having power of less than 0.24 nJ/pulse and a diameter of less than 10 μm. The lens

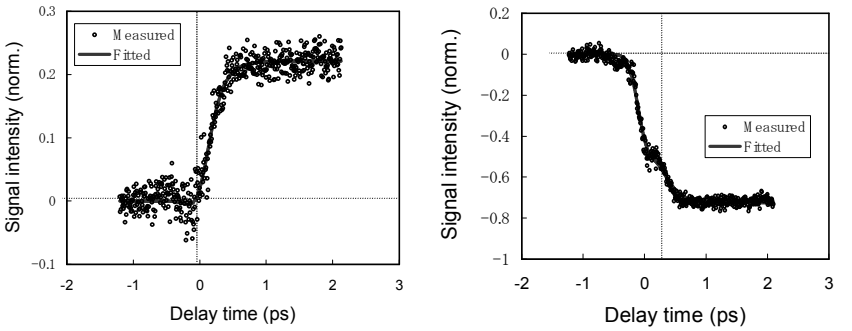

Fig. 13. Ultrafast lensing responses of rhodamine B in methanol: left, electronic response (τ = 115 fs); right, nuclear response (τ = 138 fs). The nuclear response of pure methanol has 208 fs of a rise time τ.

transiently formed in the rhodamine B solution with a thickness of 1 mm was monitored with a probe beam at 780 nm having power of less than 0.38 nJ/pulse, a diameter of less than 10 μm, and a pulse width of 68 fs. It was confirmed that the intensity of the lens was linearly proportional to the pump beam power. A quartz plano-convex lens with a focal length of 50 mm was used as the focusing lens of the pump and probe beams in the collinear configuration. The temporal resolution and sensitivity of detection depend on the focusing lens. The result of investigation on the dependence is summarized in Table 1, along with the sensitivity of the measurement of a thermal lens signal [36]. The table shows importance of the focusing lens selection serving the purpose of measurements.

Table 1
Time resolution and detection sensitivity under focusing conditions

Focusing optics	Correlation width (fs)	Sensitivity for ultrafast sig. (10^{-4}/mW)	Sensitivity for thermal lens sig. (10^{-2}/mW)
Quartz plano-convex （f = 50mm）	173	1.58	1.98
Quartz plano-convex （f = 15mm）	187	2.55	2.08
Concave mirror（R = 100mm）	366	0.67	1.79
Reflection objectives（×20, NA0.38）	185	—	—
Reflection objectives（×40, NA0.50）	180	0.17	0.0

The correlation width was evaluated with a BBO crystal by sum-frequency generation. The correlation width of 173 fs corresponds to 113 fs of the real width. The sensitivity was evaluated with a 0.1 mM methanol solution of rhodamine B (optical path length, 1mm; polarization, parallel). The signal intensity was normalized with the pump light intensity (mW).

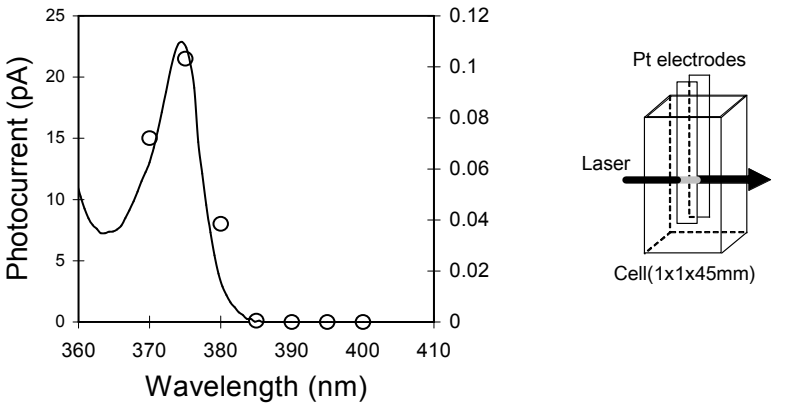

Fig. 14. Two-photon photoionization spectrum of anthracene in cycrohexane (10^{-5} M) observed with the second harmonics of Ti: sapphire laser (repetition, 76 MHz; average power, <10 mW; modulation frequency of the pump beam, 4 Hz; focal length, 50 mm; applied electric field, 5 kV/cm). The curve shows the absorption spectrum of the sample. Insert: photoionization cell used.

4.4. Nonlinear optical excitation

With a femtosecond mode-locked laser, it is easy to observe nonlinear optical phenomena, such as two-photon absorption. Two-photon excitation of fluorescence has been used in combination with an optical confocal microscope because it has two great advantages: the excitation of violet-light absorbing fluorophors by near-infrared light, in which optical damage to the biological specimens is avoidable; and achievement of a better spatial resolution than that with one-photon excitation.

Two-photon photoionization has also been observed with the second-harmonics of a Ti: sapphire laser [38]. Photoionization spectroscopy is one of the most sensitive detection methods of nonfluorescent chemical species in a liquid solution. As shown in Fig. 14, the second harmonic light of a femtosecond Ti-sapphire laser with an energy <1 nJ/pulse is sufficient to realize resonant two-photon ionization, for which two-photon photoionization is identified by the quadratic power-dependence of the signal intensity.

When microscopic photoionization detection is carried out, an ac-conductivity measurement with a couple of microelectrodes would be used. Another possibility is the use of transient absorption by solvated electrons and radical cations. It has been reported that hydrated electrons have photo-absorption with a molar absorption coefficient of 1.8×10^4 $M^{-1}cm^{-1}$ at around 700 nm [39]. It is estimated that solvated electrons generated at the laser focus increase the absorbance of a detectable magnitude [40]. The same optical setup as that for multi-colour excitation microscopic photothermal detection can be used for photoionization measurements.

5. SUMMARY

Some trials for enhanced photothermal spectroscopy for observing chemical compounds in biological cells are described. Ultraviolet excitation and photothermal signal enhancement appear to be key factors for *in-situ* and highly sensitive detection of non-labelled biological chemicals in and around the cells. Unfortunately, experimental setups and procedures presented here are far from established.

Photothermal signal enhancement by two-colour excitation is one of the ways to increase the apparent rate of photo-induced heat generation per target molecule under a certain excitation power condition for ground-state absorption. Roughly, the absorption cross-section of molecules monotonically increases up to several decades of eV [41], and, generally, solute molecules in a highly excited state have a small luminescent quantum yield. In addition, most of the excess energy of the molecules is released to the surrounding solvent molecules as heat. It will be possible to enhance the photothermal signal amplitude further by multi-colour excitation under a microscopic space; for this purpose, information on the transient absorption and dynamics of photoexcited molecules is strongly required.

At present, the most suitable laser system as a tunable laser light source at the ultraviolet wavelength region for microscopic measurements continues to be the higher harmonics of a mode-locked Ti: sapphire laser. However, the relatively high cost of the photons is less attractive in analytical applications. Use of a conventional light source for microscopic photothermal measurements could be retried for the analytical applications. Otherwise, time-resolved measurements or multi-photon excitation combined with photothermal techniques could be utilized for further analysis.

ACKNOWLEGEMENTS

This work was financially supported by a Grant-in-Aid for Scientific Research (KAKENHI) from the Ministry of Education, Culture, Sports, Science and Technology [Nos. 15205011 and 16072213 (Priority Area “Molecular Nano Dynamics”)], and by a Research Grant for the Natural Sciences from the Mitsubishi Foundation.

REFERENCES

[1] M. D. Barnes, W. B. Whitten, and J. M. Ramsey, Anal. Chem. (1995) 418A.
[2] P. M. Goodwin, W. P. Ambrose, and R. A. Keller, Acc. Chem. Res., 29 (1996) 607.
[3] W. P. Ambrose, P. M. Goodwin, J. H. Jett, A. V. Orden, J. H. Werner, and R. A. Keller, Chem. Rev., 99 (1999) 2929.

[4] Ch. Zander, J. Enderlein, and R. A. Keller eds., Single Molecule Detection in Solution, Wiley-VCH, Berlin, 2002.
[5] S. H. Leuba and J. Zlatanova eds., Biology at the Single-Molecule Level, Pergamon, Amsterdam, 2001.
[6] R. Rigler, M. Orrit, and T. Basché eds., Single Molecule Spectroscopy, Springer-Verlag, Berlin, 2001.
[7] A. J. Bard and F.-R. F. Fan, Acc. Chem. Res., 29 (1996) 572.
[8] S. Nie and S. R. Emory, Science, 275 (1999) 1102.
[9] S. E. Bialkowski, Photothermal Spectroscopy Methods for Chemical Analysis, Wiley, New York, 1996.
[10] M. Harada, M. Shibata, T. Kitamori, and T. Sawada, Anal. Chim. Acta, 299 (1995) 343.
[11] H. Kimura, M. Mukaida, T. Kitamori, and T. Sawada, Anal. Sci., 13 (1997) 729.
[12] A. Harata, T. Kitamori, and T. Sawada, J. Jpn. Soc. Colour Material, 68 (1995) 606 [In Japanese].
[13] S. Hiki, K. Mawatari, A. Hibara, M. Tokeshi, T. Kitamori, Anal. Chem., 78(8) (2006) 2859.
[14] T. G. Nolan and N. J. Dovichi, IEEE Circuites Devices Mag., 2 (1986) 54.
[15] K. Sato, H. Kawanishi, M. Tokeshi, T. Kitamori, and T. Sawada, Anal. Sci., 15 (1999) 525.
[16] M. Tokeshi, M. Uchida, K. Uchiyama, T. Sawada, and T. Kitamori, J. Luminescence, 83 (1999) 261.
[17] M. Tokeshi, M. Uchida, A. Hibara, T. Sawada, and T. Kitamori, Anal. Chem., 73 (2001) 2112.
[18] K. Mawatari, T. Kitamori, and T. Sawada, Anal. Chem., 70 (1998) 5037.
[19] M. G. Rockley and J. P. Devlin, Appl. Phys. Lett., 31 (1977) 24.
[20] L. J. Rothberg, M. Bernstein, and K. S. Peters, J. Chem. Phys., 79 (1983) 2569.
[21] J. M. Heritier and A. E. Siegman, IEEE J. Quantum. Electron., QE-19 (1983) 1551.
[22] G. G. Yee and D. S. Kliger, J. Phys. Chem., 87 (1983) 87.
[23] A. Harata and N. Yamaguchi, Anal. Sci., 16 (2000) 743.
[24] A. Harata, K. Fukushima, and Y. Hatano, Anal. Sci., 18 (2002) 1367.
[25] S. Hirashima, K. Furuya, and A. Harata, unpublished results.
[26] M. Harada, K. Iwamoto, T. Kitamori, and T. Sawada, Anal. Chem., 65 (1993) 2938.
[27] K. Sato, M. Yamanaka, H. Takahashi, M. Tokeshi, H. Kimura, and T. Kitamori, Electrophoresis, 23 (2002) 734.
[28] M. Surmeian, M. N. Slyadnev, H. Hisamoto, A. Hibara, K. Uchiyama, and T. Kitamori, Anal. Chem., 74 (2002) 2014.
[29] E. Tamaki, K. Sato, M. Tokeshi, K. Sato, M. Aihara, and T. Kitamori, Anal. Chem., 74 (2002) 1560.
[30] A. Harata, Abstract of 3rd Int. Nanophotonics Symp. Handai (Osaka, Japan, 2006) 19.
[31] M. Itoh, A. Harata, and S. Sawada, Abstract of 57th Meeting on Anal. Chem. (Bunsekikagaku-Touronkai, Matuyama, Japan, 1996) 417 (In Japanese).
[32] K. Sassa, J. Kashiwagi, M. Isoda, and A. Harata, in preparation.
[33] S. Hrashima and A. Harata, Abstract of 26th Symp. Ultrasonic Electronics (Yokohama, Japan, 2006) 333.
[34] A. Gohda, and A. Harata, in preparation.
[35] K. Ito, M. Mutoh, A. Harata, and T. Sawada, Chem. Phys. Lett., 275 (1997) 349.
[36] A. Harata, J. Taura, and T. Ogawa, Abstract of 59th Meeting on Anal. Chem. (Bunsekikagaku-Touronkai, Otaru, Japan, 1998) 106 (In Japanese).
[37] M. Terazima, Opt. Lett., 20 (1995) 25.

[38] N. Tsukiashi, A. Harata, and T. Ogawa, Abstract of 48th Annual Conf. Jpn. Soc. Anal. Chem. (Koube, Japan, 1996) 112 (In Japanese).
[39] H. Abramczyk and J. Kroh, J. Phys. Chem., 95 (1991) 6155.
[40] K. Kumamoto and A. Harata, unpublished results.
[41] Y. Hatano, Phys. Report, 313 (1999) 109.

Handai Nanophotonics, Volume 3
H. Masuhara, S. Kawata and F. Tokunaga (Editors)

Chapter 6

Probing conformational dynamics in biopolymers by contact-induced fluorescence quenching

S. Doose, H. Neuweiler, and M. Sauer

Applied Laser Physics and Laser Spectroscopy, University of Bielefeld, Universitätsstr. 25, 33615 Bielefeld, Germany

1. INTRODUCTION

The understanding and control of the functionality of biomolecular processes at the molecular level constitutes a key issue of the 21st century. Functionality describes the capability of molecules to perform specific tasks in complex systems to regulate, control, and optimize reaction efficiency and is primarily defined by structure. However, functionality is not only determined by the static structure of a macromolecule but likewise by its intrinsic dynamics. As the most important biomolecules represent biopolymers (e.g. proteins are heteropolymers made of the 20 naturally-occurring amino acids and nucleic acids are heteropolymers made of the four nucleic acids), conformational dynamics are essential for structure formation (the folding of proteins, RNA, and DNA) on one hand, and might provide functionality by itself on the other hand.

Conformational dynamics occur on a broad range of time scales ranging from nanoseconds (end-to-end contacts of unstructured polypeptides) to several minutes (prolyl-isomerization of peptide-bonds). As characteristic times for dynamic processes scale roughly with the size of the structure and the moving subunits involved, monitoring conformational changes in small biomolecules requires fast experimental techniques. Fluorescence spectroscopy has been helpful in accessing the fastest biomolecular processes, such as the folding of small proteins, or polymer dynamics of unstructured peptides, RNA, and DNA. The power of fluorescence spectroscopy and microscopy is due to its exquisite selectivity, sensitivity, and multiple observables, that are accessible through fluorescence [1].

Conformational dynamics can be probed advantageously with fluorescence spectroscopy by monitoring quenching interactions that influence the emission rate of an excited fluorophore. Two mechanisms of fluorescence quenching have

widely been employed: Förster resonance energy transfer (FRET), a non-radiative energy transfer process based on dipole-dipole coupling between two fluorophores [2], and photoinduced electron transfer (PET). Whereas FRET is sensitive to the distance between fluorophore (donor) and quencher (acceptor) in the range of 2 to 10 nm, PET is a short-range interaction and occurs efficiently only upon van der Waals contact between fluorophore and quencher.

Either quenching interaction has been measured successfully for single molecules and has been used to characterize a multitude of molecular processes [3-9]. Among them are various interactions including protein-protein, protein-DNA, and DNA-DNA interactions, as well as protein folding. In general, single-molecule fluorescence techniques allow resolving distributions and processes in time, unskewed by ensemble averaging and without the need for ensemble synchronization [1, 10-13]. In the last two decades emerging single-molecule fluorescence spectroscopic tools have been developed and adapted to analyze individual molecules under various conditions. Nowadays, single-molecule sensitive optical techniques are well established and help to increase our understanding of complex problems in different disciplines ranging from material science to cell biology [11, 13] In this book chapter, the use of selective fluorescence quenching processes of organic dyes by the amino acid tryptophan and the DNA base guanosine via PET for monitoring function and dynamics of polypeptides and nucleic acids will be presented. First, we will briefly explain the fundamentals of PET and describe experimental techniques used to study such processes with high temporal and spatial resolution. We then demonstrate that the introduced technique is ideally suited to study polymer chain dynamics of polypeptides and nucleic acids as well as protein folding dynamics under equilibrium conditions. Finally, we highlight the design of PET-based molecular probes for diagnostic applications.

2. SELECTIVE FLUORESCENCE QUENCHING OF ORGANIC FLUOROPHORES BY PHOTOINDUCED ELECTRON TRANSFER REACTIONS

2.1. Principles of Photoinduced Electron Transfer (PET) between Organic Fluorophores and Biomolecules

Electron transfer (ET) is a fundamental process in a variety of biochemical processes, with one of the most prominent examples being photosynthesis. ET between two molecules is described as a tunneling process through-space upon orbital overlap of electron donor and acceptor. A through-bond mechanism in which orbitals of intervening molecules contribute to the tunneling process has also been identified and described in terms of superexchange coupling [14, 15]. Furthermore, electrons might be transferred through-bond by a diffusive hopping mechanism.

In general, ET reactions are controlled by the free energy of the reaction, the reorganization energy, the electronic interaction geometry, and the distance between donor and acceptor. As electronic properties of a molecule change upon population of electronically excited states through absorption of a photon, ET might only become efficient after photoexcitation of a molecule. Photoinduced electron transfer (PET) is one of the fundamental mechanisms that lead to efficient fluorescence quenching of electronically excited fluorophores. Whether PET is energetically feasible can be estimated by the Rehm-Weller equation:

$$\Delta G_{CS} = E_{ox} - E_{red} - E_{0,0} + E_{Coul} \ , \tag{1}$$

where E_{ox} and E_{red} are the first one-electron oxidation potential of the donor and the first one-electron reduction potential of the acceptor in the solvent under consideration. $E_{ox/red}$ are experimentally accessible from saturated calomel electrode measurements (SCE). $E_{0,0}$ is the transition energy from the molecules ground state to the lowest excited singlet state, and E_{Coul} is the Coulomb energy term between donor and acceptor radicals. A fluorophore in the excited state can either be reduced by an electron donating quencher D or oxidized by an electron accepting quencher A (Fig. 1). The formed radical ions relax electronically by charge recombination to complete the energetic cycle. Experimental

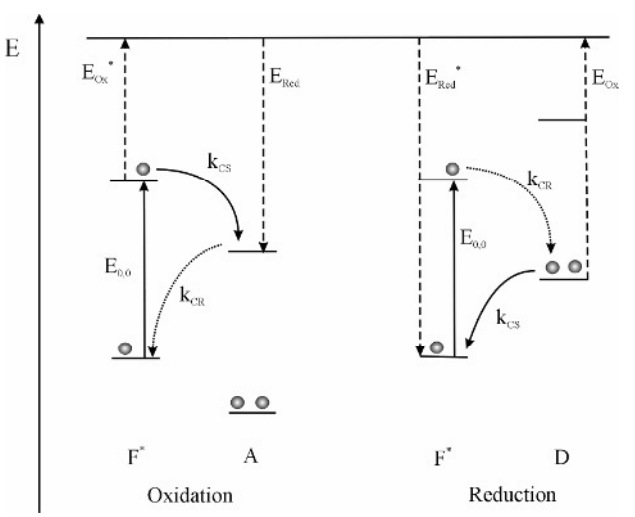

Fig. 1. Scheme of photoinduced electron transfer (PET). An excited fluorophore is oxidized by transferring an electron to a nearby molecule. After charge recombination the fluorophore has relaxed to the ground state and fluorescence is quenched. Alternatively, the fluorophore can be reduced before charge recombination completes non-radiative relaxation of the fluorophore.

investigations have confirmed the strong distance dependence as predicted by theory for both through-space and through-bond ET [14, 15]. Here, the transfer rate constant k_{ET} follows an exponential distance dependence with characteristic length scales on the order of few Angströms [14]. Characteristic time scales were estimated in pump-probe experiments and found to be in the femto- to picosecond range [16].

The strong distance dependence together with very fast reaction time qualifies PET as mechanism to probe proximity of interacting moieties and proximity changes on small length and short time scales. A variety of fluorophore-quencher pairs have been identified for which PET is an exergonic process and can thus result in complete suppression of fluorescence upon bimolecular contact. Two natural compounds of biopolymers were found that can serve as efficient electron donors when in contact with rhodamine or oxazine fluorophores: the amino acid tryptophan (Trp) and the nucleotide guanosine (G). Other components of biopolymers with aromatic groups, e.g. tyrosine or adenosine, were identified, that can also quench fluorophores but with considerably reduced efficiency [17-19]. In addition, non-natural strongly quenching compounds exist, such as the nucleotide 7-deazaguanosine, that can readily be incorporated into biopolymers. The efficiency of PET quenching depends on the reduction and oxidation potentials as well as on the transition energy from the ground to the first excited state (Eq. 1). The value of E_{Coul} in moderately polar environment is sufficiently small that it can be neglected. Experimental values for the selection of fluorophores and quenching moieties are given in [17, 18].

As PET is extremely efficient at distances of a few Angström with transfer rates above 10^{12} s^{-1}, the excited state will nearly always be depopulated via the non-radiative PET pathway as long as the fluorescence lifetime is on the order of 10^{-9} s^{-1} and the intermolecular distance of fluorophore and quencher is close to or at van der Waals contact. Contact can be provided through a transient collisional encounter during the time the fluorophore is electronically excited. The resulting non-radiative relaxation is termed collisional quenching [20].

It was also shown that organic compounds with planar aromatic moieties, such as the fluorophores Trp, or guanosine, can form stacked complexes in aqueous solutions upon collisional encounter. A combination of the various molecular forces results in an attractive total force that can stabilize planar aromatic ring systems in a face-to-face configuration. If the complexed molecules fulfill all electronic requirements for exergonic PET, fluorescence can be quenched entirely as long as the complex is stable. To distinguish this mechanism from collisional quenching it is generally termed static quenching [20].

It is well known that photon absorption and fluorescence emission spectra depend on the local environment of the fluorophore. For instance, dependent on

the fluorophore structure the absorption as well as the emission spectra is shifted with increasing hydrophobicity of the solvent. In addition excitonic interactions can entirely change spectral characteristics and result, e.g., in an additional absorption band on the blue edge of the spectrum. This is, for example, the case for homo dimer formation [11]. Complex formation in solution, however, is mostly due to intermolecular forces mediated by solvent properties, and to first approximation independent of the photophysical state. Alterations of the spectral characteristics are thus a likely indicator of but no prerequisite for complex formation. A computational example of bimolecular complex formation between fluorophores (Rhodamine 6G and the oxazine derivative MR121) and Trp was given by Vaiana et al. [21]. Molecular Dynamics (MD) simulations in explicit water were used to show formation of hydrophobic complexes and estimate a binding energy of 20-30 kJ/mol.

Bimolecular complex formation of various rhodamine and oxazine fluorophores with Trp or G was further characterized by monitoring quenching interactions using standard fluorescence spectroscopy [22, 23]. Complex formation efficiency as well as binding energy were estimated in agreement with the computational results. For the oxazine derivative MR121, which is very similar in structure and photophysical properties to the fluorophore ATTO655, complexes with Trp or G (used as guanosine monophosphate to increase water solubility) are formed at about 30% of all collisional encounters. Once formed a binding energy of 30 kJ/mol stabilizes complexes for 10-100 ns in aqueous solution before dissociation occurs [22].

2.2. Experimental Techniques to Study PET-Reactions

The molecular interplay between fluorophores and quenching moieties results in a number of experimentally accessible observables. Among them are fluorescence intensity, spectrum, lifetime, and characteristic fluctuations of either one. Using the broad range of experimental techniques in fluorescence spectroscopy gives access to these observables under various conditions. Steady-state fluorescence measurements in combination with UV/Vis absorption measurements report on variations of the fluorescence emission intensity and an apparent quantum yield. The fluorescence quantum yield (QY) of an individual molecule is defined as the ratio of total number of emitted photons and total number of absorbed photons. In a molecular ensemble, and under the assumption that the absorption characteristics do not change significantly, the reduced intensity resembles a reduced QY. However, in case of formation of non-fluorescent complexes, the measured apparent QY reflects the two subpopulations of quenched and unquenched fluorophores. Only through fluorescence lifetime measurements, using e.g. time-correlated single photon counting (TCSPC), can collisional quenching be measured independently of the formation of non-fluorescent complexes. As long as quenched complexes are

stable for a time period longer than the fluorescence lifetime, they are invisible in TCSPC measurements. Collisional quenching on the other hand reduces the fluorescence lifetime and is thus directly observable. A convenient way for quantitative analysis of both mechanisms is displaying and fitting the data in a Stern-Volmer plot [20]:

$$\frac{I_0}{I} = (1 + k_d \tau_0 [Trp])(1 + K_S [Trp]), \quad \frac{\tau_0}{\tau} = (1 + k_d \tau_0 [Trp]), \tag{2}$$

where I (I_0) and τ (τ_0) are fluorescence intensity and lifetime in presence (absence) of quenching molecules, respectively, [Q] is the quencher concentration, k_d is the dynamic quenching constant, and K_s is the static quenching constant.

Fluctuations of fluorescence emission can be analyzed via the autocorrelation function of the detected signal. Fluorescence correlation spectroscopy (FCS) was introduced by Magde, Elson, and Webb [24], and combined with confocal microscopy by Rigler et al. [25]. Meanwhile, FCS evolved to an independent fluorescence microscopy technique successfully applied in various disciplines [26]. FCS in combination with confocal fluorescence microscopy allows studying fluorescence fluctuations of fluorophores that diffuse freely through an observation volume. When investigating molecules that occupy a two-state system in thermodynamic equilibrium (e.g. complexed and solvent-separated molecules), with state A (fluorescent) and state B (non-fluorescent), populated according to an association rate constant k_+ and a dissociation rate constant k_-,

$$A \underset{k_-}{\overset{k_+}{\rightleftarrows}} B, \tag{3}$$

fluctuations in the fluorescence signal $I(t)$ can be analyzed via the autocorrelation function:

$$G(\tau) = \frac{\langle I(t) I(t+\tau) \rangle}{\langle I(t) \rangle^2}, \tag{4}$$

where < > denotes temporal averaging. Eq. (4) can be solved for the above described two-state model in combination with molecular diffusion yielding:

$$G(\tau) = \frac{1}{N} \frac{1}{(1 + \tau / \tau_D)} (1 + K_{equ} \exp\left[- \tau / \tau_{\exp} \right]), \tag{5}$$

where N is the number of detected molecules in the observation volume, τ_D is the diffusion time, $K_{equ} = k_+ / k_-$ is the equilibrium constant, and $\tau_{\exp} = (k_+ + k_-)^{-1}$ is

the exponential time constant [27]. Calculating the cross-correlation function of the signal split on two detectors, eliminates dead time and afterpulsing effects of avalanche photodiodes (APDs) and thus decreases the time resolution to a few nanoseconds. FCS hence yields access to kinetic rate constants in thermodynamic equilibrium of highly dilute solutions.

The high sensitivity of fluorescence measurements that can be achieved using a confocal microscope with single-photon sensitive APDs as detectors, can also be used to detect fluorescence bursts of individual molecules, and has thus become instrumental in single-molecule spectroscopy [1, 10-13]. In a confocal microscope the observation volume is limited to a few femtoliter, efficiently suppressing background by spatial filtering with a pinhole. With the brightest fluorophores and the most efficient quenching molecules bimolecular interactions that result in PET quenching have been detected on the single-molecule level.

3. MONITORING POLYMER DYNAMICS USING PET-PROBES

Since fluorescence quenching via PET is efficient only when fluorophore and quencher are at van der Waals contact, labeled protein/nucleotide conjugates can be designed such that conformational changes will be accompanied by intramolecular contact formation and dissociation of the attached fluorophore and the quenching moiety within the biopolymer. Changes in fluorescence intensity will thus signal conformational changes in a digital fashion with a high signal-to-noise ratio. We studied intrachain contact formation rates between site-specifically labeled fluorophore and intrinsic Trp or guanosine residues of polypeptides and nucleic acids. Biopolymers were labeled with the oxazine derivative MR121 at the N-terminus (in peptides) or 5'-end (ssDNA). A Trp or guanosine was incorporated into the sequence at the polymer's opposite end as efficient quencher (Fig. 2). Monitoring PET by FCS allows the determination of end-to-end contact formation rates, the investigation of biopolymer characteristics, and comparison with polymer theory.

3.1. Conformational Dynamics of Unstructured Polypeptide Chains

To understand the mechanisms that guide proteins through their conformational free energy landscape to the folded state it is crucial to elucidate structure and dynamics within the denatured state of proteins. Therefore, monitoring conformational transitions within unfolded polypeptides represents a topic of ongoing research in modern molecular biology.

Conformational dynamics within the originally unfolded state of proteins is of particular interest since the unfolded state represents the starting point for the protein folding process. Kinetics of end-to-end contact formation serve as valuable parameter to monitor dynamic properties of polypeptide chains. Effects

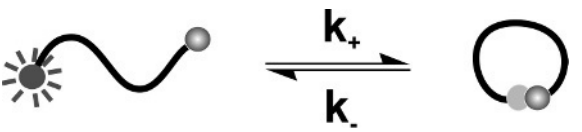

Fig. 2. Functional principle for measuring biopolymer chain dynamics using fluorescence quenching. Fluorophore and quenching moiety are incorporated at the terminal ends of the polymer. In the "open", extended configuration the fluorophore is fluorescent. Upon end-to-end contact formation of the chain (i.e. the "closed" configuration) fluorophore and quencher form a complex and the fluorescence is quenched, signaling the conformational transition. The rate constants k_+ and k_- for the corresponding conformational changes can be measured by FCS experiments.

of chain composition (polypeptide sequence) and chain length on end-to-end contact formation rates can be evaluated and deliver detailed insights into properties of polypeptides like chain stiffness or the propensities to collapse or form structures. In addition, solvent effects like ionic strength or viscosity on intrachain dynamics can be investigated.

Experimental observation of intrachain diffusion of specific sites within a polypeptide chain requires spectroscopic probes that report van der Waals contact formation with nanosecond time resolution. Currently, only a few

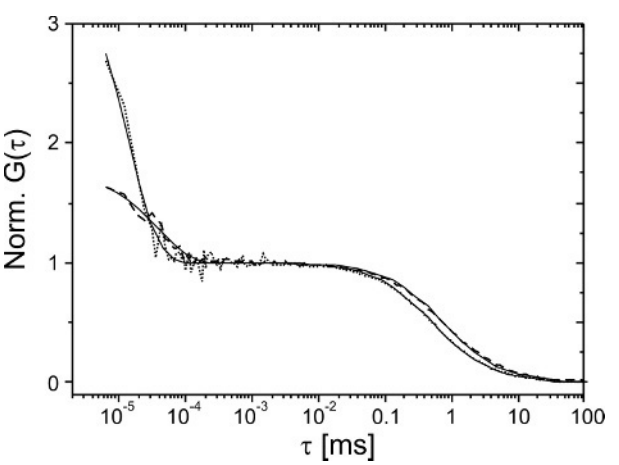

Fig. 3. Autocorrelation functions normalized to the number of molecules in the detection focus recorded from fluorescently modified poly-(GS)-peptides of various chain lengths at 20° C in phosphate buffer, pH 7.0. Dotted data represent autocorrelation functions recorded from MR121-$(GS)_5$-Trp, dashed data from MR121-$(GS)_{15}$-Trp. FCS curves are characterized by fluorescence fluctuations on the ms time scale caused by diffusion of peptides in and out of the detection volume, and fluorescence fluctuations on the ns time scale caused by end-to-end contact formation. Autocorrelation functions can be well described by an analytical model containing a single translational diffusion and a single exponential relaxation term (black curves).

techniques are available to monitor intrachain contact formation, namely triplet-triplet energy transfer (TTET) [28-30], triplet quenching [31, 32], and fluorescence quenching of long-lifetime fluorescence probes [33, 34]. We introduced the use of PET-probes in combination with FCS on a confocal fluorescence microscope setup to study intrachain diffusion of flexible peptide chains [9, 35]. Here, selective fluorescence quenching of MR121 by Trp residues present in polypeptide chains signals intrachain contact formation.

To study the dynamics of unfolded protein chains polypeptides consisting of repetitive units of glycine (G) and serine (S) residues represent a valuable model system [29, 30]. We modified poly-(GS)-peptides with MR121 and Trp at the N- and C-terminal ends, respectively, to directly monitor end-to-end contact formation by FCS. Fig. 3 shows FCS data recorded from a 10 and 30 residue long polypeptide. Data are well described by a single diffusion term on the milliseond time scale and a single exponential relaxation term on the nanosecond time scale reporting on intrachain contact formation. Single exponential relaxations observed indicate fast interconversion between different random coil conformations within the "open" state ensemble, i.e. random population of the unfolded state configurational space [36]. End-to-end contact formation rates can be revealed from FCS data following the proposed model (Eq. 3). The dependence of contact formation rates on chain length follows Gaussian chain theory [37, 38] for polypeptides of chain lengths $N > 10$ as demonstrated by the linear scaling behavior in a double-logarithmic plot of rate constant versus number of peptide bonds N (Fig. 4). The breakdown of the linear scaling law at chain lengths $N < 10$ can be explained by chain stiffness influencing dynamics over short chain segments.

Monitoring dynamics of intrachain diffusion using FCS opens the possibility to study dynamics of polypeptides even in complex biological samples applying a variety of experimental conditions (solvent viscosity or macromolecular content). Thus, such studies can shed new light on the earliest events in protein folding.

3.2. Conformational Dynamics of Single-Stranded DNA

Another important example for flexible, biological relevant polymers are single stranded nucleic acids. Oligonucleotides based on the nucleobase thymine exibit no propensity for structure formation and serve a suitable model system to study dynamics of unfolded nucleic acids. We investigated end-to-end contacts in short polythymidine oligonucleotides with MR121, attached at the 5'-end, and dG at the 3'-end: MR121-$(dT)_N$-dG. With N ranging from 4 to 10 bases, we found that complex formation and thus end-to-end contact kinetics can be described by a two-state model resulting in exponential relaxation decays similar to the behavior of polypeptides. We confirmed that ssDNA built of thymidine residues is a highly flexible biopolymer exhibiting slightly slower conforma-

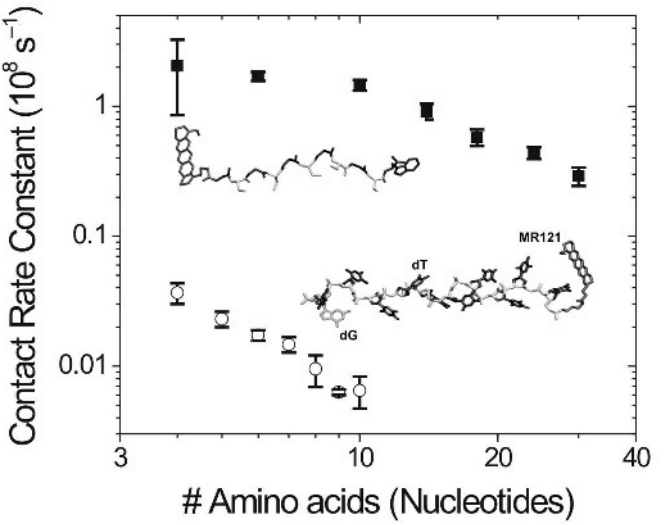

Fig. 4. Rate constants for end-to-end contact formation in flexible, unstructured biopolymers as a function of length: poly-(glycine-serine) (closed squares) and polythymine (open circles). Molecular structures are shown with fluorophore (MR121), quencher, and polymer units.

tional dynamics than were observed for polypeptides. We found end-to-end contact formation rate constants between 0.6×10^6 s^{-1} and 3×10^6 s^{-1} depending on the number of nucleotides. The length scaling is in the range of theoretical predictions for a Gaussian chain following a power law dependence N^{-b} with an exponent of b = ~2. These results are in good agreement with a less direct experimental estimation from closing rates in DNA hairpins [18], where a loop-length dependence of b = (2.0±0.2) was found.

Our data also agree with results by Nau and coworkers [39], who used collisional quenching of the fluorescence of fluorazophores (2,3-diazabicyclo[2.2.2]-oct-2-ene (DBO)) by a dG base to investigate end-to-end contact kinetics in tri- or penta-nucleotides.

Flexibility of single-stranded DNA has been extensively discussed in the context of hairpin structures. The thermodynamics of hairpin formation processes have been studied for more than 30 years by many biophysical researchers. Kinetic studies have been added, revealing opening and closing times in the range of a few tens of microseconds, slower than characteristic end-to-end contact formations kinetics [40-43]. The current understanding of hairpin folding is in agreement with a nucleation-zipping model, by which the opening rate depends on the unzipping energy of the hairpin, while the closing rate relies on the collision of the two stalks of the stem, followed by nucleation and the

propagation of base pairing [41]. Making use of PET quenching and FCS we could show that introduction of a single base pair at the ends of a loop reduces rate constants by one to two orders of magnitude [23]. The data implies that interactions between stem and loop nucleotides (in our experiment between a dC residue at the 5' end, a dG residue at the 3' end, and dT residues in the loop) rather than loop dynamics constitute the rate limiting step of DNA hairpin folding.

4. MONITORING PROTEIN FOLDING USING PET-PROBES

4.1. The Mini-Protein Trp-Cage

The early formation of sub-structures or folding intermediates in unfolded polypeptide chains represents a crucial kinetic event on the pathway of protein folding. It has been demonstrated that α-helices and β-hairpins, secondary structural elements of proteins, fold ultra-fast on time scales of hundreds of nanoseconds and microseconds, respectively [44]. These studies have raised the question of the speed-limit of protein folding [45]. One of the smallest and fastest folding proteins known to date represents the designed mini-protein Trp-cage. The 20-residue peptide has been generated by truncation and mutation of the originally only poorly folded 39-residue peptide exendin-4 from Gila monster saliva. A single Trp residue present in the sequence of Trp-cage is buried in the hydrophobic core of the fold, well shielded from solvent exposure (Fig. 5). Folding of Trp-cage has been characterized by NMR, circular dichroism, and fluorescence experiments and has been proposed to follow a highly cooperative two-state transition with a characteristic folding time of 4 μs [46, 47].

We used fluorescence quenching by PET between site-specifically labeled MR121 and the single Trp residue of Trp-cage to study folding dynamics of the mini-protein [48]. In the folded state MR121 is shielded from fluorescence quenching interactions with Trp that is "caged" in the hydrophobic core, whereas in the denatured state W6 is solvent-exposed and accessible to MR121, giving rise to fluorescence quenching interactions.

Therefore, folding and unfolding transitions result in "on" and "off" switching of the fluorescence of the attached fluorophore. FCS curves recorded from labeled Trp-cage exhibit marked, temperature dependent relaxation kinetics on microsecond time scales reporting on folding kinetics (Fig. 5). From the relaxation time and the corresponding amplitudes folding and unfolding rates measured under equilibrium conditions can be determined. Besides folding kinetics, insights into polypeptide chain dynamics in the denatured state of the mini-protein can be revealed. The absence of nanosecond relaxation kinetics in FCS data measured at temperatures beyond the thermal mid-transition point demonstrates considerably restricted conformational flexibility of the

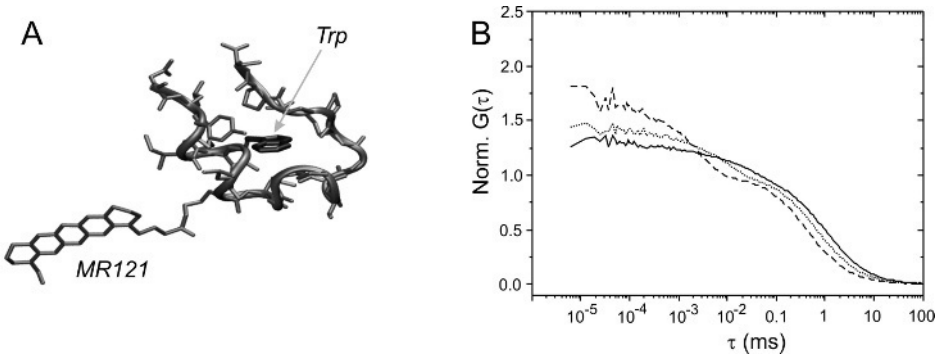

Fig. 5. Folding dynamics of Trp-Cage monitored by fluorescence quenching in combination with FCS. (A) Engineered solution structure of fluorescently modified Trp-cage. The fluorophore MR121, attached to a single lysine residue, is well shielded from quenching interactions with a single Trp residue buried in the hydrophobic core of the fold. (B) Temperature dependent autocorrelation functions recorded from labelled Trp-cage at various temperatures (data are normalized to the number of molecules in the detection focus). Solid curve: T = 5° C; dotted curve: T = 25° C; dashed curve: T = 45° C.

polypeptide in the denatured state. Experimental data are in agreement with current molecular dynamics simulations of Trp-cage predicting collapse of the unfolded mini-protein to a folding intermediate with preformed folding topology [49].

To summarize, our data demonstrate that folding dynamics of Trp-cage follows a hierarchical folding mechanism. Besides the observation of folding kinetics we revealed conformational flexibility in the denatured state of Trp-cage under various experimental conditions. Early formation of a collapsed molten globule like intermediate enhances folding efficiency of Trp-cage under physiological conditions. Strongly denaturing conditions (GdmCl) as well as introduction of a helix-breaking point-mutation lead to complete melting of the intermediate [68]. Thus, our study contrasts previous reports proposing simple two-state folding and demonstrates that reduction of protein size and simplification of folding topology does not consequently lead to simplification of the folding mechanism. It rather underscores the importance of preformed structure in the denatured state for efficient folding of even the smallest globular structure.

Furthermore, our results demonstrate for the first time that FCS in combination with selective fluorescence quenching of fluorophores by Trp can be used advantageously for the monitoring of sub-millisecond folding dynamics at the nanometer scale with nanosecond time resolution. Unlike conventional methods, FCS can be used to study ultrafast folding kinetics under equilibrium conditions and in highly dilute solutions, i.e. at the single-molecule level. We

anticipate our technique to be generally applicable in combination with protein engineering and site-specific fluorescence modification.

5. DESIGN AND DIAGNOSTIC APPLICATIONS OF PET-PROBES

The development and investigation of molecular systems and methodologies that enable the monitoring of specific recognition and molecular binding events is crucial for new refined molecular tools in medical diagnostics. In the ideal case, the molecular system should signal selective recognition or binding events via a change in a characteristic property, e.g., fluorescence or luminescence intensity, that can be conveniently transmitted into an electronic signal by the appropriate detector. In addition, the use of fluorescence characteristics for sensing is advantageous since single photons can be easily converted into electrical signals with a high efficiency of up to 80% using, for example, avalanche photodiodes as detectors. Another advantage of fluorescence microscopy relies on the fact that many structural factors of fluorescent dyes and their intra- and intermolecular interactions which finally control their fluorescence efficiency are well understood. In general, PET or FRET reactions can be used to transfer discrete and stoichiometric recognition events into an altered fluorescence signal of a fluorophore. Molecular systems in which the excited state of a fluorophore is controlled by the redox properties of a receptor module covalently attached to the fluorophore form an important class of chemosensory materials [50]. In these sensors a spacer holds the fluorophore and a receptor close to, but separate from each other. The redox properties of the receptor module are altered upon ligand binding and dissociation. Since PET reactions are controlled by the relation between the free energy of the reaction, the reorganization energy, and the distance between the donor and acceptor, careful selection of the optical, ligand-binding, and redox properties of the components allow the optimization of the signaling parameters of the PET sensor. Hence, reversible ligand-induced “off-on” and “on-off” fluorescence sensors and switches are both designable [51, 52]. The extraordinary sensitivity of fluorescence-based method is especially important for the application of “smart” fluorescent probes, used for the detection of minute amounts of target structures from biological samples. In the last few years we developed PET-sensors that use conformationally induced alterations in PET efficiency upon binding for the specific detection of DNA or RNA sequences, antibodies, and proteases as well as nucleases at the single-molecule level [53-57]. These PET-sensors take advantage of the specific quenching properties of naturally occurring DNA nucleotides (dG) and amino acids (Trp) to probe the presence of target molecules. With careful design of these conformationally flexible sensors efficient single-molecule sensitive PET sensors can be produced. If quenching interactions between the fluorophore and dG or Trp residue are deteriorated

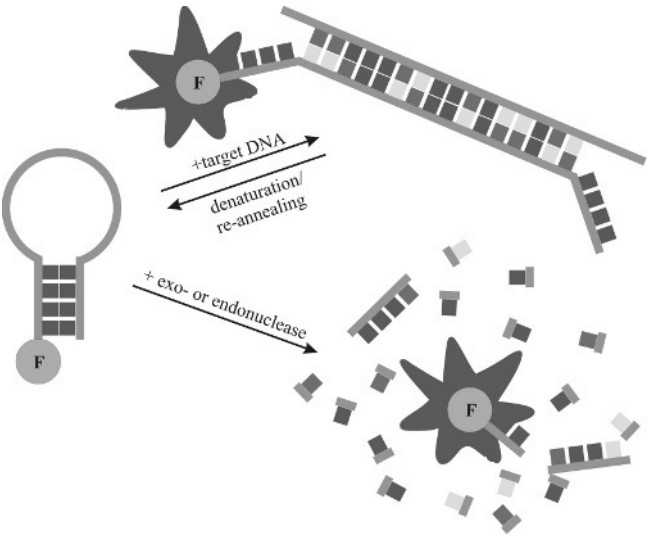

Fig. 6. Scheme of the functional principle of smart probes. The fluorophore is attached to the 5'-end of the oligonucleotide and quenched by dG residues in the complementary stem. Upon hybridization to the target sequence (complementary to the loop sequence) or exo- or endonucleolytic digestion the fluorescence is restored.

upon specific binding to the target, for example, due to binding of a complementary DNA sequence or antibody, or due to cleavage by an endonuclease or protease enzyme, fluorescence of the sensor is restored.

5.1. Detection of Specific Target DNA Sequences Using Smart Probes

With careful design of these conformationally flexible probes and the use of appropriate fluorophores (e.g. MR121) a new class of DNA-hairpins – so-called "smart probes"- can be synthesized [54]. Smart probes are single-stranded nucleic acids that adopt a stem-loop structure and are ideally suited for highly sensitive homogeneous and heterogeneous DNA binding or cleavage assays (Fig. 6). The loop consists of a probe sequence that is complementary to a portion of the target sequence, whereas the stem is formed by annealing of two complementary strands which are unrelated to the target sequence. In contrast to molecular beacons [58-60] where an additional quencher has to be attached to the oligonucleotide, in smart probes intrinsic guanosine residues terminating the 3'-end of the hairpin are responsible for strong fluorescence quenching of the dye labeled to the 3'end. If quenching interactions between the fluorophore and the guanosine residue are deteriorated, for example, due to binding of a complementary DNA sequence, or due to cleavage by an endo- or exonuclease enzyme, fluorescence of the DNA-hairpin is restored (Fig. 6). DNA-hairpins labeled with a single oxazine dye at the 5'-end increase fluorescence upon

hybridization up to 20-fold [17], which provides the basis for a cost-effective, and highly sensitive DNA/RNA detection method. The design of efficient PET-based DNA-hairpins has been achieved by a careful study of different factors that influence the photoinduced intramolecular electron transfer efficiency. Among these are the selection of suitable fluorophores, the influence of the guanosine position in the complementary stem, the attachment of additional overhanging single-stranded nucleotides in the complementary stem and the exchange of guanosine by more potent electron donors, such as 7-deazaguanosine [17]. Recently [61], we demonstrated that immobilized smart probes can be used to efficiently detect the presence of single target DNA or RNA molecules, even in the sub-picomolar concentration range within reasonable time (Fig. 7).

This has been achieved by immobilization of smart probes on coated cover slips while maintaining their native conformation. Therefore, the method is ideally suitable for the search for specific sequences using extremely low concentrations of target sequence. It is anticipated that optimization of reaction conditions (salt, temperature, etc.) and variations of the fluorophore as well as the use of modified nucleotides will lead to even higher sensitivities.

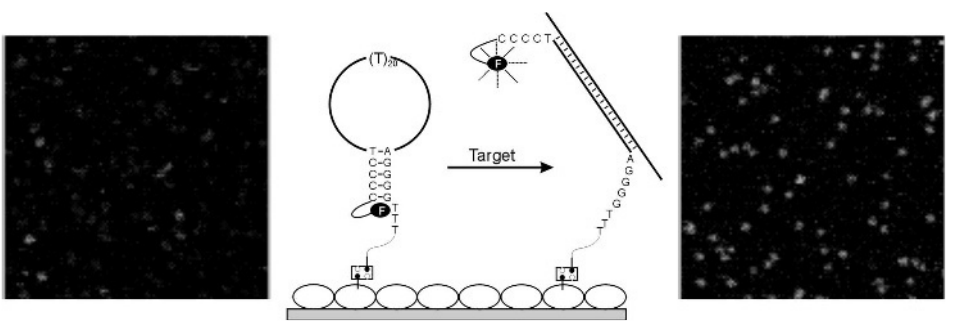

Fig. 7. Functional principle of a 3'-biotinylated DNA hairpin immobilized on a solid surface. The oxazine derivative MR121 (λ_{abs}= 661, λ_{em}=673 nm) is attached to the cytosine containing 5'-end. To immobilize smart probes onto a cover slide, the surface first binds bovine serum albumin (BSA) by physical adsorption (5 mg/ml, 10% of the BSA carries a biotin label). After an incubation time of 4 h and a washing step, streptavidin (1 mg/ml) is allowed to bind in PBS for 5 min. Finally, smart probes (10^{-10} M) are added to bind to the immobilized streptavidin. Single-molecule fluorescence scanning confocal images (20 x 20 µm) of smart probes immobilized on glass cover slips in PBS, pH 7.4 (50 nm/pixel, 3 ms integration time) are shown on the left (in the absence of target sequence) and right side (in the presence of 10^{-12} M target sequence). For excitation a pulsed diode laser (635 nm, 80 MHz, ~ 2 kW/cm^2) was used. Scanning was performed from top left to bottom down using modulated excitation. Upon hybridization to the target sequence (complementary to the loop sequence), the fluorescence is restored due to a conformational reorganization that forces the stem apart.

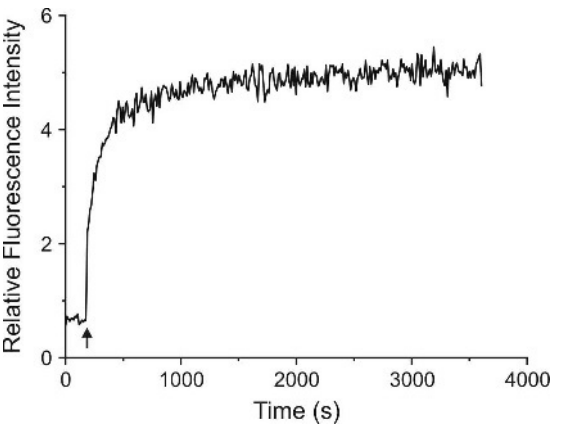

Fig. 8. Increase in fluorescence intensity with time upon addition of a 100-fold excess (denoted by the arrow) of the 240 bp PCR product of *M. xenopi* to a 10^{-8} M solution of species-specific smart probe labeled with the oxazine derivative MR121 at 50 °C using a conventional fluorescence spectrometer (λ_{exc} = 635 nm, λ_{em} = 680 nm). Measurement was performed in 10 mM Tris-HCl (pH 7.5) containing 300 mM NaCl and 1 mM EDTA.

Very recently [57], we demonstrated that smart probes can be used successfully for the sensitive and specific identification of mycobacterial strains. Both, theoretical considerations and experimental results showed that besides thermodynamic considerations also the multitude of possible secondary structures of DNA hairpins and their dynamics has to be taken into account for their efficient design. Comparison of dot plots generated by *mfold* [62] and experimentally determined fluorescence quantum yields suggests that suitable smart probes should exhibit no or only few base pairing interactions within the loop. In addition, the data imply that the formation of multiple alternative helices within the stem of the DNA hairpin maximizes fluorescence quenching. Theoretical results predict that the free energy of hairpin secondary structures should be in the range of -1.5 – -2.5 kcal/mol at 50 °C to ensure sufficient stability but likewise to enable eased hybridization to the target.

Based on these findings two smart probes SPxenopi4 and SPtuberculosis were optimzed for the specific identification of different mycobacteria (*M. xenopi* and *M. tuberculosis*). Experiments with PCR amplicons of various lengths demonstrate that the 240 bp amplicon of *M. xenopi* shows the best results with respect to increase in fluorescence intensity under the selected experimental conditions (Fig. 8). Consideration of all theoretical and experimental results allowed us to develop a reliable method for detection of *M. tuberculosis* and *M. xenopi* with a detection sensitivity of $\approx 2*10^{-8}$ M in homogenous solution. Experiments with amplicons of different mycobacterial strains demonstrate species-specific discrimination of *M. tuberculosis* and *M.*

xenopi against 15 of the most frequently isolated mycobacterial species in a single assay [57].

5.2. Development of PET-based Assays for the Specific Detection of Antibodies and Proteases

The extraordinary sensitivity of the PET-based quenching method can be used as well for the detection of antibodies using specific peptide epitopes. Recently [55, 63], we designed and synthesized peptide epitopes based on selective fluorescence quenching of an attached fluorophore by a single tryptophan residues to detect the presence of p53-autoantibodies, universal and highly specific tumor markers in cancer diagnosis [64]. P53 autoantibodies are among the most encouraging universal tumor markers in cancer diagnosis. They are found in sera of a significant number of cancer patients with different cancer types and have the potential of early-stage diagnosis for certain tumors. Common heterogeneous diagnostic tools for antibody detection, like ELISA, are time consuming and suffer from unspecificity. Hence, the development of fast and simple homogeneous formats is favored in biomedical sciences.

The amino acid sequences for synthesis of peptide-based fluorescent probes for antibody detection were selected based on the studies of Lubin et al. who mapped out immunodominant epitopes of human p53 for various cancer patients [65]. Lubin's study showed that the immune response of cancer patients is directed against a small subset of linear peptide epitopes localized mainly in the amino-terminal region (the transactivation domain) of the polypeptide chain of p53 protein. There are two immunodominant antigenic sites in the amino-terminal region of p53 (residues 11 to 35 and 41 to 59), independent of the type of cancer. Almost all of the tested p53-autoantibody positive cancer patients produce antibodies directed against one of these two peptide epitopes [66-69]. Hence, these peptides are promising systems on which to base the development of an immunoassay. The amino acid sequences of human p53 fragments used in our study are amino acid 15 to 29, SQETFSDLWKLLPEN (one-letter amino acid code), and amino acid 41 to 55, DDLMLSPDDIEQWFT. The presence of a single Trp (W) residue in both epitopes is crucial for assay development. Due to the unique quenching mechanism that requires contact formation between fluorophore and tryptophan residue both fluorescently labeled peptide-epitopes can be used as PET biosensors to detect single p53-autoantibodies. Upon specific binding to a p53-autoantibody the peptides chain adapts to the shape of the antibody cleft. Consequently, contact formation between tryptophan and MR121 is prevented (Fig. 9). The resulting increase in fluorescence intensity can be used to signal binding events. In combination with the single-molecule sensitivity the new assay allows for direct monitoring of p53 antibodies present in blood serum samples of cancer patients with picomolar detection sensitivity [55].

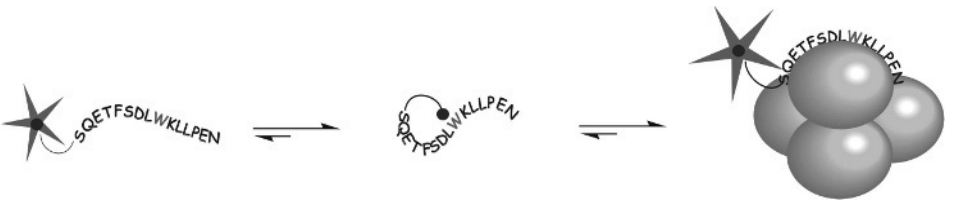

Fig. 9. Principle of operation of PET-biosensors for the specific detection of p53-autoantibodies. Driven by the conformational flexibility the peptide epitope adopts conformations where the fluorophore is efficiently quenched by Trp (W) upon contact formation. The quenched conformation coexists in equilibrium with an open, less quenched conformation. Upon specific binding to the antibody binding site, the peptide adopts a new conformation and charge transfer interactions between tryptophan and the dye are diminished. As the consequence, the fluorescence intensity increases (right side).

Our data demonstrate that the design of peptide-based molecular probes derived from the two immunodominant antigenic sites of human p53, which cover about 90% of the humoral immune response, provides a new diagnostic kit for the highly sensitive detection of human p53 autoantibodies. The development of smart PET-sensors for antibody detection, using short synthetic peptide epitopes and the principle of fluorescence quenching of selected dyes by the amino acid tryptophan opens new avenues for the detection of binding events by fluorescence intensity measurements in homogeneous solution and may thus be considered for general applications.

Alternatively, the selective quenching mechanism in tryptophan-containing peptides might be used advantageously for the detection of proteases. The interest in fast and sensitive assays for proteolytic enzymes, i.e. enzymes that specifically cleave peptide bonds, has increased considerably in the last few years. In particular, there are two medically important facts which accelerated the development of proteolytic assays. First, more and more diseases can be implicated with proteases. Because of the involvement of proteases in tumor progression and metastasis, e.g. matrix metalloproteinases, urokinase plasminogen activator (uPA), and cathepsins, such as cathepsin B, and cathepsin D, proteolytic assays play a central role in cancer diagnosis and follow-up of malignant diseases [70-75]. Second, viral infections such as HIV could be diagnosed directly by detection and monitoring of their own, specific proteases. This underscores the need for new highly sensitive and fast assays for the specific detection of proteolytic enzymes.

To date, different fluorescence-based assays have been developed to proof the presence of a specific protease in a sample using labeled enzyme substrates. Commonly, enzyme substrates, e.g. a specific peptide sequence, are doubly labeled with a donor and an acceptor fluorophore in a way that ensures efficient FRET [76, 77]. Upon cleavage of the peptide substrate by a protease the spatial contact between the donor and acceptor fluorophore gets lost. This enables the

direct monitoring of protease activity by measuring the increase in donor fluorescence intensity. Alternatively, a peptide substrate might be doubly labeled with the same fluorophore. In aqueous solution hydrophobic interactions of the fluorophores might drive the peptide into a conformation in which the fluorophores can form non- or only weakly fluorescent dimers [78]. Nevertheless, chemical modifications on peptide substrates reduce the affinity of the resulting probe to the target molecule and hence the detection sensitivity of the assay. Thus, a minimum of chemical modification is favorable for the design of high-affinity molecular probes for proteases.

We implemented our developed method using quenched peptide probes based on PET reactions between fluorophores and the amino acid tryptophan for ultra-sensitive and specific detection of proteolytic enzymes in homogeneous solution [56]. The reported new approach to assay proteolytic enzymes using quenched peptide probes based on photoinduced electron transfer between fluorophores and tryptophan residues upon contact formation offers several advantages. First, the synthesis of large quantities of quenched peptide probes is uncomplicated and inexpensive compared to the use of doubly labeled peptide probes. Second, modification of the peptide substrate is reduced to the minimum, i.e. a single reporter fluorophore, which potentially enables more accurate monitoring of enzyme activity. By monitoring the time-dependent fluorescence intensity, the presented technique permits real-time analysis of proteolysis. Third, our new protease assay enables fast, specific, and highly sensitive detection of proteolytic enzymes with a broad dynamic range (more than 6 orders of magnitude) and detection limits below the picomolar range [56]. These results raise our hopes that singly labeled quenched peptide probes can be used advantageously for the development of new fast and highly-sensitive fluorescence assays for cancer diagnosis and follow-up of malignant diseases through the detection of specific proteases.

6. CONCLUSION AND OUTLOOK

Contact-induced, selective fluorescence quenching of extrinsic fluorophores by Trp and G, elementary monomeric units of proteins and nucleic acids, represents a complementary tool to FRET-based studies both in the exploration of spatial and temporal scales, with impact on diagnostic applications. PET-based fluorescent probes, carefully designed and introduced into polypeptides and nucleic acids, provides the possibility to sense distinct conformational transitions of biopolymers and to monitor ligand binding or enzymatic reactions by translating the underlying molecular events into digital "on/off" fluorescence switching that can be detected with single-molecule sensitivity. The combination of the designed reporter systems with fast FCS experiments allows monitoring of polymer chain dynamics and protein folding events with a temporal

resolution that keeps up with the fastest state-of-the-art pump/probe experiments. Advantageously, in FCS experiments conformational dynamics are measured under equilibrium conditions without external thermodynamic perturbation and at highly dilute sample concentrations where intermolecular interactions vanish. The capability of single-molecule experiments in the far-red spectral range to study biomolecular recognition and enzymatic activity in complex biological media like human blood serum opens up the possibility to develop diagnostic tools for *in-vivo* applications and near-patient testing in the near future.

REFERENCES

[1] X. Michalet, A. N. Kapanidis, T. Laurence, F. Pinaud, S. Doose, M. Pflughoefft and S. Weiss, *Annu. Rev. Biophys. Biomol. Struct.*, *32 (*2003) 161-182.

[2] T. Förster, *Annalen der Physik*, *6 (*1948) 55-75.

[3] T. Ha, *Methods*, *25 (*2001) 78-86.

[4] H. Yang, G. Luo, P. Karnchanaphanurach, T. M. Louie, I. Rech, S. Cova, L. Xun and X. S. Xie, *Science*, *302 (*2003) 262-266.

[5] T. Ha, T. Enderle, D. F. Ogletree, D. S. Chemla, P. R. Selvin and S. Weiss, *Proc. Natl. Acad. Sci. USA*, *93 (*1996) 6264-6268.

[6] A. N. Kapanidis, N. K. Lee, T. A. Laurence, S. Doose, E. Margeat and S. Weiss, *Proc. Natl. Acad. Sci. USA*, *101 (*2004) 8936-8941.

[7] M. Cotlet, S. Masuo, G. Luo, J. Hofkens, M. Van der Auweraer, J. Verhoeven, K. Mullen, X. S. Xie and F. De Schryver, *Proc. Natl. Acad. Sci. USA*, *101 (*2004) 14343-14348.

[8] M. W. Holman, R. Liu, L. Zang, P. Yan, S. A. DiBenedetto, R. D. Bowers and D. M. Adams, *J. Am. Chem. Soc.*, *126 (*2004) 16126-16133.

[9] H. Neuweiler and M. Sauer, *Curr. Pharm. Biotechnol.*, *5 (*2004) 285-298.

[10] X. S. Xie and J. K. Trautman, *Annu. Rev. Phys. Chem.*, *49 (*1998) 441-480.

[11] S. Weiss, *Science*, *283 (*1999) 1676-1683.

[12] S. Weiss, *Nat. Struct. Biol.*, *7 (*2000) 724-729.

[13] P. Tinnefeld and M. Sauer, *Angew. Chem. Int. Ed. Engl.*, *44 (*2005) 2642-2671.

[14] D. M. Adams, L. Brus, C. E. D. Chidsey, S. Creager, C. Creutz, C. R. Kagan, P. V. Kamat, M. Lieberman, S. Lindsay, R. A. Marcus, R. M. Metzger, M. E. Michel-Beyerle, J. R. Miller, M. D. Newton, D. R. Rolison, O. Sankey, K. S. Schanze, J. Yardley and X. Zhu, *J. Phys. Chem. B*, *107 (*2003) 6668-6697.

[15] G. J. Kavarnos, Fundamentals of Photoinduced Electron Transfer, VCH Publishers, Inc., New York, 1993.

[16] D. Zhong and A. H. Zewail, *Proc. Natl. Acad. Sci. USA*, *98 (*2001) 11867-11872.

[17] T. Heinlein, J. P. Knemeyer, O. Piestert and M. Sauer, *J. Phys. Chem. B*, *107 (*2003) 7957-7964.

[18] C. A. M. Seidel, A. Schulz and M. H. M. Sauer, *J. Phys. Chem.*, *100 (*1996) 5541-5553.

[19] N. Marme, J. P. Knemeyer, M. Sauer and J. Wolfrum, *Bioconjug. Chem.*, *14 (*2003) 1133-1139.

[20] J. R. Lakowicz, Principles of fluorescence spectroscopy, Plenum, New York, 1999.

[21] A. C. Vaiana, H. Neuweiler, A. Schulz, J. Wolfrum, M. Sauer and J. C. Smith, *J. Am. Chem. Soc.*, *125 (*2003) 14564-14572.

[22] S. Doose, H. Neuweiler and M. Sauer, *Chemphyschem*, *6 (*2005) 2277-2285.

[23] J. Kim, S. Doose, H. Neuweiler and M. Sauer, *Nucl. Acids Res.*, *34 (*2006) 2516-2527.
[24] D. Magde, E. L. Elson and W. W. Webb, *Biopolymers*, *13 (*1974) 29-61.
[25] R. Rigler, U. Mets, J. Widengren and P. Kask, *Eur. Biophys. J.*, *22 (*1993) 169-175.
[26] S. T. Hess, S. Huang, A. A. Heikal and W. W. Webb, *Biochemistry*, *41 (*2002) 697-705.
[27] B. J. Berne and R. Pecora, Dynamic Light Scattering, Wiley, New York, 1976.
[28] A. Möglich, F. Krieger and T. Kiefhaber, *J. Mol. Biol.*, *345 (*2005) 153-162.
[29] F. Krieger, B. Fierz, O. Bieri, M. Drewello and T. Kiefhaber, *J. Mol. Biol.*, *332 (*2003) 265-274.
[30] O. Bieri, J. Wirz, B. Hellrung, M. Schutkowski, M. Drewello and T. Kiefhaber, *Proc. Natl. Acad. Sci. USA*, *96 (*1999) 9597-9601.
[31] L. J. Lapidus, W. A. Eaton and J. Hofrichter, *Proc. Natl. Acad. Sci. USA*, *97 (*2000) 7220-7225.
[32] L. J. Lapidus, P. J. Steinbach, W. A. Eaton, A. Szabo and J. Hofrichter, *J. Phys. Chem. B*, *106 (*2002) 11628-11640.
[33] F. Huang and W. M. Nau, *Angew. Chem. Int. Ed. Engl.*, *42 (*2003) 2269-2272.
[34] R. R. Hudgins, F. Huang, G. Gramlich and W. M. Nau, *J. Am. Chem. Soc.*, *124 (*2002) 556-564.
[35] H. Neuweiler, A. Schulz, M. Böhmer, J. Enderlein and M. Sauer, *J. Am. Chem. Soc.*, *125 (*2003) 5324-5330.
[36] R. Zwanzig, *Proc. Natl. Acad. Sci. USA*, *94 (*1997) 148-150.
[37] A. Szabo, K. Schulten and Z. Schulten, *J. Chem. Phys.*, *72 (*1980) 4350-4357.
[38] G. Wilemski and M. Fixman, *J. Chem. Phys.*, *60 (*1973) 878-890.
[39] X. Wang and W. M. Nau, *J. Am. Chem. Soc.*, *126 (*2004) 808-813.
[40] G. Bonnet, O. Krichevsky and A. Libchaber, *Proc. Natl. Acad. Sci. USA*, *95 (*1998) 8602-8606.
[41] A. Ansari, S. V. Kuznetsov and Y. Shen, *Proc. Natl. Acad. Sci. USA*, *98 (*2001) 7771-7776.
[42] Y. Q. Shen, S. V. Kuznetsov and A. Ansari, *J Phys Chem B*, *105 (*2001) 12202-12211.
[43] J. Jung and A. VanOrden, *J. Am. Chem. Soc.*, *(*2006)
[44] W. A. Eaton, V. Munoz, S. J. Hagen, G. S. Jas, L. J. Lapidus, E. R. Henry and J. Hofrichter, *Annu. Rev. Biophys. Biomol. Struct.*, *29 (*2000) 327-359.
[45] J. Kubelka, J. Hofrichter and W. A. Eaton, *Curr. Opin. Struct. Biol.*, *14 (*2004) 76-88.
[46] J. W. Neidigh, R. M. Fesinmeyer and N. H. Andersen, *Nat. Struct. Biol.*, *9 (*2002) 425-430.
[47] L. Qiu, S. A. Pabit, A. E. Roitberg and S. J. Hagen, *J. Am. Chem. Soc.*, *124 (*2002) 12952-12953.
[48] H. Neuweiler, S. Doose and M. Sauer, *Proc. Natl. Acad. Sci. USA*, *102 (*2005) 16650-16655.
[49] C. D. Snow, B. Zagrovic and V. S. Pande, *J. Am. Chem. Soc.*, *124 (*2002) 14548-14549.
[50] A. P. de Silva, H. Q. N. Gunaratne, T. Gunnlaugsson, A. J. M. Huxley, C. P. McCoy, J. T. Rademacher and T. E. Rice, *Chem. Rev.*, *97 (*1997) 1515-1566.
[51] S. C. Burdette, G. K. Walkup, B. Spingler, R. Y. Tsien and S. J. Lippard, *J. Am. Chem. Soc.*, *123 (*2001) 7831-7841.
[52] L. Zang, R. Liu, M. W. Holman, K. T. Nguyen and D. M. Adams, *J. Am. Chem. Soc.*, *124 (*2002) 10640-10641.
[53] M. Sauer, B. Angerer, W. Ankenbauer, Z. Foldes-Papp, F. Gobel, K. T. Han, R. Rigler, A. Schulz, J. Wolfrum and C. Zander, *J. Biotechnol.*, *86 (*2001) 181-201.
[54] J. P. Knemeyer, N. Marme and M. Sauer, *Anal. Chem.*, *72 (*2000) 3717-3724.

[55] H. Neuweiler, A. Schulz, A. C. Vaiana, J. C. Smith, S. Kaul, J. Wolfrum and M. Sauer, *Angew. Chem. Int. Ed.*, *41 (*2002) 4769-4773.
[56] N. Marme, J. P. Knemeyer, J. Wolfrum and M. Sauer, *Angew. Chem. Int. Ed.*, *43 (*2004) 3798-3801.
[57] K. Stöhr, B. Hafner, O. Nolte, J. Wolfrum, M. Sauer and D. P. Herten, *Anal. Chem.*, *77 (*2005) 7195-7203.
[58] S. Tyagi and F. R. Kramer, *Nat. Biotechnol.*, *14 (*1996) 303-308.
[59] L. G. Kostrikis, S. Tyagi, M. M. Mhlanga, D. D. Ho and F. R. Kramer, *Science*, *279 (*1998) 1228-1229.
[60] G. Bonnet, S. Tyagi, A. Libchaber and F. R. Kramer, *Proc. Natl. Acad. Sci. USA*, *96 (*1999) 6171-6176.
[61] O. Piestert, H. Barsch, V. Buschmann, T. Heinlein, J. P. Knemeyer, K. D. Weston and M. Sauer, *Nano Lett*, *3 (*2003) 979-982.
[62] M. Zuker, D. H. Mathews and D. H. Turner, in: J. Barciszewski and B. F. C. Clark (eds.), RNA Biochemistry and Biotechnology, NATO ASI Series, Kluwer Academic Publishers, 1999 (http://bioweb.pasteur.fr/seqanal/interfaces/mfold.html).
[63] S. Scheffler, M. Sauer and H. Neuweiler, *Z. Phys. Chem.*, *219 (*2005) 665–678.
[64] T. Soussi, *Immunol. Today*, *17 (*1996) 354-356.
[65] R. Lubin, B. Schlichtholz, D. Bengoufa, G. Zalcman, J. Tredaniel, A. Hirsch, C. C. de Fromentel, C. Preudhomme, P. Fenaux, G. Fournier, P. Mangin, P. Laurent-Puig, G. Pelletier, M. Schlumberger, F. Desgrandchamps, A. Le Duc, J. P. Peyrat, N. Janin, B. Bressac, T. Soussi and et al., *Cancer Res.*, *53 (*1993) 5872-5876.
[66] D. P. Lane, *Nature*, *358 (*1992) 15-16.
[67] J. M. Nigro, S. J. Baker, A. C. Preisinger, J. M. Jessup, R. Hostetter, K. Cleary, S. H. Bigner, N. Davidson, S. Baylin, P. Devilee and et al., *Nature*, *342 (*1989) 705-708.
[68] M. Hollstein, D. Sidransky, B. Vogelstein and C. C. Harris, *Science*, *253 (*1991) 49-53.
[69] R. Lubin, G. Zalcman, L. Bouchet, J. Tredanel, Y. Legros, D. Cazals, A. Hirsch and T. Soussi, *Nat. Med.*, *1 (*1995) 701-702.
[70] O. Simonetti, G. Lucarini, D. Brancorsini, P. Nita, M. L. Bernardini, G. Biagini and A. Offidani, *Cancer*, *95 (*2002) 1963-1970.
[71] A. Franchi, M. Santucci, E. Masini, I. Sardi, M. Paglierani and O. Gallo, *Cancer*, *95 (*2002) 1902-1910.
[72] A. Kugler, *Anticancer Res.*, *19 (*1999) 1589-1592.
[73] Y. Mochizuki, S. Tsuda, H. Kanetake and S. Kanda, *Oncogene*, *21 (*2002) 7027-7033.
[74] N. Harbeck, R. E. Kates, M. P. Look, M. E. Meijer-Van Gelder, J. G. Klijn, A. Kruger, M. Kiechle, F. Janicke, M. Schmitt and J. A. Foekens, *Cancer Res.*, *62 (*2002) 4617-4622.
[75] K. Bajou, J. M. Lewalle, C. R. Martinez, C. Soria, H. Lu, A. Noel and J. M. Foidart, *Int. J. Cancer.*, *100 (*2002) 501-506.
[76] E. D. Matayoshi, G. T. Wang, G. A. Krafft and J. Erickson, *Science*, *247 (*1990) 954-958.
[77] M. Cavrois, C. De Noronha and W. C. Greene, *Nat. Biotechnol.*, *20 (*2002) 1151-1154.
[78] B. Z. Packard, D. D. Toptygin, A. Komoriya and L. Brand, *Proc. Natl. Acad. Sci. USA*, *93 (*1996) 11640-11645.

Handai Nanophotonics, Volume 3
H. Masuhara, S. Kawata and F. Tokunaga (Editors)

Chapter 7

Second harmonic generation imaging microscopy of fibrillar structures

S. Plotnikov,[a,b] O. Nadiarnykh,[a] W. A. Mohler,[b] and P. J. Campagnola[a]

[a]Center for Cell Analysis and Modeling, Department of Cell Biology, University of Connecticut Health Center, 263 Farmington Avenue, Farmington CT 06030, USA

[b]Center for Cell Analysis and Modeling, Depart of Genetics and Developmental Biology, University of Connecticut Health Center, 263 Farmington Avenue, Farmington CT 06030, USA

1. INTRODUCTION

In the last several years, Second Harmonic Generation (SHG) has emerged as a powerful nonlinear optical contrast mechanism for biological imaging applications. SHG is a coherent process where two lower energy photons are up-converted to exactly twice the incident frequency (or half the wavelength). Like the more widespread two-photon excited fluorescence (TPEF) modality, SHG is also a nonlinear optical process. However, the underlying physical natures differ substantially, and here we present a comparison of the respective

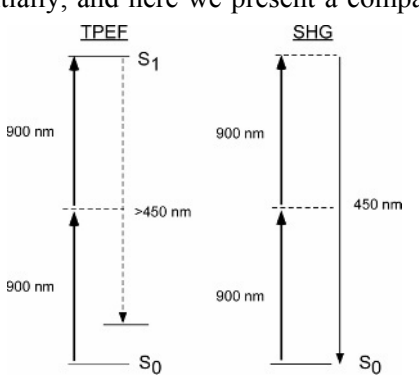

Fig.1. Jablonski diagram comparing the photophysics of two-photon excited fluorescence (left) and Second Harmonic Generation (right).

photophysics. The processes of two-photon excited fluorescence (left) and second harmonic generation (right) are shown in the Jablonsky diagram in Fig1. Consider the case of a hypothetical dye with a one-photon absorption maximum at 450 nm. Excitation can also occur via two-photon absorption at 900 nm, where the chromophore is simultaneously excited from the ground state, S_0, through a virtual state to the first excited state S_1. The resulting emission spectrum will be the same for both excitation modes since relaxation is independent of the excitation pathway. SHG, by contrast, does not arise from an absorptive process. Instead, an intense laser field induces a non-linear, second order, polarization in the assembly of molecules, resulting in the production of a coherent wave at exactly twice the incident frequency (or half the wavelength, here 450 nm.).

SHG has several advantageous features that make it an ideal approach for imaging tissues *in situ.* A particularly strong attribute of the SHG method lies in the property, that in tissues, the contrast is produced purely from endogenous species. This coupled with the physical basis that the SHG signals arise from an induced polarization rather from absorption leads to substantially reduced photobleaching and phototoxicity relative to fluorescence methods (including multiphoton). Additionally, because the excitation typically uses the same near infrared wavelengths (800-1000 nm) produced by titanium -sapphire lasers that are also used for TPEF, this method is well-suited for studying intact tissue samples since excellent depths of penetration can be obtained. For example, we have acquired optical sections into 550 microns of mouse muscle tissue with high contrast throughout the entire axial profile [1]. Furthermore, detailed information about the organization of protein matrices at the molecular level can be extracted from SHG imaging data. This is because the SHG signals have well-defined polarizations with respect to the laser polarization and specimen orientation which can respectively be used to determine the absolute orientation of the protein molecules in the array, as well as the degree of organization of proteins in tissues.

These attributes have recently been exploited to examine a wide range of structural proteins arrays in situ [1-12]. The plurality of the recent reports has focused on visualizing collagen fibers in natural tissues including skin, tendon, blood vessels, and cornea.[3, 5, 13-16]. Other work has examined the fibrillar structure of self-assembled or reconstituted collagen structures [4, 17]. Some of these efforts have focused on elucidating the physical principles that give rise to SHG in tissues as well as taking steps to use this contrast mechanism in the application of diagnosing disease states or other pathological conditions.

Here we provide an exhaustive characterization of the contrast formation in collagen and acto-myosin structural arrays. We here define SHG producing proteins as “harmonophores” to explicitly distinguish them from fluorescent dyes or fluorescent proteins (e.g. green fluorescent protein, (GFP)). Specifically

we determine the underlying biochemical and the supramolecular structural aspects that give rise to SHG contrast in collagen and actomyosin based tissues.

2. EXPERIMENTAL METHODS

A schematic of our combined SHG/TPEF microscope is shown in Fig. 2. The lasers consists of a solid state Nd:YAG laser (5-10 watts) pumped tunable (700 and 1000 nm) titanium sapphire (ti:sap) oscillator. Since SHG is not a resonant process, the choice of laser fundamental wavelength is not as critical as that of fluorescence excitation. Ti:sap lasers have divergences of 1 mrad and we compensate for the divergence with a 1 meter focal length lens in the coupling space to achieve the proper spot size and thus maximize the peak power at the specimen. Both a half wave (λ/2) and quarter wave plate (λ/4) are used to precisely control the polarization of the laser at the focal plane of the microscope. These are necessary in order to compensate for the ellipticity introduced by the scanning mirrors and other non -45 degree reflections. This level of control is important to perform accurate polarization methods that allow the determination of the structural properties of the protein array.

SHG is a coherent process and consequently the majority of the signal wave co-propagates with the laser. We typically use a long working distance 40X 0.8 N.A. (3 mm) water immersion lens and a 0.9 N.A. condenser for excitation and signal collection, respectively. The use of a higher NA condenser yields more

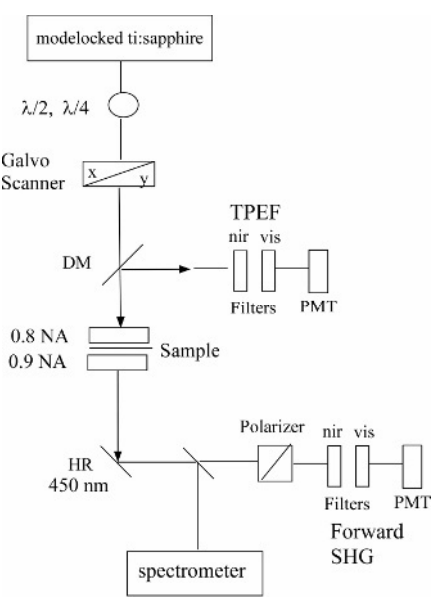

Fig 2. Schematic Diagram of the modified SHG/TPEF microscope.

efficient collection for highly scattering tissue specimens. Since unlike the epi-geometry that can be used for backscattered SHG, the transmission path does not contain an infinity space, an additional lens or telescope is required to re-collimate the SHG signal and provide a loose focus on the detector. Two additional elements are added to the transmission path. A Glan –Laser polarizer with high extinction is used for analysis of the SHG signal polarization that can be used to provide a measure of the organization of the protein array [1]. Second, a fiber-optic based spectrometer is inserted in to the collection path with a kinematic mount to verify the SHG wavelengths.

An important consideration in SHG microscopy is the efficient isolation of the desired wavelength from the fundamental laser. This is because the latter is least six orders of magnitude more intense than the desired second harmonic signal. The SHG signal is first reflected with a reflector centered around the signal (~20 nm bandwidth) which provides ~100 fold discrimination from the laser as well as autofluorescence. The SHG is further isolated from the laser and any remaining fluorescence by BG-39 color glass filters and a bandpass filter (~10 nm bandwidth) respectively. While absolute values of $\chi^{(2)}$ for structural proteins are not known, SHG signal levels are typically smaller than those of TPEF. Thus we use single photon counting electronics to maximize detection efficiency. This approach provides higher sensitivity and reduced noise over the analogue detection and integration that is used in commercial microscopes.

3. RESULTS AND DISCUSSION

3.1. Collagen Based tissues

Type I collagen is the most prevalent protein in the human body, being the primary component in such diverse tissues as skin, bone, tendon, and cornea. These tissues are all birefringent, and consist of highly-ordered structures and provide high levels of contrast in SHG imaging microscopy. The first report of SHG imaging of tissue was by Freund in 1986, [18] where they examined the polarity in type I collagen fibers from rat tail tendon (RTT). Several recent efforts have revisited the RTT at higher resolution and in greater depth, [9, 14, 15] as well as investigated the applicability of using SHG to visualize other collagen based tissues [3, 5, 16]. Here we provide demonstrative examples of our current work in this area.

Figure 3 shows representative SHG images of the bone, skin, and tendon. In all three cases, the regularity of the fibrillar structure of the collagen is observed. In particular, the collagen in rat tail tendon is one of nature's most regularly structured arrays. SHG imaging if skin allows for selective investigation of the dermis, other layers are devoid of collagen. It should be noted that elastin, the other major component of the dermis, does not produce SHG contrast. This is

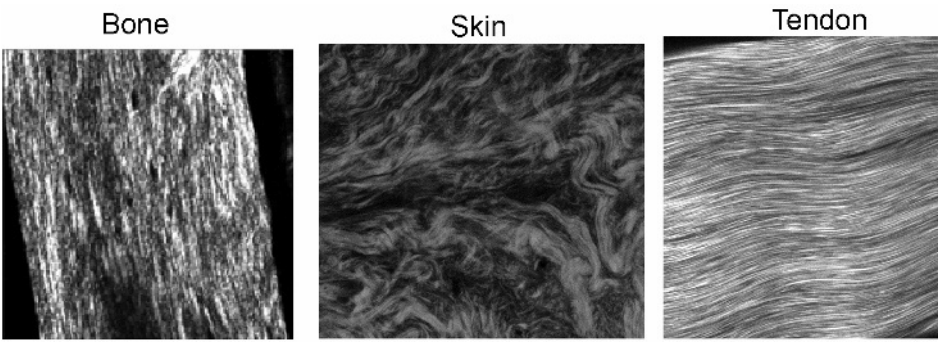

Fig. 3. Representative SHG images of collagen-based tissues ex vivo.

likely because it is comprised of α-helices, β-sheets and random coils, and as such has an essentially isotropic structure. Bone is highly turbid consisting largely of collagen and minerals. Thus the same level of penetration is not expected to be achievable as that in less highly scattering tissues such as tendon or muscle, where the mean penetration depths are ~100 microns. However, this shows that high contrast SHG images can still be obtained in the forward collection geometry. While these do not possess the striking regularity of tendon, the collagen fibers are clearly identifiable.

A fundamental question regards the molecular or supramolecular source of the SHG contrast in these tissues. Since SHG is an electric dipole process, a given molecular arrangement of SHG-emitting dipoles will yield a characteristic profile of response to varying laser polarization. For this reason, the angular dependence of the SHG intensity can be fitted to estimate the orientation of source harmonophores within the molecular assembly. The second order susceptibility, $\chi^{(2)}$, consists of 27 matrix elements. Theoretical considerations of the structure of protein filaments allow us to simplify the general case of SHG by assuming that identical harmonophores exist in collagen fibrils exist within cylindrically symmetric arrangements (C_∞ symmetry). Assuming Kleinman symmetry by using non-resonant laser excitation further simplifies the scenario. These two considerations then reduce the number of active matrix elements from 27 to 3 independent and one degenerate term and can be used to determine the angle between the symmetry axis and the dipole moment. To achieve this, we start with the general description of the second order polarization $P^{(2)}$ as given by:

$$P^{(2)} = az(z \bullet E)^2 + bz(E \bullet E) + cE(z \bullet E) \tag{1}$$

where a,b, and c are coefficients expressed in terms of the 4 non-vanishing elements of $\chi^{(2)}$, z is the unit vector, and E is the electric field vector. The values

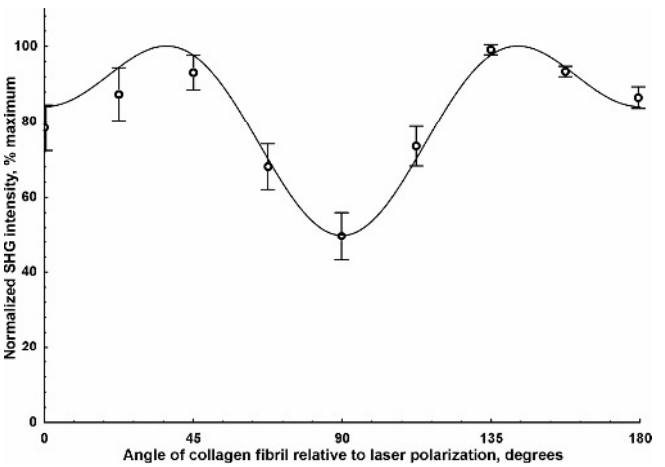

Fig. 4. Angular dependence of the SHG intensity used to fit to Eq. 1.

of these variables can be deduced by fitting the experimental SHG emission intensity as a function of laser polarization angle. The data for rat tail tendon along with the fit to Eq. 1 are shown in Fig. 4. This fits yields the angle, θ, which we interpret as the angle of maximum hyperpolarizability of the harmonophore relative to the long axis of the model cylinder. We obtain an angle θ = 50.7° for tendon collagen fibrils which coincides well with θ = 45.3°, the known pitch of the polypeptide chain in the collagen helix [19]. It should be noted that while this match with ultrastructural data is not perfect, the SHG method can be performed in situ, and may be a powerful approach for the analysis of diseased tissues.

An additional aspect of SHG imaging is the capability of probing the orientation of fibrils and fibers in tissues. Specifically, the SHG vector nature can be exploited to provide data on the spatial organization, i.e. long range order, of the helices from the size range of 500 nm and larger by using polarization anisotropy measurements of the SHG signal. For processes arising from an electric dipole process (e.g. absorption, and SHG), the angular distribution of excitation is given by the second Legendre polynomial (a $\cos^2$ function). The anisotropy parameter, β, describing the molecular orientation, is derived from this function, and when using linearly polarized light is given by:

$$\beta = \frac{I_{par} - I_{perp}}{I_{par} + 2I_{perp}} \tag{2}$$

where I_{par} and I_{perp} are the intensities of the signals whose polarizations are parallel and perpendicular to the polarization of the incident laser. This

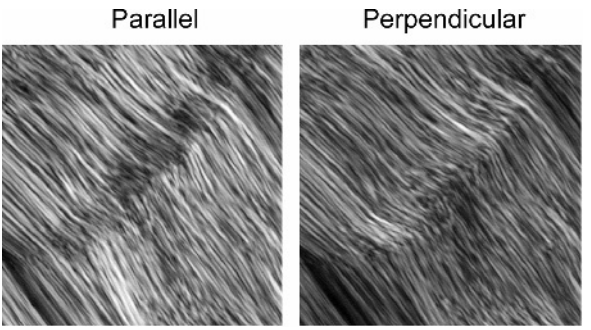

Fig. 5. SHG Polarization anisotropy of ex vivo mouse tendon where the left and right images correspond to the Glan polarizer oriented parallel and perpendicularly, respectively, to the laser polarization.

parameter can vary between –0.5,and 1. The special case of 0 represents the isotropic situation where I_{par} and I_{perp} are equal and would physically correspond to having complete randomization or disruption of the helices. The value of 1 would correspond to complete ordering relative to the incident laser, i.e. having well-aligned, well structured fibrils/fibers.. As a demonstrative example Fig. 5 shows the resulting images for mouse tendon where the analyzer was parallel (left) and perpendicular (right) to the laser polarization. By integrating the entire field of view, we obtain an anisotropy of 0.3. It should be noted that integration of smaller regions would likely result in a measurement of higher anisotropy.

3.2. Biochemical and structural characterization of the SHG harmonophore

We are also using SHG imaging to examine the muscle sarcomere structure in an effort to understand the morphological changes that happens to muscle tissue during aging as well as in diseases including muscular dystrophy. Because of the crucial importance of understanding the molecular source of sarcomeric SHG for any interpretation of experimental or medical imaging data, we present a thorough characterization of SHG from isolated myofibrils. These preparations have allowed us to perform biochemical and pharmacological manipulations of the sarcomeric filaments and myosin motor domains while imaging, and enabled high-resolution analysis of the polarization anisotropy of SHG within individual sarcomeres.

We first turn our attention to a biochemical characterization of the SHG source in acto-myosin complexes. Whereas the component protein that give rise to SHG in collagen fibrils clearly is collagen, the muscle sarcomere has a more complex structure comprising three distinct forms of major filaments and dozens of proteins [20]. Specifically, thick myosin filaments, thin actin filaments, titin filaments, or the combination of these, could comprise the SHG

harmonophore. Furthermore, either the myosin head and/or tail domains could give rise to the SHG signal.

First we directly investigate the role of myosin in SHG image formation. Treatment of myofibrils with low-ionic strength pyrophosphate solution is known to cause specific disruption of myosin filaments, but does not destroy actin or titin filaments [21, 22]. Here fluorescent actin labeled extracted myofibrils were attached to a polylysine-coated coverslip, and myosin was extracted with the pyrophosphate solution. The SHG and TPEF images before and after treatment are shown in Fig. 6A (left and center panels are SHG and TPEF respectively) prior to extraction and the right panel is the combined image following extraction. As in *C. elegans*, and in analogy to polarization microscopy, the SHG image of each sarcomere consisted of a bright double-band. We observed that the extraction essentially eliminated the SHG contrast from the isolated myofibrils but did not change the periodicity of phalloidin-stained F-actin within myofibrils, indicating that both actin and titin filaments remain intact. This result unambiguously demonstrates that myosin is necessary to produce SHG in myofibrils.

Our previous results using GFP-labeled myosin in *C. elegans* body wall muscle indicated that SHG is emitted from the region surrounding the

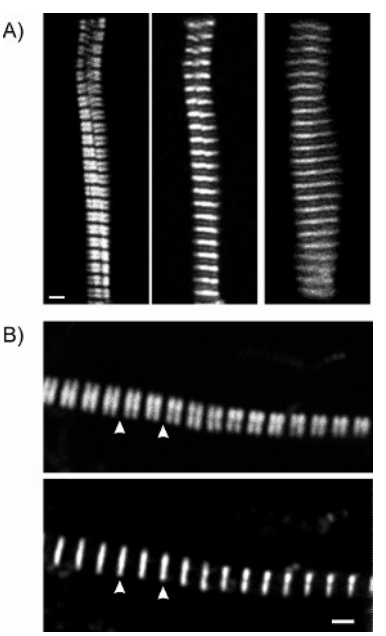

Fig 6. A) Extraction of myosin completely abolishes the SHG signal but does not change the periodicity of the phalloidin actin fluorescence. B) Comparison of the SHG sarcomere patterns (top panel) and the α-actinin labelled actin thin filaments, showing no overlap. This figure shows that the SHG arises from the myosin thick filaments.

sarcomeric M-line [1].Here we extend these findings to myofibrils by explicitly examining the spatial localization of the actin thin filaments with respect to the observed SHG signal. To this end we combined SHG with 2PEF microscopy to simultaneous visualize the spatial overlap of the SHG with either α-actinin or actin (Fig. 6B), where the top and bottom panels are SHG and TPE fluorescence, respectively) allowed us to precisely determine the localization of SHG within the sarcomere. We never observed colocalization of SHG and α-actinin indicating that the broad dark band between SHG-bright zones contains the Z-line and thin filaments.

Having uniquely identified the myosin thick filaments as the harmonophore in acto-myosin complexes, we lastly need to determine from whence the SHG arises within the myosin molecule. Specifically, the thick filaments contain both static rod domains and dynamic motor heads and we need to measure their respective contributions to the SHG contrast. Because there is no significant long-distance cooperativity between the movement of myosin heads during the contractile cycle [23], any SHG emitted from head domains should be abolished or reduced during muscle contraction. Thus we induced contraction in a myofibril (shown in Fig. 7A, left panel) and using a rapid line-scan acquisition mode (right panel) we found that SHG intensity does not change significantly during induced myofibril contraction.We concluded from this collection of experiments that myosin heads do not contribute detectably to emission of SHG from sarcomeres.

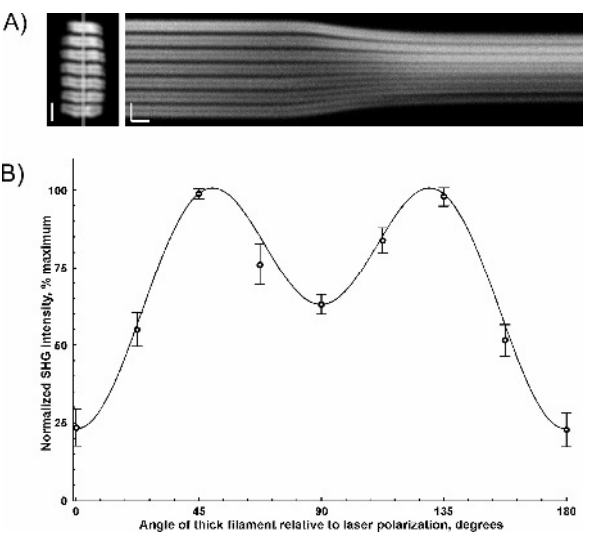

Fig. 7. A) Myofibrils were induced to contract and no change in SHG intensity was observed during rapid-line scan imaging. B) Polarization analysis as described in 3.1 indicates the SHG emanates from the coiled-coil tail domain. Together, these results suggest that the head domain does not produce significant SHG contrast.

To further verify this finding, we employ the analogous polarization analysis used in 3.1 to determine the angle between the dipole moment and the symmetry axis. The resulting fit (shown in Fig. 7B) for isolated myofibrils at 900 nm excitation gave $\theta = 61.2°$ Importantly, this value closely approximates the angle of the polypeptide chain in an α-helix relative to the helix axis, measured as 68.6° by X-ray diffraction [19]. Thus we regard the calculated angle for myosin as a viable estimate of the arrangement of excitable dipoles with myofibrils. Since $\theta = 61.2°$ matches the pitch of the peptide coil of the myosin rod domain, we concluded that sarcomeric SHG arises predominantly in the coiled rod portion of thick filaments. This assertion is in agreement with the contractile data in Fig 7A.

3.3. Optical Clearing to improve SHG image contrast

In addition to this characterization of the contrast mechanism, efforts must be taken in optimize the SHG efficiency in order to realize clinical potential. A limiting aspect of SHG imaging lies in the directionality of the emission. In the limit of a non-scattering sample with uniformly aligned molecules (or more precisely dipole moments), essentially all the SHG is forward directed [24]. This is due to the coherence of the emission. For thicker, turbid, highly scattering specimens, the SHG signal experiences multiple scattering events, and as consequence, a fraction of the SHG is backscattered. This mode of SHG imaging is more convenient to implement than that of the forward emitted wave as it requires only minimal modification of an existing multiphoton fluorescence microscope. Furthermore, this configuration allows imaging of the top layers intact skin or whole animals that cannot be performed in a transmitted geometry. On the other hand, the resulting coherence and polarization anisotropy of the backwards directed component to date has not been thoroughly investigated. It is likely that much of the structural information encoded in the SHG signal in the forward direction will be lost in the backward signal due to the multiple scattering events. It would be advantageous to exploit the purely coherent forward directed signal which retains the anisotropy and simultaneously achieve significant penetration into highly scattering tissues, including muscle.

Our approach to achieve this goal is to combine SHG imaging with the optical clearing effect. In this process, a hyper-osmotic reagent of high refractive index (e.g. glycerol) is added to the tissue to increase its transparency. There is increasing interest in this idea where recent studies have examined the clearing potential of hyper-osmotic agents (glycerol, PEG and DMSO) in such diverse tissues as skin [25-27]; blood [28]; *dura mater* [29], and gastric tissue [30]. It was demonstrated in these examples that the depth of light penetration increased to 3 fold. Here we present data on optical clearing with glycerol of ex vivo mouse muscle, using 3-D SHG imaging on intact tissue, and show that

transparency is substantially increased (~2.5 fold). We characterize the mechanism for clearing in acto-myosin and further demonstrate the non-invasive nature of the process.

In 1949, Szent-Gyorgyi [31] introduced the use of glycerol to extract muscle and this method has become a typical approach for studying muscle biology. The method is used both to isolate fibers for storage, as well as to perform physiological measurements. Here we adapt this approach to determine if increased imaging depth can be obtained. We first examine the effect with 50% glycerol, as the biochemistry of this treatment has been the most characterized [32]. Fig. 8A shows x-z projections for the control and 24 hour timepoints, where Fig. 8B shows the intensity of the SHG as a function of depth into the tissue at time points up to 24 hours. The muscle fibers are easily distinguished in this representation and the improvement in transparency is readily observed with increasing time following treatment. No further clearing

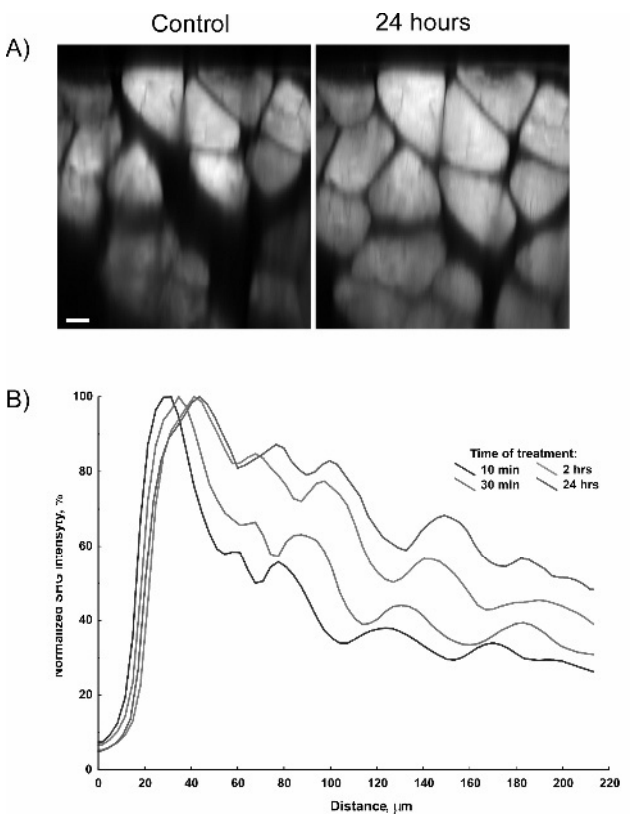

Fig. 8. Optical clearing of ex vivo muscle tissue by SHG imaging. A) X-Z projections for uncleared and cleared tissue. B) Timecourse of the process showing the SHG intensity throughout the axial extent of the tissue at intervals up to 24 hours

was observed at time points longer than 2 hours. By contrast, the control experiment of imaging muscle tissue in Tissue-Tek O.C.T. compound over 24 hours showed no optical clearing (data not shown).

Having established the power of the method, we turn our attention to determination of the mechanism of the clearing process in acto-myosin based tissue. We can analyze the SHG intensity at a given imaging depth by consideration losses due to scattering and absorption. The intensity, I(z), as a function of depth, z, is expected to scale as:

$$I(z) = I(0)e^{-\mu_{eff} z} \tag{3}$$

where I(0) is the intensity at the top of the stack and μ_{eff} is the effective attenuation coefficient and is the reciprocal of the mean penetration depth [33]. This quantity is related to the reduced scattering and absorption coefficients, μ_a and μ_s', respectively by:

$$\mu_{eff} = [3\mu_a(\mu_a + \mu_s')]^{1/2} \tag{4}$$

For SHG imaging, the total absorption and scattering coefficients are the sum of the terms corresponding to the fundamental (900 nm) and SHG wavelengths (450 nm).

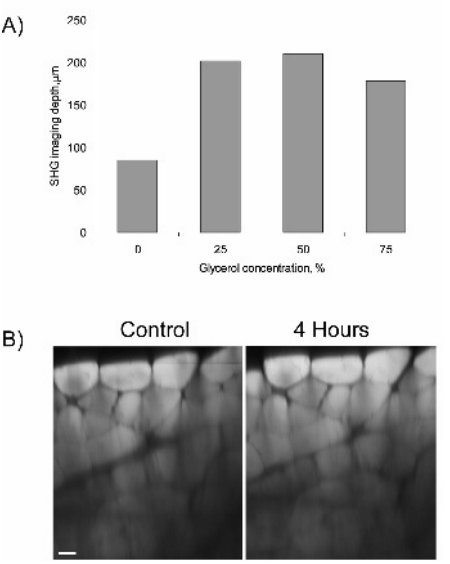

Fig 9. A) Histogram of imaging depths (1/e point) as a function of glycerol concentration. B) X-Z projections of the SHG imaging profile of fixed tissue for the control and 50% glycerol treated cases. Scale bar=20 microns. These data indicate that the clearing mechanism arises from a reduction of the secondary inner filter effect with essentially no contribution from refractive index matching.

We performed independent experiments to investigate the relative contributions of refractive index matching and reduced scattering as well as a decrease in the absorption by decreasing the effective intracellular OD. The results of fits to Eq. 3 for several trials of the control, 25%, 50%, and 75% glycerol treated muscle are shown in the bar graph in Fig 9A. We observe that the glycerol treatments all improved the mean SHG imaging depths (1/e point) from 85 ~ 210 microns, nearly a 2.5 fold improvement over the uncleared tissue. The similarity in imaging depth for all three glycerol concentrations provides insight into the clearing mechanism. In collagen based tissues, the presumed mechanism of optical clearing has been attributed to refractive index matching. [27] However, for the case of muscle, we obtained the same imaging depths of ~200 microns for all the glycerol concentrations. The higher concentrations of glycerol must result in higher intracellular refractive indices, but the degree of clearing was the same. While we have not found a published refractive index of muscle at 900 nm, the refractive index of muscle at 632 nm has been reported to be ~1.38 [34] and is comparable to the 50% glycerol case. However, given the similarity of imaging depths at all concentration we conclude that index matching only plays a small role in the optical clearing of muscle.

We must then turn to a reduction of the inner filter mechanism of the clearing in muscle with glycerol. It was shown by Huxely that this treatment permeabilizes cellular membranes, and thus extracts a fraction of the cytoplasmic proteins. This mechanism could significantly decrease light absorption and scattering within a tissue and provide much greater penetration into highly scattering tissue. This is reasonable since the SHG wavelength is 450 nm and its absorption by cytochromes and heme proteins is expected to be significant. To investigate if this is indeed the major mechanism responsible for the optical clearing n muscle, we treated muscle tissue with a mixture of 4% paraformaldehyde and 0.5% gluteraldehyde to crosslink the membrane proteins and prevent or minimize protein leaching out of the cells. Three dimensional stacks of 50% glycerol treated muscle were then acquired over a 24 hour time course as before, The resulting x-z projections for the gluteraldehyde fixed and unfixed tissue are shown in Fig 9B where the left and right panels correspond to the 0 and 4 hour time points respectively. Little clearing occurs in the fixed tissue, as only a slight increase (~10%) in SHG intensity is observed in the middle of the stack. This lack of clearing upon fixation allows us to assign the reduction of the inner filter effect as the predominant mechanism for the increased imaging depth, with refractive index playing essentially no role.

We must also consider whether the clearing process has any detrimental effects on the muscle tissue. Here we present quantitative analyses that that the structure of the tissue remains unchanged following clearing. In our first treatment, we examine the sarcomere lengths before and after glycerol application. Sarcomeres have well defined characteristic lengths for contracted

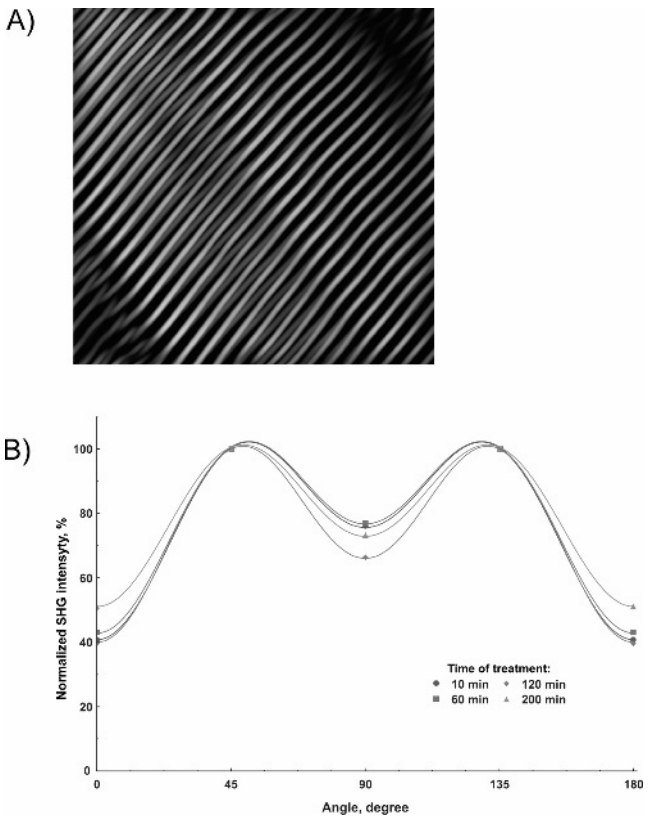

Fig. 10. A) FFT filtered image of the sarcomeres for 10 minutes and 2 hour timepoints, showing excellent overlap of the spatial frequencies. B) Dependence of the SHG intensity as a function of the laser polarization. These two data indicate that the clearing process does not alter the fiber structure or supramolecular structure of the acto myosin complexes.

and extended muscle and it is important in terms of any functional imaging that these lengths do not change during the clearing process. The highly regular periodicity sarcomeres make them amenable to analysis via a Fast Fourier Transformation (FFT). Fig. 10 shows the inverse FFT of the sarcomere pattern before and after clearing, and we see that same spatial fequency is recovered for these timepoints. This results shows that optical clearing with glycerol not only provides increased imaging depth but does so with little perturbation of the tissue structure.

We must also consider the possibility of alterations occurring on the *molecular level* due to the glycerol treatment. To determine this, we use the polarization analysis shown for collagen and myosin above, where in this case we compared the angular polarization profiles of the SHG signal before and after optical clearing. As shown in Fig. 10B we found essentially identical

angular dependences and conclude that there is no significant change in this structure of the acto-myosin complexes following the clearing process. In sum, optical clearing is a non-invasive means to achieve significantly enhanced imaging depth of acto-myosin complexes.

4. SUMMARY

Here we have performed an exhaustive characterization of the SHG in acto-myosin complexes and collagen based tissues. For the case of muscle, through biochemical and polarization analysis we have uniquely determined that the harmonophore is the myosin thick filament. Moreover, the SHG arises from the coiled-coil tail domain of the myosin, rather than from the dynamic head. Similarly, we have identified the collagen helical structure as the underlying chromophore in these tissues. We have also shown that optical clearing provides significant increase in imaging depth in muscle tissue, with no adverse effects to the underlying tissue structure. The work here then opens the door to use SHG imaging of muscle as a tool to probe muscle based pathologies, such as aging and muscular dystrophy.

ACKOWLEDGMENT

We (PJC and WAM) gratefully acknowledge support under NIH EB-1842. WAM is also supported by a New Scholar in Aging award from the Ellison Medical Foundation. SP acknowledges support from the American Heart Association.

REFERENCES

[1] P.J. Campagnola, A.C. Millard, M. Terasaki, P.E. Hoppe, C.J. Malone, and W.A. Mohler, Biophys. J., 82 (2002) 493.
[2] W. Mohler, A.C. Millard, and P.J. Campagnola, Methods, 29 (2003) 97.
[3] A.T. Yeh, N. Nassif, A. Zoumi, and B.J. Tromberg, Opt. Lett., 27 (2002) 2082.
[4] A. Zoumi, A. Yeh, and B.J. Tromberg, Proc. Natl. Acad. Sci. U S A, 99 (2002) 11014.
[5] A. Zoumi, X. Lu, G.S. Kassab, and B.J. Tromberg, Biophys. J., 87 (2004) 2778.
[6] E. Brown, T. McKee, E. diTomaso, A. Pluen, B. Seed, Y. Boucher, and R.K. Jain, Nat. Med., 9 (2003) 796.
[7] G. Cox, E. Kable, A. Jones, I. Fraser, F. Manconi, and M.D. Gorrell, J. Struct. Biol., 141 (2003) 53.
[8] D.A. Dombeck, K.A. Kasischke, H.D. Vishwasrao, M. Ingelsson, B.T. Hyman, and W.W. Webb, Proc. Natl. Acad. Sci. U S A, 100 (2003) 7081.
[9] R.M. Williams, W.R. Zipfel, and W.W. Webb, Biophys. J., 88 (2005) 1377.
[10] T. Boulesteix, E. Beaurepaire, M.P. Sauviat, and M.C. Schanne-Klein, Opt. Lett., 29 (2004) 2031.
[11] S.-W. Chu, S.-Y. Chen, G.-W. Chern, T.-H. Tsai, Y.-C. Chen, B.-L. Lin, and C.-K. Sun, Biophys. J., 86 (2004) 3914.

[12] C.-K. Sun, S.-W. Chu, S.-Y. Chen, T.-H. Tsai, T.-M. Liu, C.-Y. Lin, and H.-J. Tsai, J. Struct. Biol., 147 (2004) 19.
[13] A.T. Yeh, B. Choi, J.S. Nelson, and B.J. Tromberg, Lasers Surg. Med., (2003) 3.
[14] P. Stoller, B.-M. Kim, A.M. Rubinchik, K.M. Reiser, and L.B. Da Silva, J.Biomed. Opt., 7 (2001) 205.
[15] P. Stoller, K.M. Reiser, P.M. Celliers, and A.M. Rubinchik, Biophys. J., 82 (2002) 3330.
[16] M. Han, L. Zickler, G. Giese, M. Walter, F.H. Loesel, and J.F. Bille, J. Biomed. Opt., 9 (2004) 760.
[17] S. Ramanujan, A.Pluen, T.D. McKee, E.B. Brown, Y.Boucher, and R.K. Jain, Biophys. J., 83 (2002) 1650.
[18] I. Freund, M. Deutsch, and A. Sprecher, Biophys. J., 50 (1986) 693.
[19] K. Beck and B. Brodsky, J. Struct. Biol., 122 (1998) 17.
[20] K.A. Clark, A.S. McElhinny, M.C. Beckerle, and C.C. Gregorio, Annu. Rev. Cell. Dev. Biol., 18 (2002) 637.
[21] J. Hanson and H.E. Huxley, Biochim. Biophys. Acta., 23 (1957) 250.
[22] C.C. Gregorio and V.M. Fowler, J. Cell. Biol., 129 (1995) 683.
[23] V.A. Barnett, J. Muscle. Res. Cell. Motil., 22 (2001) 415.
[24] L. Moreaux, O. Sandre, and J. Mertz, J. Opt. Soc. Am. B, 17 (2000) 1685.
[25] M.H. Khan, B. Choi, S. Chess, K.M. Kelly, J. McCullough, and J.S. Nelson, Lasers Surg. Med., 34 (2004) 83.
[26] M. Khan, B. Choi, S. Chess, J. McCullough, K. Kelly, and J.S. Nelson, Lasers Surg. Med., (2004) 17.
[27] G. Vargas, E.K. Chan, J.K. Barton, H.G. Rylander, 3rd, and A.J. Welch, Lasers Surg. Med., 24 (1999) 133.
[28] V.V. Tuchin, X.Q. Xu, and R.K. Wang, Appl. Opt., 41 (2002) 258.
[29] A.N. Bashkatov, E.A. Genina, Y.P. Sinichkin, V.I. Kochubey, N.A. Lakodina, and V.V. Tuchin, Biophys. J., 85 (2003) 3310.
[30] X.Q. Xu, R.K. Wang, and J.B. Elder, J. Phys. D-Appl. Phys., 36 (2003) 1707.
[31] A. Szent-Gyorgyi, Biol. Bull., 96 (1949) 140.
[32] H.E. Huxley, J. Biophys. Biochem. Cytol., 3 (1957) 631.
[33] B.J. Tromberg, N. Shah, R. Lanning, A. Cerussi, J. Espinoza, T. Pham, L. Svaasand, and J. Butler, Neoplasia, 2 (2000) 26.
[34] G.J. Tearney, M.E. Brezinski, J.F. Southern, B.E. Bouma, M.R. Hee, and J.G. Fujimoto, Opt. Lett., 20 (1995) 2258.

PART II: NANO BIO DYNAMICS

This page intentionally left blank

Handai Nanophotonics, Volume 3
H. Masuhara, S. Kawata and F. Tokunaga (Editors)

Chapter 8

Imaging of enzyme catalysis by wide field microscopy

S. Rocha[a], W. Verheijen[a], K. Braeckmans[b], A. Svendsen[c], M. Skjøt[c], F.C. De Schryver[a], H. Uji-I[a], J Hofkens[a]

[a]Department of Chemistry, Katholieke Universiteit Leuven, Celestijnenlaan 200 F, 3001 Heverlee, Belgium

[b]Laboratory for General Biochemistry & Physical Pharmacy, Ghent University, Harelbekestraat 72, 9000 Ghent, Belgium

[c] Novozyme A/S, NoVo Alle, Bagsvaerd, DK-2880, Denmark

ABSTRACT

In this contribution individual lipase enzymes (PLA1) are investigated in their natural environment, more specific, when released on phospholipid bilayers. After staining the lipid layer, the enzymatic activity could be monitored by the appearance of dark features in the layers by means of wide field microscopy, assuming that the features correspond to reaction products go directly into solution. In this way, real time imaging of the activity is possible. The analysis of the desorbed surface area in the phospholipids bilayer appearing after enzyme injection is then used to estimate the catalytic activity of the enzyme. Variations in speed as a function of time and concentration are observed. Our results show that the enzymatic activity on a natural substrate can be monitored and analysed by the use of wide field microscopy. This approach represents a major step forward in single enzyme studies compared with previous fluorescence-based studies of enzymes where non-natural fluorogenic substrates were used. We also improve the time resolution as compared to AFM measurements on bilayers probing the same enzymatic process.

1. INTRODUCTION

Since the metabolic activity of the cell is mainly based on enzymatic action, the study of enzymes and their properties is a field that attracts a lot of attention. Almost all enzymes studied are proteins, generally ranging between 10 and 500

kDa in molecular weight [1, 2]. Phospholipases form a large family of enzymes that play a key role in signalling cascades [3]. They catalyse the splitting of phospholipids in the presence of water and are grouped on the basis of the specific chemical bond they split. The phospholipases include phospholipase A1 (PLA1), phospholipase A2 (PLA2), phospholipase C and phospholipase D. Phosphatide acylhydrolases (phospholipase A), catalyzes the hydrolysis of one of the acyl groups of phosphoglycerides or glycerophosphatidates. Phospholipase A2 (PLA2) hydrolyzes the acyl group attached to the 2-position and is an extensively studied membrane enzyme [4-7]. In contrast, little information is available on the catalytic activity of PLA1 that hydrolyzes the acyl group at the sn-1 position.

To investigate the enzymatic activity of a phospholipase in its natural environment, we released the enzyme (PLA1) on phospholipid layers. These layers were prepared by the spin coating method [8]. It has been shown that in this way fluid supported 1-palmitoyl-2-oleoyl-sn-glycero-3 phosphocholine (POPC) bilayers are generated. By mixing the fluorescent dye 1,1'-ioctadecyl-3,3,3',3'-tetramethylindodicarbocyanine perchlorate (DiD) in a ratio of less then 1:100 with POPC, the phospholipid layers become fluorescent. Upon hydrolysis, the dye is released in solution. The quantum yield of fluorescence of the dye is much lower in solution than when sitting in the bilayer. This drop in quantum yield together with diffusion of the dye should lead to the formation of dark patches when the enzyme is active.

This desorption of the phospholipids layers upon hydrolysis was monitored by wide field fluorescence microscopy. In this way, the risk of perturbation of the ordering of the layers by the contact of the tip in AFM measurements as previously demonstrated [9, 10] is avoided and a better time resolution is

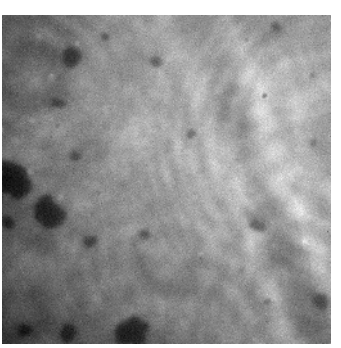

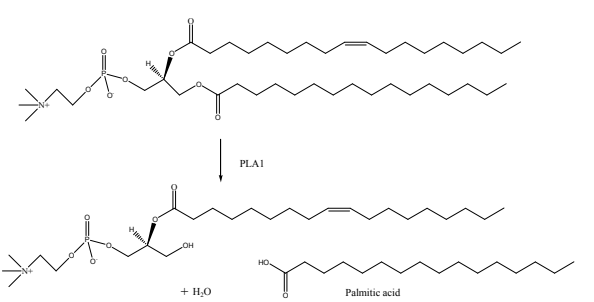

Fig. 1. Left: Typical image of POPC layers before addition of the enzyme. Dark spots show the bare mica (defect regions) while the bright regions correspond to the stained bilayer. The image size is 55 x 55 μm². Right: schematic representation of the hydrolysis of the phospholipid POPC by PLA1

achieved (ms for wide field imaging versus seconds in AFM measurements). Jensen et al. visualized the hydrolysis of fluid bilayers by PLA2 based on a similar scheme by means of fluorescence microscopy [11].

Figure 1 shows a typical wide field image of POPC layers that were stained with DiI before injection of the enzyme. The phospholipid film (bright regions) can be easily discriminated from the mica substrate (dark islands), the difference in height can be demonstrated by AFM (data not shown). The typical size of the images is 50 μm x 50 μm.

2. EXPERIMENTAL SECTION

2.1. Sample preparation

A 10 mM POPC solution in $CHCl_3$ (obtained from Avanti Polar Lipids and used without further purification) that was labelled with 0.5% of 1,1'-didodecyl-3,3,3',3'-tetramethylindocarbocyanine perchlorate (DiIC12 from Molecular Probes) is spin coated at a speed of 3000 rpm during 40 seconds on freshly cleaved sheet of mica with a thickness of approximately 70 to 100 μm. The mica samples are then dried under vacuum for a few hours. Just before measuring, the sample is hydrated by putting the mica sheets in a liquid cell holder and adding 10 mM Hepes buffer (Aldrich) that contains 150 mM sodium chloride (Sigma-Aldrich), 30 μM CaCl2 (Aldrich) and 10 μM EDTA (Sigma). The pH of this buffer solution was adjusted to 8 by adding sodium hydroxide. The sample was kept at 80°C for 3 hours and in case the liquid cell can only contain a small amount of buffer, the buffer solution is refreshed every 30 minutes. Top layers are removed by 'washing' them off gently with fresh buffer solution. PLA1 (variant of *Thermomyces* (*Humicola*) *lanuginosa* lipase) was developed, expressed and purified by Novozymes (Novo Nordisk) and details on the procedure will be published elsewhere.

2.2. Wide Field Set-up

A continuous wave laser diode laser (Uniphase, 532 nm) was used as an excitation source. Typical powers used for the fluorescence imaging are in the range of 0.2 to 0.5 mW in front of the microscope. The laser light was guided into an inverted microscope (IX 71 *Olympus*). The beam reflected by a dichroic mirror and focused at the back aperture of an objective lens (Olympus 60X air objective UplanApo, 0.9 NA). The same objective lens is used to register the required image, after expanding it 3.3 times by a camera lens, on a back illuminated EM-CCD camera (Cascade 512B, Roper Scientific Inc.), giving images with a size in the range of 50 by 50 μm². When images of larger areas are needed, this magnification lens is removed. The exposure time of the camera is mentioned in the figure caption of the different images.

2.3. Image analyses

Image analysis was performed by the program ImageJ and a routine written in Matlab™. The procedure is based on the subtraction of the images whereby the step size can be varied. In this way, areas that are hydrolyzed will appear as distinct regions and the number of pixels can be calculated from these areas. This number can then be converted to the number of square micrometers hydrolyzed between frames or to the number of phospholipids.

3. RESULTS AND DISCUSSION

As mentioned before, PLA1 hydrolyzes the sn-1 fatty acids from phospholipids and produces 2-acyl-lysophospholipids and a fatty acid chain. The overall reaction is shown in Fig.1. After preparing the dye-stained phospholipid layers, the samples are monitored at 5 minutes intervals during 30 minutes to ensure that no new features appear in the images (equilibrated system) prior to adding the enzymes. After addition of the enzyme, the hydrolysis of the bilayers can be seen by the appearance of dark features in the lipid layer. The growth of these features is followed as a function of time. Hydrolysis of the layers nearly always starts from existing defect regions. This observation is confirmed by measuring larger areas (135 x 135 μm², images not shown). Only in very few cases, the hydrolysis starts from regions where no –by wide field imaging detectable- defects are present. Small non-resolvable defects (smaller then the diffraction limit) are in that case most likely the anchoring point for the enzyme(s) to attack the layers.

Figure 2 represents three time laps series for three given concentrations of enzyme, $3.7\ 10^{-7}$ M, $1.9\ 10^{-7}$ M and $4.0\ 10^{-9}$ M, respectively. The snapshots show that for given single enzyme concentration, the black, hydrolyzed regions have a different morphological appearance. For the highest concentration of enzyme, a kind of “wave-front” like behaviour can be observed: the desorption proceeds over a larger area without really showing distinct shapes in the moving wave-front (Fig. 2A). The area that is desorbed in a certain period, expressed in number of pixels or μm² can be used as a measure for the desorption speed. For the intermediate enzyme concentration, the morphology of the hydrolyzed patches resembles what we call ‘tubes’ or ‘channels’ (Fig. 2B). The small tubes or channels have a typical width of around 1 μm. The average hydrolysis speed is reduced as compared to the higher concentration. For the lowest concentration an even lower hydrolysis speed is recorded. Now only the edges of an observed black area are “attacked”, a phenomenon we describe as “edge-nibbling” (Fig. 2C).

Note that starting from the highest concentration and for long recoding times, the morphologic features can evolve from wave front like to tube like. An example of such an image sequence is given in Fig. 3. The enzyme

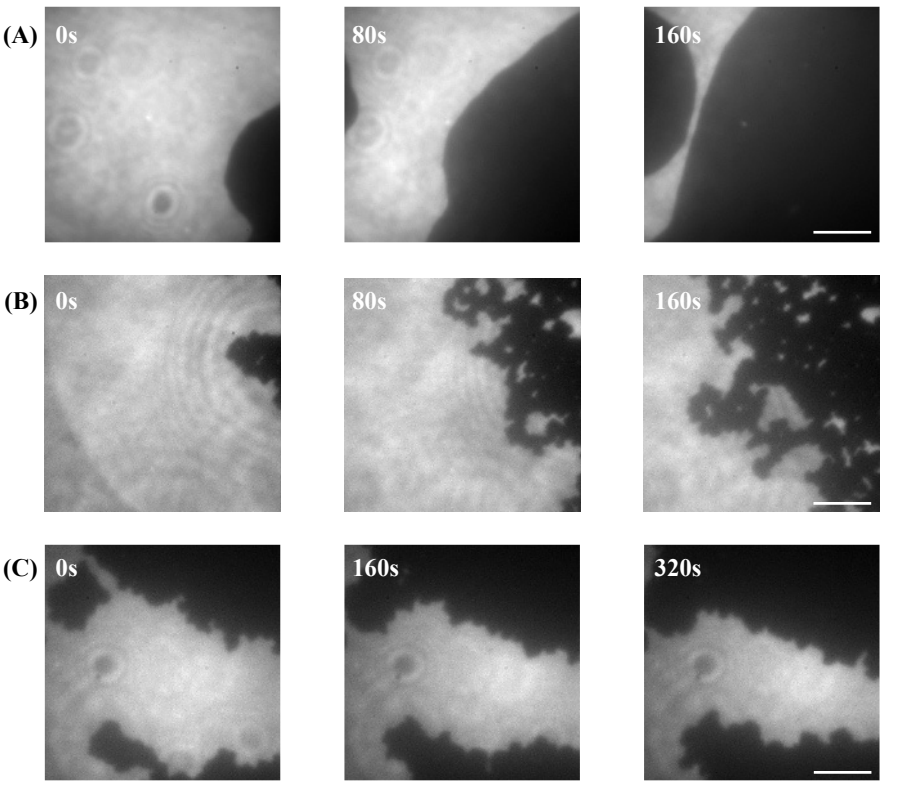

Fig. 2 Time resolved fluorescence imaging of POPC layers labelled with DiI at progressive stages of hydrolysis with diferent concentrations of PLA1. The layers were obtained by spincoating a phospholipid solution on mica. (A) Wave-front-like appearance; PLA1 3.7 x 10^{-7}M; (B) Tube-like appearance; PLA1 1.9 x 10^{-7}M; (C) Nibbling of the edges; PLA1 4.0 x 10^{-9}M. White scale 10μm. Exposure time: 500ms. Excitation wavelength: 532nm

concentration used in the movies shown in Fig. 2 is between 4.0 10^{-9} M and 3.7 10^{-7} M. In this range of concentrations, several to hundreds of enzymes are active in the region that is imaged: in a volume of 1 μm³, between 600 (1.10^{-6} M) and 0.6 (1.10^{-9}M) enzymes are present. The time lag between two images in these figures is indicated for each sequence. Comparison of image sequences, taking into account the different time lags, already shows that the hydrolysis speed is different for the different enzyme concentrations used. Analysis of these images is performed by calculating the area that has been hydrolysed during the acquisition time of an image (500 ms for all images shown). From this calculated area, the number of hydrolysed phospholipids can be calculated, taken into account that the average surface area of a single POPC molecule is 65Å^2.

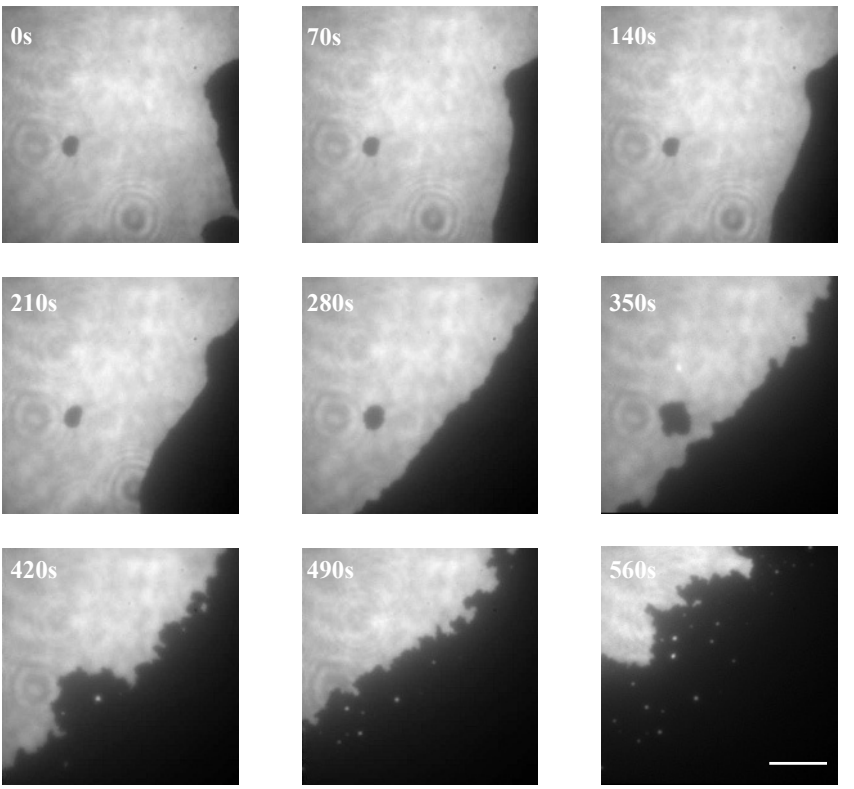

Figure 3. Time resolved fluorescence imaging of POPC layers labelled with DiI at progressive stages of hydrolysis by PLA1 (5.37 x 10^{-8}M). The layers were obtained by spincoating a phospholipid solution on mica. The images reveal a changing in the morphological appearance: passing from wave-front like to tube like appearance. White scale 10μm. Exposure time: 500ms. Excitation wavelength: 532nm. The solution used contained also BSA 1.63 x 10^{-12}M.

A plot of the number of hydrolysed phospholipids in 500 ms as a function of time for the experiments showed in Fig. 3 is presented in Fig. 4. This figure shows that the channels do not grow at a constant speed and even more, in some periods they don't grow at all. At least in the 'tube-like' regime, the hydrolysis of phospholipids seems to fluctuate with time.

How can the different morphological features, the slowdown of hydrolysis speed as well as the fluctuations in hydrolysis speed within one regime be explained?

The morphological features are most probably resulting from a combination of heterogeneity in the packing of the bilayer as well as from different amounts of enzymes that are locally adsorbed. Furthermore, the mechanical stability of the bilayer and its thermodynamical equilibrium will also play an important role

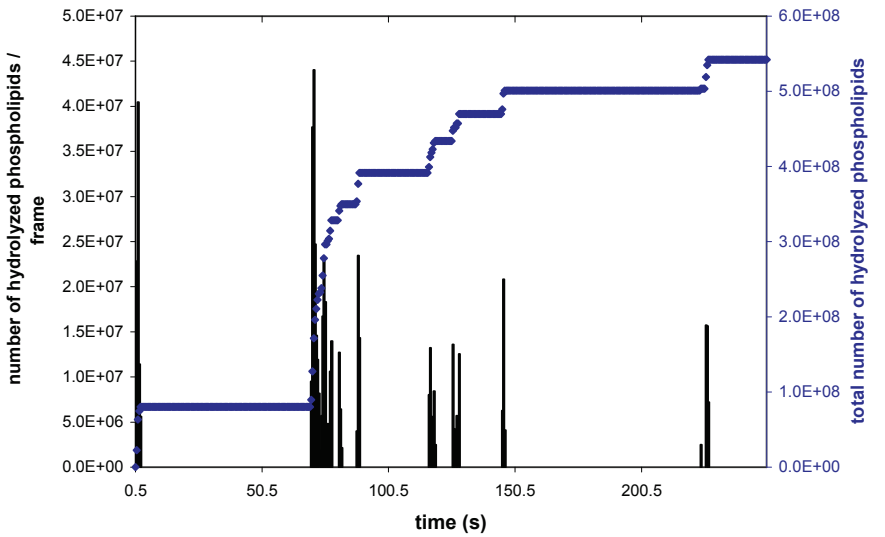

Fig.4. Black: Plot of the number of hydrolyzed phospholipids in each frame of 500 ms as a function of time for tube eating; Blue: the total number of phospholipids hydrolyzed.

In future, we will study the influence of the different parameters by changing the bilayer composition as well as by extensive modelling.

There are several possibilities to explain the time-dependent hydrolysis speed. It has been shown previously for single enzymes that they can show periods of activity followed by inactive periods, due to conformational fluctuations [12,13]. Since we are not dealing with individual enzymes here, a similar hypotesis is unlikely since such explanation would involve a concerted conformational change of several enzymes. Another possibility is that due to the formation of palmitic acid, local pH can change. This might have an influence on the enzyme activity and/or the release of the product(s). The latter possibility would correspond to product inhibition of the enzymatic activity.

In order to confirm the hypothesis of product inhibition (fatty acids [14] as well as lysophosholipids [15] are known to act as an inhibitor for other enzymes), measurements were performed in the presence of a fatty acid-binding agent. Bovine serum albumin (BSA) was used as fatty acid up-taking product. Different concentrations of BSA were applied on the phospholipids layers in order to determine the maximum concentration that can be used without destroying them by auto-hydrolysis due to the albumin. We found that the maximum BSA concentration that can be applied without destroying the bilayers is 2.5 10^{-12}M. The experiments described below were always carried out below this upper concentration in BSA. Images taken after the addition of BSA (one

albumin molecule can bind multiple palmitic acid molecules) shows that the different morphological phenomena still can be seen. However, when the hydrolysis speed for a given enzyme concentration is compared in absence with the one in presence of BSA, an increase in the hydrolysis speed can be observed. The average hydrolysis speed remains constant over a longer time window. Nevertheless, the concentrations of BSA that can be applied (below the conditions where auto-hydrolysis of the layers occurs), are still too low to take up all the palmitic acid that is formed. This explains the observation that even with BSA, the reaction still slows down after a while.

4. CONCLUSIONS

Wide-field fluorescence microscopy was used in this study to follow enzyme activity on phospholipids bilayers. Three major kinds of morphological features could be observed as a result of enzyme induced degradation of the bilayers. In the first stage of the enzymatic hydrolysis or at high enzyme concentration, a 'wave-front'-like disappearance of the layer can be observed. As a function of time, or at lower concentrations, this behaviour changes in the formation of tubes. Sometimes they grow, but also periods of inactivity can be observed when one tube is studied as a function of time. After that or at low enzyme concentrations, only the edges of the layers are nibbled off. Both effects (concentration effect as well as time dependence) are probably resulting from a complex interplay between mechanical stability of the layer, time dependent enzyme absorption and product inhibition of the enzymatic reaction. The kind of inhibition (reversible/irreversible) is not yet unambiguously determined. In order to reduce this inhibition, BSA was added and an increase in catalytic activity is observed compared to the same concentrations of enzyme without the use of a product up-taking agent. The concentrations of enzyme used are too high to be able to see single enzymes at work. On average there are between 60 and 0.6 enzymes per μm^3 present, without taking into account that due to their affinity for the bilayer, the local concentration on the phospholipid layers is probably much higher. In order to go to a single molecule level, in future dye-labelled enzymes will be used in combination with stained layers to be able to track the enzyme on its catalytic journey.

ACKNOWLEDGMENTS

The KULeuven research fund (GOA/02/2006 and grant form the Centre of Excellence CECAT to H.U.), the Federal Science Policy through IAP/V/03, the FWO and the EU (STREP project BIOSCOPE) are acknowledged for supporting this research.

REFERENCES

[1] M.T. Hyvönen, K. Öörni, P.T. Kovanen and M. Ala-Korpela, Biophys. J., 80 (2001) 565
[2] S. C. Kou, B. J. Cherayil, W. Min, B. P. English and X. S. Xie, J.Phys.Chem.B, 109 (2005) 19068
[3] E.E. Vance, and J. Vance, Biochemistry of Lipids, lipoproteins and membranes, Elsevier, Amsterdam, 1991
[4] B. Lomonte, Y. Angulo, and L Calderon, Toxicon, 42 (2003) 885
[5] S.A. Sanchez, L.A. Bagatolli, E. Gratton and T.L. Hazlett, Biophys. J. 82 (2002) 2232
[6] Dennis, E A. "Diversity of Group Types, Regulation, and function of Phospholipase A2." The American Journal of Biological Chemistry 269.18 (1994): 13057-60
[7] L.K. Nielsen, J. Risbo, T.H. Callisen, T. Bjørnholm, Biochim. Biophys. Acta 1420 (1999) 266
[8] A.C. Simonsen and L.A. Bagatolli, Langmuir 20 (2004) 9720
[9] L.K. Nielsen, K. Balashev, T.H. Callisen, T. Bjørnholm, Biophys. J., 83 (2002) 2617
[10] M. Grandbois, H. Clausen-Schaumann and H. Gaub, Biophys. J., 74 (1998) 2398
[11] U.B. Jensen, A. C. Simonsen, Biochim. Biophys. Acta 1715 (2005) 1
[12] O. Flomenbom, K. Velonia, D. Loos, S. Masuo, M. Cotlet, Y. Engelborghs, J. Hofkens, A.E. Rowan, R.J.M. Nolte, M.V. der Auweraer, F.C. de Schryver, and J. Klafter, PNAS, 102 (2005) 2368
[13] K. Velonia, O. Flomenbom, D. Loos, S. Masuo, M. Cotlet, Y. Engelborghs, J. Hofkens, A.E. Rowan, J. Klafter, R.J.M. Nolte and F.C. de Schryver, Angew. Chem. Int. Ed., 44 (2005) 560
[14] E.D. Bent and J.D. Bell, Biochim. Biophys. Acta, 1254 (1995) 349
[15] J. Piret, A. Schanck, S. Delfosse, F.V. Bambeke, B.K. Kishore, P.M. Tulkens, M.P.M. Leclercq, Chem. Phys. Lipids, 133 (2005) 1

This page intentionally left blank

Handai Nanophotonics, Volume 3
H. Masuhara, S. Kawata and F. Tokunaga (Editors)

Chapter 9

Interferometric detection and tracking of nanoparticles

V. Jacobsen, E. Klotzsch and V. Sandoghdar

Laboratory for Physical Chemistry, ETH Zurich, 8093 Zurich, Switzerland

1. INTRODUCTION

Observing and analyzing movement in biological systems is a key issue in understanding biological functions. For example, the study of the dynamics of motor proteins has helped to understand "molecular machines" and mechanical force generation in biology [1], whereas the observation of viral movement on membranes provides information about how viruses bind to the membrane and eventually enter the cell [2],[3]. An accurate knowledge about the transport of micro and nanoparticles is also of utmost importance for medical applications such as drug delivery.

Particle tracking experiments attract increasing interest from physically oriented scientists as the requirements to observe dynamic biological phenomena challenge the limits of measurement techniques. One crucial aspect for employing single particle tracking is the use of labels that are small enough not to alter the dynamic properties of the labelled object. Single molecules are the ideal label because of their negligible size and the modern fluorescence microscopy techniques available for their visualization [1],[2],[4]. However, single fluorescent molecules fare badly on several other accounts. First, fluorescence molecules generally photobleach and strongly limit the observation time. Second, after each excitation of the molecule one has to wait typically for few nanoseconds until a photon is emitted before it can be excited again. This leads to the saturation of the signal and thus a limited emitted power. As a result, a typical integration time of about 1 ms is required to accumulate sufficient statistics for accurate localization of the molecule [6]. Applications where both sub-ms temporal and sub-100 nm spatial resolution are needed become unreachable.

An alternative labeling approach uses semiconductor quantum dots which fluoresce strongly but photobleach much more slowly than dye molecules [7], [13]. However, quantum dots suffer from a severe fluorescence blinking which renders them dark for a substantial fraction of the observation time. Furthermore,

like single molecules they also suffer from saturation. Finally, although naked semiconductor dots are about 3-5 nm in size, their effective size is considerably larger, up to around 20 nm, when they have been made biocompatible (see Fig. 1). While quantum dots have become popular for conventional fluorescence microscopy, single dot experiments have not provided a notable advantage over dye molecules.

To remedy the shortcomings of fluorescent labels, gold nanoparticles have been proposed. As early as 1986, biophysicists have reported the detection of moving particles down to 10 nm and non-moving particles down to 5nm in diameter with video microscopy [14]. The principle of detection relies on light scattering instead of fluorescence. Consequently, gold nanoparticles neither photobleach nor blink. Moreover, gold nanoparticles are biocompatible and can be synthesized such that they contain a hydrophilic surface functionality, e.g. a

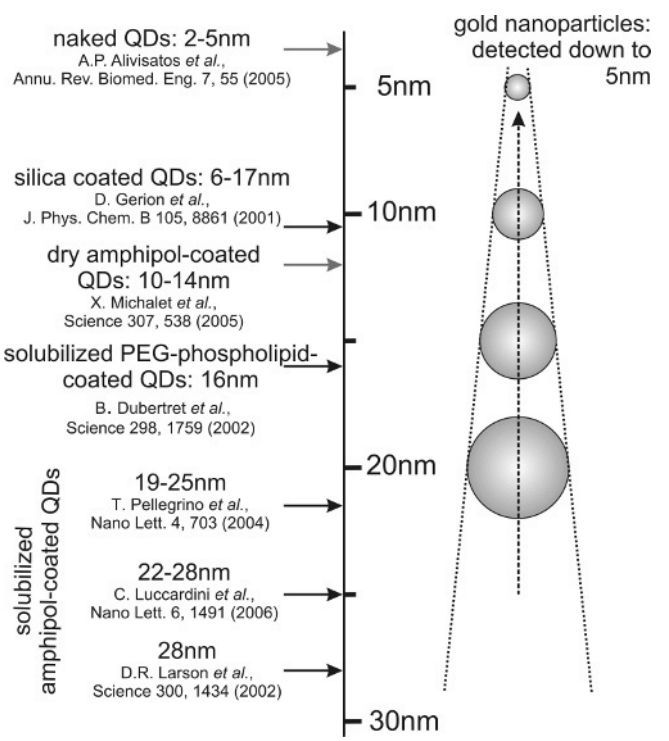

Fig. 1. Overview of the diameters of semiconductor quantum dot labels with various biocompatible coatings as compared to gold nanoparticles. Note that the diameter of the solubilized particle in water (twice the hydrodynamic radius) is the relevant size parameter for the label rather than the diameter of the dry particle, e.g. measured by electron microscop [12]. Both for the quantum dots and gold particles the specified size refers to the biocompatible but non-specific label.

carboxylic group. Furthermore, because the scattering signal does not saturate, one can obtain a large signal in a short interval of time, allowing fast tracking experiments. Although gold nanoparticle labels are rather large compared with single fluorescent molecules, their sizes are compatible with quantum dots (see Fig. 1). Specific binding to the target of interest will generally require additional chemistry which adds to the volume of the label.

Recently, Kusumi and co-workers have used gold nanoparticle labels to observe hop-diffusion in cell membranes by video microscopy [5], [15] with a time resolution of 25 μs. Although these researchers could show that in their case a 40 nm particle did not destroy the functionality of the system under observation, one is generally interested in developing methods for both fast and sensitive detection of smaller gold nanoparaticles to minimize their impact on the biological system.

2. DETECTION OF GOLD NANOPARTICLES

The optical properties of gold nanoparticles and their plasmon resonances in the visible and near-infrared spectrum of light have been subject of many excellent review articles and textbooks; see e.g. Ref. [17],[18] or Ref. [19] for a review on biological applications and Ref. [20] for gold nanoparticle synthesis. In this article we omit a general survey on gold nanoparticle optics and directly address the more recent advances in the detection of very small nanoparticles.

2.1. The unfortunate particle size-dependence of the scattering efficiency

While the detection of single fluorescent molecules has become routine in the laboratory over the last decade [21], detecting single nonfluorescent nanoparticles and clusters has remained a challenge [22]-[30]. The reason is that fluorescence emission can be easily separated from background light by spectral filtering whereas distinguishing elastically scattered light from the background is a nontrivial task. Several groups have employed dark-field [22] or total-internal reflection microscopy [23] to achieve this goal. However, these methods suffer from the fact that the scattered intensity of very small particles is proportional to the square of their static polarizability [33], which in turn depends strongly on the particle diameter. For a spherical particle with a diameter d that is much smaller than the wavelength of light λ, the polarizability can be written in the electrostatic approximation as [33]

$$\alpha(\lambda) = \frac{\pi d^3}{2} \frac{\varepsilon_p - \varepsilon_m}{\varepsilon_p + 2\varepsilon_m} \tag{1}$$

where ε_p and ε_m denote the dielectric constants of the particle and the surrounding medium respectively. Thus the scattering cross section of the

particle depends on the sixth power of the particle diameter. This means that the signal from a 5 nm particle is weaker by nearly 50000 as compared to a particle of 30 nm in diameter. This strong drop of signal is the reason that the signal from particles smaller than about 30 nm drops below the background noise even in methods such as dark-field microscopy. Some recent efforts have gotten around this problem by detecting gold nanoparticles via their absorption signal, which scales as the particle volume. This d^3 dependence causes the signal to drop below a given detection limit for smaller particles less quickly [24, 25, 28]. In what follows, we describe an alternative method that is based on the measurement of the electric field of the scattered light, which also scales as d^3 [26, 27].

2.2. Interferometric amplification of the scattered field

The scattered field $|E_s|$ is proportional to the polarizability α and thus scales as d^3. Since conventional photodetectors are sensitive to the intensity, one has to beat the electric field of interest with a reference field E_r to access the quantity E_s in an intensity measurement. It turns out that this can be easily achieved in various detection geometries if one exploits the background or reflected light. Figure 2 shows a few possibilities. The most convenient reference is the beam reflected by the sample, depicted in Fig. 2a. In this configuration, the reference and the signal are self-aligned. The detector signal will have three components consisting of the intensity of the reflected light, intensity of the scattered light and a cross term caused by the interference between the two fields. In principle, even the scattered light can serve as a reference in the dark-field and TIR

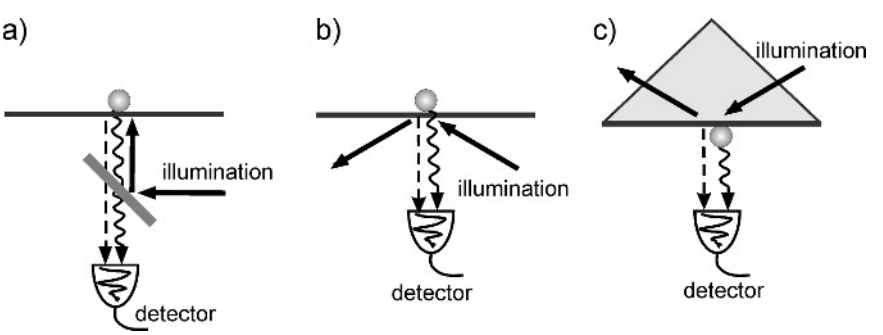

Fig. 2. Different methods employed for the detection of elastic scattering of nanoparticles. a) epi illumination: reflected and scattered light are collected in backward direction through the same objective used for the illumination. b) dark-field microscopy: reflected light is blocked by an aperture such that the detector sees scattered light only, c) TIR microscopy: incident light is totally internally reflected at the base plane of a prism such that only the scattered light can reach the detector. Solid arrows denote incident or reflected fields, curved arrows show the scattering by the particle and the dashed arrows indicate the background scattering or back-reflection from the substrate.

illuminations as sketched in Figs. 2b) and c), respectively. However, these options are not very effective because the reference is neither collected nor overlapped with the signal very efficiently.

We now discuss the optical arrangement drawn in Fig. 2a) in more detail. Let E_i denote the electric field of an incident laser beam focused onto the sample by the microscope objective. The incident light is partially reflected at the interface between the glass substrate and the cover medium (e.g. water or immersion oil), giving rise to the field $E_r = rE_i \exp(-i\pi/2)$ at the detector. Here, the real number r is the effective field reflectivity for the focused beam. The field does not experience a phase shift upon reflection from a medium of lower refractive index. However, a Gouy phase [34] of $-\pi/2$ has been accumulated by the reflected Gaussian beam with respect to E_i. The scattered field at the detector can be written as $E_s = sE_i = |s|\exp(i\varphi)E_i$, where s is proportional to the particle polarizability given in eq. (1) and φ accounts for the phase change upon scattering. For a spherical particle with a diameter that is small compared to the wavelength of light, the scattered field propagates as a spherical wave that is collimated by the microscope objective. The two fields E_r and E_s interfere so that the intensity seen by the detector is given by [26]

$$I_{\text{det}} = |E_r + E_s|^2 = |E_i|^2 \left(r^2 + |s|^2 - 2r|s|\sin\varphi\right) \tag{2}$$

The last term is the desired interference cross term. We note that the numerical aperture of the illumination has to be restricted to a value which avoids total internal reflection at the sample surface (e.g. NA $\leq$ 1.3 for the case of a glass-water interface) for this simple discussion to be applicable. In a more general case, the reflection of a tightly focused beam can have a more complicated character [35], leading to a nontrivial overlap with the scattered signal.

Figure 3 displays some examples of the experimental data. For a weakly reflecting interface between glass and an immersion oil which almost matches the index of refraction and relatively large particles of 60 nm in size (see Fig. 3a)) the pure scattering term $|E_s|^2$ dominates the signal and one observes the particles as bright spots. On the contrary, the particles appear dark (Fig. 3b) if they are smaller than a certain value because the pure scattering becomes smaller than the interference cross term. For an interface with a stronger reflectivity, the transition from bright to dark occurs for larger particles. Thus we see in Fig. 3c) that 60 nm particles appear dark at the water-glass interface. Note that particles down to 5 nm in diameter are observed at both the almost matched interface (Fig. 3b)) and the glass-water interface (Fig. 3d)). While the index-matched configuration provides an optically uniform environment desirable for single particle spectroscopy [26], [31], the latter case is important for biological application discussed later in this chapter.

We now quantify the signal obtained from the particles by defining a normalized intensity σ_N as:

$$\sigma_N = \frac{I_{\text{signal}} - I_{\text{background}}}{I_{\text{background}}} \tag{3}$$

where I_{signal} denotes the total intensity on the detector and $I_{background}$ signifies the same signal in the absence of a gold nanoparticle. As shown in Fig. 3f), 5 nm particles placed at the water-glass interface give σ_N~-3x10^{-3}. Fig. 3e) and f) plot a histogram and a line profile obtained from 5 nm particles at the glass-water interface. The width of the observed distribution of the normalized intensity

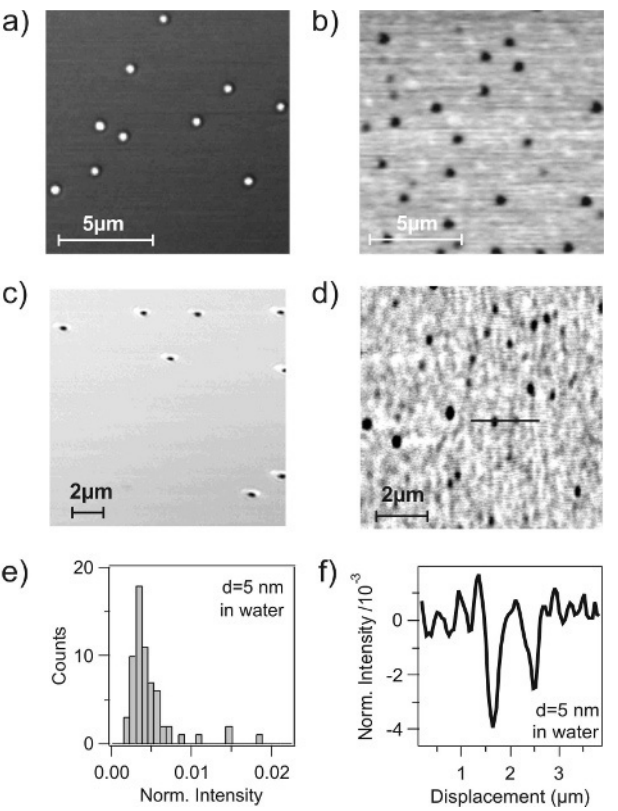

Fig. 3. Confocal images of gold nanoparticles of a) 60 and b) 5nm diameter at the oil-glass interface recorded using a white light continuum illumination [26]; confocal images of gold partices of c) 60 and d) 5nm in diameter at the water-glass interface [27] measured using green (λ=532nm) illumination; e) histogram of the normalized intensity observed for 5 nm particles at the water-glass interface, f) cross-section as indicated in d).

corresponds to the size distribution specified by the manufacturer and thus underlines that we are detecting single particles [27].

2.3. A high axial resolution

The lateral resolution of our interferometric detection method is limited by the diffraction limit in the usual manner. However, it turns out that the axial resolution of this technique can be far superior to that of a confocal microscope. This makes our method of particular interest for three-dimensional tracking of a nanoparticle. To demonstrate the performance of this method in the axial direction, we have spin-coated gold nanoparticles of 30 nm in diameter on a cover glass slip and then coated them with a SiO_x layer of various thicknesses using plasma-enhanced chemical vapor deposition (PECVD). We determined the thickness by ellipsometry on silicon reference substrates which were

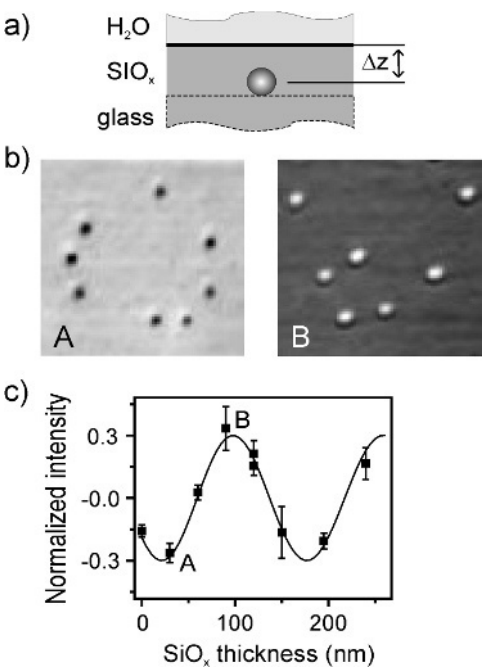

Fig. 4. a) Sketch of the experimental arrangement for a vertically displaced particle; b) 3x3µm confocal images of 30nm gold nanoparticles in this configuration. On the interface (A, without SiO_x-layer) the particles appear dark. Particles located 82nm below the interface (B, with 97nm SiO_x) appear bright due to the inversed phase of the interference cross term. c) normalized intensity σ_N of 30nm single gold nanoparticles separated from the reflecting SiO_x-water interface as a function of the thickness of the SiO_x layer, Δz. The error bars denote the standard deviation determined for more than 40 particles. The data points corresponding to the images in b) are labeled.

deposited simultaneously. Next, the samples were covered by water (see Fig. 4a) and the particles in different samples were imaged, while keeping the interface rather than the particle in the focus of the objective. In each case σ_N was determined.

As the distance Δz of the particles to the reflecting surface is increased the particles appear periodically dark and bright. Figure 4b) displays an image of particles that are at the interface (left: A) and an example of particles which are 82 nm below the interface (right: B). Figure 4c) shows the normalized intensity σ_N measured for particles covered by SiO_x layers of various thicknesses. The contrast is modulated because the distance between the interface and the particles introduces a path difference of $2\Delta z$ between the scattered field and the reflected field of twice that distance. We note that the SiO_x layer matches the refractive index of the cover glass closely so that the reflection from the interface between glass and SiO_x can be neglected. We therefore rewrite the interference cross term I_{ct} from eq. (2) as

$$I_{ct} = -2r|s|\sin\left(\varphi + \frac{4\pi n(\Delta z)}{\lambda} + \arctan\left(\frac{2\Delta z}{z_0}\right)\right) \tag{4}$$

Here we have also taken into account the Gouy phase [34] that is accumulated by the incident beam between its encounter with the particle and its return to the particle position. Because the Gouy phase is mostly accumulated within a Rayleigh range of $z_0 = n\pi w_0^2/\lambda$ [34], its contribution leads to an aperiodic evolution of the phase as a function of Δz. Equation (4) has been employed for the fit shown in Fig. 4c) using a beam waist of w_0=120 nm and a height Δz that equals the thickness of the SiO_x layer reduced by the radius of the particles to take into account that they are actually deposited on top of the glass surface.

The data in Fig. 4c show that a complete contrast reversal takes place within 75 nm. This provides a fantastic opportunity for tackling the difficult task of particle tracking along the optical axis with a localization accuracy well below 50 nm. We remark that the vertical position information is obtained in a similar fashion as compared to fluorescence interference contrast (FLIC) microscopy [38] where a sample is stained with a fluorescence dye and positioned on a transparent silica chessboard of various thickness on a reflecting silicon substrate.

2.4. Ultrafast Detection

In tracking experiments, it is often desirable to study the motion of a particle with as high of a time resolution as possible to ensure that one does not overlook processes and interactions that take place at very short time scales. In cell membranes for example, a moderate time resolution under a millisecond has

enabled the unambiguous observation of "hop-diffusion" where membrane molecules follow Brownian motion in certain compartments but change compartments on a slower time scale [5]. The experimental difficulty is that increasing the time resolution results in the reduction of the detected signal per unit time. One might imagine, this can be overcome by increasing the excitation intensity. In case of single fluorescent molecules, however, this is limited by saturation. In case of gold nanoparticles, on the other hand, the scattered power remains proportional to the incident intensity. The only restriction that has to be kept in mind is a potential heating of the local environment of the particle due to its absorption.

Gold nanoparticles have been indeed used for fast tracking. In standard video microscopy 40 nm particles have been detected with a time resolution of 25 μs to visualize hop-diffusion in cell membranes [5], [15]. We have shown that our detection scheme allows the detection of even smaller particles on a time scale as short as 1 μs [27] (see Fig. 5). To mimic the fast motion of a nanoparticle in our first demonstration experiments, a focused laser beam was scanned across the particle at a speed of 0.2 μm/μs, using a galvo-driven mirror. The curves in Fig. 5a) and b) show the traces of a single 30 and 20 nm particle, respectively, obtained using a laser power of about 2 mW. The particles are clearly observed within a passage time of about 2 μs. As shown in Fig. 5d), even a 10 nm gold particle could be easily detected after increasing the illumination power to about 30 mW. We point out that the optical powers used in these preliminary experiments have been rather high because of the laser noise. Shot-noise limited experiments would require far lower intensities.

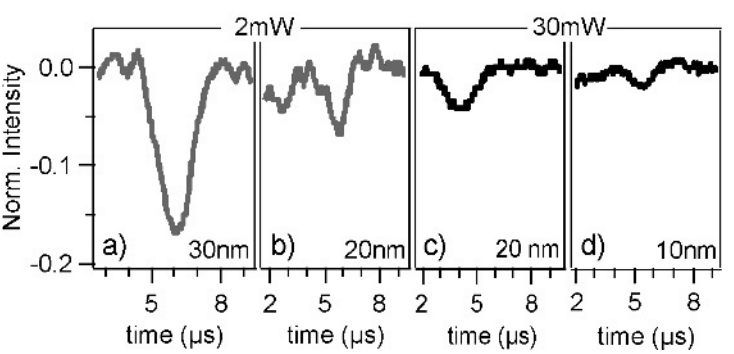

Fig. 5. Normalized intensity detected at the glass-water interface while scanning the beam laterally across the sample area selected by an enlarged pinhole. a) and b) Detection of particles 30 and 20nm, in diameter under illumination power of 2mW. c) and d) Detection of particles 20 and 10nm, in diameter under illumination power of 30mW. Reproduced from Ref. [27].

2.5. Other detection schemes

The working principle of the particle detection presented above – the amplification of a weak scattered field by a reference field – is not restricted to the confocal arrangement. The idea can be applied as long as the scattering and the reference signals are coherent. Figure 6 summarizes a few possible detection schemes. As shown in Fig. 6b), one can also detect the particle in transmission where the scattered field from the particle interferes with the transmitted field, and the signal is measured as a change in extinction. The reflectivity of a sample surface depends on the refractive index contrast and is usually a few percent or less. Consequently, the transmitted field will be much stronger than the reflected one. Although the amplification of the scattering will be stronger in this case, the transmitted (background) intensity and therefore its noise is much higher so that the extinction signal is more easily lost in the noise as compared to the situation depicted in Fig. 6a). Arbouet *et. al.* [28] have measured single gold nanoparticles down to a size of 5nm in transmission, but indeed they needed a spatial modulation of the particle and lock-in amplification to obtain a sufficiently large signal (see also the next section).

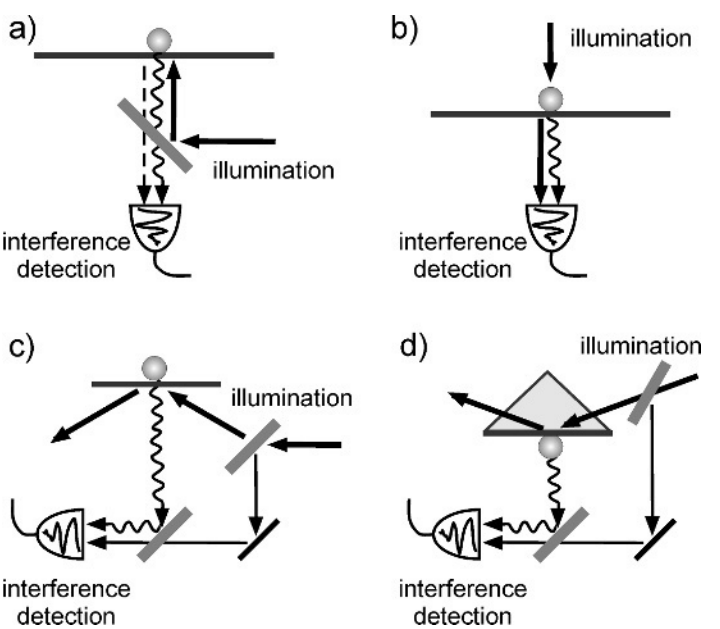

Fig. 6. Various examples of experimental arrangements for interferometric scattering detection: a) reflectivity measurement as discussed above, b) extinction measurement in transmission as applied in [28], and c) dark-field scattering detection or d) TIR scattering detection both interfered with an external reference field. Straight arrows denote incident or reflected fields, curved arrows scattered fields.

An important configuration for applications is wide-field imaging because it allows the simultaneous observation of a large area. We have previously demonstrated that our interferometric method is also possible in this imaging mode [27]. However, we found that inhomogeneities in the illumination field can give rise to systematic background features which complicate the detection of small nanoparticles. This can be remedied by employing a dark-field or total internal reflection illumination and using an external beam for obtaining interference, as indicated in Figs. 6c) and d).

An external beam can be also used in the standard configuration of Fig. 6a) [29]. An external reference offers more freedom to tailor the relative phase, amplitude and polarization of the reference and the signal. However, the use of an external reference has the important disadvantage that one loses the intrinsic alignment between the two optical fields, requiring a very stable mechanical setup.

2.6. The signal-to-noise ratio

We now address the issue of the signal-to-noise ratio (SNR) for the interferometric detection. The second and the third terms in eq. (2) constitute the signal whereby for very small particles the cross term dominates. Thus, the strength of the signal is simply proportional to the field of the reference beam. The noise can have several sources. In what follows we ignore the detector noise since various high quality detectors are available today. The most prominent noise in the measurements discussed above is the instrumental noise on the laser intensity, which is typically in the 0.1-2% range for commercial devices. The instrumental noise of the laser beam can be partly tackled in two different ways. First, active stabilization of the beam intensity using acousto-optical or electro-optical modulators can help to reduce the noise. Second, one can use an additional low-noise detector to monitor and record the laser intensity simultaneously as the measurement. The output of this detector should correlate with the beam that is incident on the sample so that it could be used for normalizing the signal and thus eliminating the noise. In practice, however, it remains extremely difficult to achieve noise levels beyond 10^{-5}.

In the ideal case that the instrumental noise has been eliminated, the shot noise, i.e. the intrinsic statistical fluctuations of the number of photons in a beam, becomes relevant. In this case, the noise of the reference beam is proportional to $\sqrt{I_r} \propto r$, while the signal scales as $2r|s|\sin\varphi$ (see eq. (2)) [26] so that σ_N becomes independent of the strength of the reference beam. Furthermore, because the shot noise scales as the square root of the intensity, its contribution becomes increasingly negligible at higher powers. The fractional ratio of the shot noise to the power of a green laser beam of 100 μW, equivalent to about 10^{14} photons per second, is about 10^{-7}. Considering that σ_N for a 5 nm particle is of the order of 10^{-3}, and that σ_N scales as d^3, we should be able to detect single

gold particles that are smaller than 0.5 nm in diameter with a shot-noise limited source.

In addition to the laser noise, one has to worry about any background "signal" seen by the detector. Here we assume that trivial sources of background such as stray light not originating from the sample are absent. However, as mentioned in the context of Figs. 2b) and d), scattering from objects other than the particle of interest also produce a signal on the detector which cannot be easily separated from the signal of the gold nanoparticle (see also section 3.2). In a wide-field detection mode this background results in a speckle-like signal on the detector.

3. DETECTION OF DIELECTRIC OBJECTS

3.1. Label-free detection of microtubules

The interferometric detection method is very sensitive to even weakly scattering object. A look at Fig. 3d) reveals that the detection picks up roughness and refractive inhomogenities of the cover glass [27]. Indeed, the detection mechanism is not limited to gold nanoparticle but can also be used for imaging other objects. Figure 7b) displays slowly moving microtubules on a kinesin surface (see Ref. [36] for the preparation method). Microtubules are asymmetric polymeric structures assembled from thousands of tubulin proteins into hollow tubes with a diameter of 24 nm stretched over a length of several micrometers (see Fig. 7a). It turns out that the dimensions and the index contrast between organic material and water is large enough to induce a change in normalized intensity of about 2%. Such biological nanostructures are conventionally detected using fluorescence labeling. It is clearly of a great advantage to be able to image them directly [37].

3.2. Distinguishing gold nanoparticles from other scattering objects

The sensitivity of the interferometric signal to very small dielectric objects

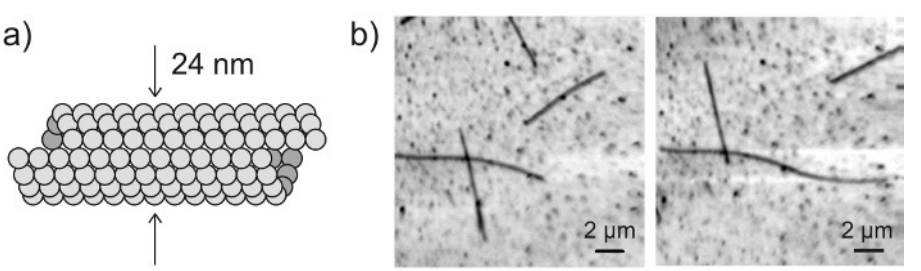

Fig. 7. a) Sketch of a microtubule as an asymmetric assembly of tubulin proteins, b) subsequent confocal scans of microtubules moving on a kinesin surface prepared as described in [36]. The microtubules cause a normalized intensity of σ_N=0.02.

opens great opportunities for label-free detection and tracking of biological nanosystems. However, it also complicates the identification of specific labels such as gold nanoparticles in a crowded environment. To address this issue, we have taken advantage of the plasmon resonance of the gold nanoparticles [27]. As shown in Fig. 8a), the scattering cross section is several times larger on the resonance than at a wavelength that is detuned by a few tens of nanometers. Dielectric objects, on the contrary, usually do not show such a strong dependence of the scattering efficiency with the wavelength. Figure 8b) and c) present confocal scans of a microtubule labeled with four gold nanoparticles on kinesin-coated glass (see Ref. [27] for details) which were simultaneously obtained at two illumination wavelengths of λ=532 nm and 488 nm, respectively. Upon subtraction of their corresponding quantities σ_N and plotting the result in Fig. 8d), the signal from the microtubule has been eliminated while the signal from the gold particles persists on a very low background.

4. TRACKING OF GOLD NANOPARTICLES

Above we have seen that we can detect gold nanoparticles and even dielectric

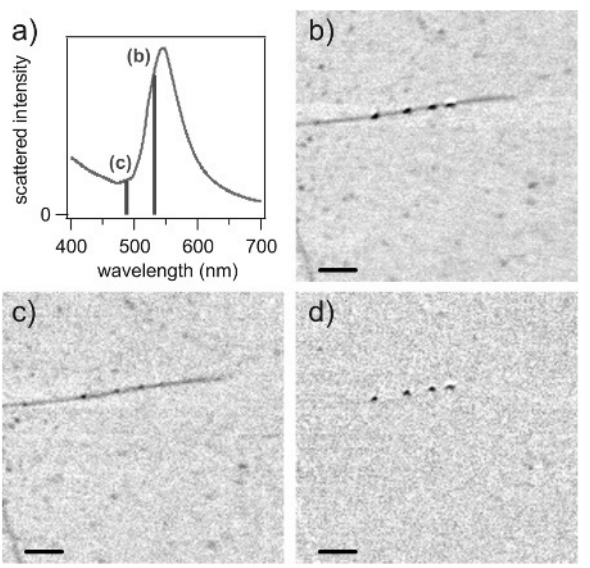

Fig. 8. a) Calculated scattering spectrum of a 20nm gold particle in the dipole approximation. The two wavelengths λ used to obtain the images shown in b), c), and d) are indicated; b) confocal scan of a microtubule labeled with gold nanoparticles of 40nm diameter (see text for details) imaged at λ=532nm; c) simultaneously acquired scan at λ=488nm. Both images show the normalized intensity σ_N in the same color scale -0.125…0.025; d) difference σ_N(532nm)-σ_N(488nm) plotted in the same color scale. Reproduced from Ref. [27].

nano-objects very sensitively. Now we discuss the possibility of tracking a single nano-object. One could imagine a wide-field configuration or a fast confocal scanning system to follow the motion of a nanoparticle. However, these options are usually fairly slow [39]. To exploit the intrinsic speed of our method, we have set out to track a single particle by locking the laser focus to its position. The information about the deflection of the laser beam will directly provide the coordinates of the particle under study. In order to achieve this, the pinhole and the detector can be replaced by a quadrant diode (Hamamatsu S6058) in the focus of the imaging lens as sketched in Fig. 9a). Taking into account the finite separation of the quadrants of 10 µm, we use a large magnification of almost 200 to image the sample focus on a sufficiently large area of the detector. Figure 9b) and c) show the sum of the signals on all quadrants and the difference between the sums of the two upper and the two lower quadrants respectively, as the particles are scanned through a fixed laser focus. It is clear that the difference signal changes its sign if the particle moves from above to below the centre of the focal area. An analogous signal is obtained from the difference of the two left and right quadrants.

Having shown that the information about the direction of the motion of the particle is recorded on the segmented photodiode, we can use closed loop electronics to track the nanoparticle. The difference signal of each direction is fed into an analog feedback amplifier (PID, Stanford Research SIM960), and the output voltage of the PID controls one dimension of a two-dimensional beam scanning unit. The beam scanner consists either of two galvanometric mirrors (Cambridge Technology) or acousto-optical deflectors (AOD, A.A. Opto-

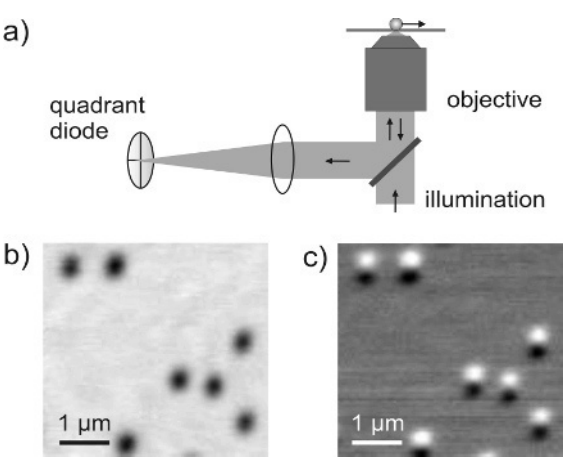

Fig. 9. a) Sketch of the quadrant detection scheme, see text for details; b) sum signal of all four quadrants observed for 30 nm particles at the water-glass interface and scanned through the focus; c) simultaneously acquired difference of the top and bottom quadrants.

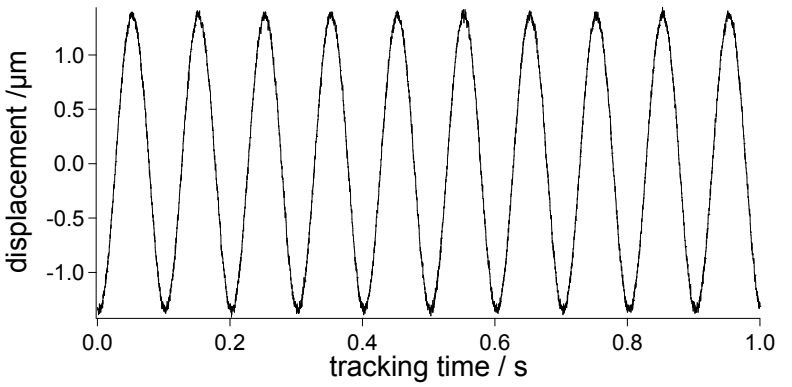

Fig. 10. Tracked trajectory of a 30 nm gold nanoparticle that is moved by a periodic sample displacement.

electronic). The acousto-optical deflection unit is limited to a maximum deflection efficiency of 50%, but it provides a high positioning speed with random access times on the order of a few µs. Figure 10 shows a proof of principle demonstration of the tracking loop. The sample containing 30 nm gold particles on glass and immersed in water is sinusoidally moved by a piezo stage. The tracking loop has been clearly successful in recording the trajectory of the nanoparticle. By using better detectors, we should be able to detect smaller particles and at higher speeds.

5. CONCLUSION

Gold nanoparticles down to a size of 5 nm can be detected and tracked at an interface. Due to their biocompatibility and indefinite photostability, these particles are very promising for application as optical label in biological studies. The detection mechanism is based on the amplification of the weakly scattered light of the object through interference with a reference beam. Improvements in the laser source and detectors will allow the detection of even smaller objects. In fact, we have shown that this method can also be used to detect and image nonfluorescent nanostructures such as microtubules. The optical measurements presented here have the potential to serve as a very powerful tool for studying dynamic nanosystems, especially when both high time resolution and long measurement times are required.

ACKNOWLEDGEMENT

We are thank F. Gruber for her contribution to the work in section 2.3 and are grateful to C. Brunner and V. Vogel for providing the microtubule samples. We

thank K. Lindfors and P. Stoller who did some of the early experiments and J. Seelig, G. Mori, M. Agio and A. Renn for fruitful discussions. This work was supported by the ETH Zurich and the Swiss Ministry of Education and Science (EU IP-Molecular Imaging).

REFERENCES

[1] A.D. Mehta, M. Rief, J.A. Spudich, D.A. Smith, R.M. Simmons, Science, 283 (1999) 1689.
[2] G. Seisenberger, M.U. Ried, T. Endreß, H. Büning, M. Hallek, C. Bräuchle, Science, 294 (2001) 1929.
[3] H. Ewers, A.E. Smith, I.F. Sbalzarini, H. Lilie, P. Koumoutsakos, A. Helenius, Proc. Natl. Acad. Sci. U.S.A., 102 (2005) 15110.
[4] M. Goulian, S.M. Simon, Biophys. J., 79 (2000) 2188.
[5] A. Kusumi, C. Nakada, K. Ritchie,K. Murase, K. Suzuki, H. Murakoshi, R.S. Kasai, J. Kondo, T. Fujiwara, Annu. Rev. Biophys. Biomol. Struct., 34 (2005) 351.
[6] R.J. Ober, S. Ram, E.S. Ward, Biophys. J., 86 (2004) 1185.
[7] A.P. Alivisatos, W. Gu, C. Larabell, Annu. Rev. Biomed. Eng., 7 (2005) 55.
[8] D. Gerion, F. Pinaud, S.C. Williams, W.J. Parak, D. Zanchet, S. Weiss, A.P. Alivisatos, J. Phys. Chem. B, 105 (2001) 8861.
[9] B. Dubertret, P. Skourides, D.J. Norris, V. Noireaux, A.H. Brivanlou, A. Libchaber, Science, 298 (2002) 1759.
[10] T. Pellegrino, L. Manna, S. Kudera, T. Liedl, D. Koktysh, A.L. Rogach, S. Keller, J. Rädler, G. Natile, W.J. Parak, Nano Lett., 4 (2004) 703.
[11] C. Luccardini, C. Tribet, F. Vial, V. Marchi-Artzner, M. Dahan, Langmuir, 22 (2006) 2304.
[12] D.R. Larson, W.R. Zipfel, R.M.Williams, S.W. Clark, M.P. Bruchez, F.W.Wise, W.W.Webb, Science, 300 (2003) 1434.
[13] X. Michalet, F.F. Pinaud, L.A. Bentolila, J.M. Tsay, S. Doose, J.J. Li, G. Sundaresan, A.M. Wu, S.S. Gambhir, S. Weiss, Science, 307 (2005) 538.
[14] M. de Brabander, R. Nuydens, G. Geuens, M. Moeremans, J. de Mey, Cell Motil. Cytoskeleton, 6 (1986) 105.
[15] T. Fujiwara, K. Ritchie, H. Murakoshi, K. Jacobson, A. Kusumi, J. Cell Biol., 157 (2002) 1071.
[16] N. Panchuk-Voloshina, R.P. Hauglanda, J. Bishop-Stewarta, M.K. Bhalgata, P.J. Millarda, F. Maoa, W.-Y. Leunga, R.P. Haugland, J. Histochem. Cytochem., 47 (1999) 1179.
[17] U. Kreibig, M. Vollmer, Optical Properties of Metal Clusters, Springer Series in Material Sciences Vol. 25, Berlin, 1995.
[18] S. Eustis, M.A. El-Sayed, Chem. Soc. Rev., 35 (2005) 209.
[19] D.A. Schultz, Curr. Op. Biotechn., 14 (2003) 13.
[20] U. Kreibig, H. Bönnemann, J. Hormes, Nanostructured Metal Clusters and Colloids, in: H.S. Nalwa (ed.), Handbook of Surfaces and Interfaces of Materials, Academic Press, San Diego, 2001.
[21] R. Rigler, M. Orrit, T. Basche (eds.), Single Molecule Spectroscopy, Springer, New York, 2001.
[22] S. Schultz, D.R. Smith, J.J. Mock, D.A. Schultz, Proc. Natl. Acad. Sci. U.S.A., 97 (2000) 996.

[23] C. Sönnichsen, S. Geier, N.E. Hecker, G. von Plesse, J. Feldmann, H. Ditlbacher, B. Lambrecht, J.R. Krenn, F.R. Aussenegg, Appl. Phys. Lett., 77 (2000) 2949.
[24] D. Boyer, P. Tamarat, A. Maali, B. Lounis, M. Orrit, Science, 297 (2002) 1160.
[25] S. Berciaud, L. Cognet, G.A. Blab, B. Lounis, Phys. Rev. Lett., 93 (2004) 257402.
[26] K. Lindfors, T. Kalkbrenner, P. Stoller, V. Sandoghdar, Phys.Rev.Lett., 93 (2004) 037401.
[27] V. Jacobsen, P. Stoller, C. Brunner, V. Vogel, and V. Sandoghdar, Opt. Express, 14 (2006) 406.
[28] A. Arbouet, D. Christofilos, N. Del Falli, F. Vallée, J.R. Huntzinger, L. Arnaud, P. Billaud, M. Broyer, Phys. Rev. Lett., 93 (2004) 127401.
[29] F.V. Ignatovich, L. Novotny, Phys. Rev. Lett., 96 (2006) 013901.
[30] O.L. Muskens, N. Del Fatti, F. Valée, J.R. Huntzinger, P. Billaud, M. Broyer, Appl. Phys. Lett., 88 (2006) 063109.
[31] P. Stoller, V. Jacobsen, V. Sandoghdar, Opt. Lett., 31 (2006) 2474.
[32] As demonstrated in Ref. [27] even higher intensities in the mW regime can be used for particle detection. The estimation of the shot-noise limit demonstrate, however, that these high intensities are generally applied to overcome the detection noise of comparable simple and cheap detectors while much less power would be sufficient if one would use optimized detector and amplification equipment.
[33] C.F. Bohren, D.R. Huffman, Absorption and Scattering of Light by Small Particles, Wiley-Interscience, New York, 1983.
[34] B.E.A. Saleh, M.C. Teich, Fundamentals of Photonics, Wiley-Interscience, New York, 1991.
[35] L. Novotny, R.D. Grober, K. Karrai, Opt. Lett., 26 (2001) 789.
[36] H. Hess, G.D. Bachand, V. Vogel, Chem. Eur. J., 10 (2004) 2110.
[37] C. Brunner, C. Wahnes, V. Jacobsen, V. Sandoghdar, V. Vogel, *in preparation*.
[38] A. Lambacher, P. Fromherz, J. Opt. Soc. Am. B, 19 (2002) 1435.
[39] Image repetition rates in confocal microscopes depend on the number of pixels (and therefore lateral resolution) per image but are usually not faster than a few 100ms.

This page intentionally left blank

Handai Nanophotonics, Volume 3
H. Masuhara, S. Kawata and F. Tokunaga (Editors)

Chapter 10

Interaction between metal-free porphine and surface Ag atoms through temporal fluctuation of surface-enhanced resonance raman scattering and background-light emission

Tamitake Itoh[a,b], Kazuhiro Hashimoto[a], Vasudevanpillai Biju[b], Mitsuru Ishikawa[b], Bayden R.Wood[c], and Yukihiro Ozaki[a]

[a]Department of Chemistry, Kwansei Gakuin University, Sanda, Hyogo 669-1337, JAPAN

[b]National Institute of Advanced Industrial Science and Technology (AIST), Takamatsu, Kagawa 761-0395, JAPAN

[c]Centre for Biospectroscopy, Monash University, Wellington Road, Clayton, Victoria 3800, AUSTRALIA

1. INTRODUCTION

Surface-enhanced resonance Raman scattering (SERRS) has been expected to be a highly-sensitive tool for structural analysis of molecules that are adsorbed on a metal surface. Indeed, SERRS enables us to identify molecular vibrations even under the single-molecule level [1-10]. It is widely accepted that both electromagnetic (EM) and chemical mechanisms contribute to SERRS [1-20]. There is no doubt that EM fields that are coupled with plasmon mainly contribute to large enhancement of Raman scattering, because recent calculations of EM fields at inter-particle junctions and at sharp edges of noble metal nanoaggregates well predict enhancement of Raman scattering by a factor of 10^8 to 10^{14} [3-10]. We have already identified that optimum polarization, spectral maxima, and Q factors of plasmon resonance are all essentials of large enhancement of Raman scattering [16-19]. However, only EM mechanism cannot provide reasons why all kinds of molecules adsorbed on inter-particle junctions and sharp edges do not always generate SERRS activities. For example, we do not observed an enhanced Raman signal of water even from Ag

nanoaggregates in an aqueous solution. Such questions strongly motivate us to consider that chemical interaction between molecules and Ag surfaces contributes to a large enhancement of Raman scattering [4,5,7,11-15,22,23]. Thus, it is important to investigate chemical interaction between SERRS-active molecules and metal surfaces to explore a SERRS-chemical mechanism.

Several spectroscopic studies on SERRS-active molecules which have non-hydrogen-terminated N atoms showed that the N atoms interact with Ag surface atoms and form Ag-N chemical bonds; however, the Ag-N stretching mode is difficult to be observed in SERRS spectra because of its low frequency of Raman shift (~250 or ~350 cm^{-1}) and weak intensity [13]. From SERRS spectroscopy of H_2TPP molecules adsorbed on Ag substrates, Itoh *et al.* identified that an Ag-N chemical bond in a pyrrole-ring enhances a SERRS band of a C_α-N stretching mode [20,21]. Thus, we expected to observe chemical interaction between SERRS-active molecules and Ag surfaces through the observation of a C_α-N stretching mode instead of an Ag-N stretching mode. Conventional ensemble spectroscopy of SERRS cannot directly reveal individual chemical interactions, thereby providing averaged information on many molecules interacting and not interacting with Ag surface atoms. Thus, it is potentially important to attempt single-molecule SERRS spectroscopy to investigate chemical interactions between H_2TPP molecules and Ag surfaces.

In the current study, we applied time-resolved SERRS spectroscopy to single Ag nanoaggregates that are adsorbed by H_2TPP molecules under the single-molecule level to reveal chemical interaction between H_2TPP molecules and Ag surfaces. We investigated temporal fluctuations of SERRS spectra and their background-light emission spectra. Background-light emission is not found in association with normal Raman scattering and has been pointed out as important characteristics of SERRS [4,7,11-15,19]. We found that both SERRS and background-light emission were temporally stable when a C_α-N stretching mode clearly appeared in SERRS spectra, suggesting that stable Ag-N chemical bonds suppress temporal fluctuations of both SERRS and background-light emission. The suppression of the temporal fluctuations by Ag-N chemical bonds implies that chemical contribution to SERRS is stabilization of adsorbed H_2TPP molecules on SERRS-active sites by formation of Ag-N bonds. Additionally, we attributed background-light emission to luminescence from complexes of H_2TPP molecules and surface Ag atoms in terms of several lines of evidence: formation of Ag-N bonds, simultaneous fluctuation of SERRS intensity with background-light emission intensity, background-light emission maxima blue shifted from the normal H_2TPP fluorescence maxima, and previous work on electronic structures of H_2TPP molecules on Ag surfaces [24-26].

2. EXPERIMENTAL

Metal-free 5, 10, 15, 20-tetraphenylporphine (H_2TPP) (ALDRICH, 99+ %, Tokyo) was used as purchased. An extinction spectrum of the Ag colloidal solution that we used showed a single maximum at 410 nm (figure not shown), thus showing that the amount of aggregated colloidal particles was negligible in the initial solution. SERRS-active Ag particles were prepared by mixing a H_2TPP aqueous solution (1.8×10^{-7} M), a NaCl aqueous solution (10 mM), and an Ag colloidal solution (1.0×10^{-10} M). An aliquot of the mixture was spin-coated on a glass plate after a 30-min incubation at room temperature (17 °C). The Ag particles on the glass plate were sandwiched with a thin film of a aquerious NaCl solution (4.0 M) to stabilize SERRS activity [5,13].The appearance of SERRS-active Ag particles was found to be clumps of several Ag nanoparticles by SEM measurements, as reported by other groups (data not shown) [2,3,4,7,9,10,19].

The spectroscopic setup is similar to the reported one [16-19].Briefly, SERRS-excitation light beam from an Ar^+ laser (457 nm) was focused on a sample glass surface using an objective lens (5×, N.A. 0.15). The incident angle of the light beam was 70° against the sample plain. Excitation intensity was 40 mW/cm^2. SERRS and background-light emission from the identical Ag nanoaggregates were collected with an objective lens (60×, N.A. 0.15), and led to a polychromator (Pro-275, Acton, Tokyo), which was equipped with a thermoelectric cooling charge-coupled device (DV434-FI, Andor, Tokyo). Two different gratings (150 and 1200 grooves/mm) were used for detection of SERRS (spectral resolution: 3 cm^{-1}) and SERRS plus background-light emission (spectral resolution: 12 cm^{-1}), respectively. White light from a 50-W halogen lamp was introduced to the common focusing area using a dark-field condenser to identify single Ag particles as isolated plasmon resonance Rayleigh scattering spots.

3. RESULTS

3.1. Dark-field and SERRS Optical Image of Ag Nanoaggregates

Figure 1A shows Rayleigh scattering spots from Ag particles the color of which varied from one spot to another. Figure 1B shows inelastic scattering spots that correspond to SERRS-active Ag particles. Many papers confirm that SERRS-active Ag particles are aggregates of several Ag nanoparticles [2,3,7,9,10,17,19];thus, we call SERRS-active Ag particles SERRS-active Ag nanoaggregates in the current paper. From the comparison between Figures 1A and 1B, we identify SERRS-active Ag nanoaggregates in Figure 1A. All SERRS-active Ag nanoaggregates in Figure 1B showed temporal intermittence known as “blinking”, as will be discussed later with reference to Figure 3. The

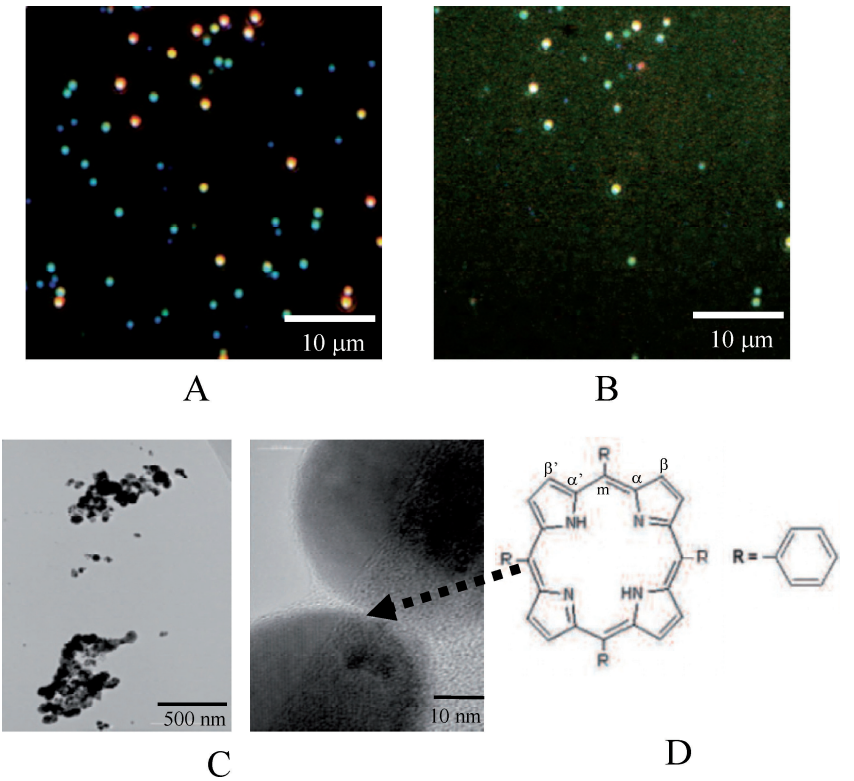

Fig 1. (A) Plasmon resonance Rayleigh scattering image of Ag nanoaggregates, (B) a corresponding SERRS image of Ag nanoaggregates, (C) a representative TEM image of Ag nanoaggregates, and (D) a molecular structure of metal-free H2TPP.

"blinking" of SERRS is attributed to either thermal translational and rotational motion of an adsorbed molecule on a SERRS-active site [1-4,6-9], or fluctuation of energy levels of a complex formed between a metal atom and an adsorbed molecule due to a change in the local work function at a SERRS-active site [5]. The left panel of Figure 1C shows a representative TEM image of Ag nanoaggregates in the current work. The right panel of Figure 1C shows an enlarged TEM image of an Ag nanoaggregate in which a junction of two Ag nanoparticles was clearly observed. Figure 1D shows a structure of a H_2TPP molecule, which is an aromatic macrocycle with four pyrrole rings connected by unsaturated (methine) carbon atoms. The symbols of α, α', β, and β' in H_2TPP molecule identify the position of carbon atoms.

3.2. Temporal Fluctuation of SERRS Spectra

Figure 2A shows a resonance Raman spectrum from H_2TPP powder on a glass surface. Figure 2B–D shows time-averaged (85 s) SERRS spectra from

three independent Ag nanoaggregates that were adsorbed by H_2TPP. The positions of SERRS bands, except for the following key band, are the same as those of the resonance Raman bands in Figure 2A within an error of ±3 cm^{-1}. This error is within the resolution of the current spectroscopic system. Thus, SERRS-active H_2TPP molecules were not decomposed or carbonized by enhanced laser fields. Figure 2B-D shows that a key Raman band was observed at 1357 cm^{-1}, which was not observed in the resonance Raman spectrum in Figure 2A. This 1357 cm^{-1} band is attributed to a C_α-N stretching mode [20,21].Note that the symbol C_α is defined as a carbon atom which is bonded to a non-hydrogenated N atom in a pyrrole ring, as shown in Figure 1D.

Figure 3A–C shows time-resolved SERRS spectra from three independent Ag nanoaggregates. Note that each SERRS spectrum in Figure 2B-D is reproduced by the summation of the time-resolved spectra in Figure 3A-C, respectively. The SERRS spectra in Figure 3A do not show a striking change with time. On the other hand, the SERRS spectra in Figure 3B and C show changes with time, as highlighted by red dotted circles. Figure 3B shows that

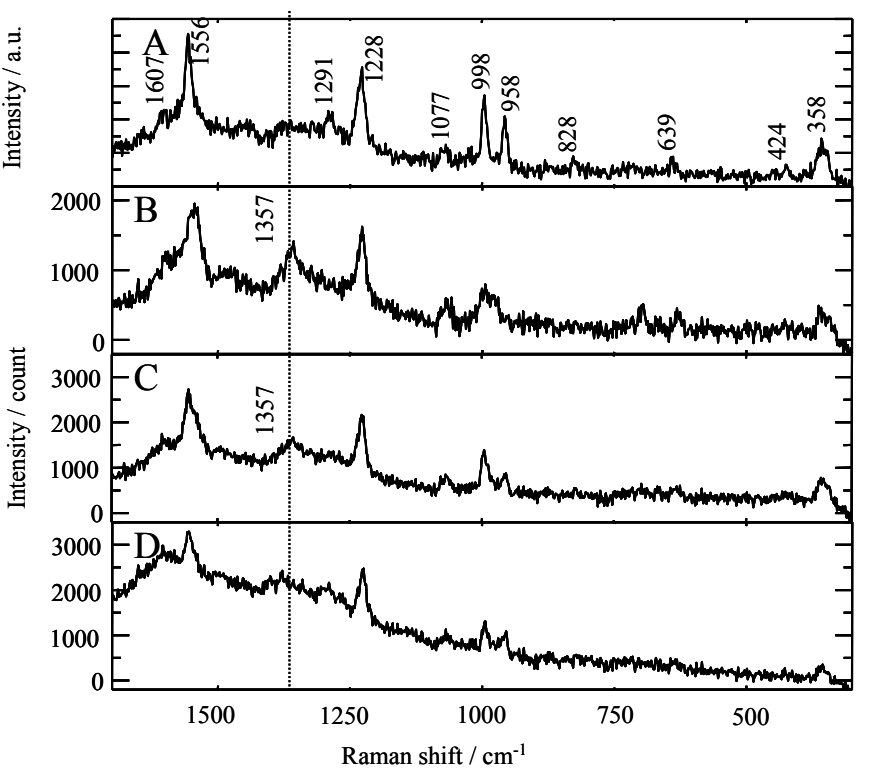

Fig 2. (A) Resonance Raman spectrum of H2TPP and (B) – (D) SERRS spectra of H2TPP molecules adsorbed on three different single Ag nanoaggregates.

Raman bands at 1602 and 1281 cm^{-1} appeared and disappeared from 15-20 to 30–35 and 30-35 to 45–50 s, respectively. The Raman bands at 1602 and 1281 cm^{-1} are attributed to a phenyl breathing mode and a C_α-C_β stretching mode, respectively [20,21,27].Figure 3C shows that SERRS spectra prominently changed in frequency and intensity. The intensity of a phenyl breathing mode at 1602 cm^{-1} increased from 10-15 to 15-20 s, and then an unknown band at 1643 cm^{-1} appeared from 20-25 to 25-30 s. This unknown band may be ν_{10} which is one of the skeletal modes with the highest Raman shift [27-29].Two bands at 1600 and 1643 cm^{-1} simultaneously disappeared at 30-35 s. Then, the SERRS spectrum at 35-40 s returned to the initial one at 0-5 s. Next, Raman bands at 1268 and 1384 cm^{-1} simultaneously appeared from 45-50 s. Furthermore, their side bands at 1295 and 1398 cm^{-1} also simultaneously appeared at 50–55 s.

3.3. Temporal Fluctuation of Background-Light Emission

We observed intermittent property of background-light emission, which is also known as “blinking” in SERRS measurements [1-9,19]. To compare

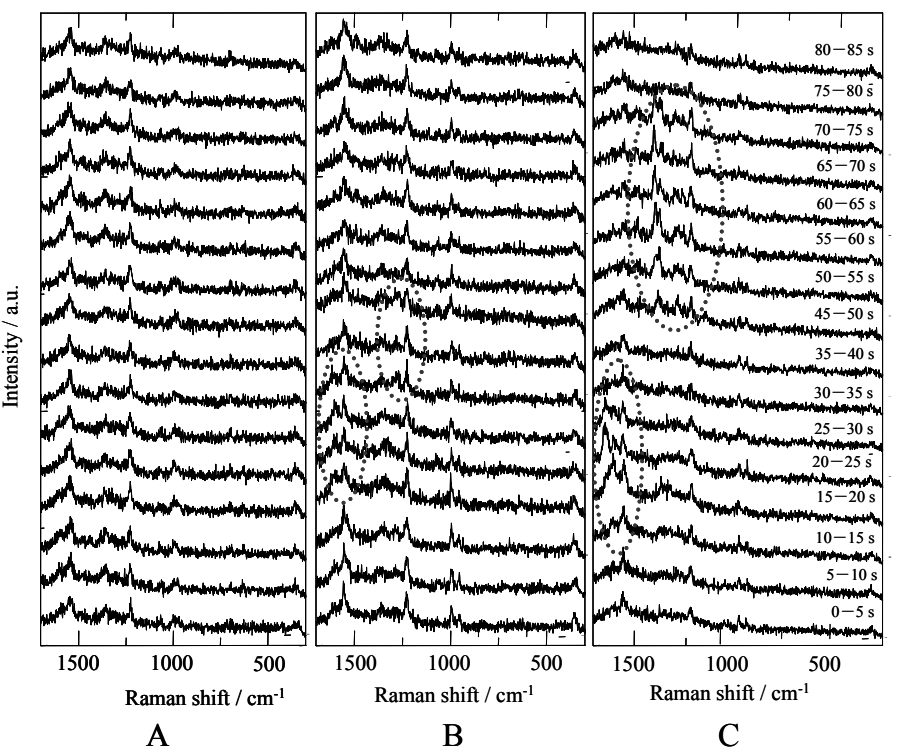

Fig 3. (A) – (C) Time-resolved SERRS spectra of H2TPP molecules adsorbed on three different single Ag nanoaggregates corresponding to those in Figure 2(B) – (D). Five seconds integration time per spectrum.

blinking of SERRS and background-light emission, we simultaneously observed SERRS and background-light emission spectra by expanding a spectral window from 50 to 250 nm. Figure 4A shows fluorescence spectra of H_2TPP. Fluorescence maxima at 650 and 720 nm are attributed to mirror-image transitions of Q-bands [30]. Figure 4B-F shows SERRS background-light emission spectra from five different Ag nanoaggregates. The highly-structured bands observed around 460 - 500 nm are attributed to SERRS bands [20,21]. The background-light emission spectra can be divided into five bands, as shown in the vertical dotted lines at 690 ± 10, 620 ± 10, 590 ± 10, 560 ± 10, and 530 ± 10 nm. These emission maxima are different from the fluorescence maxima at 650 and 720 nm.

Figure 5A-C shows time-resolved background-light plus SERRS spectra of three different Ag nanoaggregates. Figure 5A shows that background-light emission and SERRS did not fluctuate largely with time. On the other hand,

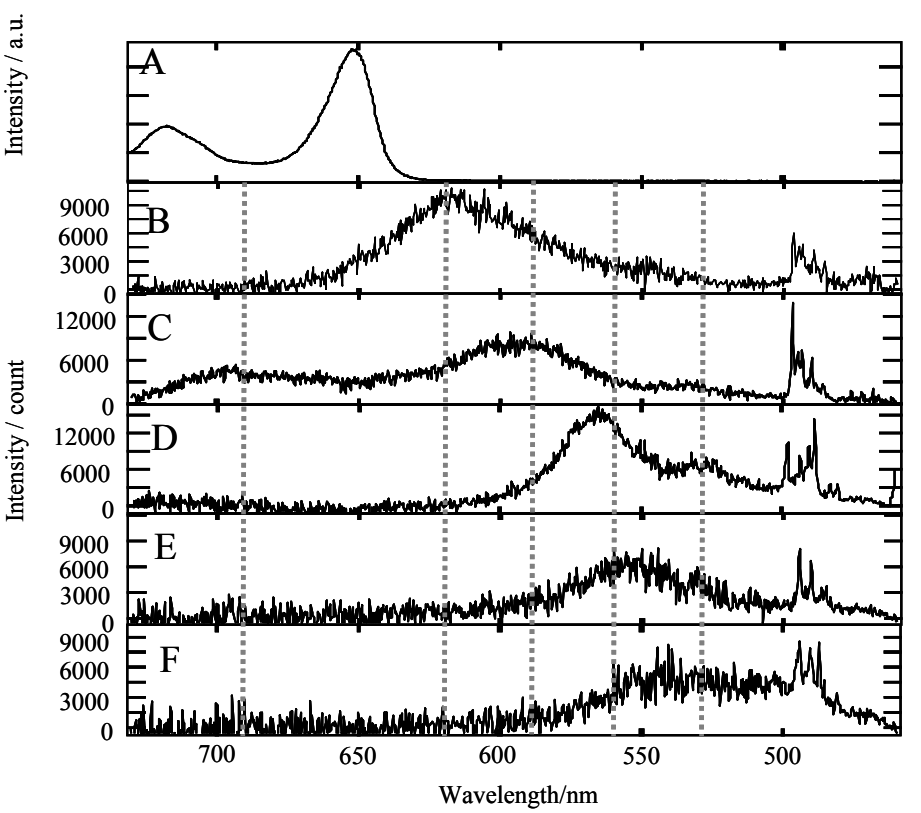

Fig 4. (A) Fluorescence spectrum of H2TPP and (B) – (F) variations in background-light emission spectra of H2TPP molecules adsorbed on single Ag nanoaggregates. The highly-structured bands around 460 - 500 nm are SERRS bands [20,21].

Figure 5B and C shows that background-light emission and SERRS fluctuated with time. Figure 5B shows that background-light emission was a combination of two maxima at 590 and 610 nm indicated by two dotted lines from 0-5 to 15-20 s. The emission maximum at 590 nm increased, decreased and disappeared from 0-5 to 30-35 s. The emission maximum at 610 nm increased and decreased from 0-5 to 30-35 s and kept its intensity from 35-40 to 80-85 s. During this temporal change, SERRS intensities and spectra also fluctuated. Figure 5C shows a background-light emission maximum at 560 nm shifted to 540 nm from 5-10 to 20-25 s, as indicated by the arrow 1. Then, the emission maximum decreased and additionally shifted to 520 nm from 50-55 to 60-65 s, as indicated by the arrow 2. During this time evolution of background-light emission, SERRS intensities and spectral shapes also fluctuated with time. Figure 5D, E, and F shows trajectories of the intensity of the background-light emission maxima at 600, 600, and 550 nm (solid line with closed circles), respectively, and of the common SERRS maximum at 490 nm (dashed line with open circles) in Figure 5A, B, and C, respectively.

4. DISCUSSION

4.1. SERRS Detection under the Single-Molecule Level

From the comparison between Figure 1A and Figure 1B, we found that the color of Rayleigh scattering of SERRS-active Ag nanoaggregates is not blue, but always red or yellow. Indeed, the color of red or yellow is an indication of aggregated Ag nanoparticles. The involvement of aggregated Ag nanoparticles as SERRS-active Ag particles is consistent with the previous work that revealed that an aggregate of Ag nanoparticles can be SERRS active [2,3,7,9,10,17,19]. From the previous work [2,3,7,9,10,19], H_2TPP molecules located at the junction of nanoparticles are likely SERRS-active. The “blinking” of SERRS is attributed to either thermal diffusion of an adsorbed molecule on a SERRS-active site [1-4,6-9] or fluctuation of energy levels of a complex formed between a metal atom and an adsorbed molecule due to a change in the local work function at a SERRS-active site [5]. Thus, the appearance of blinking in the current SERRS measurements strongly suggests that the number of adsorbed molecules per one SERRS-active site in a nanoaggregate is closed to the single molecule-level even though the initial concentration of H_2TPP (1.8×10^{-7} M) was much higher than the concentration of an Ag colloid solution (1.0×10^{-10} M).

4.2. Suppressed fluctuation of SERRS and background-light emission by Ag-N bonding

We found a key to understanding the interaction between Ag atoms and H_2TPP molecules in SERRS spectra at 1357cm^{-1}. This wavenumber is attributed to a C_α-N stretching mode by comparing SERRS spectra in Figure 2B, C, and

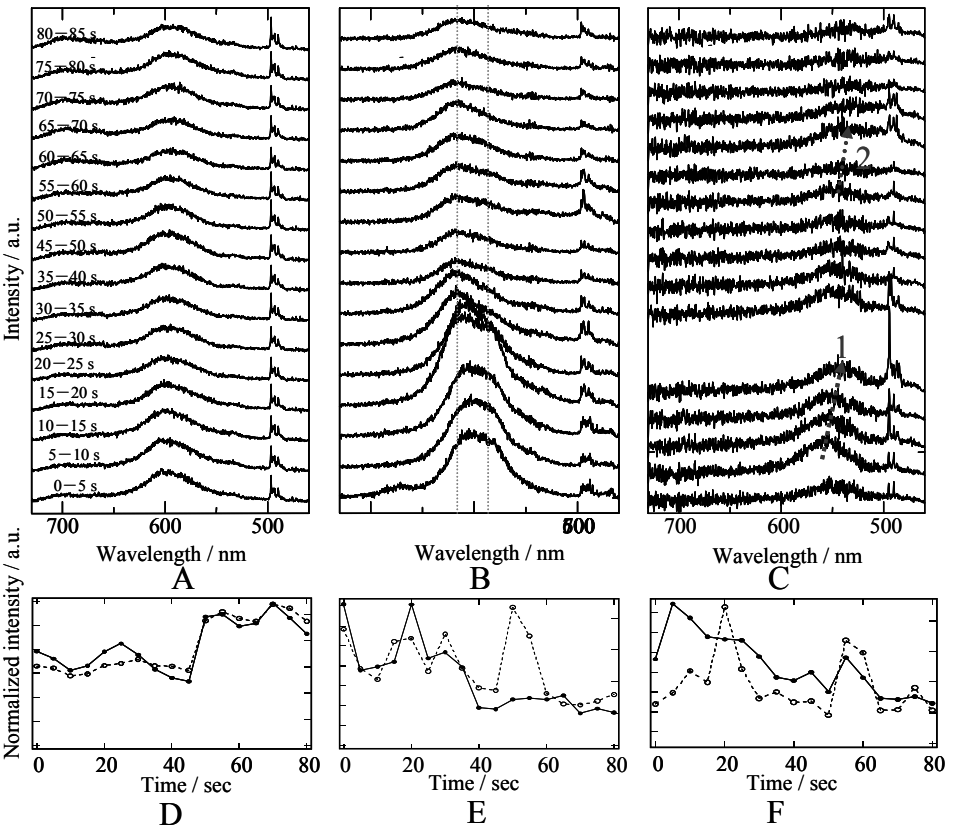

Fig 5. (A) – (C) Time-resolved background-light emission spectra of H2TPP molecules (5 s integration time) adsorbed on single Ag nanoparticle aggregates and (D) – (F) trajectories of the intensity of the background-light emission maxima at 600, 600, 550 nm (solid line with closed circles), respectively, and of the common SERRS maximum at 490 nm (dashed line with open circles) in A, B, and C, respectively. Intensities of the trajectories are normalized to their maximum intensity.

D with a resonance Raman spectrum of H_2TPP in Fig. 2A. Kobayashi *et al.* reported that resonance Raman spectra of complex of two Ag atoms and one H_2TPP molecule shows a strong band of a C_α-N stretching mode [20,21], whereas a resonance Raman spectrum of H_2TPP does not show a C_α-N stretching mode. Thus, formation of an Ag-N bond is evidenced by the appearance of a C_α-N stretching mode in the SERRS spectra in Figure 2B, C and D. Furthermore, formation of Ag-N bonds between adsorbed molecules with non-hydrogenated N atoms and Ag surface atoms is favored by reduction of the work function of Ag surfaces, as revealed by ultraviolet photoemission spectroscopy (UPS) [31]. Thus, our identification of the Ag-N bonds between

H_2TPP molecules and Ag surfaces in SERRS spectra is consistent with the previous experimental observations.

Recently, Jarzecki and Spiro applied a method of density functional theory (DFT)/configuration interactions with single-excitation (CIS) to analyze resonance Raman spectra of metal-free porphines [28]. Changes in the current SERRS spectra are quite similar to a change in their calculated spectra which is caused by electronic excitation splitting (Figure 3 in Ref. 28). The electronic excitation splitting is caused by two kinds of N atoms in a pyrrole-ring, one is hydrogenated and the other is non-hydrogenated, as shown in Figure 1D. The two kinds of nitrogen atoms in a pyrrole-ring split the excitation into two kinds of polarization [28]. In particular, a temporal change in the observed spectra in Figure 3B and C, which are highlighted by dotted circles, are in agreement with the transition from one polarized resonance Raman spectrum to the other polarized one of H_2TPP [28]. Considering that the current measurement is implemented at the single-molecule level per one SERRS-active site, the temporal change in SERRS bands in Figure 3B and C may provide evidence for rotation of a H_2TPP molecule against a SERRS-excitation electromagnetic field localized on a SERRS-active site.

The SERRS spectrum in Figure 2B, which was averaged over stable time-resolved spectra in Figure 3A, clearly shows a C_α-N stretching mode at 1357 cm^{-1}, whereas the SERRS spectra in Figure 2C and D, which were averaged over unstable time-resolved spectra in Figure 3B and C, respectively, do not clearly show the C_α-N stretching mode. Thus, the clearly observed C_α-N stretching mode in Figure 2B supports the idea that a H_2TPP molecule forms a stable Ag-N bond with a surface Ag atom. On the other hand, an unclear C_α-N stretching mode in Figure 2C and D supports the idea that a H_2TPP molecule forms an unstable Ag-N bond with a surface Ag atom. From the two types of appearance of a C_α-N stretching mode, we consider that the origin of temporal fluctuation of SERRS spectra is due to fluctuation of an Ag-N bond between a surface Ag atom and a H_2TPP molecule. We consider one possible origin of stale and unstable Ag-N bond is temporal fluctuation of local work function of an Ag surface, which changes barrier height of electron tunneling from a chemisorbed molecule to an Ag surface or an Ag surface to a molecule [5].

We identified in the previous paragraph a C_α-N stretching mode which is an indication of an Ag-N bond between a H_2TPP molecule and a surface Ag atom when SERRS spectra is temporally stable. Figure 5D shows that background-light emission was well synchronized with SERRS when the emission and SERRS was temporally stable. Figures 5E and F show that background-light emission is out of synchronization with SERRS when both the emission and SERRS are temporally unstable. The out-of-synchronization, together with the synchronization, suggests that the Ag-N bond determines not only the temporal fluctuation of SERRS but also of background-light emission.

4.3. Possible mechanism of SERRS and background-light emission in the current H_2TPP/Ag nanoaggregate system

We discuss in this section a possible mechanism of SERRS and background-light emission. Figure 4A-F shows blue shifts of background-light emission maxima from fluorescence maxima. These blue shifts suggest that background-light emission is not fluorescence of monomer of H_2TPP molecules. Background-light emission of SERRS has been considered to be luminescence or electronic Raman scattering from complexes of chemisorbed molecules and surface metal atoms [4,7,11,12,19,22]. We observed lack of excitation-wavelength dependence of background-light emission maxima for H_2TPP/Ag nanoaggregate system (data not shown). The lack of excitation-wavelength dependence supports the idea that background-light emission is not Raman scattering but luminescence. Blue shifts of luminescence maxima from monomer fluorescence maxima suggest that H_2TPP molecules form H-aggregates on Ag surfaces [32]. Furthermore, we identified in the previous section that SERRS-active H_2TPP molecules form Ag/N bonds with surface Ag atoms. From the lack of excitation-wavelength dependence and formation of Ag-N bonds, we attribute the background-light emission to luminescence of H_2TPP/Ag complexes. From the point of the origin of luminescence, we assume that the observed five background-light emission maxima in Figure 4B-F are luminescence from several conformations of H_2TPP/Ag complexes, because surface conformations of chemisorbed molecules on metal surfaces strongly change electronic orbital of the molecules [5,11,15]. However, there is still difficulty in identifying the origin of luminescence because the out-of-synchronization between SERRS and background-light emission suggests a possibility that SERRS is occasionally detected without background-light emission, and vice versa. We consider that SERRS without background-light emission is Raman signals of H_2TPP molecules, not forming complexes with Ag atoms, enhanced by EM field at SERRS-active sites, and that background-light emission without SERRS is luminescence from Ag-atom clusters [33,34], which enhanced by a strong EM field at SERRS-active sites.

We have difficulty in identifying electronic structures of H_2TPP/Ag complexes because no general rules are available to identify the structures. Furthermore, formation of orbital mixing between molecules and metal surfaces depends strongly on the combination of molecules and metals [11,15]. Ishii *et al.* investigated electronic structures of H_2TPP molecules on several kinds of metal surfaces by UPS [24-26]. They showed that decreases in vacuum level energy of H_2TPP/Mg, H_2TPP/Ag, and H_2TPP/Au system are 0.3, 0.6, and 1.0 eV, respectively, and noted that these variations in the reduction of vacuum level indicate existence of an electronic state at an interface between H_2TPP molecules and a metal surface [24-26]. They also commented that decreases in vacuum level energy indicate charge transfer (CT) from H_2TPP molecules to

metal surfaces through the interface electronic state [25]. Lombaridi *et al.* developed SERRS mechanisms including the CT from adsorbed molecules to metal surfaces (Figure 1C in Ref. 14). According to the CT-SERRS mechanisms [14] and a comprehensive dipole-dipole interaction theory [23], one possible quantum mechanical picture of SERRS and background-light emission of H_2TPP/Ag nanoaggregate system is summarized in the following manner. The incident light that is enhanced by a plasmon dipole excites an electron in one of HOMO states of a molecule to an interface electronic state between a molecule and a Ag nanoaggregate, and then the excited electron is scattered back to the initial HOMO state. The coupling between the transition-up dipole, which is induced by excitation from a HOMO state to an interface state, and a plasmon dipole enhances the scattering process. This enhanced scattering is an origin of SERRS.[23] On the other hand, a portion of the population of an excited electron in the interface electronic state can radiatively decay to the initial HOMO state. The coupling between the transition-down dipole, which is induced by radiative decay from the excited interface electronic state to the initial HOMO state and plasmon dipole enhances the radiative decay process. This enhanced radiative process is an origin of background-light emission.

5. CONCLUSIONS

We investigated, under the single Ag nanoaggregate and the single-molecule level, both temporal changes in SERRS and background-light emission spectra of H_2TPP. When SERRS spectra were temporally stable, a C_α-N stretching mode was clearly observed in SERRS spectra. On the other hand, when SERRS spectra were temporally unstable, this mode was not clearly observed. Furthermore, when SERRS spectra were temporally stable, the intensity of background-light emission was synchronized with the intensity of SERRS. On the other hand, when SERRS spectra were temporally unstable, the intensity of background-light emission was also temporally unstable and was not synchronized with the intensity of SERRS. A C_α-N stretching mode is enhanced when H_2TPP molecules form Ag-N bonds with surface Ag atoms [20,21]. Thus, we attributed the spectral fluctuation of SERRS and background-light emission to fluctuation of Ag-N bonds, the control of which plays an important role in suppression of spectral fluctuation. Furthermore, we attributed background-light emission to luminescence of complexes between H_2TPP H-aggregates and surface Ag atoms, considering possible Ag-N bonds, synchronized SERRS intensity with background-light emission intensity, and blue shifted background-light emission maxima from normal H_2TPP fluorescence maxima, and published work of electronic structure of H_2TPP molecules on Ag surfaces [24-26].

ACKNOWLEDGMENTS

This study was supported by MEXT under the 'Open Research Center' project for private universities.

REFERENCES

[1] K. Kneipp, Y. Wang, H. Kneipp, L. T. Perelman, I. Itzkan, R. Dasari and M. S. Feld, Phys. Rev. Lett. 78 (1997) 1667.
[2] S. M. Nie and S. R. Emory, Science 275 (1997) 1102.
[3] H. Xu, E. J.Bjerneld, M. Ka¨ll and L. Borjesson, Phys. Rev. Lett. 83 (1999) 4357.
[4] A. M. Michaels, M. Nirmal, L. E. Brus, J. Am. Chem. Soc. 121 (1999) 9932.
[5] A. Weiss, G. Haran, J. Phys. Chem. B 105 (2001) 12348.
[6] C. J. L. Constantino, T. Lemma, P. A. Antunes, R. Aroca, Anal. Chem. 73 (2001) 3674.
[7] K. A. Bosnick, J.Jiang, L. E. Brus, J. Phys. Chem. B 106 (2002) 8096.
[8] S. Habuchi, M. Cotlet, R. Gronheid, G. Dirix, J. Michiels, J. Vanderleyden, F. D. Schryver and J. Hofkens, J. Am. Chem. Soc. 125 (2003) 8446.
[9] Y. Maruyama, M. Ishikawa, M. Futamata, J. Phys. Chem. B 108 (2004) 673.
[10] H. X. Xu, J. Aizpurua, M. Kall, P. Apell, Phys. Rev. E 62 (2000) 4318.
[11] A. Otto, I. Mrozek, H. Grabhorn, W. Akemann, J. Physics-Condensed Matter 4 (1992) 1143.
[12] A. Campion, and P. Kambhampati, Chem. Soc. Rev. 27 (1998) 241.
[13] P. Hildebrant and S M.tockburger, J. Phys. Chem. 88 (1984) 5935. reference there in
[14] J. R. Lombardi, R. L. Birke, T. Lu and J. Xu, J. Chem. Phys. 84 (1986) 4174.
[15] J. F. Arenas, J. Soto, I. L. Tocon, D. J. Fernandez, J. C. Otero and J. I. Marcos, J. Chem. Phys. 116 (2002) 7207.
[16] T. Itoh, K. Hashimoto, A. Ikehata and Y. Ozaki, Appl. Phys. Lett. 83 (2003) 5557.
[17] T. Itoh, K. Hashimoto, Y. Ozaki, Appl. Phys. Lett. 83 (2003) 2274.
[18] T. Itoh, K. Hashimoto, A. Ikehata and Y. Ozaki, Chem. Phys. Lett. 389 (2004) 225.
[19] T. Itoh, V. Biju, M. Ishikawa, Y. Kikkawa, K. Hashimoto, A. Ikehata and Y. Ozaki, J. Chem. Phys. 124 (2006) 134708.
[20] Y. Kobayashi and K. Itoh, J. Phys. Chem. 89 (1985)5174.
[21] K. Syoji, Y. Kobayashi and K. Itoh, Chem. Phys. Lett. 102 (1983) 179.
[22] P. C. Andersen, M. L. Jacobson and K. L. Rowlen, J. Phys. Chem. B 108 (2004) 2148.
[23] B. J. Pettinger, Chem. Phys. 85 (1986) 7442.
[24] D. Yoshimura, H. Ishii, S. Narioka, M. Sei, T. Miyazaki, Y. Ouchi, S. Hasegawa, Y. Harima, K. Yamashita, and K. Seki, J. Electron Spectrosc. 78 (1996) 359.
[25] K. Seki and H. Ishii, J. Electron. Spectrosc. vol. 88-91 (1998) 821-830.
[26] H. Ishii, S. Hasegawa, D. Yoshimura, K. Sugiyama, S. Narioka, M. Sei, Y. Ouchi, K. Seki, Y. Harima and K. Yamashita, Mol. Cryst. Liq. Cryst. 296 (1997) 427-444
[27] P. Stein, A. Ulman and G. Spiro., J. Phys. Chem. 88 (1984) 369
[28] A. A. Jarzecki, T. G. Spiro, J. Phys. Chem. A 109 (2005) 421.
[29] K. Prendergast, T. G. Spiro, J. Phys. Chem. 95 (1991) 9728.
[30] S. Ohshima, T. Kajiwara, M. Hiramoto, K. Hashimoto and T. Sakata, J. Phys. Chem. 90 (1986) 4474.
[31] C. W. Kim, J. C. Villagran, U. Even and J. C. Thompson, J. Chem. Phys. 94 (1991) 3974.

[32] C. M.Nakul, M.Shyamalava, and N. Periasamy, J. Phys. Chem. 102 (1998) 1528.
[33] S. Fedrigo, W. Harbich, J. Buttet, J. Chem. Phys. 99 (1993) 5712.
[34] M. Treguer, F. Rocco, G. Lelong, A. L. Nestour, T. Cardinal, A. Maali, B. Lounis, Solid State Sci. 7 (2005) 812.

Handai Nanophotonics, Volume 3
H. Masuhara, S. Kawata and F. Tokunaga (Editors)

Chapter 11

General importance of anomalous diffusion in biological inhomogeneous systems

Kiminori Ushida and Akiko Masuda

Eco-Soft Materials Research Unit, Riken, 2-1 Hirosawa, Wako, Saitama, 351-0198 JAPAN

1. INTRODUCTION

From the viewpoint of material science, all biological systems from primitive to higher ones are complex compositions of various inhomogeneous substances, for example, polymers, gels, membranes, solutions, and other so-called soft materials. Life is the total activity of the construction, one aspect of which is expressed as material transports within this inhomogeneous space followed by some chemical reactions, including molecular association induced by weak intermolecular interactions. Transporting substance involves gases such as oxygen and carbon dioxide, liquids such as bloods, nourishing matters, hormones, and various signaling molecules which exist both inside and outside of cells. Activity of life, or "live or dead" in other straightforward words, can be distinguished by the conditions of material transports among various organisms in many practical cases. Moreover, organisms with diseases may causes some troubles or difficulties in material transports and therefore their observation can be used as diagnosis of various biological systems. Different from other superficial observations checking the structure or morphology of the biological organs, this new approach through material transports is more closely related to the real life activities.

Material transports in media are quantitatively characterized by diffusion coefficients. Diffusion coefficients can be measured by various methods including several spectroscopic methods, such as fluorescence correlation spectroscopy (FCS) [1-4]. However, diffusion coefficients within inhomogeneous space are not constant showing complex behavior called "Anomalous diffusion (AD)"[5]. AD is defined as the transport phenomenon where the mean-square displacement (MSD) of diffusing particle is not in

proportion to the time progression. Normal diffusion (ND) coefficient cannot be defined any more in such cases.

In this chapter, we discuss the importance of AD in biological systems realizing various bio-activity in life.

2. GENERAL DESCRIPTION OF ANOMALOUS DIFFUSION

2.1. General review about the description of normal diffusion

Diffusion coefficient, which is widely accepted in many fields of science and technology, was first found in Fick's second law [6, 7]. Fick had no microscopic imagination based on molecules but seemed to have derived this concept from thermal conduction theory. Diffusion coefficient namely started as the coefficient in diffusion equation which provides phenomenological explanations about material transports.

Now a day, however, widely accepted definition of diffusion coefficient by physical scientists is given by the relationship with the MSD of diffusing particles which is a statistical quantity obtainable by some experimental techniques [1,8]. This is originally predicted by Albert Einstein for the diffusion induced by Brownian motion [8]. As shown in Fig.1, MSD is often given by a function of time t as $<r(t)^2>$ In normal diffusion (ND), MSD increases in proportion to t and diffusion coefficient D is defined as

$$< r(t)^2 >= 2dDt \qquad (1)$$

where d is the dimension of diffusion, or in other words, the freedom of diffusion. For 3-dimentional isotropic (Euclid) diffusion (1) becomes

$$< r(t)^2 >= 6Dt \qquad (2)$$

t must be sufficiently long to reach a stationery stage where we can rule out the effect of the initial inhomogeneity and local fluctuations but this criteria is fulfilled in normal experimental observation such as in spectroscopy or in diffraction methods.

Diffusion equation describing ND is generally successful in the explanation of the diffusions in ordinal but ideal liquids where the proportional relationship between MSD and t is valid over surprisingly wide time region, from picoseconds to, probably days or years. This success implies the fact that any material transports in normal liquids are induced and driven by microscopic Brownian motions of molecular scale, i.e. the spatial scale is smaller than 0.01 nm and the time scale is smaller then picoseconds. Einstein expressed this concept providing very simple equation called Einstein's equation as

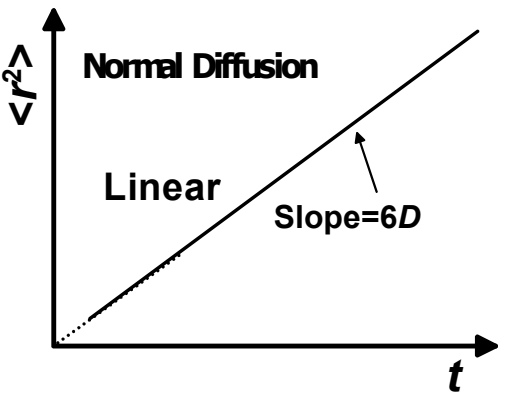

Fig. 1. The definition of diffusion coefficient derived from the time dependent function of mean square displacement (MSD), $<r(t)^2>$. See eq. (1).

$$D = \frac{\beta kT}{m} \tag{3}$$

at temperature T using a parameter β, where m and k stand for the mass of diffusing particle and Boltzmann factor, respectively [8]. Microscopic Brownian motion can be introduced to the diffusion equation by adding some stochastic terms such as random forces. One well-known stochastic differential equation of this kind is Langevin equation [9, 10] where the nature of Brownian motion appears in the time-correlation function of a stochastic random force $F(t)$ as

$$\ddot{x} + \beta\dot{x} = \frac{F(t)}{m} \tag{4}$$

in a style of the equation of motion. The nature of $F(t)$ can be analyzed using its auto-correlation function as

$$R(\tau) =< F(t)F(t+\tau) > \tag{5}$$

When the $F(t)$ is a pure random force (Brownian motion in homogeneous media), $R(t)$ takes a form expressing "white noise" with a delta function as

$$R(\tau) = R_0\delta(\tau) \tag{6}$$

In the diffusion process in homogenous media, the time integrals of $F(t)$ are supposed to show a Gauss distribution and the process belongs to Wiener process. However, this is not a unique solution for general diffusing transports and others are conceivable such as Levy-Flight motion [11, 12]. As far as we

treat homogenous systems classically as ND, we have almost no opportunity to encounter non-Wiener process and no necessity to use these extensions. However it can be revealed in the treatment of AD occurring in inhomogeneous space as simply discussed in the later sections of this article.

2.2. Extention of diffusion coefficient applicable to inhomogeneous systems

The majority of substances existing in this actual world, especially in the biological community, belong to inhomogeneous systems. The diffusion processes in such real substances are affected not only by spatial structures of diffusing spaces but also by some potential forces all of which have some typical scales, from nanometers to meters. One example of spatial structure is the meshwork structure in gels, glasses, or polymer solutions [1, 13-16]. One example of potential forces is the electrostatic interactions in colloidal solutions [17]. As the result, the physical properties concerning material transports (including D) may have some correlations to (or dependence on) the spatial scale [1]. Similarly, the structure of diffusing space also changes gradually along the progress of the time by some fluctuations and the above-mentioned physical properties may also have some correlations to the time scale. Accordingly, the static property in eq. (2) is changed to depend on the time and space scales in inhomogeneous systems as

$$< r(t)^2 >= 6D(t)t \tag{7}$$

or

$$< r(t)^2 >= 6D(L)t \tag{8}$$

where L is a typical length of diffusion traveling (we refer "diffusion length") and one can choose the square root of MSD for this parameter as

$$L = \sqrt{< r(t)^2 >} \tag{9}$$

It should be noted that eq. (2) can be used as the inter-conversion equation between t and L as

$$L = \sqrt{6D(t)t} \text{ or } L = \sqrt{6D(L)t} \tag{10}$$

regarding $D(t)$ and $D(L)$ as simple proportional factors for t [18, 19]. In the later sections of this article, we borrow this inter-conversion in the analyses of our observation of D since any experimental results have there typical t or L in their sampling as far as some spectroscopic or diffraction methods are employed. We

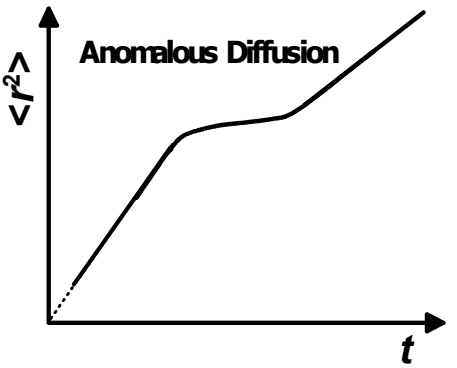

Fig. 2. An example of the lineshape of MSD for anomalous diffusion (AD). $\langle r(t)^2 \rangle$ becomes a variable function of t. (Compare with Fig.1)

call this kind of experiment as "single point measurement of D" and mark the observed results of D as D_{obs} to distinguish them. Even for inhomogeneous diffusions, we allow to use the following equation to obtain rough but sufficiently correct estimation for both t and L in treating a "single" experimental result.

$$L = \sqrt{6D_{obs}t} \tag{11}$$

In recent years, the term of "Anomalous diffusion" is widely used, the definition of which is the diffusion process where MSD is not in proportion to t as indicated in Fig.2. When plotted against linear t, MSD of normal diffusion is a straight line started from the origin (Fig. 1). For AD, however, the lineshape of observable (but actual observation is not easy) MSD is generally a free function of t as shown in Fig. 2. There is one question how we can define the time dependent diffusion coefficient $D(t)$ from the curve in Fig. 2. Another question is what is the relationship between $D(t)$ and experimentally obtained D_{obs}.

3. RELATIONSHIP OF THE OBSERVED DIFFUSION COEFFICIENT (D_{OBS}) WITH THE SAMPLING FUNCTIONS OF EACH EXPERIMENTAL METHOD

In AD, the measurement of diffusion coefficients (we refer this as diffusiometry in this chapter) cannot be straightforwardly connected with the real MSD function. Observation of D is performed under the experimental regulation in the scales of the time and space. If we choose one molecule, the value of D is approximately constant, however, the time scale can be changed by orders depending on the experimental scales which covers, for example, 10^{-9} – 10^{-0} m.

Since most of the experimental techniques have their own setups with a typical spatial scale, one experiment never covers this full time scale of MSD plot in Fig.2.

Another problem is the statistical sampling always accompanied by diffusiometry. When the real displacement ($r_i(t)^2$) of each single particle (i) can be monitored, the definition of MSD is expressed as

$$< r(t)^2 >= \lim_{N\to\infty} \frac{1}{N} \sum_{i=1}^{N} r_i(t)^2 \tag{12}$$

For diffusion of the particles smaller than the optical resolution limit such as ordinary molecules, we have no way to observe the real displacement $r_i(t)$. Instead of this, we choose an event which reflects the particle displacement and measure the period (sometimes statistical) in which the event undergoes. This is one-way derivation and we can never reproduce $r_i(t)$ from MSD.

Here we examine several examples of diffusiometry with spectroscopic techniques.

In FCS [1-4], the event in the view is decrease or increase of the molecules caught in the confocal volume (CV). The fluctuation (i.e. its correlation time) of the fluorescence intensity reflects the period of the stay for single molecule in the CV. In this case, the spatial condition (the size and shape of CV) is defined at first, the event (molecular motion intersecting the CV border) is defined next, and then, a time-dependent behavior (autocorrelation function) is monitored as the experimental result. A fitting function is used for the autocorrelation function to obtain the mean stay period (τ_R) inside CV. Typical size of CV in FCS is hundreds nm in horizontal diameter and typical τ_R is longer than μs.

For PFG-NMR method [18,19], as another example, the spatial resolution realized by magnetic field gradient is defined first, the escape of molecule from the area is used as the event, and a time-dependent behavior (signal decay versus the duration of two pulses) is obtained. Typical size of field gradient resolution is μm and typical decay constant is longer than ms.

FRAP (fluorescence recovery after photobleaching) has also connect the spatial information observed by microscopes with a time-dependent behavior (fluorescence recovery) induced by the diffusion of dye molecules. When a laser scanning microscope is used, the typical size of diffusing space is larger than μm and time scale is longer than ms.

All these experimental methods were developed and designed only for ND. When ND is expected for the system to be investigated, the effect of the shape of sampling function on the result is negligible since the true D value is only one at any t or L range. In most cases in ND, simple averaged values are used to obtain D.

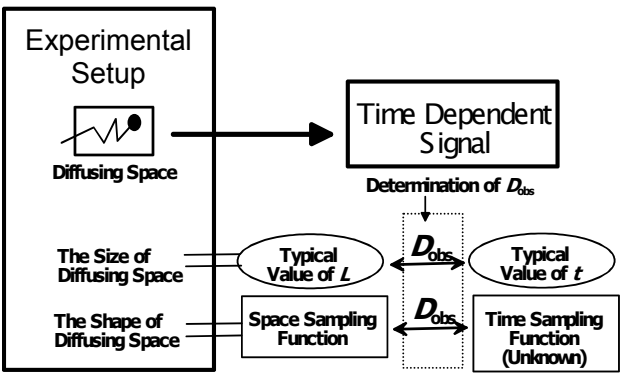

Fig. 3. A schematic diagram describing the effect of the experimental regulation of diffusiometry. The time sampling function is indirectly controlled by the shape and the size of diffusing space.

In Fig.3 we schematically indicate this situation. All these methods have their own space where the particles diffuse and time-dependent signals from the particles are recorded and accumulated. After appropriate analysis, D_{obs} is determined. Each method has its own size of diffusing space and L takes typical values depending on this size. Then this typical L is connected with typical t by

the value of D_{obs}. Therefore the typical value of t is indirectly regulated by the size of the diffusing space. In the same way, the shape and the size of the diffusing space indirectly controls the statistical distribution of the data in the time region through the space sampling function. This distribution, which is precisely unknown, can be regarded as the time sampling function for MSD. Obtained values of D_{obs} are the reflection of this time sampling function and sometimes deviate from the value of $D(t)$.

In AD, where the lineshape of MSD is not linear as shown in Fig.2, there is no guarantee that we can reproduce the true lineshape of $D(t)$ in connecting number of data points of D_{obs} obtained by various diffusiometries. Nevertheless, we dared to have done this approach in the series of our previous works [2-4, 18,19] which seems rather informative and useful in spite of its lack of precise background.

4. DIFFERENTIATION OF MSD AND ANOMALOUS DIFFUSION COEFFICIENT

In the last section we aware that the sampling method in the experiment is essential to discuss the relationship between D_{obs} and $D(t)$. In this section, we provide another remark on the differentiation of MSD in AD. Differentiation can be regarded as a limit ($\Delta t \to 0$) style of the sampling function in the time region.

For ND, eq.(2) is permanently correct and

$$\frac{d < r(t)^2 >}{dt} = 6D \tag{13}$$

is obtained. For AD, however,

$$\frac{d < r(t)^2 >}{dt} = 6D(t) + 6D'(t) \tag{14}$$

is obtained from eq. (7) and

$$\frac{d < r(t)^2 >}{dt} = 6D(t) \tag{15}$$

is incorrect because the second term in eq. (14) is neglected. In Fig 4, we show the difference between $d<r(t)^2>/dt$ and $6D(t)$ on the MSD curve. In real diffusiometry, for which the sampling function is ambiguous, both cases are possible that obtained D_{obs} is close to $d<r(t)^2>/dt$ or $6D(t)$.

5. EXAMPLES OF DIFFUSIOMETRY FOR INHOMOGENEOUS SYSTEM WITH ANOMALOUS DIFFUSION

In resent years, we performed diffusiometry on aqueous solutions of hyaluronic acid (HA) using several kinds of spectroscopic methods.[2-4, 18, 19] We collected the several numbers of data on single measurement (D_{obs}) and aligned

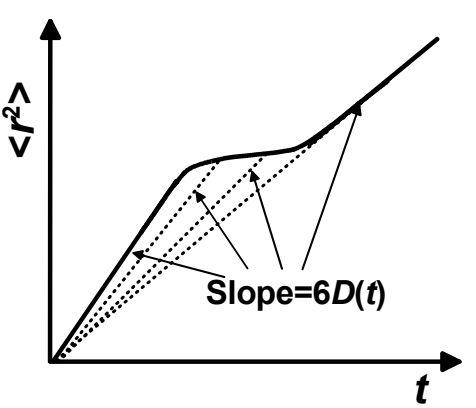

Fig. 4. The $6D(t)$ in the MSD curve of AD is the slope of linear line connecting the origin and $<r(t)^2>$ data points. The $d<r(t)^2>/dt$ is not equal to $6D(t)$. (See eq . (14))

them against the diffusion distance L or the diffusion time t. We could obtain a smooth line in each systems as shown in Fig. 5 and suppose that the resultant lines indicate rough profiles of $D(t)$ or $D(L)$.

The details of experiments were already presented in elsewhere. We used three kinds of diffusiometries for cytchrome c: Photochemical bimolecular reaction (PCBR), SVC-FCS, and PFG-NMR. A smaller molecule Alexa 488 showed a nice AD curve in SVC-FCS results. The value of t was determined as follows: (1) For PCBR, the time constant of the exponential decay of the excited state (fluorescence lifetime) was used. (2) For SVC-FCS, the average stay period in CV (τ_R) was used. (3) For PFG-NMR, the duration between two field

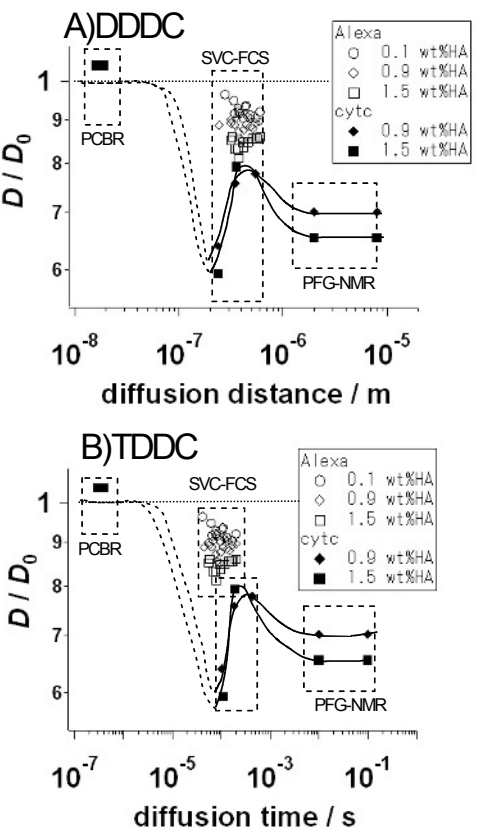

Fig. 5. A) The distance dependence of diffusion coefficient (DDDC) and B) the time dependence of diffusion coefficient (TDDC) plots for Dobs obtained in the aqueous solution of hyaluronan (HA). Diffusing molecules are Alexa 488 and cytchrome c. Use diffusiometries are PCBR (photochemical biomolecular reaction), SVC-FCS (sampling volume controlled fluorescence correlation spectroscopy), and PFG-NMR (pulsed field gradient nuclear magnetic resonance). (Reproduced from Ref. 4)

gradient pulses were used. We obtained corresponding L value for each data point by eq. (11). Both the distance dependence of diffusion coefficient (DDDC) plot and the time dependence of diffusion coefficient (TDDC) plot are shown in Fig. 5. These data points are D_{obs} which involve small deviation from true $D(L)$ or $D(t)$ because of the varieties of the sampling functions for each D_{obs} point.

Since the HA solutions are believed to form meshwork structures, it is reasonable that the profile of $D(L)$ becomes a step function as shown in Fig.6. For HA solutions used in our experiment, the typical mesh size (μ) was 5 - 30nm which was one order larger than the ordinary gel solutions. In the short distance limit (Plateau I: $L \rightarrow 0$), the line was flat and D_{obs} was constant and close to the value in water (buffer solution) without HA. In the long distance limit (Plateau II: $L >> \mu$), the line was flat again because the mesh size was sufficiently small to be regarded as homogenous media in this large scale of L. The interactions between the diffusing molecules and the HA mesh act as if friction in the continuous media. Different from plateau I, the position of plateau II depends on the mesh size, i.e. the concentration of HA. The HA concentration (C_{HA}) dependence of D_{obs} in plateau II exhibits an exponential curve as

$$D_{obs} = D_0 \exp(-\xi C_{HA}{}^{0.5}) \tag{16}$$

as suggested by Ogston et al [2-4, 21] for general gel solutions.

Between these two plateaus a step was found around which the value of D_{obs} dramatically changes. SVC-FCS method, which we developed recently, is a powerful technique to resolve the lineshape of curvature around the step. The position of the step in the spatial scale was 1-2 order larger than μ and also depends on the size of diffusing particles. The step shifts to lower t and L for larger molecules and realizes the size selection of the molecule like molecular sieving.

The mechanism of decrease in D_{obs} is explained as gradual decrease of the volume of reachable space within diffusing period along which the molecules are occasionally inhibited from their free motions encountering the polymer chains. The term “Ant in the labyrinth” [13, 22, 23] is used to describe this situation. Since the area where the value of D_{obs} changes is restricted in very narrow region of TDDC or DDDC plots, we call this region “local anomalous diffusion area” [4] as shown in Fig. 6. Appearance of local AD area is an importance character of gel-like fluid containing meshwork space.

Since meshwork structures are generally found in almost all biological systems, anomalous diffusion, especially the local anomalous diffusion, should be essential to regulate the biological activity through the material transports. In next section we discuss a typical example of extracellular matrix.

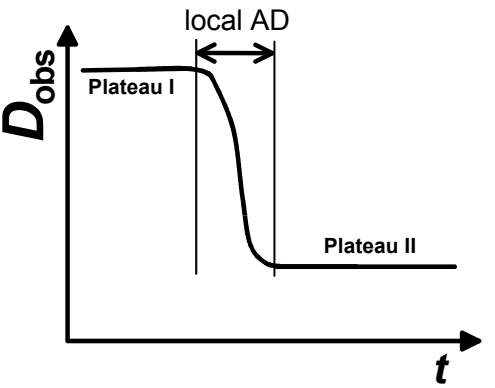

Fig. 6. A typical TDDC curve observed for inhomogeneous solutions containing mesh structure.

6. GENERAL IMPORTANCE OF ANOMALOUS DIFFUSION IN MATERIAL TRANSPORTS IN EXTRACELLULAR MATRICES (ECM)

Extracellular matrix (ECM) [24, 25] is the generalized name of variety of organs in animals other than cells. About a half volume of animal body is constructed by ECM. ECM is generated from cells, surrounds cells, interacts with cells, and is occasionally decomposed by cells. Sometimes cell itself migrates through the ECM space as seen in tumor cell migration.

Until recently, the role of ECM had been thought to be limited to ones of less importance in bio-activity such as constructing the body, holding moisture, etc.. However, recent studies reveal the significance of ECMs which communicate with cells continuously in their life activities. One example is the role of cell adhesion molecules (CAMs). The most famous CAM, cadherins act as connectors in cell-cell adhesion [26]. There are another group of CAMs which interact with ECMs such as integrins [27] (interacting with collagens) and CD44 [28] (interacting with HA). They act as the anchors of the cell contacting with ECM. Cells select cell-cell adhesion or cell-ECM adhesion in their activity and CAMs and ECMs are believed to play crucial roles in development and tumor migrations.

In Fig. 7, a cartoon of typical ECM (assuming ECM in cartilage) is indicated. The ECM is composed of largely of collagen fibrils which forms a stiff mesh structure. Rather small amount of glycoproteins, HA, and proteoglycans exist to fill up the large space between collagens. These glycomaterials form soft meshwork of hydrated gels and also hinder the materials that diffuse in ECM. Our previous results indicate that even a small amount (0.1 wt%) of HA affects the diffusion modes significantly. Therefore, material transports in ECM should be AD including local AD.

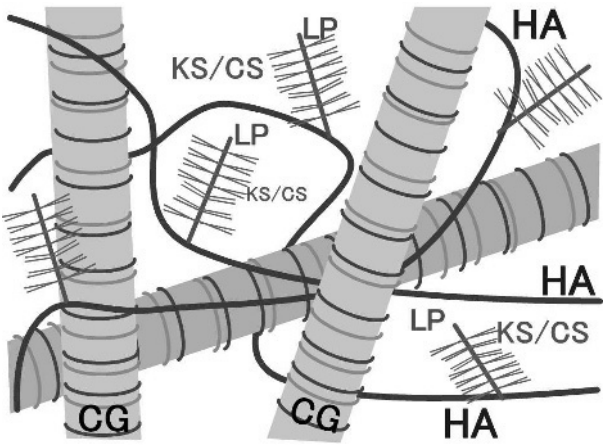

Fig. 7. A cartoon showing the structure of a typical ECM (assuming ECM in cartilage) composed of collagen (CG), hyaluronan (HA), link protein (LP), chondroitin sulfate (CS), keratan sulphate (KS). The LP+CS/KS are called aggrecan.

Now we scope on the cell surface activity in contact with ECM simply comparing two situations with and without ECM as shown in Fig. 8. The cell in the lower position secrets some materials including signaling molecules from P and Q. In free diffusion without ECM, materials secreted from P disperse into open space. Very small number of molecules can reach A, B and C and the majority will be lost in outer space. However, in the existence of ECM, the materials from P are not lost but held in ECM forming a gradient of concentration. The probability to reach B and C is still low but the selectivity to be conveyed to A is improved. In the same way, the material secreted from Q is easily accepted by the adjacent cell in the existence of ECM. The ECM seems to control the yield of chemical reactions by AD especially for the cell-cell communications.

This strategy to improve the yield of chemical reactions is adequately designed. The rate of bimolecular reaction between R and S is naively expressed as

$$v = 4\pi(D_R + D_S)[\mathrm{R}][\mathrm{S}] \tag{17}$$

If S is an acceptor fixed on the cell surface, (17) is simplified to be

$$v = 4\pi D_R[\mathrm{R}]S_0 \tag{18}$$

where S_0 is a constant. To increase the magnitude of v, we have two possibilities to increase [R] or to increase D_R. In biological system, however, the first

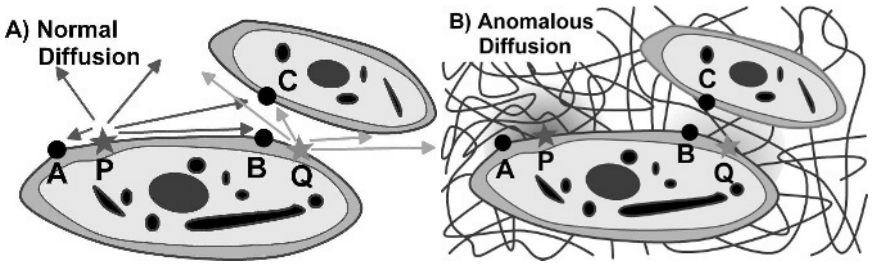

Fig. 8. Two cartoons comparing the cell with and without ECM. Some materials are secreted from P and Q to be accepted at A, B or C. A) Normal diffusion without ECM. B) Anomalous diffusion with ECM.

strategy to increase [R] is inadequate because the excess R is generated and the whole biological system needs to find a way to clean up the existing R which large amount of R and in sweeping up the excess R. Instead of this, the second strategy to increase (or control) D_R is the most rational one in sustaining the life activity.

7. CONCLUSIONS

In this chapter, we described the theoretical background for describing AD, the experimental techniques to resolve AD in spectroscopy together with their results, and one example of ECM showing important roles of AD. Needless to say, AD also occurs in intracellular material transports as observed by FCS and molecular migrations in membranes. Although we have no space to discuss all of them, the general importance of AD in total activity of biological system is apparent.

ACKNOWLEDGEMENTS

This research is partly supported by The Cosmetology Research Foundation, and the Grant-In-Aid for Scientific Research (Kakenhi) Grant No. 17034067 in Priority Area “Molecular Nano Dynamics” and Grant No. 17300166 from the Ministry of Education, Culture, Sports, Science and Technology (MEXT) of Japan.

REFERENCES

[1] Fluorescence Correlation Spectroscopy: Theory and Applications, edited by R. Rigler and E. S. Elson (Springer, Berlin, 2001).
[2] A. Masuda, K. Ushida and T. Okamoto, Biophys. J. 88, 3584 (2005).
[3] A. Masuda, K. Ushida and T. Okamoto, Phys. Rev. E 72, 6, 060101 (2005).

[4] A. Masuda, K. Ushida and T. Okamoto, J. Photochem. Photobiol. A 183, 304 (2006).
[5] P. A. Netz and T. Dorfmüller, J. Chem. Phys. 107, 9221 (1997).
[6] A. Fick, Phil. Mag. 10, 30 (1855).
[7] A. Fick, Poggendorff's Annel Physik 94, 59 (1855).
[8] A. Einstein, Annalen der Physik 17, 549 (1905).
[9] W. T. Coffey , Yu. P. Kalmykov, and J. T. Waldron, The Langevin Equation : With Applications to Stochastic Problems in Physics, Chemistry and Electrical Engineering 2ND Edition,World Scientific Pub Co Inc, USA (2004).
[10] D. S. Lemons, P. Langevin, and A. Gythiel, An Introduction to Stochastic Processes in Physics : Containing 'on the Theory of Brownian Motion' by Paul Langevin, Translated by Anthony Gythiel, Johns Hopkins Univ. Press, USA, (2002).
[11] M. Sclesinger, G. Zaslavsky, and U. Frisch eds. Levy Flights and Related Topics in Physics, Springer, Berlin (1995).
[12] J. Klafter, M. F. Shlesinger, and G. Zurmofen, Physics Today, 1996, 2, 33 (1996).
[13] Y. Gefen, A. Aharony, and S. Alexander, Phys. Rev. Lett. 50, 77 (1983).
[14] L.-S. Luo and G. D. J. Phillies, J. Chem. Phys. 105, 598 (1996)
[15] A. A. Gusev, S. Arizzi, U. W. Suter and D. J. Moll, J. Chem. Phys. 99, 2221 (1993).
[16] M. Mustafa and P. S. Russo, J. Coll. Interface Sci. 129, 240 (1989).
[17] R. Klein, in Structure and Dynamics of Polymer and Colloidal Solution, ed. by R. Borsali and R. Pecora, Kluwer Academic Publisher, 83 (2002)
[18] A. Masuda, K. Ushida, H. Koshino, K. Yamashita and T. Kluge, J. Am. Chem. Soc. 123, 11468 (2001).
[19] A. Masuda, K. Ushida, G. Nishimura, M. Kinjo, M. Tamura, H. Koshino, K. Yamashita, T. Kluge, J. Chem. Phys. 121, 10787 (2004).
[20] S. A. Adelman, J. Chem. Phys. 64, 123 (1976).
[21] A. G. Ogston, B. N. Preston, J. D. Wells and J. M. Snowden, Proc. R. Soc. London, A 333, 297 (1973).
[22] D. Stauffer and A. Aharony, Introduction to Percolation Theory, Taylor & Francis, London (1994).
[23] J. P. Straley, J. Phys. C, 13, 2991 (1980).
[24] B. Alberts, A. Johnson, J. Lewis, M. Raff, K. Roberts, P. Walter, Molecular Biology of The Cell 4th ed. Garland Science, New York, (2001).
[25] S. Ayad, R. Boot-Handford, and M. Humphries, Extracellular Matrix Factsbook, Academic Press, London (1998).
[26] M. Beckerle ed. Cell Adhesion, Oxford Univ. Press, Oxford (2002).
[27] N. H. Brown, S. L. Gregory, and M. D. Martin-Bermudo, Dev. Biol. 223, 1 (2000).
[28] D. Naor, S. Nedvetzki, I. Golan, L. Melnick, and Y. Faitelson, Crit. Rev. Clin. Lab. Sci. 39, 527 (2002).

Handai Nanophotonics, Volume 3
H. Masuhara, S. Kawata and F. Tokunaga (Editors)

Chapter 12

Two-color picosecond time-resolved infrared super-resolution microscopy

M. Sakai[a], T. Ohmori[b] and M. Fujii[a, b]

[a]Chemical Resources Laboratory, Tokyo Institute of Technology, 4259 Nagatsuta-cho, Midori-ku, Yokohama, 226-8503, Japan

[b]Integrated Research Institute, Tokyo Institute of Technology, 4259 Nagatsuta-cho, Midori-ku, Yokohama, 226-8503, Japan

1. INTRODUCTION

Molecular vibrations are known as the "finger print" of a molecule because they sensitively reflect geometry and circumstance of a molecule. If we can map a specific IR absorption band with sub-micron spatial resolution, we will be able to visualize the reaction dynamics in a non-uniform environment such as a cell. However, the IR absorption is weak in comparison to visible/UV absorption, thus a highly sensitive detection method is necessary. More seriously, the diffraction limit [1] prevents improvement of the spatial resolution of IR absorption to greater than a micron, because the wavelength of IR light is several micrometers. Therefore both high sensitivity and super-resolution beyond the diffraction limit are indispensable to achieve the nano-scale mapping of the IR absorption. In addition, the time-resolution of the IR light must be picosecond to facilitate the measurement of dynamics.

In this chapter, we introduce a new far-field infrared super-resolution microscopy proposed by combining laser fluorescence microscope and two-color picosecond time-resolved transient fluorescence detected infrared spectroscopy. We also report a principle inspection experiment of infrared super-resolution microscopy by using a sample of rhodamine 6G in chloroform-d_1 solution.

1.1. Picosecond time-resolved IR spectroscopy by transient fluorescence detection

Figure 1 shows the principle of the picosecond time-resolved IR spectroscopy by transient fluorescence detection, which was developed about 30 years ago by Kaiser and Laubereau [2-3]. We will call this technique transient fluorescence detected IR (TFD-IR) spectroscopy, because various IR-visible/UV double-resonance spectroscopies have been developed, and the name "IR-visible/UV double resonance method" is confusing [4]. Briefly, tunable IR light is introduced together with visible/UV light of which the wavelength is fixed to slightly longer than the visible/UV absorption band. If the frequency of the IR light is not resonant to the vibrational level, no fluorescence will appear because the wavelength of visible/UV light does not match the absorption band. When the IR frequency is resonant to the vibrational level, the vibrationally excited molecule generated by the IR absorption can absorb the visible/UV light, and gives the fluorescence. Thus we can detect the vibrational transition as this transient fluorescence. TFD-IR spectroscopy has high sensitivity because it is zero-background, and the IR absorption can be detected by the electronic transition, which has a large absorption cross-section. Moreover, we can also observe the population dynamics of vibrational cooling by adjusting the time delay between the IR and visible light.

1.2. Application to infrared super-resolution microscopy

IR super-resolution microscopy is achieved by applying picosecond time-resolved TFD-IR spectroscopy to a fluorescence microscope. A sample is irradiated with IR and visible/UV light. At a focal point, IR or visible light is focused by their respective diffraction limits. The transient fluorescence due to IR excitation appears only in the spatial region where both IR and visible/UV are overlapped. This overlapped region can be smaller than the diffraction limit of IR or visible/UV light (see figure 2). Thus we can obtain the IR absorption

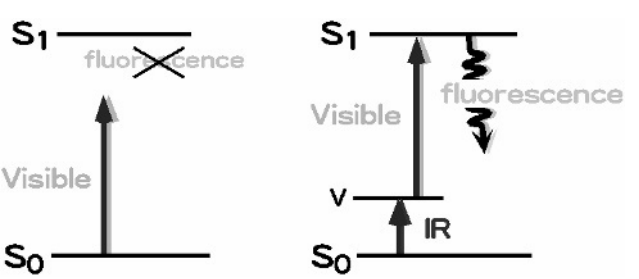

Fig. 1. Excitation scheme of transient fluorescence detected IR (TFD-IR) spectroscopy. The IR light excites a molecule to a vibrationally excited level. The visible light further excites to the electronically excited S_1 state, where the transient fluorescence is emitted.

spectrum of a region smaller than the diffraction limit. More realistically, IR and visible light is co-linearly irradiated to a sample. Also in this case, the super-resolution is achieved in the IR light. When the same objective lens is used, the diffraction limit is proportional to wavelength. The IR wavelength is much longer than the visible wavelength. Visible light can be focused much smaller than IR light. Transient fluorescence appears only in the overlapping region of IR and visible light, and the size of the overlapping region is completely the same as the diffraction limit of visible light. This means that IR information is observed with visible spatial resolution, i.e., the IR is super-resolved.

Furthermore, picosecond TFD-IR spectroscopy gives time-evolution of vibrationally excited molecules. Therefore, the measurement of picosecond dynamics is possible with IR super-resolution in this microscopy.

2. EXPERIMENTAL

2.1. Picosecond laser system

In IR super-resolution microscopy, we monitor the transient fluorescence pumped from a vibrationally excited level. In a vibrationally excited level, vibrational relaxation occurs in the picosecond timescale. Therefore, it is necessary for us to use a picosecond laser system. The laser setup for IR microscopy is essentially the same as that for the transient fluorescence detected IR spectroscopy [4-5]. Seed pulses from a cw mode-locked Ti:sapphire laser (Spectra Physics, Tsunami) were introduced into a regenerative Ti:sapphire amplifier (Quanta Ray, TSA-10). The amplified output pulse was composed of 2-3 ps pulses with energies of 6 mJ at 800 nm. 20% of the output pulse was used to pump a traveling-wave optical parametric amplifier system (Light conversion, TOPAS 400) after frequency doubling in BBO, to provide tuneable visible light. The remaining 80 % of the output pulse was split into two beams, and one was

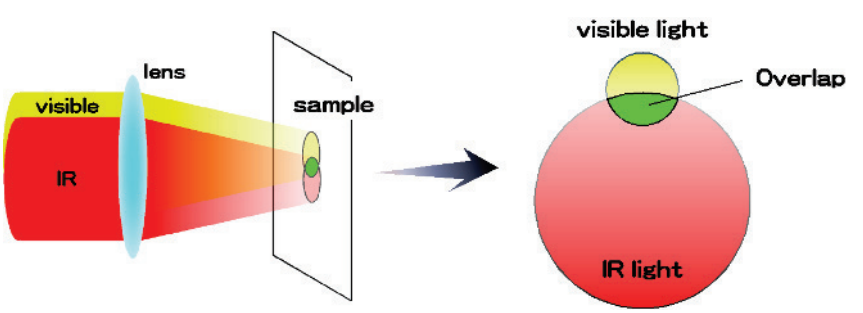

Fig. 2. The principle of IR super-resolution microscopy. If the visible light is collected onto a part of some focused IR light on a sample, the transient fluorescence due to IR excitation takes place in the area where the two lights overlap.

introduced into another OPA system (Light conversion, TOPAS 800). The second harmonic of the idler wave from the OPA and the remaining output pulse were differentially mixed in a KTA crystal to generate tuneable IR light.

2.2. Fluorescence detection system

Both the IR and visible light (~3 ps, ~15 cm^{-1}) generated by the picosecond laser system were introduced into a home-made laser fluorescence microscope [6-7]. Both beams were adjusted on a co-linear pass by a beam-combiner and focused into a sample by an objective reflection lens (Sigma, OBLR-20, NA = 0.38). Here, the sample used was rhodamine 6G dissolved in chloroform-d_1 to give a concentration of 5 x 10^{-4} mol dm^{-3}. This sample was held in a quartz cell. The transient fluorescence from the focal point was corrected by the same objective lens and was projected onto a CCD camera (Princeton Instruments Inc., PI-MAX-512). The delay time between IR and visible lights was varied by an optical delay system (Sigma, LTS-400X).

2.3. Sample

Rhodamine 6G, a typical dye for fluorescence probes, has a S_1-S_0 absorption around the 500–550 nm region, with the maximum at 530 nm (see figure 3). The visible light was fixed to 621 nm, which is longer than the S_1-S_0 absorption. The IR light was scanned in the region of CH and NH stretching vibrations of rhodamine 6G (2700 nm - 3700 nm). Under these conditions, the total energy of visible plus IR reaches somewhere around the absorption maximum at 530 nm. On the other hand, the fluorescence region of rhodamine 6G is from 550 to 590 nm, with the maximum at 565 nm shown in figure 3. Therefore, the transient fluorescence was monitored through the 555-575 nm band-pass filter. The visible light at 621 nm was cut off by a notch filter.

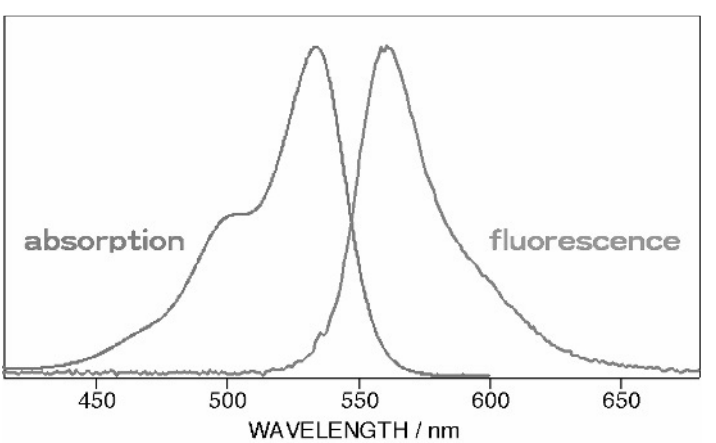

Fig. 3. Absorption and fluorescence spectra of rhodamine 6G

3. RESULTS AND DISCUSSION

3.1. Transient fluorescence image with an IR super-resolution

Figure 4 shows the transient fluorescence images of Rhodamine 6G in chloroform-d_1 solution (concentration, 5 x 10^{-4} mol dm^{-3}) observed by introducing (a) only infrared (IR wavelength, 3400 nm; diameter, 2.5 mmϕ), (b) only visible (visible wavelength, 621 nm; diameter, 7 mmϕ), and (c) both infrared and visible lights. No fluorescence appears in (a) only infrared and (b) only visible light. The transient fluorescence is clearly observed by introducing both infrared and visible lights (c). Moreover, the fluorescence images disappear again when the visible light is introduced earlier than the IR light or the IR wavelength is changed from 3400 nm to 2750 nm. 2750 nm is not in the range of IR absorptions of rhodamine 6G [8]. It is clear that transient fluorescence image is the IR-visible double resonance signal that appears via the vibrationally excited level.

As can be seen in the figure 4(c), the observed diameter of the transient fluorescence image was 6.8 μm. Since the theoretical diffraction limit for the IR light (3400 nm, 2.5 mmϕ, f=10 mm) is 16.6 μm FWHM in this measurement, this result clearly proves that the proposed technique breaks the diffraction limit. The spatial resolution of this infrared microscope can be improved by at least 2 times.

3.2. Picosecond time-resolved measurement

Another important function of this method is time-resolved IR imaging. Originally TFD-IR spectroscopy was used to investigate vibrational relaxation processes [2-4]. Thus in this spectroscopy, we can observe the population

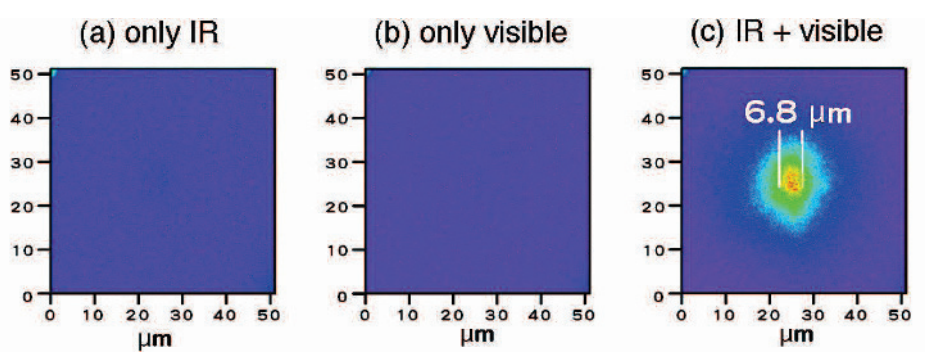

Fig. 4. Transient fluorescence images of rhodamine 6G in a chloroform-d_1 solution (concentration, 5 x 10^{-4} mol dm^{-3}) observed by introducing (a) only infrared (IR wavelength, 3400 nm; diameter, 2.5 mmϕ), (b) only visible (visible wavelength, 621 nm; diameter, 7 mmϕ), (c) both infrared and visible light into a quartz cell.

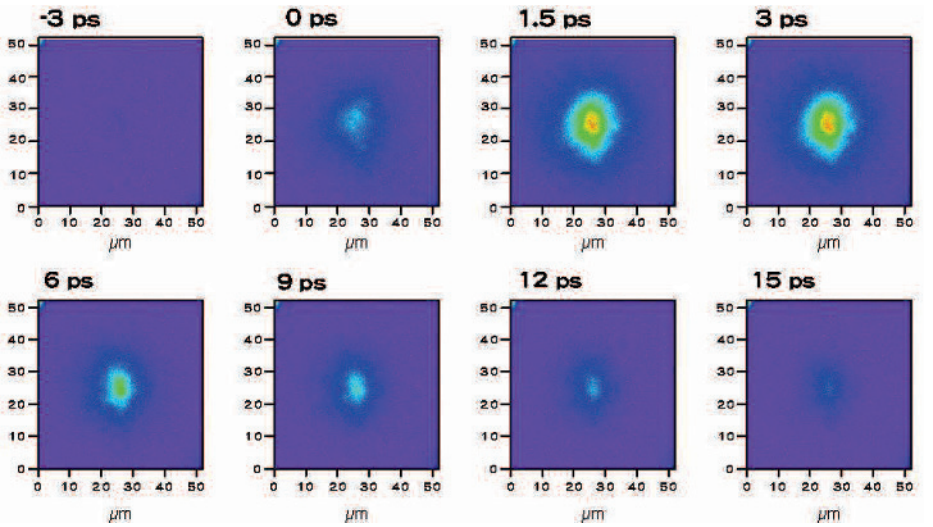

Fig. 5. Picosecond time-resolved transient fluorescence images at several delay times when the IR (diameter, 2.5 mmϕ) and visible (diameter, 7 mmϕ) lights are fixed to 3400 nm and 621 nm, respectively.

dynamics by the time-evolution of transient fluorescence images when we adjust the delay time between IR and visible light. Figure 5 shows picosecond time-resolved transient fluorescence images when the IR and visible lights are fixed to the 3400 nm and 621 nm, respectively. At the -3 ps delay time when the visible irradiates before IR, the signal is not observed at all. At 0 ps when the visible and IR irradiate at the same time, a transient fluorescence image clearly appears. The transient fluorescence increases in intensity up to 3 ps and decays with delay time. The observed time-evolution of the fluorescence image

represents the population decay from the vibrational level prepared by the IR laser together with the spatial mapping of the hot molecules at a specific time. This time-resolved imaging will be a good tool for space and time-resolved spectroscopy, which is necessary for the study of non-uniform systems such as catalysts, or biological systems like a cell.

4. CONCLUSION

We have performed far-field infrared super-resolution microscopy by combining a laser fluorescence microscope with picosecond time-resolved TFD-IR spectroscopy. In this chapter, we indicated that the spatial resolution of the infrared microscope improved to more than 2 times the diffraction limit of IR light. It will not be so difficult for the spatial resolution to improve to less than 1

μm by building a con-focal optical system in the near future. Furthermore, this new infrared super-resolution microscopy is capitalizing on TFD-IR spectroscopy's ability to study vibrational relaxation processes. Therefore, by using this infrared super-resolution microscopy, we will be able to carry out space- and time-resolved vibrational micro-spectroscopy in the infrared super-resolution region. Considering that IR absorption is regarded as the "finger print" of a molecule, the new infrared super-resolution microscopy will become an extremely important tool in not only microscopy but also spectroscopy.

In the near future, the spatial resolution of the infrared microscope will be improved to a sub-micron scale. Tunable picosecond IR light will also be generated in the mid-IR region up to 10 μm. The spatial resolution of our infrared microscope is determined by the diffraction limit of visible light. Therefore, the IR super-resolution will be kept in the 10 μm region. Probing in the 10 μm region will also mean that we will avoid the strong IR absorptions of water, which have been known to confound our results. By using this infrared super-resolution microscope, we will be able to visualize the structure and reaction dynamics of molecules in non-uniform environments such as cells.

ACKNOWLEDGMENT

The present work was financially supported in part by a Grant-Aid for Scientific Research (KAKENHI) on Priority Areas [432] MEXT, Japan. The authors would like to thank Dr. T. Watanabe and Dr. Y. Iketaki for the technical support of laser fluorescence microscope.

REFERENCES

[1] M. Born and W. Wolf, Principle of Optics, Springer, Berlin, 1933.
[2] A. Seilmeier, W. Kaiser, A. Laubereau and S. F. Fischer, Chem. Phys. Lett., 58 (1978) 225.
[3] N. H. Gottfried, A. Seilmeier, W. Kaiser, Chem. Phys. Lett., 111 (1984) 326.
[4] M. Sakai and M. Fujii, Chem. Phys. Lett., 396 (2004) 298.
[5] M. Sakai, T. Ueda, T. Yamanaka and M. Fujii, Bull. Chem. Soc. Jpn., 76 (2003) 509.
[6] T. Watanabe, Y. Iketaki, T. Omatsu, K. Yamamoto, S. Ishiuchi, M. Sakai and M. Fujii, Chem. Phys. Lett., 371 (2003) 634.
[7] T. Watanabe, Y. Iketaki, T. Omatsu, K. Yamamoto, M. Sakai and M. Fujii, Opt. Express, 11 (2003) 3271.
[8] SDBSWeb: http://www.aist.go.jp/RIODB/SDBS/ (National Institute of Advanced Industrial Science and Technology, March 2004).

This page intentionally left blank

Handai Nanophotonics, Volume 3
H. Masuhara, S. Kawata and F. Tokunaga (Editors)

Chapter 13

Molecular motion under the trapping potential of optical tweezers

Syoji Ito, Takashi Sugiyama, Naoki Toitani, and Hiroshi Miyasaka

Division of Frontier Materials Science, Graduate School of Engineering Science, Osaka University, 1-3 Machikaneyama-cho, Toyonaka, Osaka 560-8531, Japan

1. INTRODUCTION

Since the pioneering work of Ashkin in 1986 [1], laser trapping (optical tweezers) has been used as a powerful microscopic manipulation tool in various small systems. In these years the target of this method has been downsized from micrometer-scaled objects to nanometer-sized systems, such as patterning of individual nanoparticles onto substrates in solution using photochemical/ photothermal reactions [2-5], formation of polymer microparticles with characteristic internal structure by assembling polymer chains with the photon force [6,7], force measurement of individual motor proteins in molecular cell-biology [8,9], and so on. A focused near infrared (NIR) laser beam creates optical force potential providing only one stable trapping point. The feature enables us to manipulate small objects three-dimensionally without any mechanical contact. This is indeed one of the biggest advantages of the laser trapping as a nano-manipulation method in solution. For stable trapping of small objects, intense NIR laser light is focused into a spot close to the diffraction limit by a high numerical aperture (NA) objective. This tight focusing can induce local heating near the spot although the system has very small absorption of the trapping light. The local heating can affect the trapping stability of the laser manipulation method. Hence, a current interest about the topic is experimental determination of particle size range where the laser trapping is applicable in solution at room temperature for further application of the manipulation technique to quantum dots and molecules. It motivated us to investigate molecular motion in optical force potential well using fluorescence correlation spectroscopy (FCS) that allows us to determine the number of molecules in the confocal volume and their diffusion coefficient.

2. EXPERIMENTAL

2.1. FCS system combined with laser trapping

A schematic illustration of our experimental setup for the FCS measurement at the optical trapping point is shown in Figure 1. As an excitation light source for the fluorescence correlation measurement, a CW blue (wavelength: 488 nm) light from an Ar^+ laser (LGK7872M, LASOS lasertechnik GmbH) was coupled to a single mode optical fiber (Newport, F-SA-C) to isolate the laser device from the optical bench. This excitation laser light transmitting through the optical fiber was re-collimated with a pair of lenses, and then was focused by a

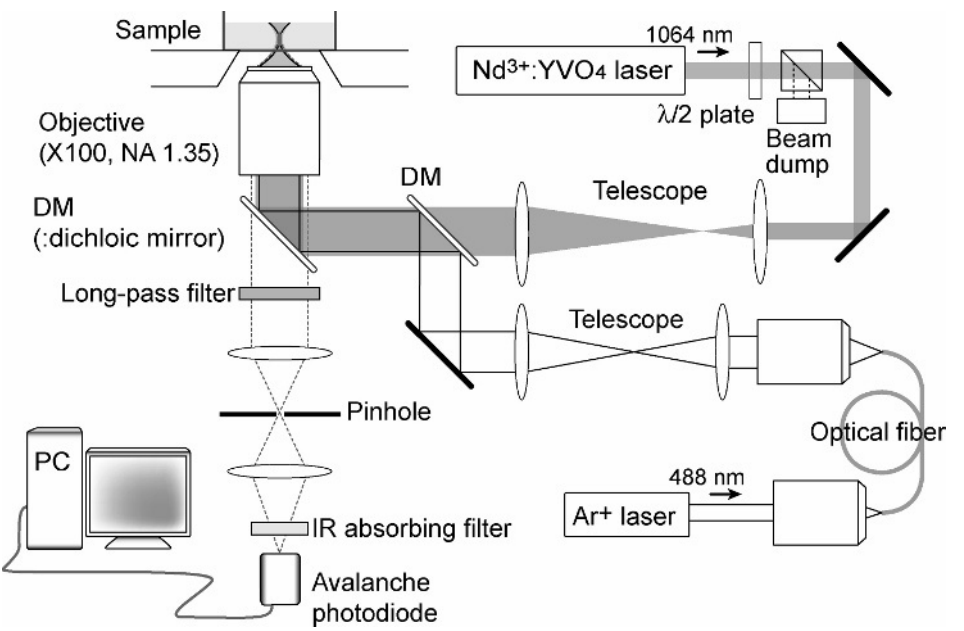

Fig. 1. Experimental setup for monitoring the translational motion of molecules under the radiation pressure of the focused NIR laser beam by fluorescence correlation spectroscopy. The NIR beam from a Nd:YVO_4 laser (1064 nm) was expanded by lenses of f=100 mm and f=300 mm, then was focused by a high NA objective (NA = 1.35, ×100) close to its diffraction limit. The power of the NIR laser beam was adjusted to desired value using a half-wave plate and a polarizing beam splitter. The 488 nm laser beam from an Ar^+ laser was focused in a similar manner without magnification; two lenses in the optical path were the same in focal length. The focusing points of these two laser beams were three dimensionally controlled by the pairs of lenses. Fluorescence from the confocal volume in sample solution was detected by an avalanche photo-diode; the sampling area was typically 350 nm in diameter in the focal plane.

microscope objective lens (UPlanApo 100X Oil Iris3, NA: 1.35, Olympus). For realizing a confocal optical configuration, a pinhole with diameter of 25 mm was set at the backward image plane of a microscope (IX70, Olympus). The emitted photons from dye molecules inside the confocal area were detected with an avalanche photodiode (SPCM-AQR-14, Perkin Elmer) connected with a counting board (M9003, Hamamatsu photonics K.K.). Scattered light from the sampling volume was blocked by an edge (long-pass) filter (Semrock, LP01-488RU) for the 488 nm light and an IR absorbing filter (Sigma Koki, HAF-50S-30H) for the 1064 nm light. Autocorrelation function of the fluorescent light was obtained using FCS software (U9451, Hamamatsu photonics K.K.). The CW NIR laser beam of 1064 nm from a Nd:YVO_4 laser (J20-BF-106W, Spectra-Physics) was focused by the microscope objective in a similar manner with the blue light. The Laser power of the NIR light in solution through the objective was estimated by a reported method by Masuhara et al. in 1991 [10].

2.2. Samples

Rhodamine-123 (abbreviated as Rh123, Acros Organics) was dissolved in water (Wako) and ethanol (Kshida) as samples for investigation of the diffusion behavior of a small fluorescent molecule. Single stranded DNA molecules consisting of 40 bases were also examined for elucidation of the effect of molecular weight. Fluorescein was tagged to the 5' end of the DNA chain as a fluorescent probe. The fluorescein tagged DNAs were dissolved in the TE buffer (mixture of aqueous solutions of HCl and of ethylene-diamine-tetraacetic acid). These sample solutions were injected into a glass-bottom culture dish (MatTek) for measurement. Through all measurements, both focusing points of the blue laser light and the NIR light were located 30 mm above from the bottom of the culture dishes.

3. DATA ANALYSIS OF FLUORESCENCE CORRELATION SIGNALS

3.1. Analytical model expressing the fluorescence correlation function

Fluorescence correlation spectroscopy provides the information on the diffusive motion of molecules, translational diffusion coefficient, on the basis of the fluctuation of fluorescence intensity in the time region originating from the variation of molecular number in the confocal volume. Taking into consideration of the actual experimental condition, autocorrelation function, G(t), of this fluorescence fluctuation is analytically derived as the following equation [11,12].

$$G(\tau) = 1 + \frac{1}{N}\left(1 + \frac{p}{1-p}\exp\left(-\frac{\tau}{\tau_T}\right)\right)\left(1 + \frac{\tau}{\tau_D}\right)^{-1}\left(1 + \frac{\tau}{w^2\tau_D}\right)^{-1/2} \quad (1)$$

where N is the average number of molecules in the confocal volume, V_{conf}, with cylindrical shape, p is the fraction of the contribution of triplet state, t_T is triplet lifetime, and w is structure parameter defined by $w = w_z/w_{xy}$. Here, w_z and w_{xy} are respectively the axial and radial radii of the cylindrical confocal volume ($V_{conf} = 2\pi w_z w_{xy}^2$). t_D is called diffusion time related with translational diffusion coefficient, D, by eq(2). Diffusion time is defined as an average time in which a fluorescent molecule goes across the sampling volume.

$$\tau_D = \frac{w_{xy}^2}{4D} \quad . \quad (2)$$

3.2. Analysis of fluorescence correlation signals using the analytical model

Figure 2 shows fluorescence autocorrelation curves of Rh123 in ethanol at 294.4 K. The solid line in the trace is the curve analyzed by the nonlinear least

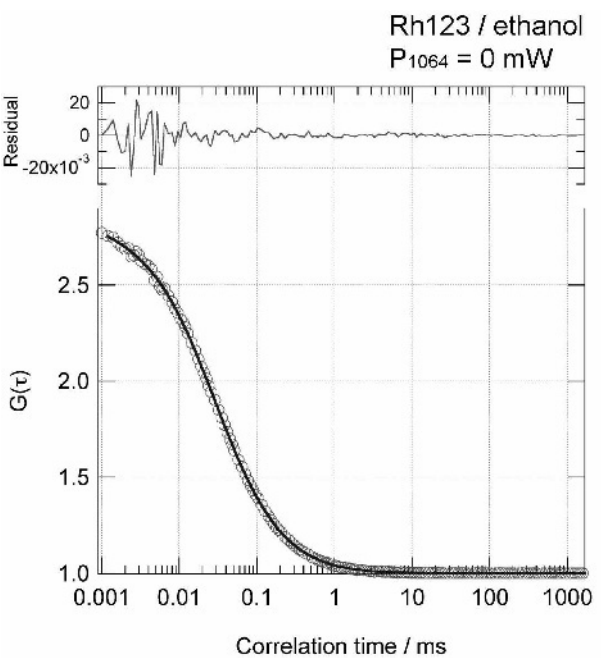

Fig. 2. Typical fluorescence autocorrelation function curve of the Rh123 in ethanol without the NIR laser irradiation. The fitting curve based on eq. (1) (solid line) well reproduce the experimental result. Its residual is also shown in the top of the figure.

square method with eq. (1), determining the parameters, N, t_D, w, t_T, and p. The residual is also plotted together at the top of the fluorescence autocorrelation curve. The experimental result was well reproduced by the calculated curve based on eq. (1). Also for other solutions of the samples, it was confirmed that the analysis based on eq. (1) well reproduced the experimental results.

Next, we confirmed the validity of the data analysis using eq. (1) for the fluorescence correlation function under tight focusing of the NIR light. Figure 3 shows a fluorescence correlation signal for the Rh123 solution of ethanol under the irradiation of the NIR laser at 240 mW. The curve calculated by using eq. (1) and the residual are plotted together with the experimental result. The correlation function curve under the irradiation of the NIR laser beam is also well reproduced by eq. (1), as was shown in Figure 2 without incident NIR laser light. For other solutions of the dye molecules, it was confirmed that the analysis based on eq. (1) well reproduced the experimental results. The results, thus, clearly support the analysis using eq. (1) is available for the fluorescence correlation signals obtained under the irradiation of the NIR laser beam.

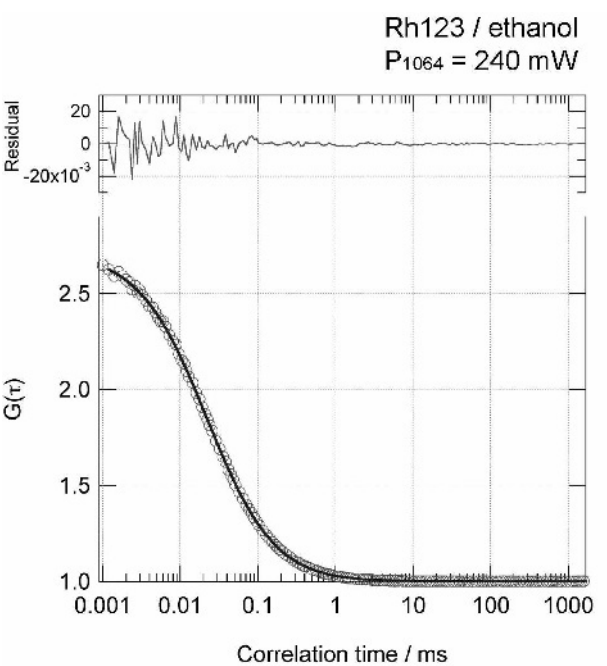

Fig. 3. Typical fluorescence autocorrelation function curve of the Rh123 in ethanol under irradiation of the NIR laser light at 240 mW. The curve calculated by eq. (1) (solid line) well reproduces the experimental result even in the presence of the NIR beam. The residual is shown together in the top of the trace.

4. EFFECT OF NEAR INFRARED LASER IRRADIATION ON TRANSLATIONAL MOTION OF MOLECULES IN SOLUTION

4.1. Estimation of optical force potential depth for nanometer sized particles

When we consider interaction between a nanoparticle and NIR light, the nanoparticle can be regarded as a point dipole (Rayleigh approximation) and the photon force potential, U, is given by the following equation [1, 13].

$$U = \frac{n_m}{c} 4\pi a^3 \frac{\varepsilon_p - \varepsilon_m}{\varepsilon_p + 2\varepsilon_m} I \tag{3}$$

where I is the intensity of the NIR light, a is the radius of the particle, e_p is the dielectric constant of the particle, e_m is the dielectric constant of medium, n_m is the refractive index of medium, c is the speed of light. As easily understood from eq. (3), optical force that a particle experiences is dependent on its size and the intensity of the incident laser light. This simple model based on Rayleigh approximation predicts that the optical force potential depth for ~ a 10 nm particle under the incident beam of several hundreds of mW was equal to the averaged energy of thermal motion at room temperature (~ 4.0×10^{-21} J). In other words, particle size of ~ 10 nm in diameter is at least necessary for effective optical trapping.

4.2. Effect of optical force potential on the translational diffusion of small dye molecules

From the radius of the Rhodamine molecule < 1nm estimated from the fluorescence correlation curves and the relation between the optical force potential depth and the volume of the particle, the optical force potential the molecule experiences is estimated to be < 10^{-3} kT, indicating that the change in diffusion time under the NIR laser irradiation can be attributed to the acceleration of the molecular motion by temperature elevation. Figure 4 shows changes in diffusion time as a function of the incident NIR power for Rh123 in water (Figure 4(a)) and Rh123 in ethanol (Figure 4 (b)). In both cases, the decrease in diffusion time with an increase in the incident laser power is ascribed to local heating at the focusing point of the NIR beam due to the absorption of the incident light by the solvents.

4.3. Effect of optical force potential on the translational diffusion of DNA

The fluorescein-tagged single stranded DNAs consisting of 40 bases exhibited larger diffusion time than that of the small dye molecules as shown in Figure 6(a). Comparing the diffusion time of the DNA with that of the Rh123 indicates that the hydrodynamic radius of the DNA in the solution was ~ four

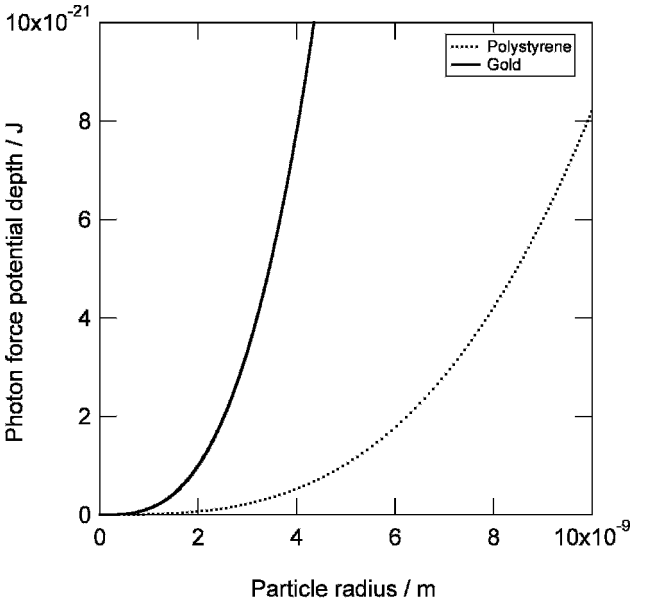

Fig. 4. Calculation of optical trapping potential depths for gold nanoparticle (solid line) and polystyrene nanoparticle (dotted line) as a function of particle radius based on eq. (3).

times larger than Rh123. From the simple estimation based on the Stokes-Einstein relation, $D = kT/6\pi\eta a$, the hydrodynamic diameter of the DNA was estimated ~ 5 nm. This size is about half of the critical particles size for optical trapping estimated in the section 4.1. It is expected that the relatively larger molecules experience the optical for potential that is not deep enough for their stable trapping but might affect their translational diffusion behaviors. As in the case of Rh123 shown in Figure 5, the diffusion time of the DNA decreased with an increase in the NIR laser power as shown in Figure 6. The decrease in the diffusion time of the DNA is ascribed to the local heating at the focusing point of the NIR beam due to the absorption of the incident light by the solvents as discussed in the previous section. Whereas the number of the DNA in the sampling volume increased with increasing the NIR laser power as shown in Figure 6b. This result suggests the competition between optical trapping and local heating in this size range (~ few nm hydrodynamic diameter estimated from the FCS measurement). This result also suggests a possible application of the optical trapping to controlling local concentration of molecules in nm-sized region. We are now continuing the elucidation of this interesting phenomenon and the development of a method that enables us to exert optical force to molecules more effectively.

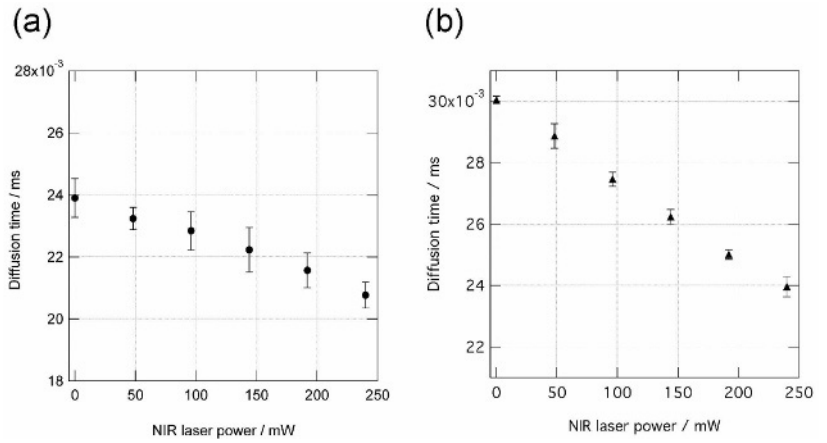

Fig. 5. Changes in diffusion times of fluorescent molecules as a function of the incident NIR laser power; (a), Rh123 in water and (b), Rh123 in ethanol.

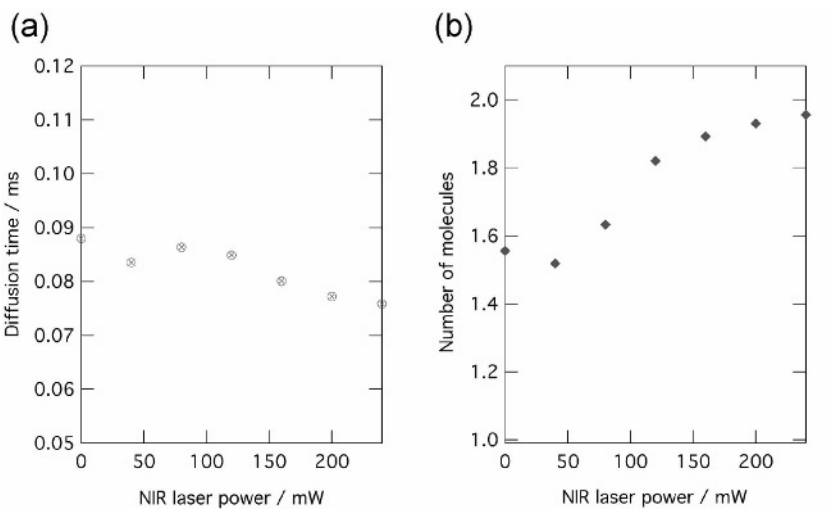

Fig.6. Incident laser power dependences of diffusion time (a) and the average number of molecules (b) for the DNA consisting of 40 bases.

5. SUMMARY

We have applied FCS to elucidating the diffusion behavior of molecules in solution under the optical force potential of the focused NIR laser beam. For the small dye molecules < 1 nm hydrodynamic radius, irradiation of the NIR laser beam induced temperature elevation at the focusing point with negligible optical

trapping effect. For larger DNA molecules consisting of 40 bases with ~ 5 nm hydrodynamic diameter, radiation pressure induced increase in the average number of the molecules inside the optical force potential, which suggested the control of molecular concentration by the radiation pressure even in the size range of few nm.

ACKNOWLEDGMENT

The present work was financially supported by The Mazda Foundation's Research Grant, by The Iketani Science and Technology Foundation, by the Ministry of Education, Culture, Sports, Science, and Technology (MEXT), Grant-in-Aid for Scientific Research on Priority Area "Molecular Nano Dynamics" and Grant-in-Aid for Young Scientists (B), and by the 21st Century COE Program from the Japan Society for the Promotion of Science (JSPS).

REFERENCES

[1] Ashkin, A.; Dziedzic, J. M.; Bjorkholm, J. E.; Chu, S. *Opt. Lett.* **11**, 288 (1986).
[2] S. Ito, H. Yoshikawa, and H. Masuhara, *Appl. Phys. Lett.* **78**, 2566 (2001).
[3] S. Ito, H. Yoshikawa, and H. Masuhara, *Appl. Phys. Lett.* **80**, 482 (2002).
[4] S. Ito, H. Yoshikawa, and H. Masuhara, *Jpn. J. Appl. Phys.,* **2004**, 43, L885.
[5] S. Ito, T. Mizuno, H. Yoshikawa, and H. Masuhara, *Jpn. J. Appl. Phys. submitted***.**
[6] J. Hofkens, J. Hotta, K. Sasaki, H. Masuhara, and K. Iwai, *Langmuir*, **13**, 414 (1997).
[7] J. Hofkens, J. Hotta, K. Sasaki, H. Masuhara, T. Taniguchi, and T. Miyashita, J. Am. Chem. Soc. 119, 2741 (1997).
[8] K. Svoboda, C. F. Schmidt, B. J. Schnapp, and S. M. Block, Nature, 365, 721 (1993).
[9] H. Kojima, E. Muto, H. Higuchi, and T. Yanagida, Biophys. J. 73, 2012 (1997).
[10] H. Misawa, M. Koshioka, K. Sasaki, N. Kitamura, and H. Masuhara, J. Appl. Phys. 70, 3829 (1991).
[11] Fluorescence Correlation Spectroscopy, R. Rigler and E. S. Elson Eds.; Springer Series in CHEMICAL PHYSICS 65, Springer, Berlin, 2001.
[12] Krichevsky and G. Bonnet, Reports on Progress in Physics, 65, 251 (2002).
[13] K. Svoboda and M. Block, Opt. Lett. 19, 930 (1994).

This page intentionally left blank

Handai Nanophotonics, Volume 3
H. Masuhara, S. Kawata and F. Tokunaga (Editors)

Chapter 14

Nanoscale fluid motion via molecular pores and polymer actuators

M. B. Cannell[1], P. Kilmartin[2], M. Jacobs[1,] S. Valiavalappil[2], J. Travas-Sejdic[2] and C. Soeller[1]

[1]Department of Physiology University of Auckland, Private Bag 92019, Auckland, New Zealand

[2]Department of Chemistry, University of Auckland, Private Bag 92019, Auckland, New Zealand

1. ABSTRACT

To develop "lab-on-a-chip" devices, it would be useful to develop microscopic pumping systems as well as ways of separating reactants. We have been developing methods to study a protein based molecular filter based on connexin proteins found in cells. The connexins form gap-junctions with a molecular weight cut-off of ~1kDa. To probe the porosity of a native gap-junction system we have combined two-photon excited flash photolysis and confocal microscopy to study diffusion through gap-junctions. To move sub-picolitre solution volumes, we have been examining volume changes within conducting polymers with atomic force microscopy (AFM).

Rat lenses (a cell system with extensive gap-junction mediated cell-cell permeability) were loaded with CMNB-caged fluorescein and positioned on the stage of a confocal microscope. By focusing the light from a Ti:Sapphire laser into a selected fiber cell a point source of free fluorescein was created. The movement of released fluorescein within and between fiber cells was monitored using an Argon ion laser. Parameter fits to experimental data gave estimates for both intracellular and intercellular diffusion coefficients. From this analysis, the gap junctions in eye lens fiber cells permit exchange of low molecular weight compounds between cells at about 0.4% of the rate of free diffusion.

Out-of-plane volume changes of microscopic polypyrrole strips were monitored with a Nanoscope II AFM. The actuator polymerization was carried out on gold strip electrodes patterned onto a glass slide. After polymerisation, alternate strips were oxidized and reduced to measure swelling and shrinkage as

voltage was changed (+/- 1V). With suitable electrolytes, 20% (or more) volume change occurred. Since the volume change is reversible by reversing the electrical polarity, there is net movement of electrolyte into the conducting polymer matrix. The resulting movement could be used to propel solute and provide a pumping action. Additionally, the swelling of the polymer could be used as a valve to direct different solute streams to a reaction chamber.

2. INTRODUCTION

To develop "lab-on-a-chip" devices a number of basic technologies for reactant metering, reactant handling and ways of analyzing fluid motion need to be developed at scales that are suitable for future nano-scale fabrication. Our work at Auckland has focused on two areas: (1) using optical techniques to measure microscopic motion of tracer dyes and new methods for analyzing diffusive fluxes across semi-permeable membranes and (2) examination of the behavior of prototypic conducting polymer actuators at microscopic scales.

Two-photon excitation (TPE) microscopy [1] can provide three-dimensionally resolved fluorescence excitation and carries the benefit that a confocal pinhole is not needed to limit fluorescence from out side the focal plane. Another advantage of TPE microscopy resides in the focally restricted nature of TPE where photodamage [2] and phototoxicity [3] are restricted to the focal volume which permits extended periods of imaging and collection of extended volumetric data in fragile specimens [4,5]. The spatially restricted nature of TPE also allows photolysis of precursor caged compounds to release active molecules in femtoliter volumes [6-8] or diffusion measurements by two-photon fluorescence photobleaching recovery [9] (for a review of TPE microscopy see [10]). In this paper we will describe some experiments that exploit TPE to measure diffusion in small volumes with high temporal resolution using photolysis of caged fluorescein to provide a fluorescent probe that can be simultaneously tracked with confocal microscopy. With this system, we have used TPE of CMNB-caged fluorescein to measure the rate of fluorescein production in test solution as well as the diffusion of fluorescein in drops of solution and within and between between eye lens fiber cells with high temporal and spatial resolution. The fiber cells are joined by an effective molecular sieve with a cutoff of about 1kDa formed by gap junction proteins [11] linking cells. Diffusion of uncaged fluorescein was about an order of magnitude slower inside fiber cells than in aequeous solution and diffusion between cells could be explained by the gap junctions acting as a restrictive barrier.

Conducting polymers (CP) such as polypyrrole (PPy) are creating considerable interest in the area of micro-device fabrication due to their ability to behave as low voltage physical actuators [12-14]. The dimensional change of the CP is due to the movement of ions into and out of the CP matrix as the CP is

either oxidized or reduced. This creates osmotic forces and a change in the dimensions of the matrix. Although the degree of volume change of the CP matrix may not be large, considerable forces can be developed and these processes have been described for a large number of electrolytes and solvents [15,16]. The motion takes the form of the linear length change for conducting polymer strips (in-plane actuation) and induced volume change (out-of-plane actuation) (for review see [17]). On the other hand, the nature of the ion flow, even for polypyrrole actuators, can be complicated by the existence of swelling and an increase of volume under both oxidising conditions (with an influx of anions) and reducing conditions (where cations move into the films). In this report we show preliminary results obtained by atomic force microscopy (AFM) of the out-of-plane swelling of thin films of polypyrrole [18] formed electrochemically on patterned gold strips. By choice of solvent and electrolyte, swelling can be achieved at either more positive or more negative potentials. The results are promising; the ability to change the actuation by changes in electrolyte (which can also modulate strain) coupled with the low voltage operation and amenity to micro- and nano-fabrication by lithographic techniques suggest that actuators based on these principles could form pumps and valves for the construction of "on-a-chip" solvent and reactant handling systems.

3. METHODS

3.1. Two-photon flash photolysis

A schematic of the optical apparatus is shown in Fig. 1. A modified Zeiss LSM410 laser scanning confocal microscope (Zeiss, Oberkochem) was used for imaging and 2-photon excitation. Illumination for 2-photon excitation was provided by a tunable, passively modelocked Ti:Sapphire (Ti:S) laser (Mira 900, Coherent, Santa Clara, CA) capable of generating ultra-short (<100 fs at 730 nm) pulses at 76MHz. The Ti:S laser was pumped by a 532 nm 10W solid state pump laser (Verdi, Coherent, Santa Clara, CA). Typical pump power was 8W. The light from the Ti:S laser was modulated by a Pockels cell (Conoptics, California, USA) whose command signal was derived from the LSM 410 frame, line and pixel timing pulses by custom electronics designed by the authors. For most experiments shown here, a slightly longer pulse of ~150fs with a bandwidth of just under 10nm was used which did not require group velocity correction. The beam was then coupled into the LSM 410 light path by way of a beam steering mirrors (Melles Griot, Irvine, CA), focusing lens and a custom short wave pass dichroic mirror centered at 680 nm (Chroma, Battleboro, New Jersey, USA). The latter element was incorporated into a modified field diaphragm housing in the Axiovert 100TV microscope body (Zeiss, Oberkochem) of the LSM410. The divergence of the Ti:S laser beam over the extended beam path (~3m long) with some magnification from the focusing lens

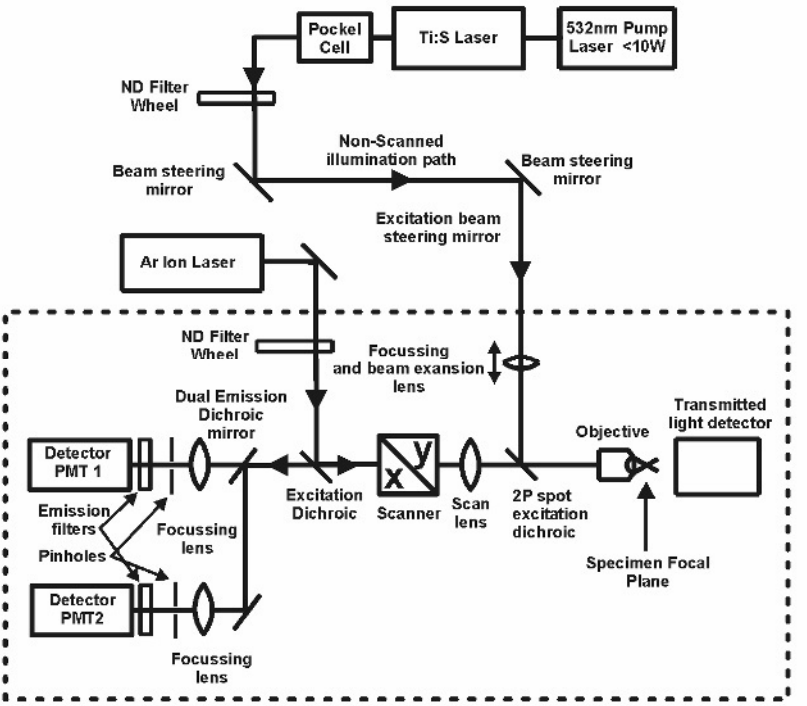

Fig. 1. Schematic of the two-photon photolysis system. The components associated with the LSM410 confocal microscope are shown in the dotted box. The Pockel cell provided fast intensity modulation of the beam from the Ti:S laser which was passively mode locked to provide ~150 fs pulses at 80 MHz. This beam was coupled into the microscope by beam steering mirrors and bypassed the confocal scanning optics, thereby providing a stationary spot for flash photolysis.

ensured that no additional beam expansion was necessary to fill the objective rear aperture. For 2-photon flash photolysis, the Ti:S laser center wavelength was set to 750nm. Illumination power for two-photon excited flash photolysis (TPEFP) varied (depending on the experiment) but was usually <300 mW (measured at the side port aperture) in test solutions and <80mW inside cells.

With a measured throughput of ~36% at the objective rear aperture (a loss related to the need to overfill the objective rear aperture) this corresponds to powers <20 mW in cell samples. To measure the resolution of the TPEFP system, DMNB-caged fluorescein dextran, 70KDa (Molecular Probes) was embedded in a 15% acrylamide gel to achieve an effective cage concentration of ~1mM (based on a concentration of 8.5 mol caged fluorescein/mol) and a short pulse used to release some fluorescein. This was subsequently imaged in three dimensions by the confocal microscope. After taking blurring into account (due

to the limited resolution of the confocal microscope), a full width at half maximum (FWHM) diameter of 0.5 μm in plane (x-y) and of 1.4 μm along the axial direction (z) for the photolysis volume was measured [19]. This corresponds to an effective photolysis volume of ~0.4 x 10^{-15} l. While the size of the photolysis volume is somewhat larger than might be expected from the diffraction limit associated with a 1.2 NA objective lens, this increase in size probably results from the moderate degree of rear-aperture overfilling used. For a Gaussian input beam, the beam needs to be expanded to a size ~10x that of the rear aperture to obtain diffraction limited performance. Such a large degree of beam expansion is impractical since 10x beam expansion implies very low throughput efficiencies (about 1%). By using a beam 3 times the diameter of the rear aperture we obtained a reasonable compromise; the photolysis PSF was approximately twice the size of the diffraction limited PSF while sufficient power was available to achieve a maximum photolysis rate of ~75% of the maximum rate possible (limited by both intensity and diffusion into the photolysis volume). Light for conventional confocal imaging was supplied by an air-cooled Ar-ion laser (Uniphase, California, USA) that was coupled into the LSM 410 via the main dichroic mirror (see Fig. 1). Fluorescence changes in response to focal photolysis of caged compounds were monitored with the 488 nm line of the Ar-ion laser in confocal mode in order to measure the spatio-temporal properties of the indicator signal. When images were acquired in confocal mode, the pinhole was adjusted to a diameter of ~1.2 Airey units resulting in a confocal point spread function with a full width at half maximum (FWHM) diameter of 300 nm in plane and 700 nm in the axial direction. In some cases, images were acquired in the line scan mode of the microscope where one line through the sample was repetitively scanned to retain spatial information (along the scan line) while achieving millisecond time resolution (see [20] for a more detailed description of line scanning). A 40x 1.2NA water immersion objective (Zeiss, Oberkochem) was used for all imaging in the aqueous samples. Excitation and emission filters were custom made (Chroma Technology, Battleboro, New Jersey, USA) to the authors' specifications. The main dichroic filter separating 488 nm illumination and 530 nm emission wavelength from each other was a long pass filter with an edge centred at 500nm. The emission bandpass filter was centered at 535nm (HQ535/50, bandwidth 50nm). Fluorescence was measured with a photomultiplier tube (PMT) internal to the LSM 410 via a confocal pinhole and wavelength selection filters. Lenses from 21-day-old Wistar rats (killed by CO_2 asphyxiation in accordance with protocols approved by the University of Auckland Animal Ethics Committee) were dissected into phosphate buffered saline at 37°C and then transferred to a plate where they were bathed in intracellular medium containing (in mM) $MgCl_2$ 1, EGTA 0.5, NaCl 10, Na_2ATP 2, KCl 20, K-gluconate 120, HEPES 10, pH 7.3, 300 mOsm/kg. Lenses were cut through the

equator using a scalpel blade and the hemispheres were examined for structural integrity under a dissecting microscope. Hemispheres were then transferred to a small chamber sealed at the bottom with a coverslip, so that the cut surface of the lens faced the coverslip. The chamber was filled with 0.15 ml of solution containing 1 mM CMNB-caged fluorescein and (optionally) 0.10 mg/ml WGA in intracellular medium to selectively label cell membranes.

Solutions: Flash photolysis in drops of salt solution containing 140mM KCl and 10mM phosphate buffer, pH 7.0 was carried out with CNMB caged fluorescein (Molecular Probes, Eugene, Oregon, USA).

3.2. Polymer-based actuators

Pyrrole monomer (Aldrich) was distilled prior to use and stored under a nitrogen atmosphere in the dark. Tetrabutylammonium phosphorous hexafluoride ($TBAPF_6$), tetrabutylammonium triflouromethanesulfonate ($TBACF_3SO_3$), and propylene carbonate (PC) (Aldrich) were used as supplied.

Polypyrrole (PPy) was deposited on patterned parallel gold strips evaporated onto a chip-like substrate on a 1.5 cm x 1.5 cm glass plate using a common connector for the working electrodes to ensure uniform PPy thickness on all strips. PPy in the doped form was prepared potentiostatically at 0.85 V against Ag/AgCl at a gold electrode in solutions containing 0.1 M pyrrole in propylene carbonate (PC) with either (a) 0.1 M $TBAPF_6$, or (b) 0.1M $TBACF_3SO_3$, as the supporting electrolyte, which also provides the dopant anions and cations species needed to balance charges created within the PPy films during oxidation and reduction. The electrochemical polymerization was stopped once the consumed charge reached 1 mC (for a working electrode area of 0.024 cm^2), to obtain a film thickness of about 2 μm.

The PPy strips were cycled in pyrrole-free PC solutions with the same supporting electrolyte as used during formation. The alternative strips were then oxidized and reduced at a constant potential of +1 V or -1 V for 3 minutes. After the oxidation/reduction step, the chip was taken out of the electrolyte solution, patted briefly to remove the electrolyte solution from the surface and measured by AFM. No corrrection was made for potential solvent loss from the matrix.

Atomic Force Microscopy (AFM) was used to determine the out of plane (volume change) actuation of the PPy strips polymerized onto the chip electrodes. Thickness changes for the oxidized and reduced state of PPy films in PC were measured using a Nanoscope II AFM and each sample was measured on at least 5 different positions . Section analysis of each sample was carried out in order to obtain the thickness difference between alternative oxidized and reduced strips. The thickness of the gold layer, determined using bare strips, was subtracted from the recorded value to get the actual thickness of the PPy films. From these values the percentage volume change for each section could be calculated.

4. RESULTS

4.1. TPE flash photolysis in drops of solution

Figure 2A shows release of caged fluorescein in a drop of solution evoked by TPE flash photolysis (TPEFP). In this X-Y confocal scan, fluorescence spreads from the diffraction-limited photolysis volume in a radially symmetric pattern as would be expected for free diffusion. As the illumination power was increased, the intensity of the pattern increased and at higher powers (Fig. 2B), a spot of reduced fluorescence in the center developed. This loss of fluorescence in the center may be explained by the simultaneous destruction of some (uncaged) fluorescein molecules by the photolysis beam (or some other loss process -see below). By repeatedly scanning a single line through the center of the photolysis region a higher time resolution (2 ms) can be achieved at the expense of one spatial dimension [20]. Since the diffusion is radially symmetric, the line plot captures the same spatial information as an X-Y scan. The raw data can be displayed as a "line scan image" where the intensity along the line is plotted and with each line the displayed line offset (Fig. 2C) so that, in these data, the horizontal axis shows position and the vertical axis time (increasing downward). The spread of fluorescence from the focal volume can be seen and, as input power is increased, the intensity of fluorescence increases. The central panel shows the appearance of the dark region in the center of the photolysis volume at intermediate powers which persist for the duration of the uncaging beam exposure. At higher input power (upper panel), when the uncaging beam is turned off, there is a rapid increase in fluorescence above the level seen while the uncaging beam is on and which subsequently decays. The time course of fluorescence change at the center of the photolysis volume is shown in Fig. 2D.

Although at low powers the intensity of fluorescence follows a square power law dependence (as expected for TPE), the peak intensity during photolysis saturates and when the photolysis beam is switched off there is a further rapid increase in fluorescence. At the highest power level used in these experiments, the peak fluorescence was ~40% lower than the level observed immediately after the uncaging beam is turned off. The simplest explanation for this secondary increase in fluorescence is that, at higher power levels, fluorescein molecules are rapidly bleached by the photolysis beam and when the beam is turned off the uncaging reaction continues for some time liberating new fluorescein molecules (which are not now subject to photobleaching). This idea is supported by the observation that the rate of rise of the secondary increase is the same as the initial rate of rise of fluorescence (shown at higher time resolution in Figs. 2E and 2F) and was 2500 s^{-1}. By fitting the decay of the diffusion profile to the equation for spherical diffusion we obtained a value of $4 \cdot 10^{-6}$ cm^2/s, a value close to the reported diffusion coefficient of fluorescein in aqueous solution of $5.1 \cdot 10^{-6}$ cm^2/s at 25ºC. It should be noted that this

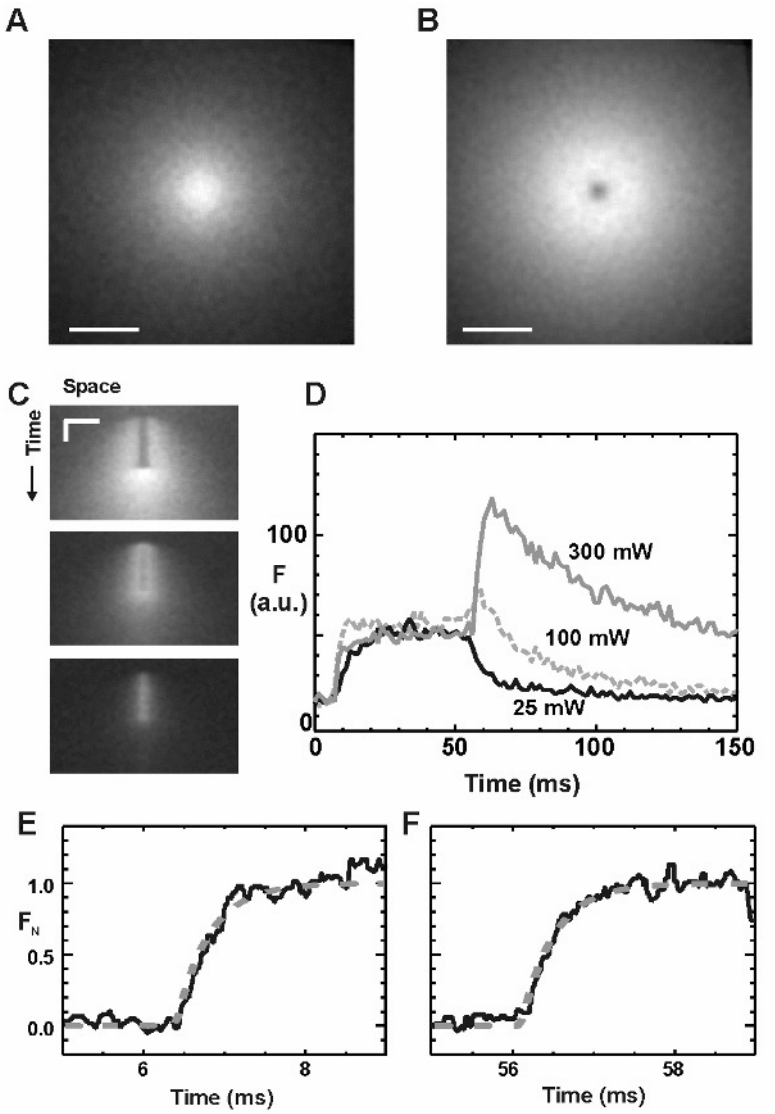

Fig. 2. TPEFP of caged fluorescein in test solution. **A**. X-Y scan of fluorescence in response to a flash lasting 500 ms at 50 mW. Scale bar 10 micron. **B.** A similar x-y scan recorded during uncaging with a beam power of 300 mW. Note the central dark spot due to fluorescein photobleaching by the uncaging beam. **C**. Three line scans show the spatiotemporal spread of fluorescein uncaged using beam powers of 300, 100 and 25 mW (top to bottom). Flash duration 50ms. Scale bars 5 micron and 20 ms. **D**. Time course of fluorescence at the center of the uncaging spot. Note the overshoot of fluorescence following termination of the uncaging flash at powers of 100 and 300 mW. Panels **E** and **F** show at higher time resolution normalized fluorescence during the onset of photolysis (**E**) and during the rising phase of the overshoot after flash termination (**F**). Both time courses had an exponentially rising curve with a time constant of 0.4 ms suggesting that it reflects the kinetics of the dark reaction of caged fluorescein. Similar time courses were obtained at beam powers between 50 and 500 mW.

determination has been obtained over a distance of <10 μm in <100 ms incorporating a volume of ~4 x 10^{-15}l (4 fl) and about ~20,000 caged molecules.

4.2. TPEFP of fluorescein in fiber cells

The eye lens consists of two cell types: an epithelial cell layer that covers the anterior surface of the lens and elongated fiber cells that make up the bulk of the lens (for review see [21]). These fiber cells have an approximately hexagonal cell profile when viewed in cross section that facilitates cellular packing and reduces light scattering. When viewed in a longitudinal plane the fiber cells form a parallel array of elongated cells. It is clear, from data shown earlier, that TPEFP can create a near 'point source' of fluorescein which should allow

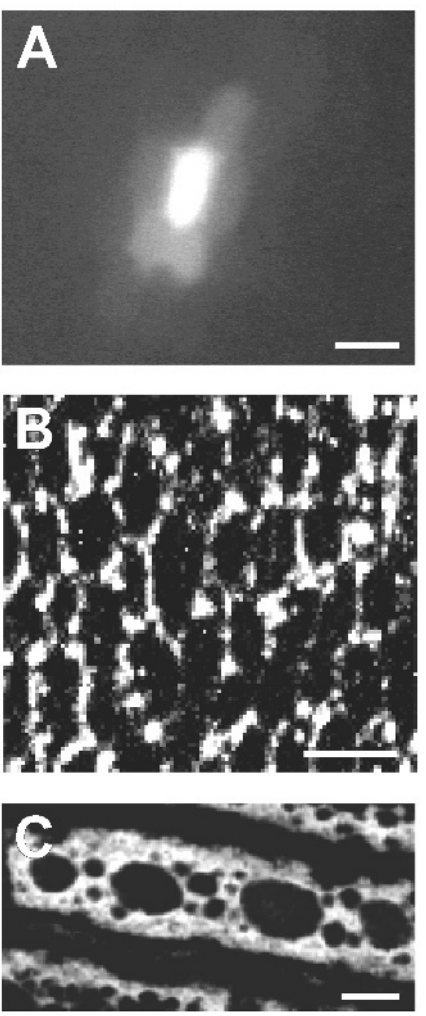

Fig. 3. TPEFP in fiber cells and gap junction protein distribution. Panel **A** shows an X-Y confocal image of fluorescein distribution when the uncaging beam is placed in the center of a selected fiber cell. Note the non-uniform dye distribution that develops. Although fluorescence in the central cell is bright, adjacent cells are more weakly labeled and the labeling is non-uniform. This image was taken 3s after the start of photolysis. Scale bar 0.005 mm. Panel **B** shows a lens cross section labeled to show the distribution of gap junction protein (Cx46) in another lens in a similar region to that used for the experiment shown in A. Scale bar 0.002 mm. Panel **C** shows a longitudinal section where the surface membrane has been labeled. The plaques of gap junction protein are now seen as holes in the cell surface labeling. Again, there is marked heterogeneity in gap junction distribution. Scale bar 0.002 mm.

determination of diffusion along and between fiber cells. Caged fluorescein (1mM) was added to the intracellular solution that was used to bathe bisected (equatorial section) rat lenses. After allowing time for diffusion of caged fluorescein into the cut fiber cells, TPEFP was used to liberate fluorescein inside a target cell by placing the stationary spot from the Ti:S laser ~40 μm from the cut surface. Figure 3A shows a typical TPEFP experiment on lens fiber cells. In these experiments, input power was kept to <50mW to avoid photobleaching the fluorescein which would complicate subsequent analysis. In the selected cell, fluorescence increased rapidly and then spread to adjacent cells via the gap junctions that allow intercellular communication [11,22]. The spread of fluorescence is no longer radially symmetric as seen in the case of free solution (c.f. Fig. 2), a result explained by the irregular cell surface membrane forming a barrier to diffusion between cells and which varies from cell to cell. We suggest that this variation should be explained by variations in the amount of gap junction protein linking the different cells. Support for the view that there are local variations in the amount of gap junction protein is shown in fig. 3B which shows antibody labeled connexin-46 (a gap junction protein) in a transverse lens section. The distribution of protein is non-uniform and the gap junction protein is organized in plaques (e.g. see [23]). In the axial direction, (Fig 3C) the gap junction plaques are also non-uniformly distributed with quite large variations in the local gap junction density. It is therefore apparent that there are marked non-uniformities in cell-cell coupling over small distances which may be explained by the local levels of gap junction protein expression.

4.3. Analysis of TPEFP induced fluorescein signals.

To evaluate fluorescence diffusion across and between fiber cells, line scanning was employed to increase time resolution to 2ms. Fig. 4A shows the fluorescence profile across the cell plotted at two time points. The decay of fluorescence with distance is expected from diffusion from the source. To analyze these data, a finite element model was constructed whose geometry mimicked the shape of the cell. Fig. 4B shows the time course of fluorescence change expected when no diffusion across cell boundaries occurred. The edge of the cell is sharply defined and the simulated region of photolysis can also be seen. These data appear quite different to the data shown in 4A as blurring by the microscope has not been considered. When the data is blurred by a Gaussian function with a half width comparable to that of the point spread function of the microscope (middle panel) the difference between the simulation and experimental data is reduced, but not eliminated. When the barrier to diffusion between cells was removed in the simulation (Fig. 4C) gradients of fluorescence within the cell became steeper and rapidly spread into adjacent cells. Again, this simulation poorly describes the experimental data. These two limiting cases

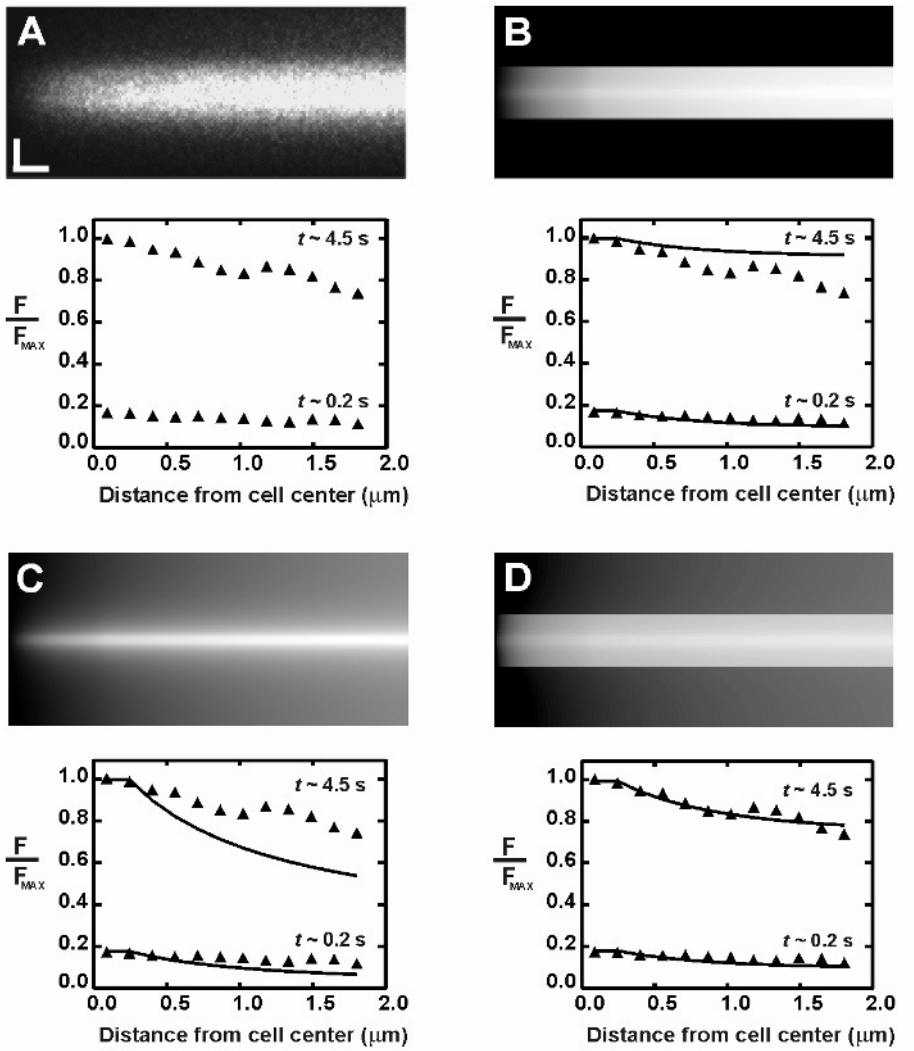

Fig. 4. Analysis of TPEFP in fiber cells by line scanning and modeling. Panel A shows a line scan image across a fiber cell any its neighbors with position in the vertical direction and time horizontal. When the TPE beam is switched on fluorescence rapidly increases and the spreads to adjacent cells. The graph below shows the distribution of fluorescence across the selected cell 0.2s and 4.5s after the start of photolysis. Scale bar 0.002mm and 1s. Panel B shows a simulation without cell-cell coupling. In this case, fluorescence is restricted to the cell containing the photolysis spot. The upper panel shows model output and the lower panel the same data with microscopic blurring included. Note that the fluorescence gradients are more shallow than actually observed except at the cell boundary. Panel C shows a simulation with no diffusion barriers between cells. In this case, the spread of fluorescence is greater than observed and steeper intracellular gradients develop. Panel D shows a best fit simulation to the experimental data. After blurring (lower panel), the extent of cell-cell diffusion is comparable to that observed as are the intracellular gradients of fluorescence. The effective barrier between cells was 0.4% of free diffusion. The intracellular diffusion coefficient was 4×10^{-7} cm^2/s

show that there must be a partial diffusion barrier between cells which restricts the movement of fluorescein above that seen in the cell cytoplasm. By allowing the computer model to alter the strength of cell-cell coupling as well as the intracellular diffusion coefficient, a reasonable fit to the data could be obtained (after blurring) rapidly. This is shown in Fig. 4D where the best fit to the data was obtained by stetting the intracellular diffusion coefficient to $4x10^{-7}$ cm^2/s with a cell to cell barrier that was equivalent to a free diffusion coefficient of 0.4% of that in the cytosol. The large reduction in fluorescein diffusion coefficient compared to that measured in free solution might be expected from the high fixed protein concentration inside the fiber cell which increases the lens refractive index and gives it a crystalline like quality. From Fick's first law of diffusion, the reduced diffusion between cells this implies that the free area through which the fluorescence diffuses must be no more than 0.4% of the total membrane area since tortuosity associated with passage through the 10nm cell membrane can be ignored on this spatial scale. From inspection, this area is considerably smaller than the area occupied by gap junction plaques (~20% in Fig. 4C), however this difference can be explained by the pore of the gap junction complex being smaller than the complex itself [22].

4.4. Height changes in PPy films with different dopants

When PPy was doped with $TBAPF_6$ (see Fig. 5), oxidation at +1V caused an expansion of the film while reduction at the adjacent electrode caused a shrinkage (see Fig. 5A). The differential change (from the original height) was of the order of 20%. In this case, positive charges (polarons and bipolarons) were created on the polymer backbone during oxidation to create the conductive form of the polymer. To balance the positive charges on the polymer, PF_6^- anions and accompanying solvent enter the PPy film and the polymer swells considerably as a result:

$$PPy + PF_6^- \rightarrow PPy^{+\cdot} PF_6^- + e^- \quad (1)$$

In contrast to that, through simple change of dopant/electrolyte to $TBACF_3SO_3$ / PC we obtained a situation in which the reduced form of the polymer was the more highly swollen (Fig. 5B). Section analysis by AFM showed that the magnitude of the differential height change was about the same.

We can explain the reduced state having a larger volume due to a cation insertion process (see below), due to $CF_3SO_3^-$ anions being immobilized deep within the polymer structure during electropolymerisation. As the polymer is reduced and positive charges removed from the polymer, TBA^+ cations and solvent need to move in to the film to balance the negative charge of the residual $CF_3SO_3^-$ ions:

$$PPy^{+\cdot} CF_3SO_3^- + TBA^+ + e^- \rightarrow PPy\ TBACF_3SO_3 \quad (2)$$

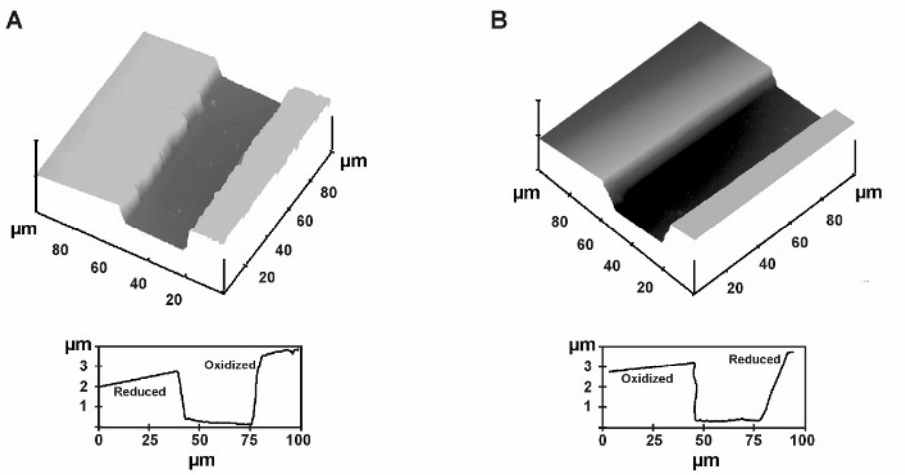

Fig. 5. Panel A shows an AFM topographic picture of reduced (-1V, to the left of the channel) and oxidized strips (+1 V, to the right and swollen) of PPy in $TBAPF_6$ / PC, showing the volume change with applied potential. The channel down the middle was formed by the lack of gold substrate so that no polymer was deposited there. Each pair of electrodes had opposite voltages applied. Panel B shows an AFM picture of oxidized (+1 V, to the left of the channel) and reduced strips (-1 V, to the right and swollen) of PPy in $TBACF_3SO_3$ / PC, showing the volume change with applied potential.

This results in the film swelling. On the other hand, in the presence of mobile anions, polymer reduction results in movement of the charge balancing anions moving out of the film drawing solvent with them thus reducing film thickness (e.g. [24,31]).

In-plane [25] and out-of-plane [18] actuation at cathodic potential has previously been observed for PPy films in aqueous solution containing dodecyl benzene sulfonate (for review see [18]). However, our AFM measurements do not show the marked distortion of the edge of the film noted by Smela and Gadegaard [18] so that the change in height appears nearly isotropic. It should also be noted that the change in film height is much larger than the approximate 2-5 % change in in-plane stress typically seen in PC actuators.

5. DISCUSSION

5.1. Utility of TPEFP to measure microscopic diffusion

In this article, we have described how TPEFP can be used to probe microscopic diffusion in very small (fl) volumes at high (ms) time resolution. This technique has some advantages over the more common fluorescence recovery after photo-bleaching (FRAP) method: (1) The probe concentration is

changed by a different wavelength of light than that used to monitor probe concentration. This means we can alter the probe concentration while *simultaneously* measuring its concentration. The difference in wavelength also reduces interference between measurement and the generation of probe concentration gradients. (2) The source is spatially restricted in 3D (and time) so that photo-release can be restricted to selected micro-volumes. This simplifies the selection of the volume of interest as well as producing a defined geometry for subsequent quantitative analysis. (3) By generating the fluorescent probe (by photolysis) we produce signal on a dark background so that small probe concentration differences can be measured. (4) The region involved in producing the change in probe concentration is small; reducing the risk of widespread system damage.

Despite these advantages, the focal volume is small (as determined by the diffraction limited resolution of the objective lens) so that the liberated quantities of fluorescein (or other caged molecules) are small. In the case of a typical probe molecule concentration of ~1 mM, about 30,000 molecules are within the focal volume of the objective lens used here. However, not all these molecules can be photolysed at once since we have not been able to achieve a power level that causes the effective ground state depletion. If the beam power is increased to help offset the small excited volume and excitation rate, photo-bleaching can occur which complicates the time course of fluorescence liberation. It is our impression that we can achieve no more than ~10% of the maximum possible excitation rate before TPE damage becomes a potentially serious problem. TPE induced damage has also been noted in other cell systems [3]. In our experience, this starts to occur at an input power of ~5 mW at the sample (corresponding to ~15 mW input). Nevertheless, we showed that it is possible to release sufficient quantities of fluorescein for determination of diffusion constants at powers that do not lead to this complication. By using confocal line scanning coupled with computer modeling we can evaluate both intracellular and cell-cell diffusion of fluorescein which should permit detailed analysis of gap junction regulation in identified cells with high time resolution. This method also carries the advanatge that noisy signals are less of a problem as entire data sets can be model fit simultaneously. Our data also shows marked heterogeneity in diffusion between different adjacent cells (cf. Fig. 3A). The high spatial resolution of TPEFP allows such non-uniformity to be detected and studied and these differences might not be anticipated for a reasonably homogeneous tissue such as the lens. In this case, the highly restricted nature of TPEFP enabled fine control over the region probed -a property that cannot be reproduced by any other optical method which does not produce three dimensionally resolved excitation. A common alternative approach to probe intercellular permeability and diffusion is to use fluorescence recovery after photobleaching (FRAP). After selectively bleaching the fluorochrome in a small

region of tissue, the observed rate of fluorescence recovery should be a function of the intercellular coupling to cells that were not exposed to the bleaching illumination (which serve as a reservoir of dye). In principle, it should be possible to use two-photon excitation to selectively bleach the dye within a target cell also and achieve similar local resolution as shown here the uncaging approach. However, as noted earlier, the reduced contrast associated with FRAP methods decreases signal-to-noise ratio. For example, in experiments using conventional one-photon illumination the directed transport of tubulin was detected using caged fluorochromes [26] but could not be resolved in FRAP experiments [27]. It also is possible that the light dose needed to produce significant photobleaching for FRAP may be more damaging to the cell than a pulse designed to break a labile cage molecule.

TPEFP can also be used to study the kinetics of chemical reactions. We were able to measure the dark reaction of a CMNB cage as 2500 s^{-1} by recording the rate of rise of fluorescence at the start of the TPEFP pulse. This dark reaction represents a first order chemical reaction from the induction of the excited state to the appearance of the broken cage components. This reaction also leads to a complicated release time course when significant photobleaching of the released fluorescein is present. For analysis of diffusion, one can examine the dissipation of the profile immediately after the pulse or keep to powers below that needed to cause significant photobleaching. This observation directly supports the idea that the light dose needed to produce significal photobleaching for FRAP may be more damaging than that associated with a pulse designed to break a labile cage molecule.

The methods described here can be readily extended to other types of molecular sieves where local diffusive properties need to be measured. In addition, it is possible to synthesize molecules with different sizes and shapes to probe the local microenvironment.

5.2. Conducting polymer volume changes by AFM

Using AFM we have carried out initial characterization of height changes of PPy films doped by various compounds. AFM has also been used by Suarez and Compton [28] and Smela and colleagues [18] who found comparable percentage changes to those shown here. However, the results presented here clearly demonstrate that the volume change is highly dependent on the nature of the dopant, and by switching from $TBAPF_6$ to $TBACF_3SO_3$ we were able to reverse the volume change associated with oxidation/reduction. The films examined by Smela and colleagues [18] exhibited fairly strong edge effects where the height change at the edge of the film was much less that that in the center of the film. This led to the appearance of a “rim” at the edge of the film which was most obvious when oxidized but also present when reduced. This sub structure within the film was not observed in the experiments reported here and the cause of the

difference is unclear. It is possible that it may be related to the use of a surfactant in the polymerization solution, different film growth rates and difference in the experimental set up.

The out-of-plane strain is much larger than the in-plane change of typically only a few percent [25,29,30]. This may be related to the adhesion of the film to the gold (or other) substrate(s) which would limit in-plane movement, or more likely, to the anisotropic structure of the polymer formed during the electrodeposition. The out-of-plane height change associated with oxidation/reduction is of the order of 25% which would be sufficient to allow various forms of micro-actuation and since the actuation is known to be associated with high stress levels, one can envision the construction of various valve gates and fluid displacement systems based on this action. The high stress (on the order of 40 MPa) which can be developed by the PPy actuator would greatly aid the action of such devices.

Further experiments are needed to identify new dopants and chemical systems that increase the stress/strain behavior of such thin CP films. For longevity, the solvent system and CP film should be electrochemically stable in the voltage range of the interest. In addition, repeated cycling and the resulting in-plane strain will tend to cause de-adhesion of the film and it would be desirable to develop cross linked substrate-CP systems to increase mechanical strength. Whether this is best achieved by using a microstructured substrate, electrically conductive bonding intermediates or covalent substrate attachment has yet to be explored. Nevertheless, the useful size of the out-of-plane changes we have observed offer great promise for the future of such actuators and although the actuators are generally slow, their large forces may be translated to higher speeds by mechanical means.

ACKNOWLEGEMENTS

Funding for this work was provided by the Health Research council (NZ), the Marsden fund (NZ) the Lottery Board, the New Zealand Foundation for Research and Technology (New Economy Research Fund, contract No. UOAX0408). The authors also wish to thank Dr. Thierry Livache (CEA-Grenoble, France) for providing the patterned chips used for AFM measurements.

REFERENCES

[1] Denk W, Strickler JH, Webb WW. Two-photon laser scanning fluorescence microscopy. *Science*. 1990; 248: 73-76. 2.

[2] Patterson GH, Piston DW. Photobleaching in two-photon excitation microscopy. *Biophysical Journal* 2000; 78: 2159- 2162.

[3] Hopt A, Neher E. Highly nonlinear photodamage in two-photon fluorescence microscopy. *Biophysical Journal* 2001; 80: 2029-3206.

[4] Cannell, M.B. & Soeller, C. (1997) High resolution imaging using confocal and 2-photon molecular excitation microscopy. *Proceedings of the Royal Microscopical Society* 1997; 32(1):3-8.
[5] Jones, K.T., Soeller, C. & Cannell, M.B. The passage of Ca2+ and fluorescent markers between the sperm and egg after fusion in the mouse. *Development* 1998; 125: 4627-4635.
[6] DelPrincipe F, Egger M, Niggli E. Calcium signalling in cardiac muscle: refractoriness revealed by coherent activation. *NatureCell Biology* 1999; 1: 323-329.
[7] Brown EB, Shear JB, Adams SR, Tsien RY, Webb WW. Photolysis of caged calcium in femtoliter volumes using two-photon excitation. *Biophysical Journal* 1999; 76: 489-499
[8] Soeller C, Cannell MB. Estimation of the sarcoplasmic reticulum Ca^{2+} release flux underlying Ca^{2+} sparks. *Biophysical Journal* 2002; 82: 2396-2414.
[9] Brown EB, Wu ES, Zipfel W, Webb WW. Measurement of molecular diffusion in solution by multiphoton fluorescence photobleaching recovery. *Biophysical Journal* 1999; 77: 2837-2849.
[10] Rubart M. Two-Photon Microscopy of Cells and Tissue. *Circulation Research* 2004; 95:1154-1166.
[11] Sohl G, Willecke K. Gap junctions and the connexin protein family. *Cardiovascular Research* 2004 ;62(2):228- 232.
[12] R. H. Baughman, *Science (Washington, DC, United States)* 2005, *308*, 63.
[13] Spinks, G., Xi, B., Campbell, T., Whitten, P., Mottaghitalab, V., Bahrami Samani, M., Wallace, GG. *Proceedings of SPIE-The International Society for Optical Engineering* 2005, *5759*, 314.
[14] Hara, S., Zama, T., Tanaka, N., Takashima, W., Kaneto, K. *Chemistry Letters* 2005, *34*, 784.
[15] Zama, T., Hara, S., Takashima, W., Kaneto, K. *Bulletin of the Chemical Society of Japan* 2005, *78*, 506.
[16] Maw, S., Smela, E., Yoshida, K., Stein, RB. *Synthetic Metals* 2005, *155*, 18.
[17] Smela, E. Conjugated polymer actuators for biomedical applications. *Adv. Mat.* 2003; 15: 480-194.
[18] Smela, E & Gadegaard, N. Volume Change in Polypyrrole Studied by Atomic Force Microscopy. *J. Phys. Chem. B* 2001; 105: 9395-9405
[19] Soeller, C. & Cannell, MB. Two-photon microscopy: Imaging in scattering samples and three-dimensionally resolved flash photolysis. *Microscopic Research Techniques* 1999 47:182-195.
[20] Cannell, MB., Cheng, H. & Lederer, WJ. Spatial non-uniformities in $[Ca^{2+}]_i$ during excitation-contraction coupling in cardiac myocytes. *Biophysical Journal* 1994; 67: 1942-1956.
[21] Kuszak JR.The ultrastructure of epithelial and fiber cells in the crystalline lens. *International Review of Cytolology* 1995;163:305-350.
[22] Cannell, MB, Jacobs, M., Donaldson, P. & Soeller, C. Probing microscopic diffusion by 2-photon flash photolysis: Measurement of isotropic and aniostropic diffusion in lens fiber cells. *Microscopic Research Techniques* 2004; 63(1):50- 57.
[23] Jacobs MD, Soeller C, Sisley AM, Cannell MB, Donaldson PJ. Gap junction processing and redistribution revealed by quantitative optical measurements of connexin46 epitopes in the lens. *Investigative Ophthalmology and Visual Science* 2004; 45(1):191-199.
[24] Naoi, K., Lien, M., Smyrl, W. H. Quartz Crystal Microbalance Study: Ionic Motion across Conducting Polymers. *J. Electrochem. Soc.* 1991, *138*, 440.

[25] Pei, Q., Inganas, O. Electrochemical Applications of the Bending Beam Method. 2. Electroshrinking and Slow Relaxation in Polypyrrole. *J.Phys. Chem.* 1993, *97*, 6034.
[26] Okabe S, Hirokawa N. Differential behavior of photoactivated microtubules in growing axons of mouse and frog neurons. *Journal of Cell Biology* 1992;117(1):105-120.
[27] Lim S.S, Edson KJ, Letourneau PC, Borisy GG. A test of microtubule translocation during neurite elongation. Jou*rnal of Cell Biology* 1990;111(1):123-130.
[28] Suarez, MF.; Compton, RG. In Situ Atomic Force Microscopy Study of Polypyrrole Synthesis and the Volume Changes Induced by Oxidation and Reduction of the Polymer. *J. Electroanal. Chem.* 1999, *462*,
[29] Pei, Q.; Inganas, O. Electrochemical Applications of the Bending Beam Method; A Novel Way to Study Ion Transport in Electroactive Polymers. *Sol. State Ion.* 1993, *60*, 161.
[30] Pei, Q., Inganas, O., Lundstrom, I. Bending Bilayer Strips Built from Polyaniline for Artificial Electrochemical Muscles. *Smart Mater. Struct.* 1993, *2*, 1.
[31] Bay, L., Jacobsen, T., Skaarup, S., West, K. Mechanism of Actuation in Conducting Polymers: Osmotic Expansion. *J. Phys. Chem. B* 2001, *105*, 8492.

PART III: NANO BIO PROCESSING

This page intentionally left blank

Handai Nanophotonics, Volume 3
H. Masuhara, S. Kawata and F. Tokunaga (Editors)

Chapter 15

Femtosecond nonlinear processing in solution: From crystallization to manipulation and patterning

H. Masuhara[a,c,f], Y. Hosokawa[a,f], H. Y. Yoshikawa[a,b,f], K. Nakamura[a,c], Y. Sora[a], Y. Mori[b,f], Y. Q. Jiang[a], I. Oh[a], T. Kaji[a], H. Mori[d,f], Y. Hiraki[e,f], A. Yamaguchi[a] and T. Asahi[a]

[a]Department of Applied Physics and Venture Business Laboratory, Osaka University, 2-1 Yamada-oka, Suita, Osaka, 565-0871, Japan

[b]Department of Electrical Engineering and Venture Business Laboratory, Osaka University, 2-1 Yamada-oka, Suita, Osaka, 565-0871, Japan

[c]Graduate School of Frontier Biosciences, Osaka University, 1-3 Yamada-oka, Suita, Osaka, 565-0871, Japan

[d]Department of Applied Biology and Insect Biomedical Research Center, Kyoto Institute of Technology, Matsugasaki, Sakyo-ku, Kyoto, 606-8585, Japan

[e]Department of Cell Differentiation, Institute for Frontier Medical Sciences, Kyoto University, 53 Kawamachi Shogoin, Sakyo-ku, Kyoto, 606-8507, Japan

[f]CREST-JST

1. INTRODUCTION

Laser has high performance in developing superior methodologies for the studies on molecular and bio systems. Particularly time- and space- resolved spectroscopy and imaging based on pulsed lasers and microscopes enable us to analyze primary dynamic processes in photo-induced phenomena and its spatial distribution [1]. When laser intensity is high, photophysical and photochemical processes become nonlinear with respect to the laser intensity and its electronic processes evolve to morphological changes. Namely, melting, fragmentation, explosive vaporization, and so on are induced by efficient photothermal conversion and photochemical decomposition, which is well recognized as laser

ablation [2]. The laser beam can be focused, patterned, and/or scanned freely, so that spatial control of laser ablation phenomenon will be a useful perturbation for material processing.

Laser ablation which is defined as explosive vaporization and material ejection having certain threshold values in laser fluence. The phenomena are never observed even when irradiated for very long time with weak intensity below the threshold. By developing and applying time-resolved spectroscopy and imaging we have elucidated evolution dynamics from electronic excitation to surface morphology change [3, 4]. Now it is possible to explain ablation dynamics of molecular materials in the framework of Jablonski diagram of molecular electronic structure. For nanosecond and femtosecnd laser ablation photothermal ablation mechanism based on cyclic multiphotonic absorption and photomechanical mechanism [3, 4] were proposed by us, respectively. Understanding the mechanisms has led us to find new ways to fabricate materials and to develop new tools for molecular and bio sciences. As the former example organic nano particle preparation by ablation in solution is well known [5-9], while crystallization and manipulation in solution are newly developed and being demonstrated successful to open new research fields.

Through these systematic studies on laser ablation dynamics and mechanism, we have understood that high potential of our methodology is in application to bio systems and have come to new ideas. Large cells are often too heavy to manipulate in solution by laser trapping, furthermore the cells adhered on the surface cannot be removed by pushing or pulling by the photon force of laser trapping. However, we consider that laser ablation generates a force stronger than that of laser trapping. Intense focused femtosecond laser induces multiphoton absorption at the focal point, and results in local ablation. This means that manipulating the focused femtosecond laser pulse three-dimensionally in transparent solution enables us to input energy at an arbitrary small spot. As a result, mechanical force, high temperature, high pressure, high density, concentration fluctuation, and so on can be generated locally and transiently. These are very useful perturbation for the solution system, on which we have explored new phenomena of biological molecular systems and bio cells, and proposed very original dynamics. In the present review recent results on protein molecules, protein cubes, and living bio cells are presented, explained, and considered.

2. CRYSTAL GROWTH TRIGGERED BY FEMTOSECOND LASER ABLATION

Most of femtosecond laser ablation studies have been done in air and in vacuum, and fragmented materials are ejected and dispersed. The morphology of etched surface is usually rough, at least in a few tens nm level, while ejected materials

had not been made clear. In laser ablation transfer experiment, a source molecular film is covered with a transparent polymer film and a femtosecond laser pulse was focused to the molecular film through the polymer film. Laser ablation with single shot femtosecond laser left a small hole on the source film, while ejected small materials are now received by the target polymer film [10], and their size and its distribution can be evaluated by AFM observation. In case of laser ablation in solution, ejected materials are dispersed in the medium, sometimes, as nano colloids [5-9]. The latter is deposited on a substrate and characterized after drying; their size is directly confirmed by SEM and AFM observation. On the basis of these results it is summarized that the laser ablation leaves some surface roughness on the etched area and ejects nano particles.

When such femtosecond laser ablation is conducted for a single urea crystal in its saturated aqueous solution, the etched surface and ejected nano particles may work as a nucleus and trigger crystallization [11, 12]. This idea is schematically shown in Fig. 1. A single crystal of urea was prepared, while the solution is still saturated. A single shot femtosecond laser pulse was introduced from the bottom of an inverted microscope and induced laser ablation of the single crystal. The result obtained by femtosecond 1470 nm pulse irradiation is given in Fig. 2. Initially some time lag was found after the irradiation and the convection flow perpendicular to the focused surface was generated. Then the crystal was found by eye and it grew up to millimeter dimension with a rate of 100 μm/s. It is surprising that a single shot irradiation results in crystal generation and growth, and this new phenomenon is observed for a single femtosecond excitation at 800 and 1470 nm. A distinct single crystal grew when the power was above a certain threshold, which means laser ablation is a key primary process of the crystal growth. When the power was increased, plural crystals grew with some angle distribution from the perpendicular direction.

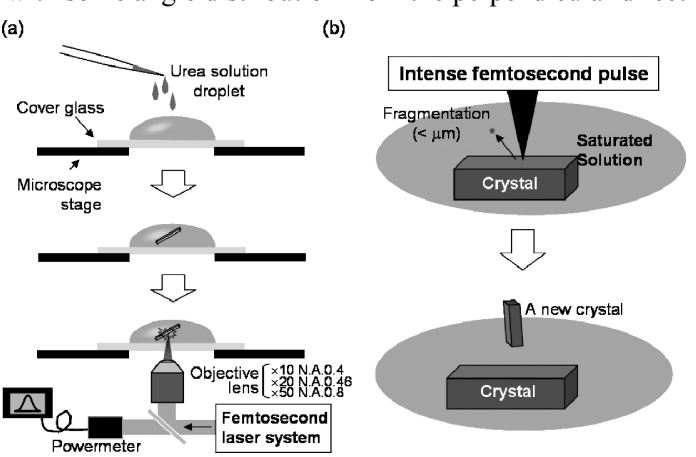

Fig. 1. Schematic illustration for (a) sample preparation of crystal growth triggered by femtosecond laser ablation and (b) a possible explanation of the crystal growth.

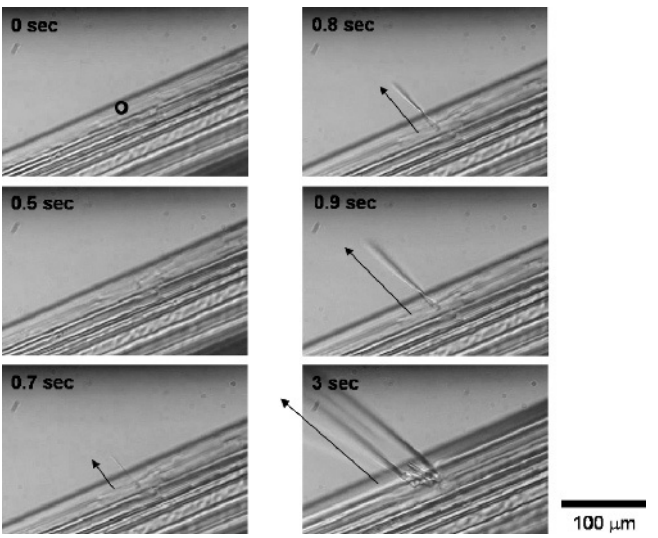

Fig. 2. Subsequent crystal growth of urea from the laser irradiation area marked with an open circle by a single shot of 1470 nm pulse at 3.8 μJ/pulse through ×20 objective lens.

The ablation should be triggered by multiphoton absorption of 1470 nm laser pulse, as urea and water have no electronic absorption at these wavelengths. Furthermore no such behaviour of crystal growth was realized when the CW laser at 1470 nm was irradiated. Instead the irradiated area of the crystal was melt, its rate along the depth is about 10 μm/s. Surprisingly, the dug area recovered by crystallization form the surroundings after switching off the CW laser.

3. FEMTOSECOND LASER-INDUCED CRYSTALLIZATION OF PROTEINS AND MOLECULES

Multiphoton excitation of neat liquids and solution had received much attention in early 1980's [13-15], and formation and relaxation dynamics of solvated electron were studied by using picosecond electronic absorption spectroscopy. Even in nonpolar cyclohexane ionization and following recombination were involved in primary processes and their similarity to radiation chemical processes was considered. Further increase in excitation intensity does not constitute topics for physical chemistry, while it is reported frequently that plasma state, shockwave, and bubbling are generated. Recently we found that the intense femtosecond laser excitation of protein solution results in its efficient crystallization. The examples that our group has prepared are lysozyme, glucose isomerase, Ribonuclease H, trypanosome brussei, and so on [16]. Even crystal quality is better than that of the crystals prepared by conventional methods.

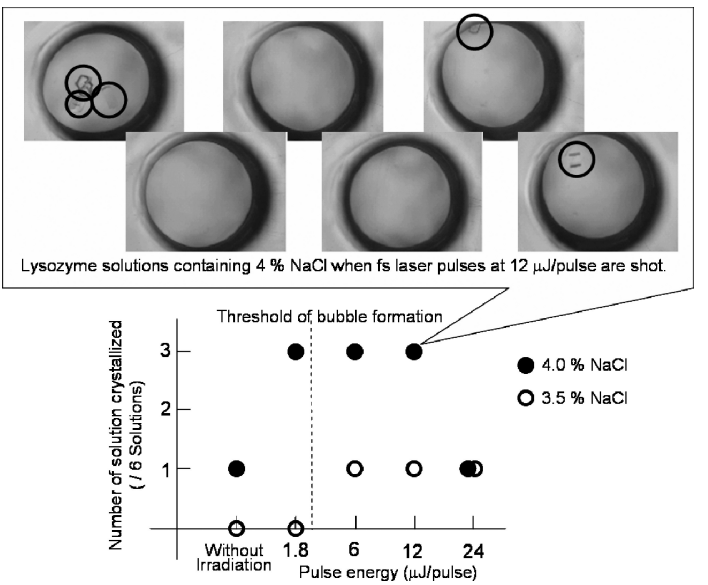

Fig. 3. Pulse energy dependence of femtosecond laser-induced crystallization in lysozyme solution, indicating the number of solutions that crystallized at a given pulse energy as shown in the inset.

The irradiation of aqueous solution of egg-white lysozyme [16] and 4-(dimethylamino)-N-methyl-4-stilbazolium tosylate (DAST) [17] with 800 nm femtosecond laser pulse led to its more efficient and better crystallization compared to the conventional methods. One typical example is shown in Fig. 3 where femtosecond irradiation gives clearly larger and nicer crystals compared to a non-irradiated sample. As the mechanism of laser-induced crystallization the following two had been proposed before our works. Garetz et al. reported nanosecond Nd^{3+}:YAG induced crystallization of urea and explained the mechanism in view of electric field of laser light [18-20]. As urea has no absorption and the nanosecond laser intensity is not so high to induce multiphoton absorption, they considered that the molecular orientation due to electric field assists the association of urea molecules leading to nucleation. On the other hand Okutsu et al. demonstrated photochemical crystallization for anthracene and benzophenone whose photochemical products are less insoluble compared to mother molecules [21, 22]. This photochemical mechanism is extended to proteins where tryptophan residue forms its dimer upon excitation, and the dimmer triggers the nucleation of lysozyme. In our femtosecond case both mechanism seems not applicable, as the 100 femtosecond pulse width is too short to orient molecules efficiently and photochemical mechanism is excluded by the following experiment.

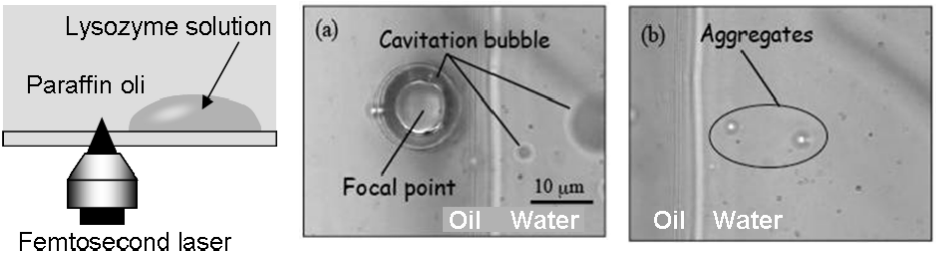

Fig. 4. Femtoseocnd laser induced crystallization of lysozyme when the laser was shot in paraffin oil surrounding the lysozyme aqueous solution.

In Fig. 4, a single droplet of lysozyme aqueous solution was covered by paraffin oil and both phases were excited by femtosecond pulse respectively. In this case we set the condition to see aggregate precipitants of visible size immediately after the irradiation, as the crystallization needs at least few hrs or sometimes a few days. When the aqueous solution was irradiated, some bubbles appeared and then some precipitants were observed. The femtosecnd pulse was introduced into the oil phase and some bubbles were observed not only in the oil but also in the aqueous phase. As the intensity is enough high, bubbles were observed in both phases and in a few sec the precipitants came to the image. This experiment clearly indicates multiphoton excitation of the aqueous solution is not necessary for crystallization and photochemical products are never involved in aggregation. It was confirmed phenomenologically that the crystallization is mostly accompanied with laser-induced bubbling.

To show the relation between the crystallization and the bubbling more directly, we prepared viscous lysozyme solution by adding PEG (polyethylene glycol) to increase viscosity and irradiated the solution. Since the solution is viscous, the formed bubbles remained relatively long, during which the crystallization proceeds. One representative picture is shown in Fig. 5, where the femtosecond pulse was scanned in the viscous solution [23]. The bubbles, which looked black shadows, and crystals are associated with the bubbles, and less crystals were found far from the bubbles. Thus we consider that femtosecond laser-induced bubbling is critical to protein crystallization. In the textbook the crystallization is usually explained in the framework of phase diagram such as shown in Fig. 6. It is considered that crystallization is brought about by elevating temperature, by increasing concentration of solute, and then by cooling it. In the present femtosecond case, the solution is over-saturated, which means the system is in the metastable zone. The femtosecond bubbling may increase local concentration transiently and nucleation is induced near the bubbling surface. Of course this explanation is very primitive and needs systematic study, which is being conducted in our group.

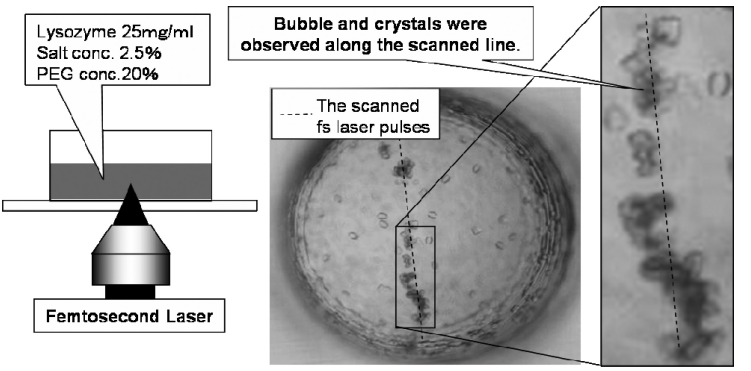

Fig. 5. Femtoseocnd laser induced crystallization of lysozyme in gel medium. The laser was scanned on dashed line in the microphotograph, which is at 1 day after the laser irradiation.

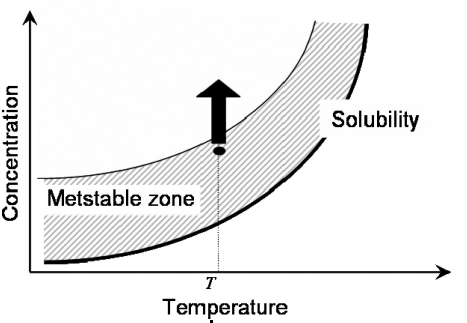

Fig. 6. A possible scheme explaining the femtosecond laser-induced crystallization based on the phase diagram.

4. MANIPULATION OF SINGLE BEADS BY FEMTOSECOND LASER-INDUCED BUBBLING

The femtosecond laser-induced bubbling and accompanying convection have high potential as providing local and transient force, leading to various applications. This force can push and pull micro targets such as polymer beads and living cells in solution, which is schematically drawn in Fig. 7. Initially the cavitation bubbles formed by femtosecond multiphoton excitation push away a single bead, but upon its collapse the bead is pulled back to certain amount. Simultaneously convection flow from all directions to the focal point is induced, which is again push the bead away. The behaviour depends upon the geometries where the bead and the focal point are, whether they are close to each other or not, and how far a focal point is from a substrate. These are summarized in Fig. 7, where a stream in water is illustrated to come from the sides to the upper. This stream is very useful for manipulating a single particle around 100 nm size.

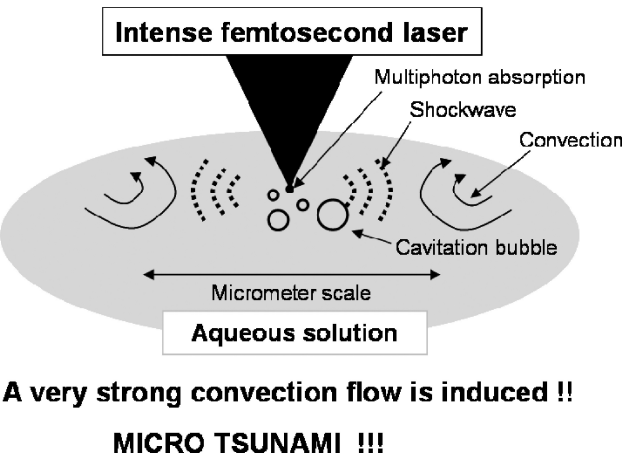

Fig. 7. Nonlinear phenomena in aqueous solution induced by intense focused femtosecond laser irradiation.

Many years ago we reported an original work on laser manipulation of μm-sized metal particles by a focused CW laser beam [24]. This beam is typical of conventional laser trapping and exerts repulsive force upon optically reflective metal particles. As we are the first group to combine laser trapping and beam scanning technique using Galvano mirror, we came to the proposal that a single metal particle should be surrounded by a circle locus formed by a scanning laser beam. As the force generates repulsive force, the metal particle was confined by the repulsive potential. The particle does not receive any attraction force but cannot escape from the inside of the locus.

This idea is now applied to the femtosecond bubbling phenomenon. The femtosecond laser pulse was scanned as a circular and a single polymer bead on a substrate was pushed from all the directions. Here 10 shots per circular per sec were introduced, so that the bead receives the force almost equivalently from 10 positions. The force is transient as it is caused by each laser irradiation, but the water flow due to bubbling does not respond so quickly. Thus the bead was surrounded by the water pressure from all the directions. When the microscope stage on which the substrate was set was driven, the bead was shifted from position to position arbitrarily. The femtosecond pulse is focused not on the bead but in the water, so that even multiphoton excitation of the bead is not involved and damage is never induced. The amplitude of the force is extremely large to be in the μN order as described below. Of course we know advantages of the conventional laser trapping, but the present manipulation method is very original and complementary to well known laser trapping method.

5. PATTERNING OF PROTEIN CUBES AND BIO CELLS IN SOLUTION BY FEMTOSECOND LASER-INDUCED SHOCKWAVE AND BUBBLING

When femtosecond laser was focused and irradiated in water, shockwave and cavitation bubble are created, causing water convection. The water flow pushes μm-sized objects in solution without any damages, namely, femtosecond laser ablation generates mechanical force which can be applied for patterning various μm-sized materials. In our group we chose protein cubes and bio cells, and demonstrated our new patterning method [25, 26]. The protein cube is a proteinous occlusion body called polyhedron which insect virus produces at the late stage of the infection [27]. The insect viruses within the polyhedra are protected from hostile environmental conditions such as high temperature and dryness. The polyhedron is composed of crystalline matrix of proteins, and the insect viruses are well protected from outside. The shape and size of polyhera are cubic and a few μm, respectively, which means that the conventional laser trapping method is useful. Actually we have prepared various patterns composed of polyhedra and indicated high potential of trapping technique [25]. One disadvantage of this trapping method is its relatively slow process. Each cube should be independently caught, transferred, and fixed on a substrate. Alternatively we present new idea based on femtosecond laser-induced shockwave and cavitation bubble to form protein cube patterns more efficiently [28]. An ensemble of protein cubes can be transferred and distributed arbitrarily. It is worth noting that functional proteins such as green fluorescent protein, antibody, cell growth factors, and so on can be occluded into polyheda by gene technology and that they are stable against high temperature and dryness. Therefore patterning of protein cubes are expected useful to constitute protein chips and bio sensors with high performance.

The experimental set up and our approach is schematically illustrated in Fig. 8. Protein cubes were distributed on a glass substrate and it was set as a source substrate on water layer. Femtosecond laser was introduced into the solution, but its focal point is at a few μm below the substrate. Shockwave, bubble, and water flow propagate up to the substrate like “Micro Tsunami” and remove the attached protein cubes from the substrate. Then the cubes fall down to the bottom target substrate. Repeating this procedures for protein cubes with different functional proteins, we can form various protein cube tips with different functional distribution. We are clarifying dynamics and mechanisms of this femtosecond laser-induced phenomena and examine conditions and parameters for fabricating the pattering.

A representative result on protein cubes is shown in Fig. 9. The resolution is practically in the order of 10 μm, while any kind of patterns can be fabricated well. A typical example for protein cubes is “JST” which is one of our funds. On

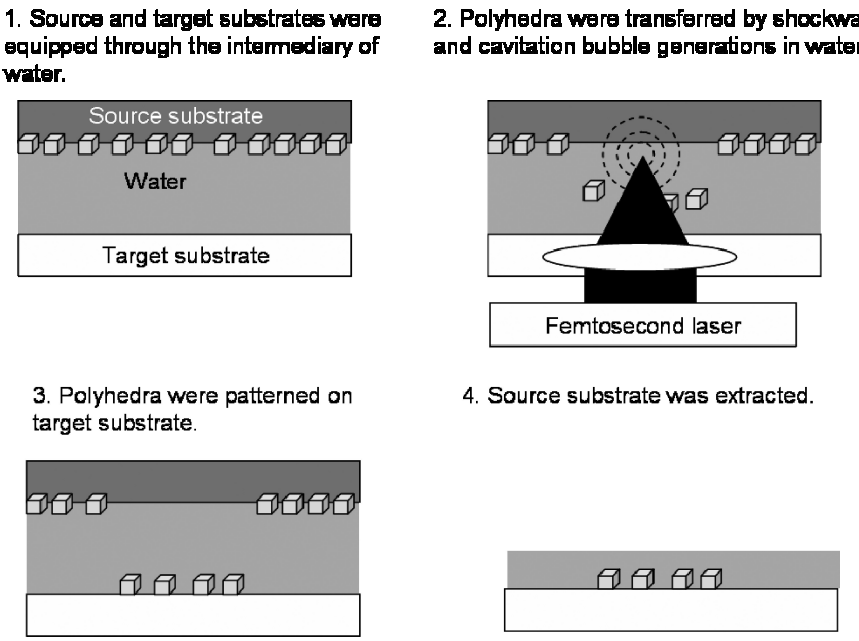

Fig. 8. Schematic illustration of micro-patterning of protein cubes by focused femtosecond laser irradiation in the water medium.

the protein cube patterns, we have already succeeded in cultivating bio cells indicating protein cubes are biologically active. The same method was applied to living bio cells. Mouse NIH3T3 cells are set on the source substrate on the upper side, and the femtosecond pulse was used to cause shockwave and bubble generation, and consequently the cells were removed and transferred to the target substrate. In Fig. 10 bio cells images of the substrates before and after laser scanning are shown. Before scanning and irradiation cells are only on the source substrate, which looked flat shapes, while after the scanning and irradiation cells around the scanning locus were removed and transferred to the target film. The picture focus is on the target substrate and the cells forming a line looked same flat shape. On the other hand cells left on the target substrate which distributed except the line looked small spheres, which is ascribed the fact that the focus is on the target and not on the source substrate. It was confirmed that most of the transferred cells were not damaged, thus it is clear that the bio cells are successfully transferred and patterned well.

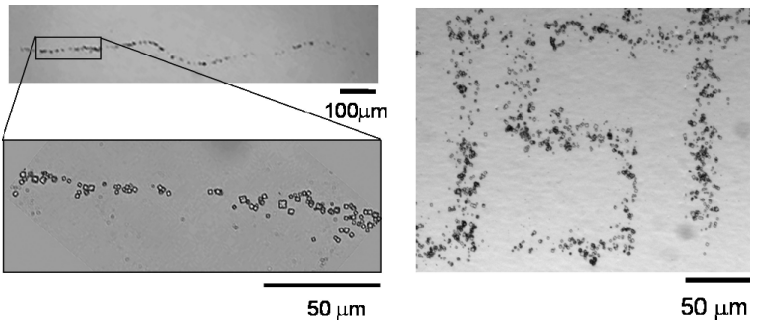

Fig. 9. Representative example of micro-patterning of protein cubes.

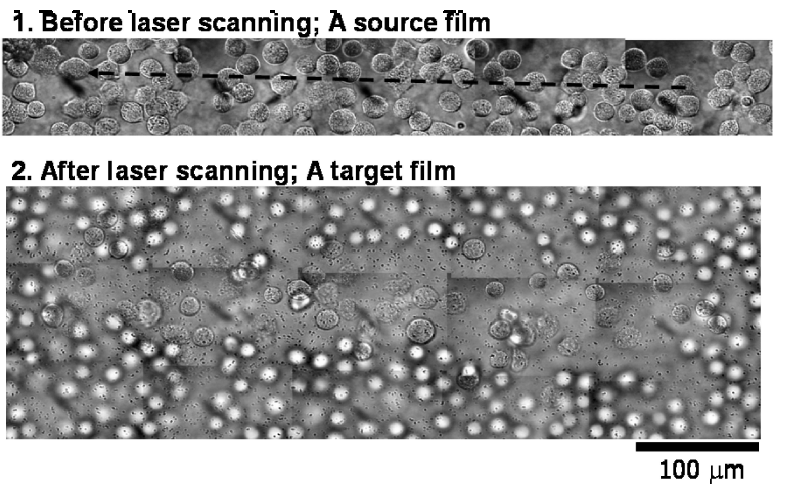

Fig. 10. Representative example of micro-patterning of living animal cell.

6. FEMTOSECOND LASER-INDUCED INJECTION OF NANO PARTICLES INTO SINGLE BIO CELLS

The femtosecond laser-induced shockwave and bubble formation generate transient mechanical force, which is now applied to inject nanoparticles in single bio sells. The idea is illustrated in Fig. 11, where the laser pulse was again focused into the water not to hit to a mouse fibroblast NIH3T3 cell itself. The size of the focal point was 1 μm and the distance between the focal point and the edge of the cell was 20 μm. When the laser was hit, the cell shrunk a little, so that its membrane structure should be changed at least transiently. The force exerted on the cell was estimated to be a few tens pN/μm^2, under which power the cell was not detached. Polystyrene nanoparticle was dispersed in the culture medium and some particles were put on the cell. In 24 hrs the cells underwent

endocytosis of many nanoparticles but negligible amount was transferred to the cell in 1 hr. At this time the femtosecond laser was introduced to a location a little far from the end of the cell, and after that the cell was monitored by a confocal microscope. The results are summarized in Fig. 12. The focal point was located in the top-left side of the cell (Fig. 12 (a)) and the cell was not detached by the femtosecond irradiation. The three dimensional observation of the cell after the irradiation is given in Fig. 12 (b), where right and the bottom pictures represent cross sections of the YZ and XZ planes, respectively. The bright spots observed at the right-upper and left-lower sides can be ascribed to the fluorescent polymer nanoparticles which were injected by the laser. The height of the cell is larger than 6 μm and the bright spots are located close to the bottom but not on the bottom. Some spots give a long shape suggesting the aggregation of the nanoparticles. The particle on the white lines (cursors) seems single, and its cross view along the z-axis is compared with those of the membrane stained with fluorescent dyes in Fig. 12 (c). Fluorescence intensity distribution of the stained dye has two peaks in the vertical profile, corresponding to the bottom and top surface membranes of the cell. On the other hand the fluorescence from the nanoparticle is located just between them, clearly indicating that the particle is injected into the cell. The shockwave and bubbling are very useful also for injecting large nanoparticles in single bio cells.

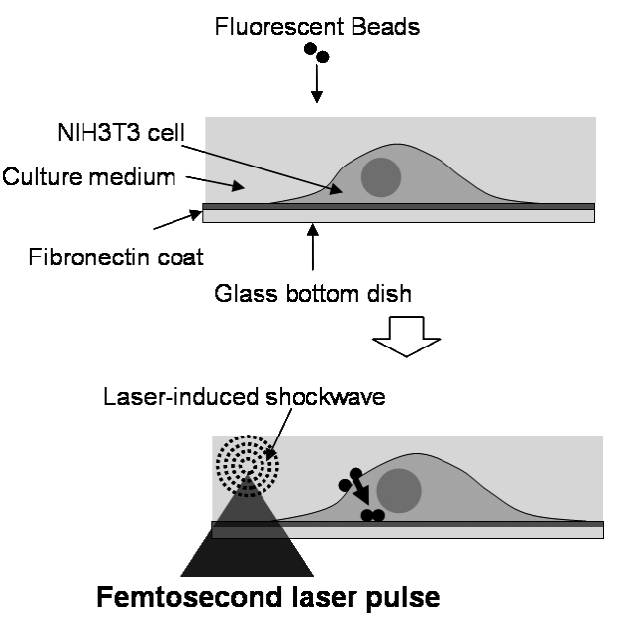

Fig. 11. Schematic illustration for the femtosecond laser-induced injection of nano particles into a single animal cell.

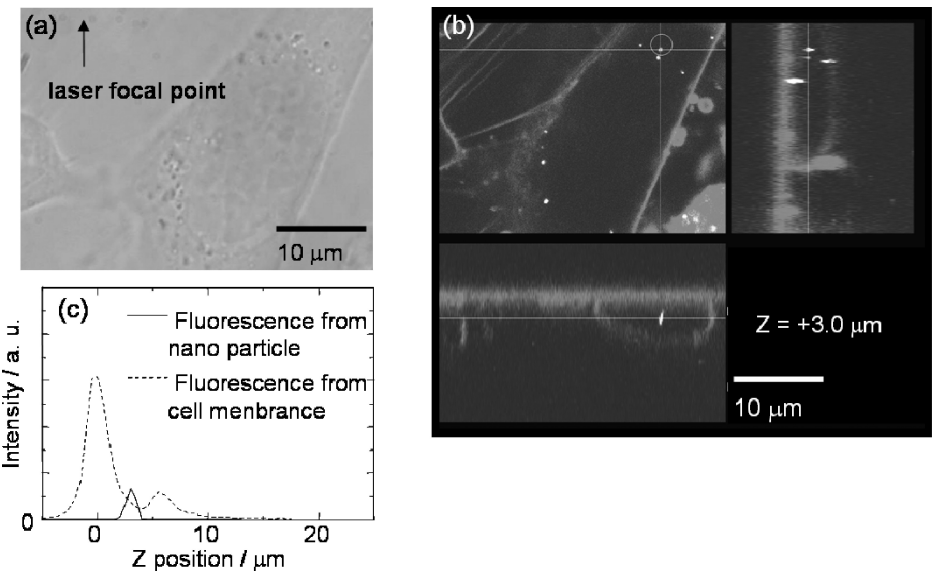

Fig. 12. Transmission (a) and confocal fluorescence (b) images of single animal cell after femtosecond laser-induced injection of nanoparticles. The cross section of fluorescence at the horizontal white line in (b) right is shown in (c).

7. FEMTOSECOND NONLINEAR PROCESSES AND MECHANICAL EFFECTS

We have described our recent results that the focused femtosecond laser irradiation brings about crystallization and crystal growth, makes it possible to manipulate large particles, patterns protein cubes and bio cells, and even injects nanoparticles into single cells. Quite diverse phenomena can be caused and applied by femtosecond irradiation, which is due to multiphoton absorption of aqueous solution leading to cavitaiton bubble, shockwave, convection flow, and so on. The polymer beads, protein cubes, and bio cells are pushed away mechanically, while they are not photoexcited. In order to demonstrate this mechanical effect more directly, how a single polymer bead in water is affected by the irradiation was examined. The result is summarized in Fig. 13, where a schematic illustration of the experiment, images showing the movement of a single bead upon excitation, and a graph showing its relation between the distance and the time (laser shot) are given. Initially the distance between the focal point and the bead was 8 μm, and upon each femtosecond irraditation the bead shifted further and further. This clearly indicates that the bead receives the force and it becomes weaker as the distance longer. When the bead is located beyond 25 μm, the shift upon 1 shot irradiation is about a few μm.

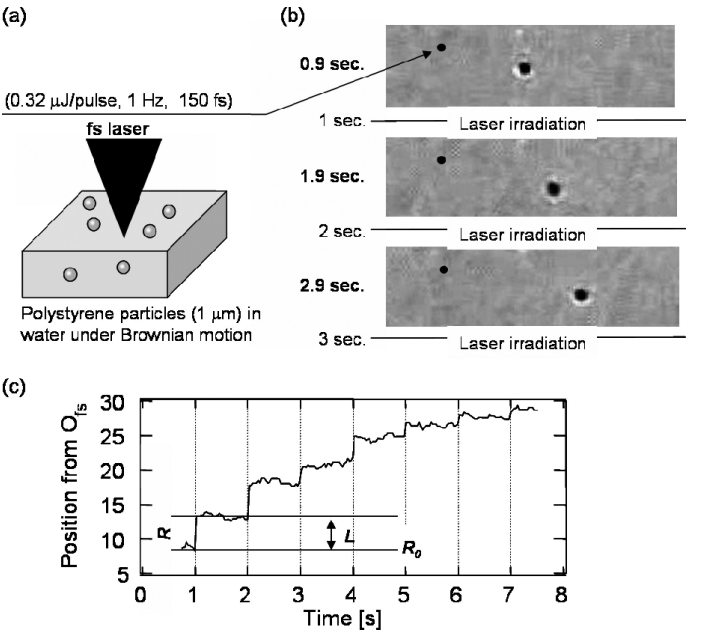

Fig. 13. A schematic (a) and microphotographs (b) of a single polystyrene particle in a culture medium after the femtosecond laser irradiation. Time evolution of the distance between the particle and the focal point is summarized in (c).

Analyzing this behavior, we can estimate the mechanical force. A schematic model and accompanying parameters are given in Fig. 14. The force is regarded to be generated instantaneously, then we introduce δ-function and give the force as

$$f = F_0 \frac{\pi r^2}{4\pi R_0^2} \delta(t) \,. \tag{1}$$

The equation of the particle motion is

$$m\frac{d^2R}{dt^2} = -6\pi\eta r\frac{dR}{dt} + f \,, \tag{2}$$

so that the total shift of the particle is given as

$$L = R(t=\infty) - R_0 \,. \tag{3}$$

Thus, the following relation which can be fit to experimental data is derived as

$$L = \alpha \cdot \frac{1}{R_0^2}$$
$$\alpha = \frac{F_0 \cdot r}{24\pi\eta} \,. \tag{4}$$

The fittings in Fig. 4 give us the result listed in Table 1. Examining the relation

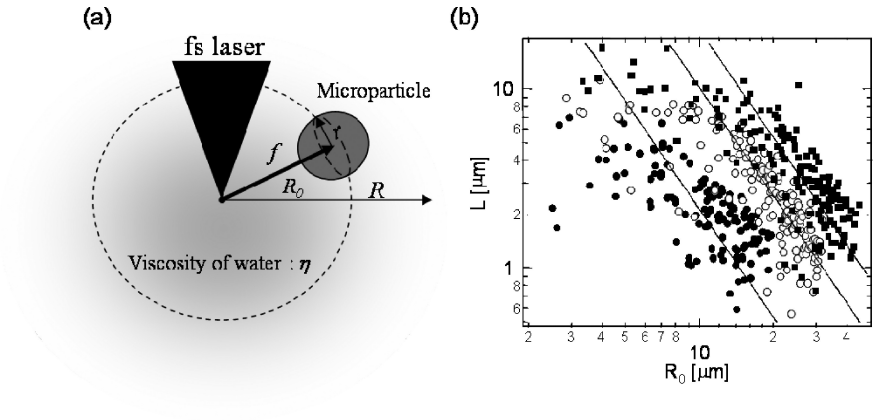

Fig. 14. (a) Model to calculate the motion of micro particles after femtosecond laser irradiation and (b) plots of initial position of the particle, R_0, vs. the shift after the laser irradiation, L, at the pulse energy 0.28(●), 0.33(○), and 0.56(■) μJ/pulse.

Table 1
Pulse energy dependence of force induced by femtosecond laser irradiation

Pulse energy [μJ/pulse]	α	F_0 [μN]
0.28	183	13.8
0.33	525	39.6
0.56	2367	178

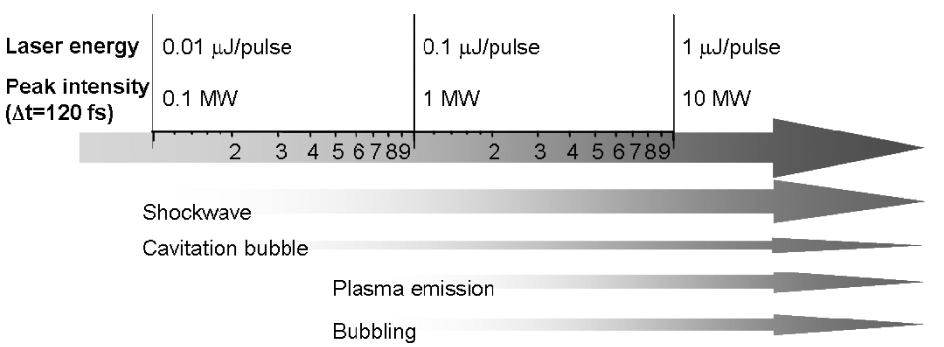

Fig. 15. Nonlinear processes in aqueous solution induced by single-shot femtosecond laser.

between the force and the pulse energy, it was found that the former is proportional to 2.17 power of the energy. The force at a few μm distance is estimated to be about a few μN, although it is transiently exerted. It is worth

noting that the force is larger than that of conventional laser trapping by a few orders of magnitudes. This extremely large force enables us to manipulate a bead of about 100 μm order in solution and furthermore various new methodologies are developed.

The origin of the force is considered to be cavitation bubble, shockwave, and convection flow as we described frequently. The relation among these nonlinear processes was investigated by examining their threshold laser fluence. The results are summarized in Fig. 15. The shockwave and bubbles were identified by eye under a microscope, while the plasma emission was detected by high speed CMOS camera. We conduct crystal growth, crystallization, manipulation, pattering, and injection by changing laser fluence, and we guess the origins of these interesting phenomena. The crystal growth is triggered by laser ablation, polymer bead can be shifted and injection is made possible by shockwave, and crystallization, manipulation, and patterning are closely related to bubbling and convection flow. The femsosecond nonlinear processing in solution is very promising, particularly, for soft matters and living systems, and various applications are being explored.

ACKNOWLEDGEMENTS

Some of the works described here is due to the collaboration with Prof. Takatomo SASAKI and Dr. Hiroaki ADACHI of Department of Electrical Engineering, Osaka University. The financial supports are given by KAKENHI (Grant-in-Aid for Scientific Research) on Priority Area “Molecular Nano Dynamics” from MEXT (Ministry of Education, Culture, Sport, Science and Technology of Japan), CREST Project on “Nano Manipulation-μm Multiplication” from JST, and Intelligent Cluster Project from MEXT.

REFERENCES

[1] H. Masuhara, T. Asahi and Y. Hosokawa, Pure Appl. Chem. in press (2006).
[2] K. Hatanaka, Y. Tsuboi, H. Fukumura and H. Masuhara, J. Phys. Chem. B, 106 (2002) 3049.
[3] Y. Hosokawa, M. Yashiro, T. Asahi and H. Masuhara, Proc. SPIE, 4274 (2001) 78.
[4] Y. Hosokawa, M. Yashiro, T. Asahi and H. Masuhara, J. Photochem. Photobio. A, 142 (2001) 197.
[5] Y. Tamaki, T. Asahi and H. Masuhara, Jpn. J. Appl. Phys., 42 (2003) 2725.
[6] Y. Tamaki, T. Asahi and H. Masuhara, J. Phys. Chem. A, 106 (2002) 2135.
[7] Y. Tamaki, T. Asahi and H. Masuhara, Appl. Surf. Sci., 168 (2000) 85.
[8] T. Sugiyama, T. Asahi, H. Takeuchi and H. Masuhara, Jpn. J. Appl. Phys., 45 (2006) 384.
[9] T. Sugiyama, T. Asahi and H. Masuhara, Chem. Lett., 33 (2004) 724.
[10] T. Asahi, H. Y. Yoshikawa, M. Yashiro and H. Masuhara, Appl. Surf. Sci., 197-198 (2002) 777.

[11] H. Y. Yoshikawa, Y. Hosokawa and H. Masuhara, Cryst. Growth Des., 6 (2006) 302.
[12] H. Y. Yoshikawa, Y. Hosokawa and H. Masuhara, Jpn. J. Appl. Phys., 45 (2006) L23.
[13] H. Miyasaka, H. Masuhara and N. Mataga, J. Phys. Chem., 94 (1990) 3577.
[14] H. Miyasaka, H. Masuhara and N. Mataga, Laser Chem., 7 (1987) 119.
[15] H. Miyasaka, H. Masuhara and N. Mataga, Chem. Phys. Lett., 118 (1985) 459.
[16] H. Adachi, K. Takano, Y. Hosokawa, T. Inoue, Y. Mori, H. Matsumura, M. Yoshimura, Y. Tsunaka, M. Morikawa, S. Kanaya, H. Masuhara, Y. Kai and T. Sasaki, Jpn. J. Appl. Phys., 42 (2003) L798.
[17] Y. Hosokawa, H. Adachi, M. Yoshimura, Y. Mori, T. Sasaki and H. Masuhara, Cryst. Growth Des., 5 (2005) 861.
[18] B. A. Garetz, J. E. Aber, N. L. Goddard, R. G. Young, A. S. Myerson, Phys. Rev. Lett., 77 (1996) 3475.
[19] J.Zaccaro, J. Matic, A. S. Myerson and B. A. Garetz, Cryst. Growth Des., 1 (2001) 5.
[20] B. A. Garetz and J. Matic, Phys. Rev. Lett., 89 (2002) 175501.
[21] T. Okutsu, K. Nakamura, H. Haneda and H. Hiratsuka, Cryst. Growth Des., 4 (2004) 113.
[22] T. Okutsu, K. Isomura, N. Kakinuma, H. Horiuchi, M. Unno, H. Matsumoto, and H. Hiratsuka, Cryst. Growth Des., 5 (2005) 461.
[23] K. Nakamura, Y. Sora, H. Y. Yoshikawa, Y. Hosokawa, Y. Mori, T. Sasaki and H. Masuhara, Submitted to Appl. Surf. Sci. (2006).
[24] K. Sasaki, M. Koshioka, H. Misawa, N. Kitamura, and H. Masuhara, Appl. Phys. Lett., 60 (1992) 807
[25] H. Y. Yoshikawa, Y. Hosokawa, K. Suzuki, K. Ikeda, H. Mori and H. Masuhara, Jpn. J. Appl. Phys., 45 (2006) 323.
[26] Y. Hosokawa, S. Matsumura, H. Masuhara, K. Ikeda, A. Shimo-oka, H. Mori, J. Appl. Phys., 96 (2004)2945.
[27] K. Ikeda, H. Nakazawa, A. Shimo-Oka, K. Ishio, S. Miyata, Y. Hosokawa, S. Matsumura, H. Masuhara, S. Belloncik, R. Alain, N. Goshima, N. Nomura, K. Morigaki, A. Kawai, T. Kuroita, B. Kawakami, Y. Endo and H. Mori, Proteomics, 6 (2006) 54.
[28] Y. Hosokawa, T. Kaji, C. Shukunami, Y. Hiraki, E. Kotani, H. Mori and H. Masuhara, Biomed. Microdevices in press (2006).

This page intentionally left blank

Handai Nanophotonics, Volume 3
H. Masuhara, S. Kawata and F. Tokunaga (Editors)

Chapter 16

Single living cell processing in water medium using focused femtosecond laser-induced shockwave and cavitation bubble

Y. Hosokawa[a,e], R. Yasukuni[a], J.-A. Spitz[a,c,d], T. Tada[a], T. Negishi[a], C. Shukunami[b,e], Y. Hiraki[b,e], T. Asahi[a], R. Méallet-Renault[c] and H. Masuhara[a,e]

[a]Department of Applied Physics and Venture Business Laboratory, Osaka University, 2-1 Yamadaoka, Suita, Osaka, 565-0871, Japan

[b]Department of Cell Differentiation, Institute for Frontier Medical Sciences Kyoto University, 53 Kawahara-cho Shogoin, Sakyo-ku, Kyoto, 606-8507, Japan

[c]Laboratoire de Photophysique et Photochimie Supramoléculaires et Macromoléculaires (UMR 8531), Ecole Normale Supérieure de Cachan, 61, avenue du Pdt Wilson, 94235 Cachan Cedex, France

[d]Laboratoire de Biotechnologies et Pharmacologie génétique Appliquée (UMR 8113), Ecole Normale Supérieure de Cachan, 61, avenue du Pdt Wilson, 94235 Cachan Cedex, France

[e]CREST-JST

1. INTRODUCTION

When a near-infrared femtosecond laser is focused by a high-numerical-objective lens, the cell and tissue are three-dimensionally processed at the laser focal point through multiphoton absorption. Such phenomenom is possible due the transparency of cells and tissues in the near-infrared region. Recently, the 3D processing of biological material has attracted much attention as a new method for cell and tissue dissection with fine spatial selectivity [1-7]. In addition, the femtosecond laser processing has an advantage for biological materials which are sensitive to thermal damage. Indeedthe femtosecond laser processing in

water (which is main component of biomaterials) is normally dived not only by thermal evaporation but also by shockwave and cavitation bubble generation. Although the latter generation can be induced also by near-infrared nanosecond and picosecond lasers [8], an efficient multi-photon absorption by femtosecond laser initiates these generations with relatively low pulse energy [9, 10]. The shockwave and cavitation bubble generated are localized at the laser focal point and produce local processing of cell and tissue with less thermal damage. In fact, our group succeeded in the manipulation of single animal cell without thermal damage by applying the compact shockwave and cavitation bubble [11]. In this chapter, we explain the effective generation process of shockwave and cavitation bubble on the basis of photomechanical ablation process, and describe femtosecond laser processing for living animal cell.

2. SAMPLE AND MICROSCOPE

As a representative animal cell, NIH 3T3 fibroblast was prepared. The fibroblasts were plated onto glass-bottom Petri dishes which had been coated by fibronectin (5 mg/ml) and cultured in Dulbecco's Modification of Eagle's Medium supplemented with 5 % fetal bovine serum. The specimen was set on an inverted microscope (Olympus, IX71), to which a regeneratively amplified femtosecond Ti:Sapphire laser (Spectra-Physics, Hurricane, 800 nm, 120 fs) was led as shown in Fig. 1. The laser pulse was focused by a microscope objective lens. Single shot laser pulses were picked up from the pulse train with a repetition rate of 125 Hz by a mechanical shutter. Laser power was tuned by a half-wavelength plate and dual polarizers.

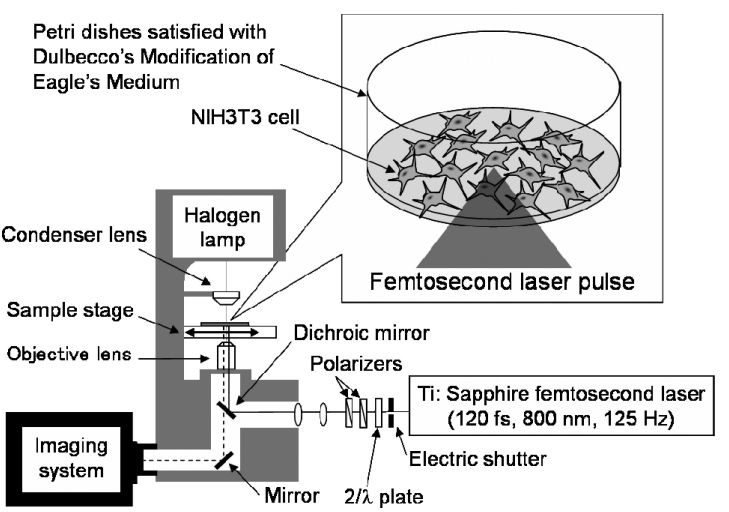

Fig. 1. Experimental setup of femtosecond laser processing for living animal cell.

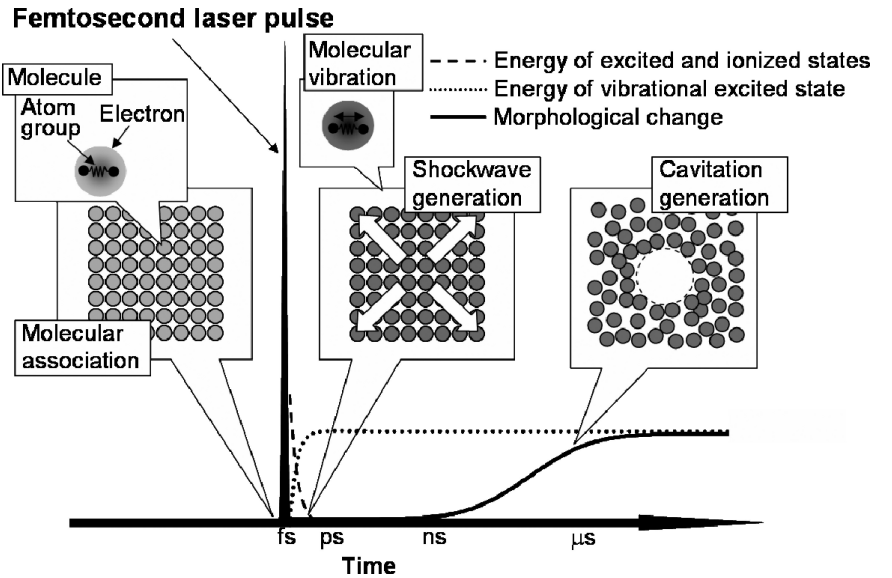

Fig. 2. Schematical illustration of the mechanism of shockwave and cavitation bubble generation

3. SHOCKWAVE AND CAVITATION BUBBLE GENERATION PROCESSES

The mechanism of shockwave and cavitation bubble generation has been investigated on the basis of femtosecond laser-induced breakdown [8-10]. More precisely, the mechanism for femtosecond laser irradiation has been detailed on the basis of photomechanical mechanism of femtosecond laser ablation [10, 12-15], which should be schematically summarized as shown in Fig. 2. The energy of the femtosecond laser pulse is efficiently deposited in a part of a material, consisting of molecular association, through the multiphoton absorption at the laser focal point. Then, excited and/or ionic states are locally generated, whose energy could be quickly converted to vibrational excited states of molecules composing of number of frequency modes, then to the lattice motion with low frequency modes. Such vigorous molecular motions enhanced in a confined space do not only a temperature increase but also a pressure elevation. In the case of liquid, the excessive pressure will relax as a shockwave. After the shockwave propagation, the pressure at the laser focal point will decrease and induce an explosive vaporization, which results in a cavitation bubble formation [8]. The cavitation bubble soon collapses and forms a jet flow of liquid.

The time-evolution of the shockwave and cavitation bubble generated in water was monitored with a high-speed CMOS camera (Photron, FASTCAM).

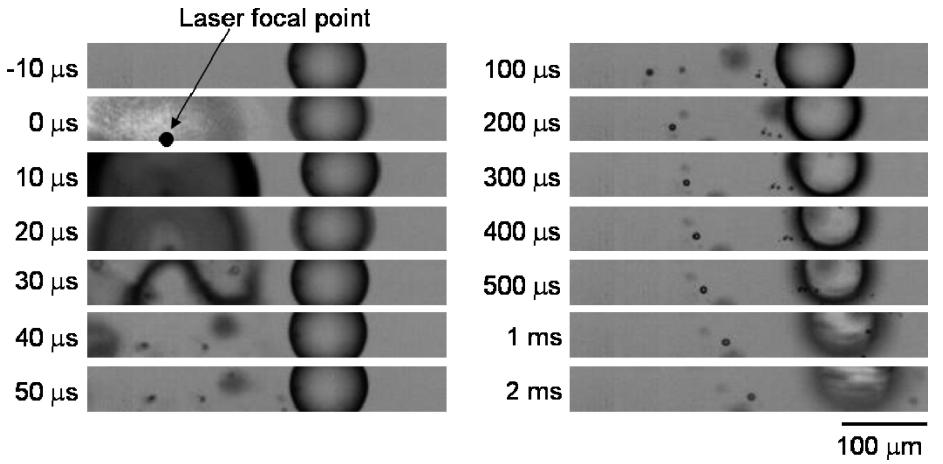

Fig. 3. Time-evolution of shockwave and cavitation bubble monitored by a high-speed imaging device.

Here, instead of NIT3T3 cells described at the inset of Fig. 1, water containing 90 μm polystyrene beads was used as a model sample in order to monitor its convection. The transmitted images, whose light source was a halogen lamp equipped on the microscope, were acquired with gate time and frame rate of 166 ns and 100 000 frame/sec, respectively. The representative result is shown in Fig. 3, in which the laser pulse (24 μJ/pulse) was focused by a 10x objective lens (NA 0.45). Immediately after the laser shot (0 μs), an emission which will be attributed to plasma emission of water was observed. Simultaneously, the silhouette of the bead was blurred. This means that the bead was accelerated by the impact of the shockwave in the time scale less than 10 μs. Then a cavitation bubble was generated and collapsed within 30 μs, where the motion of the bead was synchronized with shape change of cavitation bubble. The collapse of the cavitation bubble initiated a jet flow and small lasting bubbles, by which the bead was further shifted. When the femtosecond laser was focused on the culture medium, similar behaviour of the shockwave and cavitation bubble was observed. Since the size of the bead is in the same order to that of a cell, we can analyze these phenomena to estimate an external force for processing the single cell.

4. MOTIONS OF SINGLE ANIMAL CELL CULTURED ON A SUBSTRATE

The behaviour when the femtosecond laser pulse was shot near the NIH3T3 cell in the culture medium was investigated by high-speed imaging. The

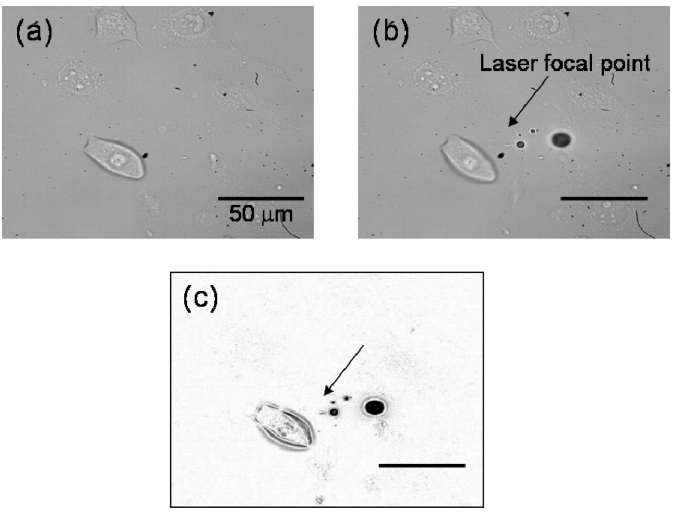

Fig. 4. High-speed microphotographs of NIH3T3 cell before (a) and at 500 μs (b) after a single-shot femtosecond laser irradiation. Image (c) is difference between (a) and (c).

representative example of transmission images of the NIH3T3 cell is shown in Fig. 4. The laser with 0.8 μJ/pulse was focused and shot by a 100x objective lens (NA 1.25) and shot at the position of 20 μm away from the cell. In order to see the modification more clearly, a difference image between microphotographs (a) and (b) was calculated as shown in Fig.4 (c). Immediately after the laser irradiation, black spots with size of 1 ~ 25 μm were observed at the vicinity of the laser focal point. Simultaneously, the position of the cell was shifted at the opposite side of the laser focal point. Since the shift of the cell is about 5 μm, it is estimated that the cell was moved with velocity over 10 mm/s, though the cell adheres tightly on the substrate.

The black spots will be bubbles generated after collapse of the cavitation bubble, so that the cell will be attacked by forces due to shockwave and cavitation bubble generations in this time scale. Namely it is considered that the cell motion is induced by mechanical force. Although there is another possibility that the cell motion is led by cellular biological processes, such as synthesis, polymerization, and depolymerization processes of cytoskeleton, this time scale is too short to initiate them (See section 6). On the other hand, we have also tried to manipulate the NIH3T3 cells using a conventional laser trapping, where optical pressure by near infrared laser was applied, however, it was impossible. This result obviously indicates that the mechanical force due to the shockwave and cavitation bubble is stronger than that of the trapping and will be an effective perturbation enabling manipulation of single cells.

5. REGENERATION PROCESS OF CELL MONITORED BY TOTAL INTERNAL REFLECTION FLUORESCENECE IMAGING

The regeneration process of the cell after the detachment was evaluated by monitoring actin stress fibres connected with the substrate. Actin is a cytoskeleton protein and forms actin filament. Three-dimensional network of actin stress fibre, which is an association of actin filaments, provides mechanical support for the cell, determines the cell shape, and enables cell movements. Here, the actin stress fibre was visualized by binding it with enhanced green fluorescence protein (EGFP). The NIH 3T3 cells were transfected with pEGFP-actin plasmid (Clontech) and transfectin (Biorad) according to the standard procedures and hatched in a CO_2 incubator (5 % CO_2 in air) at 37 °C for 2 days. The actin stress fibres at the interface between the cell and substrate were selectively monitored by total internal reflection fluorescence (TIRF) imaging, whose experimental setup is schematically shown in Fig. 5. A diode pumped solid state (DPSS) laser (473 nm) led to the edge of a 60x objective lens (NA 1.45) shines up through a glass coverslip at a shallow angle and an evanescent wave probes only an interface layer of the cell adhered on the substrate. Alternatively, the epi-fluorescence image was also acquired by shifting the DPSS laser beam to the centre of the objective lens. These images were acquired by an electron multiplier CCD camera (HAMAMATSU, C9100).

Transmission, epi-fluorescence, and TIRF images before laser irradiation are shown in Figs. 6 (a), (b), and (c), respectively. Although the pEGFP-actin is expressed in the whole cell at the centre of the pictures, only the actin fibres at the interface between the cell and substrate were selectively detected in the TIRF image (c). Hence, the bright lines in TIRF image can be attributed to actin stress fibres which adhered on the substrate. The time evolution of the cell when the laser with 0.3 μJ/pulse was focused at the ventral side of the cell by the 60x objective lens is summarized in Figs. 6 (d-f). Immediately after the laser shot,

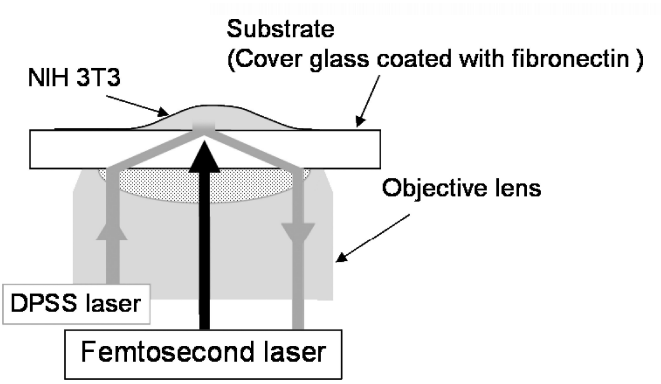

Fig. 5. Schematic illustration of TIRF imaging using high NA objective lens.

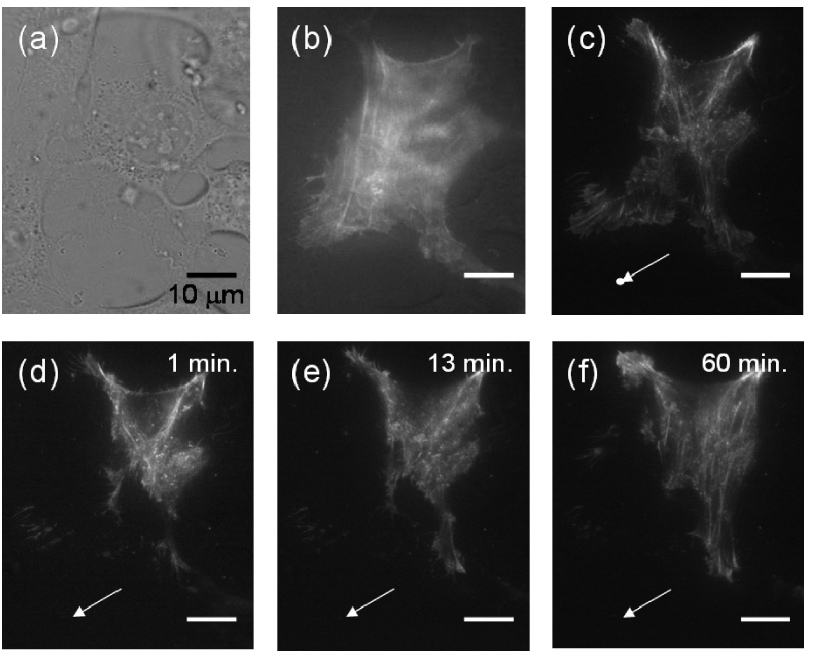

Fig. 6. Transmission (a), Epi-Fluorescence (b), and TIRF (c-f) images of NIH3T3 cell before (a-c) and after (d-f) the femtosecond laser irradiation. Arrows indicate the laser focal point.

fluorescence of actin filaments near the laser focal point were lost. Simultaneously, the averaging intensity of the fluorescent of the actin was increased in the area far from the laser focal point.

The loss of the actin filaments near the laser focal point will be due to the detachment of the cytoskeleton from the culture substrate. The detachment will also induce relaxation of a tension of the cytoskeleton, which is originated in the process of cell adhesion and migration. On the other hand, at the area far from the laser focal point, there is a possibility that the generation of cytoskeleton in the cell is enhanced, because the increase of the fluorescence intensity means that the actin molecules are accumulated at the adhesion area.

At a few tens minutes after the laser irradiation, the actin filament was regenerated from the adhesion area, and the regeneration proceeded as shown in Figs. 6 (e) and (f). Of course, the actual cell viability can not be evaluated by this method, because the cell regeneration strongly depends not only on the laser irradiation but also on the cell culture conditions. For example, even under the normal culture condition, the activity of the cell is prevented when much amount of the pEGFP-actin is expressed. When the pEGFP-actin is not expressed in the cell, about 80 % cells perfectly detached from the culture substrate were adhered again on the culture substrate, which has been already reported [11].

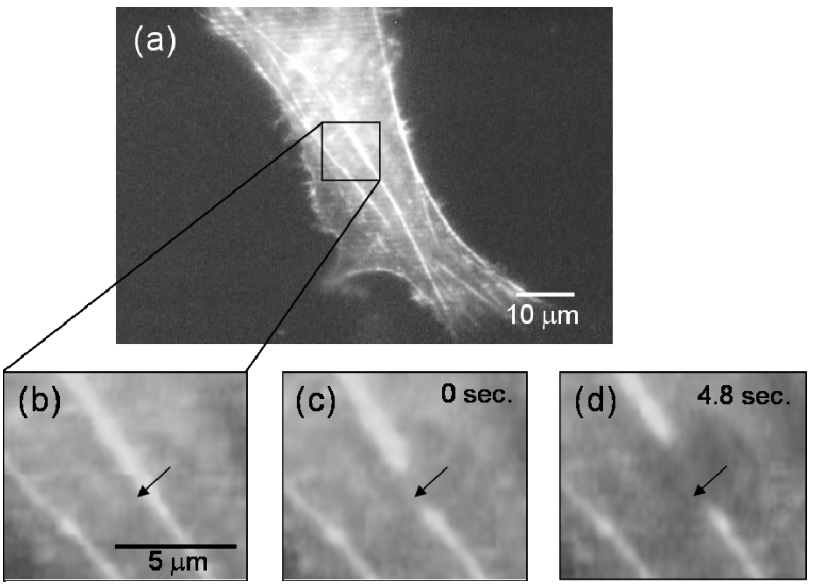

Fig. 7. Fluorescence images of actin stress fibres in NIH3T3 cellafter before (a, b) and after (c, d) a single-shot femtosecond laser irradiation. Arrows indicate laser focal point.

6. DIRECT CUTTING OF SINGLE ACTIN STRESS FIBRE

The actin stress fibre was locally cut by direct irradiation of femtosecond laser and the generation process was monitored. In order to obtain fluorescence images, a diode pumped solid state (DPSS) laser (473 nm) was led to the centre of a 100x objective lens (NA. 1.25). The fluorescence of the pEGFP-actin inside the cell before and after the laser irradiation was imaged by a cooled CCD camera (Roper Scientific, CoolSNAP-HQ).

The fluorescence images when a single-shot femtosecond laser with energy of 4 nJ was focused on the actin stress fibre are shown in Figs. 7. The focal spot darkened immediately after the laser irradiation (c) and the dark area was increased along the actin stress fibre with time (d). This behaviour will arise from contraction of the actin stress fibre, which is considered to be due to the release of elastic energy of the actin stress fibre. Indeed, Kumar et al, recently reported the same behavior of an actin stress fibre [6]. After the contraction, the fibre was further shrunk in the time scale of a few minutes. In this process, the distance between cut edges was increased linearly. It suggests that an actin depolymerization was initiated in this time scale.

Fig. 8 shows fluorescence images after the relaxation of the cell tension, where the realignment process of the actin stress fibre was observed in a few tens of minutes. Its recovery progressed with the appearance of thin individual microfilaments. It is worth noting that the actin stress fibre did not lose its

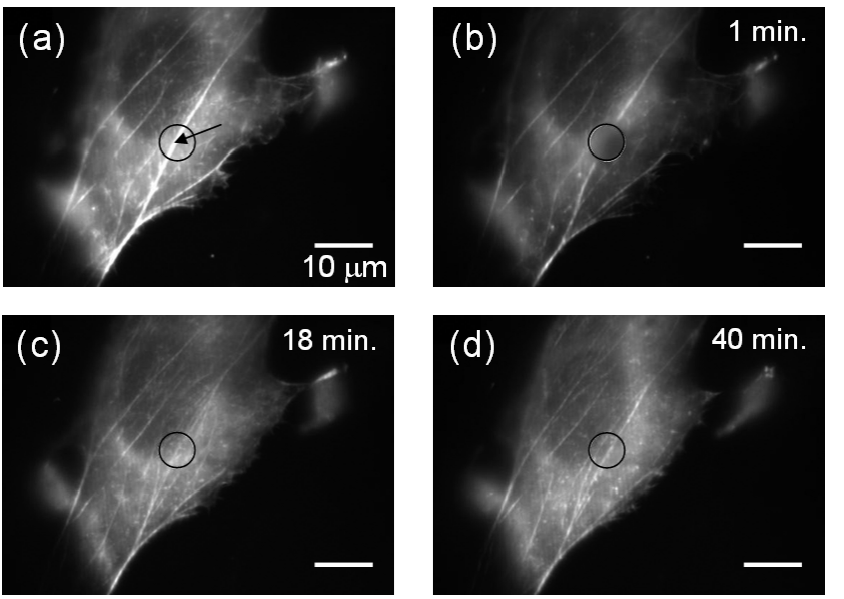

Fig. 8. Fluorescence images of actin stress fibres before (a) and after (b-d) a single-shot laser irradiation. Arrow in circle indicates the laser focal point.

directionality of the elongation even after the femtosecond laser dissection. The realignment process of the actin stress fibres has been also investigated by affecting an external stress to the scaffold, where the actin stress fibres detached from the scaffold was adhered again and realigned in the time scale of a few tens minutes [16]. Since the realignment speed is in good agreement with that after the femtosecond laser dissection, it is suggested that the cell activity was not much changed by the mechanical stress induced by the femtosecond laser irradiation.

7. CONCLUSION

In this chapter, we have summarized cellular events when an animal cell is processed by a single-shot focused femtosecond laser. The mechanical influence due to the laser irradiation is not localized at the laser focal point but propagated to the whole of the cell. This result indicates that the focused femtosecond laser has original characteristic as a mechanical perturbation to stimulate the cell. In parallel with the present work, this perturbation of shockwave and cavitation bubble should be applied to develop new methodology for single cell control, such as micro injection of extracellular materials to a single cell, single cell patterning, and so on.

ACKNOWLEDGEMENTS

This work was partly supported by CREST of JST (Japan Science and Technology Corporation) and the Grant-in-Aid Project on Scientific Research (KAKENHI) on Priority Area on “Molecular Nano Dynamics” from the MEXT.

REFERENCES

[1] K. König, Histochem. Cell Biol., 114 (2000) 79.
[2] U. K. Tirlapur and K. König, The Plant J., 31 (2002) 365.
[3] M. F. Yanik, H. Cinar, H. N. Cinar, A. D. Chisholm, Y. Jin and A. Ben-Yakar, Nature, 432 (2004) 882
[4] W. Watanabe, N. Arakawa, S. Matsunaga, T. Higashi, K. Fukui, K. Isobe and K. Itoh, Opt. Express, 12 (2004) 4203.
[5] A. Heisterkamp, I. Z. Maxwell, E. Mazur, J. M. Underwood, J. A. Nickerson, S. Kumar and D. E. Ingber, Opt. Express, 13 (2005) 3690.
[6] S. Kumar, I. Z. Maxwell, A. Heisterkamp, T. R. Polte, T. P. Lele, M. Salanga, E. Mazur and D. E. Ingber, Biophys. J., 90 (2006) 3762.
[7] R. Yasukuni, J. A. Spitz, R. Méallet-Renault, T. Negishi, Y. Hosokawa, T. Asahi, C. Shukunami, Y. Hiraki and H. Masuhara, submitted to Appl. Surf. Sci. (2006).
[8] J. Noack, D. X. Hammer, G. D. Noojin, B. A. Rockwell and A. Vogel., J. Appl. Phys., 83 (1998) 7488.
[9] A. Vogel and V. Venugopalan, Chem. Rev., 103 (2003) 577.
[10] A. Vogel, J. Noack, G. Hüttman and G. Paltauf, Appl. Phys. B, 81 (2005) 1015.
[11] Y. Hosokawa, J. Takabayashi, S. Miura, C. Shukunami, Y. Hiraki and H. Masuhara, Appl. Phys. A, 79 (2004) 795.
[12] Y. Hosokawa, M. Yashiro, T. Asahi and H. Masuhara, J. Photochem. Photobio. A, 142 (2001) 197.
[13] Y. Hosokawa, M. Yashiro, T. Asahi, H. Fukumura and H. Masuhara, Appl. Surf. Sci., 154-155 (2000) 192.
[14] G. Paltauf and P. E. Dyer, Chem. Rev., 103 (2003) 487.
[15] L. V. Zhigilei and B. J. Garrison, J. Appl. Phys., 88 (2000) 1281.
[16] K. Naruse, T.Yamada and M. Sokabe, Am. J. Physiol., 43 (1998) 1532.

Handai Nanophotonics, Volume 3
H. Masuhara, S. Kawata and F. Tokunaga (Editors)

Chapter 17

Subcellular effects of femtosecond laser irradiation

N. I. Smith[a], S. Iwanaga[b], H. Niioka[a], K. Fujita[b], and S. Kawata[b,c]

[a]Department of Frontier Biosciences, Graduate School of Frontier Biosciences, Osaka University, Yamadaoka 1-3, Suita, Osaka 565-0871, Japan

[b]Department of Applied Physics, Graduate School of Engineering, Osaka University, 2-1 Yamadaoka, Suita, Osaka 565-0871, Japan

[c]Riken, 2-1 Hirosawa, Wako, Saitama, 332-0012, Japan

1. INTRODUCTION

When living biological systems are put under the microscope, researchers can observe a fascinating array of dynamics and reactions. The most useful observations occur when the observation is combined with a method of interacting with, or perturbing the system of interest. In the case of living cells, the perturbation is often genetic, chemical, electrical or mechanical in nature. Each method of perturbing the existing state in the cell can provide unique information about the basic nature of the cell itself, as well as the mechanisms that regulate cell behaviour and response.

In this chapter we will discuss using optical methods as a means of interacting with cells. For several decades, lasers have been used as "optical tweezers" for cell manipulation [1], and as "optical scissors" for cell surgery [2]. More recently, laser sources are becoming more popular as a basic research tool, and researchers are exploiting the unique properties of laser radiation, particularly the nonlinear effects resulting from high intensity pulsed irradiation to unlock biological mechanisms. This has led to increased understanding of cell damage thresholds [3], as well as clues regarding the complex interaction between optical stimulation and cell reactions [4-6]. While there remain difficulties in acquiring complete knowledge of the laser-cell interaction mechanisms, the key significance of using laser irradiation to probe and interact with the cell is the ability to position the laser focal spot at any location within the cell. By additionally exploiting known properties of nonlinear absorption, it

is possible to restrict the laser effect to a micrometer-sized region at arbitrary depths within the cell, something that is unique to optical methods.

In particular, here we will look at laser-induced calcium signaling, and investigate some of the general interactions of focused laser light with living cells. The results presented in this chapter are relevant for femtosecond pulsed 800nm laser irradiation in the majority of mammalian cell types.

1.1. Calcium signaling in living cells

In this chapter, the cell function we are particularly interested in the calcium ion (Ca^{2+}) signaling pathway, where the information is passed from region to

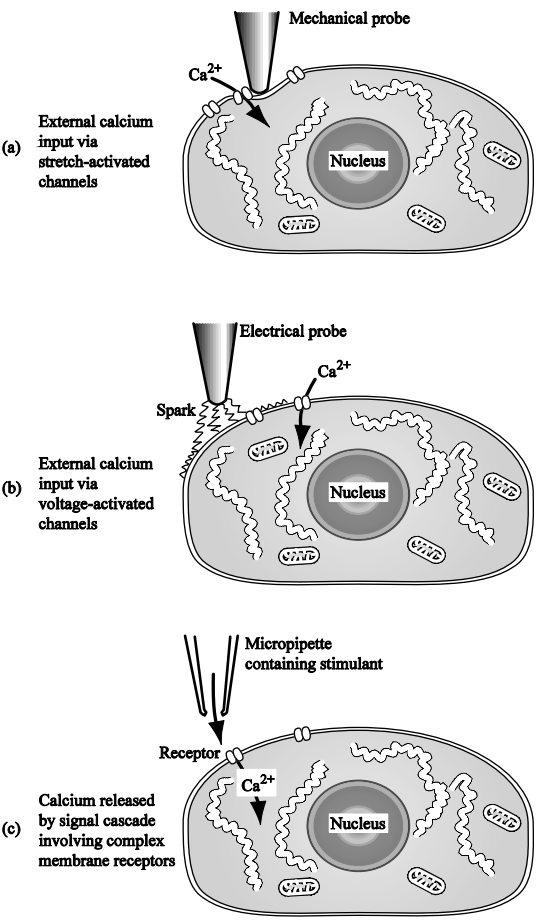

Figure 1: Three conventional methods a), mechanical, b) electrical, and c) chemical for stimulating the release of a small amount of calcium into a living cell. The endoplasmic reticulum of the cell (shown as a white fibrous line) is responsible for amplifying the initial rise in calcium to form a wave of concentration increase over the entire cell.

region by modulating the levels of calcium inside the cell. For the calcium signaling pathway alone, cells can communicate information related to some of the most fundamental responses available to a cell, including fertilization processes in an egg, contraction in muscle cells, and apoptotic programmed cell death [7,8]. It is phenomenal that the concentration of a single ion can be simultaneously responsible for so many different processes. This is achieved by the use of amplitude and frequency modulation (AM/FM) of the concentration levels and the use of ion concentration waves to communicate information [9].

1.2. Techniques to influence cellular calcium signaling

The importance of Ca^{2+} waves and the Ca^{2+} ion as a signaling molecule has led to significant interest in developing techniques to control the Ca^{2+} levels and signaling pathways in living cells. In order to recreate the natural changes in cellular Ca^{2+} concentration that occur during fundamental biological processes, researchers have sought methods to influence the resting cytosolic Ca^{2+} concentration ($[Ca^{2+}]_i$) in cells in vitro. Until now there have been a variety of methods for stimulating Ca^{2+} release in cells (Fig. 1.), including stimulation by a mechanical probe [10], electrostimulation of the membrane [11], and chemical stimulation of membrane receptors [12]. All of these methods are in current use and can be used to stimulate Ca^{2+} release in cultured cells.

However, many of the naturally-occurring stimuli that provoke a Ca^{2+} elevation are caused by events within the cell, rather than as a response to external stimulation. To reproduce such events in the laboratory requires a means of creating a localized Ca^{2+} elevation inside the cell. The Ca^{2+} elevation is self-amplifying and a whole-cell Ca^{2+} response can be evoked by a local concentration spike in $[Ca^{2+}]_i$ by calcium-induced calcium release (CICR) [9]. Such a local increase in $[Ca^{2+}]_i$ can be created by photolytic uncaging (Fig. 2)., where caged Ca^{2+} is added to the cell, and is then liberated by exposure to focused UV light [13]. Uncaging has also been performed by 2-photon absorption [14,15], where the initial amount of liberated Ca^{2+} is localized to the region around the 2-photon focal spot.

2. CELL-LEVEL EFFECTS INDUCED BY LASER IRRADIATION

2.1. Femtosecond laser-induced calcium dynamics

We have observed that the direct action of focused NIR femtosecond pulsed irradiation can cause sufficient release of Ca^{2+} from within the existing stores in a cell to trigger a Ca^{2+} wave [5,16]. Fig. 3 shows the process in rat PC12 cells. The photogeneration of Ca^{2+} waves can be used as a method of whole-cell Ca^{2+} stimulation, without the requirement for additional caged Ca^{2+}. Since the Ca^{2+} release occurs around the laser focus region, and is demonstrated to be independent of extracellular conditions, the location of the initial release can be

positioned anywhere that Ca^{2+} stores exist inside the cell, including locations where caged compounds may not easily penetrate.

An implication of this photogeneration technique for the uncaging method is the possibility of direct laser-induced calcium that is not related to the caged

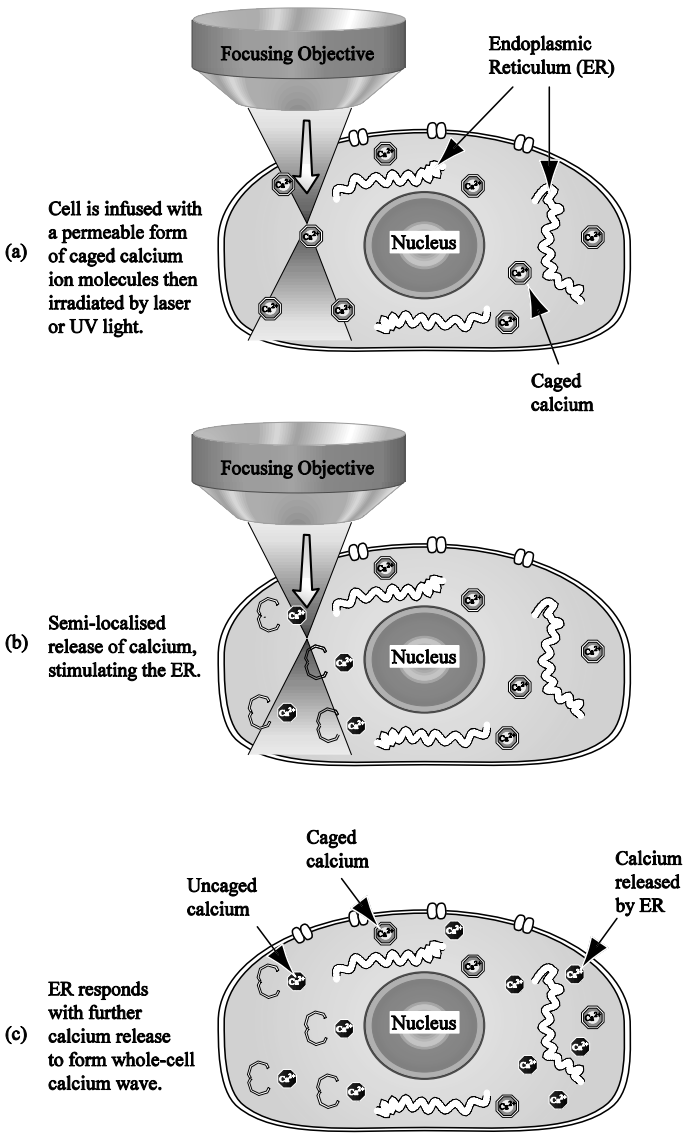

Figure 2: The processes involved in uncaging of calcium causing a calcium wave response in the cell. The endoplasmic reticulum in the cell is responsible for the amplification of the initial rise in calcium. Time between (a) and (b) is less than a millisecond; (b) and (c) is approximately 1 second.

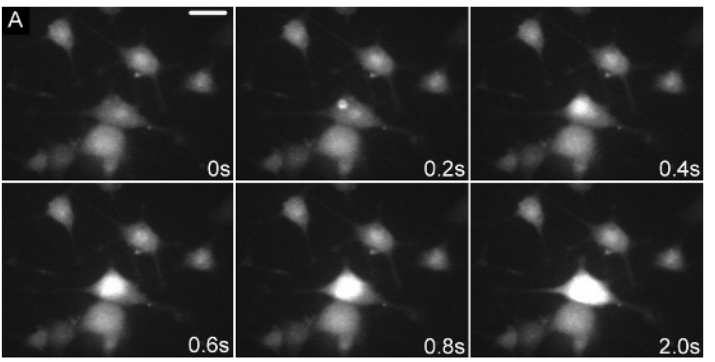

Figure 3: Intracellular Ca^{2+} wave in rat PC12 neural-type cells. The laser focus is positioned adjacent to the nucleus in the cell at the center of the image. At the indicated time of 0.2 s, irradiation of 50 mW average power for a period of 13 ms causes the release of intracellular Ca^{2+} ions, which then act as the trigger for a whole-cell Ca^{2+} wave. The scale bar is 20 μm.

compounds in the target cell. Although photolytic uncaging is usually performed at lower laser powers than are used here, the potential for laser-induced calcium release should also be considered.

We also observed a measurable detrimental effect on the cell viability as a result of intracellular irradiation, although the onset of cell damage occurred at a higher laser power than the onset of Ca^{2+} wave generation. Setting the average laser power in a range between 20 to 50 mW allows the photogeneration of Ca^{2+} waves without significant cell damage. At an average power of 50 mW, a high repetition rate femtosecond laser has a peak pulse power that is orders of magnitude higher than the average power. This leads to the highly localized effects in the energy deposition zone that have been observed in subcellular surgery and other experiments [3].

2.2. Power dependence

The induction of Ca^{2+} waves by laser was dependent on the nonlinear interaction that occurs at high peak power irradiation when the Ti:sapphire laser is used in mode-locking (pulsed) operation. It is worth noting that continuous-wave 780 nm irradiation, even at an average power of up to 300 mW, did not generate Ca^{2+} waves. In pulsed operation, the femtosecond laser source outputs 80 fs pulses at a repetition rate of 82 Mhz, leading to a peak power of $7.7*10^5$ higher than the average power. Even though the peak power is a more critical parameter for investigating laser effects, we chose to define the phenomenon in terms of average power, as measured at the position of laser focus. This allows for an easier comparison with existing publications on power-related anomalies in scanning two-photon microscopy and photolytic uncaging of caged compounds [6,15].

We examined the dependence between average irradiation power and the probability of the intracellular Ca^{2+} wave generation with the laser in mode-locking (pulsed) mode and in continuous mode. The laser was focused in the cytoplasm, halfway between the upper and lower membrane, and several μm distance from the nucleus, at an exposure time of 13 ms. The percentage of cells where Ca^{2+} waves were generated increased with the average power of the pulsed laser, as shown in Fig. 4. 20 mW or lower average power rarely produced Ca^{2+} waves, while almost all cells exhibited Ca^{2+} waves in response to irradiation at 60 mW or higher. Due to the variability in shape between cells in each trial, up to 310 cells (see figure caption) were used at each laser power for the data shown in Fig. 2.

The dependence of the Ca^{2+} wave probability on the laser power is sigmoidal (Fig. 4), and does not show a particular dependence on the square of the laser power, as might be expected from two-photon absorption. The relationship between laser irradiation and Ca^{2+} waves is complicated by the self-catalyzing effect of laser-induced Ca^{2+} release. On a cellular scale, a threshold amount of cytosolic Ca^{2+} is sufficient to produce a whole-cell Ca^{2+} wave. The amount of laser-induced Ca^{2+} release may depend on multiphoton absorption, but the whole-cell Ca^{2+} wave depends on the presence or absence of the trigger amount of Ca^{2+}. If experiments could be repeated in the same cell, the resulting probability function should therefore resemble a step response, even if the trigger Ca^{2+} was generated through multiphoton absorption. However, to create the distribution function shown in Fig. 4 a different cell must be used for each trial, which causes the specific absorption, laser focus position, stored vs. cytosolic Ca^{2+} levels, and other factors to vary between trials. If we assume that for each trial, a given laser power is required to generate the Ca^{2+} trigger, and that a higher laser power will also trigger a Ca^{2+} wave, then the measured Ca^{2+}

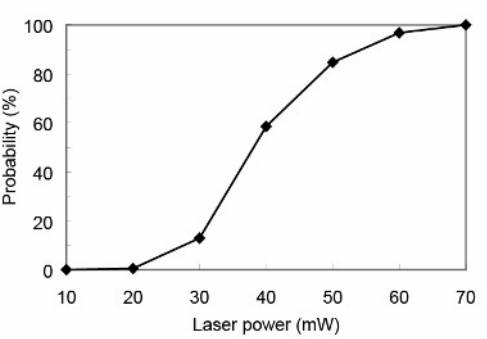

Fig. 4. Average power dependence of femtosecond laser induced Ca^{2+} waves in HeLa cells. Laser powers of 20 to 60 mW produced sufficient nonlinear interaction to generate Ca^{2+} waves. Number of cells per data point is as follows: 10 mW, n=20; 20 mW, n=210; 30 mW, n=310; 40 mW, n=301; 50 mW, n=301; 60 mW, n=220; 70 mW, n=60.

wave probability forms the cumulative distribution function (CDF). The sigmoidal shape of the measured CDF indicates that the factors which differ between individual trials have a normal distribution.

2.3. Thermal effects at the laser focus

In biological samples, laser modification of a sample can be generalized as some combination of the following three effects: thermal, photochemical/ionization, or electromechanical/photomechanical interactions [17] For thermal effects to occur, light energy must first be absorbed, either by single or multiple photon absorption. Depending on the thermal diffusion speed and rate of energy deposition, the laser irradiation may lead to a buildup of heat in and around the focal zone.

It is difficult to quantify the absorption modes in a cell due to the range of potential absorbers, however some assumptions can produce an estimation that indicates the overall temperature rise is less than one degree. The single-photon absorption by water and subsequent temperature rise in the focal zone of a high numerical aperture water-immersion lens resulting from pulsed (or cw) irradiation has previously been analyzed [18]. It was found that, for wavelengths less than 1070 nm, and irradiation of 100 mW average power, the temperature rise will not be higher than 3°K. In particular, for 800 nm, the expected temperature rise resulting from focusing 100mW power by a 1.2 NA objective lens is ~0.12°K after 1 ms irradiation time. Steady-state heat transfer solutions were also calculated by Denk et al. [19] and estimated to be in the order of several degrees.

This temperature rise can be modeled using the linear absorption coefficient (γ=2.5 m^{-1} at 780 nm), incident laser power (60 mW) and specific heat of water (4.181kJ/kg°K) to estimate the temperature at the focus resulting from one pulse. In a cubic micron volume, the temperature rise will be $4.4*10^{-4}$ °K per pulse.

Now considering the thermal effect resulting from two-photon absorption, Chirico *et al.* have demonstrated a significant temperature rise, tens of degrees, resulting from two-photon absorbing dyes spin-cast onto a substrate [20]. In a solution, the temperature rise will not be as dramatic since heat can diffuse in three dimensions away from the focal spot, however, some temperature rise is still to be expected. The Fluo-4 dye used in this experiment is excited by a mercury lamp and is not intended to be a two-photon absorber, it does however, have a significant two-photon absorption cross-section (on the order of 10 GM) and the presence of Fluo-4 in the cytosol during laser irradiation can therefore be expected to contribute to thermal effects due to thermal relaxation during fluorescence, or from non-radiative decay of excited molecules in the focal zone. By assuming that the two-photon absorption cross section for Fluo-4 is similar to that for Fluo-3 (10 GM) [21], we can estimate the absorbed energy due to the dye. Since the quantum yield of the fluorescent dye is significantly lower in the

condition of low cytosolic Ca^{2+} during the laser exposure, we can further assume that all of the absorbed photon energy is converted to heat. For parameters of 60 mW average power, 140 fs pulses at a 12 ns period, focused by a water-immerion 0.9 NA lens, into a dye with 10 GM two-photon absorption at 780 nm, the temperature rise resulting from a single pulse is $3.7*10^{-4}$ °K in a one cubic micron volume around the focus. Even though Fluo-4 has a relatively high two-photon absorption cross-section, the number of dye molecules in the focal volume is low compared to water and the single pulse heating effect is similar for dye and water absorption-based heating. Combining the single pulse temperature rise due to the two effects, we can calculate the total temperature rise over time.

During an exposure time of 13 ms at 82 MHz pulse repetition rate, cells are exposed to $1.07*10^6$ pulses in each Ca^{2+} stimulation experiment. The thermal diffusion equation provides the time and space dependent temperature profile:

$$r^2 \frac{\partial T}{\partial t} = \alpha \frac{\partial}{\partial r}\left(r^2 \frac{\partial T}{\partial r} \right) + r^2 \frac{\dot{q}}{\rho c_p} \tag{1}$$

where $T(r,t)$ is the spherically symmetric time-dependent temperature distribution above ambient temperature, α is the thermal diffusivity, ρ is the density , c_p is the specific heat, and q is the heat generation term. Iteration of the above equation with the addition of pulse energy at a period of 12 ns and a step size of 0.5 ns in time and 10 nm step size in space with radial symmetry produces a peak temperature at the centre of the focus of 0.07°K after 13 ms. The contributions by linear absorption in water and two-photon absorption of Fluo-4 are approximately equal (54% and 46%, respectively). This result using 60 mW average power is lower than, but comparable to the water absorption results reported by Schönle and Hell [18], who predict a temperature rise of approximately 0.12°K for similar parameters and 100 mW average power.

Other endogeneous absorbers exist in the cytosol, but are not homogenously distributed and are difficult to analyze. However, the water absorption and two-photon dye absorption calculation implies that the combined temperature rise of all absorption-based heating should not be higher than several degrees. To induce significant thermal effects, a temperature rise of several degrees at the focus might be sufficient to cause some lipids in the endoplasmic membrane to undergo lipid transition causing an increase in permeability and consequently, Ca^{2+} leakage. However, since the experiments here were performed at 23°C, even a temperature rise of 5°K would still produce lower than normal operating temperature of the cells and would not be expected to have a significant effect.

At the laser intensities reached in these experiments, some photoionization will occur in the focal zone [17]. While falling short of the power levels required

for full optical breakdown (with subsequent plasma generation), photon density is sufficiently high for 2-photon absorption and structural modification of the sample [22]. If the cellular Ca^{2+} stores overlap the focal zone, laser-induced damage to the membrane of Ca^{2+} stores can cause leakage of Ca^{2+}. Laser-induced singlet oxygen formation may also cause subsequent damage to local cellular structure as well as causing changes in the mitochondrial and cytoplasmic Ca^{2+} concentrations [23,24].

2.4. Generation of Ca^{2+} trigger

There are several possible independent mechanisms for the laser-induced Ca^{2+} release. In biological tissue, Ca^{2+} waves can naturally be generated through several pathways, for example the influx of $[Ca^{2+}]_{ex}$, signal transduction cascade by receptor activation, and the release of $[Ca^{2+}]_i$ from intracellular stores [7]. In any case, once a seed amount of $[Ca^{2+}]_i$ is present inside the cell, CICR can then amplify the concentration to evoke a Ca^{2+} rise over the entire cell. For laser-induced Ca^{2+} waves, there are three possible mechanisms (Fig. 5) by which enough free Ca^{2+} can be generated to trigger the wave. The first possible mechanism is the influx of $[Ca^{2+}]_{ex}$ by the local destruction of plasma membrane (Fig. 5a). The second possible mechanism is the activation of the stretch activated or other channels, either by light-induced pressure on the membrane or

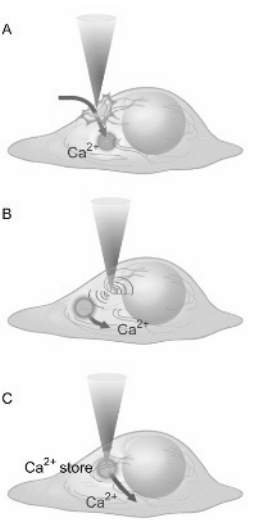

Fig. 5. Three possible mechanisms of Ca^{2+} wave generation by laser irradiation. a. Influx of Ca^{2+} from outside of the cell by the local destruction of the plasma membrane. b. Activation of the stretch activated or other channels by light-induced pressure on the membrane or by shock waves generated from the focal spot. c. Leakage of Ca^{2+} from the destruction of intracellular stores.

by shock waves generated from the focal spot (Fig. 5b). Activation of these channels causes signal transfer through the G-protein, phospholipase-C, IP_3 and Ca^{2+} pathways. The third possible mechanism is the leakage of Ca^{2+} from the destruction of the intracellular Ca^{2+} stores, such as the ER, Golgi apparatus, and mitochondria (Fig. 5c).

To determine which of the three mechanisms shown in Fig. 5 were involved in laser-induced Ca^{2+} wave generation, we investigated the effect of a Ca^{2+}-free extracellular solution with the addition of the chelator EGTA. Additionally, the effect of the presence of a phospholipase-C inhibitor (U-73122) in the extracellular solution was tested. The results are shown in Fig. 6. The following four cases were tested, each of which produced the same probabilities for Ca^{2+} generation: 1 mM $[Ca^{2+}]_{ex}$ (normal condition); negligible $[Ca^{2+}]_{ex}$ and 0.1 mM EGTA; 1 mM $[Ca^{2+}]_{ex}$ and U-73122 inhibitor; 1 mM $[Ca^{2+}]_{ex}$ and U-73343 (inactive U-73122 analogue). Therefore, influx of $[Ca^{2+}]_{ex}$ and activation of stretch-activated or other channels did not significantly influence the laser-induced Ca^{2+} wave so long as the laser was focused in the cytoplasm.

Due to the self-catalyzing influence of CICR on the Ca^{2+} release, the data points shown in Fig. 4 result from experiments that could be well-classified as "wave" or "no wave". The amount of Ca^{2+} released by the irradiation was either sufficient or not sufficient to evoke a Ca^{2+} wave, with very few cases requiring some judgement for classification. If the laser-induced release of stored Ca^{2+} acts as the trigger for the whole-cell Ca^{2+} wave, then the Ca^{2+} wave probability should be affected by a decrease in the concentration of stored Ca^{2+}. To investigate this, we added 1 μM thapsigargin to the extracellular solution, inhibiting the ER Ca^{2+}-ATPase and preventing Ca^{2+} uptake by intracellular stores, which in turn decreases the ER-stored Ca^{2+} over time. The amount of decrease in ER-stored Ca^{2+} in HeLa cells is difficult to quantify, and depends strongly on the temperature and basal leakage rate [25]. However, application of 2 μM thapsigargin has been seen to cause a reduction of non-mitochondrial store Ca^{2+} concentration of ~85% from the initial value [26] after 35 min in A7r5 cells at 25°C. To significantly decrease but not fully deplete the ER-stored Ca^{2+} we used 1μM thapsigargin with a loading time of 35 min at 25°C. As expected, the probability of Ca^{2+} wave generation was found to decrease when thapsigargin was present (Fig. 6). Although the depletion of the ER-stored Ca^{2+} by thapsigargin would be expected to decrease the probability of a Ca^{2+} wave response, the observation of the expected decrease supports the presumption that Ca^{2+} is being released from internal stores and not by influx of $[Ca^{2+}]_{ex}$. It also confirms that the actual laser-induced release is small compared to the whole-cell Ca^{2+} rise, and is self-amplified to the much larger observed response. The Ca^{2+} wave probability dropped significantly when the ER Ca^{2+} stores were partially depleted by thapsigargin, but the results could still be classified as "wave" or "no wave". If the laser action was to release an amount of stored Ca^{2+}

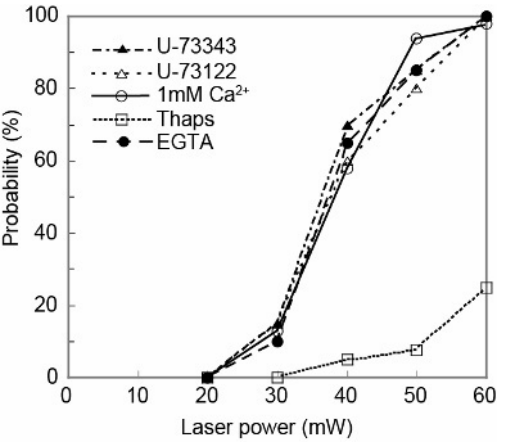

Fig. 6. Probability of Ca^{2+} wave generation after femtosecond laser irradiation of the cytoplasm for different inhibitors. Inhibiting external Ca^{2+} influx (EGTA), and PLC signal transduction (U73122&U73343) produced a negligible effect on the Ca^{2+} wave probability. The probability was reduced significantly by inhibiting the ER Ca^{2+}-ATPase (Thaps). n=20 per data point.

from the ER that could diffuse through the cell and was responsible for the observed fluorescence, the effect of thapsigargin should manifest more as a decrease in fluorescence signal than a marked decrease in Ca^{2+} wave probability. In summary, the probability of the intracellular Ca^{2+} wave generation was independent of $[Ca^{2+}]_{ex}$ influx, independent of phospholipase-C signal transduction, and diminished when the ER-stored Ca^{2+} was decreased, indicating that the seed Ca^{2+} was provided by laser-induced leakage from internal stores.

2.5. Laser repetition rate dependence ROS

We considered the generation of diffusing free radical or other reactive oxygen species production in triggering the Ca^{2+} response. The presence of laser-induced radicals near the cellular calcium stores can cause lipid peroxidation [27] and direct inhibition of the Ca^{2+}ATPase [28]. Hydrogen peroxide has been implicated in increased Ca^{2+} activity in cultured endothelial cells [29]. The generation of at least some amount of laser-induced ROS is probable, and has been observed in other experiments using mode-locked infrared lasers to generate H_2O_2 and other ROS in a variety of cell types [6,23,30,31]. The combination of HEPES buffer (used in our culture media) and ultraviolet-A (320-400 nm) illumination (which is close to the two-photon absorption wavelength) has recently been reported and may also contribute to intracellular ROS generation [32]. We applied Trolox, a water-soluble and cell-permeable analogue for vitamin E and powerful scavenger of cytosolic ROS, to obtain a 200 μM concentration in the extracellular solution. We observed

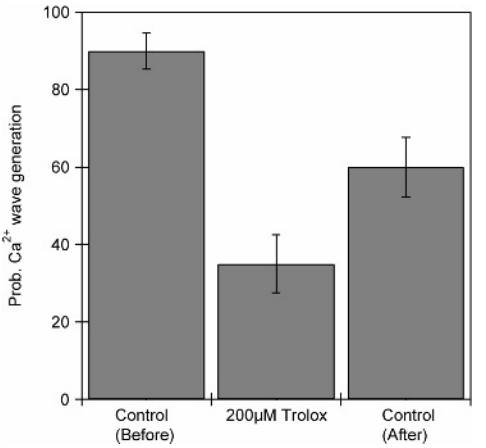

Fig. 7. The probability of intracellular Ca^{2+} wave generation with or without Trolox. The laser (780 nm wavelength, 100 kHz repetition rate, 520 μW average power, 10 s exposure time) was focused into the cytoplasm of the HeLa cell. Error bar is calculated from standard deviation in binominal distribution. (n=40)

whether the Ca^{2+} waves could still be induced when the cellular antioxidant cascades are enhanced. Trolox can be expected to disperse evenly throughout the cellular cytosol. In contrast, laser-induced ROS was expected to be localized, existing in a narrow region surrounding the laser focus. The types of generated ROS differ in their chemical activity, as well as lifetime and therefore diffusion radius. The lifetime of singlet oxygen reported in water or biological tissue is on the order of several μs or lower [33,34], leading to a mean diffusion distance of less than 0.5 μm. The hydroxyl radical has a mean diffusion distance of only ~30 Å, while the hydrogen peroxide radical is stable enough that it can cross cell membranes [35]. Some types of ROS, such as singlet oxygen and hydroxyl radicals (highly reactive), can therefore be expected to be confined to the focal zone by localization due to both two-photon absorption and inherent ROS lifetime. Since the generation of ROS was expected to be localized at the focal spot, Trolox must be able to diffuse into the focal spot in order to be effective. We therefore tested ROS inhibition at different repetition rates, where the ability of Trolox to diffuse into the focal region and inhibit generation of ROS was expected to change with repetition rate.

The laser pulse rate was varied using a pulse picker with an extinction ratio of 300:1. At low output pulse rates (where the pulse picker is blocking the majority of input pulses) the average power leaked through the pulse picker is actually higher than the power in the output pulse train. Therefore, careful consideration of the effect of large numbers of leaked pulses with low peak power is necessary. Further information can be found in Ref. 30, where the

outcome of experiments on pulse leakage indicates that leakage pulses do not have a significant effect on laser-induced Ca^{2+} wave generation.

With a 100 kHz pulse train, and a pulse energy of 1.3 nJ, cells were stimulated at 100 kHz, then the intracellular Ca^{2+} wave generation rate was measured 10 minutes after application of 200 μM Trolox to the cell culture dish. The probability of intracellular Ca^{2+} wave generation was measured again. The application of 200 μM Trolox caused a reduction of the probability of intracellular Ca^{2+} wave generation. Partial recovery of the Ca^{2+} wave generation was then observed after removing Trolox (Fig. 7). This result was unique to the low repetition rate experiments.

Figure 8 shows the effect of 200 μM Trolox application at repetition rates of 100 kHz, 400 kHz, and 82 MHz. These results show that the generation of ROS in the focal zone is a contributing factor to laser-induced Ca^{2+} release of Ca^{2+} from stores such as the endoplasmic reticulum, although they only demonstrate the effect at repetition rates below 1 MHz. From this, we must conclude either that effects resulting from ROS occur only at low repetition rates, or that Trolox is not an effective inhibitor at high repetition rates. Since photochemical effects leading to ROS formation cannot be expected to decrease when the repetition rate is raised, we suggest that Trolox scavenging is ineffective at the higher repetition rates. If, as previously mentioned, several strongly reactive types of ROS are confined to the focal zone, Trolox may become depleted in the focal zone and the effectiveness of Trolox on ROS inhibition will then be determined by the rate of diffusion into the focal zone.

To determine the rate at which Trolox can diffuse into the focal zone, the 1D diffusion equation in spherical coordinates with angular symmetry is:

$$\frac{\partial U}{\partial t} = \kappa\left(\frac{2}{r}\frac{\partial U}{\partial t} + \frac{\partial^2 U}{\partial r^2}\right) \tag{2}$$

where U represents (arbitrary) concentration and κ is the diffusion constant for the molecule. Based on the molecular weight, the diffusion constant of Trolox can be taken to be approximately 5×10^{-10} $m^2 s^{-1}$. If Trolox is fully depleted by one laser pulse, the concentration will recover to reach 50% of the original value within 100 μs. At the repetition rate of 10 kHz, 100 μs is the arrival time of the next pulse. If Trolox is not completely depleted by one laser pulse, then the repetition rate can be higher than 10 kHz without losing the ROS scavenging effect. As shown in Fig. 8, the effect of Trolox is still observable at repetition rates up to 400 kHz, indicating that the effect of a single laser pulse of up to 1.75 nJ does not produce enough ROS to deplete locally available Trolox scavengers. It is worth noting that even though ROS generation was suppressed by the addition of 200 μM Trolox, 100% probability of intracellular Ca^{2+} wave

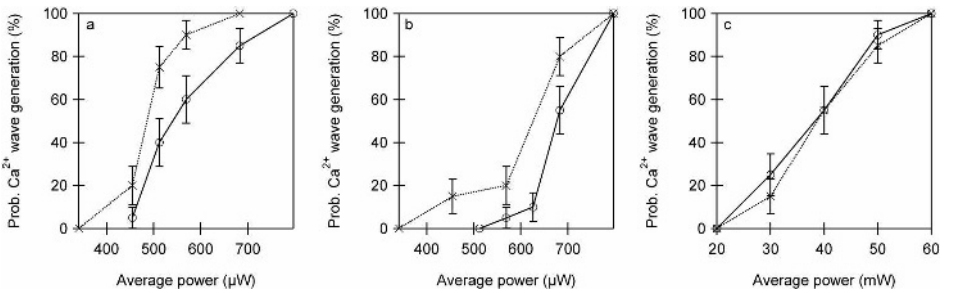

Fig. 8. The probability of intracellular Ca^{2+} wave generation at each average power with or without Trolox. The laser (780 nm wavelength) was focused into the cytoplasm of the HeLa cell. Error bar is calculated from standard deviation in binominal distribution. (n=20) (a) 100 kHz repetition rate, 10 s exposure time (b) 400 kHz repetition rate, 10 s exposure time (c) 82 MHz repetition rate, 13 ms exposure time

generation at sub-MHz repetition rates could still be observed by compensating for the Trolox effect with higher laser pulse energy. Additionally, the shape of the Ca^{2+} wave probability vs. laser power relationship (Fig. 8a, 8b) does not change significantly under the influence of Trolox. The decrease in Ca^{2+} wave probability attributable to Trolox observed at 400 kHz was similar to that at 100 kHz, though the time available for Trolox diffusion between pulses was 4 times longer. This implies that ROS generation is not the only mechanism involved in intracellular Ca^{2+} wave generation, but instead works in combination with direct photoionization of other targets, including endogenous and exogenous fluorophores in the cytosol.

The overall Ca^{2+} response probability dependence on an increase in laser pulse energy was remarkably similar for repetition rates varying over three orders of magnitude (Fig. 8). The shape of the power dependence curve is similar to those previously measured at high repetition rates [5]. At all repetition rates, the average power (corresponding to pulse energy) at the onset of laser-induced Ca^{2+} waves was approximately half of the average power required to generate laser-induced Ca^{2+} waves with 100% probability. Given the femtosecond pulse width, by examining the the results shown in Fig 8, we can state that the NIR laser pulse energy and number of exposed pulses are the most important parameters governing the laser-induced Ca^{2+} release. The interaction is mediated by ROS, but the observed inhibition of ROS effects by Trolox does not preclude other mechanisms of laser-induced Ca^{2+} release, such as photoionization. As the repetition rate decreases, the total number of pulses required to generate Ca^{2+} waves becomes constant. This demonstrates that low repetition rate laser-induced Ca^{2+} release is based on photo-induced changes that are not strongly diffusing in the cell.

2.6. Physical evidence of laser irradiation effects in cells

The action of high intensity laser irradiation can produce physical modification of the intracellular structure, including ablation of mitochondria, poration of the endoplasmic reticulum, and bubble formation in the cytoplasm itself. The difficulty in quantifying these effects in the cell stems mainly from the instability over time of laser-induced modifications. For example, microbubbles formed in the cytoplasm may have poor contrast under optical microscopy, and may not be stable enough to survive the sample preparations required for ultra-high resolution microscopy such as scanning or tunneling electron microscopy (SEM or TEM).

Nevertheless, it is worthwhile to attempt direct observation of subcellular changes resulting from laser irradiation. Transmission electron microscopy has the potential to image nanometer-sized modifications in existing cellular structure. The main disadvantage is that in order to observe the intracellular structure with TEM, cells need to be carefully treated, including fixing, staining, and mounting. The methods we used are described as follows. Cells were fixed with 2.5% glutaraldehyde in 0.1 M cacodylate buffer for 30/min, either before or after laser irradiation. Samples were post fixed with 1% OsO_4 in 0.1 M cacodylate buffer for 1 hour at 4°C. This was followed by graded ethanol dehydration, and embedding in epoxy resin. Ultrathin sections (80-100 nm) were

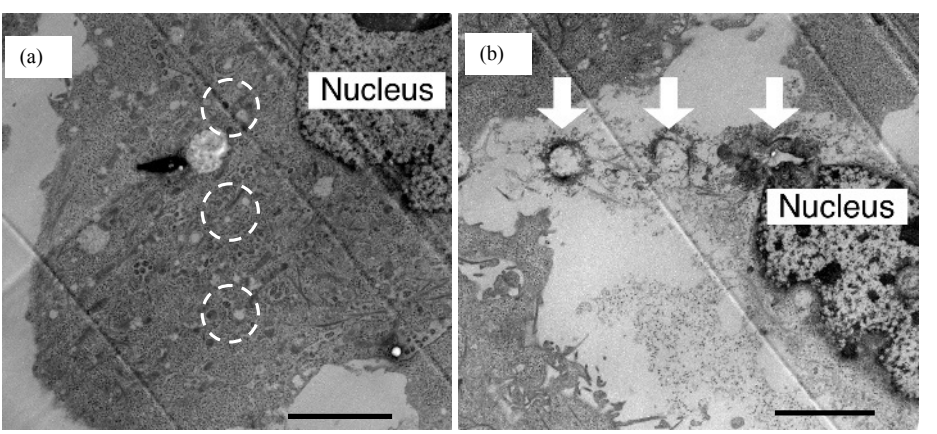

Fig. 9 TEM image of laser-irradiated HeLa cell. The laser was focused in cytoplasm at a power of 60 mW in each spot for a period of 13 ms. After laser irradiation, cells were immediately fixed with glutaraldehyde. a) no obvious physical effects induced by laser were observed. Other sections from the same sample similarly do not show strong laser effects. The white circle shows the laser irradiated regions, inside which there are some ambiguous indications of holes. b) using a polystyrene cell substrate, when the laser focus overlapped the substrate, substrate damage occurred and was accompanied by bubble formation. Arrows indicates laser-irradiated spots. Bar = 5 μm

cut and successive sections were mounted on carbon-coated copper grids. After staining with uranyl acetate and lead citrate, sections were viewed by TEM (Hitachi H-7100).

Fig. 9 shows the sections from HeLa cell samples following immediate fixationg by glutaraldehyde. Fig. 9a shows three regions where the laser was focused at 60 mW average power for 13 ms. The areas of laser irradiation do not clearly show the laser effects. This may be due to one of the following considerations: laser affected areas diffusing out of the focal zone, laser effects reverting to the pre-irradiation state over time, or the lack of any induced visible effects. Phase contrast images were also taken during experiments (not shown), but do not have sufficient resolution to resolve visible changes. Laser induced changes were readily visible only when the focal spot overlapped the plastic substrate (Fig 9b)

Laser-induced changes were not readily visible for femtosecond irradiation of living cells at a few tens of milliwatts for exposures of 13 ms. It is not surprising that laser irradiated of the cytoplasm did not leave physical effects that remained long enough to be visible by fixing and then observing with TEM. The cytoplasm is not purely liquid, but contains a substantial amount of water and is more liquid than solid. Laser effects on a micrometer scale can diffuse out of the target region, or disappear completely by the time the cell is fixed. Fixation inherently takes some time due to the requirement of diffusion of the fixative (in this case glutaraldehyde) into the cells. For the fixative to stabilise

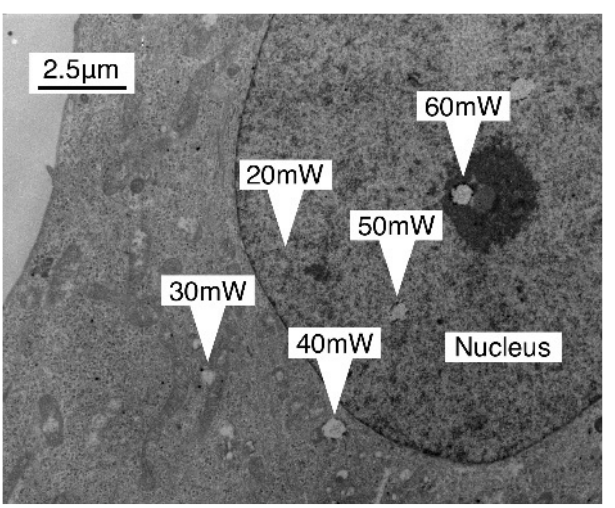

Fig. 10 TEM image of laser-irradiated HeLa cell. By using pre-fixation, laser induced changes were observed. After glutaraldehyde fixation, the laser was focused in the cytoplasm and nucleus while increasing the laser power from 20 mW to 60 mW in steps of 10 mW. The exposure time was 13ms in each spot.

the laser affected area, cell penetration and fixation must occur within seconds of glutaraldehyde application, and preferably faster. Effective glutaraldehyde fixation occurs on a timescale of minutes [36]. Laser-induced changes (such as bubble formation) can easily disappear within seconds, and for that reason, we have considered using pre-fixation to "freeze" the laser effects in the cell.

We observed micrometer-sized laser induced changes when the laser was irradiated after glutaraldehyde fixation. The glutaradehyde prefixing of laser targets may therefore allow nanoscale investigation of laser-induced effects. When the laser power was 20 mW or lower, no discernable structural changes were observed. The threshold power to induce cellular structural change under the stabilising effect of glutaraldehyde, and with the same laser parameters and focusing conditions as described above is therefore between 20 mW and 30 mW. However, the effects of glutaraldehyde are complex and require further consideration. If glutaradehyde can be shown not to significantly affect the laser-cell interaction, we can use it as a new tool to study laser biophysics and cell interactions at the nanometer resolution of electron microscopy.

3. CONCLUSION

This chapter has discussed some of the effects that focused laser irradiation can have in living cells. The attention has been on the laser effects on intracellular calcium dynamics, and some of the physical mechanisms of interaction. Experimentally, such laser effects on cell behaviour can be beneficial or unfavourable, depending on the aims of the experiment, and need to be quantified and controlled for. The work presented in this chapter has implications for multiphoton microscopy, where the high peak power and long exposure times could potentially cause artificial changes in calcium levels. It is also important to consider and compare the amount of trigger calcium released directly from intracellular stores to that in experiments using photolytic uncaging. Work remains to be done in this area. It is also interesting to consider laser induced calcium waves as a tool to interact with the existing cell dynamics. For example, if we account for the cell viability and are careful with the total cell exposure to laser irradiation, we can use focused irradiation as a means to modulate the calcium dynamics in the cell over minutes or hours. Focused laser irradiation has interesting and unique properties; it is an inherently sterile, membrane-penetrating tool that has nanoscale three-dimensional positioning accuracy.

REFERENCES

[1] Ashkin, Phys. Rev. Lett. 24 (1970) 156.
[2] M.W. Berns, R.S. Olson and D.E. Rounds, Nature, 221 (1969) 74.
[3] K. König, I. Riemann, P. Fischer and K.–J. Halbhuber, Cell. Mol. Biol., 45 (1999) 195.

[4] A.B. Uzdensky, and V.V. Savransky, J. Photochem. Photobiol. B Biology, 39 (1997) 224.
[5] N.I. Smith, K. Fujita, T. Kaneko, K. Kato, O. Nakamura, T. Takamatsu, and S. Kawata, Appl. Phys. Lett., 79 (2001) 1208.
[6] H. Hirase, V. Nikolenko, J.H. Goldberg, and R. Yuste, J. Neurobiol., 51 (2002) 237.
[7] M.J. Berridge, P. Lipp, and M.D Bootman, Nat. Rev. Mol., 1 (2000) 11.
[8] H. Cheng, W.J. Lederer, and M.B. Cannell, Science, 262 (1993) 740.
[9] M.D.Bootman, M.J. Berridge, and P. Lipp, Cell, 91 (1997) 367.
[10] K. Paemeleire, P.E.M. Martin, S.L. Coleman, K.E. Fogarty, W.A. Carrington, L. Leybaert, R.A. Tuft, W.H. Evans, and M.J. Sanderson, Mol. Biol. Cell, 11 (2000) 1815.
[11] T. Fauquier, ,N.C. Guérineau, R.A. McKinney, K. Bauer, and P. Mollard, Proc. Natl. Acad. Sci. USA, 98 (2001) 8891.
[12] R. Jacob, J.E. Merritt, J.E. Hallam, and T.J. Rink, Nature, 335 (1998) 40.
[13] V. Parpura, and P.G. Haydon, Proc. Natl. Acad. Sci. USA, 97 (2000) 8629.
[14] E.B. Brown, J.B. Shear, S.R. Adams, R.Y. Tsien, and W.W. Webb, Biophys. J., 76 (1999) 489.
[15] P. Lipp, and E. Niggli, J. Physiol., 508 (1998) 801.
[16] N.I. Smith, S. Iwanaga, T. Beppu, K. Fujita, O. Nakamura, and S. Kawata, Las. Phys. Lett., 3 (2006) 154.
[17] A. Vogel, , and V. Venugopalan, Chem. Rev., 103 (2003) 577.
[18] A. Schönle and S.W. Hell, Opt. Lett., 23 (1998) 325.
[19] W. Denk, D.W. Piston, and W.W. Webb, (J.B. Pawley, ed.), Two-Photon Molecular Excitation in Laser Scanning Microscopy, Plenum, New York, 1995, pp. 445-458.
[20] G. Chirico, F. Cannone, G. Baldini, and A. Diaspro, Biophys. J., 84 (2003) 588.
[21] C. Xu, , R.M. Williams, W. Zipfel, , and W.W. Webb, Bioimaging, 4 (1996) 198.
[22] N.I. Smith, K. Fujita, O. Nakamura, and S. Kawata, Appl. Phys. Lett., 78 (2001) 999.
[23] U.K. Tirlapur, K. König, C. Peuckert, R. Krieg, and K.J. Halbhuber, Exp. Cell Res., 263 (2001) 88.
[24] L. Jornot, P. Maechler, C.B. Wollheim, and A.F. Junod, J. Cell Sci., 112 (1999) 1013.
[25] M.J. Barrero, M. Montero, and J. Alvarez, J. Biol. Chem., 272 (1997) 27694.
[26] L. Missiaen, H. De Smedt, J.B. Parys, L. Raeymaekers, G. Droogmans, L. Van Den Bosch, and R. Casteels, Biochem J., 317 (1996) 849.
[27] S.H. Kang and Q. Chae, Bull. Korean Chem. Soc., 14 (1993) 371.
[28] T.T. Rohn, T.R. Hinds, and F.F. Vincenzi, Biochem. Pharmacol., 51 (1996) 471.
[29] Q. Hu, S. Corda, J.L. Zweier, M.C. Capogrossi, and R.C. Ziegelstein, Circulation., 97 (1998) 268.
[30] S. Iwanaga, N. Smith, K. Fujita, S. Kawata, and O. Nakamura, Opt. Express, 14 (2006) 717.
[31] P.E. Hockberger, T.A. Skimina, V.E. Centonze, C. Lavin, S. Chu, S. Dadras, J.K. Reddy, and J.G. White, Proc. Natl. Acad. Sci. USA, 96 (1999) 6255.
[32] A. Mahns, I. Melchheier, C.V. Suschek, H. Sies, and L.O. Klotz, Free Radic. Res., 37 (2003) 391.
[33] M. A. J. Rodgers, and P. T. Snowden, J. Am. Chem. Soc., 104 (1982) 5541.
[34] M. S. Patterson, J. Photochem. Photobiol. B, 5 (1990) 69.
[35] C. Batandier, E. Fontaine, C. Kériel, and X.M. Leverve, J. Cell Mol. Med., 6 (2002) 175.
[36] J.A. Kiernan, Microsc. Today, 1 (2000) 8.

Handai Nanophotonics, Volume 3
H. Masuhara, S. Kawata and F. Tokunaga (Editors)

Chapter 18

Femtosecond laser nanosurgery of biological cells and tissues

A. Vogel[a], J. Noack[a], G. Hüttmann[a], N. Linz[a], S. Freidank[a] and G. Paltauf[b]

[a]Biomedizinische Optik, Universität zu Lübeck, Peter-Monnik Weg 4, 23562 Lübeck, Germany

[b]Institut für Physik, Karl-Franzens-Universität, Universitätsplatz 5, A-8010 Graz, Austria

1. INTRODUCTION

Nonlinear absorption of short and ultrashort laser pulses focused through microscope objectives of high numerical aperture (NA) can be used to achieve very fine and highly localized laser effects inside of biological media that are transparent at low irradiance as well as in the bulk of photonic materials [1]. Very large numerical apertures are required both to minimize the diffraction limited focus diameter and to avoid self-focusing and filamentation.

To make use of the full potential of femtosecond pulses for highly localized material processing and modification of biological media, it is essential to understand the underlying mechanisms. We have therefore investigated the evolution of plasma formation and the chemical, thermal, and thermomechanical effects arising from femtosecond optical breakdown in aqueous media. Details about numerical and experimental methods applied in this study can be found in Ref. [1].

2. PLASMA FORMATION

While nanosecond breakdown is very abrupt (Figs. 1a, b), we found that in femtosecond laser optical breakdown free electrons are produced in a fairly large irradiance range below the optical breakdown threshold, with a deterministic relationship between free electron density and irradiance (Figs. 1c, d). This provides a large 'tuning range' for the creation of spatially confined chemical, thermal and mechanical effects via free electron generation that can be used for

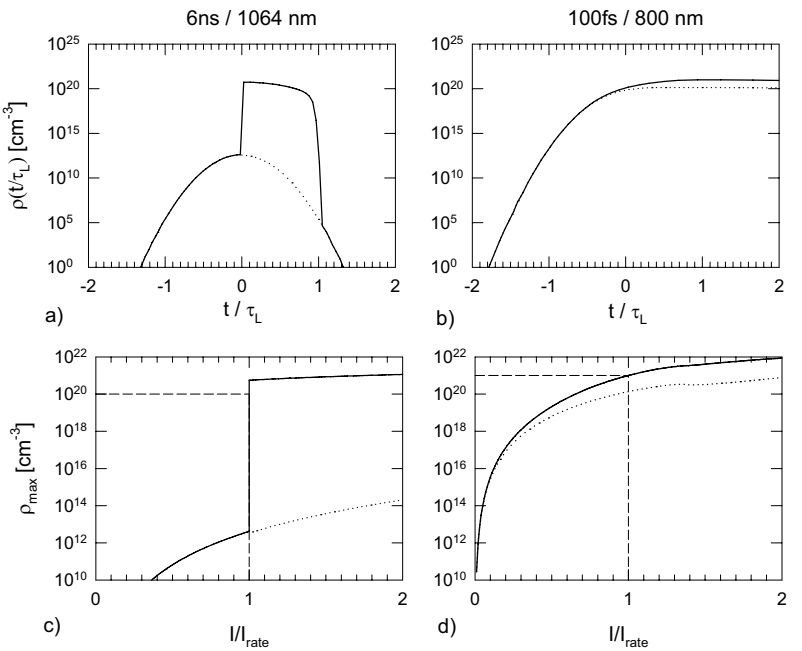

Fig. 1. Evolution of the free-electron density during the laser pulse at the optical breakdown threshold for 6 ns, 1064 nm pulses (a) and for 100-fs, 800-nm pulses (c). The time t is normalized with respect to the laser pulse duration τ_L. The contribution of multiphoton ionization to the total free-electron density is plotted as a dotted line. The maximum free electron density ρ_{max} achieved during the laser pulse as a function of irradiance is, for the same laser parameters, shown in (b) and (d). The irradiance I is normalized with respect to the threshold $I_{rate.} = 10^{21}$ cm^{-3} that is commonly assumed in numerical calculations of the breakdown. The threshold I_{rate} and the corresponding value of ρ_{max} are marked by dotted lines. Reprinted with permission from Ref. [1].

cell surgery. The prediction of low-density plasmas at irradiances below the threshold for bubble formation (Fig. 1d) was experimentally confirmed by Mao et. al. [2]. For larger irradiances, plasmas in bulk media grow beyond the region of the beam waist, which keeps the plasma energy density small. By contrast, at surfaces the energy deposition becomes confined to a thin, dense layer once the free electron density reaches the critical density [3, 4], and the regime of low-density plasma generation has little practical importance.

3. IRRADIANCE AND FREE ELECTRON DISTRIBUTION WITHIN THE FOCAL VOLUME

The temperature and stress distribution in the focal region depend on the distribution of quasi-free electrons produced during femtosecond optical break-

down. Therefore, we must explore the shape of the irradiance and free-electron density distributions within the focal volume before we can investigate the resulting temperature and stress effects. For a plane wave focused by a microscope objective, the focal region has an ellipsoidal shape. The short axis d of the ellipsoid is identified with the diameter of the central maximum of the Airy pattern in the focal plane

$$d = 1.22\,\lambda / NA\,. \tag{1}$$

The symbol λ refers to the vacuum wavelength of light, and $NA = n_0 \sin\alpha$ is the numerical aperture of the objective. The ratio l/d of the long and short axes is

$$l / d = (3 - 2\cos\alpha - \cos 2\alpha)^{1/2} / (1 - \cos\alpha) \tag{2}$$

for optical setups with very large solid angles [1,5]). Here α is the half angle of the light cone such as used in the definition of the numerical aperture. For NA 1.3, which in water corresponds to an angle of $\alpha = 77.8°$, we find $l/d = 2.4$ and, for $\lambda = 800$ nm, $d = 750$ nm and $l = 1800$ nm. For our calculations, we approximate the ellipsoidal region of high irradiance in the focus center by a Gaussian distribution, and the boundaries of the ellipsoid are identified with the $1/e^2$ values of this distribution.

When long pulses (μs to ms) are used for cell surgery and energy deposition is based on linear absorption, the possible spatial resolution is related to the temperature distribution in the focal region that is directly related to the irradiance distribution. By contrast, for femtosecond laser pulses, the spatial resolution is defined by the free electron distribution, which, for 800 nm wavelength, is proportional to the 5^{th} power of the irradiance distribution [1]. Due to the nonlinear absorption process underlying optical breakdown, the free-electron distribution is much narrower than the irradiance distribution. For $\lambda = 800$ nm, the diameter of the free -electron distribution at the $1/e^2$- values amounts to 336 nm, the length to 806 nm. Femtosecond-laser nanoprocessing can thus achieve a 2-3 fold better precision than cell surgery using cw irradiation, and enables manipulation at arbitrary locations.

4. CHEMICAL EFFECTS OF LOW-DENSITY PLASMAS

The lower end of the irradiance range useful for cell surgery is defined by the regime where the free electron density is still too low to cause any thermal or thermo-mechanical effects but sufficiently high to cause chemical changes arising from the action of the free electrons. One very important chemical effect

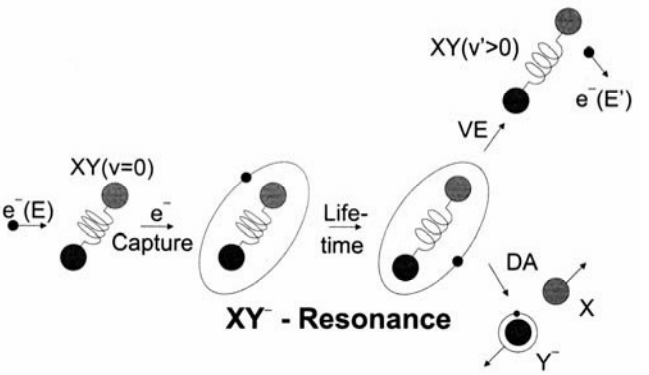

Fig. 2. Dynamics of vibrational excitation and dissociative electron attachment in resonant electron-molecule scattering. Reprinted with permission from Ref. [7].

is molecular bond breaking that can result from resonant interactions between electrons of 3 -20 eV kinetic energy and biomolecules (Fig. 2) [6].

The irradiance threshold for chemical changes can be assessed using the plot of free-electron density versus irradiance presented in Fig. 1d. At NA = 1.3 and λ = 800 nm, one free electron per focal volume corresponds to a density of $\rho = 2.1\times10^{13}$ cm^{-3}. This value is reached at an irradiance of $I = 0.26\times10^{12}$ W cm^{-2} which is 0.04 times the irradiance threshold for breakdown defined as $\rho_c = \rho_{cr} = 10^{21}$ cm^{-3}.

When long oscillator pulse series of ≈ 80 MHz repetition rate consisting of 10^4 to 10^6 pulses are employed, their accumulative chemical effects can lead to cell damage and, for larger irradiances, to dissection [1]. According to our calculations, the irradiance required for intranuclear chromosome dissection [8] amounts to 1/6 of the irradiance required to produce $\rho_{cr} = 10^{21}$ cm^{-3}, and about 1000 free electrons per pulse are produced with the parameters used for chromosome dissection [1].

5. THERMAL EFFECTS

The deposition of laser energy into the medium is mediated by the generation of free electrons. When the energy carried by the free electrons is subsequently transferred to the heavy particles in the interaction volume through collisions and nonradiative recombination, this results in a heating of the atomic, molecular and ionic plasma constituents.

The temperature rise can be determined by calculating the volumetric energy density gained by the plasma during the laser pulse. This calculation is particularly easy for femtosecond pulses because the pulse duration is

considerably shorter than the electron cooling and recombination times. Therefore, hardly any energy is transferred during the laser pulse, and the energy density deposited into the interaction volume is simply given by the total number density ρ_{max} of the free electrons produced during the pulse multiplied by the mean energy gain of each electron. The mean energy gain of an electron is, in turn, given by the sum of ionization potential and average kinetic energy. To calculate the temperature rise from the plasma energy density, we assumed that the thermal constants of tissue are equal to those of water. The evolution of the temperature distribution was then calculated by solving the differential equation for heat diffusion [1].

The results are presented in figure 3. They demonstrate that for repetition rates in the MHz range accumulative thermal effects are observed. For 80 MHz, the peak temperature after many pulses is up to 6.8 times higher than after a single pulse for NA = 1.3, and up to 45 times higher for NA = 0.6 (Figs. 3a, b). However, when the repetition rate is reduced to 1 MHz or smaller, heat accumulation disappears even for NA = 0.6 (Fig. 3c) because the narrow free electron distribution, which is the source of the heat deposition, leads to a very rapid heat diffusion.

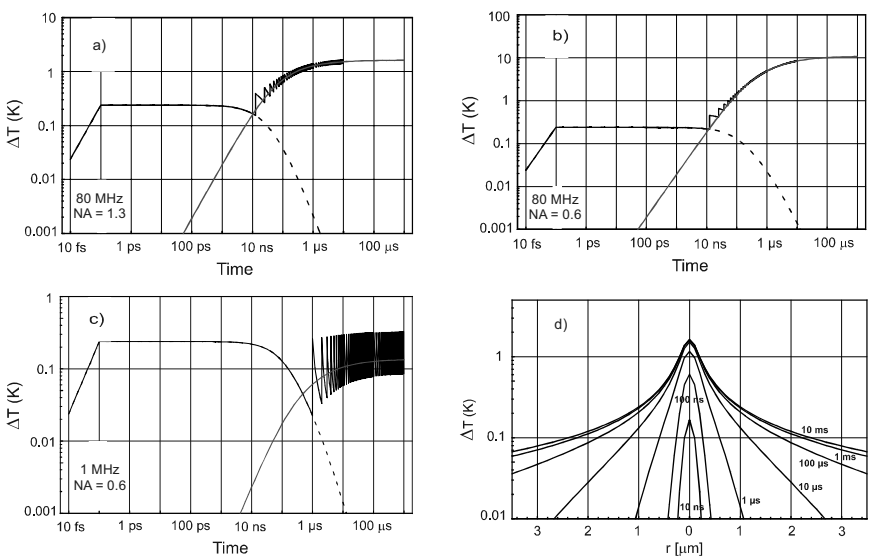

Fig. 3. Temperature evolution at the center of the laser focus produced by a series of 800-nm, 100-fs pulses focused into water (a-c), and the corresponding temperature distribution (d). a) 80 MHz repetition rate, NA = 1.3; b) 80 MHz repetition rate, NA = 0.6; c) 1 MHz repetition rate, NA = 0.6, d) 80 MHz repetition rate, NA = 1.3. The volumetric energy density deposited per pulse was always assumed to be 1 Jcm^{-3} at the focus center. The dashed lines in a) – c) represent the temperature decay after a single pulse. For comparison, the temperature evolution during cw irradiation with the same average power as for pulsed irradiation is also shown. Reprinted with permission from Ref. [1].

When laser surgery is performed with 80 MHz pulse series focused at NA = 1.3, the boiling temperature of 100°C will, due to the 6.8-fold temperature accumulation, be reached when each individual pulse produces a temperature rise of 11.8°C (starting from 20°C room temperature). For 800-nm, 100-fs pulses this temperature rise requires a free-electron density of $\rho_c = 2.1\times10^{19}$ cm^{-3}, which is reached at an irradiance of 0.51 times the value required for optical breakdown ($\rho_{cr} = 10^{21}$ cm^{-3}).

For NA = 1.3, the heat distribution exhibits a half-width in the submicrometer-range, as shown in Fig. 3d. Thermal effects are thus confined to a very small volume, even for long pulse series for which the thermal distribution resembles that of cw irradiation. However, it needs to be kept in mind that no purely thermal effects can be produced with femtosecond pulses, because due to the nonlinear absorption of the laser light heat generation is always mediated by the production of free electrons. For example, each pulse of a series leading to a final temperature of 100°C (at NA = 1.3) produces ≈ 2 Mill. free electrons. The thermal effects are, therefore, always accompanied and probably dominated by free-electron-mediated chemical effects.

For even larger irradiances, thermo-mechanical effects (bubble formation) come into play. When bubbles are formed during cell surgery with oscillator pulse series (≈ 80 MHz), they arise from accumulative chemical bond breaking and photothermolysis. They are long lasting, can grow to a fairly large size, and their appearance defines the upper limit of the useful parameter range for cell surgery with oscillator pulse series.

6. THERMOELASTIC STRESS EVOLUTION

In the single pulse regime ≤ 1 MHz, where no temperature accumulation occurs, bubbles are produced by thermo-elastically induced tensile stress. In femtosecond optical breakdown, laser pulse duration and thermalization time of the energy of the free electrons are much shorter than the acoustic transit time from the center of the focus to its periphery. Therefore, no acoustic relaxation is possible during the thermalization time, and the thermo-elastic stresses caused by the temperature rise stay confined in the focal volume, leading to a maximum pressure rise [9, 10]. Conservation of momentum requires that the stress wave emitted from the focal volume must contain both compressive and tensile components such that the integral of the stress over time vanishes. In water or biological cells, the tensile stress wave will cause the formation of a cavitation bubble when the rupture strength of the liquid is exceeded. For cell surgery in the single pulse regime, the threshold for bubble formation defines the onset of disruptive mechanisms contributing to dissection.

To determine the evolution of the thermo-elastic stress distribution in the vicinity of the laser focus, we solved the three-dimensional thermo-elastic wave

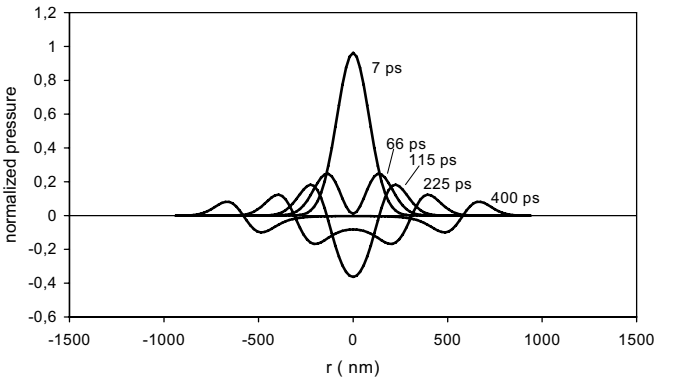

a)

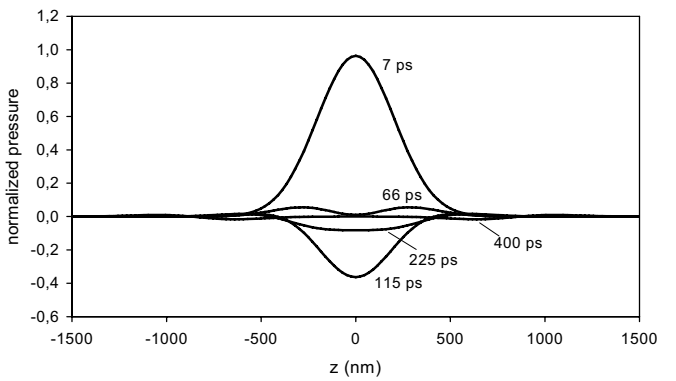

b)

Fig. 4. Stress distribution produced by a single 800-nm, 100-fs pulse focused into water (NA = 1.3). The evolution of the distribution is shown (a) in radial direction, and (b) in axial direction for various times after the release of the laser pulse. The pressure amplitudes are normalized to the peak compressive stress created in the focal volume. Reprinted with permission from Ref. [1].

equation arising from the temperature distribution at the end of a single femtosecond laser pulse [1]. The result is presented in figure 4.

7. BUBBLE FORMATION

Because the region subjected to large tensile stress amplitudes is very small, the presence of inhomogeneous nuclei that could facilitate bubble formation is unlikely, and we have to consider the tensile strength of pure water to estimate the bubble formation threshold. We use the crossing of the "kinetic spinodal" as defined by Kiselev [11] as threshold criterion for bubble formation. In the thermodynamic theory of phase transitions, the locus of states of infinite

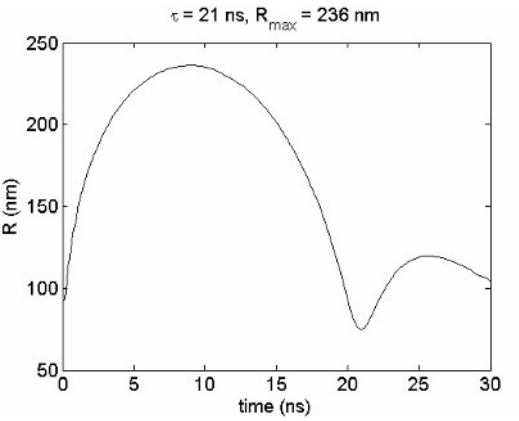

Fig. 5. Calculated radius time curve of the cavitation bubble produced by a single 800-nm, 100-fs laser pulse focused at NA = 1.3 that leads to a peak temperature of T_{max} = 200 °C at the focus center. Isothermal conditions for the bubble content with respect to the surrounding liquid were assumed. Reprinted with permission from [1]

compressibility $(\delta p / \delta V)_T = 0$, the spinodal, is considered as a boundary of fluid metastable (superheated) states. Physically, however, the metastable state becomes short-lived due to statistical fluctuations well before the spinodal is reached. The "kinetic spinodal" is the locus in the phase diagram where the lifetime of metastable states becomes shorter than a relaxation time to local equilibrium. For 20°C start temperature, the kinetic spinodal of water is reached at ΔT = 131.5°C, and p = - 71.5 MPa.

For superthreshold pulse energies, the size of the bubble nucleus was identified with the extent of the region in which the negative pressure exceeds the kinetic spinodal limit. The bubble dynamics was then calculated by means of the Gilmore model, taking the tensile stress around the bubble and the vapor pressure inside the bubble into account as driving forces for the bubble expansion. In these calculations, we considered the temperature-dependence of the surface tension at the bubble wall. An example for the bubble dynamics after a temperature rise from room temperature to 200°C is given in Fig. 5, and the dependence between maximum bubble size and end temperature is presented in Fig. 6. Our experimental results on stress amplitudes at the bubble formation threshold agree very well with the calculated values, as described in Ref [1].

The most prominent feature of the transient bubbles produced close to the threshold of femtosecond optical breakdown is their small size and short lifetime. The bubble radius in water right at threshold is as small as 50 nm, and it amounts to about 200 nm for a peak of 200°C temperature in the focus center. The bubbles will be even smaller in a visco-elastic medium such as the

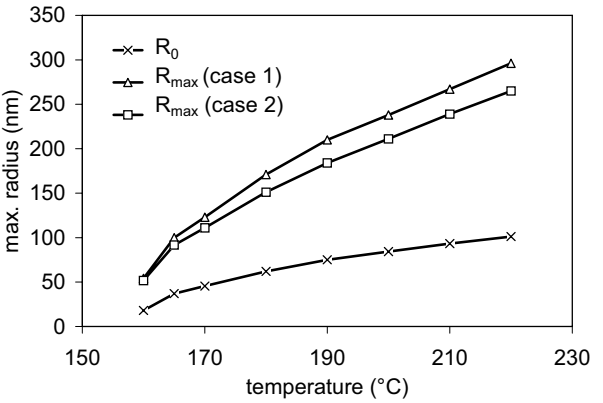

Fig. 6 Maximum bubble radius R_{max} as a function of the peak temperature in the center of the focal volume, together with the radius of the nucleus, R_0. Cases 1 and 2 stand for isothermal and adiabatic conditions for the bubble content with respect to the surrounding liquid. The calculation were pefformed for 800-nm, 100-fs pulses. Reprinted from Ref. [1]

compatible with intracellular nanosurgery, in contrast to nanosecond optical breakdown where the minimum bubble radius in water observed for NA = 0.9 and λ = 532 nm was R_{max} = 45 μm [12]. The small bubble size corresponds to a small energy of only 53 femtoJoule of the expanded bubble for the case presented in Fig. 5. The smallness of the bubble energy is largely due to the minute energy content of the stress transient creating the bubble. For the case of Fig. 5, the energetic conversion efficiency from heat into the thermo-elastic wave is only 0.46%, and the conversion efficiency from thermo-elastic energy into bubble energy is 6.8%.

The stress-confinement of the energy deposition in femtosecond laser induced material processing results in large compressive and tensile stress amplitudes already after a moderate temperature rise. Therefore, a temperature rise as little as 131.5 °C is sufficient for bubble generation in a liquid without any pre-existing nuclei. The low volumetric energy density required for thermoelastically induced cavity formation, which is only about 1/5 of the vaporization enthalpy, is a reason for the lack of thermal side effects in femtosecond laser dissection and the small conversion rate of laser energy into mechanical energy. Nevertheless, for sufficiently large pulse energies, bubble expansion and shock wave pressure can cause effects far beyond the focal volume that lead to cell death. This is especially important for applications such as optotransfection (transient cell membrane permeabilisation for transfer of genes or other substances into live cells). To avoid unwanted side effects, irradiances should be used that are only slightly above the bubble formation threshold.

8. EXPERIMENTAL DETERMINATION OF BREAKDOWN THRESHOLD AND BUBBLE SIZE

Figure 7 shows a schematic drawing of the experimental setup for our experimental investigations of femtosecond optical breakdown in water at large NA. The laser pulses are generated by an Yb:glass laser system IC-1045-30-fs Reg Amp/SHG/THG (High Q Laser Production). This laser system delivers amplified pulses with 315 fs duration, a center wavelength of $\lambda = 1040$ nm, and up to 30 μJ pulse energy at 1 kHz repetition rate. With a combination of two fast shutters (Uniblitz electronics), single pulses can be selected out of the 1 kHz repetition rate signal. The oscillator leakage is suppressed by means of an external pockels cell (Linos LM0202P).

The precise energy adjustment of the pump beam required for a determination of the optical breakdown threshold is achieved by combinations of $\lambda/2$ plates and thin film polarizers, the transmission of which depends on the polarization angle of the incident light. The energy of the laser pulses is measured by diverting a part of the pump beam onto an energy meter (Ophir PD10-pJ).

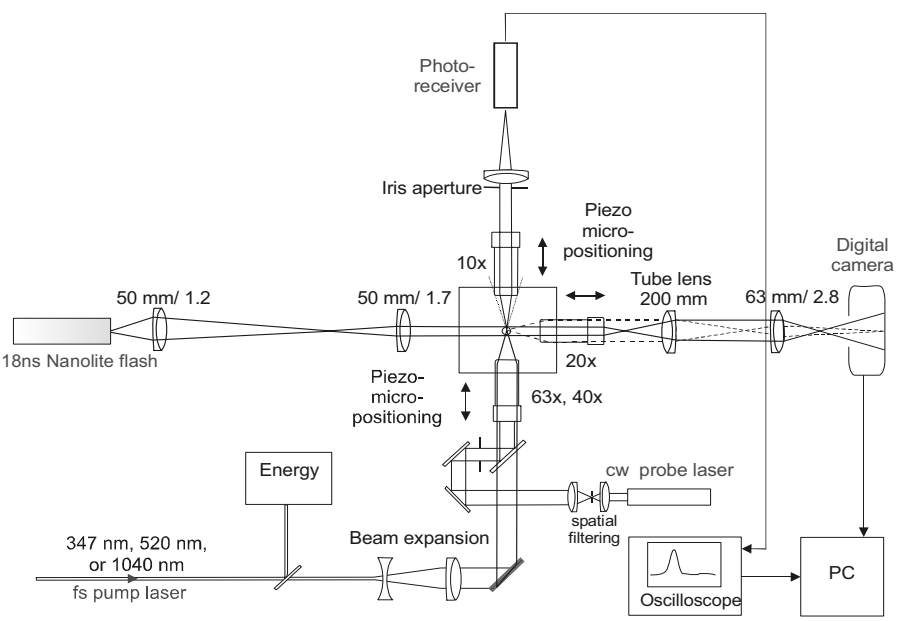

Fig. 7. Setup for the determination of the breakdown threshold and the energy-dependent maximum cavitation bubble size.

The calculations in the previous section showed that for optical breakdown at large NA the bubble size expected near threshold is well below the optical resolution limit (Fig. 6). Therefore, a direct photographical observation is impossible. Instead, we used a time-resolved detection of the scattering of a probe laser beam to determine the bubble size via a measurement of its oscillation time. To validate the scattering technique, its results for energies well above the bubble formation threshold were compared with photographically determined bubble sizes.

The core of the setup is a water-filled cuvette with three water immersion microscope objectives built into the cuvette walls that can be confocally adjusted. The cw probe laser beam (658 nm, 25 mW) is aligned collinear with the fs-pump beam and delivered through the focusing objective. The transmitted light is collected by a second microscope objective built into the opposite cell wall. Larger bubbles could be photographed through a third microscope objective (20x) oriented perpendicular to the optical axis of the pump and probe beams.

Axial adjustment for precise focusing and confocal alignment of the three objectives is achieved by piezo-driven micropositioners. When the 40x objective was used to focus the fs-pulses, we could achieve a confocal arrangement with the 20x imaging objective at correct working distance for all objectives. This was not possible with the 63x objective. For illumination of the focal region, we used a Nanolite flash lamp with 18 ns pulse duration. To be able to image very small bubbles near the optical resolution limit, the image formed by the 20x objective and tube lens was further magnified using a Nikkor objective (63mm/1:2,8) that is corrected for 8x magnification. This way, we achieved a total magnification factor of 162.

The scattering signal is detected by an AC-coupled high speed photoreceiver (FEMTO, HCA-S) with a signal bandwidth from 25 kHz to 200 MHz and an additional monitor output of the DC signal that is important for the basic alignment of the entire setup. When the bubble size is much smaller than the focus of the probe laser beam, the scattering signal is much smaller than the total amount of the light transmitted through the focal volume. AC coupling is very useful to remove this bias. The duration of the scattering signal equals the oscillation time of the bubble in the focal volume.

The bubble formation threshold energy was 22.6 nJ for the 40x, NA = 0.8 objective, corresponding to a radiant exposure of 1.15 J/cm^2 averaged over the focal spot. The maximum bubble radius $R_{\max}$ was calculated from the bubble oscillation time T_{osc} using the Rayleigh equation

$$R_{\max} = (T_{osc} / 1.83)\left[(p_\infty - p_{v_0}) / \rho_0\right]^{1/2}, \tag{3}$$

where p_∞ is the hydrostatic pressure, p_v the vapor pressure inside the bubble, and ρ_0 the mass density of the liquid [13]. Figure 8 shows the results of the probe beam scattering technique, together with the photographically determined values of the bubble size.

For large bubbles, the agreement between the results obtained with both measurement techniques is very good. Close to threshold, the maximum cavitation bubble radius is well below the optical resolution limit and very close to the values predicted by our model calculations (see Fig. 6). However, it must be noted that for bubble sizes close to the optical resolution limit, the Rayleigh equation yields radius values that are considerably smaller than the photographic values. This discrepancy can be explained by the fact that the Rayleigh formula was derived without consideration of surface tension, which exerts a pressure $p = 2\sigma/R$ in addition to the hydrostatic pressure. The pressure by surface tension can be neglected for large bubbles but becomes important for bubble radii of a few μm or below. In water at room temperature, the surface tension against air is 0.073 N/m, and the corresponding pressure acting on bubbles of for example 100 nm radius is 1.46 MPa. Since this value is much larger than the hydrostatic pressure of 0.1 MPa, surface tension will considerably alter the relationship between bubble oscillation time and maximum radius. It will shorten the oscillation time for a given radius and, vice versa, the actual radius for a measured oscillation time will be larger than the radius predicted by Eq. (3).

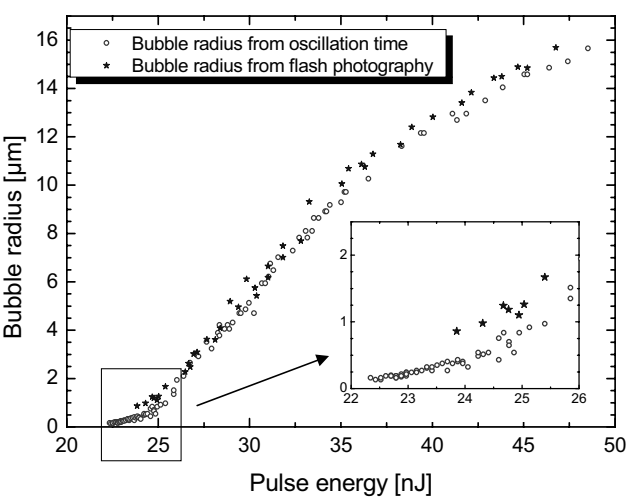

Fig. 8. Bubble radius determined by photography and probe beam scattering. 40x objective, NA = 0.8, λ = 1064 nm.

9. IMPLICATIONS FOR LASER EFFECTS ON CELLS AND TISSUES

An overall view of physical effects induced by femtosecond laser pulses in comparison to experimental data on cell surgery is given in figure 9. It allows to assess the working mechanisms in the different regimes of nanosurgery. Dissection at 80 MHz repetition rate is performed in the low-density plasma regime at pulse energies well below the optical breakdown threshold. It is mediated by free-electron-induced chemical decomposition (bond breaking) in conjunction with multiphoton-induced chemistry, and not related to heating or thermo-elastic stresses. When the energy is raised, long-lasting bubbles are produced by accumulative heating and tissue dissociation into volatile fragments that are usually unwanted. By contrast, dissection with 1 kHz repetition rate is performed using about 10-fold larger pulse energies and relies on thermo-elastically-induced formation of minute transient cavities with life times < 100 ns. Both modes of fs-laser nanoprocessing can achieve a 2-3 fold better precision than cell surgery using cw irradiation (see section 3) and enable manipulation at arbitrary locations [1].

Besides for nanoprocessing of biological materials, femtosecond laser induced plasmas can also be used to modify other transparent materials and enable the generation of photonic elements in bulk glass and fused silica. The

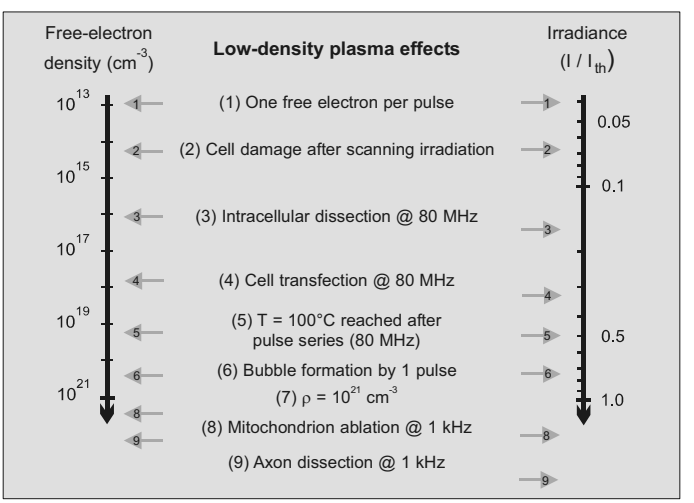

Fig. 9. Overall view of physical breakdown phenomena induced by femtosecond laser pulses, together with experimental damage, transfection and dissection thresholds on cells, scaled by free-electron density and irradiance. The irradiance values are normalized to the optical breakdown threshold I_{th} defined by $\rho_{cr} = 10^{21}$ cm^{-3}. All data refer to plasma formation in water with femtosecond pulses of about 100 fs duration and 800 nm wavelength. Reprinted from [1].

process of plasma generation and void formation in the bulk of dielectrica like fused silica and glass resembles the process in water, and the methods developed in our study can also be applied to solid dielectrica. However, differences in the band gap energy and material properties will lead to somewhat larger threshold values for chemical and thermo-mechanically induced changes in solids compared to aqueous media.

REFERENCES

[1]A. Vogel, J. Noack, G. Hüttman, and G. Paltauf, Appl. Phys. B 81 (2005) 1015.
[2]S. S. Mao, F. Quéré, S. Guizard, X. Mao, R.E. Russo G. Petite, and P. Martin, Appl. Phys. A 79 (2004) 1695.
[3]B. C. Stuart, M.D. Feit, S. Hermann, A.M. Rubenchik, B.W. Shore, and M.D. Perry, Phys. Rev. B 53 (1996) 1749.
[4]A.P. Joglekar, H. Liu, E. Meyhöfer, G. Mourou, and A.L. Hunt, Proc. Nat. Acad. Sci. 101 (2004) 5856.
[5]S. Grill, and E. H. K. Stelzer, J. Opt. Soc. Am. A 16 (1999) 2658.
[6]B. Boudaiffa, P. Cloutier, D. Hunting, M.A. Huels, and L. Sanche, Science 287 (2000) 1658.
[7]H. Hotop, Proceedings of the International Symposium on Gaseous Dielectrics, ed. by L.G. Christophorou and J.K. Olthoff, Kluwer Academic/Plenum, New York, 2001, p. 3.
[8]K. König, I. Riemann, P. Fischer, and K. Halbhuber, Cell. Mol. Biol. 45 (1999) 195.
[9]A. Vogel, and V. Venugopalan, Chem. Rev. 103 (2003) 577.
[10] G. Paltauf, and P. Dyer, Chem. Rev. 103, (2003) 487.
[11] S.B. Kiselev, Physica A 269 (1999) 252.
[12] V. Venugopalan, A. Guerra, K. Nahen, and A. Vogel, Phys. Rev. Lett. 88, (2002) 078103.
[13] L. Rayleigh, Philos. Mag. 34 (1917) 94-98

Handai Nanophotonics, Volume 3
H. Masuhara, S. Kawata and F. Tokunaga (Editors)

Chapter 19

Femtosecond laser nanomachining of silicon wafers and two-photon nanolithography for stem cell research

K. König[1,2], F. Bauerfeld[1], D. Sauer[1], H. Schuck[1], A. Uchugonova[1], E. Lei[1], M. Stark[1], T. Velten[1], R. Bückle[3], R. LeHarzic[3]

[1]Fraunhofer Institute of Biomedical Technology (IBMT),
D-66386 St. Ingbert, Germany

[2]Saarland University, Faculty of Mechatronics and Physics,
Saarbrücken, Germany

[3]JenLab GmbH, www.jenlab.de, Schillerstrasse 1, D-07745 Jena, Germany

1. INTRODUCTION

Conventional laser ablation of materials with high energy laser systems, such as ultraviolet (UV) nanosecond excimer lasers, picosecond solid state lasers, and amplified near infrared (NIR) femtosecond lasers, is a well established technology. Major disadvantages include difficulties to realize precise in-bulk processing and the requirement of expensive and large-dimension equipment. Typical laser pulse energies are in the range of microjoule up to millijoule. So far, high energy laser pulses in the UV are required to realize sub-100nm features in silicon wafers.

König et al. [1] demonstrated the possibility to fabricate sub-100 nm features in biological materials by multiphoton effects with low nanojoule energy NIR laser pulses at high MHz repetition frequency. Applications include chromosome nanodissection [1], nanohole drilling in cellular membranes for targeted transfection [2], and intracellular and intratissue nanosurgery [3-4]. The sub-wavelength cut size was found to be far below the diffraction-limited spot size and can be explained by multiphoton effects induced in a sub-femtoliter volume within the central part of the focused beam. When employing single metallic nanobeads coupled to specific genomic regions of a human chromosome, the damage zone can be further reduced to a 50 nm hole. To our knowledge, this is the smallest laser induced feature in biological specimens [5].

The procedures do not require expensive amplified femtosecond laser systems and can be performed with ultracompact turn-key laser resonators in combination with high numerical aperture (NA) focussing optics at low 0.5 – 5 nJ pulse energies and high 80/90 MHz repetition frequency.

Goal of this study was to explore the feasibility of nanojoule NIR MHz femtosecond laser pulses for nano- and microprocessing of non-biological materials, such as silicon wafers, metal films, and polymers based on multiphoton ablation as well as two-photon polymerization.

Three-dimensional microstructuring based on two-photon polymerization has been pioneered by Kawata's group in Japan [6]. They used NIR titanium:sapphire lasers in combination with stage-scanning and high NA focussing optics to realize mask-less illumination of photoresists.

Here we report on nanostructuring based on two-photon polymerization and direct laser writing with beam scanning units and high-NA objectives. In particular, the compact laser scanning microscope FemtOcut (JenLab GmbH) with fast galvoscanners attached to the microscope`s side/back ports have been employed to realize rapid prototyping of nanonstructures in silicon and photoresists and to study the cell-nanostructure interaction.

2. MATERIALS AND METHODS

2.1. Laser microscopes for nanoprocessing and high-resolution imaging

The laser microscope system FemtOcut (JenLab GmbH) was employed to perform nanoprocessing in combination with 3D-imaging for target search and the proper adjustment of the laser beam for nanoprocessing. FemtOcut is based on an inverted compact fluorescence microscope with x,y galvoscanner and piezodriven high-NA objective in combination with the compact tunable Ti:sapphire lasers MaiTai (Spectra Physics, 80 MHz, <100 fs pulse width, 720 – 960 nm) and Chameleon (Coherent, 90 MHz, <100 fs, 730 – 960 nm). The microscope is further equipped with a Hamamatsu photomultiplier of short rise time, short pass safety filters and safety shutter, beam expander, power sensor, step-motor driven beam attenuator, a control unit, and a fast shutter to vary the number of applied pulses for nanomachining from about 300,000 to 90 million pulses. Typically, a 40x NA 1.3 oil objective has been used to focus the laser beam onto the target which was positioned on a coverslip. In part, a motorized stage (object scanning) has been employed in addition to the galvoscanners (beam-scanning). Fig. 1 shows a photograph of the compact laser tool for nanomachining, maskless nanolithography, and high-resolution imaging.

The JenLab Scan software allows full-frame scanning, scanning of region of interests, single line scanning for cutting as well as single-point illumination for drilling. Conventional imaging can be realized by reflectance, transmission and one-photon fluorescence detection. In addition, two-photon fluorescence and

detection of second harmonic generation (SHG) can be realized by correlation of the luminescence signal with the scanner position as defined by the parameters frame sync, line sync, pixel clock, and piezo voltage.

FemtOcut can also be transferred into an additional 5D imaging tool with submicron spatial resolution, <250 ps temporal resolution and <10 nm spectral resolution when combined with time-correlated single photon counting (TCSPC) units and spectral imaging devices such as the Spectra Cube based on a Sagnac interferometer or polychromators with multiple PMT arrays.

The laser power after transmission through the whole microscope was measured in air using a Fieldmaster power meter (Coherent, USA) with the two detector heads LM-2 and LM-3. In order to correct for the true photon flux through oil and the glass window as well as for the limited detection angle of the power detector heads, correction values of 1.1 and 2.0 had been determined using a sandwich system consisting of two objectives aligned in such a way that the have the same focus position. The overall transmission at 800 nm was found to be typically in the range of 30 % (depends on the ratio of laser beam diameter - objective's aperture).

Optical dispersion results in pulse broadening during transmission through the microscope optics. Typically, the pulse width at the sample was about 200 fs – 270 fs as measured with a special autocorrelator with nonlinear semiconductor sensor positioned at the microscopes focus of the high NA objective. This correlates to dispersion values of about 5000 fs^2.

At 80 mW mean power (80 MHz fs pulses, 1 nJ pulse energy), the peak power and the peak intensities reaches values of ~6 kW and 10^{13} W/cm^2 (10 TW/cm^2), respectively, when assuming a full width half maximum (FWHM) beam size of $\lambda/(2NA)\approx310$ nm. A typical beam dwell time (time of exposure per pixel) during one 512x512 pixel scan was about 30 µs which resulted in a frame rate of 8 s/frame. At zoom setting 2, 512 x 512 pixels covered an area of 160 µm x 160 µm. The mechanical shutter allowed minimum exposure times of 1/125 s and 640,000 laser pulses, respectively.

In addition to the compact microscope FemtOcut, the ZEISS microscope LSM510-NLO-Meta with the feature of spectral imaging has been employed for nanoprocessing.

2.2. Principle of multiphoton nanoprocessing

Light intensities in the TW/cm^2 range can cause optical breakdown phenomena resulting in plasma formation and destructive thermomechanical effects. The threshold for optical breakdown decreases with the pulse width. In water, the threshold for 100 fs pulses was found to be 2 orders lower than for 6 ns pulses. The primary cause for optical breakdown in the case of femtosecond pulses in transparent material is efficient multiphoton absorption. Inverse Bremsstrahlung and collision processes are not dominant. The onset of optical

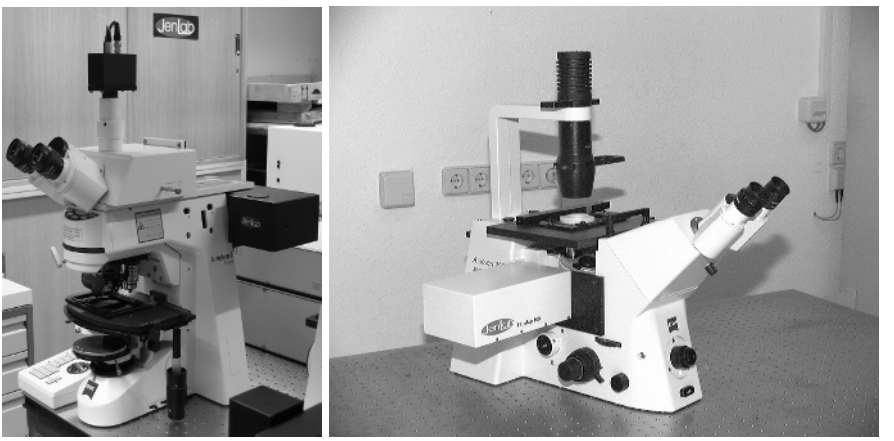

Fig. 1. Photographs of the compact laser scanning microscope FemtOcut™ (JenLab GmbH) for nanoprocessing and multidimensional imaging

optical breakdown depends on the material. For some materials, femtosecond laser pulses at light intensities of about 0.1 TW/cm^2 are sufficient to induce destructive low-density plasma effects [7].

Non-destructive two-photon induced photochemical reactions such as photopolymerization occur when working at lower GW/cm^2 laser intensities and pJ laser pulse energies, respectively. The epoxy based photoresist SU8 absorbs mainly below 400 nm. In conventional lithography SU-8 is illuminated with 365 nm light of a mercury lamp or by UV lasers. In this study, the polymer was excited by 730 nm laser light by the flying-spot technology within the bulk of the photoresists.

.2.3. Materials

Silicon wafers, gold films, and polymers such as the photoresist SU-8 50 (MicroChem Corporation, Newton, MA) has been used as materials for laser nanoprocessing. The photoresist was spun on 4" Si wafers at a typical final thickness of 50 µm. The wafers were precleaned by water rinsing to remove particles, heated to remove OH-groups, and activated to improve adhesion. Afterwards, the photoresist was applied by spin-coating at up to 3000 rpm and three-stage soft baking.

2.4. Cells

CHO (Chinese Hamster Ovary) cells grown at 37°C, 5% CO_2, in culture medium HAMs F12 (Biochrom KG, Berlin) with 10 % FCS and Pen/Strep/Amp antibiotica-mix (Sigma) were used to probe cell-nanopattern interaction. In addition, adult human dental pulpa stem cells (DPSC) have been employed.

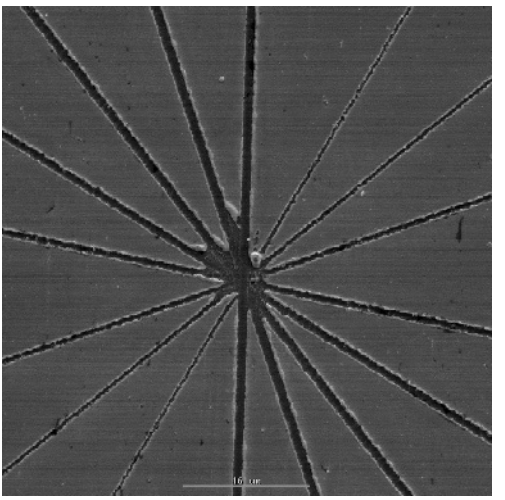

Fig. 2. Nano- and microprocessing of thin gold films

3. RESULTS

3.1. Nanostructering based on multiphoton ablation

Experiments on direct laser writing were typically performed in the line-scan mode with 512 pixels per line, a beam dwell time of up to 400 μs per pixel (200 ms per line), a wavelength of 800 nm, and pulse energies of 1–3.5 nJ. The laser exposure was performed at atmospheric pressure. Interestingly, a variety of materials including silicon, polymers and gold could be laser-processed with high accuracy and cut widths in the submicron range. Fig. 2 demonstrates laser-processed 40nm thin gold films. Different line scans have been performed in dependence on pulse energy. Using 1 nJ, sub-200nm laser dissections have been achieved.

More interestingly, laser-processing of silicon wafers resulted in the formation of two types of nanostructures: nanocones and ripples. The superficial layer contained non-homogeneously distributed laser-induced nanocones representing non-coherent structures. A second highly coherent "ripple" structure was detected after removing this layer by etching with ammonium fluoride. Surprisingly, these symmetric laser-induced periodic structures (LIPPS) possessed a wavelength (distance) of 50–80 nm only which is one order below the laser wavelength and far below the "Abbe's diffraction limit" (Fig. 3). Note that normally deep UV sources are required to realize sub-100 nm features on wafers. We used the possibility to generate nanoripples for regular nanostructuring of certain areas of the silicon wafer by a combination of beam-scanning and stage-scanning. Fig. 4 demonstrates a chess-like nanostructured field.

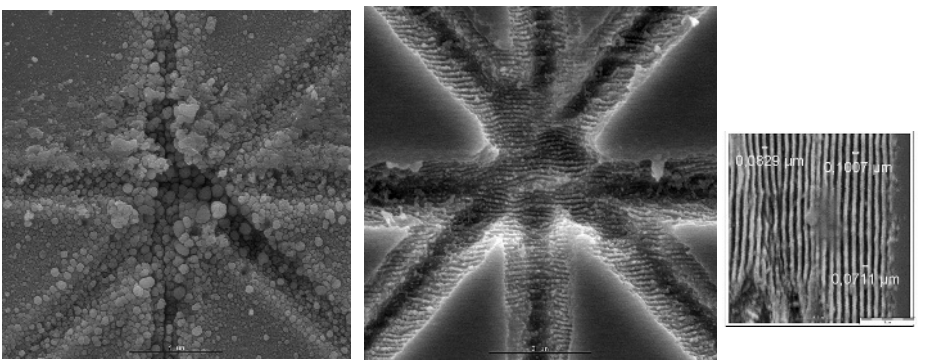

Fig. 3. Nanostructering of silicon wafers. Non-coherent nanocones and coherent sub-100nm ripples are fabricated [8].

3.2. Two-photon polymerization

Two-photon polymerization was realized based on the mask-less laser exposure of a 50µm thin photoresist SU8 layer on silicon substrates with tight focussed femtosecond laser beams at 730 nm and 250 pJ laser pulse energy. A typical scan field of 230x230 μm^2 representing 512x512 pixels was chosen and exposed within with a beam dwell time per pixel of 1.6 µs. We performed x,y galvoscanning from the bottom to the top by a piezodriven variation of the focal plane in z-steps of 250 nm. Subsequent etching led to the formation of two-photon-fabricated microcages. When probing the bottom of such laser-fabricated cages by means of atomic force microscopes we found regular nanopatterns aligned along the x-scan direction with a typical depth of 150 nm (Fig. 4). The space between these regular nanofeatures were found to be depend on the lateral

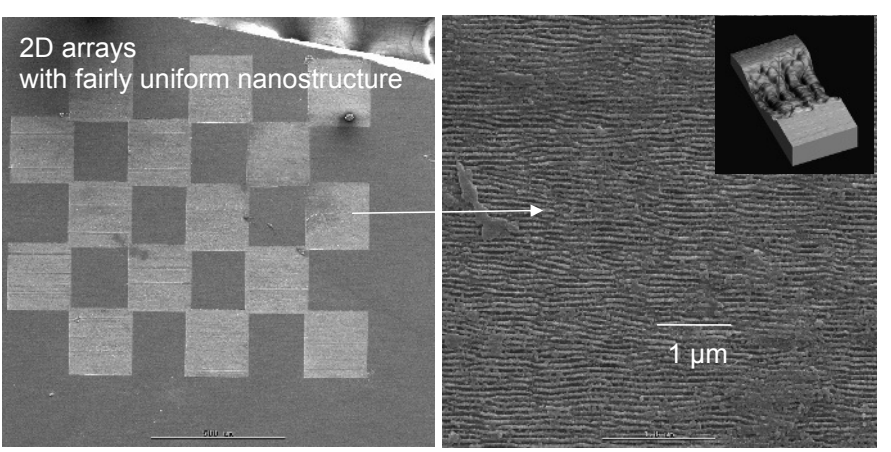

Fig. 4 Nanostructured chess patterns in silicon wafers

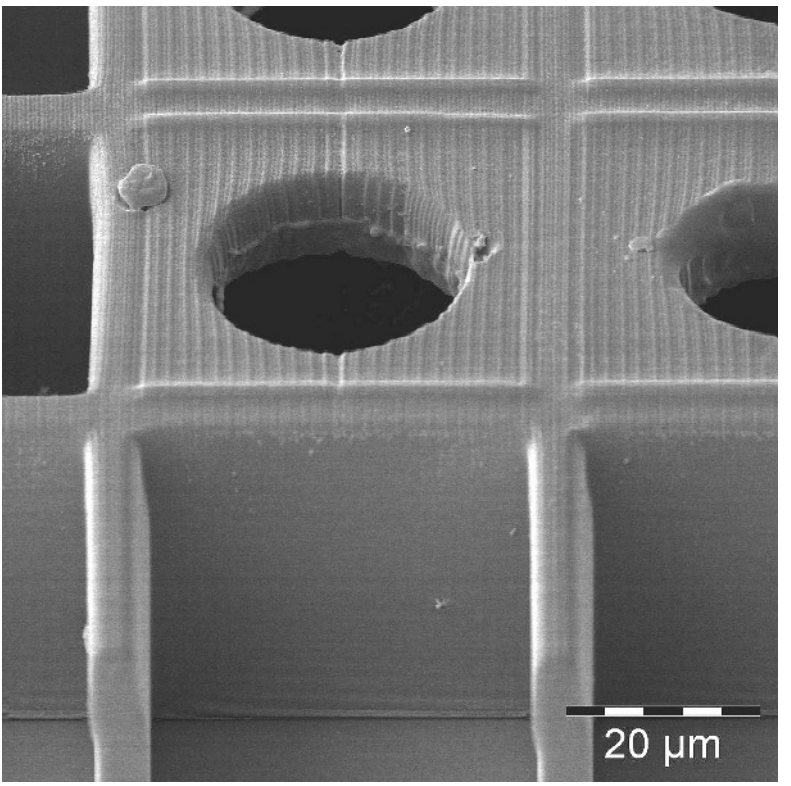

Fig. 5. Photofabricated microcage with nanostructured surfaces.

distance between two subsequent scans. For 512 lines covering a distance of 200 µm, the spacing was found to be 200 µm/512 = 400 nm.

First studies on the interaction of CHO and DPSC stem cells with these nanostructured microcages showed the biocompability and the impact of the nanostructured surfaces. Single cells attached to the surfaces and aligned with an orientation predominantly along the parallel nanofeatures. In contrast, cells attached to surfaces without nanotopography in the periphery show random orientation. We were also able to produce 3D spiral cages with different diameters. Interestingly, stem cells aligned along these curved surfaces and spread as curved cells with exactly the same geometry (Fig. 6).

4. CONCLUSIONS

Multiphoton absorption in highly confined sub-femtoliter focal volumes based on the application of low pJ and nJ NIR femtosecond laser pulses can be used to realize complex three-dimensional nano- and microstructures by ablation as well

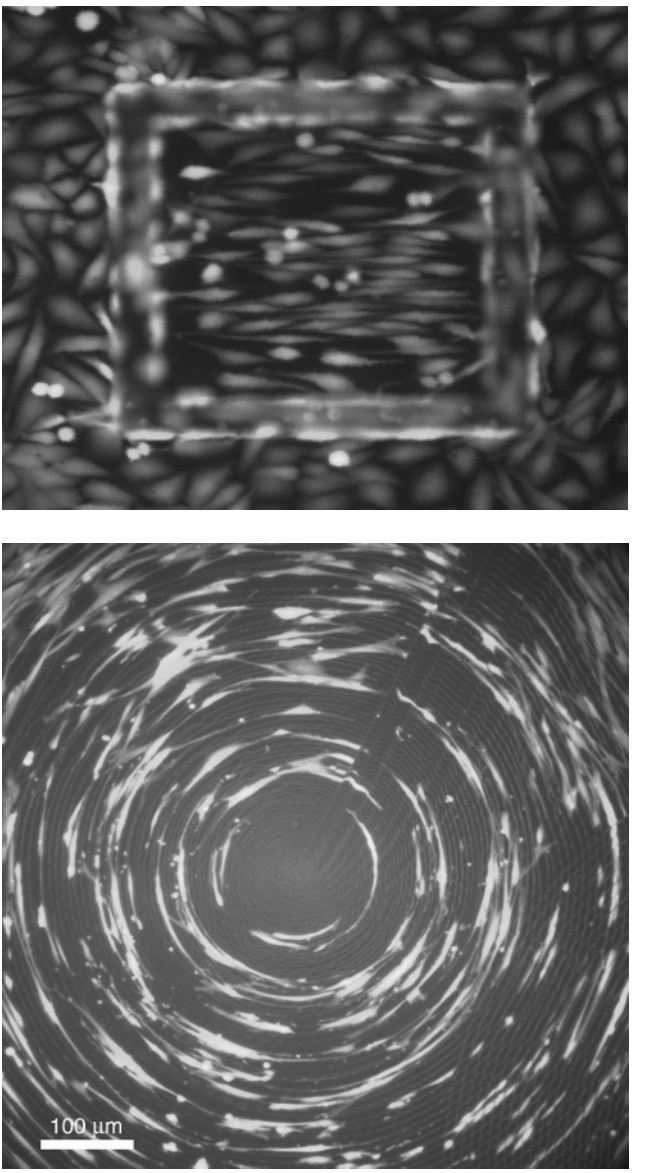

Fig. 6. Cell alignment along sub-100nm parallel nanostructures within a microcage and along femtosecond laser fabricated spirals.

as by two-photon polymerization. The compact galvoscan laser microscope FemtOcut™ based on turn-key MHz femtosecond laser resonator technology was found to be a promising tool for rapid prototyping of 3D nanostructures.

Interestingly, coherent nanopatterns in silicon with sub-100 nm features due to the formation of laser induced periodic surface structures (LIPSS, ripples) have been obtained with long-wavelength near infrared photons. The ripple formation is a well known phenomenon which was first described by Birnbaum 4 decades ago after he exposed semiconductor surfaces with a ruby laser[9]. In general, LIPPS can be generated in a variety of materials. The required laser intensity for ripple formation in semiconductors is significantly lower as in metals likely due to the lower melting threshold. It is assumed that ripples originate from the interference of the incident and the reflected light with the scattered (diffracted) laser light which may excite a real surface electromagnetic wave (SEW) near the interface. Typically, the resulting size of the emerging structures (distance between ripples) is on the order of the laser wavelength. It was believed that the ripple period d has to be related to Rayleigh's diffraction condition $d = \lambda/(1\pm\sin\alpha)$ with the angle α of laser beam incidence where the negative and the positive signs correspond to forward and backscattered light, respectively.

However, ripple formation with a size up to 5 times smaller than the laser wavelength has been reported on crystalline III-V semiconductors and sapphire when using NIR femtosecond laser pulses of 0.3 – 2 μJ pulse energy provided by an optical parametric amplifier pumped by another 50 fs Ti:sapphire regenerative amplifier[10,11]. Daminelli et al. reported on λ/8 ripples (λ: 800nm) when using liquid microenvironment and 3-250 μJ laser pulses[12]. Sub-wavelength ripple formation was not obtained in air.

Here we report on λ/11 ripple formation in silicon wafers with 3 nJ laser pulses at a high repetition frequency of 80 MHz pulses and the use of oil immersion objectives. Further studies have to be performed in order to understand the mechanism and to prove if self-organization processes starting after the multiphoton excitation process are responsible for this phenomenon.

One of the potential applications of surfaces with nanotopography is the manipulation of biological specimens, in particular the differentiation of stem cells[13,14]. It should be mentioned within this context, that collagen as the major component of our extracellular matrix which provides the 3D environment for intratissue cell organization is based on fibrils with a typical diameter in the range of 20–200 nm.

We believe that sub-200nm laser nanomachining with the novel tool of nanojoule MHz NIR femtosecond laser scanning microscopes is potentially useful for the fabrication of optical data storage devices, waveguides, photonic crystals, gratings, nano- and microfluidic systems, nano- and microcontainers, and cell sensors as well as to manipulate cells including the controlled differentiation of stem cells and to create biomaterials and scaffolds for tissue nanoengineering and implant technology.

ACKNOWLEDGEMENTS

This project is supported by the European Commission (CellPROM, no. NMP4-CT-2004-500039).

REFERENCES

[1] K. König, I. Riemann and W. Fritzsche, Opt. Lett. 26 (2001) 819.
[2] U.K. Tirlapur and K. König, Nature 418 (2002) 290.
[3] K. König et al., Optics Express 10 (2002) 171.
[4] K. König et al., Med. Laser Appl. 20 (2005) 169.
[5] K. König et al,. SPIE-Proceed. 5462 (2005).
[6] S. Kawata et al., Nature 412 (2001) 697.
[7] A. Vogel et al., Appl. Phys. B 81 (2005) 1015.
[8] R. LeHarzic et al., Optics Express 13 (2005) 6651.
[9] M. Birnbaum, J. Appl. Phys. 36 (1965) 3688.
[10] A. J. Pedraza et al., Appl Phys A 77 (2003) 277.
[11] Borowiec and H.K. Haugen,. Appl. Phys. Lett. 82 (2003) 4462.
[12] G. Daminelli et al., Thin Solid Films 467 (2004) 334.
[13] D.G. Anderson et al., Nature Biotech 22 (2004) 863.
[14] G.A. Silva et al. Science 27 (2004) 1352.

Handai Nanophotonics, Volume 3
H. Masuhara, S. Kawata and F. Tokunaga (Editors)

Chapter 20

Gold nanorods: application to bioscience and medicine

Y. Niidome[a] and T. Niidome[a,b]

[a]Department of Applied Chemistry, Kyushu University
744 Moto-oka Nishi-ku, Fukuoka 819-0395 Japan

[b]Center of Future Chemistry, Kyushu University
744 Moto-oka Nishi-ku, Fukuoka 819-0395 Japan

1. INTRODUCTION OF GOLD NANORODS

1.1. Synthesis

Gold nanorods are rod-shaped gold nanoparticles. In many cases, those were synthesized in micellar solutions of cationic amphiphiles. The first report about gold nanorods, which was titled as "Preparationof Rodlike gold particles by UV irradiation using cationic micelles as a template", was reported by Esumi et al. in 1995[1]. In that paper, rod-shaped nanoparticles were prepared in a micellar solution of hexadecyltrimethylammonium chloride by irradiation of ultraviolet (UV) light. In 1997, Zande and co-workers reported that electrodeposition of gold in meso-porous aluminium oxide gave rod-shaped gold nanoparticles, and the nanorods could be dispersed in aqueous solutions with assistance of amphiphilic molecules [2]. Their method could give uniform nanorods, because the size of their nanoparticles was restricted by the pour-size of the aluminium oxide and electric charge to deposit the gold. The electrochemically deposited showed two surface absorption bands which were assignable to transverse and longitudinal modes of surface plasmon oscillations [3].

Electrochemical synthesis of gold nanorods in hexadecyltrimethyl-ammonium bromide (CTAB) solutions was reported by Yu et al. in 1997[4]. This method could give concentrated nanorods solution through constant current electrolysis. They used gold and platinum plates as anode and cathode, respectively (Fig. 1). Constant current electrolysis under sonication induced dissociation of gold clusters from the gold anode, and gave gold nanorods dispersing in CTAB micellar solutions. The resultant nanorods were rather uniform in spite of absence of rigid template such as the mesoporous aluminum oxide. In this case, the formation of gold nanorods probably comes from aniso-

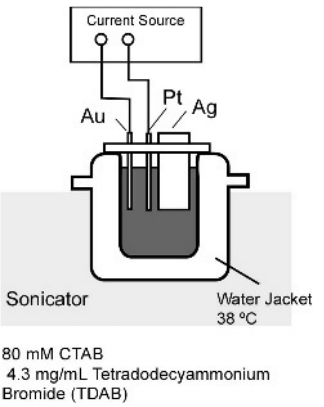

Fig. 1. Schematic illustration of electrochemical synthesis of gold nanorods in a sonicator [4].

tropic crystal growth of gold assisted by the adsorbed layer of CTAB on the nanorods [5, 6]. Aspect ratio of the nanorods could be controlled by silver plates immersed in electrolyte. It is notable that the silver plates were not electrodes; if larger silver plates were immersed in the electrolyte, longer nanorods were obtained. Yu et al. added small amount of cyclohexane and acetone in the electrolyte other than CTAB [7]. We confirmed that these chemicals assisted the formation of nanorods; especially, acetone was essential to the nanorod-formation.

Murphy et al. and co-workers reported chemical synthesis of gold nanorods using seed particles [8-11]. The seed particles were prepared in CTAB solutions by using $NaBH_4$-reduction of tetrachloroaurate. The resultant seed particles were small (~ 2 nm) and spherical. The seed particles were added in a growth solution that contained CTAB (80 mM in a typical case) and $AuBr_2^-$ (Fig. 2). The $AuBr_2^-$ was generated by ascorbic-acid-reduction of teterachloroaurate. The Murphy's method could give high aspect ratio of gold nanorods. You can see remarkable TEM images in their papers [9, 10]. As long as our following experiments, this method was sensitive to the conditions of seed particles; however, this is a

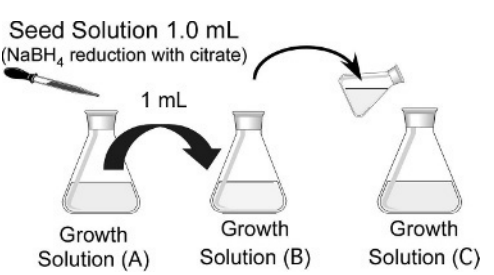

Fig. 2. Schematic illustration of seeding synthesis of gold nanorods. Three steps of growth reactions gave high aspect ratio of gold nanorods [10].

popular recipe to synthesize practical amount of gold nanorods. El-Sayed and coworkers also reported chemical synthesis of gold nanorods[12]. They added amphiphilic pyridinium salts in a growth solution containing CTAB to order to assist the formation of gold nanorods. Their method gives uniform gold nanorods, and is another popular technique to synthesize gold nanorods.

Photochemical methods are another important technique to have gold nanorods [1, 13, 14]. The first report by Esumi et al. [1] was a photochemical method. Recently, Yang et al. also reported photochemical synthesis of gold nanorods using CTAB [15]. They irradiated ultra-violet (UV) light on tetrachloroaurates in a CTAB micellar solution, and obtained gold nanorods through the one-pot and the single-step photoreaction. This method is very simple and reproducible, and gives very uniform nanorods after few hours of UV irradiation [15]. We reported that chemical reduction of tetrachloroaurates in a CTAB micellar solution, which gave $AuBr_2^-$, accelerated photoreactions to generate the gold nanorods [14]. It was shown that a few minutes of UV irradiation on $AuBr_2^-$ gave gold nanorods. This chemical reduction process did not disturb the reproducibility and the uniformity of the photochemical synthesis of the gold nanorods. Based on our combination method, Mitsubishi Materials Corp. and Dai Nihon Toryo Co. Ltd. realized a large-scale synthesis of gold nanorods. Additional information about the large-scale synthesis can be seen in our web site (http://www.nanorod.net).

1.2. Spectroscopic Properties

Maxwell's equations for the optical response of metal nanoparticles to an electromagnetic field of light wave were solved analytically for a homogeneous isotropic sphere by Mie [16]. For the gold nanorods, the Mie theory and the discrete dipole approximation (DDA) method have been readily used for a quantitative study of the optical properties of different size, shape, and aggregation state. Link et al. applied the Mie theory for gold nanorods using an ellipsoidal model [17, 18]. It was shown that the intensities and wavelength-position of the two plasmon-bands depended on the aspect ratio of gold nanorods and dielectric constants of the mediums. Using same ellipsoidal models, Gluodenis and Foss discussed the effect of mutual orientation on the spectra of metal nanoparticles pairs; rod-rod and rod-sphere [19]. They indicated that interaction between two gold nanorods drastically changes their longitudinal surface plasmon bands. Their theoretical treatments were advantageous to qualitatively estimate peak positions of the longitudinal surface plasmon bands depending shape, size, and aggregation states of gold nanorods.

On the other hand, the DDA is a finite element method for light scattering of small particles [20, 21]. This method is the most powerful and flexible electrodynamic methods for computing the optical scattering of particles with an arbitrary geometry [21]. Schatz and Van Duyne, and their co-workers [22-25]

proved that the DDA is suited for optical calculations of metallic systems with different geometries and environments through the extensive studies on the extinction spectrum and the local electric field distribution in metal particles. In DDA calculations, the target geometries are approximated by a cubic array of point dipoles, so that it is necessary for the number of dipoles N to be large enough to reproduce a satisfactory target surface and thus diminish the inaccuracy originating from the surface granularity. However, because the computational effort scales with the volume of the system, there exists a limit in the number of dipoles that can be used. The optimum number N is somewhat arbitrarily taken as a number for which the numerical results converge to a certain value and change little by further increase in N. A Fortran code library for the DDA calculation was developed by Draine and Flatau, and that is freely available on their web site [26]. Theoretical calculations of gold nanorods using the DDA model were reported by Lee and El-Sayed [27]. You can consult their paper about the detailed consideration of surface plasmon bands of gold nanorods depending on size and shape.

As predicted by the Mie theory and the DDA calculation, the surface plasmon bands of metallic nanoparticles consist of absorption and scattering. In the case larger particles than ~50 nm, contribution of light scattering is not negligible[28]. Thus, the gold particles larger than ~50 nm can be a probe material for light scattering observation. In the case of gold nanorods, surface plasmon bands can be observed in near-IR region; that is, the nanorods act as a light-scattering-probe particle in near-IR region[27]. El-Sayed and co-workers indicated that gold nanoparticles and nanorods were taken up in living cells and gave light scattering images in visible region [29]. Their pioneer works proved possibilities of gold nanorods as a novel probe for light scattering (dark field) observation in near-IR region.

The light scattering imaging is expected to be a new method to observe a bio-system, such as single cell or a tissue. It is well known that fluorescence microscopic imaging is the most popular technique to have qualitative and/or quantitative information from a bio-system. For example, time resolution of fluorescence spectroscopy is less than 10^{-12} second, if the most sophisticated system can be used. This time resolution is sufficient to analyze the reaction speed of every biochemical reaction. A modern confocal fluorescence microscope, which gives a three-dimensional fluorescence image, is widely used for biochemical research activities. By the combination with fluorescence resonance energy transfer (FRET), a confocal system can visualize the distribution and functionality of probe molecules in a living cell or a tissue. The light scattering imaging has same advantage with that of the fluorescence imaging. In addition, the scattering is never quenched by light irradiation, because the scattering does not associate with excitation of electric states of probe materials. It is the advantageous point of the light scattering imaging. The

light scattering imaging has been known as dark field imaging for many years, and an apparatus to have a microscopic dark field image is commercially available; however, this has not been a popular technique to make quantitative discussion of a bio-system, because light scattering can be observed every where in a cell or a tissue. Due to the high background scattering, it is difficult to specify a target organelle in a cell or a target cell in a tissue. Thus, highly efficient light-scattering probe is essential to realize the practical light scattering imaging. We believe the nanorod is the most possible candidate for the light scattering probe, because the nanorod can scatter deep-red or near-IR light. The longer wavelength light hardly affects a bio-system, and can penetrate deeply in a tissue. Optimization of light scattering efficiency, which depends on size and shape of the nanorods, is the most important point to obtain the practically applicable nanorod probe.

2. BIOCOMPARTIBLE GOLD NANORODS

2.1. Cytotoxicity of gold nanorods

Despite the unique characteristics, gold nanorods have hardly ever been used in the bioscience field. This is due to cytotoxicity of CTAB. The CTAB is a cationic detergent which degrades biomembranes and peptides; however, the CTAB is essential as a stabilizing agent in the preparation of gold nanorods. Nikoobackt and El-Sayed [5] and Gao et al. [6] reported characteristics of the CTAB layers on the surface of nanorods. Their works indicated that the CTAB bilayers formed on the gold nanorods, and that the bilayers were essential for the anisotropic growth of the gold nanorods. On the other hand, the CTAB layers are obstructive for surface modification of gold nanorods. Moreover, the large amount of CTAB dispersed in the solution interferes with biological processes and shows high cytotoxicity. The toxicity is not due to the CTAB layers that are statically bound to the nanoparticles [30]. It was shown that 1 mM of CTAB-passivated nanoparticles did not cause cytotoxicity to cultivated cells after three times of centrifugation; that is, unbound CTAB was toxic to cultivated cells [31]. Thus, to obtain “biocompatible” gold nanorods, excess CTAB other than in the bilayers [5, 6] on nanorods surface should be removed. Repeated centrifugation to decrease the excess CTAB has already reported. After the centrifugation, partial modification of the nanorods is possible. In all cases, however, the CTAB bilayers remained on the nanorods surfaces. The CTAB bilayers on the nanorods are not static; in other words, the CTAB molecules can desorb from the NR surfaces. Thus, it is hard to eliminate all of the unbound CTAB without aggregation of nanorods, if the nanorods are passivated only with CTAB molecules. Replacement of the CTAB with alternative stabilizing agents is essential for the realization of functional nanorods that can be used in cultivated cells as concentrated NR solutions [31].

2.2. Phosphatidylcholine modified gold nanorods

Phospatidylcholine (PC) is a typical phospholipid that is found in the most of the biological systems. PC is amphiphilic but not so water soluble. We tried to use the PC as an alternative stabilizing agent of gold nanorods. To realize the replacement of CTAB with PC, nanorod solutions were extracted with chloroform containing PC. In brief, chloroform solution of PC (10 mg/mL, 10 mL) was added in a CTAB-passivated gold nanorods solution (20 mL). These solutions are immiscible. After shaking the solutions, water phase containing gold nanorods was separated from the chloroform phase. Three times of extraction gave a reddish colour solution of gold nanorods.

Absorption spectra after the extraction procedure are shown in Fig. 3a. The spectra show similar characteristics to that of initial gold nanorods solution (Fig. 3b). The absorption spectrum immediately after the extraction procedure (followed by once centrifugation) (b) is almost identical with that obtained after 15 days (c) and shows no remarkable changes even after 30 days (d). This indicates that the nanorods can disperse without forming aggregates. The zeta-potential of the nanorods after the three extractions with PC was +15 ± 1 mV. Thus, though the magnitude is smaller than that in the case of as-prepared gold nanorods (+67 ± 1 mV), the colloidal dispersion of the nanorods is retained in the long term. Considering that PC is a zwitter-type molecule, the decrease of zeta potential indicates the replacement of CTAB with PC, and the sign of the zeta potential indicates that some CTAB molecules are retained on the nanorod surfaces. As a control experiment, a PC-liposome solution prepared by a conventional method was added to the initial nanorod solution. Centrifugation of the nanorod solution after addition of resulted in irreversible aggregation. Thus, the colloidal dispersion of the nanorods can be attributed to a so-called hydration repulsive force between the PC layers on the nanorod surfaces [31].

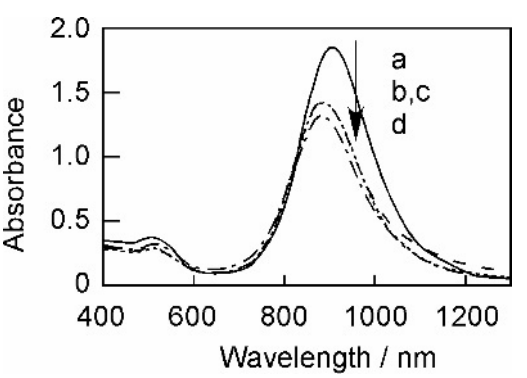

Fig. 3. extinction spectra of gold nanorods before (a) and after (b, c, d) extraction with PC-containing chloroform phases. (a) before extraction, (b) soon, (c) 15, (d) 30 days after the extraction.

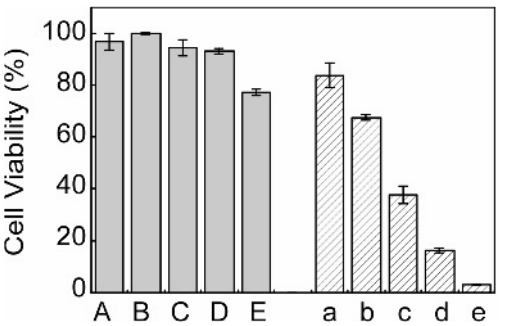

Fig. 4. Viabilities of HeLa cells after contacting with the PC-NR solutions (A-E) and twice-centrifuged NRs solutions (a-e). Final concentrations of NR solution: 0.09 (A, a), 0.18 (B, b), 0.36 (C, c), 0.72 (D, d) and 1.45 (E, e) mM (Au atoms). The cells were incubated for 24 hours in the presence of the NRs.

Cytotoxicity of the phosphatidylcholine modified nanorods (PC-NRs) was estimated using HeLa cells after 24 hours of incubation in the presence of PC-NRs [31]. The cell viabilities are shown in Fig. 4 (A-E). The same procedure as that for the PC-NR was applied to twice-centrifuged nanorods (a-e), to investigate residual CTAB. In the case of the 0.09-0.72 mM PC-NR solutions (A-D), cytotoxicity was not remarkable. When the concentration of PC-NR was increased to 1.45 mM, about 20% of the cells died. On the other hand, the twice-centrifuged nanorod solutions (a-e) showed significant cytotoxicity. Even when 0.09 mM of the centrifuged nanorod (a) was present in the medium, the viability was about 85% after 24 hours of incubation. The viability decreased drastically with increasing concentration of nanorods (b-e). Thus, the twice-centrifuged nanorods are much more toxic than the PC-NRs. Under our experimental conditions, the 50% inhibitory concentration (IC_{50}) of CTAB was about 9.1 mM. This indicates that the concentration of unbound CTAB was much lower than 9.1 mM in the PC-NR solutions even when 1.45 mM of PC-NRs was present in the medium. The PC layers on the nanorod surfaces probably suppress dissociation of CTAB molecules which retained on the nanorod surface and gave positive zeta potentials.

2.3. Polyethylenegrychol modified gold nanorods

We also prepared poly(ethylenegrychole) (PEG) modified gold nanorods (PEG-NR) as an alternative candidate of biocompatible nanorods [32]. PEG is a typical material showing high biocompatibility. Surface modification of gold nanorods with PEG chains is the most possible way to give biocompatibility for the nanorods. To prepare PEG-modified gold nanorods, a solution of gold nanorods containing CTAB (as-prepared solution) was centrifuged at 14,000 g for 10 min, decanted, and resuspended in water to remove excess CTAB. PEG_{5000}-SH (200 mL, 5 mM, Nektor) was added to 1 mL the centrifuged gold

nanorod solution (1 mM gold atoms). The mixture was stirred for 24 hours at room temperature, and was dialyzed for 3 days. Cytotoxicity of the PEG-modified gold nanorods was estimated from cell viabilities of HeLa cells using MTT assay, which was same with the case of the PC-modified gold nanorods.

After the dialysis the gold nanorods showed negative zeta potential (-0.5 mV). TEM observations of the nanorods that were treated with WO_3^- ions showed PEG layers on the surface of the nanorods (Fig. 5) [32]. The nanorod solutions could be kept with forming aggregates at least for few weeks. Thus, PEG_{5000}-SH certainly adsorbed on the nanorod surfaces and the PEG chains contributed to stabilize the colloidal dispersion of the nanorods. Cytotoxicity of the PEG-modified gold nanorods is shown in Fig. 6. The PEG-modified gold nanorods showed high cell viability (90%), even when 0.5 mM (gold atoms) of nanorods was added in the medium. It is shown that the PEG-modification gave biocompatible gold nanorods that showed same order of compatibility of PC-modified gold nanorods.

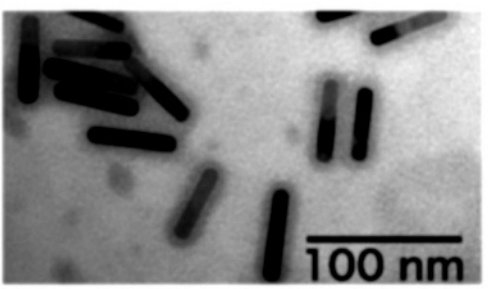

Fig. 5. TEM image of the PEG-modified gold nanorods.

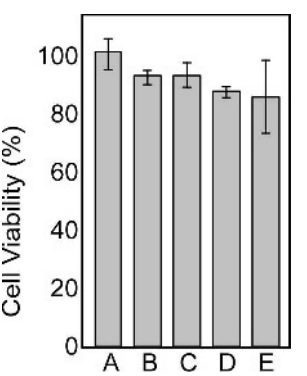

Fig. 6. Viabilities of HeLa cells after contacting with the PEG-NR solutions (A-E). Final concentrations of NR solution: 0.01 (A), 0.05 (B), 0.1 (C), 0.5 (D, d) and 1.0 (E) mM (Au atoms). The cells were incubated for 24 hours in the presence of the NRs.

3. BIODISTRIBUTION OF GOLD NANORODS

To apply gold nanorods to medical fields including tumor imaging, photothermal therapy, gene therapy, and gene/drag delivery, targeted delivery of nanorods after systemic injection is a key parameter. For the targeted delivery *in vivo*, a stealth character is certainly required. Providing the stealth character to nanorods will enable efficient delivery to a specific site. It will also produce higher contrast images, and a more effective photothermal therapy compared to current techniques. We injected the surface-modifed gold nanorods intravenously into mice to investigate biodistribution of the gold nanorods[32].

Male ddY mice (kyudo Co. Ltd., Fukuoka, Japan) were used in all experiments. Gold nanorods in 300 mL 5% glucose were injected into the mice via the tail vein. Mice were sacrificed 0.5, 3, 6, 12, 24, 72 hours later. Blood and tissue samples were completely lysed in aqua regia, and centrifuged at 1000 g for 5 min. Following evaporation, resulting precipitates were dissolved in 0.5 M HCl. Quantitative analysis of gold was performed by an ICP mass spectrometry.

With original gold nanorods stabilized with CTAB, from which excess CTAB was washed with 5% glucose and centrifugation, 30% of the injected dose of gold was found in liver at 30 min after the injection, while only a small amount of gold was found in other organs (Fig. 7). PC-nanorods showed same characteristics for the biodistribution; most of those were found in liver. In contrast, with PEG-modified gold nanorods, 54% of the injected dose of gold was found in blood at 30 min. The amount of gold in the blood was decrease in a time-dependent manner, then, no gold was found observed at 72 hours. A small

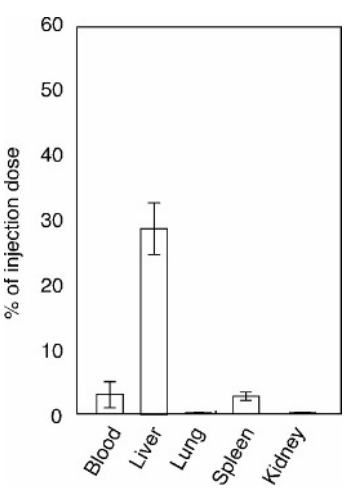

Fig. 7. Biodistribution of CTAB passivated gold nanorods in mice after intravenous injection. The nanorods were washed with 5% glucose to decrease the amount of CTAB. Gold amount in tissue samples were evaluated by ICP mass spectroscopy 30 min after injection.

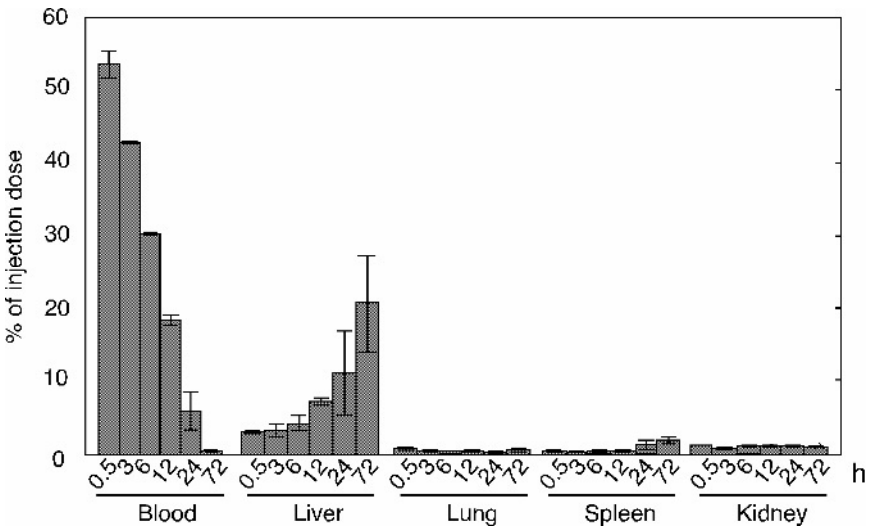

Fig. 8. Biodistribution of PEG-modified gold nanorods in mice after intravenous injection. After 0.5, 3, 6, 12, 24, and 72 h after injection, gold amounts in tissue samples were evaluated by ICP mass spectroscopy.

amount of gold was found in other organs (Fig. 8). PEG-modification of gold nanorods drastically changed biodistribution of nanorods, and provided the nanorods with a stealth character in the blood flow. PEG-modification enabled long lasting circulation in blood. Due to the stealth character that was introduced by the PEG-capping, modification of ligands such as RGD peptide and antibodies with gold nanorods will allow development of targeted delivery systems. Then, combination with near-IR laser irradiation will allow simultaneous imaging and therapeutic systems.

4. CONCLUSION

Surface modification of nanorods was a key to have practical gold nanorods for the bio-related science. Now, we prepared two kinds of surface-modified gold nanorods; that is, PC- and PEG-modified gold nanorods. Both of those were biocompatible for cultivating cells. The PEG-modified nanorods indicated long lasting circulation in blood. These nanorods will afford new application in biochemistry utilizing the unique spectroscopic properties of gold nanorods.

REFERENCES

[1] K. Esumi, K. Matsuhisa and K. Torigoe, Langmuir, 11, (1995), 3285.
[2] B. M. I. v. d. Zande, M. R. Böhmer, L. G. J. Fokkink and C. Schöneberger, J. Phys. Chem. B., 101, (1997), 852.

[3] C. G. Blatchford, J. R. Cambell and J. A. Creighton, Surf. Sci., 120, (1982), 435.
[4] Y.-Y. Yu, S.-S. Chang, C.-L. Lee and C. R. C. Wang, J. Phys. Chem. B, 101, (1997), 6661.
[5] B. Nikoobakht and M. A. El-Sayed, Langmuir, 17, (2001), 6368.
[6] J. Gao, C. M. Bender and C. J. Murphy, Langmuir, 19, (2003), 9065.
[7] S.-S. Chang, C.-W. Shih, C.-D. Chen, W.-C. Lai and C. R. C. Wang, Langmuir, 15, (1999), 701.
[8] N. R. Jana, L. Gearheart and C. J. Murphy, J. Phys. Chem. B, 105, (2001), 4065.
[9] N. R. Jana, L. Gearheart and C. J. Murphy, Adv. Mater., 13, (2001), 1389.
[10] B. D. Busbee, S. O. Obare and C. J. Murphy, Adv. Mater., 15, (2003), 414.
[11] T. K. Sau and C. J. Murphy, Langmuir, 2004, (2004), 6414.
[12] B. Nikoobakht and M. A. El-Sayed, Chem. Mater., 15, (2003), 1957.
[13] F. Kim, J. H. Song and P. Yang, J. Am. Chem. Soc., 124, (2002), 14316.
[14] Y. Niidome, K. Nishioka, H. Kawasaki and S. Yamada, Chem. Commun., (2003), 2376.
[15] F. Kim, J. H. Song and P. Yang, J. Am. Chem. Soc., 124, (2002), 14316.
[16] G. Mie, Ann. Phys. (Lipzig), 25, (1908), 377.
[17] S. Link, M. B. Mohamed and M. A. El-Sayed, J. Phys. Chem. B, 103, (1999), 3073.
[18] S. Link and M. A. El-Sayed, J. Phys. Chem. B, 109, (2005), 10531.
[19] M. Gloudenis and J. Colby A. Foss, J. Phys. Chem. B, 106, (2002), 9484.
[20] E. M. Purcell and C. R. Pennypacker, Astrophys. J., 186, (1973),
[21] B. T. Draine and P. J. Flatau, J. Opt. Soc. Am. A, 11, (1994), 1491.
[22] W.-H. Yang, G. C. Schatz and R. P. V. Duyne, J. chem. Phys., 103, (1995), 869.
[23] T. Jensen, L. Kelly, A. Lazarides and G. C. Schatz, J. Cluster Sci., 10, (1999), 295.
[24] K. L. Kelly, E. Coronado, L. L. Zhao and G. C. Schatz, J. Phys. Chem. B, 106, (2003), 668.
[25] E. M. Hicks, X. Zhang, S. Zou, O. Lyandres, K. G. Spears, G. C. Schatz and R. P. V. Duyne, J. Phys. Chem. B, 109, (2005), 22351.
[26] B. T. Draine and P. j. Flatau, User Guide for the Discrete Dipole Approximation Code DDSCAT 6.1, (2004),
[27] K.-S. Lee and M. A. El-Sayed, J. Phys. Chem. B, 109, (2005), 20331.
[28] P. K. Jain, K. S. Lee, I. H. El-Sayed and M. A. El-Sayed, J. Phys. Chem. B, 110, (2006), 7238.
[29] X. Huang, I. H. El-Sayed, W. Qian and M. A. El-Sayed, J. Am. Chem. Soc., 128, (2006), 2115.
[30] E. E. Connor, J. Mwamuka, A. Gole, C. J. Murphy and M. D. Wyatt, Small, 1, (2005), 325.
[31] H. Takahashi, Y. Niidome, T. Niiodme, K. Kaneko, H. Kawasaki and S. Yamada, Langmuir, 22, (2006), 2.
[32] T. Niidome, M. Yamagata, Y. Okamoto, Y. Akiyama, H. Takahashi, T. Kawano, Y. Katayama and Y. Niidome, J. Controlled Release, 114, (2006), 243.

This page intentionally left blank

PART IV: NANO BIO DEVICES

This page intentionally left blank

Handai Nanophotonics, Volume 3
H. Masuhara, S. Kawata and F. Tokunaga (Editors)

Chapter 21

Protein modules: Functional proteins incorporated in viral polyhedra

N. Hamada[a], R. Nakamura[b], H. Ijiri[a], Y. Takeda[a], F. Tokunaga[c], Y. Kanematsu[b] and H. Mori[a]

[a]JST-CREST, Division of Applied Biology, Kyoto Institute of Technology, Matsugasaki, Sakyo-ku, Kyoto 606-8585, Japan

[b]JST-CREST, Venture Business Laboratory, Center for Advanced Science and Innovation, Osaka University, 2-1 Yamada-oka, Suita 565-0871, Japan

[c]JST-CREST, Graduate School of Science, Osaka University, Toyonaka 560-0043, Japan

1. INTRODUCTION

Proteins are the building blocks of the biological body. They work as structural elements, storage and transport systems, and catalysts. In effect, they perform most of the tasks carried out by biological systems. Our project toward biological systems is based on what we call the "Protein Module", in which proteins are clustered. In November 2002 we started a project entitled, "Protein Module: From Nano Assembling to Micro Multiplication" (project leader, Fumio Tokunaga, Osaka University) at Core Research for Evolutional Science and Technology (CREST). This project and nine other projects among CREST programs have formed the research area: Creation of Novel Nano-material / System Synthesized by Self-organization for Medical Use (http://www.self-org.jst.go.jp/; research supervisor, Koji Kaya, RIKEN). This research project aims to establish the fundamental principles and methodologies for the synthesis of nanometer-scale materials with novel functional properties. This synthesis can be achieved by the well-designed control of molecular arrangement based on the concept of self-organization. The other important topic of this research project is to attempt the integration of nanotechnology and biotechnology, to create fields such as "nano-photonics". The results of this research project will be applicable to the development of advanced medical treatments as well as

information and environmental technology. Our final goal is to use the Protein Module to develop new methods in cellular and molecular biology.

In general, hierarchical structures can be recognized in the biological body: molecules, polymers, organelles, cells, tissues, organs, and so on. These components have specific functions and are located at specific positions. In biological systems, such components automatically assemble and construct new, higher level units to realize new functions. Our project aims to create artificial modules at various levels that correspond to biological systems, and which induce the automatic assembling of the components and the construction of structures at a higher level. The basis of our project toward creating a biological system is the Protein Module. Protein Modules are constructed by several original methods involving self-organized membranes and crystals. The Protein Modules are assembled with a highly ordered structure arising from the construction of a patterned sub-cellular module by means of nano self-organization and laser nano/micro processing. Further integration of this module will lead to the generation of the tissue module, on which stimulating patterns for living cells cause differentiation/proliferation and lead to self-multiplication of the system.

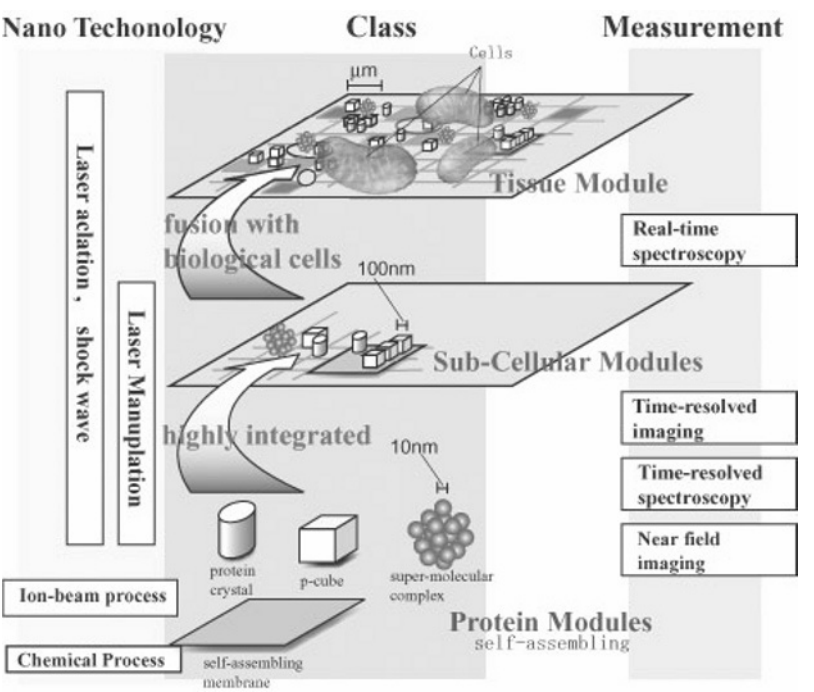

Fig. 1. An image of aim and strategy of the CREST project. The creation of artificial modules at various levels, corresponding to biological systems.

With these concepts in mind, we have begun the development of Protein Modules. Since Protein Modules are integrated, target proteins are expected to be properly immobilized on a carrier or support. Three immobilization methods have been tested for this purpose: formation of general protein crystals, self-organized membranes, and viral polyhedra. The following features are required in Protein Modules:

1) Stability of various agents;
2) Simple purification or synthesis steps; and
3) Availability for various types of proteins.

For construction of the Protein Module, we decided to develop a method for the immobilization of proteins based on an insect virus strategy since, among the three candidate strategies, only the insect virus strategy has the potential to satisfy all three features described above. Viral polyhedra are cytoplasmic crystalline particles produced by insect viruses known as cypoviruses. The polyhedra occlude progeny virions produced during infection and play a role in protecting these virions from hostile environmental conditions. The virions are immobilized on and in polyhedra through linkage with a signal protein called VP3. In previous studies, Mori and co-workers found that a target protein tagged with VP3 is successfully immobilized on and in polyhedra. Unlike other protein crystals, polyhedra crystalline particles cannot be broken by sonication or other operations involved in general protein purification. The size of the polyhedra, which is around 5 μm, confers another advantage because it enables ease of handling.

Cypoviruses are insect viruses that produce a cytoplasmic crystalline particle called a polyhedron in which progeny virions are occluded. The polyhedra produced by some insect viruses could be a useful platform for protein immobilization without loss of biological activity. As mentioned above, previous work showed that the Bombyx mori cypovirus (BmCPV) outer capsid protein, VP3, acts as the immobilization signal for the incorporation of protein molecules in polyhedra [1]. Fusion of enhanced green fluorescent protein (EGFP) to the C-terminal of VP3 resulted in its incorporation in polyhedra when the chimeric protein was co-expressed with polyhedrin during BmCPV infection [1].

In order to evaluate the usefulness and readiness of production, we carried out the immobilization in polyhedra of cartilage-derived morphogenetic protein 1 (CDMP1), which was selected as an example of a growth and differentiation factor while confirming the immobilization in the polyhedra of EGFP. Fluorescence microscopy has been used to visualize EGFP-incorporated polyhedra, and since EGFP has a fluorescent chromophore, protein function can be evaluated by whether or not fluorescence can be detected. Normally, however, CDMP1 is non-fluorescent and it functions by interaction with its receptor protein. In our experiments, we endeavored to observe the interaction of

CDMP1 with its antibody. To this end, fluorescence immunoassay was performed, combined with microscopy for visualization of CDMP1 so as to evaluate whether the binding affinity with the antibody is maintained or not. In Section 3, we report the successful construction of Protein Modules.

The Protein Module acts through functional proteins incorporated in the protein polyhedra. Protein-protein interactions are extremely important to the functionality of proteins. For successful interactions between functional proteins to occur, a sufficiently high concentration of the interacting proteins is necessary. In some cases, structural changes are also required. Here, two questions arise: 1) Can incorporated protein move around freely? and 2) How many incorporated proteins are active in the polyhedra?

We have already made clear that S-modulin, which is a calcium-binding calmodulin-like protein held in the octahedral, actually causes structural changes when calcium ions are added (this observation will be reported elsewhere). The related optical changes were clearly observed. S-modulin plays an important role in light-signal transduction. Therefore, this is the first case to confirm that a structural change directly related to biological function actually occurs despite being held in the Protein Module. Thus, question 1) is partially answered by this observation. However, the general mobility of the protein remains to be addressed.

In Section 4, we report experimental results concerning the functional aspects of the Protein Module—that is, the dynamic aspects and the number of active proteins incorporated in the polyhedra. Concluding remarks are presented in Section 5.

2. EXPERIMENTAL

2.1. Virus and cells

The *Spodoptera frugiperda* cell line IPLB-Sf21-AE (Sf21) was maintained in tissue culture flasks in TC-100 medium (GIBCO/BRL) with 10% fetal bovine serum [2]. A recombinant form of BmCPV (AcCP-H), which produces cubic polyhedra [3], was used in this study.

2.2. Construction of recombinant baculoviruses

A cDNA derived from BmCPV segment 4, which encodes VP3 [1], was cloned into the baculovirus transfer vector pVL1392 (PharMingen) to produce a plasmid designated pAcVP3. To produce pAcVP3(N)/EGFP, a baculoviral transfer plasmid encoding the N-terminal VP3-EGFP fusion protein, the EGFP gene was excised from pEGFP-N3 (CLONTECH) with *NheI* and *XbaI* and subcloned into the *XbaI* site of pAcVP3. To produce pAcEGFP/VP3(C), a baculoviral transfer plasmid encoding the C-terminal EGFP-VP3 fusion protein, the EGFP gene was excised from pEGFP-N3 with *Eco47III* and SmaI and

subcloned into the *BglII* (repaired)-*MscI* sites of pAcVP3. Gateway cloning technology (Invitrogen) was used to facilitate high-throughput expression and immobilization of various human proteins. Briefly, a "destination" vector was constructed by inserting a cassette consisting of an *att*R1 site at the 5'-end, and the chloramphenicol resistance gene, the *ccd*B gene, and the *att*R2 site at the 3'-end, into the *XbaI* site of pAcVP3. Open reading frame (ORF) regions of full-length human cDNA analyzed in the NEDO full-length cDNA sequencing project were amplified by PCR, in which *att*B1 and *att*B2 sequences were included in the primers. To construct the "entry vector", the *att*B-flanked PCR products were cloned into a donor vector containing a cassette consisting of the *att*P1 site, the chloramphenicol resistance gene, the *ccd*B gene, and the *att*P2 site, inserted by BP reactions with the BP clonase enzyme mixture. The ORFs were cloned between the *att*L1 and *att*L2 sites of the resulting "entry" vectors, then transferred to the destination vector via LR reactions using the LR clonase enzyme mixture. The resulting expression vectors consisted of the N-terminus of VP3 fused in-frame to various human ORFs in the background of the baculovirus transfer vector pVL1392. The recombinant transfer vectors, pAcVP3(N)/EGFP and pAcEGFP/VP3(C), and the various expression vectors were co-transfected into Sf21 cells together with linearized AcNPV DNA (Baculogold Baculovirus DNA, PharMingen). The recombinant AcNPVs produced by rescue of the linearized viral DNA were harvested and isolated by plaque purification. The recombinant baculoviruses obtained using pAcVP3(N)/EGFP and pAcEGFP/VP3(C) were designated AcVP3(N)/EGFP and AcEGFP/VP3(C), respectively. To make VP3 deletion mutants, pAcVP3(N)/EGFP was digested with *XbaI* and *KpnI*, followed by use of the Deletion Kit (TAKARA). The deleted recombinant plasmids were prepared by standard techniques and sequenced with the ABI PRISM terminator cycle sequencing kit (PE Applied Biosystems) and the PE Applied Biosystems Model 373A automated sequencer.

The sequence data for CDMP1 were taken from DDBJ/EMBL/GenBank databases, using accession number BC032495. The CDMP1/VP3 recombinant plasmid vector was prepared in the same manner.

2.3. Purification of polyhedra

Sf21 cells (5×10^7 cells per 75 cm^2 flask) were inoculated with the recombinant virus at a multiplicity of infection (MOI) of 10 PFU/cell. For double infections, each virus was added at an MOI of 5 PFU/cell. The infected cells were collected, washed with PBS (20 mM NaH_2PO_4, 20 mM Na_2HPO_4, 150 mM NaCl, pH 7.2) and homogenized in a blender on ice. The homogenates were washed with 1% Tween 20 and polyhedra were partially purified by differential centrifugation. Further purification was carried out by discontinuous sucrose density gradient centrifugation in 1.5~2.2 M sucrose at 50,000 g for 45

min. The polyhedra were recovered with a syringe, washed with PBS, and finally collected by centrifugation at 15,000 g for 10 min.

2.4. Measurement of fluorescence by EGFP immobilized in polyhedra

Sf21 cells (5×10^7 cells per 75 cm^2 flask) were co-infected with AcVP3(N) /GFP and AcCP-H or with AcEGFP and AcCPH, using an MOI of 5 PFU/cell for each virus. Polyhedra were isolated from the infected Sf21 cells at 4 days postinfection (DPI), as described in Section 3.3. Samples of the purified polyhedra were suspended in 1 mL PBS (pH 7.2), and, after a 30 min incubation at 30°C, EGFP fluorescence was measured by excitation at 475 nm and emission at 510 nm using a F-2000 fluorescence spectrophotometer (Hitachi).

2.5. Western blot analysis

Samples were mixed with a sample buffer (10% SDS, 10% β-mercaptoethanol, 0.3M Tris-HCl (pH 6.8), 0.05% bromophenol blue, and 50% glycerol), boiled for 5 min, and resolved by 12.5% sodium dodecyl sulfate-polyacrylamide gel electrophoresis (SDS-PAGE), followed by electrophoretic transfer to a Hybond™-PVDF membrane (Amersham Pharmacia Biotech) for Western blot analysis. After blocking for 1 h in Tris-buffered saline (TBS; 20 mM Tris-HCl, pH 7.5, and 500 mM NaCl) containing 5% non-fat dry milk, the membrane was incubated in an antibody solution (1% non-fat dry milk in TBS containing rabbit anti-CDMP1 monoclonal antibodies (1:1,000 v/v) (Santa Cruz Biotechnology, Inc.)).

2.6. Detection of CDMP1 immobilized in polyhedra

Purified polyhedra were arrayed and fixed on a glass slide. The slide was then treated with 1% v/v hydrogen peroxide and incubated for 30 min with 5% normal horse serum (NHS) in PBS containing 0.3% Triton X-100 (PBST). This was followed by treatment with anti-CDMP1 antibody diluted 1000-fold in PBST for 3 h at 37°C, biotinylated anti-mouse IgG (Vector) diluted 100-fold in PBST containing 5% NHS for 1 h at 37°C, and ABC reagent (Vector) diluted 100-fold in PBST for 1 h. Finally, the horseradish peroxidase reporter was detected by incubating the slide glass with 0.05% DAB in 50 mM Tris-HCl, pH 7.4. The slide was sealed with glycerol-PBS and a coverslip, and examined under a microscope (Olympus IX71) equipped with a DP50 digital camera. One microliter of a suspension (108 polyhedra/mL) of polyhedra containing immobilized CDMP1 or control polyhedra containing no CDMP1 was also spotted onto a glass slide. Subsequently, the polyhedron-fixed glass slide was treated with anti-CDMP1 antibody (Santa Cruz Biotechnology) diluted 1000-fold in PBST for 3 h at 37°C. After washing, the glass slide was incubated with FITC-conjugated anti-mouse IgG secondary antibody diluted 20-fold in PBST for 2 h at 37°C. Finally, samples were examined with an Axioplan-2MOT

epifluorescence microscope coupled to a Carl Zeiss laser-scanning confocal imaging system.

2.7. Setup for time-resolved fluorescence microscopy

Light pulses (pulse duration of 0.2 ps) from an optical parametric amplifier (OPA), which was pumped by a regenerative Ti:sapphire amplifier operating at a repetition rate of 200 kHz (Coherent, RegA9000), were used to excite the samples. The wavelength of the output pulse from the OPA was tuned to 485 nm to be resonant with the absorption band associated with the anionic form of the chromophore. The excitation light was introduced into a microscope equipped with a ×100 objective lens (Carl Zeiss, NA 1.25). The fluorescence from the sample was focused on the slit of a monochromator and detected by a microchannel plate (MCP) photomultiplier (Hamamatsu, R3809U). The wavelength range of fluorescence detection was set to 515-535 nm. The amplified signal from the MCP was directed to a time-correlated single-photon counting module (PicoQuant, TimeHarp200). For time-resolved anisotropy measurements, fluorescence of parallel and perpendicular polarization was selected using a Glan-Thompson prism inserted in front of a monochromator.

3. IMMOBILIZATION OF EGFP AND CDMP1 PROTEINS

3.1. Expression of a chimeric gene consisting of EGFP and VP3 genes

Optical microscopy of the polyhedra co-infected with AcVP3/EGFP and AcCp-H showed that the green fluorescence was localized to BmCPV polyhedra (Fig. 2). Infection with AcVP3/EGFP only, on the other hand, resulted in diffuse green fluorescence in the cytoplasma (data not shown). This localized green fluorescence around BmCPV polyhedra suggested that specific interactions

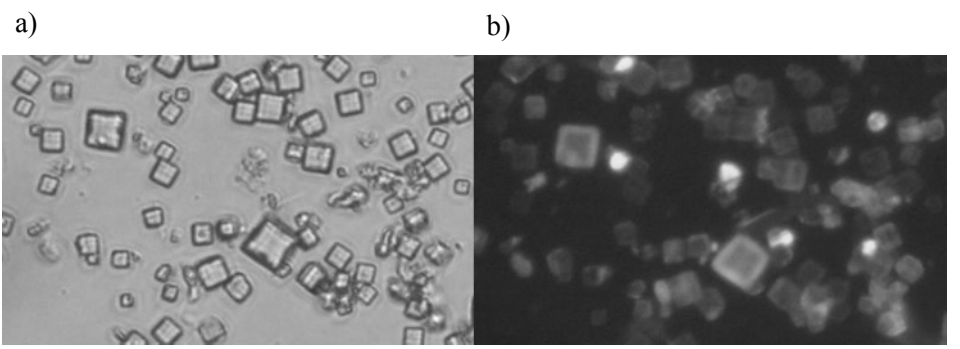

Fig. 2. Analysis of polyhedra containing a recombinant VP3-EGFP fusion protein by optical microscopy. Polyhedra were isolated from cells doubly infected with AcVP3(N)/GFP and AcCP-H. Panel a) show a phase contrast image of polyhedra, while panel b) shows a fluorescence image of polyhedra.

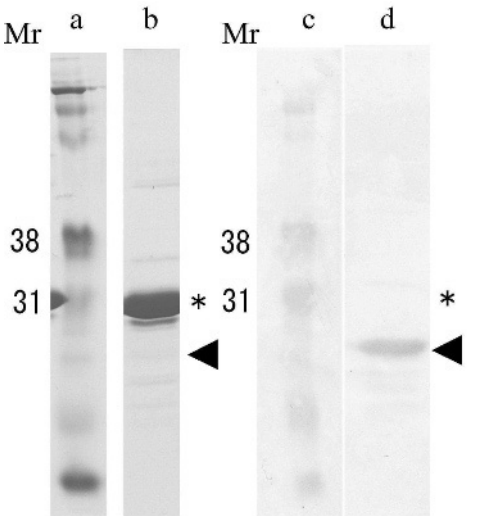

Fig. 3 SDS-PAGE and Western blot analysis of CDMP1/VP3 immobilized polyhedra. Proteins were detected by Coomassie brilliant blue straining (a and b) and Western blot analysis (c and d). The arrowhead indicates CDMP1/VP3 protein and * indicates polyhedorin protein. Molecular weights are in thousands.

occur between BmCPV polyhedrin and VP3. However, it was unknown whether the VP3-EGFP chimeric protein is occluded in BmCPV polyhedra or whether the specific interactions facilitate BmCPV virion occlusion in polyhedra. A study that reported EGFP fluorescence on a surface newly exposed by alkali-dissolution [1,4] confirmed that co-infected polyhedra incorporate the VP3-EGFP chimeric protein.

3.2. Western blot analysis

The mature peptide of CDMP1 consists of 120 amino acids with a molecular mass of 15 kDa. The CDMP1/VP3 protein was expected to show a slightly higher mobility than intact CDMP1 due to the addition of the VP3 tag. Figure 3 shows the results of SDS-PAGE followed by Western blot of CDMP/VP3 immobilized polyhedra. The 31 kDa band was strongly detected in panel b, indicating the presence of polyhedrin protein. The 20 kDa band in panel d indicates CDMP1/VP3.

3.3. Immunolocalization of CDMP1 polyhedra

The polyhedra-spotted slide glass was incubated for 1 h with monoclonal antibody against CDMP1. After washing, the glass slide was incubated with an anti-mouse IgG secondary antibody. Finally, secondary antibody binding was

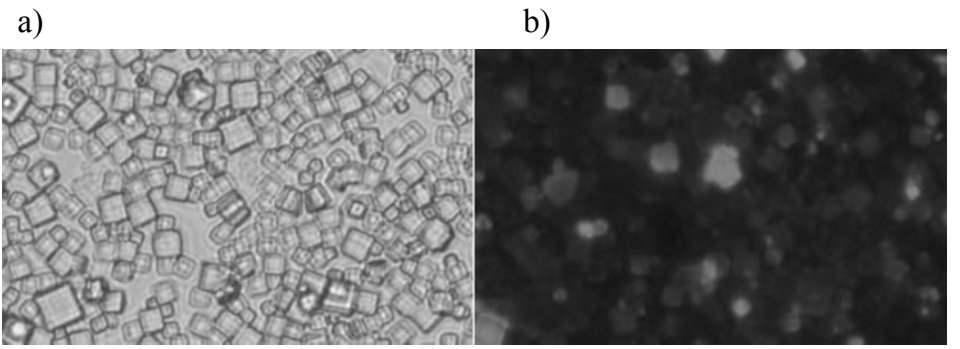

Fig. 4 Detection of fluorescence from CDMP1/VP3-immobilized polyhedra. Panel a) shows a bright-field image, and b) shows a fluorescence image.

assessed using a horseradish peroxidase method. Panel b) in Fig. 4 shows an immunoreactive pattern of CDMP1/VP3-immobilized polyhedra. FITC fluorescence was observed on CDMP1/VP3-immobilized polyhedra. Immunoreactivity of an anti-CDMP1 antibody was not observed for polyhedra (data not shown). The surfaces of the CDMP1/VP3-immobilized polyhedra were clearly immunoactive, while the control polyhedra lacking CDMP1/VP3 were not. These results suggest that incorporation in polyhedra could be an excellent way to immobilize diverse recombinant proteins without loss and, perhaps, with stabilization of their structures and functions.

It should be noted that Protein Modules obtained in this manner can be applied to the attractive methodology for constructing a protein micro-array described below. The three requirements of the Protein Module, as mentioned in the Introduction, are also necessary conditions for the protein micro-array. The immobilization of biologically active molecules is important for diagnostic screening as well as for micro-technology. Protein micro-arrays enable us to carry out high-throughput analysis of protein-protein, substrate-enzyme, DNA-protein, RNA-protein, and ligand-protein interactions. Although a wide variety of protein immobilization methods are available, most are not sufficiently robust in terms of stability, structure and surface conditions. This renders them impractical for use with micro-arrays. An array constructed by patterning Protein Modules is considered to be a promising method for the creation of protein micro-arrays.

4. EVALUATION OF PROTEINS IN POLYHEDRA BY TIME-RESOLVED FLUORESCENCE

Figure 5 shows the temporal behaviour of the fluorescence intensities of EGFP polyhedra during irradiation at various excitations. At an excitation power

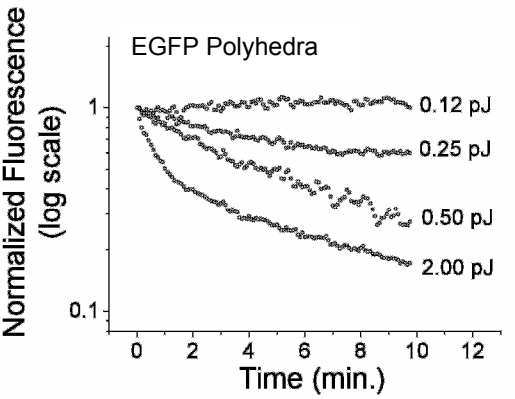

Fig. 5. Temporal behaviours of fluorescence intensities of EGFP in polyhedra during irradiation with various excitation powers.

of 2.0 pJ, the fluorescence intensity rapidly decreases in a few minutes. Photobleaching becomes slower as excitation power is decreased, and becomes negligible below 0.12 pJ. In the case of EGFP solution, photobleaching was negligible with an excitation power below 0.50 pJ. Taking into account the pulse width of 0.2 ps and the beam waist of ~1 μm for the excitation light, the power of 0.12 pJ corresponds to a photon flux of 10^{26} $cm^{-2}s^{-1}$. The following time-resolved spectroscopies were performed at this excitation power.

4.1. Rotational dynamics of EGFP in polyhedra

The inset in Fig. 6 shows the fluorescence time profiles of parallel and perpendicular polarizations for EGFP in polyhedra. The major component of the fluorescence decay was 1.6 ns (85%), which is faster than the decay of 2.8 ns for the EGFP solution [5-7].

It is well known that the anisotropic decay of EGFP in solution shows a single exponential pattern and its time constant (rotational correlation time) of ~14 ns is explained by a cylinder-shape structure with a size of 4.2 nm in length and 2.4 nm in diameter. That is, whole proteins undergo rotational diffusion and the chromophore is fixed inside a barrel-shaped cage. In addition, the rotational correlation time linearly depends on the solvent viscosity, the gradient of which is 14 ns/cp [8]. Therefore, it is expected that the environment surrounding EGFP in polyhedra can be probed by anisotropic decay experiments.

Figure 6 shows the time-resolved fluorescence anisotropic decay of EGFP in polyhedra obtained by the time-resolved fluorescence of parallel and perpendicular polarizations shown in the inset. Anisotropic decay clearly occurs in this time window. This result provides evidence that EGFP in polyhedra still keep a degree of freedom of rotation. From fitting the experimental data using a single exponential function, a rotational correlation time of 30 ± 10 ns was

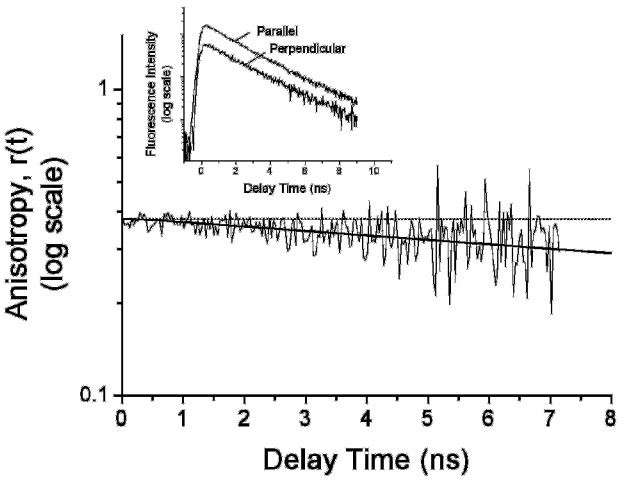

Fig. 6. The fluorescence anisotropy decay of EGFP in polyhedra. The inset shows time profiles of fluorescence of parallel and perpendicular polaizations for EGFP in polyhedra.

obtained. This time constant observed for EGFP polyhedra is 2 times slower than the rotational time in EGFP solution.

4.2. Average concentration of EGFP in polyhedra

Recently confocal microscopy revealed that only EGFP near the surface of polyhedra is active (fluorescent), although EGFP molecules are uniformly incorporated inside the polyhedra [4]. Here, we estimated the average concentration of active EGFP in polyhedra by time-resolved fluorescence, by comparison with a standard sample (EGFP solution with known concentration).

The number of photons emitted from the sample is given by

$$F \propto J_{ex} \varepsilon C \Phi A l \qquad (1),$$

where J_{ex} is excitation photon flux per unit area; ε is molar extinction coefficient; C is average concentration of molecules; Φ is fluorescence quantum yield; and Al is irradiated volume of the sample. The quantum efficiency Φ is related to the radiative rate constant k_r and the nonradiative rate constant k_{nr} by $\Phi = k_r/(k_r + k_{nr})$. We assumed that J_{ex}, ε, and A do not differ between EGFP in polyhedra and EGFP in solution under the same experimental condition. In this case, the average concentration of C for EGFP in polyhedra is given by the time-resolved fluorescence with relative intensity, the depth length l of the excited volume, and known concentration of EGFP solution.

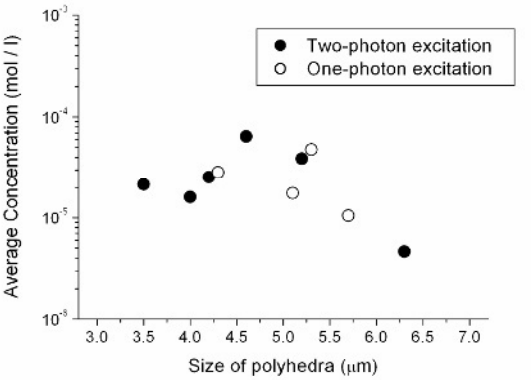

Fig. 7. The average concentration of EGFP in polyhedra estimated from time-resolved fluorescence experiments by one-photon and two-photon excitations.

In order to avoid ambiguity when determining the depth length l of the excited volume, we performed two kinds of experiments involving one-photon and two-photon excitation configurations, the depth resolutions of which were 70 and 3 μm, respectively. In the case of the EGFP solution, we assumed that the depth length l is the same as the depth resolution because the sample thickness is much larger than the resolution. On the other hand, in EGFP polyhedra, we assumed that l is the same as the size of measured polyhedra in one-photon excitation and that it is 3 μm (depth resolution) in two photon excitation.

Figure 7 shows estimated results of the average concentration for EGFP in polyhedra of various sizes. The concentrations are within a range of 10^{-4} to 10^{-5} mol/l except for large polyhedra. The concentration estimated here corresponds to active (fluorescent) EGFP, which are localized near the surface of the polyhedra. A detailed discussion of the depth of the active surface would be possible if we could obtain enough information on how many EGFP molecules are incorporated in the polyhedra.

5. CONCLUDING REMARKS

We have succeeded in the construction of Protein Modules based on polyhedra incorporated with target proteins, as well as spectroscopic analysis for protein-protein interactions and biological activities. Interaction between the protein and EGFP-tagged protein was observed by microscopic fluorescence spectroscopy. The CDMP1/VP3-immobilized polyhedra were found to be immunoactive.

Rotational freedom was found to still be active for EGFP incorporated in the polyhedra by measurement of time-resolved fluorescence anisotropy.

Furthermore, based on fluorescence lifetime and intensity measurements in comparison to those of the reference solution, we have estimated the number of active EGFP molecules, considered likely to be localized on the surface of the polyhedra. Our observations indicate that the immobilized protein molecules maintain the biological activities on the surface of polyhedra.

Our evaluation of Protein Modules based on viral octahedra suggests that they show promise for biological application. In fact, interaction with living cells was investigated and reported by Professor Hajime Mori in this book of proceedings. In order to break new ground in cellular and molecular biology, further investigation toward ascertaining the structure, dynamics, function and mechanism of Protein Modules is now in progress.

ACKNOWLEDGEMENT

This work has been supported by CREST of JST (Japan Science and Technology Agency).

REFERENCES

[1] K. Ikeda, S. Nagaoka, S. Winkler, K. Kotani, H. Yagi, K. Nakanishi, S. Miyajima, J. Kobayashi, and H. Mori, J. Virol., 75 (2001) 988.
[2] J. L. Vaughn, R .H. Goodwin, G. J. Thompkins, and P. McCawley, In Vitro, 13 (1997) 213.
[3] H. Mori, R. Ito, H. Nakazawa, M. Sumida, F. Matsubara, Y. Minobe, J. Gen. Virol. 74 (1993) 99.
[4] K. Ikeda, H. Nakazawa, A. Shimo-Oka, K. Ishio, S. Miyata, Y. Hosokawa, S. Matsumura, H. Masuhara, S. Belloncik, R. Alain, N. Goshima, N. Nomura, K. Morigaki, A. Kawai, T. Kuroita, B. Kawakami, Y. Endo, and H. Mori, Proteomics, 6 (2006) 54.
[5] G. Striker, V. Subramaniam, C. A. M. Seidal, and A. Volkmer, J. Phys. Chem. B, 103 (1999) 8612.
[6] M. Cotlet, J. Hofkens, M. Maus, T. Gensch, M. van der Auweraer, J. Michiels, G. Dirix, M. van Guyse, J. Vanderleyden, A. J. W. G. Visser, and F. C. De Schryver, J. Phys. Chem. B, 105 (2001) 4999.
[7] A. A. Heikal, S. T. Hess, and W. W. Webb, Chem. Phys., 274 (2001) 37.
[8] K. Suhling, D. M. Davis, and D. Phillips, J. Fluorescence, 12 (2002) 91.

This page intentionally left blank

Handai Nanophotonics, Volume 3
H. Masuhara, S. Kawata and F. Tokunaga (Editors)

Chapter 22

Immobilization of protein molecules into insect viral occlusion body and its application

H. Mori[a,b], Y. Hosokawa[c], H. Masuhara[c], C. Shukunami[d], and Y. Hiraki[d]

[a]Insect Biomedical Research Center, Kyoto Institute of Technology, Matsugasaki, Sakyo-ku, Kyoto 606-8585, Japan

[b]Protein Crystal Corporation, 2-3-8, Honmachi, Chuo-ku, Osaka 541-0053, Japan

[d]Department of Applied Physics, Osaka University, Suita, Osaka 565-0871, Japan

[d]Department of Cellular Differentiation, Institute for Frontier Medical Sciences, Kyoto University, Sakyo-ku, Kyoto 606-8507, Japan

1. CYTOPLASMIC POLYHEDROSIS VIRUS

Cytoplasmic polyhedrosis viruses (CPVs) are classified as the genus *Cypovirus* in the family *Reoviridae* (1). These viruses produce large proteinaceous occlusion bodies called polyhedra in the cytoplasm of infected midgut epithelial cells of a wide range of insects (1, 2) (Fig.1). The polyhedra are the result of the crystallization of a viral encoded protein, polyhedrin, late during the viral infection and many virus particles are occluded into the polyhedra (1, 2). One of the functions of these polyhedra is to protect the virions from hostile environmental conditions during the horizontal transmission of the disease (2). The polyhedra are highly resistant to both nonionic and ionic detergents and to solubilization at neutral pH. Another function of the polyhedra is to assure the delivery of virus particles to the target intestinal cells. Here the polyhedra are dissolved by the strongly alkaline pH of the insect midgut, thereby releasing the virions and allowing the infection to proceed.

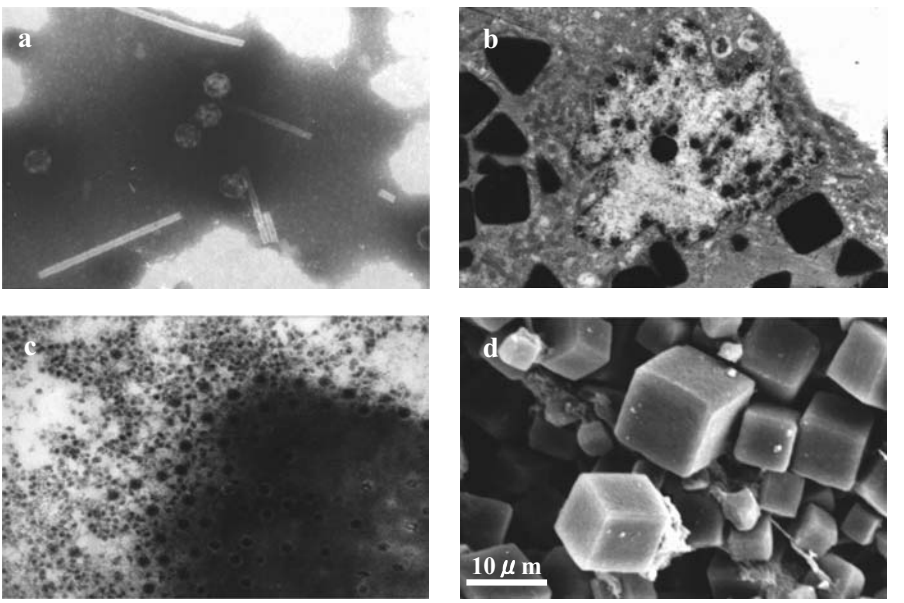

Fig. 1. Electron microscopy of BmCPV. (a) purified BmCPV particles, (b) infected cells with BmCPV, (c)

1.1. Polyhedrin

The CPV's viral genome is composed of 10 discrete equimolar double-stranded (ds) RNA segments (S1-S10) (1). Based on the variations in the electrophoretic migration patterns of the genomic dsRNA segments, 14 types of CPV have been identified (1). The polyhedrin has a molecular mass ranging from 27 kDa to 31 kDa, and the smallest genome segment encodes the polyhedrin. The polyhedrin genes of type 1 Bombyx mori CPV (BmCPV) and type 5 CPVs including Euxoa scandens CPV (EsCPV), Orgya pseudotsugata CPV (OpCPV), and Heliothis armigera CPV (HaCPV) were cloned and the nucleotide sequences were determined (1). No similarities were found in the DNA sequences of the polyhedrin gene of two distinct virus types type1 (BmCPV) and type 5 (EsCPV). The amino acid sequence of BmCPV and EsCPV polyhedrin however shows a weak homology in three regions. Especially, the hydrophilic profiles and predicted secondary structures of both BmCPV and EsCPV polyhedrin show some similarities, mainly in the amino-terminal half of the polypeptides (1).

Virus particles of BmCPV are composed of VP1 (151 kDa), VP2 (142 kDa), VP3 (130 kDa), VP4 (67 kDa), and VP5 (33 kDa) (1). The *in vitro* labeling of

BmCPV with ^{125}I indicated that VP1 and VP3 were outer components (3). Recently, it was reported that BmCPV particle has a single shell capsid and there are two sizes of protrusions on the capsid shell (4). The coding assignments of dsRNA segments for BmCPV were performed by in vitro translation studies with rabbit reticulocyte (5). The nucleotide sequences of S6 and S7 encoding BmCPV-VP4 and VP5 and those of S8 and S9 encoding two nonstructural proteins have been determined. Using in vitro translation studies it was speculated that BmCPV outer components VP1 and VP3 are encoded by S1 and S4 respectively, however these two dsRNA segments have not been characterized.

1.2. Viral protein

The complete nucleotide sequence of the genome segment 4 (S4) of *Bombyx mori* cytoplasmic polyhedrosis virus (BmCPV) was determined. The 3,259 nucleotide sequence contains a single long open reading frame spanning nucleotides 14 to 3,187 which is predicted to encode a protein with a molecular mass of about 130 kDa (6). Western blot analysis showed that S4 encoded BmCPV protein VP3 which is one of the outer components of the BmCPV virion.

2. IMMOBILIZATION OF PROTEIN MOLECULES INTO POLYHEDRA

A chimeric protein consisting of most of the complete sequence of BmCPV-VP3 and green fluorescent protein (GFP) was constructed and expressed with BmCPV polyhedrin using a baculovirus expression vector. The VP3-GFP chimera was incorporated into BmCPV polyhedra and released in alkaline conditions. The results indicate that specific interactions occur between BmCPV polyhedrin and VP3 which might facilitate BmCPV virion occlusion into the polyhedra (6).

In order to map an immobilization signal for incorporation of protein molecules to a fragment of the BmCPV VP3 protein, we isolated recombinant baculoviruses encoding chimeric proteins in which either the N-terminal or C-terminal half of VP3 was fused to EGFP (7) (Fig.2). One of these viruses, designated AcVP3(N)/GFP, encoded amino acids 1-448 of VP3 fused to EGFP and the other, designated AcGFP/VP3(C), encoded EGFP fused to amino acids 428-1057 of VP3. Each recombinant virus was used for double infections together with AcCP-H, which is a third recombinant that produces a cubic form of BmCPV polyhedra. Polyhedra were purified from the co-infected host cells,

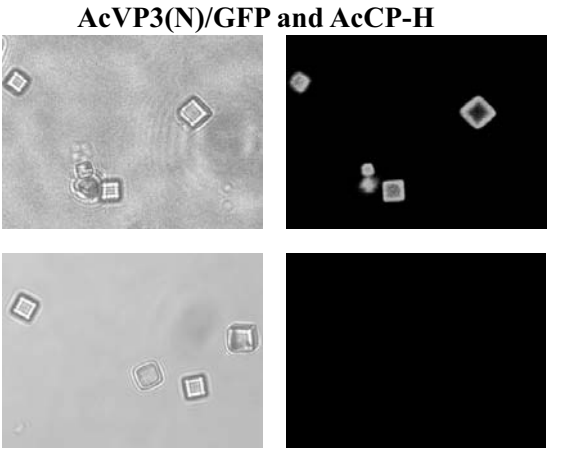

Fig. 2. Immobilization of EGFP into BmCPV polyhedra. The VP3 domain between amino acids 1 and 79 directed to the immobilization into the polyhdra.

suspended in PBS (pH 7.2) and examined by laser-scanning confocal microscopy. Green fluorescence was observed, predominantly on the surface, with polyhedra isolated from cells that had been doubly-infected with AcVP3(N)/GFP and AcCP-H. In contrast, no green fluorescence was observed with polyhedra isolated from cells that had been doubly-infected with AcGFP/VP3(C) and AcCP-H (7).

We subsequently constructed a large number of recombinant baculoviruses encoding different VP3-GFP fusion proteins. Sf 21 cells were co-infected with these recombinant baculoviruses and AcCP-H, polyhedra were purified from each doubly-infected culture, and then the presence of each fusion protein in the polyhedra was examined by confocal microscopy. Based upon the results of these analyses, which are summarized in Table 1, we were able to conclude that the occlusion of cypovirus particles into polyhedra requires the VP3 domain between amino acids 1 and 79 and this amino acid sequence also was able to direct the immobilization signal for incorporation of foreign proteins into polyhedra (7).

3. PROTEIN MICROARRAYS

Protein microarrays have important applications for the analysis of protein-protein, substrate-enzyme, DNA-protein, RNA-protein, and ligand-protein

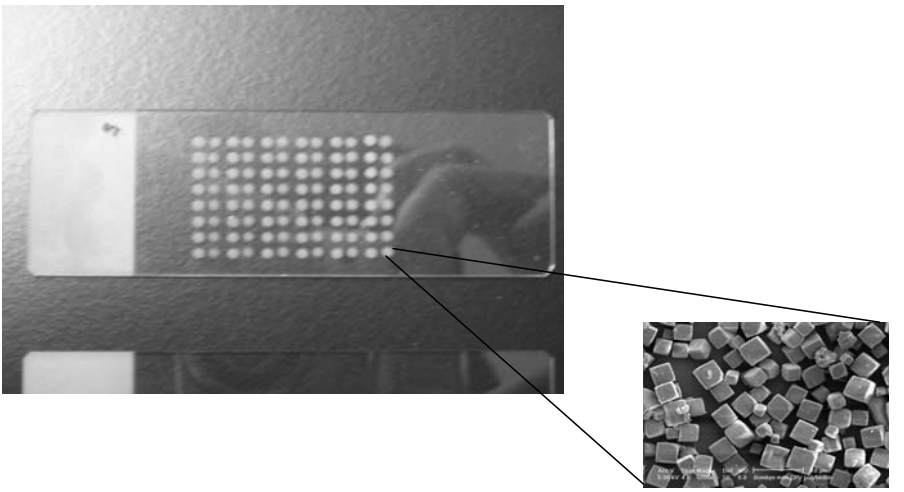

Fig. 3. Protein microarrays using BmCPV polyhedra. Many protein molecules were immobilized into BmCPV polyhedra and each polyhedron was spotted on the glass slide.

interactions. However, proteins are composed of twenty different amino acids, which result in the production of diverse molecules with highly different properties. Proteins may be hydrophilic or hydrophobic, acidic or basic, and may acquire many different covalent chemical modifications, such as phosphorylation and glycosylation. The diversity of individual protein structures, together with the need to maintain all these proteins in a functional state, pose significant problems that must be overcome to develop a broadly useful protein microarray technology.

The polyhedra, which occlude progeny virions produced during infection and function to protect these virions from hostile environmental conditions. It has been postulated that the polyhedra produced by certain insect viruses could be a useful platform for protein immobilization without destruction of biological activity. We determined the immobilization signal for incorporation of protein molecules into polyhedra and showed that many human proteins can be successfully immobilized into polyhedra without loss of function (7).

4. SCAFFOLD FOR CELL PROLIFERATION

Hormones and cytokines in circulation represent a typical mode of cell-cell communication via diffusible extracellular signal molecules. Extracellular concentrations and affinities to cell-surface receptors are the major determinants

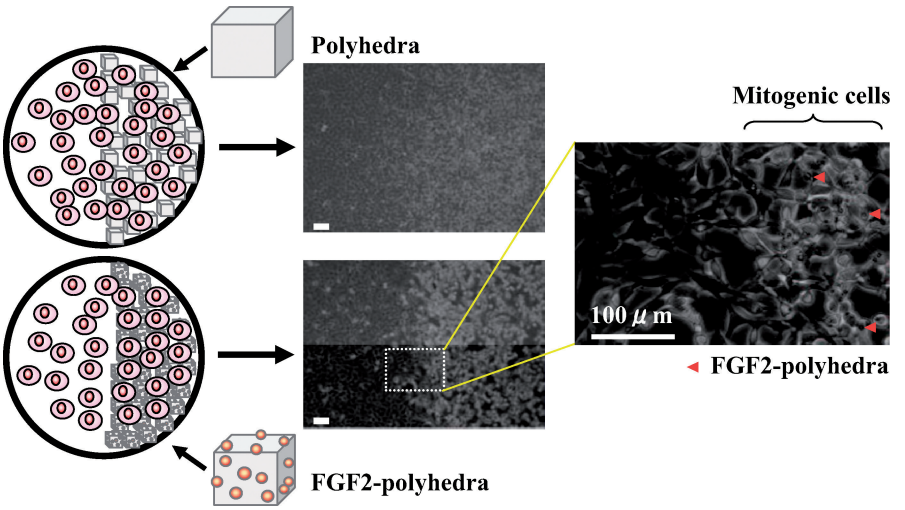

Fig. 4. Effects of FGF-2 polyhedra on proliferation of ATDC5 cells. The ATDC5 cell is an embryonal carcinoma derived chondrogenic cell line. Polyhedra or FGF2-polyhedra were spotted on the one side of Thermanox coverslips and completely desiccated. The coverslips were put on the well of an 8-well plate and ATDC5 cells were seeded at a density of $1x10^4$ cells per well. After 2 days incubation, the effect on the proliferation of ATDC5 cells was investigated.

of the potency of signaling proteins. However, with the exception of hematopoietic and/or blood cells, all single cells throughout the various organs receive their signaling cues from the extracellular matrix (ECM). The basal lamina underlying the epithelial cell sheets, and the specialized ECM in the mesenchyme such as cartilage and bone, play a crucial role in this regard during the regulation of cellular behavior. The ECM provides a supramolecular architecture for the disposition of specific accessory molecules that exist in low abundance, such as growth factors, which are released after proteolytic cleavage to effect a downstream alteration in the behavior of the responding cells. Conversely, cells that regulate remodeling (or degradation under certain conditions) of the ECM do so via the production and secretion of proteases and protease inhibitors. Thus, each individual cell sends and receives spatio-temporally restricted signals from its extracellular environment. However, only limited tools are currently available that can generate signaling cues in a spatially restricted manner at the cellular or subcellular level *in vitro* to enable further studies of these events. As fibroblast growth factor-2 (FGF2) is one of

well characterized heparin binding growth factors and regulates cell proliferation, differentiation, or migration, we attempted here to produce polyhedra immobilized growth factors using this technology, including human FGF2.

The supramolecular architecture of the extracellular matrix (ECM) and the disposition of its specific accessory molecules give rise to variable heterotopic signaling cues for single cells. We describe here the successful occlusion of human FGF2 into the BmCPV polyhedra. The polyhedra are proteinous cubic crystals of several microns in size that are insoluble in the extracellular milieu. Purified FGF2-polyhedra were found to stimulate proliferation and phosphorylation of p44/p42 MAP kinase in cultured fibroblasts. Moreover, cellular responses were blocked by a synthetic inhibitor of the FGF signaling pathway, SU5402, suggesting that FGF2-polyhedra indeed act through FGF receptors. Furthermore, FGF2-polyhedra retain potent growth stimulatory properties even after desiccation. In contrast, purified recombinant FGF2-protein that has been solubilzed in saline completely loses its mitogenic activity after desiccation. We demonstrate that BmCPV polyhedra microcrystals that occlude extracellular signaling proteins are a novel and versatile tool that can be employed to analyze cellular behavior at the single cell level (under submission).

REFERENCES

[1] Belloncik, S. and Mori, H. Cypoviruses. In The Insect Viruses. (eds. Miller, L. K. & Ball, L. A.) 337-369 (Plenum, New York; 1998).

[2] Rohrmann, G.F. Polyhedrin structure. J Gen Virol 67, 1499-1513 (1986).

[3] Lewandowski, L. J., and B. L. Traynor. Comparison of the structure and polypeptide composition of three double-stranded ribonucleic acid containing viruses (Diplorna viruses). Cytoplasmic polyhedrosis virus, wound tumor virus and reovirus. J. Virol. 10: 1053-1070 (1972).

[4] Hill, C. L. et al. The structure of a cypovirus and the functional organization of dsRNA viruses. Nat. Struct. Biol. 6: 565-568 (1999).

[5] McCrae, M. A., and P. P. C. Mertens. In vitro Translation Studies on and RNA Coding Assignments for Cytoplasmic Polyhedrosis Viruses, p. 35-41; R. W. Compans and D. H. L. Bishop (eds.), Double-Stranded RNA Viruses. Elsevier Biomedical, New York (1983).

[6] Ikeda, K. et al. Molecular characterization of Bombyx mori cytoplasmic polyhedrosis virus genome segment 4. J Virol 75, 988-995 (2001).

[7] Ikeda, K. et al. Immobilization of diverse foreign proteins in viral polyhedra and potential application for protein microarrays. Proteomics 6, 54-66 (2006).

This page intentionally left blank

Handai Nanophotonics, Volume 3
H. Masuhara, S. Kawata and F. Tokunaga (Editors)

Chapter 23

All-optical switching in rhodopsin proteins

S. Roy

Department of Physics and Computer Science
Dayalbagh Educational Institute (Deemed University)
Dayalbagh, Agra 282 005, India

1. INTRODUCTION

Light sustains life on earth. It is one of the most important signals providing important information to biological systems. Plants, seaweeds, and photo-synthesizing bacteria absorb sunlight and convert it into their life energy [1-3]. In addition to human vision, light controls movement, growth, differentiation, development, circadian clock and a host of gene-expression responses in diverse organisms from prokaryotic microbes to eukaryotic plants and animals [4, 5].

Every form of living matter uses information processing [6]. While the principles governing natural computing are so far not understood, it is evident that natural implementations utilize matter in a markedly different way than conventional information processing systems. Although the basic ideology in information processing so far has been to mimic the way nature processes information through semiconductor electronics, present day capabilities are no way near to the complex tasks performed in natural processes whether in a small cell or the human brain [7-10].

The fact that natural biomolecules exhibit an efficient nonlinear optical response is extremely fascinating. Driven by the dual needs of understanding natural information processing and adopting a cost-effective and environmentally safe technology that has the potential to meet our future needs, has provided the impetus to investigate natural photosensitive biomolecules for a variety of photonic applications [3, 11-14]. The ability to harness the power of nano and biotechnologies for information technology forms an important application of the niche multidisciplinary area of *Nano-Bio-Photonics*.

One of the most light sensitive biomolecules that has been the subject of great interest is the rhodopsin protein contained in the cone cells of the human retina. Retinal (Vitamin A aldehyde) is a chromophore that binds integral membrane proteins (opsins) to form light absorbing pigment called rhodopsins.

Rhodopsins are currently known to belong to two distinct protein families, i.e. the visual rhodopsins found in eyes throughout the animal kingdom that are photosensory pigments, and archael rhodopsins found in extreme halophiles, which function as light driven proton pumps (bacteriorhodopsins), chloride-ion pumps (halorhodopsins), or photosensory receptors (sensory rhodopsins) [15-20]. Many of the same halobacteria that use bacteriorhodopsin as a transducer to convert light energy to chemical free energy also have two other retinal proteins that are involved in photosignaling: sensory rhodopsins I and II. The amino acid sequences of these retinal proteins are quite similar. They also have many properties in common. For example, transduction is initiated by photo-isomerization, leading to a reversible sequence of changes in the pigment, the "photocycle." All four pigments use the all-*trans* isomer of retinal as the chromophore configuration for their initial active state. Upon radiation of the chromophoric center of any rhodopsin, the retinal molecule undergoes conformational changes in the protein. This process is reflected in the changes in the absorption spectrum of the molecules. While originally thought to occur only in higher animals capable of vision, retinal proteins recently have also been found in unicellular plant organisms, in fungi, in bacteria and, most diverse in function, in halophilic archaea [4, 5, 13].

The photochromic protein bacteriorhodopsin (bR), which is found in the purple membrane of *Halobacterium halobium,* has been the focus of intense research as it serves as a model to understand the basic transport processes fundamental to all forms of life, and due to its unique charge transport, photoelectric and photochromic properties [11-13, 18, 21-24]. It has become a paradigm for membrane proteins in general and transporters in particular [19, 20]. The bR molecule initially excited by photons undergoes several structural transformations in a complex photocycle that generates intermediates exhibiting absorption spectra spanning the entire visible spectrum, Fig.1. Under certain conditions, a branching reaction takes place in the typical photocycle of bR [21-26]. A long-lifetime state containing *9-cis* retinal in its photochromic group is obtained by photochemical excitation of an all-*trans*-retinal alongwith protonation of Asp85 with red light. This state (P-state) is thermally stable and is no longer catalyzed to transform to the all-*trans* configuration of the initial state. It can be formed in wild-type (WT)-bR either by low pH values, de-ionization, replacing Asp85 for an amino acid having a different pK_a value that stays in its uncharged form or by removing the carboxylate group by mutation.

A typical example of such a mutation is Asparagine (bR-D85N). The P-state has a maximum absorption at 490 nm and can be photochemically reconverted to the initial B-state with blue light. In the dark, a thermal decomposition of the P-state into the Q product has also been observed. The long lifetime P and Q states can hence be used for permanent optical data storage leading to bR based 3D volumetric memories with extremely high optical data storage [21-25].

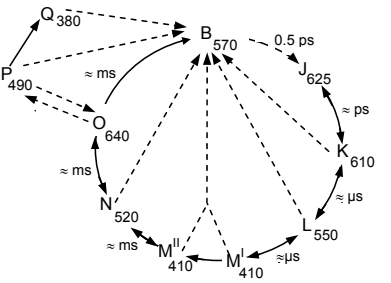

Fig.1. Schematic of the photochemical cycle of bR molecule. Subscripts indicate absorption peaks in nm. Solid and dashed arrows represent thermal and photo-induced transitions, respectively.

Bacteriorhodopsin protein exhibits high quantum yield and efficiency of converting light into a state change, large extinction coefficients and optical nonlinearities, low isomerization time, robustness to degeneration by environmental perturbations and high thermal stability towards photo-degradation. The low production cost, capability to form thin films in polymers and gels and flexibility to tune its kinetic and spectral properties by genetic engineering techniques, have made bR a potential candidate for device applications [11-13, 18, 21-24].

Numerous applications have been proposed based on its unique properties. Its proton pumping and photo-electric properties have been used to design artificial retinas, desalination of sea water, photovoltaic cells, photo-electrochemical splitting of water to generate hydrogen, biosensors, ultrafast light detectors and photon counters. Its photochromic property has resulted in applications that include pattern recognition systems, information recording, photographic film, associative and 3D memories, holography, second harmonic generation, saturable absorption, wave mixing and phase conjugation, nonlinear optical filtering, interferometric systems, optical bistability, mode-locking, optical limiting, spatial light modulation, optical image processing, neural networks, incoherent to coherent conversion, optical displays, logic gates, beam deflection, photochromic and electrochromic inks, as a natural efficient photonic crystal and even slow light for all-optical information processing [11-13, 21-28].

The purification of sensory rhodopsin (sR I) and phoborhodopsin (pR), also called sRII, is very difficult. However, it has been synthesized from *Natronobacterium pharaonis*, a halophilic alkaliphilic bacterium termed *pharaonis* phoborhodopsin (*p*pR) and has received much attention due to its stability and its recent structure elucidation [29-36]. Among the archaeal sensory rhodopsins, *p*pR has the most robust properties and is able to function during photosignaling in *N. pharaonis*, *H. salinarium* and *E. coli.* It remains stable both in the dark and under prolonged illumination, and it retains its native absorption

spectrum and photocycle in different membranes; in a range of detergents; in salt concentrations from 25 M to 4 M, and over a broad range of pH. These exceptional properties have made it the prototypical sensory rhodopsin for crystallography and structure-function studies [35, 36]. It exhibits unique properties that are distinct from other retinal proteins. It exhibits a photocycle similar to bR with shorter absorption maximum wavelength (blue-shifted) with vibration fine structure. Its unique absorption spectrum has spectral shoulders at wavelengths shorter than their absorption maxima in contrast to other retinal proteins that have broad bell-shaped spectra. A spectroscopically distinct *p*pR$_N$ intermediate is absent that has only been observed to be composed of an equilibrium mixture of intermediates. It has high thermal stability of the *p*pR$_K$ intermediate at low temperatures, more extended structural changes with considerably longer lifetime of intermediate states in its photocycle; and no light-dark adaptation of all-*trans* and 6S-*trans* retinal ground state [28-35]. The WT-*p*pR molecule undergoes several structural transformations in a photocycle by absorbing green light: $p\text{pR}_{498} \xrightarrow{h\nu} p\text{pR}_{K540} \xrightarrow{50ns} p\text{pR}_{KL512} \xrightarrow{990ns} p\text{pR}_{L488} \xrightarrow{32\mu s} p\text{pR}_{M390} \xrightarrow{1.7s} p\text{pR}_{O560} \xrightarrow{770ms} p\text{pR}_{498}$. The intermediates are named in analogy to those in the bR photocycle [29-33]. Recently, mutamts have been generated that exhibit *p*pR$_M$ and *p*pR$_O$ intermediate lifetimes of the order of those in bR (~ms) [34].

Recently, proteorhodopsin (pR), a light-activated proton pump homologous to bR has been discovered in oceanic γ-proteobacteria [37, 38]. Proteorhodopsin is a 249-amino acid membrane protein native to several uncultured species of γ-proteobacteria, which are a component of marine plankton. Addition of retinal to *E. coli* expressing pR has been shown to cause a reddish coloration of the bacteria with an absorption maximum near 520 nm [37-41]. The pR contained in the bacterial membranes has been shown to act as a light-activated proton pump only in the presence of the retinal. A time-resolved UV/Vis study at pH 8 has also revealed that the protein undergoes a photocycle, similar to that of WT-bR [41]. WT-pR also exhibits a photocycle on absorption of light: $\text{pR}_{520} \xrightarrow{h\nu} \text{pR}_{K555} \xleftrightarrow{43ms\,/\,14ms} \text{pR}_{MI405} \xrightarrow{222ms} \text{pR}_{MII405} \xleftrightarrow{0.53ms\,/\,1.9ms} \text{pR}_{N560} \xleftrightarrow{18.8ms\,/\,119ms} \text{pR'}_{520} \xrightarrow{153ms} \text{pR}_{520}$, where on double arrows, the time mentioned first is for forward reaction and the second for back reaction [41].

Since its discovery, as many as 800 relatives have been identified in samples throughout the world's oceans. Microorganisms containing rhodopsin genes inhabit diverse environments including salt flats, soil, fresh water, surface and deep sea water, glacial sea habitats and human and plant tissues as fungal pathogens. They comprise a broad phylogenetic range of microbial life, including haloarchaea, proteobacteria, cyanobacteria, fungi, dinoflagellates, and green algae [4, 5]. Nano-biotechnology has effectively been used to synthesize and design several mutants and genetic variants [5, 11-13, 15-26].

A switch is the basic building block of information processing systems [42-46]. The anticipated need for high speed high bandwidth communication and computing has given the impetus to realize all-optical information processing, to overcome the electronic bottleneck [46-52]. Photosensitive molecules can be used as switches that can be converted from one state to another by an external light stimulus. They would offer unique advantages such as small size and weight, low power operation, high quantum efficiency, fast response, high stability, low cost and most important, the ability to tailor molecular properties by chemical, physiochemical or genetic engineering techniques [51, 52].

The efficient photochromic property of rhodopsins can be used to perform all-optical switching for potential applications in optical computing [51]. All-optical switching and logic operations in bR have been demonstrated though various techniques such as sequential photo-excitation [53], dynamic holographic gratings [54, 55], degenerate four-wave mixing [56], photo-induced dichroism and birefringence [57-59], integrated-optic waveguide [60], complementary suppression-modulated transmission [61-63], self-diffraction [64-67] and excited-state absorption (ESA), with cw and pulsed beams [22, 26, 68-81]. All-optical switching in *p*pR and pR has also been reported recently [82-86].

Molecular conformation is a key process in many biological functions. A wide range of photo-sensitive proteins exhibit conformational changes in a well defined photocycle. Photo-induced conformational switching of proteins between different states with multiple laser beams leads to all-optical switching. The photochemistry of retinal proteins is similar to rhodopsin [18]. In this Chapter, we present a brief review of all-optical switching in archael rhodopsin proteins (bR, *p*pR and pR) with cw and pulsed pump laser beams, based on the phenomena of intensity-induced ESA. They exhibit similar photocycles and their respective properties can be tailored to match with corresponding intermediates [33]. Moreover, either by varying the physical conditions under which the molecules operate or by minor genetic modifications, the functions of the retinal proteins of halobacteria are interconvertible [13]. Hence, analysis of all-optical switching presented here is applicable in general to a wide variety of proteins. We discuss its application in the design of switches, spatial light modulators and logic gates and present issues that emerge from the analysis, that need to be addressed by nano-biotechnology to meet practical requirements.

2. THEORETICAL MODEL

The phenomenal capability to control '*light with light*', requires the application of the principles of nonlinear optics. The nonlinear interaction of light with matter can be classified into resonant (absorbing matter) and non-resonant (transparent matter) interactions with both coherent and incoherent light

respectively. In case of incoherent resonant interaction, the nonlinear behavior can be described by an intensity-dependent absorption-coefficient $\alpha(I')$ [87].

In simple cases such as under stationary conditions (steady-state) and for optically thin samples, these absorption-coefficients can be written analytically as rational polynomials of the intensity. The nonlinear incoherent absorption results from the change in population of absorbing or emitting energy states of matter and the absorption-coefficient for a given light beam can be written as,

$$\alpha = \sum_i \pm\sigma_i(\lambda)N_i(I',r,t) \tag{1}$$

where σ_i is the cross-section of the i^{th} eigenstate (or energy level) of matter and N_i is its population density. The summation includes all possible absorption and emission transitions with positive and negative signs respectively, between the various energy levels. Light intensity-induced population changes of m different energy levels can be described by the rate equations in the form,

$$\frac{dN_i}{dt} = \hat{O}N \tag{2}$$

where the operator $\hat{O}$ is defined in terms of absorption, stimulated and spontaneous transitions taking place between energy states expressed in terms of the absorption cross-sections, rate constants and quantum efficiencies, and

$$\sum_{i=1}^{m} N_i = N \tag{3}$$

This linear system of equations can be solved numerically for stationary and non-stationary conditions. In general, for stationary models an analytical expression for the nonlinear absorption coefficient can be obtained in the form,

$$\alpha(I) = \frac{\alpha_0(1 + A_1 I_m + A_2 I_m^2 + \ldots\ldots + A_r I_m^r)}{(1 + B_1 I_m + B_2 I_m^2 + \ldots\ldots + B_r I_m^r)} \tag{4}$$

where α_0 is the small-signal absorption coefficient, I_m is the modulating photon flux density ($I'_m/h\nu$), r is the number of absorption transitions in the model and the power of the highest possible nonlinearity, and $A_1, A_2, \ldots, A_r$ and $B_1, B_2, \ldots, B_r$ are algebraic functions of the cross-sections and decay times of the material [86]. A general exact analytical expression for $\alpha(I'_m, I'_n, \ldots)$ at steady-state, for multiple modulation pump laser beams, has been derived based on a generalized model of the photocycle of bR (Fig.1), that takes into account all possible states

and transitions [26]. Assuming optically thin samples and a strong cw or quasi-cw modulation laser beam with broad light pulses, the propagation of a weak probe beam through a nonlinear medium, is governed by the equation,

$$\frac{dI'_p}{dx} = -\alpha_p(I'_m)\,I'_p \tag{5}$$

where, x is the distance in the medium and α_p is the absorption-coefficient at probe wavelength. In addition to the pump beam, absorption due to the probe beam has to be considered in Eqns. (1)-(5), when its intensity is comparable. A modulating super-gaussian pump laser pulse is given by,

$$I'_m = I'_{mo}\,exp\left(-2^{2q}\,ln\,2\left(\frac{(t-t_O)}{\Delta t}\right)^{2q}\right) \tag{6}$$

where t_o is the time at which the pulse maxima occurs, q is the pulse profile parameter and Δt is the pulse width [75-78].

3. ALL-OPTICAL SWITCHING WITH CW PUMP BEAMS

We consider retinal proteins to be excited by a cw pump beam corresponding to the peak absorption of the initial state. On excitation, the proteins undergo conformational changes in a photocycle, populating various intermediate states, before relaxing back to the initial state. The transmission of a weak probe beam corresponding to the peak absorption of any intermediate state, through the protein sample, gets modulated due to absorption by molecules in that state and in other states, if there is an overlap of their absorption spectra. Since the population of the excited-states can be controlled by varying the pump intensity, the probe transmission can be continuously modulated based on ESA, which depends on spectral and kinetic parameters [22, 26, 69-73].

All-optical switching based on ESA, using a pump-probe configuration, is a simple, flexible and convenient technique for practical applications, compared to other methods, for instance, those based on phase conjugation and interference phenomena. The transmission characteristics, namely the variation in normalized transmitted probe intensity (NTPI) with the modulating pump intensity (I'_m) can be obtained by computer simulations using Equations (1)-(5) for bR, *p*pR or pR, considering their typical photocycles with respective kinetic and spectral parameters [22, 26, 69-73, 79, 82, 83, 86].

The variation in NTPI of D96N-bR genetic variant at probe wavelength of 410 nm corresponding to the peak absorption of M-state with I'_m at 570 nm are

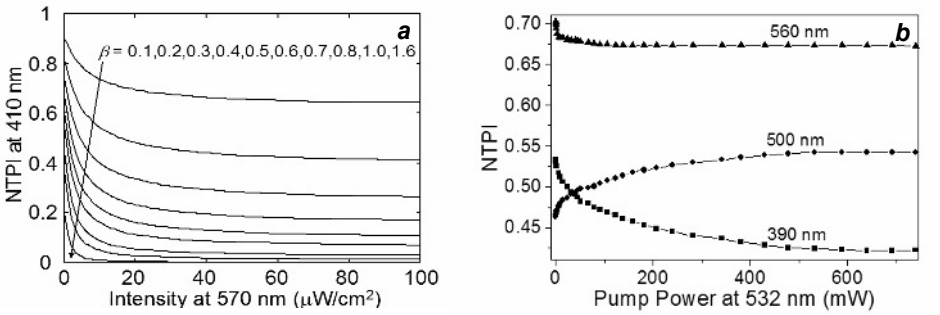

Fig. 2 (a). Simulated amplitude modulation of an input probe beam at 410 nm in D96N-bR with I'_m at 570 nm for various values of β, with $k_{MII} = 4 \times 10^{-4}$ s^{-1}[74], (b) Measured variation in NTPI in WT-*p*pR for different probes with I'_m at 532 nm, $C = 2.65$ μM and $L = 5$mm.

shown in Fig. 2 (a), for different values of the normalized small-signal absorption coefficient $\beta\,(=N\sigma_{Bp}L)$ [74]. The NTPI decreases with increase in the modulation laser beam intensity and finally saturates for considerably low intensity values compared to the wild-type(WT)-bR. There exists an optimum value of β (β_{opt}) for which maximum percentage modulation can be achieved. The β_{opt} value for which maximum percentage modulation, which in this case is 50 %, can be achieved is 0.4, at I'_m = 50 μW/cm^2. For a 2.5 pW laser, this requires focusing the laser beam to a 5 μm^2 spot area [74].

This switching mechanism can be utilized for the construction of a molecular SLM based on bR molecules. Such a SLM would be free from the problems encountered in conventional liquid crystal or semiconductor SLMs due to diffusion process, since the excitation is localized in the molecules. In this case, the resolution depends on the focusing geometry. Typical SLM properties can be estimated in the present case assuming the modulation beam as the write beam and the probe beam as the read beam. For example, the dynamic range, defined as the ratio of the transmitted intensity of the read beam through a sample of length L in the presence of the write beam, to that in the absence of the write beam, can be calculated from the expression, $\delta = exp[\alpha_R(0)L-\alpha_R(I'_w)L]$, where, α_R is the same as α_P and I'_w is the same as I'_m defined earlier. Another important SLM parameter is the sensitivity, defined as $S = -(ln\delta)/I'_w$ [70, 74]. The variation in the dynamic range and sensitivity is more for larger β values. For example, for $\beta = 0.4$, $\delta = 0.27$, for I'_w = 50 μW/cm^2 at 570 nm and hence the sensitivity $S = 26.2$ cm^2/mW. For same intensity, $\beta = 1.3$, $\delta = 0.02$ and $S = 78.2$ cm^2/mW and the minimum value of β for which the dynamic range is maximum is 1.6 [74].

Figure 2(b) shows the experimental results of modulation of three different probe beams corresponding to the peak absorption of *p*pR$_M$ (390 nm), *p*pR (500

nm) and *p*pR$_O$ state (560 nm), by a modulating pump beam at 532 nm. As expected, the transmission at 500 nm shows saturable absorption at 500 nm and reverse saturable absorption at 390 nm and 560 nm. The initial B-state absorption spectrum of D96N-bR shows small absorption at the read beam wavelength of 410 nm. Thus, the probe beam is absorbed by both M and B states, which reduces the linear transmission and hence the contrast. The percentage modulation can thus be increased by reducing the absorption cross-section of the B-state at probe wavelength (σ_{Bp}), which in the ideal case is zero [74]. For such a case, for β_M (=$N\sigma_{Mp}L$) = 2.6, the probe beam gets modulated by 90 % and δ = 0.1 and S = 46.1 cm^2/mW, for I'_m = 50 μW/cm^2. For this case, as high as 100 % modulation of the probe beam can be achieved with β_M = 5.8.

The kinetic and spectral properties of retinal proteins can be altered through physical, chemical and biotechnological procedures such as variation in the polymer environment, including pH, temperature, degree of hydration and addition of chemicals [11-13, 21-25, 29-34, 41]. For instance, addition of azide affects the absorption spectra and the *p*pR$_M$ state lifetime and replacing the amino acid (Val-108) by methionine (V108M mutant of *p*pR) causes three times faster decay of *p*pR$_M$ state and removes the shoulder of the *p*pR$_M$ spectrum [34, 88].

Figure 3(a) shows the variation in NTPI at 390 nm corresponding to peak absorption of *p*pR$_M$ state, modulated by I'_m at 498 nm for different values of k_M and k_O, corresponding to two mutants of *p*pR at different pH values [84]. It is interesting to note that variation in NTPI is contrasting (increasing or decreasing) for WT-*p*pR and its mutants. Even for the same system, in this case F86D-ppR, it can be varied to large proportions. Its characteristics at low pH = 5 can be used to realize XOR logic by considering the two pump intensities, with I'_m = 0 (off) or on at a particular value, as logic '0' and '1', respectively, while the corresponding output as NTPI, can be considered, above and below a threshold level, as logic '1' and '0', respectively.

For instance, considering the combinations of the two input intensities to be I'_m = 9.0 mW/cm^2 and 0, as logic '1' and '0' respectively, the output becomes high in presence of either one of the inputs and becomes low in absence and presence of both inputs. This conforms to an all-optical XOR logic gate, Fig. 3(b) [84].

The variation in the NTPI at 512 nm corresponding to the peak absorption of the *p*pR$_{KL}$ state of WT-*p*pR with I'_m at 498 nm has been shown in Fig. 4(a). Initially, NTPI is low due to high absorption by the initial state. As I'_m increases, the population of the *p*pR$_{KL}$ state decreases, as it absorbs the pump wavelength itself at 498 nm and hence leads to increase in NTPI and large percentage modulation. For instance, for β = 7, the probe beam can be modulated by 96.22 % with I'_m = 1 W/cm^2. For an optimized SLM for this case, β_{opt} = 5.25, for I'_m = 1 W/cm^2, for which 96.70% modulation can be achieved, as shown in inset of

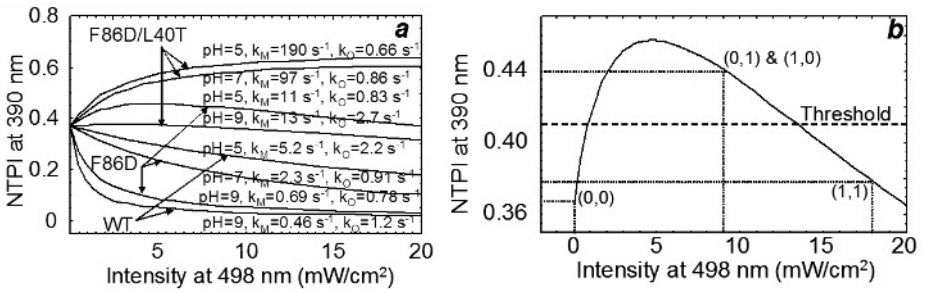

Fig. 3. Amplitude modulation of an input probe beam at 390 nm in *p*pR with I'_m at 498 nm (a) for WT-*p*pR and two mutants that exhibit different values of the rate constant of the *p*pR$_M$ (k_M) and *p*pR$_O$ state (k_O) with $\beta = 1$. (b) Magnified view of the variation with F86D-*p*pR with $k_M = 11$ s^{-1}, $k_O = 0.83$ s^{-1} at pH = 5, and implementation of an all-optical XOR logic gate. Adapted from Ref. [84].

Fig. 4 (a). As I'_m increases, β_{opt} increases. The percentage modulation in this case is larger than *p*pR$_O$ case, although at relatively higher I'_m values. The corresponding variation in NTPI at 560 nm is shown in Fig. 4(b). Initially, the transmission of the probe beam is high due to low absorption by the initial *p*pR state only. As the intensity of the pump beam (I'_m) increases, the NTPI decreases due to increase in the population of the *p*pR$_O$ state, which results in greater absorption of the probe beam at relatively low pump intensities. However, at higher I'_m, increased absorption of the pump beam by the *p*pR$_O$ state itself results in a dip in the modulation characteristics. The NTPI can be made to increase monotonically at larger values of k_O (10 s^{-1}), i.e., the dip can be removed, due to lower population of the *p*pR$_O$ state and hence less absorption of the probe and also by increasing k_M and decreasing σ_O [79, 83]. A decrease in σ_O results in a decrease in the off-on percentage modulation, i.e., NTPI saturates and does not increase at higher I'_m values. The dip in the transmission characteristics can only be obtained for the O-state dynamics in bR or *p*pR, due to spectral overlap between their respective initial and the O-intermediates at pump wavelength. Hence, increasing I'_m leads to a transition from reverse saturable absorption to saturable absorption [79, 83].

For NTPI having positive slope with I'_m, β_{opt} increases with increase in I'_m, inset of Fig. 4(a), whereas, for NTPI having negative slope with I'_m, β_{opt} decreases with increase in I'_m. There is also a β_{opt} value between two I'_m values, i.e., exposing *p*pR sample to a low and then a high pump intensity, as shown in inset (ii) of Fig.4(b), for which maximum modulation of the probe beam [79, 83]. The transmission characteristics corresponding to O-state dynamics in bR or *p*pR can be used to design multiple input all-optical NOT, NOR, NAND, OR, AND and XNOR logic gates by considering the transmission of the probe beam as output and multiple pump beams as inputs for two cases (i) using the same

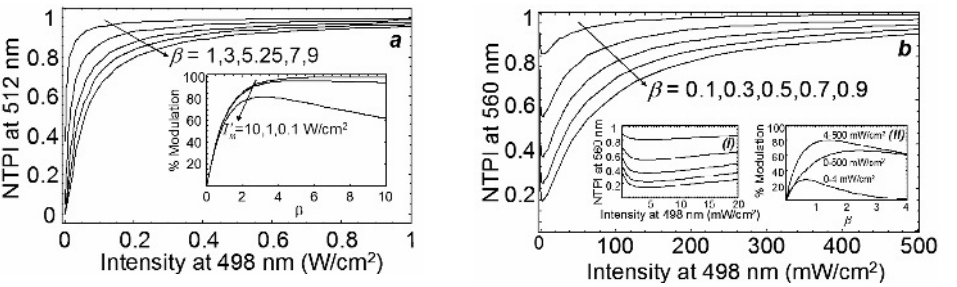

Fig. 4. (a) Variation of NTPI at 512 nm in WT-*p*pR with I'_m at 498 nm for various values of β. The inset shows the variation of percentage modulation of probe beam with β for different pump intensity values, Adapted from [84], (b) Variation of NTPI at 560 nm in *p*pR I'_m at 498 nm for various values of β with k_O = 1.3 s^{-1}. Inset (i) shows the corresponding variation at lower pump intensity values. Inset (ii) shows the percentage modulation of the probe beam versus β for different pump intensity ranges. Adapted from Ref. [83]

medium and only changing the output threshold level and (ii) using media with different β values and considering a common threshold. Using the same setup, different logic operations can be generated by considering different parts of the transmission characteristics by varying the input intensities only [79, 83].

4. ALL-OPTICAL SWITCHING WITH PULSED PUMP BEAM

We consider the transmission of a cw probe laser beam of intensity I'_p, ($I'_p << I'_m$) at 410 nm corresponding to the absorption maximum of the M intermediate in the bR photocycle, modulated by excitation of bR molecules by a gaussian pulsed pump laser beam at 570 nm. In WT-bR, the lifetime of the M-state ~ ms. Initially, in the absence of the modulating pulse, all protein molecules stay in the initial bR state, hence, the NTPI is high (on-state) due to less linear absorption of signal beam by initial bR state only. As the modulating pulse excites the bR molecules, the population of longer-lived M intermediate increases, which leads to increased absorption of the signal beam and hence switching-off of the NTPI. This results in the basic all-optical switching mechanism, as shown in Fig. 5(a-dashed lines), (b) and (c) [73, 76-81].

Variation in NTPI with time for different values of the absorption cross-sections of B-state at probe wavelength (σ_{Bp}), is also shown in Fig. 5(a), for two values of M-state lifetime τ_M = 0.26 ms and 10 ms. For the case when τ_M is small, the population of the M-state is less than that of the longer lifetime N and O states. As σ_{Bp} decreases, absorption due to M-state becomes significant as the absorption of the probe beam by the B-state decreases. The variation in NTPI at 410 nm with time, as σ_{Bp} decreases, as shown by solid lines, is similar to variation in NTPI with increase in τ_M [77]. The linear absorption (initial and final values) of the NTPI shift to higher values, as σ_{Bp} decreases, due to less

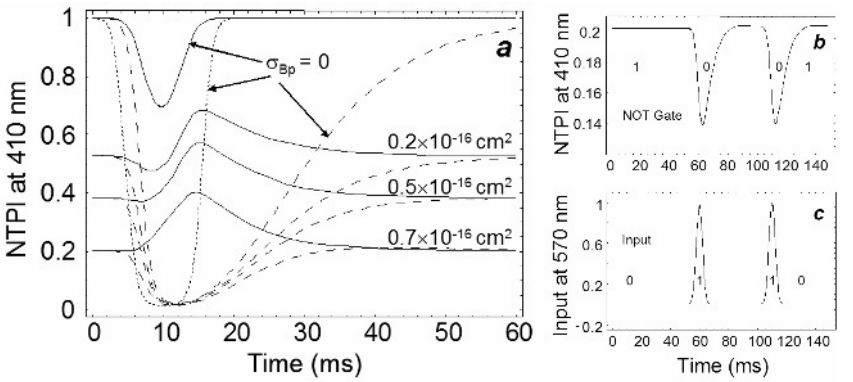

Fig. 5(a). Variation in NTPI at 410 nm with time in bR for different values of σ_{Bp} with Δt = 5 ms, I'_{m0} = 1 W/cm^2 and L = 20 μm for τ_M = 0.26 ms (solid lines) and τ_M = 10 ms (dashed lines). The dotted line corresponds to τ_M = 0.26 ms at I'_{m0} = 55 W/cm^2, (b) All-optical inverter (NOT) logic gate: variation in NTPI at 410 nm as output with time; (***c***) normalized input pulse profile at 570 nm [77].

absorption by the B-state. For σ_{Bp} = 0, the probe beam is switched due to absorption by only the M-state and gets modulated by 31 %. Complete switching i.e. 100 % modulation can be achieved by increasing I'_{m0} to 55 W/cm^2 for σ_{Bp} = 0, as shown by the dotted line, that can be achieved by a 2.8 μW laser focused to a 5 μm^2 spot size. The switch-off and on-time for this case is 8.6 ms and 9.1 ms respectively [77]. The corresponding variation for higher values of τ_M = 10 ms, is also shown in Fig. 5(a) with dashed lines. In this case, the percentage modulation increases as σ_{Bp} decreases. There is also an optimum value of concentration for maximum contrast in this case as β_{opt} in the cw case. For σ_{Bp} = 0.5×10^{-16} cm^2 and 0.2×10^{-16} cm^2, 20 % and 55 % modulation of the probe beam can be achieved respectively, for I'_{m0} = 1 W/cm^2. For σ_{Bp} = 0, 100 % modulation of the probe beam can be achieved for the same intensity. The switch-off and on-time for this case is 9.4 ms and 55.2 ms respectively. For τ_M = 250 s as shown for D96N [89], 100 % modulation of the probe beam can be achieved for I'_{m0} = 0.4 W/cm^2. Thus, for larger lifetime of an intermediate, the corresponding switching takes place at lower I'_{m0}, although it results in slower switching. Hence, for σ_{Bp} = 0, complete switching for larger values of τ_M can be achieved at lower I'_{m0}, although the switch-on time increases. The switching characteristics become more asymmetric with increase in τ_M due to increase in the total photocycle time in comparison to the pump pulse width.

The switching characteristics can be used to design all-optical NOT, OR, AND and the universal NOR and NAND logic gates with multiple pulsed pump laser beams Fig. 6 [73, 76-81]. For lower value of τ_M = 0.26 ms, the NTPI exhibits an increase as each pulse pumps the sample as shown in Fig. 5 (a) and 6(c). Two- input OR and AND logic operations can be realized by considering

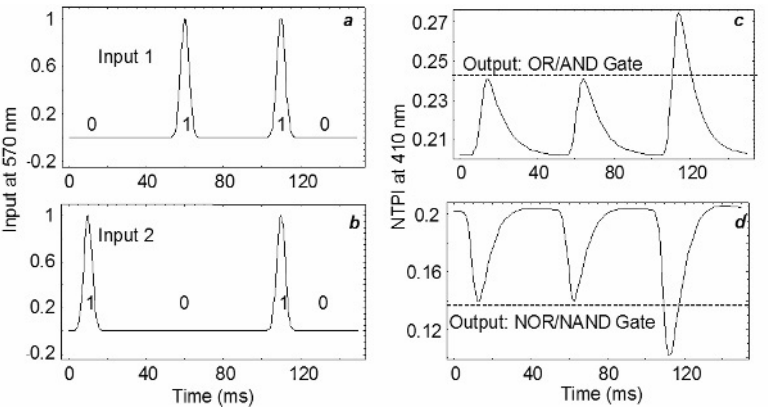

Fig. 6. All-optical logic operations in bR with NTPI as output with time: (a) and (b) are normalized pulse profiles of the two inputs 1 and 2 at 570 nm, with Δt = 5 ms, L = 20 μm and I'_{m0} = 70 mW/cm^2 (c) OR gate (without threshold) and AND gate (with dashed line as the threshold level), with τ_M = 0.26 ms, (d) NOR gate (without threshold) and NAND gate (with dashed line as the threshold level), with τ_M = 10 ms. Adapted from Ref. [77].

two pulsed pump laser beams (I'_{m1} and I'_{m2}) at 570 nm, as the two inputs 1 and 2 Fig. 6 (a), (b), and amplitude modulation of the probe beam, i.e., NTPI as the output, Fig. 6 (c), (d). The output is high for each incident pulse and it increases further when both pump simultaneously, as the total pump intensity increases. These characteristics correspond to the all-optical OR logic gate, as the output is high when either one or both the input pulses are present and is low only when none of the pulses is present, as is shown in Figs. 6(c). The same configuration can also result in an all-optical AND logic gate, if a threshold level is considered as shown by the dashed line in Fig. 6(c). In this case, the output can be considered to be low when either one or none of the pulses are present and high only when both the input pulses are present simultaneously.

The switching characteristics can also be used to design the universal NOR and NAND logic gates with the same configuration, for a bR film with a larger value of τ_M = 10 ms. In this case, the NTPI would decrease due to absorption by the M-state, as its population is large. For the all-optical NOR logic gate, the output is low when either one or both the pulses are present and is high when none of the two pulses is present, as is shown in Fig. 6(d). The same configuration can also result in an all-optical NAND logic gate by considering a threshold level shown by the dashed line in Fig. 6(d). In this case, the output can be considered to be high when either one or none of the pulses are present and low only when both the input pulses are present simultaneously [77].

The switching time can be reduced by increasing the relaxation rates of the intermediate states so that the excitation time from B→M is reduced and also by

decreasing the thermal relaxation time from M→B. Life time of the M state (τ_M) is an important parameter and the switching characteristics can be tailored by changing τ_M. The switching time can also be reduced by considering switching of the probe beams corresponding to the peak absorption wavelength of the earlier intermediate K or L states. The K-state is thermally stable at very low temperatures (83 K), when the transition to the next state is inhibited [21]. Hence, a genetic variant that exhibits a truncated photocycle at higher temperatures, with early states that exhibit shifted absorption spectra relative to the initial B-state (σ_{Bp}~0), would lead to fast switching with high contrast.

The switching contrast can be enhanced by reducing the absorption cross-section of the initial B-state at the probe wavelength for longer τ_M values, to design the NOT, NOR and NAND logic gates. The percentage modulation increases with increase in I'_{m0} and saturates after a certain value. Hence, the difference between the NTPI for single and double input pulses decreases for AND and NAND logic gates. There is thus an optimum value of the peak pump intensity for which the difference in the NTPI for the two input pulses and the threshold intensity level is maximum [77]. For a fixed value of τ_M, the respective logic gate combinations can be realized with the same experimental setup, only by suitably defining the threshold level for the transmission of the probe laser beam. Both the input and output are in digital form. These designs offer advantages of small size, simple and low power digital operation, small linear absorption coefficient, mirror-less structure, and flexibility for optimization.

The conventional pump-probe spectroscopy, considers a strong pump beam for excitation and monitors the excited-state dynamics in terms of the transmission of a weak probe beam through the sample. Practical switching applications require arrays or network of switches in circuits, for which cascading of devices is necessary. This requires the probe beam to also be strong.

Figure 7(a) shows the variation in NTPI at 390 nm with time for different probe beam intensity (I'_p) values for F86D/L40T-*p*pR at pH = 5, which exhibits a short *p*pR_M state lifetime, for a gaussian pump pulse at 50 mW/cm^2. Interestingly, as is evident from Fig. 7(a), increasing I'_p, the switching characteristics can be inverted, the total switching time can be reduced, and the switched beam profile made more symmetric, due to decrease in effective life-time of *p*pR_M-state for photo-induced transformation. This is evident from the variation in the normalized population density (NPD) with increase in I'_p, Fig. 7(b)-(d). Initially, the NTPI for a weak probe beam exhibits positive switching due to depletion of initial *p*pR-state and less population of *p*pR_M-intermediate. In the absence of the pump pulse at 498 nm, the intense probe beam pumps the sample exciting molecules from the initial *p*pR-state to the excited *p*pR_O-intermediate, whose population increases to a high value due to its larger lifetime than the *p*pR_M-state, Fig. 7(d). The presence of the modulating pump pulse now leads to absorption by the *p*pR_O-state reducing its population that

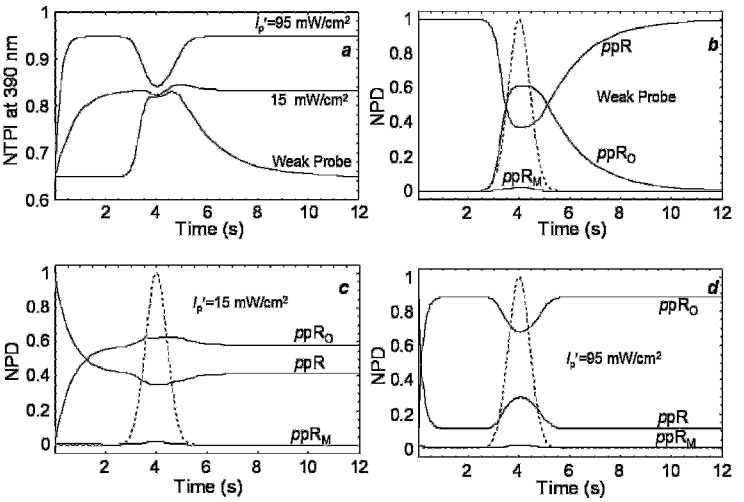

Fig. 7.(a) Variation in NTPI at 390 nm with time for different values of I_p' in F86D/L40T-*pp*R at pH = 5; and variation of the normalized population density of *pp*R, *pp*R$_M$ and *pp*R$_O$ states for normalized input pulse at 498 nm (dashed line) with time, for (b) I_p'~ 0 (weak), (c) I_p'= 15 mW/cm^2 and (d) I_p'= 95 mW/cm^2, with Δt = 1 s, I_{m0}' = 50 mW/cm^2 for C = 44.8 μM, L = 5 mm, k_M = 190 s^{-1} and k_O = 0.66 s^{-1}.

leads to a corresponding increase in the initial *pp*R population, which results in increased absorption of the probe beam, as shown in Fig. 7(a)-(d). Switching the probe intensity from a low to a high value thus affects positive to negative switching [80].

Since the intermediates in the rhodopsin photocycles exhibit absorption spectra spanning the entire visible region, they provide flexibility in modulating the NTPI by switching the intermediates, by multiple pump and bias beams. Figure 8 shows the effect of a bias beam intensity (I'_B) at 390 nm on NTPI at 560 nm with time, in *pp*R, with a modulating pulsed pump beam at 498 nm. It is

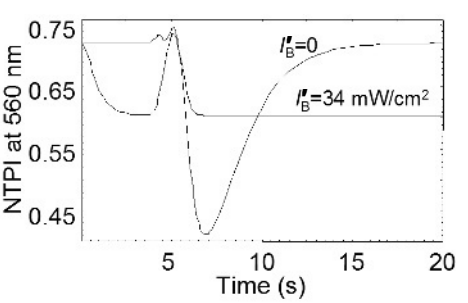

Fig. 8. Variation in NTPI at 560 nm in WT-*pp*R with time with a pump pulsed beam at 498 nm, I'_{m0} = 50 mW/cm^2, Δt = 1 s, t_0 = 5 s, σ_{1p} = 1.6×10^{-17} cm^2, k_M = 0.59 s^{-1}, k_O = 1.3 s^{-1}, L = 5 mm and conc. = 67.75 μM. The bias beam I'_B is at 390 nm.

interesting to observe that in the absence of the bias beam, the NTPI switches-off as the pump pulse excites the sample (negative-switching), due to absorption by the *p*pR$_O$-intermediate. Whereas, in the presence of the bias beam at 390 nm, the molecules switch from the *p*pR$_M$-intermediate to the initial state, thereby reducing the population of the *p*pR$_O$-intermediate. The NTPI thus increases (positive-switching) in the presence of the bias beam. Hence, the relative phase of the switched NTPI can be effectively controlled with the bias beam.

For all-optical information processing, it is important to have the capability to effectively control the switching characteristics. Moreover, for digital operation, it is necessary to perform all-optical switching with a train of modulating pulses. The switching characteristics using the pump-probe configuration, with pulse train excitation, would be similar to the single modulating pulse excitation, provided the time period of the modulating pulse train is greater than the switching time of switched probe beam due to single modulating pulse excitation. An increase in modulating pulse frequency would affect the nature and contrast of switching characteristics [85].

Figure 9 shows the experimental results for *p*pR$_O$-state dynamics, i.e., variation of transmitted probe (signal) intensity (TPI) at 560 nm that corresponds to peak absorption of *p*pR$_O$-intermediate state, switched by a modulating pulse train at 532 nm, for different modulating pulse frequencies. The switched signal beam exhibits out-of-phase characteristics with respect to modulating pulse (negative-switching), for single pulse excitation or for a pulse train at low frequencies as shown in Fig. 9(a). Increase in modulating pulse frequency to larger values results in an apparent phase shift of TPI with respect to the modulating pulses as shown in Fig.9(b)-(e). For a modulating pulse train, the presence of a second successive pulse at a time interval less than the relaxation time of the photocycle, results in the TPI not reaching the steady-state off-on values [85]. This results in a decrease in contrast and an asymmetric switched probe profile, while maintaining out-of-phase switching behaviour, as is evident from Fig. 9(b). Increasing the frequency further, results in further increase in the relative phase-shift of TPI, which saturates after a certain value. Increase in frequency also results in a change in the switched TPI profile, from symmetric to asymmetric and then again to a symmetric profile. The profile changes from an initial square to a triangular and then to a sine-like wave, alongwith a continuous decrease in contrast [85].

As the modulating pulse appears, the TPI switches off after a certain time-lag. This time-lag appears due to the time taken by the molecules to relax from the long-lifetime *p*pR$_M$-intermediate that does not absorb the signal beam at 560 nm, to the probed *p*pR$_O$-state. In general, the apparent phase-shift appears when the modulating pulse width (~1/2*f*) becomes of the order of the rate constant of an earlier longer lifetime intermediate, in the range in which experiments have been conducted. The variation of apparent phase-shift in this frequency range

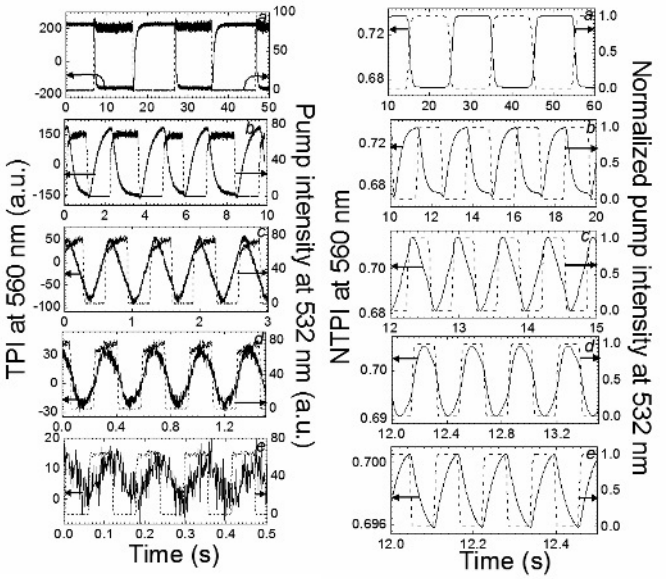

Fig. 9(a)-(e) Measured TPI and simulated NTPI at 560 nm (solid lines) and input modulating beam at 532 nm (dashed lines) for modulating pulse frequency (a) 0.05 Hz, (b) 0.42 Hz, (c) 1.53 Hz, (d) 2.86 Hz, (e) 8.57 Hz, for modulating pulse frequency for peak modulating power of 1 mW and signal beam of 0.2 mW. Adapted from Ref. [85].

depends on the lifetimes of the probed excited state and its earlier intermediates. A theoretical fit of the experimental switching curves at different modulating frequencies would result in the estimation of the lifetimes of $p\text{pR}_\text{M}$ and $p\text{pR}_\text{O}$ states. This time-lag appears to be significant at higher modulating pulse frequencies, when it becomes comparable to the modulating pulse width, which is evident from Fig 9(d) and (e). Theoretical simulations carried out by numerically solving the nonlinear time-dependent Eqns. (1) to (6), considering the experimental conditions and pulse profile parameter $q = 8$, are also shown in Fig. 9. It is evident that simulated results are in good agreement with experimental results [85].

The apparent phase-shift of NTPI with respect to modulating pulses is sensitive to the probe beam intensity and wavelength, frequency of the modulating pulses, and the kinetic and spectral response of the photo-intermediates [85]. Theoretical simulations show that it can be continuously varied between some specific ranges for different probe beam wavelengths, for a given frequency range. The apparent phase-shift of the switched probe beam at 560 nm and 600 nm respectively, with respect to modulating pulsed beam can be varied to exhibit negative to positive switching. Increasing the probe beam intensity continuously, results in an apparent phase-shift of NTPI at 500 nm only, such that switching characteristics get converted from positive to negative

switching. The profile of the switched NTPI is also sensitive to the wavelength of the probe beam. Since, the apparent phase-shift in switching characteristics appears due to time taken by excited molecules to relax from the long-lived *p*pR$_M$-state to the probed *p*pR$_O$-state, hence, for a fixed modulating frequency (*f*), increase in *p*pR$_M$-state lifetime (τ_M) would result in a similar variation as in Fig. 9. Hence, the effect of τ_M is analogous to the change in frequency. On the other hand, an increase in τ_O leads to a continuous variation in the apparent phase-shift, contrast and profile of the switched NTPI at 560 nm. There is also an optimum value of pump pulse width Δt, for O-state dynamics for maximum switching contrast in WT-*p*pR, for which the M-state lifetime is greater than that of the O-state [85].

All-optical switching characteristics in proteorhodopsin (pR) exhibit special features in comparison to bR and *p*pR [86]. This is due to an additional small absorption of pR$_M$-state at 520 nm [41]. The switching characteristics corresponding to pR$_M$-state dynamics exhibit a peak in NTPI at 405 nm, at higher pump intensity at 520 nm, due to absorption of pump intensity by pR$_M$-state molecules. As the modulating pulse appears, initially, the NTPI decreases due to increased absorption of probe beam by highly populated pR$_K$ and pR$_M$ states and then increases due to photo-induced conversion of pR$_M$ state molecules to the initial state by absorbing 520 nm intense pump beam. This peak in NTPI saturates to a particular value at higher pump intensities, which can be removed by decreasing the absorption cross-section of pR$_M$ state at 520 nm.

Bacteriorhodopsin and its derivatives exhibit photo-induced anisotropy and birefringence [58, 59], which can be enhanced by using two laser beams of different wavelengths with orthogonal polarization. Almost 20 times intensity enhancement of photo-anisotropy has been observed as compared to one color exciting beam [58]. Transient switching of 633 nm probe beam by a combination of a modulated pulsed 442 nm and cw 568 nm beams has also been studied using this technique. Positive-switching is achieved when the applied 568 nm beam is polarized perpendicular to the 442 nm beam, as this combination causes positive enhancement of photoanistropy, while negative-switching is achieved when the 568 nm beam is polarized parallel to the blue beam, due to disappearance of photoanistropy which blocks the probe beam [58]. Photonic switching with a pump-probe combination at 532 nm and 660 nm, based on photo-induced birefringence, has also been demonstrated with ~ 1000:1 contrast ratio, ~ 0.6 s rise and ~1.5 s decay time [59].

CONCLUSION

There are interesting aspects that emerge out of all-optical switching in rhodopsin proteins. One can exercise all-optical control over various features of the switching characteristics such as the switching contrast, switching time,

switching pump intensity, switched probe profile and phase and relative phase-shift. The effect of varying the pump pulse frequency, is analogous to the effect of the change in the lifetime of the intermediate earlier to the probed state in the photocycle. The probe intensity and a bias beam can control the relative phase of the switched beam to realize positive or negative switching and also reduce the switching time. Hence, controlling these parameters, one can realize the desired switching response from the same sample, instead of using genetic variants with different kinetic parameters. There are optimized values of the small-signal absorption coefficient β (for cw case), the pump pulse width and concentration for maximum switching contrast (for pulsed case). Although for high contrast for negative-switching, there should not be any spectral overlap between the initial and the excited intermediate states, it can be advantageous in case of positive-switching and for applications such as the realization of optical logic based on the dip and peak in the switching characteristics and their inversion by varying the probe intensity. There is a trade-off between switching time, contrast and pump power. For ultrafast operation, the earlier intermediates in the photocycle have to be accessed, which would require higher peak pump pulse intensities and result in lower contrast for negative-switching. All-optical switching in retinal proteins based on ESA has been analyzed in the ms-s time scale, which is due to the slower photocycle time, which results in higher switch-on time Fig. 4(b) and Fig. 5(a) (dashed lines) [53-86].

All-optical switching based on ESA, using the pump-probe technique, has also been reported in a variety of materials that include C_{60} in toluene [90-93], organometallic phthalocyanines [94, 95], platinum:ethynyl complex [96, 97], metalloporphyrins [96, 98], polymethine dyes [99], polydiacetylene [100], 2-(2'-hydroxyphenyl) benzoxazole (HBO) [101], poly(vinyl carbazole) (PVK) with azobenzene [102], and PMMA films doped with azobenzene chromophore [103-104]. Although faster switching ~ ns in C_{60} and organometallics can be obtained, the pump intensities required are ~ kW-GW/cm^2 [90-99].

The efficient photo-response of rhodopsins leads to switching at very low pump powers, compared to other molecular configurations. It opens up the possibility of compact nano-biophotonic computing with low power sources such as LEDs, laser diodes and even white light sources. As large, high-density arrays of switches and gates can be realized that can operate at very low switching energies with high thermal stability, they would be useful in parallel optical processing. The results show the applicability of these novel molecules to achieve this important capability, with advantages of simple design, low power operation, multi-wavelength operation, flexibility in design to achieve different operations, control over spectral and kinetic photo-response and an environmentally safe and cost-effective proposition.

The efficient multifunctional photo-response of these proteins, which has resulted in a wide range of proposed applications, and the sophisticated control

and manipulation by nano-biotechnological techniques of self-assembly and genetic engineering, offer good prospects for practical implementations. Although evolution has optimized proteins for many characteristics relevant to device application, further optimization is usually desirable [25]. For ultrafast switching, nano-biotechnological tools need to be applied to generate mutants or variants that exhibit a faster photocycle; a truncated photocycle with thermally stabilized early intermediates at higher temperatures; or invoke considerable thermal relaxation from the early intermediates back to the initial state (J, K→B).

There is also the possibility of using other natural photoreceptors with a faster photoresponse, for all-optical switching. Recently, a detailed photochemical and mutational analysis and structural elucidation of phototropin the plant blue-light photoreceptor has been undertaken, which is involved in phototropic plant movement, chloroplast relocation and stomatal opening in guard cells [2, 4, 5, 105-109]. Phototropins are a family of membrane-associated flavoproteins with at least two kinds of phototropin photoreceptors namely Phot1 and Phot2 that contain two flavin mononucleotide (FMN)-binding LOV (light-, oxygen-, voltage-sensitive) domains at the N-terminus, each consisting of approximately 100 amino acids, and differences in their sequences define them as either LOV1 or LOV2. These photoreceptors have been identified in several species that include *Arabidopsis thaliana*, *Avena sativa* (oat), *Oryza sativa* (rice), *Zea mays* (corn) and *Chlamydomonas reinhardtii* [2, 4, 5, 105-109]. Recently, the isolated LOV2 domain from *Avena sativa* (oat) Phot1 expressed in *E. coli* has been shown to undergo a simple three-state photocycle with unique properties, especially reverse saturable absorption over a wide spectral range (500-700 nm) [105]. Although the total photocycle time is quite large (~ 70 s), as many as 50% molecules photo-excited to its first L-state (peak absorption 660 nm) relax back to the initial D-state (peak absorption 447 nm) and $\sigma_{Dp} = 0$, which leads to faster switching based on L-state dynamics. All-optical switching in μs has recently been reported in this phototropin [110].

Although the present study has been conducted with the objective of performing nature-inspired bio-molecular computing, biological information processing is very different from classical computing architectures. The elementary components of biological systems, respond slowly compared to solid-state switches, but they implement much higher-level operations. Moreover, they exhibit self-assembly that helps achieve high interconnection densities, and biological systems are implemented without being planned [7-10].

The large rhodopsin family of proteins, especially bR, is a model system. Although the discussion has concentrated on bR, *p*pR and pR retinal proteins, the analysis of all-optical switching described herein, is relevant to any protein that exhibits an analogous photoreponse. Tuning the response of rhodopsins, fabrication of tailor-made bio-molecules, discovery of new natural photoreceptors, advancement in our understanding of their photoresponses and

rapid improvements in the techniques for genetic manipulation and screening would hopefully open up new vistas in nano-biophotonics for information processing.

REFERENCES

[1] H. Smith, Nature, 407 (2000) 585.
[2] W.R. Briggs and J.M. Christie, Trends Plant Sci., 7 (2002) 204.
[3] P.N. Prasad, Introduction to Biophotonics, Wiley Interscience, New Jersey, 2003.
[4] A. Batschauer (ed.), Photoreceptors and Light Signalling, Royal Society of Chemistry, Cambridge, 2003.
[5] W. R. Briggs and J.L. Spudich (eds.), Handbook of Photosensory Receptors, Wiley-VCH Verlag, Weinheim, 2005.
[6] E. Schrödinger, What is Life?, Cambridge University Press, Cambridge, 1945.
[7] K.P. Zauner, Crit. Rev. Solid State Mat. Sci., 30 (2005) 33.
[8] P. Warren, IEE Proc. Nanobiotechnol., 151 (2004) 1.
[9] N. Shadbolt, IEEE Intel. Syst., 1 (2004) 2.
[10] M. H. Garzon and R. J. Deaton, IEEE Trans. Evolut. Comp., 3 (1999) 236.
[11] D. Oesterhelt, C. Brauchle and N. Hampp, Quart. Rev. Biophys., 24 (1991) 425.
[12] N. Vsevolodov, Biomolecular Electronics: An Introduction via Photosensitive Proteins, Birkhauser, Boston, 1998.
[13] N. Hampp and D. Oesterhelt, in Nanobiotechnology: Concepts, Applications and Perspectives, C.M. Niemeyer and C.A. Mirkin (Eds.), Wiley-VCH, Weinheim, 2004.
[14] R. Das, P.J. Kelley, M. Segal, J. Norville, A.A. Yu, L. Wang, S.A. Trammell, L.E. Reddick, R. Kumar, F. Stellacci, N. Lebedev, J. Schnur, B.D. Bruce, S. Zhang and M. Baldo, Nanolett., 4 (2004) 1079
[15] D. Oesterhelt and W. Stoeckenius, Nature New Biol., 133 (1971) 149.
[16] R.R. Birge, Ann. Rev. Phys. Chem., 41 (1990) 683.
[17] D. Oesterhelt, Curr. Opin. Struct. Biol., 8 (1998) 489.
[18] F.T. Hong, Prog. Surf. Sci., 62 (1999) 1.
[19] U. Haupts, J. Tittor, D. Oesterhelt, Ann. Rev. Biophys. Biomol. Struct., 28 (1999) 367.
[20] J.K. Lanyi, Annu. Rev. Physiol., 66 (2004) 665.
[21] N. Hampp, Chem. Rev., 100 (2000) 1755.
[22] A. Popp, M. Wolperdinger, N. Hampp, C. Brauchle and D. Oesterhelt, Biophys. J., 65 (1993) 1449.
[23] R.R. Birge, Am. Sci., 82 (1994) 348.
[24] R.R. Birge, N.B. Gillespie, E.W. Izaguirre, A. Kusnetzow, A.F. Lawrence, D. Singh, Q.W. Song, E. Schmidt, J. A. Stuart, S. Seetharaman, K.J. Wise, J. Phys. Chem. B, 103 (1999) 10746.
[25] K.J. Wise, N.B. Gillespie, J.A. Stuart, M.P. Krebs, R.R. Birge, Trends Biotechnol., 20 (2002) 387.
[26] S. Roy, C. P. Singh and K. P. J. Reddy, J. Appl. Phys., 90 (2001) 3679.
[27] D.V.G.L.N. Rao, F.J. Aranda, D.N. Rao, J. Joseph, J.A. Akkara and M. Nakashima, in Photonic Polymer Systems: Fundamentals, Methods and Applications, D.L. Wise, G. E., Wnek, D. J. Trantolo, T.M. Cooper, J. D. Gresser (eds.) Marcel Dekker, New York, 1998.
[28] P. Wu and D.V.G.L.N. Rao, Phys. Rev. Lett., 95 (2005) 253601.
[29] N. Kamo, K. Shimono, M. Iwamoto and Y. Sudo, Biochem., 66 (2001) 1277.
[30] M. Miyazaki, J. Hirayama, M. Hayakawa and N. Kamo, Biochim. Biophys. Acta, 1140 (1992) 22.

[31] Y. Imamoto, Y. Shichida, J. Hirayama, H. Tomioka, N. Kamo and T. Yoshizawa, Photochem. Photobiol., 56 (1992) 1129.
[32] M. Iwamoto, Y. Sudo, K Shimono, N. Kamo, Biochim. Biophys. Acta, 1514 (2001) 152.
[33] M. Iwamoto, K Shimono, M. Sumi and N. Kamo, Biophys. Chem., 79 (1999) 187.
[34] M. Iwamoto, Y. Sudo, K. Shimono, T. Araiso and N. Kamo, Biophys. J., 88 (2005) 1215.
[35] J.L. Spudich and H. Luecke, Curr. Opin. Struct. Biol., 12 (2002) 540.
[36] R. Moukhametzianov, J. P. Klare, R. Efremov, C. Baeken, A. Göppner, J. Labahn, M. Engelhard, G. Büldt and V. I. Gordelie, Nature, 440 (2006), 115.
[37] O. Béjà, L. Aravind, E.V. Koonin, M.T. Suzuki, A. Hadd, L.P. Nguyen, S.B. Jovanovich, C.M. Gates, R.A. Feldman, J.L. Spudich, E.N. Spudich and E.F. DeLong, Science, 289 (2000) 1902.
[38] O. Béjà, E.N. Spudich, J.L. Spudich, M. Leclerc, E.F. DeLong, Nature, 411 (2001) 786.
[39] T. Friedrich, S. Geibel, R. Kalbbach, I. Chizov, K. Ataka, J. Heberle, M. Engelhard and E. Bamberg, J. Mol. Biol., 321 (2002) 821.
[40] A.V. Dioumaev, L.S. Brown, J. Shih, E.N. Spudich, J.L. Spudich and J.K. Lanyi, Biochem., 41 (2002) 5348
[41] G. Váró, L.S. Brown, M. Lakatos and J.K. Lanyi, Biophys. J., 84 (2003) 1202.
[42] M.A. Reed and J.M. Tour, Sci. Am., (June 2000) 68.
[43] B.L. Feringa, Molecular Switches, Wiley-VCH, New York, 2001.
[44] T. Sienko, A. Adamatzky, N.G. Rambidi and M. Conrad (eds.), Molecular Computing, MIT Press, Cambridge, 2003.
[45] B.W. Vought and R.R. Birge, in Wiley Encyclopedia of Electrical and Electronics Engineering, J.G. Webster (ed.), Wiley, New York, 1999.
[46] F.M. Raymo, Adv. Mater., 14 (2002) 401
[47] D.J. Bishop, C.R. Giles and S.R. Das, Sci. Am., 284 (2001) 88.
[48] F.M. Raymo, and S. Giordani, J. Am. Chem. Soc., 124 (2002) 2004.
[49] F.M. Raymo and S. Giordani, Proc. Natl. Acad. Sci., USA 99 (2002) 4941.
[50] A. Forchel, Nature Mater., 2 (2003) 13.
[51] F.M. Raymo and M. Tomasulo, Chem. Eur., 12 (2006) 3186.
[52] S. R. Marder, Chem. Commun., 2 (2006), 131.
[53] J.A. Stuart, D.L. Mercy, K.J. Wise and R.R. Birge, Synth. Met., 127 (2002) 3.
[54] A. L. Mikaelian and V. K. Salakhutdinov, Proc. SPIE, 2144 (1994) 84.
[55] S. Thai, J. Malowicki and Q. Song, Proc. SPIE, 3384 (1998) 107.
[56] D.V.G.L.N. Rao, F.J. Aranda, D.N. Rao, Z. Chen, J.A. Akkara, D.L. Kaplan and M. Nakashima, Opt. Commun., 127 (1996) 193.
[57] J. Joseph, F.J. Aranda, D.V.G.L.N. Rao and B.S. DeCristofano, Opt. Mem. Neural Net., 6 (1997) 275.
[58] P. Wu, D.V.G.L.N. Rao, B.R. Kimball, M. Nakashima and B.S. DeCristofano, Appl. Phys. Lett., 81 (2002) 3888.
[59] Y. Huang, S. T. Wu, Y. Zhao, Appl. Phys. Lett., 84 (2004) 2028.
[60] P. Ormos, L. Fábián, L. Oroszi, E. K. Wolff, J. J. Ramsden and A. Dér, Appl. Phys. Lett., 80 (2002) 4060.
[61] L. Gu, C. Zhang, A. Niu, J. Li, G. Zhang, Y. Wang, M. Tong, J. Pan, Q.W. Song, B. Parson and R.R. Birge, Opt. Commun., 131 (1996) 25.
[62] T. Zhang, C. Zhang, G. Fu, G. Zhang, Y. Li, Q.W. Song, B. Parsons and R.R. Birge, J. Infrared Mill. Waves, 18 (1999) 177.
[63] T. Zhang, C. Zhang, G. Fu, Y. Li, L. Gu, G. Zhang, Q.W. Song, B. Parsons and R.R. Birge, Opt. Eng., 39 (2000) 527.
[64] Y. Li, Q. Sun, J. Tian and G. Zhang, Opt. Mater., 23 (2003) 285.

[65] G. Chen, C. Zhang, X. Shang, Z. Guo, X. Wang, J. Tian, and Q.W. Song, Opt. Commun., 249 (2005) 563.
[66] G. Chen, C. Zhang, Z. Guo, X. Wang, J. Tian and Q.W. Song Q. W., J. Appl. Phys., 98 (2005) 044504.
[67] G. Chen, Z. X. Guo, K. Chen, C.P. Zhang, J.G. Tian, Q.W. Song, Optik, 116 (2005) 227.
[68] R. Thoma, N. Hampp, C. Brauchle and D. Oesterhelt, Opt. Lett., 16 (1991) 651.
[69] Q.W. Song, C. Zhang, R. Blumer, R.B. Gross, Z. Chen and R.R. Birge, Opt. Lett., 18 (1993) 1373.
[70] K.P.J. Reddy, J. Appl. Phys., 77 (1995) 6108.
[71] A. Peda'el, R. Daisy, M. Horowitz and Fischer B., Opt. Lett., 23 (1998) 1173.
[72] S. Roy and K. P. J. Reddy, Curr. Sci., 78 (2000) 184.
[73] S. Roy, C.P. Singh and K.P.J. Reddy, Curr. Sci., 83 (2002) 623.
[74] C.P. Singh and S. Roy, Optik, 113 (2002) 373.
[75] C.P. Singh, S. Roy, J. Photosci., 9 (2002) 317.
[76] C.P. Singh and S. Roy, Curr. Appl. Phys., 3 (2003) 163.
[77] C.P. Singh and S. Roy, Opt. Commun., 218 (2003) 55.
[78] S. Roy, P. Sharma, A. K. Dharmadhikari, D. Mathur, Opt. Commun., 237 (2004) 251.
[79] P. Sharma and S. Roy, IEEE Trans. Nanobiosci., 3, (2004) 129.
[80] Y. Huang, S. T. Wu, Y. Zhao, Opt. Exp., 12 (2004) 895.
[81] R. K. Banyal and B. R. Prasad, Appl. Opt., 44 (2005) 5497.
[82] C.P. Singh, P. Sharma and S. Roy, IEE Proc. Cir. Dev. Syst., 150 (2003) 563.
[83] P. Sharma, S. Roy, J. Appl. Phys., 96 (2004) 1687.
[84] P. Sharma, S. Roy and C.P. Singh, Thin Solid Films, 477 (2005) 227.
[85] S. Roy, T. Kikukawa, P. Sharma and N. Kamo, IEEE Trans. Nanobiosci., 5 (2006) 178.
[86] S. Roy and P. Sharma, Optik (In Press).
[87] R. Menzel, Photonics, Springer-Verlag, Berlin, 2001.
[88] K. Shimono, M. Iwamoto, M. Sumi and N. Kamo, J. Biochem., 124 (1998) 404.
[89] T. Juchem and N. Hampp, Opt. Lett., 26 (2001) 1702.
[90] C. Li, L. Zhang, R. Wang, Y. Song, Y. Wang, J. Opt. Soc. Am. B, 11 (1994) 1356.
[91] F.Z. Henari, K.H. Cazzini, D.N. Weldon, W.J. Blau, Appl. Phys. Lett., 68 (1996) 629.
[92] S. Roy, C.P. Singh and K.P.J. Reddy, Appl. Phys. Lett., 77 (2000) 2656.
[93] C.P. Singh and S. Roy, Opt. Engg., 43 (2004) 426.
[94] C. Li, L. Zhang, M. Yang, H. Wang and Y. Wang, Phys. Rev. A, 49 (1994) 1149
[95] F.Z. Henari, J. Opt. A: Pure Appl. Opt., 3 (2001) 188.
[96] S. Roy and K. Kulshrestha, Opt. Commun., 252 (2005) 275.
[97] C.P. Singh, K. Kulshrestha and S. Roy, Optik (In Press).
[98] C.P. Singh, K.S. Bindra, B. Jain, S.M. Oak, Opt. Commun., 245 (2005) 407.
[99] P. Sharma, S. Roy and C.P. Singh, Thin Solid Films, 477 (2005) 42.
[100] H. Xu, S. Guang, D. Xu, D. Yuan, Y. Bing, M. Jiang, Y. Song and C. Li, Mat. Res. Bull., 31 (1996) 351.
[101] G. Zhang, H. Wang, Y. Yu, F. Xiong, G. Tang, W. Chen, Appl. Phys. B, 76 (2003) 677.
[102] S. Wu, M. Liu, W. She, K. Yun and Z. Huang, Mat. Chem. Phys., 83 (2004) 29.
[103] S. Wu, S. Yao, D. Luo, H. Wang, J. Mater. Sci., 38 (2003) 401.
[104] Y. Luo, W. She, S. Wu, F. Zheng and S. Yao, Appl. Phys. B, 80 (2005) 77.
[105] T.E. Swartz, S.B. Corchnoy, J.M. Christie, J. Lewis, I. Szundi, W.R. Briggs and R. Bogomolni, J. Biol. Chem., 276 (2001) 36493.
[106] S.M. Harper, L.C. Neil and K.H. Gardener, Science, 301 (2003) 1541.
[107] J.T.M. Kennis, I.H.M.V. Stokkum, S. Crosson, M. Gauden, K. Moffat and R.V. Grondelle, J. Am. Chem. Soc., 126 (2004) 4512.

[108] A. Penzkofer, L. Endres, T. Schiereis and P. Hegemann, Chem. Phys., 316 (2005) 185.
[109] M. Kimura and T. Kagawa, Curr. Opin. Plant Biol., 9 (2006) 503.
[110] S. Roy and K. Kulshrestha, IEEE Trans. Nanobiosci. (In Press).

Handai Nanophotonics, Volume 3
H. Masuhara, S. Kawata and F. Tokunaga (Editors)

Chapter 24

A photoisomerization study on photoactive yellow protein model chromophores from solution to crystalline phases

Anwar Usman, Hiroshi Masuhara, and Tsuyoshi Asahi

Department of Applied Physics, Osaka University, 2-1 Yamadaoka, Suita, 565-0871 Osaka, Japan

1. INTRODUCTION

The families of photoreceptor proteins have a light-triggered functionality and a dynamic role in natural photoprocesses [1,2]. Upon photon absorption these proteins initiate a change in configuration of chromophore buried in their binding pocket. This ultrafast process leads to a chain of reactions; the formation of a signaling state that triggers intraprotein and then intracellular reactions. Crystallographic studies with sufficient resolutions, which provide detailed information on the structural features of these proteins, including the structure of the buried chromophore and its interactions to surrounding amino acid residues, are essential to understand both the structural dynamics of the chromophore in the photoprocess and the conversion of photon energy into a biological function [3]. In addition to this fundamental interest, applications of the photoreceptor proteins in the optical field and photobiosensor become important topics in recent research activities [4].

Among the photoreceptor proteins, the photoactive yellow protein (PYP) [5,6], a protein isolated from the bacterium Halorhodosphira halophila, is an ideal system to study the protein structure-function relationship, because PYP is a small (14kDa) and water soluble protein. The buried chromophore in the PYP is a p-hydroxycinnamic thioester covalently bonded via a thioester bond to a cystein Cys69 residue in a hydrophobic protein pocket [6]. In the ground state, this chromophore is in deprotonated form of the trans configuration, linked by several hydrogen bonds to the side of the protein pocket, and electronically stabilized by an argenium cationic Arg52 residue as shown schematically in Fig 1. The structure of the ground state P, which has been determined using X-ray diffraction [7] and time-resolved Fourier-transform infrared (FTIR) [8] spectroscopy, shows a slight deviation of the carbonyl out of the aromatic ring

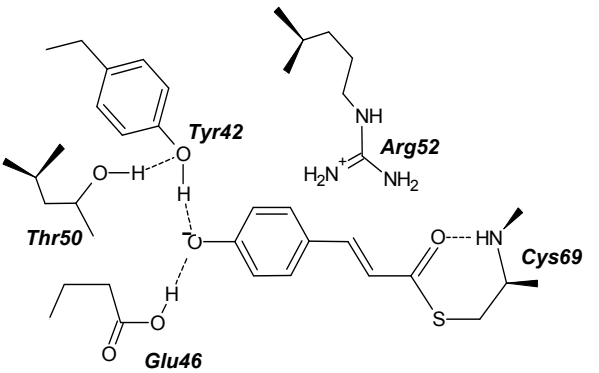

Fig. 1. Schematic representation of PYP chromophore in the ground state; deprotonated trans p-hydroxycinnamic thioester covalently bonded to Cys69, hydrogen bonded to Tyr42, Glue 46, and Cys69, and stabilized by positively charged guanidinium group of Arg52.

plane. Like other protein of rhodopsin family, the PYP chromophore undergoes an ultrafast trans-cis photoisomerization. This isomerization, which occurs in the primary stage of its photocycle, is a key structural dynamic process of the overall photocyclic process [9-11]. After a sequence of fast and intricate events following the isomerization, involving several intermediates, the proton transfer from the side group of the protein pocket to the phenolate group of the cis isomer occurs in a later stage of the photocycle. The intermediate I_1 and I_2 states, deprotonated and protonated cis isomers, respectively (shown in Fig. 2), which appear on time scales from nano to milliseconds, have been structurally analyzed in detail using time-resolved X-ray diffraction [12,13] and step-scan IR [14] experiments.

A highly distorted geometry involving twisting by a flipping of the thioester bond, induced by an intramolecular charge transfer, is believed to take place in early time of the photoexcitation. However, the structural evolution of the chromophore that occurs directly upon photoexcitation was less known until ultrafast time-resolved FTIR spectroscopy was recently invented [15,16]. Using this method, an early intermediate of the photocycle (I_o state), which appears within 3 ps after excitation and already has a cis geometry without a relocation of the phenolate group, has been reported [16]. This species has been proposed to be a precursor of the well characterized cis I_1 intermediate. However, the planar enone moiety (C7=C8-(C9=O)-S) of the early intermediate observed in solution [16] differs from that of a low temperature-trapped early intermediate in protein single crystals which shows a rotated thioester bond 166° relative to the aromatic plane evidenced by X-ray structure determination [7]. This discrepancy could be addressed to temperature and environment surrounding effects, because at low temperature the PYP photocycle is known to involve additional

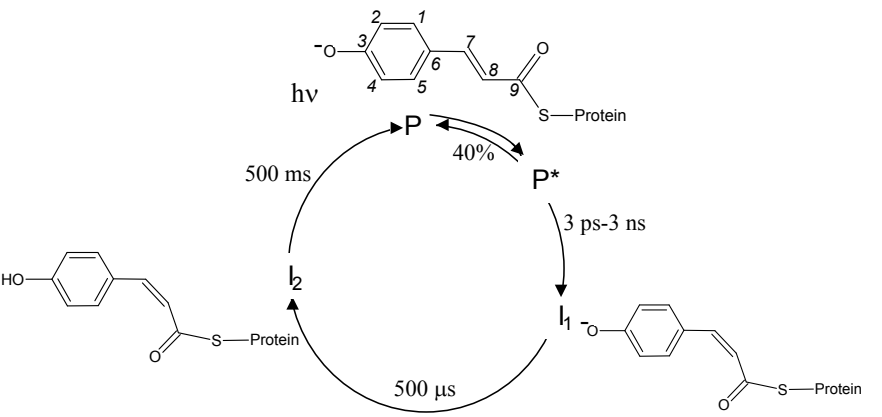

Fig. 2. Scheme of the photocycle of native PYP after photoexcitation showing only the two main intermediate states (I_1 and I_2) and their lifetime identified at room temperature. The P and P* represent the ground and excited states.

intermediate formations whose structures may be similar to those observed at room temperature, but no direct correspondence has been established. Nevertheless, the ground state PYP_{dark} and intermediate PYP_M state in the later stage of PYP photocycle at low temperature [17] can be related to the ground state P and intermediate I_2 state, respectively, of the room temperature PYP photocycle. On the other hand, the kinetic and photoprocess of the chromophore in the protein are altered by constrains of the crystal lattice compared with those in solution [17]. Experiments on several PYP mutants and hybrids have also elucidated the influence and important role of the amino acid residues surrounding the chromophore on the PYP photocycle, where a partial disruption of hydrogen bonds linking the chromophore leads to longer excited-state lifetimes than those in the native PYP [18].

2. PYP MODEL CHROMOPHORES

An interesting issue of the trans-cis photoisomerisation process is to find whether it can be attributed to an intrinsic property of the chromophore or if it is controlled by the surrounding amino acids of the protein. To help answering this question, the photoexitation dynamics of several free chromophores in various solutions, which mimic the chemical structure of the PYP chromophore, have been investigated recently by several groups [19-26]. These so-called PYP model chromophores are mainly the analogues of trans p-hydroxycinnamate (also known as deprotonated p-coumaric acid) with or without thioester group

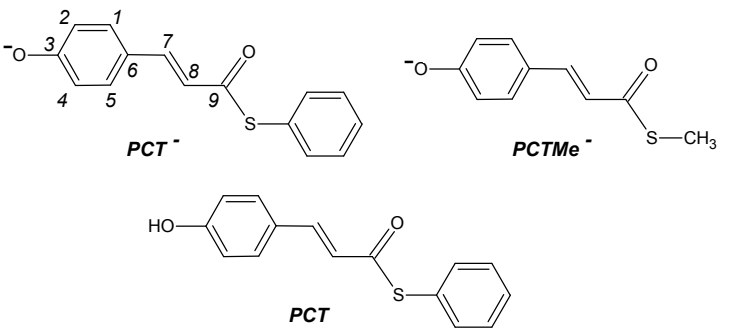

Fig 3. Chemical structures of deprotonated PCT^- and $PCTMe^-$, and protonated PCT.

substituent. Determination of their structural dynamics upon photoexcitation has become an important issue in those research topics.

The role of the thioester group of model chromophores has been a subject of experimental and theoretical studies. It is interesting to note that, in experiments, the thioester bond has been found to induce a red-shifted absorption spectrum that will be addressed later. Owing to these distinct differences in electronic structures, chromophores with the thioester group were found to show different photoexcitation dynamics compared with those without thioester group [20a-c]. This fact highlights the determining role of the thioester bond in the primary molecular event in the PYP photocycle. On the other hand, the theoretical calculations demonstrated that the red-shift of absorption spectrum upon oxygen to sulfur substitution is due to an energetic lowering of n-π* state. More interestingly, such a substitution also leads to a lengthening of the intrinsic C_7=C_8 bond geometry which is expected to play a role in the trans-cis isomerization because this bond could be the center of the process [23].

In this short contribution, recent studies on the photoinduced isomerization of PYP model chromophores, especially those having thioester group, e.g. p-hydroxycinnamic-thiophenyl ester (PCT) and p-hydroxycinnamic-thiomethyl ester (PCTMe), are reviewed. The photoexcitation dynamics of their deprotonated form (PCT^- and $PCTMe^-$ in Fig. 3), in various solutions, which have been studied over a wide range of methods, and comparisons with those of PYP and denaturated PYP are discussed. The photoexcitation dynamic of the protonated form of PCT in crystalline phase is also presented, since it displays an interesting crystalline state photochromism.

2.1. Solvent polarity dependent

The steady state absorption and fluorescence spectra of PCT^- and $PCTMe^-$ in solutions are strongly dependent on solvent polarity. In general, the absorption maximum of the model chromophores shows a markedly tunable spectrum,

which is red-shifted when the solvent polarity decreases. For instance, the absorption peak of PCT^- is shifted from 395 nm in pure water [20a] to 445 nm in 1:10 water:DMSO mixture [22a]. Such a massive shift of the absorption spectrum is not found in other PYP model chromophores which do not contain a thioester group [20c], hinting that the thioester group induces a larger difference between dipole moments in the Frank-Condon excited state and in the ground state. The absorption and fluorescence spectral data of PCT^- and $PCTMe^-$ in various solvents are gathered in Table 1 along with those of PYP and denatured PYP for comparison.

The fluorescence band of PCT^- is also solvent polarity dependent, being opposite to the electronic absorption tendency, it is red-shifted when the polarity decreases. As a result, its Stoke shift becomes larger in high polarity solvents. In each solvent, the fluorescence band and its respective absorption spectrum, however, are not mirror images [20c,22a]; the latter is broader, which is attributed to the existence of two electronic transitions under the main absorption band, especially in the blue side of the spectra, below 325 nm [20c]. The fluorescence band of the chromophore has also been shown to be insensitive to hydrogen donor ability of the solvent. This strongly indicates that after excitation, though there could be hydrogen bonding rearrangements in the excited state, upon radiative relaxation process to the ground state their overall energy is essentially unchanged [20c].

It is interesting to note that the steady state absorption and fluorescence spectra of PCT^- in 1:10 water:DMSO mixture [22a] are comparable to those of PYP. These facts indicate that both their electronic transition energy and Stoke shift are coincident, although PCT^- and chromophore in PYP have differences in the surrounding environment and hydrogen bonding networks around them. For PCT^-, the large red-shifted absorption spectrum is believed to be due to the presence of the thioester group and to a particular solvent polarity, which both affect intramolecular charge mobility and arrangement of the negative charge. On the other hand, the absorption spectrum of PYP depends on the hydrogen bonding interactions, where disruption of the specific hydrogen bond interactions of the chromophore to the side of protein pocket in denatured PYP (a solvated PYP in basic solvent with an addition of highly concentrated denaturing agent) leads to a considerably blue-shifted absorption [20c] (see Table 1).

2.2. Photoisomerization of PYP model chromophores in solution

The photodynamic of the deprotonated form of PYP model chromophores, especially PCT^- and $PCTMe^-$ in liquid solutions, have been studied by several research groups employing ultrafast time-resolved resonance Raman [19], UV-vis absorption [20], fluorescence up-conversion [21] and Fourier-transform infrared (FTIR) spectroscopies [22]. In general, within a few hundreds fs to a

few tens ps after photoexcitation, the observed transient spectra cover the excited state structure, intermediate and photoproduct state (not in every case) along with repopulated ground state.

Lifetime of the excited state structure of the model chromophores in liquid solutions is in the range of 3-15 ps time scale depending on solvent polarity (see Table 1). This demonstrates that the solvent polarity is also a determining factor of the excited state decay time, where the polarity effect is considered as the result of changes in both mobility of intramolecular charge delocalization and the excited state dynamics. It is interesting to note that the decay time of the excited state PCT^- and $PCTMe^-$ in aqueous solution is very close to that of PYP (3 ps). On the contrary, when the electronic transition energy and Stoke shift of PCT^- in 1:10 water:DMSO and those of PYP are coincident, the excited state decay time of PCT^- is 15 ps, being severely different to that of PYP. From these findings it has been concluded that the electronic transition energy and Stoke shift are less to do with the excited state relaxation [22a].

However, the equivalent rate of the excited state decay of the model chromophores to PYP does not represent the similarity of excited-state relaxation pathway. In fact, the photoexcitation dynamics of both model chromophores in the solutions differ markedly from that of PYP. For the model chromophores, the relaxation process has been proposed to involve an intermediate species prior to the formation of long-lived photoproduct along with a possible branching relaxation pathway [20,21]. The cis photoproduct, as the result of trans-cis isomerization, has been suggested with very low quantum yields (less than 5%) in the water-DMSO mixture solutions [22] or it would be a similar small amount that has been observed as long-lived photoproduct absorption band in basic aqueous solution [20,21]. The low quantum yield is thought to be related to unstable ground-state cis isomer, because there is no evidence of the cis isomer formation in steady state photolysis measurement [20a-c]. This is in contrast to the double deprotonated 4-hydroxycinnamic acid

Table 1
Solvent dependent absorption and fluorescence spectra and excited state decay time

Chromophore	Solvent	λ_{abs} (nm)	λ_{em} (nm)	τ (ps)	Reference
$PCTMe^-$	H_2O	385	n.m.	3	21
	H_2O:DMSO 1:1	390	n.m.	15	22b
PCT^-	H_2O	395	500	3	20a
	H_2O:DMSO 1:1	415	504	10	22a
	H_2O:DMSO 1:10	445	498	15	22a
PYP	H_2O/protein	446	496	3	15,16
Denaturated PYP	H_2O/protein	398	500	3 ; 18	20c

λ_{abs} = absorption peak, λ_{em} = emission peak, τ = excited state decay time, n.m. = not measured.

(PCA^{2-}), a model chromophore without thioester bond, which shows a stable ground state cis isomer [20a-c]. To this discrepancy there have been two possible reasons proposed, i.e. (i) destabilization by the thioester bond, although the ground state energy of the cis PCT^- isomer and activation barrier of the cis formation are 5 and 30 kcal mol^{-1}, similar to those of PCA^{2-}, and (ii) a possible non-radiative process faster than photo-isomerization reaction. This later hypothesis has been considered as a main reason because such a formation of photoinduced charge transfer showing a possible geometrical change that occurred in competition with the photoisomerization process has been observed for several derivatives of stilbenes, merocyanine dyes and polyenes [27].

It has been pointed out by Nibbering's group that, for both model chromophores, the excited state decays faster in a higher solvent polarity as when the chromophore has a larger electronic transition energy and Stoke shift [22]. This indicates an inconsistency with the energy-gap law formulation, where internal conversion rate to the ground state increases with the lowering electronic transition energy or with the smaller Stoke shift. This inconsistency must be related to the alvation dynamics induced by the intramolecular charge translocation upon excitation, leading to an intricate excited state relaxation pathway or even different reaction coordinates. The alvation dynamics have been reported in great details by Martin's group for the photodynamics of several PYP model chromophores in various polarity and viscosity of protic solvents [20d,e]. The main observation was slowing down of the excited state decay time with the increase of the solvent viscosity. Although such a solvent friction effect occurs for all model chromophores, it has a larger impact on PCT^- compared with other model chromophores without thioester group, because the thioester group is believed to have an important role to induce a larger charge translocation. This is a strong indication of differences in reaction coordinate and kinetic between PCT^- and the model chromophores without thioester group. The PYP model chromophores with thioester group, especially PCT^-, has been proposed by Martin's group to have a relaxation pathway and reaction coordinate involving only the torsional motion of the ethylenic double bond, whereas the relaxation pathway and reaction coordinate of other PYP chromophores without thioester bond resemble the trans-stilbene-like concerted motions of the ethylenic double bond and one adjacent single bond [20c]. The excited state relaxation of PCT^- has also been proposed to involve a participation of an intermediate species as the gateway of cis photoproduct related to a new minimum at the perp configuration in the ground state. In accordance with this relaxation pathway, the electron withdrawing nature of the thioester group was also believed to induce an energy lowering of the perp excited state. Thus, the potential barrier from the perp configuration in the local minimum of the ground state to the apparently unstable cis isomer would be higher than that leading

back to the initial trans configuration, resulting in a very low quantum yield as mentioned above [20b-d].

The excited state structure of the model chromophores in solution, in such a way, repopulates the ground state efficiently, which is in contrast to about 60% quantum yield for the I_o state formation in the native PYP. Although the electron donor-acceptor strength of the substituents at either ends of the chromophore has also been pointed out to be another determining factor for the decay kinetics and the relaxation pathway [24], both PCT^- and $PCTMe^-$ have a deprotonated hydroxyl group at one end and a thioester group at the other end, resembling both the ground state structure and charge distribution of the PYP chromophore. Therefore, remarkable differences between relaxation pathways of the model chromophores in liquid solutions and that of PYP must be attributed to the differences in the environment surrounding the chromophore (solvent molecules for the free chromophore in solutions and the amino acid residues for the PYP chromophore).

3. DENATURED PYP

Experimental studies on photodynamics of denatured PYP by Martin's group [20b,c] and several PYP mutants and hybrids by Mataga's group [18] are important to provide a better understanding of the role of amino acid residues surrounding the chromophore in the PYP. In these modified proteins, the chromophore remains in the deprotonated form and is covalently bonded to Cys69 residue in the protein pocket via thioester bond as it is in the native PYP, but the specific hydrogen bonds linking the chromophore to the side of protein pocket are disrupted as the chromophore is exposed to the solvent in denatured PYP or the specific surrounding amino acid residues are modified in mutated PYP.

The surrounding effects on the excited state relaxation in the denatured or mutated PYP were found in rather different from the solvent polarity and viscosity effects on the model chromophores. In those modified proteins, the hydrogen bonds apparently play a key role, in which destruction of the hydrogen bond interactions in the denatured or mutated PYP was found to lengthen the time of a twisted state formation or a flipping of the thioester bond. Most importantly, they have different relaxation pathways and quantum yields compared with those of the native PYP. For instance, the denatured PYP was found to have an effective ground state recovery with biexponential excited-state decay time of 3 and 18 ps [20b,c]. Although mechanism of the modified PYP is yet not clear, the decay rate of some mutated PYP (single exponential with 11 ps decay time) [18] is comparable to that of PCA^{2-} in aqueous solution (single exponential with 10 ps decay time) [20b,c]. On the other hand, emission band of the denatured and mutated PYP has been shown to have a similar dynamic Stoke

shift with that of PCT^- in alcohols [20b-d]. The differences in the excited state kinetics between the modified PYP and the PYP model chromophores must be related to their different reaction coordinate and relaxation pathway, since, as it was mentioned above, the dynamic Stoke shift has less effects. Thus, from these facts, it can be concluded that the reaction coordinate and relaxation pathway of the excited structure of the chromophore are controlled by the specific hydrogen bonds for the chromophore in the native PYP and by polarity and viscosity of solvent for the free molecules in solutions.

Recently, Martin's group has also reported an observation of a small persistent bleaching band detected up to a delay time of 1000 ps after the photoexcitation, which reveals that the ground state of denatured PYP is not completely repopulated [20b,c]. At the same delay time, a long-lived absorption band was detected, suggesting the signature of the photoproduct state. The formation of such a long-lived photoproduct state which absorbs at 360 nm has also been reported for PCT^- [20a-c]. The presence of the photoproduct band suggests that the long-lived species observed for the model chromophores in aqueous solution or that for denatured PYP is most probably the cis photoproduct state. This is strongly supported by the similarities of the 450-nm intermediate absorption of both PCT^- and denatured PYP with the early intermediate of the native PYP photocycle. Such a cis photoproduct has been suggested for the PCT^- in water:DMSO in the transient IR spectroscopy measurement, although an accurate structure could not be determined [22]. If this trans-cis photoisomerization in the denatured PYP (and PCT^-) indeed takes place, it must occur in delay times of a few ps to a few ten ps. This is supported by an observation that, at short delay times, the transient absorption spectra of the denatured PYP was also similar to those of the native PYP, although its long delay time transient spectra resembled that of PCT^- [20b,c].

4. PHOTOISOMERIZATION OF PCT IN CRYSTALLINE STATE

With the assumption mentioned above, we propose that the trans-cis photo-isomerization is most likely an intrinsic character of the p-hydroxycinnamic thioester chromophore with a strong control by surrounding environment. The low quantum yields of the model chromophores in solutions or the modified PYP are apparently due to the lacking of anisotropic amino acid residues surrounding the chromophore and the specific hydrogen-bond interactions, respectively, which lead the excited state structures to repopulate the ground state efficiently. Therefore, a disparate environment is expected to give a dissimilar photoexcitation dynamic. Recently, we have reported the photo-excitation dynamic of the protonated form of PCT in crystalline state [25], which is a different environment from either solution or protein.

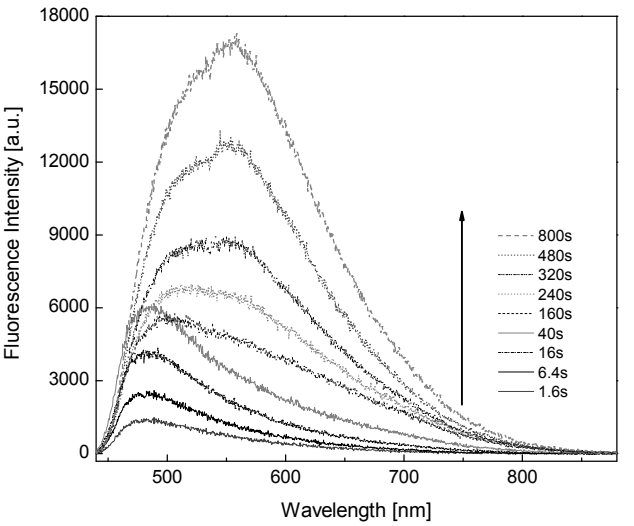

Fig. 4. Fluorescence spectra of a single microcrystal of PCT at 1.6 s to 800 s after UV light irradiation (λ=405 nm, 1.9 mW) showing a shift of fluorescence peak from 490 nm in a few seconds after irradiations to 560 nm upon continues irradiation

In microsized crystals, the photophysics of PCT is indeed different. By monitoring of fluorescence band upon UV irradiation and inspection of the IR-vibrational marker bonds, we reported the unequivocal demonstration of conversion from the trans to cis state of PCT [25]. Upon continuous UV irradiation the emission color of a PCT microcrystal shifts from blue to greenish yellow as indicated by a red-shift of fluorescence band from 490 nm after a few seconds of UV irradiation (Fig. 4). A new band around 560 nm which arose after an incubation time was assigned to the fluorescence from distinctly different excited species, which must be the structural geometry converted from the initial trans form, apparently cis configuration.

The new band has been found to have a unique enhanced emission upon continuous irradiation rather than a fluorescence intensity decrease that often occurs in crystalline or liquid phase due to a fluorescence quenching process, which can be caused by such as excitonic couplings, excimer formations, and excitation energy migrations. The temporal profile of the new band has been fitted to double exponential components, indicating that the photoinduced trans-cis isomerization involves a complex pathway upon the excited state relaxation and is not a simple four electronic state photochromism [25]. An interesting observation is that the reverse reaction can be induced by a subsequent visible light irradiation. By repeated UV and visible irradiations, the fluorescence from initial trans configuration was reproducible, although there is a sign of degradation. This suggests that only a partial amount of the trans configuration is recovered upon visible irradiation, as the photoisomerization may involve a

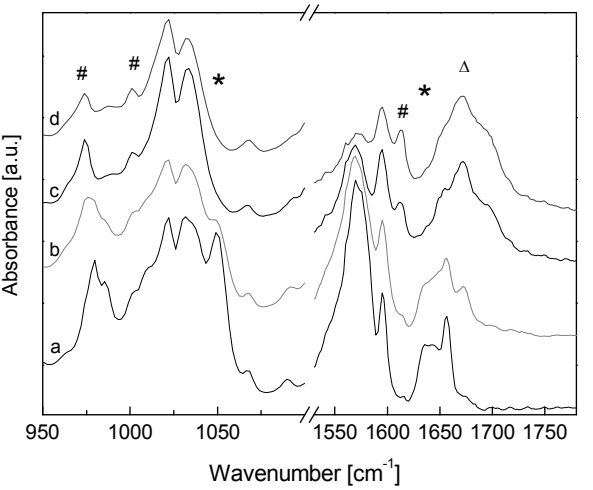

Fig. 5. IR spectrum of PCT before (a) and after UV irradiation (1.9 mW) at 60 s (b), at 500 s (c) and at 750 s (d). The asterisk (*), pound (#), and triangle (Δ) denote the disappearing, newly raised, and frequency-shifting bands, respectively.

branched pathway with an intermediate species as a gateway prior to the cis photoproduct. This has been revealed by an increase of fluorescence intensity of the trans and cis configurations in dark condition after UV irradiations, indicating a recovery from the intermediate species between the trans and cis form.

Conversion from trans to cis structural configuration was revealed by inspection of IR vibrational marker modes. The changes in vibrational spectrum upon photoisomerization of PCT were comparable with those of the trans-cis isomerization marker modes of the PYP chromophore. Notably, when PCT isomerizes into the cis form, it also resembles the later stage of the chromophore, I_2 or PYP_M intermediate state in the PYP photocycle, therefore, their specific vibrational modes should be identical. We have shown in our previous work [25], that the IR spectral changes assigning the photo-isomerization were the disappearance of both the γCH=CH hydrogen out-of plane bending and $\nu C_8–C_9$ stretching vibrational bands around 1050 cm^{-1} of the trans-PCT [22] upon UV irradiation, which was followed by the appearance of a clear band at 973 cm^{-1} and a tiny band at 994 cm^{-1} (Fig. 5). These bands have been assigned to the cis γCH=CH and $\nu C_8–C_9$ vibrational modes, respectively [16,22]. In comparison to PYP_M, the conversion from PYP_{dark} to PYP_M clearly exhibited similar frequency downshift of the $\nu C_8–C_9$ modes of the chromophore from 1058 to 994 cm^{-1} [26,28]. On the other hand, the cis photoproduct of deprotonated PCT^- in water:DMSO solution arose in the 980-995 cm^{-1} region, although the band was extremely small for an accurate structure determination [22]. The vibrational mode of ethylenic double bond indicating the trans-cis isomerization was also

observed as a pair of the disappearance/appearance band at 1639/1613 cm^{-1} with the latter band assigned to the νCC(8a)+νC=C(A_1) mode of cis configuration (similar mode was at 1599 cm^{-1} in the PYP_M) [26,28]. There are other several vibrational changes in the fingerprint region following the trans-cis isomerization. For instance, the disappearance/appearance band of the ethylenic mode from the *trans* δCH=CH(B_u) at 1291 cm^{-1} to a coupled of *cis* νC_3–O and δCH=CH(A_1) modes at 1283 cm^{-1}. A recent IR study on *trans*-4-hydroxycinnamic acid has shown the related pair of bands at 1294/1288 cm^{-1} upon isomerization [26c], while the *cis* δCH=CH(A_1) vibrational mode in the PYP_M, is assigned to the band at 1286 cm^{-1} [28].

A direct insight into the trans-cis isomerization was provided by a frequency upshift of the carbonyl νC=O stretching mode from 1656 cm^{-1} to a broad band peaking at 1672 cm^{-1} (Fig. 5). The twisting or flipping of the thioester bond is believed to set the carbonyl group relatively free and less substantial couplings with other nuclear vibrations resulting in higher frequency position of the νC=O mode. A similar frequency upshift of the carbonyl stretching mode from 1631 cm^{-1} in PYP_{dark} to 1653 cm^{-1} in PYP_M was also observed upon trans-cis isomerization of the PYP chromophore [26,28]. In addition to those isomerization maker modes, the frequency positions of the phenolic moiety vibrations also slightly shifted from 1169, 1435, 1513, and 1595 cm^{-1} [22,26] to 1178, 1448, 1517, and 1590 cm^{-1}, respectively, due to couplings with other vibrational motions, although the phenolic moiety is structurally unchanged. On the other hand, localized vibrational modes of the thiophenyl moiety (SC_5H_5) [22] at 1067, 1108, 1476 cm^{-1} remain unchanged. These provide a conclusive evidence that the vibrational motions of these two moieties are not significantly altered upon the twisting or isomerization, but the detailed mechanism is still an open question.

The crystal packing has been pointed out to apparently stabilize the cis photoproduct [25]. This is in contrast to the unstable ground state cis isomer of PCT^- in liquid solutions or even to the short-lived cis configuration of the PYP chromophore. Although the crystal lacks anisotropic binding pocket and amino acid residues that likely stabilize the efficient photoprocess in the native PYP, the stability could be due to possible hydrogen bonds or other intermolecular interactions in the tight packing structure. The striking difference between the photodynamics of PCT in crystals and that of PCT^- in solutions can be addressed to environment surrounding effects, intermolecular couplings and interactions in the tight crystal packing and polar solvent molecules in solutions. An effect of the protonation of hydroxy group should also be taken into account since the photoisomerization channel would be influenced by protonation of the hydroxy group as such an effect has been observed for several 4-hydroxycinnamate acid derivatives having different fluorescence lifetime and quantum yield upon protonation [24].

5. CONCLUSION AND PERSPECTIVE

In these few years, attempts to understand the key structural dynamics of PYP chromophore, which has a complicated photocycle and an important biological functionality, have been devoted on photoexcitation dynamic of PYP and several of its model chromophores employing ultafast time-resolved spectroscopies, X-ray diffraction, as well as steady state fluorescence and IR spectroscopies. The cis photoproduct formation which was observed for the PYP model chromophores and for the denatured PYP provided a conclusive evidence that the trans-cis photoisomerization is most probably an intrinsic character of the p-hydroxycinnamic thioester chromophores with strong effects and controls from surrounding environment. Strikingly different photodynamics of the PYP model chromophores and the native PYP, therefore, must be due to the differences in the environment surrounding the chromophore. In the native PYP, the role of amino acid residues, including specific hydrogen bonds linking the chromophore to the side of protein pocket and an important electrostatic stabilizer Arg52 nearby the chromophore, is to facilitate the trans-cis photoisomerization efficiently and to drive the excited state structure of the chromophore along a particular reaction pathway of the photocycle [29]. The markedly different excited state lifetime and relaxation pathway upon disruption of the specific hydrogen bonds in denatured or mutated PYP have emphasized the role of the surrounding amino acid residues. Such an important role the amino acids in the PYP still can not be mimicked by surrounding solvent polarity or by intermolecular couplings and interactions for the model chromophores in solutions or in crystals.

Although an intermediate species has been considered to involve in photoisomerization of the PYP model chromophores as a gateway prior to cis photoproduct, but it still remains an interesting task to elucidate finer details of the isomerization mechanism and the surrounding effects. The main excited-state relaxation channel in every PYP model chromophore is yet to be clarified, therefore, further studies to understand the reaction coordinates and particularly vibrational modes responsible for the excited state evolution and relaxation pathway for the PYP model chromophores are required. The ultrafast time-resolved vibrational spectroscopic studies would be useful to probe such vibrational modes as well as changes in structural geometry, which possibly have a non-radiative nature. These future studies would provide a better understanding of the photoprocess of the PYP chromophore. In addition, theoretical approaches should be addressed to the photoisomerization mechanism including the twisting bonds, excited-state relaxation and conical intersection upon different surrounding environment.

The observation of PCT photoisomerization in crystalline state with a stable cis photoproduct becomes important, since there are only few examples of

compounds known to show crystalline state photochromism [30]. This rarely occurring process is generally due to that the compounds have unstable photoproduct isomers or they have a fluorescence quenching effect in crystalline state, although they are compounds of high fluorescence efficiency in solutions. Intermolecular interactions and available free volumes that allow the molecular rearrangement in the crystal are also important factors. Thus, X-ray crystallographic studies are necessary to provide such information, and such a study of PCT single crystals is indeed required. On the other hand, studies of the photoexcitation dynamics of the protonated form of PCT in solution phase, solvent effects on the excited-state relaxation, and structural geometry reorganization are also crucial.

Finally, it would be of fundamental and technological interest to explore further the photochromic properties of PCT from the microsized to nanosized crystals in future. The bottom line of this interest is the unique physical properties originating from crystal quantum-size effects that are attractive for various potential photonic applications. Lastly, the PCT and PCTMe would also be of biological interest, since p-hydroxycinnamic acid, the mother compound of the PYP model chromophores, is the known anti-cancer active chromophore through its interference with the development of cancer-causing nitrosamines [31].

ACKNOWLEDGEMENTS

The present work has been supported by the Grant-in-Aid for Scientific Research (KAKENHI) in Priority Area “Molecular Nano Dynamics” from Ministry of Education, Culture, Sports, Science and Technology of Japan. A.U. is grateful to the Japan Society for the Promotion of Science (JSPS) for a Postdoctoral Fellowship.

REFERENCES

[1] K. J. Hellingwerf, J. Photochem. Photobiol. B: Biol. 54 (2000) 94.
[2] I. M. Pepe, Photochem. Photobiol. B: Biol. 48 (1999) 1.
[3] G. Gröbner, I. Burnett, C. Glaubitz, G. Chol, A. J. Mason A. Watts, Nature 405 (2000) 810.
[4] F. Noll, D. Braga and N. Hampp, Biofutur 226 (2002), 61.
[5] T. E. Meyer, Biochim. Biophys. Acta 806 (1985) 175.
[6] T. E. Meyer, E. Yakali, M. A. Cusanovich and G. Tollin, Biochemistry 26 (1987) 418.
[7] U. K. Genick, S. M. Soltis, P. Kuhn, I. L. Canestrelli and E. D. Getzoff, Nature 392 (1998) 206.
[8] J. Heberle and T. Gensch, Nat. Struct. Biol. 8 (2001) 195.
[9] M. A. Cusanovich and T. E. Meyer, Biochemistry 42 (2003) 4759.
[10] K. J. Hellingwerf, J. Hendriks and T. Gensch, J. Phys. Chem. A 107 (2003) 1082.

[11] Y. Imamoto, M. Kataoka, F. Tokunaga, T. Asahi and H. Masuhara, Biochemistry 40 (2001) 6047.
[12] Z. Ren, B. Perman, V. Šrajer, T.-Y. Teng, C. Pradervand, D. Bourgeois, F. Schotte, T. Ursby, R. Kort, M. Wulff and K. Moffat, Biochemistry 40 (2001) 13788.
[13] H. Ihee, S. Rajagopal, V. Šrajer, R. Pahl, S. Anderson, M. Schmidt, F. Schotte, P. A. Anfinrud, M. Wulff and K. Moffat, Proc. Natl. Acad. Sci. USA 102, (2005) 7145.
[14] R. Brudler, R. Rammelsberg, T. T. Woo, E. D. Getzoff, and K. Gerwert, Nat. Struct. Biol. 8 (2001) 265.
[15] M. L. Groot, L. J. G. W. van Wilderen, D. S. Larsen, M. A. van der Horst, I. H. M. van Stokkum, K. J. Hellingwerf and R. van Grondelle, Biochemistry 42 (2003) 10054.
[16] K. Heyne, O. F. Mohammed, A. Usman, J. Dreyer, E. T. J. Nibbering and M. A. Cusanovich, J. Am. Chem. Soc. 127 (2005) 18100.
[17] Y. Imamoto, M. Kataoka and F. Tokunaga, Biochemistry 35 (1996) 14047.
[18] (a) H. Chosrowjan, N. Mataga, Y. Shibata, Y. Imamoto and F. Tokunaga, J. Phys. Chem. B 102 (1998) 7695. (b) N. Mataga, H. Chosrowjan, Y. Shibata, Y. Imamoto and F. Tokunaga, J. Phys. Chem. B 104 (2000) 5191.
[19] M. Kim, R. A. Mathies, W. D. Hoff and K. J. Hellingwerf, Biochemistry 34 (1995) 12669.
[20] (a) P. Changenet-Barret, A. Espagne, N. Katsonis, S. Charier, J.-B. Baudin, L. Jullien, P. Plaza and M. M. Martin, Chem Phys. Lett. 365 (2002) 285. (b) P. Changenet-Barret, A. Espagne, P. Plaza, K. J. Hellingwerf and M. M. Martin, New J. Chem. 29 (2005) 527. (c) P. Changenet-Barret, A. Espagne, S. Charier, J.-B. Baudin, L. Jullien, P. Plaza, K. J. Hellingwerf and M. M. Martin, Photochem. Photobiol. Sci. 3 (2004) 823. (d) A. Espagne, P. Changenet-Barret, P. Plaza and M. M. Martin, J. Phys. Chem. A 110 (2006) 3393. (e) A. Espagne, P. Changenet-Barret, J.-B. Baudin, P. Plaza and M. M. Martin, J. Photochem. Photobiol. A: Chemistry (2006), in press, available online on 24 July 2006.
[21] (a) D. S. Larsen, M. Vengris, I. H. M. van Stokkum, M. A. van der Horst, R. A. Cordfunke, K. J. Hellingwerf and R. van Grondelle, Chem Phys. Lett. 369 (2003) 563. (b) D. S. Larsen and R. van Grondelle, ChemPhysChem 6 (2005) 828.
[22] (a) A. Usman, O. F. Mohammed, K. Heyne, J. Dreyer and E. T. J. Nibbering, Chem Phys. Lett. 401 (2005) 157. (b) O. F. Mohammed, K. Heyne, A. Usman, J. Dreyer, E. T. J. Nibbering and M. A. Cusanovich "Ultafast Polarization-Sensitive Infared Spectroscopy od Photoactive Yellow Protein and Model Compounds" in R. J. D. Miller, A. M. Weiner, P. B. Corkum, and D. M. Jonas (Eds.), Ultrafast Phenomena XV, Springer Series Chemical Physics, Springer, Berlin, 2006 (in press).
[23] E. V. Gromov, I. Burghardt, H. Koppel, L. S. Cederbaum, J. Phys. Chem. A 109 (2005) 4623.
[24] H. El-Gezawy, W. Rettig, A. Danel, G. Jonusauskas, J. Phys. Chem. B 109 (2005) 18699.
[25] A. Usman, H. Masuhara and T. Asahi, J. Phys. Chem. B (2006) in press.
[26] M. Unno, M. Kumauchi, N. Hamada, F. Tokunaga and S. Yamauchi, J. Biol. Chem. 279 (2004) 23855. (b) M. Unno, M. Kumauchi, J. Sasaki, F. Tokunaga and S. Yamauchi, Biochemistry 41 (2002) 5668. (c) M. Unno, M. Kumauchi, J. Sasaki, F. Tokunaga and S. Yamauchi, J. Phys. Chem. B 107 (2003) 2837.
[27] D. H. Waldek, Chem Rev. 91 (1991) 415.
[28] Y. Imamoto, K. Mihara, O. Hisatomi, M. Kataoka, F. Tokunaga, N. Bojkova and K. Yoshihara, J. Biol. Chem. 272 (1997) 12905. (b) Y. Imamoto, Y. Shirahige, F. Tokunaga, T. Kinoshita, K. Yoshihara and M. Kataoka, Biochemistry 40 (2001) 8997.

[29] G. Groenhof, M. Bouxin-Cademartory, B. Hess, S. P. de Visser, H. J. C. Berendsen, M. Olivucci, A. E. Mark and M. A. Robb, J. Am. Chem. Soc. 126 (2004) 4228.
[30] M. Irie, Chem. Rev. 100 (2000) 1685.
[31] http://www.vitamins-minerals.tv/phytochemicals/para_coumaric_acid.htm

Handai Nanophotonics, Volume 3
H. Masuhara, S. Kawata and F. Tokunaga (Editors)

Chapter 25

Defect mode and laser action in cholesteric liquid crystal

M. Ozaki, Y. Matsuhisa, H. Yoshida, Y. Takao, R. Ozaki and A. Fujii

Department of Electrical, Electronic and Information Engineering,
Osaka University, 2-1 Yamada-Oka, Suita, Osaka 565-0871, Japan

1. INTRODUCTION

Photonic crystals (PCs) having a three-dimensional (3-D) ordered structure with a periodicity of optical wavelength have attracted considerable attention from both fundamental and practical points of view, because in such materials novel physical concepts such as photonic band gap have been theoretically predicted and various applications of photonic crystals have been proposed [1, 2]. Especially, the study of stimulated emission in photonic band gap is one of the most attractive subjects, since, in the band gap, a spontaneous emission is inhibited and low-threshold lasers based on photonic crystals are expected [1, 3-6]. So far intensive studies on one- and two- dimensional band gap materials have been performed. In order to realize the photonic crystal, a large number of intensive studies on a micro-fabrication based on a semiconductor processing technology [7-9] and a self assembly construction of nano-scale spheres [10, 11] have been carried out.

Liquid crystals (LCs) including chiral molecule have a self-organized helical structure which can be regarded as a 1-D periodic structure. In such systems, there is a so-called stop band in which the light can not propagate, which is considered as a 1-D pseudo-bandgap. Lasing at the band edge has been reported in the cholesteric liquid crystal (CLC) [12, 14], chiral smectic liquid crystal [15-17] and polymerized cholesteric liquid crystal (PCLC) [18-21]. These laser action in the 1-D helical structure of the chiral liquid crystals are interpreted to be based on the band edge of the 1-D photonic band gap in which the photon group velocity is suppressed [22].

On the other hand, the localization of the light based on the defect mode caused by the imperfection in periodic structure has been expected as potential applications such as low threshold lasers and micro waveguides [7-9, 23, 24]. The introduction of the defect layer into the periodic helical structure of the

CLCs has been theoretically studied [25, 26]. Especially, Kopp et al. have predicted the existence of a localized state for single circularly polarized light in the twist defect of the CLCs [26]. However, in spite of the theoretical demonstration of the twist defect mode (TDM) in the CLC, evident experimental demonstration on such defect mode has not been carried out.

LCs have a large optical anisotropy and are sensitive to an external stress such as an electric field. Based on such optical anisotropy and field sensitivity, a tunable photonic crystal has been proposed in opal or inverse opal infiltrated with LC [27-31]. Although opal and inverse opal are simple and inexpensive approach to realize 3-D PC using self-organization of colloidal particles [10, 11], the introduction of defects into the 3-D periodic structure is a problem that must be resolved. Not only 3-D PCs but also one-dimensional (1-D) PCs are an attractive subject. Although, the 1-D PC does not have a complete PBG, there are plenty of applications using extraordinary dispersion of the photon and localized photonic state in a defect layer. So far, intensive studies on 1-D PC applications have been reported: air-bridge microcavities [7], the photonic band-edge laser [22], nonlinear optical diode [32] and the enhancement of optical nonlinearity [23, 33]. Recently we have introduced a LC layer in dielectric multilayer structure as a defect in 1-D PC [24], in which the wavelength of defect modes were controlled upon applying electric field in a basis of the change in optical length of the defect layer caused by the field-induced molecular reorientation of LC.

In this chapter, we review our recent work on the introduction of the optical defect into periodic nano-structured liquid crystals and the realization of the tuning of the defect mode in the photonic crystal containing liquid crystal as a defect. We experimentally demonstrate the TDM in the 1-D photonic band gap of the CLC film having a twist defect [21]. The laser action based on the TDM is also observed in the dye-doped PCLC composite film with the twist defect [20]. Although the TDM has a high quality (Q) factor, its frequency can not be tuned by an external field in this system. We propose a novel approach to introduce a defect into the helical structure of CLC [34]. Namely, using a direct laser writing technique with femtosecond pulse laser, we fabricate a local modification of the CLC helix pitch based on a two-photon polymerization. Finally, we propose a hybrid photonic crystal (HPC) structure based on a combination of CLC and a 1-D PC, in which CLC layer having a periodic helix structure is introduced into the periodic structure of 1-D PC as a defect [35]. In the HPC, a single-mode laser action with low pumping threshold is observed, which is based on the defect mode with a high Q factor peculiar to the CLC defect having periodic structure [36].

2. PHOTONIC BAND GAP AND BAND EDGE LASING IN CHOLESTERIC LIQUID CRYSTAL

In a periodically structured medium, when the Bragg condition is satisfied, reflected lights at each point interfere with each other. As a result, the light can not propagate and only the standing waves exist. This means the lights in a certain range of energy can not propagate in the medium, and the lights at both edges of this energy range have zero group velocity. This energy range is so called “photonic band gap”.

In the helical periodic structure of the CLCs, light propagating along the helical axis is selectively reflected depending on the polarization states if the wavelength of the light matches to the optical periodicity of the helical structure, which is a so-called selective reflection. In this case, there are two types of circularly polarized standing waves with zero group velocity at the edges of the stop band as shown in Fig.1. Here, the rods indicate the molecular long axis of the CLC and the arrows show the polarization direction of the standing waves. For one of standing waves, the polarization direction of the light is parallel to the molecular long axis and, if we dope laser dye, the polarization is parallel to the transition moment of the doped dye. This light feels extraordinary refractive index of the liquid crystal and has lower energy with respect to a traveling wave, which corresponds to the longer edge of the stop band. Moreover, this circularly polarized standing wave effectively interacts with the laser medium and we can expect the low threshold laser action at the longer wavelength edge of the band gap.

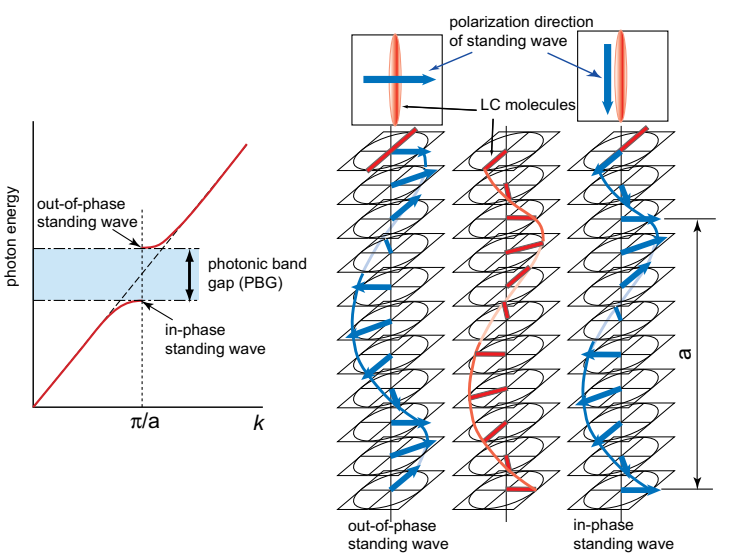

Fig. 1. Schematic explanation of the appearance of photonic band gap in spiral periodic structure.

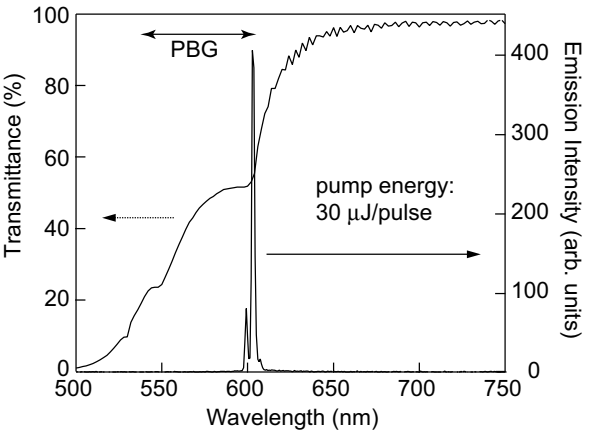

Fig. 2. Transmission and emission spectra of dye-doped PCLC. A sharp lasing peak appears at the longer edge of the PBG.

The emission spectrum of the dye-doped PCLC film for excitation energy of 30 J/pulse is shown in Fig.2 [20]. For the fabrication of PCLC, two types of photo-polymerizable CLC mixtures (Merck KGaA) were used, which have right-handed helix and reflection bands around 779 nm and 440 nm. The helical pitch of the CLC sample, that is, the wavelength of the optical stop band can be adjusted by mixing these two CLC compounds at a proper ratio. The free-standing CLC polymer film was prepared as follows. The monomer sample was inserted by a capillary action into the sandwiched cell that is composed of two grass plates. In order to obtain a homogeneously aligned cell, the surfaces were coated with a polyimide (JSR, AL1254) and rubbed. The cell gap was 25 m. The CLCs in this cell align their director parallel to the glass plates, that is, the helical axis is perpendicular to the glass substrates. UV light irradiation was performed using a Xe lamp to induce the photo-polymerization of the UV-curable CLC monomer. After UV light irradiation, two glass substrates were removed and the free-standing PCLC film was obtained. As a laser dye dopant in the CLC, [2-[2-4-(Dimethylamino)phenyl]ethenyl]-6-methyl-4H-pyran-4-ylidene] propanedinitrile, DCM (Exciton) was used. The concentration of the dye was 0.4 wt.-%. A second harmonic light of Q-switched Nd:YAG laser was used for an excitation light source, whose wavelength, pulse width and pulse repetition frequency were 532 nm, 8 ns, and 10 Hz, respectively. The illumination area on the sample was about 0.2 mm^2.

When the excitation energy is low (<3.0 J/pulse), the spectrum is dominated by a broad spontaneous emission. At high excitation energy, laser action is confirmed at the edge of the stop band which is observed as a suppression of the transmittance. The full width at half maximum (FWHM) of the emission peak is about 2 nm, which is limited by the spectral resolution of our spectrograph. At

lower excitation energies, the emission intensity increases in proportion to the pump energy, while above the threshold, the emission intensity increases steeply. The linewidth of the emission spectrum also drastically decreases above the threshold. This laser action is achieved without any substrates and is observed even when PCLC film is bent. This suggests that 1-D helical structure required for the laser action is maintained even in the deformed film. This flexibility may enable us to fabricate optical devices with new functionalities.

3. TWIST DEFECT MODE IN CHOLESTERIC LIQUID CRYSTAL

Laser actions reported so far in chiral liquid crystals are observed at the edge wavelength of the stop band and are associated with the group velocity anomaly at the photonic band edge. On the other hand, low threshold laser action based on the photon localization at the defect in periodic structure can also be expected. The introduction of the defect into the periodic helical structure of the CLCs has been theoretically studied. Especially, Kopp et al. have predicted the existence of a single circularly polarized localized mode in the twist defect of the CLCs (Fig.3(b)) [26].

The PCLC film with the twist defect was prepared as follows [21]. The photo-polymerizable CLC monomer was spin-coated from a toluene solution on a glass substrate on which a polyimide (AL-1254) was coated and rubbed in one direction. In order to obtain a uniform planer alignment, the coated CLC was annealed at the temperature just below a clearing point. The CLC on the substrate aligns their director parallel to the glass plate, that is, the helical axis is perpendicular to the glass substrate. UV light irradiation was performed using a Xe lamp to induce the photo-polymerization of the UV-curable CLC monomer. Two PCLC films were put together as the directors of liquid crystal molecules at an interface of these films make a certain angle. In other words, there is a discontinuous phase jump of the azimuthal angle of the helical structures between these PCLC films at the interface, which acts as a twist defect in the helicoidal periodic structure.

Fig. 3(c) shows the transmission spectrum of the dye-doped double PCLC composite film containing a discontinuous defect interface. A stop band, 1-D photonic band gap, is confirmed in the spectral range from 580 nm to 640 nm. It should be noted that a sharp peak appears at 611 nm within the photonic band gap, which might be related to the defect mode induced by the introduction of the twist defect interface.

We have performed theoretical calculation of light propagation in PCLC films with and without twist defect interface, using a method of characteristic matrices. This method is a numerical analysis based on the Maxwell equation which can be used to quantitatively calculate the light propagation in the medium with refractive index varying along one direction. Assuming that the

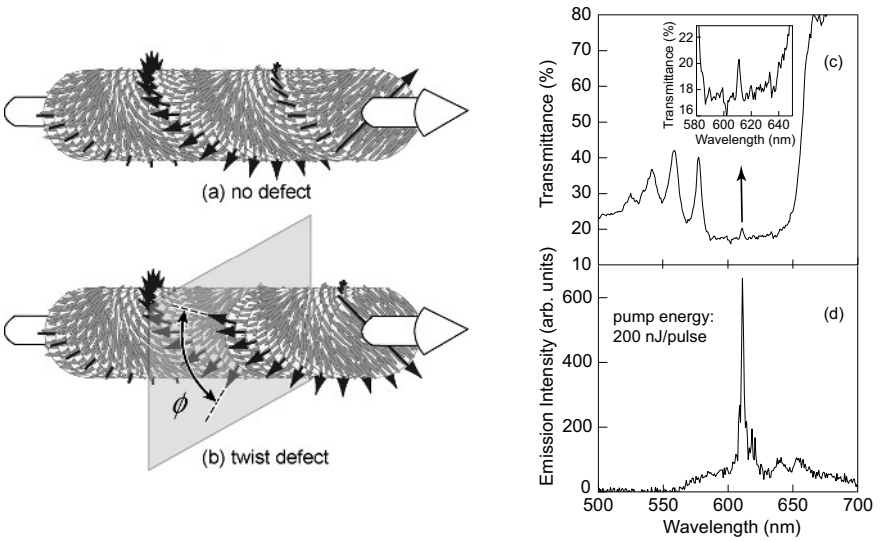

Fig. 3. The helix structures without (a) and with (b) twist defect interface. (c) Transmission spectrum of the dye-doped double PCLC composite film with twist defect. (d) Emission spectrum of the double PCLC composite film at above the threshold pump pulse energy (200 nJ/pulse).

phase jump of the director angles at the interface of two PCLC layers is 4/9 rad, the theoretically calculated results are in good agreement with the experimental ones. This result indicates that the sharp peak observed in the photonic band gap corresponds to the TDM in the double PCLC composite film with the twist defect interface.

Fig. 3 (d) shows the emission spectrum of the dye-doped double PCLC composite film with the defect interface at pump energy of 200 nJ/pulse. For an excitation source, second harmonic light of a mode-locked Nd:YAG laser (Ekspla, PL2201) was used. The pulse width, wavelength and pulse repetition frequency of the pump laser beam were 100 ps, 532 nm and 1 kHz, respectively. The illumination area on the sample was about 0.2 mm^2. At high excitation energy (200 nJ/pulse), laser action appears at 611 nm which is within the band gap and coincides with the TDM wavelength. The FWHM of the emission peak is about 2 nm, which is limited by the spectral resolution of our experimental setup. Above the threshold at a pump pulse energy of about 100 nJ/pulse, the emission intensity increases. The FWHM of the emission spectrum also drastically decreases above the threshold. These results confirm that laser action occurs above the threshold of the pump energy at the wavelength of the TDM in the photonic band gap.

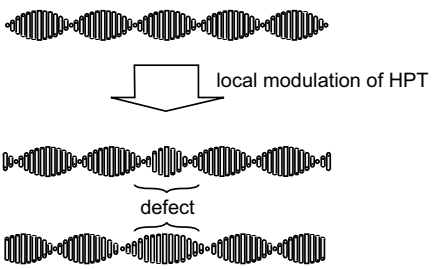

Fig. 4. Schematic explanation of the chiral defect based on the partial deformation of the helix pitch.

4. CHIRAL DEFECT MODE INDUCED BY PARTIAL DEFORMATION OF HELIX

TDM based on the composite film of two PCLCs has been achieved. However, its wavelength can not be tuned by an external field such as the electric field or light. We have proposed a new type of defect mode in the helix which can be dynamically tuned by the external field [37]. Fig. 4 shows schematic explanation of a photonic defect in CLC. If the periodicity (pitch) of the helix is partially changed, that is, the pitch is partially squeezed or expanded, these irregularities in the periodic structure should act as a defect and cause the light localization. As a method to induce partial change in helix pitch, we suppose that the local modification of helical twisting power (HTP) is induced by a focused Gaussian laser light. Optical control of HTP can be realized using photochemical effects of the doped azobenzene, nonlinear optical effects, or by simple heating. Photoinduced reversible control of HTP of CLC has been demonstrated in the CLC containing photochromic azobenzene, and applications to a reflection-type display devices, an optical shutter, an optical memory, and so on have been studied [38, 39]. By the trans-cis photoisomerization of the doped azobenzene, HTP of the host CLC changes, so that photoinduced control of HTP can be realized.

We have also proposed a novel approach to introduce chiral defects (local modulation of the helix pitch) into the helix structure of CLC [34]. A schematic explanation of the fabrication procedure is shown in Fig. 5(a). A 100 fs pulse of a Ti:Sapphire laser at wavelength of 800 nm and repetition rate of 80 MHz were focused on the sample cell by an objective lens with N.A.1.4. The right-handed PCLC material doped with 1 wt% of DCM dye was aligned homogeneously in a cell with a gap of 6-7 m. The direct laser writing was performed with a confocal laser scanning microscope. The laser was scanned over an area of 146.2 m x 146.2 m, with a scan-line resolution of 2048 lines per scan-area. First, the laser light is tightly focused near the substrate surface in the CLC cell. Tow-photon polymerization occurs at the laser focusssing point and a locally polymerized

PCLC thin film is obtained on the substrate surface. The sample is then flipped over and laser writing performed again near the opposite surface of the cell. As a result, a hybrid structure is fabricated in which an unpolymerized CLC region is left between two PCLC films on the cell surfaces.

Fig. 5(b) shows the transmission spectra for right-handed circularly polarized light of the fabricated CLC defect structure. A single defect mode is observed within the selective reflection band of the CLC. The theoretical transmission spectrum was calculated using Berreman's 4x4 matrix, which showed a good agreement with the experimental result. Fig. 5 (c) shows the emission spectrum at high pumping energy of the CLC single-defect structure along with the corresponding transmission spectrum. Single mode laser action is observed at 628 nm, which corresponds to the defect mode wavelength. Lasing threshold for the defect mode structure is 16.7 mJ/cm^2, which is less than half of the threshold of CLC without defect structure. The reduction of the lasing threshold in the defect structure supports a high-Q cavity formed by the defect.

5. TUNABLE DEFECT MODE LASING IN A PERIODIC STRUCTURE CONTAINING LC LAYER AS A DEFECT

We have introduced a LC layer in a 1-D PC as a defect, in which the wavelength of defect modes were controlled upon applying electric field in a basis of the change in optical length of the defect layer caused by the field-induced molecular reorientation of LC [24]. We also proposed a wavelength tuneable laser based on an electrically controllable defect mode in a 1-D dielectric

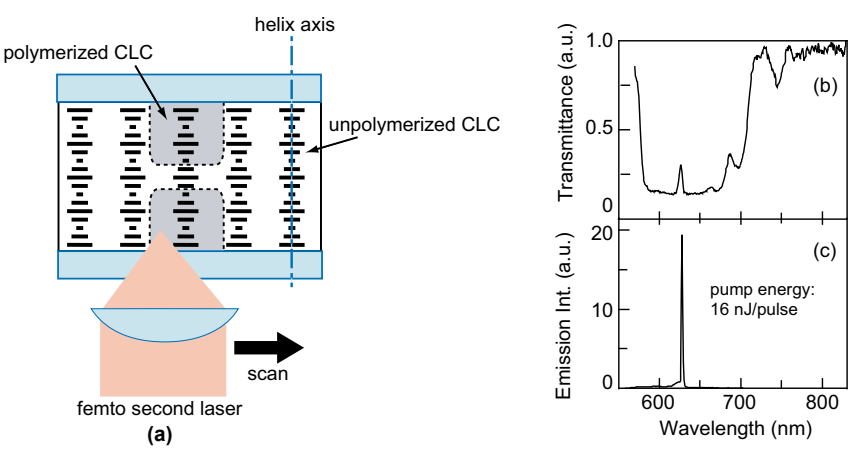

Fig. 5. (a) Schematic explanation of the fabrication procedure of the PCLC with chiral defect based on local photo-polymerization using scanning confocal microscope. Transmission (b) and emission (c) spectra of the CLC with chiral defect.

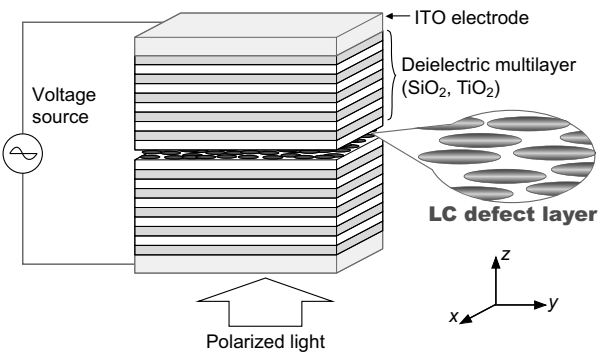

Fig. 6. Schematic explanation of 1-D PC containing liquid crystal as a defect.

periodic structure containing a dye-doped LC as a defect layer [40, 41]. Fig. 6 shows the 1-D PC with a LC defect. A dielectric multilayer consisting of an alternating stack of SiO2 and TiO2 layers deposited on an In-Sn oxide (ITO) coated glass substrate is used as the 1-D PC. In order to introduce the defect layer, a dye-doped nematic liquid crystal (Merck, E47) was sandwiched between substrates with dielectric multilayer using 2 m spacers. The refractive index anisotropy n of E47 is 0.209 at room temperature. In the absence of an electric field, the long molecular axis of the LC is aligned parallel to the substrates (y-axis).

In order to investigate the characteristics of defect mode, the transmission spectrum of the linearly polarized light propagating along the z-axis was measured from the opposite side of the cell using a CCD multi-channel spectrometer. The peaks of the defect modes shift to shorter wavelengths upon applying voltage. This peak shift originates from the decrease in the optical length of the defect layer caused by the field-induced reorientation of the LC molecules. Consequently, we confirmed that the wavelength of the defect mode in 1-D PC with the LC layer as a defect can be controlled upon applying voltage. On the basis of this defect mode tuning, the lasing wavelength can be controlled upon applying electric field [40, 41].

We have also introduced a CLC layer in a 1-D PC as a defect [35, 36, 42]. Fig. 7(a) shows the theoretical transmission spectrum of a 10-pair multilayer without a CLC defect (solid line), and a simple CLC without a PC structure (dashed line). The PBG of the CLC was observed between 605 nm and 680 nm, which is inside that of the multilayer. Fig. 7(b) shows the calculated transmission spectrum of a 1-D HPC with a CLC defect. Many peaks appeared at regular intervals in the PBG of the HPC. These peaks are related to the defect modes resulting from the introduction of the CLC defect. However, additional peaks were observed, as indicated by arrows, which disrupted the regular interval between the defect mode peaks at both band edges of the CLC.

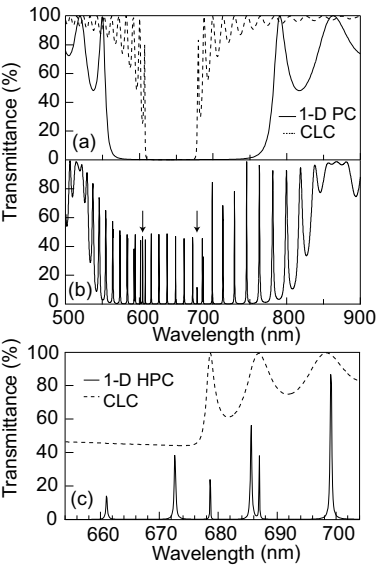

Fig. 7. (a) Theoretical transmission spectra of a 1-D PC without any defect (solid line) and a CLC without a PC structure (dashed line). (b) Theoretical transmission spectra of 1-D PC containing CLC as a defect. (c) Magnified transmission spectra corresponding to (b).

The transmission spectra in Fig. 7(b), around the longer edge of the PBG of the CLC, are shown magnified in Fig. 7(c). Four main peaks due to the defect modes appeared at regular intervals (661 nm, 673 nm, 687 nm and 699 nm), although the peak at 687 nm splits. The splitting of the peak at 687 nm is attributed to the optical anisotropy of the CLC. Therefore, two kinds of defect mode corresponding to left- and right-handed circularly polarized lights could exist out of the PBG of the CLC. On the other hand, one additional peak was observed at 678.6 nm, which corresponds to the band-edge wavelength of the CLC. From detailed consideration of the polarization states of transmitted light, the additional peak was clearly distinguished from the other defect mode peaks. Such a peak was not observed in a 1-D PC with a uniform defect such as an isotropic medium or nematic liquid crystals [24, 43]. Namely, this peak is a defect mode peculiar to the helix defect in the 1-D PC, and is associated with photon localization originating from the band-edge effect of the CLC helix. Note that this defect mode peak is very sharp and the full width at half-maximum (FWHM) of this peak was 0.05 nm, which is more than four times smaller than that of the other defect mode peaks (0.23 nm). From the peak width, the Q-factor of the additional mode at the band edge of the CLC was estimated to be 14000, which was much higher than that of the other defect modes.

In order to clarify the appearance of the high-Q defect mode in the double periodic structure, we have performed theoretical estimation of electric field

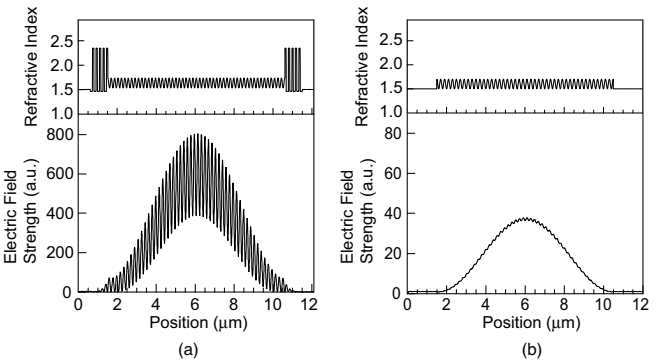

Fig. 8. Calculated electric field strength in the cell of a 1-D PC containing CLC defect (a) and a simple CLC (b).

distribution in three types of one-dimensional periodic structures described above using a finite difference time domain (FDTD) method. This method is numerical analysis based on the Maxwell differential form equations. In this calculation, light absorption is neglected in simulation space and the first Mur method is applied as the absorbing boundary condition to absorb the outgoing light in simulation space edges. Fig.8 shows the calculated electric field distributions and refractive indices in two types of periodic structures. We assumed that the thickness, the helical pitch and the extraordinary and ordinary refractive indices of the CLC are 9.1 μm, 350 nm, 1.735 and 1.530, respectively. The wavelength of the incident light to the periodic structures corresponds to the high-Q defect mode wavelength. It should be noted that light is localized strongly in the double periodic structure and the maximum electric field intensity is more than 15 times as much as that of a simple CLC. Light is localized at the center of the CLC layer in the double periodic structure shown in Fig. 8(a) and its field pattern is similar to that in the CLC shown in Fig. 8(b), which indicates that light in the double periodic structure is confined by the band edge effect of CLC. Additionally light confinement is effectively enhanced by the outer periodic structure because the wavelength of light is within the PBG of the outer periodic structure. Namely, from the contribution of both band edge effect of CLC and defect mode effect of the outer periodic structure, light is localized strongly in the double periodic structure.

We have investigated the laser action in a 1-D HPC with a CLC defect. As a laser dye dopant, DCM was compounded in a CLC, whose concentration was 1 wt%. The PBG of the CLC shifts with a temperature change, which is attributed to the temperature dependence of the helical pitch of the CLC. The band edge of the CLC was adjusted to 644 nm by temperature regulation in this experiment because of the emission wavelength window of the laser dye. The pumping wavelength was 532 nm. The excitation laser beam irradiated the sample

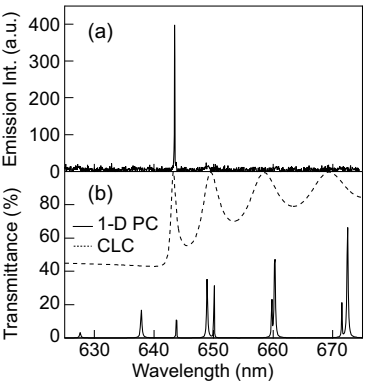

Fig. 9. (a) Emission spectrum of 1-D PC containing dye-doped CLC defect layer. (b) Theoretical transmission spectra corresponding to the emission spectrum.

perpendicularly to the glass surface, whose illumination area on the sample was about 0.2 mm^2. The emission spectra from the 1-D HPC were measured using a CCD multichannel spectrometer. At a low pumping energy, the emission peaks appear, which were attributed to spontaneously emitted light passing out through narrow spectral windows owing to the defect modes. At a high pumping energy of 18 nJ/pulse, as shown in Fig. 9(a), only one sharp lasing peak appeared at 643.5 nm. The calculated transmission spectrum of this system is also shown in Fig. 9(b). Comparing Figs. 9(a) and (b), the lasing peak coincides with the wavelength of the peculiar defect mode. Note that the laser action was single-mode based on one additional mode, although many modes exist because of the high Q-factor. The threshold of laser action in the 1-D HPC with a CLC defect was lower than that in simple CLC without a 1-D PC [35]. This result is attributed to strong optical confinement due to the high Q-factor of the additional mode. Similar results have been confirmed in the 1-D PC containing ferroelectric liquid crystal as a defect [44].

6. SUMMARY

Two types of laser actions were demonstrated using PCLC. They originated from the band edge effect of the one-dimensional photonic bands gap and the defect mode within the band gap. We experimentally demonstrated the TDM in the 1-D photonic band gap of the CLC film having a twist defect which was a discontinuity of the director rotation around the helix axis at an interface of two PCLC layers. The laser action based on the TDM was also observed in the dye-doped PCLC composite film with the twist interface. We proposed a new type of defect mode based on the chiral defect in which the partial modulation of the helix pitch was induced. In the new chiral defect mode, the tuning of the mode

frequency could be expected by partial modulation of the helical twisting power. In order to realize chiral defect in CLC, we also proposed a novel approach using a direct laser writing technique with femtosecond pulse laser. We fabricated a local modification of the CLC helix pitch based on a two-photon polymerization. Finally, we proposed double periodic structure in which the defect has also periodicity, and we demonstrated a hybrid photonic crystal (HPC) structure based on a combination of a 1-D PC and CLC defect. In the HPC, a single-mode laser action with low pumping threshold is observed, which is based on the defect mode with a high Q factor peculiar to the CLC defect having periodic structure.

ACKNOWLEDGEMENTS

This work is supported by a Grant-in-Aid for Scientific Research from the Japan Ministry of Education, Culture, Sports, Science and Technology. We would like to show our acknowledgements to Merck KGaA for providing the photo-polymerizable CLC materials.

REFERENCES

[1] E. Yablonovitch, Phys. Rev. Lett., 58 (1987) 2059.
[2] S. John, Phys. Rev. Lett., 58 (1987) 2486.
[3] J. D. Joannopoulos, R. D. Meade, and J. N. Winn, Photonic crystals, Molding the Flow of Light, Princeton Univ. Press, Princeton, NJ, 1995.
[4] J. Martorell, and N. M. Lawandy, Phys. Rev. Lett., 6 (1990) 1877.
[5] K. Yoshino, S.B. Lee, S. Tatsuhara, Y. Kawagishi, M. Ozaki, and A.A. Zakhidov, Appl. Phys. Lett., 73 (1998) 3506.
[6] K. Yoshino, S. Tatsuhara, Y. Kawagishi, M. Ozaki, A.A. Zakhidov, and Z.V. Vardeny, Appl. Phys. Lett., 74 (1999) 2590.
[7] J.S. Foresi, P.R. Villeneuve, J. Ferrera, E.R. Thoen, G. Steinmeyer, S. Fan, J.D. Joannopoulos, L.C. Kimerling, H.I. Smith, and E.P. Ippen, Nature, 390 (1997) 143.
[8] O. Painter, R.K. Lee, A. Scherer, A. Yariv, J.D. O'Brien, P.D. Dapkus, and I. Kim, Science, 284 (1999) 1819.
[9] S. Noda, K. Tomoda, N. Yamamoto, and A. Chutinan, Science, 289 (2000) 604.
[10] K. Yoshino, K. Tada, M. Ozaki, A.A. Zakhidov, and R.H. Baughman, Jpn. J. App. Phys., 36 (1997) L714.
[11] Y.A. Vlasov, K. Luterova, I. Pelant, B. Honerlage, and V.N. Astratov, Appl. Phys. Lett., 71 (1997) 1616.
[12] V.I. Kopp, B. Fan, H.K. Vithana, and A.Z. Genack, Opt. Lett., 23 (1998) 1707.
[13] B. Taheri, A.F. Munoz, P. Palffy-Muhoray, and R. Twieg, Mol. Cryst. Liq. Cryst., 358 (2001) 73.
[14] K. Funamoto, M.Ozaki, and K.Yoshino, Jpn. J. Appl. Phys., 42 (2003) L1523.
[15] M. Ozaki, M. Kasano, D. Ganzke, W. Haase, and K. Yoshino, Adv. Mater. 14 (2002) 306.
[16] M. Ozaki, M. Kasano, D. Ganzke, W. Haase, and K. Yoshino, Adv. Mater. 15 (2003) 974.

[17] M. Kasano, M. Ozaki, D. Ganzke, W. Haase, and K. Yoshino, Appl. Phys. Lett., 82 (2003) 4026.
[18] H. Finkelmann, S.T. Kim, A. Munoz, P. Palffy-Muhoray, and B. Taheri, Adv. Mater. 13 (2001) 1069.
[19] J. Schmidtke, W. Stille, H. Finkelmann, and S.T. Kim, Adv. Mater. 14 (2002) 746.
[20] T. Matsui, R. Ozaki, K. Funamoto, M. Ozaki, and K. Yoshino, Appl. Phys. Lett., 81 (2002) 3741.
[21] M. Ozaki, R. Ozaki, T. Matsui, and K. Yoshino, Jpn.J.Appl.Phys., 42 (2003) L472.
[22] J.P. Dowling, M. Scalora, M.J. Bloemer, and C.M. Bowden, J. Appl. Phys., 75 (1994) 1896.
[23] T. Hattori, N. Tsurumachi, and H. Nakatsuka, J. Opt. Soc. Am., 14 (1997) 348.
[24] R. Ozaki, T. Matsui, M. Ozaki, and K. Yoshino, Jpn. J. App. Phys., 41 (2002) L1482.
[25] Y.C. Yang, C.S. Kee, J.E. Kim, H.Y. Park, J.C. Lee, and Y.J. Jeon, Phys. Rev. E, 60 (1999) 6852.
[26] V.I. Kopp, and A.Z. Genack, Phys. Rev. Lett., 89 (2002) 033901.
[27] K. Yoshino, S. Satoh, Y. Shimoda, Y. Kawagishi, K. Nakayama, and M. Ozaki, Jpn. J. Appl. Phys., 38 (1999) L961.
[28] K. Yoshino, Y. Shimoda, Y. Kawagishi, K. Nakayama, and M. Ozaki, Appl. Phys. Lett., 75 (1999) 932.
[29] K. Busch, and S. John, Phys. Rev. Lett., 83 (1999) 967.
[30] Y. Shimoda, M. Ozaki, and K. Yoshino, Appl. Phys. Lett., 79 (2001) 3627.
[31] M. Ozaki, Y. Shimoda, M. Kasano, and K. Yoshino, Adv. Mater., 14 (2002) 514.
[32] M. D. Tocci, M.J. Bloemer, M. Scalora, J.P. Dowling, and C.M. Bowden, Appl. Phys. Lett., 66 (1995) 2324.
[33] Y. Dumeige, P. Vidakovic, S. Sauvage, I. Sgnes, and J.A. Levenson, Appl. Phys. Lett., 78 (2001) 3021.
[34] H. Yoshida, C.H. Lee, Y. Matsuhisa, A. Fujii, and M. Ozaki, Adv. Mater, in press.
[35] Y. Matsuhisa, R. Ozaki, M. Ozaki, and K. Yoshino, Jpn. J. Appl. Phys., 44 (2005) L629.
[36] Y. Matsuhisa, R. Ozaki, K. Yoshino, and M. Ozaki, Appl. Phys. Lett., 89 (2006) 101109.
[37] T. Matsui, M. Ozaki, and K. Yoshino, Phys. Rev. E, 69 (2004) 061715.
[38] E. Sackmann, J. Am. Chem. Soc., 93 (1971) 7088.
[39] H.K. Lee, K. Doi, H. Harada, O. Tsutsumi, A. Kanazawa, T. Shiono, and T. Ikeda, J. Phys. Chem. B, 104 (2000) 7023.
[40] R. Ozaki, T. Matsui, M. Ozaki, and K. Yoshino, Appl. Phys. Lett., 82 (2003) 3593.
[41] R. Ozaki, Y. Matsuhisa, M. Ozaki, and K. Yoshino, Appl. Phys. Lett., 84 (2004) 1844.
[42] Y. Matsuhisa, R. Ozaki, K. Yoshino, and M. Ozaki, Thin Solid Films, 509 (2006) 189.
[43] R. Ozaki, T. Sanda, H. Yoshida, Y. Matsuhisa, M. Ozaki, and K. Yoshino, Jpn. J. Appl. Phys., 45 (2006) L493.
[44] Y. Matsuhisa, W. Haase, A. Fujii, and M. Ozaki, Appl. Phys. Lett., 89 (2006) in press.

Handai Nanophotonics, Volume 3
H. Masuhara, S. Kawata and F. Tokunaga (Editors)

Chapter 26

Integrated photonic devices using semiconductor quantum-well structures

Toshiaki Suhara and Masahiro Uemukai

Department of Electrical, Electronic and Information Engineering
Graduate School of Engineering, Osaka University
2-1 Yamada-Oka, Suita, Osaka, 565-0871 Japan

1. INTRODUCTION

Quantum-well (QW) structures of III-V semiconductors with nanometer layer thickness offer a number of advantages as an active structure for semiconductor lasers [1]. Use of strained QWs enables enhancement of the performances and expansion of functions.

QWs are so thin that the atoms in the well can be intermixed with atoms of the surrounding barriers by appropriate heat treatment. Area-selective QW disordering techniques based upon patterned capping or patterned doping, followed by rapid thermal annealing (RTA), provide an effective means for tailoring of effective bandgap energy and optical loss reduction in passive waveguide. The technique enables implementation of monolithic integrated photonic devices consisting of active and passive components. The authors developed an area-selective QW disordering technique based on impurity-free vacancy diffusion using silica caps and RTA [2].

Periodic fine structures with nanometer precision in semiconductor waveguides can be used not only as a distributed Bragg reflector (DBR) for wavelength-selective feedback but also as elements for various wavefront conversion and beam shaping based upon the principle of holography [1, 2]. Therefore they are an important element for integrated photonic devices.

This chapter reviews the research work of the authors' group on the integrated semiconductor lasers and monolithic integrated photonic devices using QW and waveguide gratings. Applications include optical communications, information processing and sensing. The area-selective QW disordering as an effective technique to reduce the absorption loss in the passive waveguide is described, and the design and fabrication of the semiconductor

waveguide grating components are outlined. Then, design, fabrication and experimental results are presented on high-performance DBR lasers using curved gratings, an integrated master oscillator power amplifier (MOPA) with outcoupler, a tunable extended-cavity laser using tapered amplifier and a curved grating coupler, and surface-emitting DBR laser for biosensing applications.

2. AREA-SELECTIVE QUANTUM-WELL DISORDERING

Monolithic integration of semiconductor lasers with passive elements like grating components requires reduction of propagation loss in the passive waveguide, since the semiconductor waveguide sections without carrier injection exhibit large absorption loss at the lasing wavelength. One of the effective techniques for the loss reduction is effective bandgap modification by compositional disordering (intermixing) of quantum well [3]. QW disordering through impurity-free vacancy diffusion (IFVD) by capped rapid thermal annealing (RTA), in particular, offers several advantages; it allows postgrowth bandgap modification by simple processing using inexpensive standard deposition and RTA apparatus, and possibly allows loss reduction larger than that by impurity-induced QW disordering. Deposition of a SiO_2 cap layer on a QW structure followed by RTA induces absorption of the Ga atoms into the cap layer and generates vacancies in the III-V semiconductor crystal [3]. The vacancies diffuse toward the QW and promote interdiffusion between the atoms

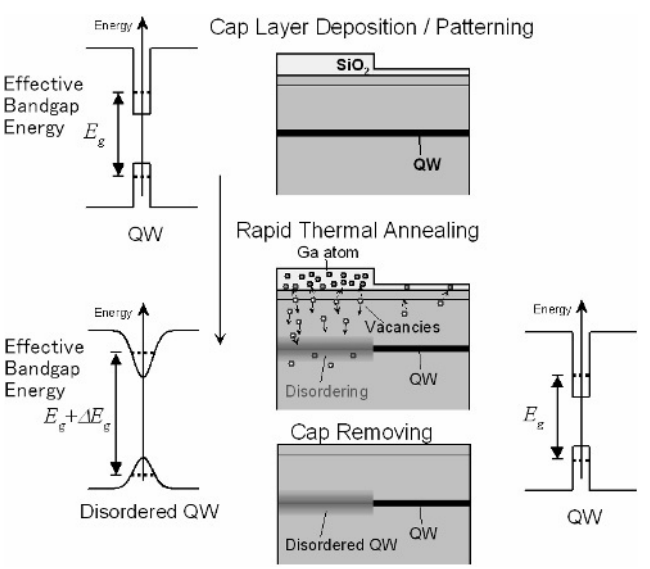

Fig.1. Area-selective QW disordering by impurity-free vacancy diffusion using SiO_2 caps of different thicknesses.

in the QW and barriers. As a result, the effective bandgap of the QW is widened. If the QW is capped with a layer which does not substantially absorb Ga atoms, disordering is suppressed. A very thin SiO_2 layer is also expected to work as a suppression cap because of saturation of Ga absorption. In fact, for GaAs-AlGaAs QW, it was reported that a thinner SiO_2 cap gives smaller bandgap widening [4, 5]. We have developed selective disordering technique using SiO_2 caps of different thicknesses and RTA [6, 7]. The technique is illustrated in Fig.1.

The selective bandgap broadening was examined by photoluminescence measurement and lasing wavelength measurement of Fabry-Perot (FP) lasers. We deposited SiO_2 layers of 300nm and 30nm thickness, for the disordering and suppressing caps, respectively, by plasma-enhanced chemical vapor deposition (PCVD) on separate areas of the InGaAs/GaAs QW structure. Then RTA was performed at 900ºC, 920ºC and 940ºC for 15s. The FP laser configuration and the measured lasing wavelengths are shown in Fig.2. For the RTA temperature of 920°C, lasing wavelength difference as large as 23 nm was obtained. The lasing wavelength of a laser using as-grown QW was 980nm. These results were consistent with the results of photoluminescence measurements. The internal differential quantum efficiency η_i and the internal loss α_i were

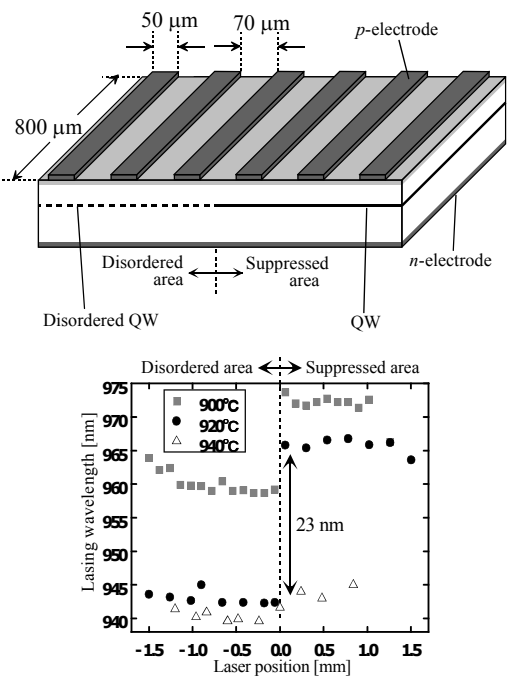

Fig.2. FP lasers fabricated in select-ively disordered QW structure and the lasing wavelengths.

determined from the measured injection current dependence of the output power. There was no substantial difference in these parameters between the as-grown lasers and the lasers in the suppressed area.

The loss reduction was evaluated by fabricating FP lasers with disordered passive waveguides as shown in Fig.3. Lasers of different passive guide lengths L_{pf}+L_{pb}=0, 400, 800μm were fabricated, and the *I-P* characteristics were measured to determine the external differential quantum efficiency η_d. By fitting the result to the theoretical expression of η_d dependent on the passive waveguide loss α_p and laser parameters, the α_p for the disordered waveguide was determined as 3cm^{-1}, while the α_p for the undisordered waveguide was roughly 40cm^{-1}.

3. GRATING COMPONENTS FOR SEMICONDUCTOR INTEGRATED PHOTONIC DEVICES

Periodic structures or gratings in optical waveguides can perform various functions, such as phase matching, mode conversion, deflection, input/output coupling, wavelength-selective reflection, and wavelength dispersion for guided waves [8, 9]. Complicated wavefront conversion functions can also be incorporated based on the principle of holography. The authors have demonstrated the usefulness of such gratings as a component of semiconductor integrated photonic devices by implementation of a monolithic integrated-optic interferometer position/displacement sensor [10] and a monolithic integrated-optic disc pickup head [11]. In this section, design of such grating components is outlined.

3.1. Design of grating patterns for wavefront conversion

Gratings in a planar waveguide can perform various wavefront conversion functions [8, 9]. The pattern of such gratings can be determined from the

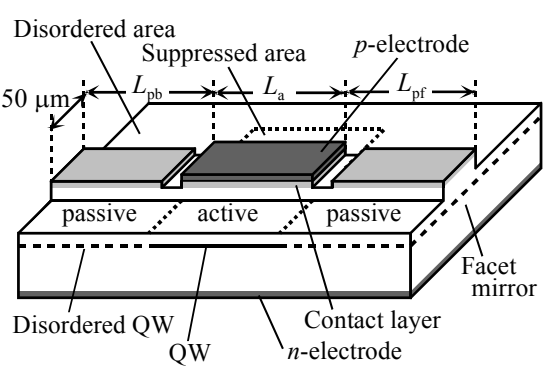

Fig.3. FP laser integrated with passive waveguides for evaluation of loss reduction.

wavefront difference between the input wave and the desired ouptput wave. For conversion between input and output waves described by phase distributions $\Phi_i(x,y)$ and $\Phi_o(x,y)$ on the grating (xy) plane, the shape of the m-th line of q-th order grating is given by $\Phi_o(x,y)-\Phi_i(x,y)=2qm\pi+\text{const}$. An example of gratings for in-plane coupling is a curved distributed Bragg reflection (DBR) grating which reflects a 2-dimensional (2D) diverging Gaussian beam into a focusing Gaussian wave as depicted in Fig.4(a). The pattern is given by [12]

$$2N_e ky + \frac{N_e kyx^2}{y^2 + (N_e kw_0^2/2)^2} - \tan^{-1}\left(\frac{2y}{N_e kw_0^2}\right) = 2qm\pi, \quad k = 2\pi/\lambda, \tag{1}$$

where N_e is the mode index, and w_0 the $1/e^2$ half width of the beam waist. An example of gratings for out-of-plane coupling is a focusing grating coupler [13] that converts a diverging 2D spherical guided wave into a converging spherical wave in free space as depicted in Fig.4(b). The grating pattern is given by

$$k\sqrt{x^2 + (y - f\sin\theta)^2 + (f\cos\theta)^2} + N_e k\sqrt{x^2 + (y+r)^2} = 2m\pi + kf + N_e kr, \quad k = 2\pi/\lambda, \tag{2}$$

where f, r, θ denote the outer and inner focal lengths, and the exit angle. The pattern of a grating coupler for output beam collimation is given by Eq. (2) with $f\to\infty$. These grating patterns can be written by curved-line scanning of an electron beam. In order to obtain diffraction-limited performances, appropriate writing accuracy is required to ensure the RMS aberration of the output wavefront on the grating plane smaller than $\lambda/15(=0.07\lambda)$ (Maréchal criterion).

3.2. Design of cross-sectional structure for high coupling efficiency

The coupling efficiency, i.e., the reflectivity R and the transmissivity T, of a DBR grating (Fig.4(a)) of length L, at the Bragg wavelength for q-th order coupling, can be written as

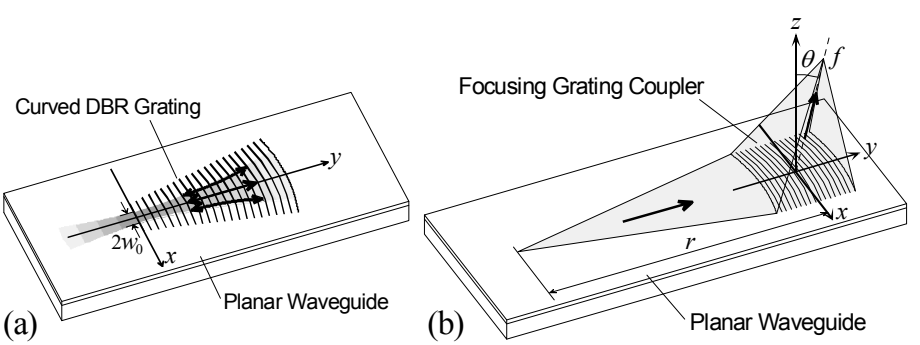

Fig.4. Waveguide grating components for wavefront conversion and coupling.

$$R=\left|\frac{\kappa_q \sinh \gamma L}{\gamma \cosh \gamma L+(\alpha_p/2)\sinh \gamma L}\right|^2,\quad T=\left|\frac{\gamma}{\gamma \cosh \gamma L+(\alpha_p/2)\sinh \gamma L}\right|^2,\quad \gamma=\sqrt{\kappa_q^2+(\alpha_p/2)^2}, \quad (3)$$

where κ_q denotes the coupling coefficient, α_p the passive waveguide loss factor. The coupling coefficient κ_q depends on the grating groove depth, and can be calculated as an overlap integral of the guided mode and the q-th order Fourier amplitude of the permittivity distribution of the grating. To accomplish a high reflectivity, the loss α_p must be minimized. Reduction of α_p at the lasing wavelength can be accomplished by selective QW disordering. The grating length L can be designed to maximize R or to obtain required R and T. The outcoupling efficiency η_{out} of a grating coupler of length L (Fig.4(b)) can be written as

$$\eta_{out}=P^{(a)}{}_1\{1-\exp(-2\alpha_{tot}L)\},\ P^{(a)}{}_1=\alpha^{(a)}{}_1/\alpha_{tot},\ \alpha_{tot}=\alpha_p/2+\Sigma_{q,i}\alpha_q{}^{(i)}\ \alpha_q{}^{(i)}=\pi|\kappa^{(i)}{}_q|^2, \quad (4)$$

where $\alpha^{(a)}{}_q$ ($\alpha^{(s)}{}_q$) denotes the decay factor for radiation into air (substrate) by q-th order coupling, $\kappa^{(i)}{}_q$ ($^{(i)=(a),(s)}$) the coupling coefficient, α_p the loss factor, α_{tot} the total decay factor, $P^{(a)}{}_1$ the power distribution ratio for 1-st order beam into air. The coupling coefficient $\kappa^{(i)}{}_q$ can be calculated as an overlap integral of the guided and radiation modes and the Fourier amplitude of the grating. In order to have a high efficiency, $P^{(a)}{}_1$ and $\alpha_{tot}L$ should be large. Reduction of α_p can be accomplished as mentioned above. The upward radiation from the grating interferers with the reflection of the downward radiation by the multilayer reflector. Therefore $P^{(a)}{}_1$ can be maximized up to approximately 1 by selecting a grating period so as to eliminate higher-order radiation and optimizing the separation between the grating and the reflector (the lower cladding thickness). If $a_{tot}L>1$, the effective aperture length $1/a_{tot}$ is smaller than L, and the wavefront conversion performances are deteriorated. A design guideline to obtain a high efficiency together with good beam shaping is to determine the grating groove depth so as to satisfy $a_{tot}L\sim1$.

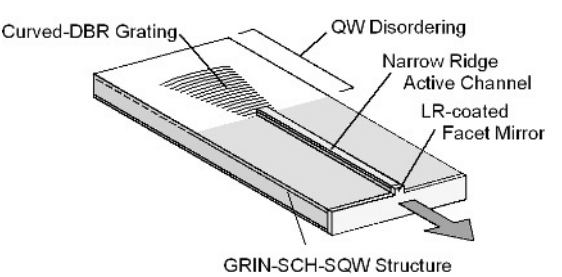

Fig.5. Schematic illustration of a DBR laser consist-ing of a ridge active channel and a curved surface DBR grating.

4. DBR LASERS USING CURVED SURFACE GRATING

4.1. Prototype QW DBR laser description

Figure 5 illustrates a DBR laser configuration proposed by the authors [12]. The laser consists of a narrow active channel and a curved surface DBR grating. The active channel is in the form of a narrow ridge structure, which ensures the lateral single-mode operation. The curved-DBR grating of a pattern given by Eq.(1) provides a high reflectivity for the guided wave diverging from the end of the channel. The grating is in the form of surface relief etched on the waveguide where the upper cladding is removed. Whereas the fabrication of DFB laser usually requires crystal regrowth over a grating, the use of surface grating allows simple fabrication without regrowth procedure.

The prototype of the DBR lasers was fabricated by using an InGaAs/AlGaAs graded-index separate confinement heterostructure (GRIN-SCH) strained single quantum well (SQW) waveguide [14, 15] grown by MOVPE. The cross sections of the GRIN-SCH-SQW structure and the surface DBR grating are shown in Fig. 6. The structure contains an $In_{0.2}Ga_{0.8}As$ QW as an active layer, a GaAs etch stop layer. In the first prototype DBR laser using a third-order DBR grating without QW disordering, a stable single-mode oscillation at around 970nm wavelength was obtained with 14.5mA threshold and 32.5mW maximum CW output power.

4.2. Performance improvements

The performances of the DBR laser were improved by use of a first-order DBR grating, enhancement of the DBR reflectivity through loss reduction by area-selective QW disordering, optimization of the output facet reflectivity by low-reflection (LR) coating, and forming a transparent window structure near

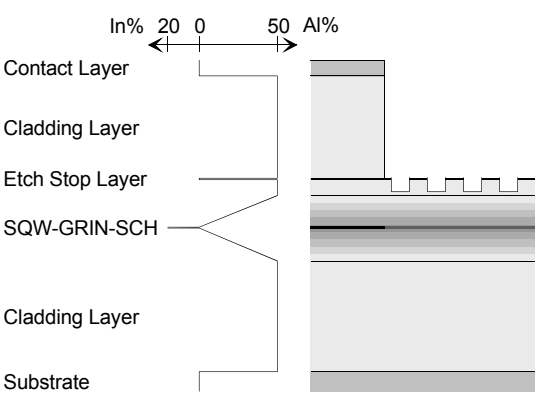

Fig.6. Cross section of the SQW-GRIN-SCH waveguide and grating structure.

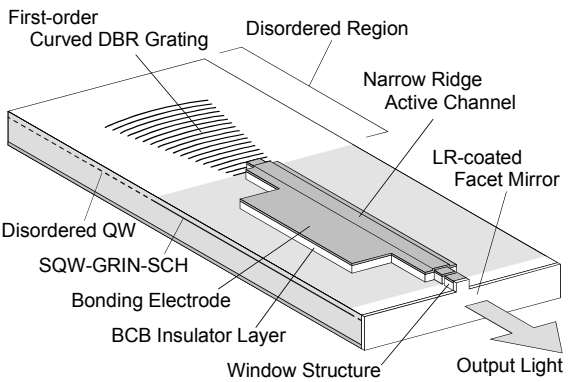

Fig.7. Configuration of the improved DBR laser using curved surface DBR grating with QW disordering in the grating and output window regions.

the output facet by area-selective QW disordering to enhance the catastrophic optical damage (COD) threshold level [16,17]. The improved device configuration is shown in Fig.7.

The improved curved-DBR lasers were fabricated using the strained-layer SQW-GRIN-SCH epitaxial structure as shown in Fig.6. Selective area QW disordering was performed by rapid thermal annealing (RTA) using SiO_2 caps

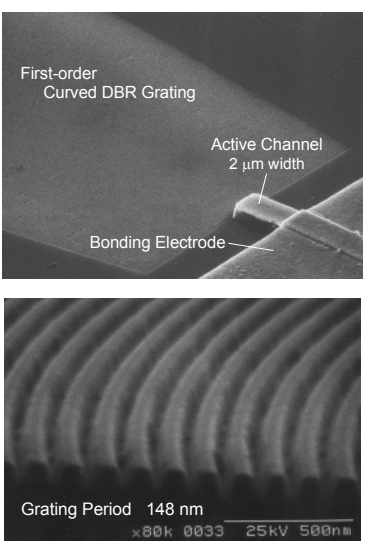

Fig.8. SEM microphotographs of the fabricated DBR laser: perspective view and enlarged view of curved grating.

of different thicknesses [6,7]. SiO_2 caps of 300nm and 30nm thickness were deposited by plasma chemical vapor deposition (CVD) for the disordering and suppressing caps, respectively. Then RTA was performed at 860 °C for 60 s and the both SiO_2 caps were removed by buffer etching. After the evaporation of a Cr/Au *p*-electrode, the ridge structure was formed by reactive ion etching (RIE) in CH_4/H_2 gas using the electrode as a mask. The etch depth was accurately controlled by in-situ monitoring with a semiconductor laser probe using the etch-stop layer as a reference layer. The first-order curved DBR grating was fabricated by electron beam (EB) writing and two-step RIE. A thin SiO_2 layer was deposited and an EB resist was spin-coated. The DBR grating pattern (200μm interaction length) with a 148nm grating period was written by curved scanning of the EB. The pattern was transferred to the SiO_2 layer by the first RIE in CF_4/H_2 gas and then transferred into the semiconductor layer to a depth of 70nm by the second RIE in CH_4/H_2 gas. The reflectivity and the wavelength bandwidth of the DBR grating were estimated as 96% and 1.6nm, respectively. A benzocyclobutene (BCB) layer for electrical insulation was spin-coated. The planarized surface of the BCB layer was etched by RIE with CF_4/O_2 gas to open a self-aligned contact window. Following bonding electrode deposition, the BCB layer on the DBR grating region was removed by RIE to avoid a decrease of the reflectivity. After the wafer was thinned to 100μm, an Au-Ge/Au *n*-electrode was evaporated on the backside. A facet mirror was formed by cleaving, and an Al_2O_3 LR layer with a thickness of 170nm was evaporated on the cleaved facet to obtain 5% reflectivity. The device was soldered on a Cu heatsink. SEM microphotographs of the fabricated curved-DBR laser are shown in Fig. 8.

Figure 9 shows a measured lasing spectrum. Single-mode lasing with a side-mode suppression ratio (SMSR) as high as 52dB was obtained. Figure 10

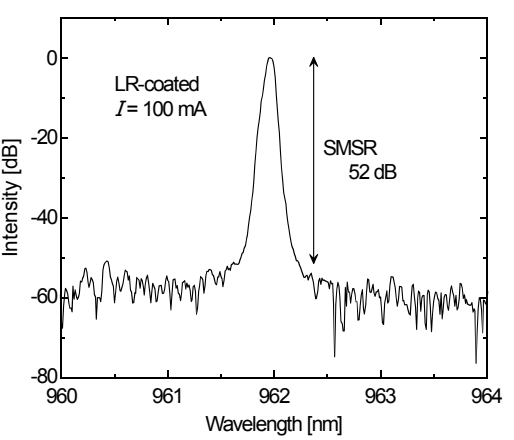

Fig.9. Measured lasing spectrum of the DBR laser with LR-coated output facet.

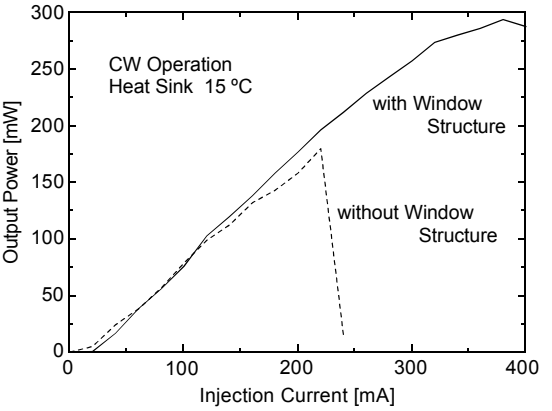

Fig.10. Dependence of output power on injection current of DBR lasers with and without output window structure.

compares the output powers dependent on the injection current of the DBR lasers with and without the window structure. Whereas the maximum output of the lasers without the window structure was limited by the COD below 200mW, maximum output power of 294mW was obtained in the DBR laser with window structure.

The high-efficiency, high-power, low-noise, stable single-mode operation of the improved lasers allows various applications in optical communications, signal processing and sensing, including uses as a pumping source for fiber optical amplifiers and waveguide nonlinear-optic devices.

4.3. Squeezed light generation

We demonstrated squeezed light generation by the high-efficiency InGaAs QW DBR laser [18]. Figure 11 shows the dependence of the output power and

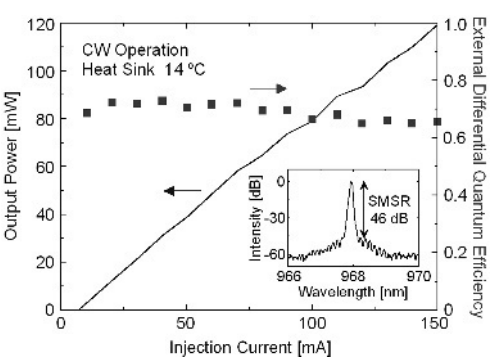

Fig.11. Dependence of the output power and the external differential quantum efficiency on the injection current.

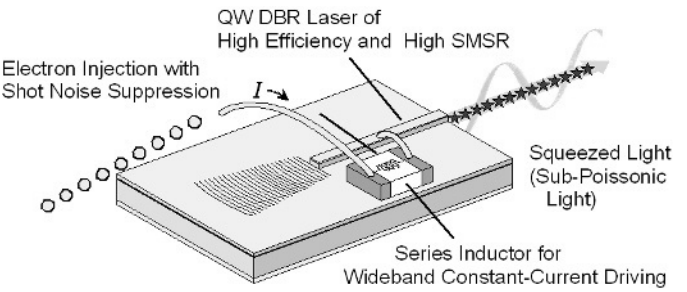

Fig.12. Generation of squeezed light by wide-range constant current driving.

the external differential quantum efficiency on the injection current of the DBR laser fabricated and used for this purpose. The threshold current was 7mA, and the maximum output power of 120mW was obtained. The differential quantum efficiency was as high as 0.71, and the quantum efficiency was 0.63 at 80mA injection. Single-mode 968nm lasing with SMSR of 50dB was obtained. The laser was driven by a constant current source with a series inductor (1.5mH) for constant-current driving over a wide radio frequency (RF) range required for pump noise suppression, as shown in Fig.12. The quantum intensity noise relative to the standard quantum limit (SQL) was measured by the balanced detection technique using a beam splitter, two Si-PIN photodiodes, low-noise preamplifiers an RF switch and an RF spectrum analyzer. The result of the measurement at 80mA injection is shown in Fig.13, which indicates that the noise level is 0.5dB below the SQL level. Compensating for the overall quantum efficiency of the detection system 0.57, the result shows that the laser generated squeezed light (sub-Poissonic light) with an ultralow noise level of 0.8dB below the SQL level. This is the first demonstration of generation of single-mode squeezed light by a monolithic semiconductor laser at room temperature.

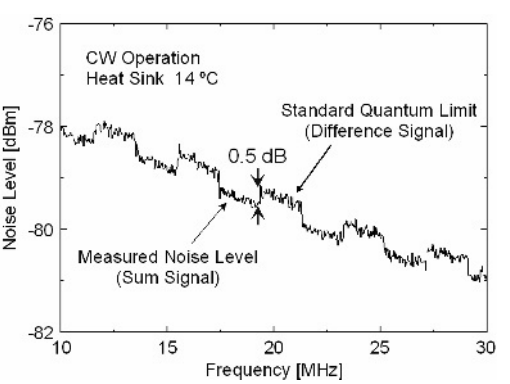

Fig.13. Noise spectrum relative to SQL measured by balanced detection technique.

4.4. GaInP/AlGaInP QW DBR laser emitting red light

There are many potential applications of integrated optics, e.g., implementation of integrated optical disk pickup head and integrated biosensing devices, that require expansion of the lasing wavelength to shorter visible region. For such applications, we are developing GaInP/AlGaInP QW DBR lasers emitting coherent red light [19]. The device configuration is same as that shown in Fig.5.

The DBR laser was fabricated by using a GaInP/AlGaInP MQW SCH structure. At first, area-selective QW disordering was performed by within the grating region by Zn diffusion [20]. A 10nm thick ZnO film was deposited on the grating region by RF sputtering and photolithoghraphic patterning, and then a surface-protecting SiO_2 cap layer of 100nm thickness was deposited over the entire surface. Then Zn was indiffused by thermal annealying at 600°C for 40min in N_2 atmosphere. The preliminary photoluminescence measurement showed that this process gave rise to substantial QW disordering. The follwing process is very similar to that presented in the previous sections. An active channel of 800μm length and 2μm width, and a DBR grating of third order of 294nm period and 300μm interaction length were formed by EB writing and RIE. Then the ridge was buried with BCB and the electrodes were formed. The laser performances were examined under pulse operation. Single-mode lasing at 656nm was obtained. The threshold current was 18mA, and a maximum peak output power of 44mW was obtained at 120mA injection.

5. MONOLITHIC MOPA WITH INTEGRATED OUTCOUPLER

High-power semiconductor lasers which emit a highly-coherent diffraction-limited output beam are required for many applications, such as free-space communications, pumping of fiber amplifiers and nonlinear-optic devices. Several laser device configurations have been developed to broaden the gain region for high power without spoiling the beam quality. They include

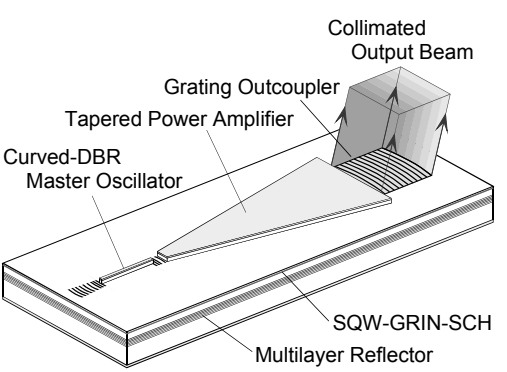

Fig.14. Monolithic integrated master oscillator power amplifier with a grating coupler.

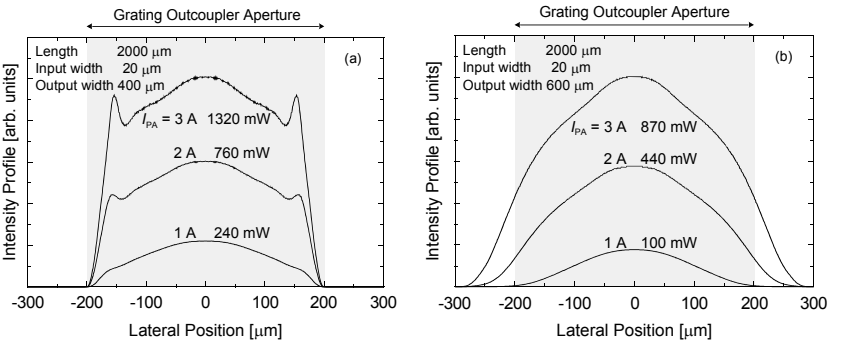

Fig.15. Lateral intensity profiles at the PA output end calculated by the BPM simulation.

monolithic master oscillator power amplifier (MOPA) lasers [21-24]. The output wave from edge-emitting MOPA lasers, however, is astigmatically divergent, and a composite external lens system is required for beam collimation or focusing. We proposed and demonstrated monolithically integrated MOPA with an integrated grating coupler [25-27]. Various beam-forming functions, such as collimating, focusing into a spot or a spot array [28] can be realized. The device has advantages of high power, diffraction-limited output beam, high coherence, and compact and stable lensless module implementation.

5.1. Device description and design

The device is constructed with a DBR master oscillator (MO), a tapered power amplifier (PA) and a curved grating coupler (GC), as shown in Fig.14. The output from the MO is amplified and broadened in the tapered PA. Then the GC couples the amplified wave out of the waveguide as a collimated beam. Various beam-forming functions and/or correction of wavefront distortion caused in the PA can be incorporated by appropriate design of the GC.

The integrated MOPA was fabricated by using an InGaAs SQW GRIN-SCH structure similar to that shown in Fig.6, but a 10-period GaAs-AlAs multilayer

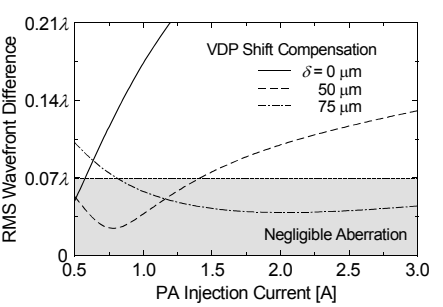

Fig.16. Dependence of the RMS wavefront difference on the PA injection current.

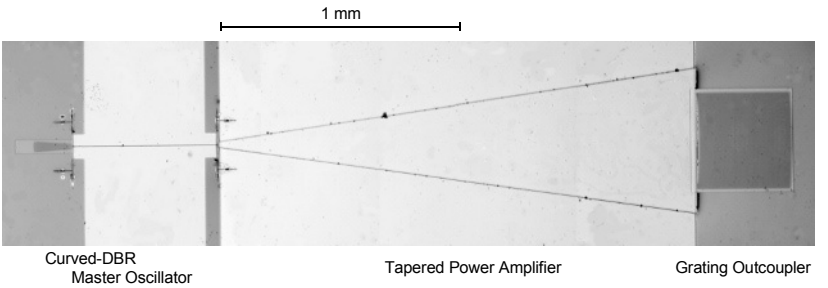

Fig.17. Top view of the fabricated monolithic MOPA with integrated grating outcoupler.

reflector was inserted below the lower cladding to enhance the output coupling efficiency of the grating coupler. A DBR laser similar to that described in the previous section was used as a MO. The width and length of the ridge were designed as 2.0μm and 600μm, respectively. The full angle of beam divergence in the PA from the channel is 6.6°. The wide divergence angle is advantageous to reduce gain saturation in the PA. The Bragg wavelength was slightly detuned to 985nm longer than the wavelength of gain maximum to reduce the absorption loss. The length of the rear DBR was 160μm to provide high reflectivity, and that of the front DBR was 10μm to obtain a semitransparent reflector.

To design the tapered PA, simulation was performed based on the beam propagation method (BPM) by taking nonuniform gain saturation, temperature and mode-index distributions into account [29]. The simulations were performed for various electrode configurations and working conditions, and the PA output powers, intensity profiles and wavefronts were calculated. Figure 15 shows the calculated lateral intensity profiles at the PA output end. The full width of the PA output wave is expanded by the nonuniform gain saturation and is wider than 300μm, while the width corresponding to the divergence of the

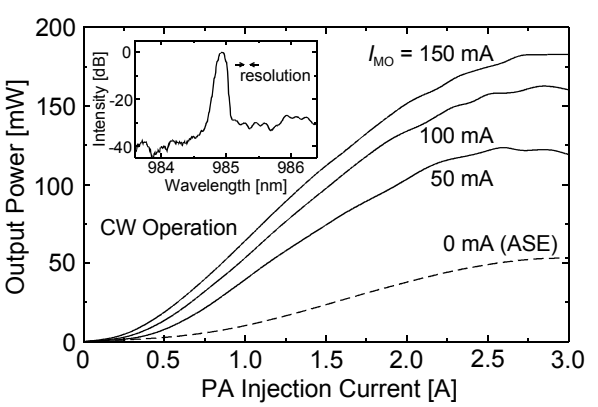

Fig.18. Dependence of the outcoupled power on the PA injection current.

beam from the MO is about 230μm. To obtain both high PA output power and minimum wavefront distortion, the length, input and output widths of the tapered PA were determined as 2000μm, 20μm and 600μm, respectively. Figure 15(b) shows the simulation results for the optimized PA electrode. The simulation predicts that a PA output of 440-870mW is obtained for a 10mW incident power and a 2-3A PA injection current.

The PA output wavefront deformed by the propagation and amplification in the PA can be approximated by a two-dimensional (2D) spherical wave diverging from a virtual divergence point (VDP). The simulation showed that the ray in the PA is slightly refracted toward the light axis. As a result of the thermal lens effect, the VDP is shifted from the front end of the MO active channel toward the back end with increasing PA injection. By designing the GC with compensation for an appropriate VDP shift δ, a well-collimated output can be expected even for high PA injection. In order to determine δ, the power-weighted RMS wavefront difference $\Delta\Phi_{RMS}(\delta)$ between the calculated PA output wave and the 2D spherical wave diverging from the point corresponding to the shift δ was calculated. Figure 16 shows the dependence of $\Delta\Phi_{RMS}(\delta)$ on the PA injection current with δ as a parameter. The result shows that the wavefront distortion for a 2-3A PA injection can be well compensated ($|\{\Delta\Phi_{RMS}(\delta)/2\pi\}\lambda|<0.07\lambda$ (Maréchal criterion)) by designing the GC focal length to be the distance between the GC and the VDP shifted by δ=75μm to match with the VDP of the PA output wavefront. The collimator GC using a curved surface grating of a $400\times400\mu m^2$ aperture in the GRIN-SCH waveguide with a multilayer reflector was designed. The grating pattern is given by Eq. (2) with $f\rightarrow\infty$ and r including the VDP shift δ. For simple fabrication, simultaneous etching of DBR and GC gratings was assumed, and the duty ratio of the GC was taken as a parameter.

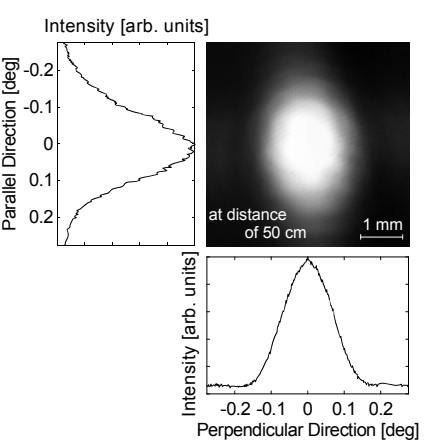

Fig.19. Far-field pattern and the intensity profile of the output beam.

The radiation decay factor α_{rad} for the GC groove depth was calculated. As a result of optimization to minimize the divergence angle of the output beam parallel as well as perpendicular to the exit plane, the groove depth and the duty cycle were determined as 90nm and 0.75, respectively. Then α_{rad} and the directionality into air P_{air} (the fraction of the power radiated into air to the total radiation power) were calculated as 50cm^{-1} and 96%, respectively.

5.2. Fabrication and experimental results

At first, *p*-electrodes for the MO active channel and the tapered PA were formed. After writing the electrode patterns in an EB resist, Cr-Au were evaporated and lifted off. The ridge structures were formed by RIE using H_2/CH_4 gas and the electrodes as masks. The etch depth was accurately controlled by in-situ monitoring with a laser probe using the etch stop layer as a reference layer. The grating patterns of the DBR and the GC gratings were written simultaneously by EB writing. Then they were transferred to the remaining upper cladding layer by reactive ion beam etching (RIBE). An SiO_2 insulation layer was deposited by PCVD, and contact windows were opened. Following bonding electrode formation, the SiO_2 layer on the DBR grating and the GC was removed to avoid the reduction of reflectivity and coupling efficiency. After the wafer was thinned to 100μm, an *n*-electrode was evaporated on the backside and the device was soldered on a heat sink. The top view is shown in Fig.17. The MOPA performances were measured under CW operation at room temperature. The dependence of the power outcoupled by the GC on the PA injection current is shown in Fig.18. The inset shows the spectrum at I_{MO}=100mA and I_{PA}=1.0A. Stable single-mode lasing up to 183mW with a side mode suppression ratio of about 25 dB was obtained.

The near-field pattern of the output wave on the GC and the intensity profiles were observed. The evolution of the lateral intensity profile with

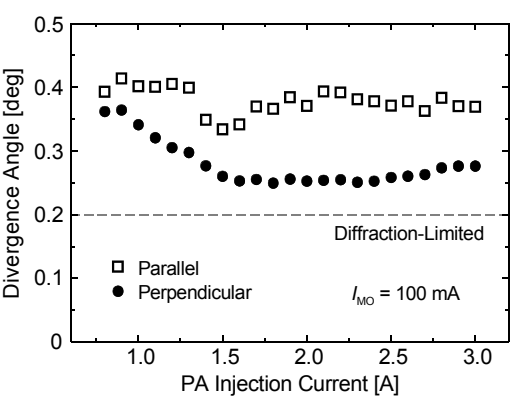

Fig.20. Dependence of divergence angles of output beam on PA injection current.

increasing injection was consistent with the simulation result. For the GC aperture length of 400μm and the directionality into air of 0.96, the coupling efficiency into air was estimated as 52%. The total power at the PA output end was estimated as 390mW. The reason for discrepancy between the predicted and experimental results would be deterioration of the PA gain due to insufficient heat sinking. As a result of the VDP shift compensation and the radiation factor optimization, a well-collimated output beam with a nearly circular profile was obtained. Figure 19 shows the far-field pattern and the intensity profiles. The divergence angles of 0.26°(perpendicular to the exit plane)×0.33°(parallel), close to the theoretical values of 0.20°×0.20°, were obtained at I_{MO}=100mA and I_{PA}=1.5A. The dependence of the divergence angles of the output beam on the PA injection current is shown in Fig.20. The collimated output beam with small divergence angles was maintained for larger PA injection. Output power and collimation can be improved by more effective heat sinking and reduction of absorption loss in the grating region through selective QW disordering.

6. TUNABLE EXTENDED-CAVITY LASER

6.1. Device description and design

We proposed and demonstrated a high-power tunable extended-cavity laser using an integrated tapered amplifier (TA) and curved grating coupler (GC) as shown in Fig.21 [30, 31]. The GC serves as a collimator for the output beam, and simultaneously enables wavelength tuning by device rotation through the wavelength dispersion. The laser cavity consists of a facet mirror, a narrow active channel, a tapered amplifier (TA), a curved grating coupler (GC), and an external half mirror (HM). The narrow-ridge channel is incorporated to ensure lateral single-mode lasing. The curved GC couples a 2D spherical guided wave amplified in the TA into air as a collimated beam, and a collimated output beam

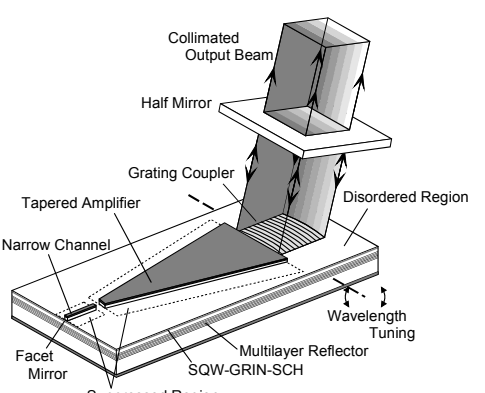

Fig.21. Tunable extended-cavity laser using tapered amplifier and grating coupler.

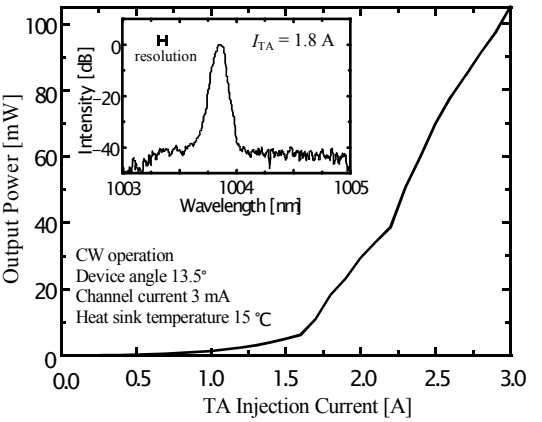

Fig.22. Dependence of the output power on TA injection current.

is obtained through the HM. Due to the wavelength dispersion of the GC, the beam exit angle depends on the wavelength. Therefore, the lasing wavelength can be tuned by rotating the semiconductor device with respect to the HM.

The lasing wavelength λ is determined by the grating coupling condition: $\sin\theta = N - \lambda/\Lambda$, where N is the mode index, Λ the grating period, and θ is the tilt angle of the waveguide device with respect to the HM (the beam exit angle at the GC). The input coupling efficiency exhibits sharp wavelength selectivity due to the discreteness of the guided mode. The wavelength bandwidth estimated for an aperture L=400μm is 0.3nm. Such sharp wavelength selectivity assures precise wavelength tuning. The tuning range is not limited by the

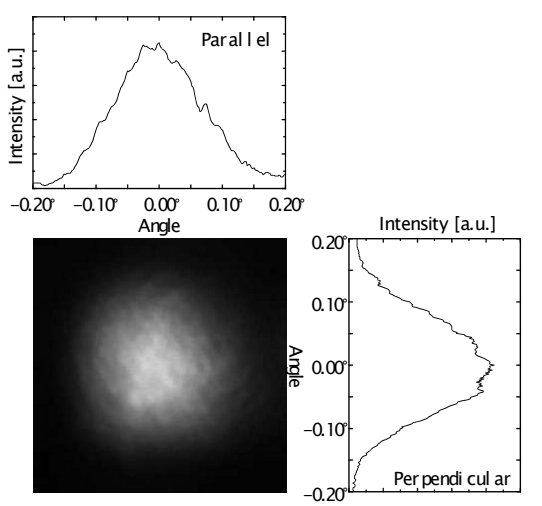

Fig.23. Far field pattern and the intensity profile of the output beam.

wavelength selectivity but is determined by the gain bandwidth of the amplifier.

The width and length of the active channel were designed as 2.0μm and 300μm, respectively. The channel supports single lateral mode, and the $1/e^2$ full angle of divergence in the TA from the channel is 6.6°. The TA was designed by the same method as described in the previous section. The widths of the narrow and wide ends were 20μm and 600μm, and the length as 2000μm. The BPM simulation of the amplifier performances suggests that maximum output power of several hundred mW is feasible. The channel and the TA are separated by a 10μm gap, which was inserted to enable independent control of injection currents. The GC pattern was designed to incorporate aberration correction for a TA injection current of 2.5~3A.

Loss reduction by the selective QW disordering was considered. A GC with a $400\times400\mu m^2$ aperture was designed for coupling of the guided wave at a wavelength of 995nm into air as a collimated beam at an exit angle θ_0=15°. The groove depth was determined as 60nm to have a radiation decay factor optimized for good output beam collimation and high coupling efficiency. The calculated radiation decay factor and the directionality into air of the GC with the multilayer reflector were $61cm^{-1}$ and 92%, respectively. For passive waveguide loss α_p of $3cm^{-1}$ (disordered) and $40cm^{-1}$ (undisordered), the effective GC aperture L_{eff} was calculated as 310μm and 200μm, respectively, and the output coupling efficiency η_{out} as 81% and 55%. This estimation shows that the loss reduction by the selective QW disordering results in large expansion of L_{eff} and significant increase of η_{out}.

6.2. Fabrication and experimental results

Selective QW disordering was performed through RTA at 920ºC for 15s. After deposition of *p*-electrodes for the channel and the TA, the ridge structure was formed by RIE. The GC (330nm period) with a depth of 60nm was

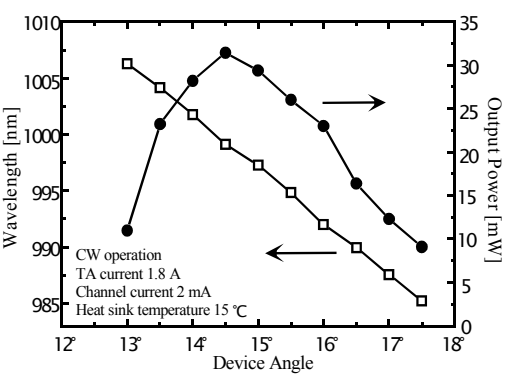

Fig.24. Dependence of lasing wavelength and output power on the device angle.

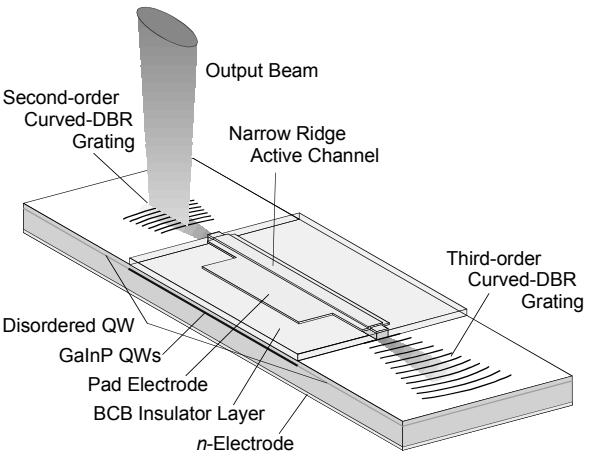

Fig.25. Grating-coupled surface-emitting DBR laser.

fabricated by EB writing and two-step RIE. After formation of *n*-electrode and cleaving for facet formation, the device was soldered on a heat sink.

The device was mounted on a rotary stage, and a HM with 50% reflectivity was aligned at a distance of 10 mm from the GC. Figure 22 shows the dependence of the output power through the HM on the TA injection current I_{TA}, measured for CW lasing at an exit angle θ of 13.5° with injection into the channel I_{ch} of 3mA. The lasing threshold was I_{TA} ~1.5A, and the maximum output power of 105mW was obtained at I_{TA}=3A. It was demonstrated that the loss reduction by the disordering contributed to enhancement of the output power. The inset of Fig.22 shows the measured lasing spectrum. The 3dB full width was within the resolution (0.08nm) of the measurement.

Figure 23 shows the far-field pattern and the intensity profiles of the output beam observed at a distance of 40cm from the device. The full divergenceangles at half maximum were 0.16° (parallel to the exit plane)×0.18° (perpendicular), while the diffraction-limited values are 0.13°×0.14°. Wavelength tuning characteristics were examined by rotating the device. Figure 24 shows the dependence of the lasing wavelength and the output power on the device angle θ for I_{TA}=1.8A and I_{ch}=2mA. Quasi-continuous tuning over a range of 21.1nm (985.2 -1006.3nm) was obtained. The single-peak spectrum (<0.08nm width) was observed in the whole tuning range.

7. GRATING-COUPLED SURFACE-EMITTING LASER

Figure 25 shows a GaInP/AlGaInP QW grating-coupled surface-emitting DBR laser [32]. The laser consists of a narrow ridge active channel, and second- and third-order curved DBR gratings. Surface emission is obtained from the second-

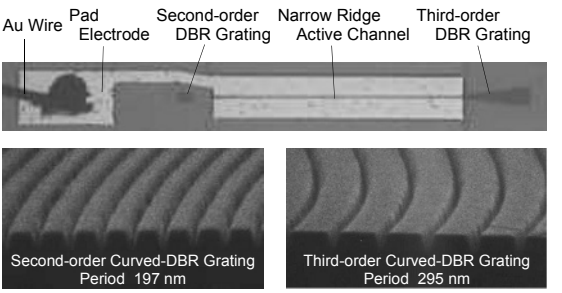

Fig.26. Fabricated surface-emitting DBR laser and SEM microphotographs of curved DBR gratings.

order DBR grating. The DBR gratings were designed for lasing oscillation at a wavelength of 655nm. The second-order DBR grating provides feedback by second-order Bragg reflection and surface emission into air by first-order diffraction. By appropriate design of the grating, the diverging angle of the emitted light can be controlled. To obtain the beam spot of a 50μm width at a distance of 150μm from the laser, the DBR length and the active channel to DBR grating distance were determined as 50μm and 50μm, respectively. To obtain a high reflectivity and a high coupling efficiency into air, the grating depth and duty ratio were determined as 120nm and 0.7, respectively. The reflectivity and coupling efficiency into air were calculated as 35% and 13%, respectively. The third-order DBR grating was designed, and the reflectivity for a 200μm DBR length was estimated as 67%.

The surface-emitting DBR laser was fabricated using a GaInP/AlGaInP MQW SCH structure. To reduce the absorption loss in the passive region, area-selective QW disordering was performed by ZnO deposition and thermal annealing [20]. After the fabrication of an 800μm long, 2μm wide *p*-electrode, a ridge structure was formed by RIE using the electrode as a mask. The curved

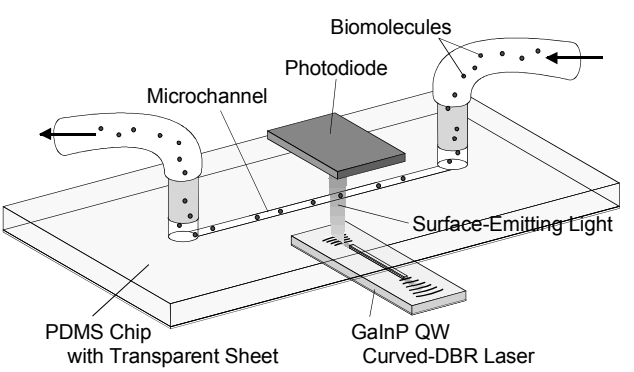

Fig.27. Schematic of microfluidic bioparticle sensing using surface-emitting DBR laser.

DBR gratings were fabricated simultaneously by EB writing and two-step RIE. A bonding pad electrode was formed using a BCB layer as an insulator. After thinning the wafer to 120μm, an *n*-electrode was evaporated on the backside. Figure 26 shows the fabricated laser and SEM micrographs of the curved DBR gratings.

The laser oscillated with a threshold of 28mA. A maximum CW output power emitted from the second-order DBR grating was 1.4mW at 100mA injection. Single-mode lasing at 654.4nm wavelength with 35.5dB SMSR was obtained.

A preliminary experiment for biosensing application was performed by combining the laser with a microfluidic structure and a Si photodiode as shown in Fig. 27. A microfluidic structure with a channel of 57μm width and 23μm height was fabricated by photolithographic molding of PDMS, and was covered by a 60μm thick transparent sheet. The beam spot at the channel was of an elliptical shape with a size of 60μm (⊥ channel)×20μm(//). A test was done by flowing polystyrene black-dyed microspheres of 6μm diameter in 0.25% aqueous suspension through the channel. Each microsphere was detected well as the reduction of the photocurrent.

8. CONCLUSION

Implementations of various semiconductor integrated photonic devices based upon the area-selective QW disordering technique and the EB lithograph fabrication of waveguide grating elements were reviewed. The effectiveness of the QW disordering technique for reducing the passive waveguide losses and enhancing the performances, as well as the versatility of the waveguide gratings as wavelength-selective feedback, wavelength dispersion and wavefront conversion elements were demonstrated. Research and development work is being continued to improve the performances and extend the wavelength range and applications including biosensing.

REFERENCES

[1] T.Suhara, Semiconductor Laser Fundamentals, Marcel Dekker, New York, 2004.
[2] T.Suhara, M.Uemukai, N.Shimada and A.Larsson, Proc. SPIE, 4995 (2003) 10.
[3] E.H.Li, ed., Semiconductor quantum wells intermixing, Gordon and breach science publishers, 2000.
[4] E.S.Koteles, B.Elman, P.Melman, J.Y.Chi and C.A.Armiento, Opt. Quantum Electron., 23 (1991) S779.
[5] S.Burkner, M.Maier, E.C.Larkins, W.Rothemund, E.P.O'Reilly and J.D.Ralston, J. Electron. Mater., 24 (1995) 805.
[6] N.Shimada, Y.Fukumoto, M.Uemukai, T.Suhara, H.Nishihara and A.Larsson, Jpn. J. Appl. Phys., 39, Pt.1 (2000) 5914.

[7] N.Shimada, Y.Fukumoto, M.Uemukai, T.Suhara, H.Nishihara and A.Larsson, IEEE J. Selected Topics Quantum Electron., **7** (2001) 350.
[8] T.Suhara and H.Nishihara, IEEE J. Quantum Electron., 22 (1986) 845.
[9] H.Nishihara, M.Haruna and T.Suhara, Optical Integrated Circuits, McGraw-Hill, New York, 1989.
[10] T.Suhara, T.Taniguchi, M.Uemukai, H.Nishihara, T.Hirata, S.Iio and M. Suehiro, IEEE Photon. Tech. Lett., 7 (1995) 1195.
[11] T.Suhara, T.Taniguchi, M.Uemukai, A.Yoshimoto, H.Nishihara, T.Hirata, S.Iio and M.Suehiro, Jpn. J. Appl. Phys., 35, Pt.1 (1996) 369.
[12] M.Uemukai, A.Yoshimoto, N.Matsumoto, T.Suhara, H.Nishihara, N.Eriksson and A.Larsson, Electron. Lett., 33 (1997) 1464.
[13] T.Suhara, K.Okada, T.Saso and H.Nishihara, IEEE Photon. Tech. Lett., 4 (1992) 903.
[14] T.Kjellberg, M.Hagberg and A.Larsson, IEEE Photon. Tech. Lett., 5 (1993) 1149.
[15] N.Eriksson, M.Hagberg and A.Larsson, IEEE J. Quantum Electron., 32 (1996) 1038.
[16] M.Uemukai, K.Kitano, N.Shimada and T.Suhara, Jpn. J. Appl. Phys., 43, 8B (2004) 5918.
[17] M.Uemukai, S.Nozu and T.Suhara, Trans. IEICEJ, J89-C (2006) ****.
[18] M.Uemukai, S.Nozu and T.Suhara, IEEE J. Selected Topics Quantum Electron., 11 (2005) 1143.
[19] K.Hamana, P.K.Das, O.Omachi, N.Shimada, M.Uemukai and T.Suhara, Jnp. J. Appl. Phys., 43 (2004) 642.
[20] S.Arimoto, M.Yasuda, A.Shima, K.Kadoiwa, T.Kamizato, H.Watanabe, E.Omura, M.Aiga, K.Ikeda and S.Mitshi, IEEE J. Quantum Electron., 29 (1993) 1874.
[21] S.O'Brien, D.F.Welch, R.A.Parke, D.Mehuys, K.Dzurko, R.J.Lang, R.Waarts and D.Scrifes, IEEE J. Quantum Electron., 29 (1993) 2052.
[22] J.S.Osinski, K.M.Dzurko, J.S.Major Jr., R.A.Parke and D.F.Welch, IEEE Photon. Tech. Lett., 6 (1994) 885.
[23] J.S.Osinski, D.Mehuys, D.F.Welch, K.M.Dzurko and R.J.Rang, IEEE Photon. Tech. Lett., 6 (1994) 1085.
[24] S.O'Brien, R.Lang, R.Parke, J.Major, D.F.Welch and D.Mehuys, IEEE Photon. Tech. Lett. 9 (1997) 440.
[25] T.Suhara, M.Uemukai, A.Yoshimoto, N.Matsumoto, H.Nishihara, S.Iio, M.Suehiro and M.Wada, Electron. Lett., 33 (1997) 1228.
[26] M.Uemukai, N.Matsumoto, T.Suhara, H.Nishihara, N.Eriksson and A.Larsson, IEEE Photon. Tech. Lett., 10 (1998) 1097.
[27] M.Uemukai, M.Miyata, N.Shimada, T.Suhara, H.Nishihara, N.Eriksson, P.Modh and A.Larsson, Jpn. J. Appl. Phys., 39, Pt.1 (2000) 1503.
[28] M.Li, J.Bengtsson, M.Hagberg, A.Larsson, T.Suhara and H.Nishihara, IEEE J.Selected Topics Quantum Electron., 2 (1996) 226.
[29] R.J.Lang, A.Hardy, R.Parke, D.Mehuys, S.O'Brien, J.Major and D.W.Welch, IEEE J. Quantum Electron., 29 (1993) 2044.
[30] M.Uemukai, T.Suhara, K.Yutani, N.Shimada, Y.Fukumoto, H.Nishihara and A.Larsson, IEEE Photon. Tech. Lett., 12 (2000) 1607.
[31] N.Shimada, K.Yutani, M.Uemukai, T.Suhara and A.Larsson, IEICE Trans., E85-C (2002) 79.
[32] M.Uemukai, H.Miyamoto, Y.Yamada, Y.D.Sharma and T.Suhara, Jpn. J. Appl. Phys., 45 (2006) 6738.

This page intentionally left blank

Handai Nanophotonics, Volume 3
H. Masuhara, S. Kawata and F. Tokunaga (Editors)

Chapter 27

Process control and new developments in crystal growth from solution: oxide, organic, protein and nitride

Y. Mori[1-3], Y. Takahashi[1], F. Kawamura[1], H. Adachi[1-3], M. Yoshimura[1], Y. Kitaoka[1], and T. Sasaki[1,2].

[1]Graduate School of Eng., Osaka University, Japan

[2]SOSHO Inc., Japan

[3]CREST JST, Japan

1. INTRODUCTION

High quality bulk crystals are required in the areas of semiconductors and lasers in order to develop devices and equipment with enhanced performance. Crystal quality generally determines the quality level of devices and equipment. Technological advances are important for growing high quality crystals with fewer defects and dislocations. Technologies were developed to improve the quality of Ge bulk crystals in early work, and subsequently the quality of Si, GaAs, *etc*. for semiconductors and oxide crystals of ruby, YAG, sapphire, *etc*. for lasers. Among these, the quality of Si single crystals grown from a melt using the Czochralski method has been most successfully improved. Silicon is considered to be a highest-quality crystal, since it is composed of a single element and the crystal can be grown from a melt. However, development of new technologies has been recently required to upgrade the quality of crystals that are composed of materials with more complicated structures and therefore not grown from a melt. The flux method becomes necessary for crystal growth when structure molecules composed of many elements are too large to convert to a melt state. Researchers have attempted various methods of crystal growth by changing the experiment parameters, such as the flux and crystal-growing conditions. They often determine such parameters based on their empirical knowledge of each material. There is a common theory in the methodology of growing crystals.

The authors have studied nonlinear optical (NLO) crystal growth using the flux method and succeeded in developing $CsLiB_6O_{10}$ crystals in 1993. We have also engaged in crystallization of organic materials, such as DAST crystals. Moreover, we began to develop protein crystallization techniques in our laboratory in an attempt to grow crystals of materials with larger molecules. We succeeded in developing novel techniques, such as the solution-stirring technique and the laser-irradiated growth technique. We are also developing a liquid-phase epitaxy method for growing large high-quality GaN crystals from Na flux as our research activity to advance crystal-growing techniques for semiconductor materials. From these studies, we have learned that controlling the nucleation and growth processes are important for growing high-quality, large crystals of oxide, nitride, or protein from solution. So we must understand to what extent the solution can be controlled. This is a universal principle that is applicable for the various materials, such as oxide, protein and nitride. We introduce the specifications of the methods to grow the relevant crystals in this report and discuss the common principles.

2. GROWTH OF HIGH QUALITY $CSLIB_6O_{10}$ CRYSTAL

The high photon energy and short wavelengths of coherent ultraviolet (UV) light play important roles in various industrial and medical applications. Corrosive gas-based excimer lasers are now utilized as UV light sources despite their high-voltage gaseous discharges, regular maintenance requirements, and bulky dimensions. In contrast, solid-state lasers potentially have longer lifetimes and lower operating costs than conventional excimer lasers. The lasing frequency in the infrared region is readily converted to a UV frequency with nonlinear optical (NLO) crystals. For example, high-repetition-rate, high-power UV light at 355 nm or 266 nm can be generated from Nd-doped solid-state lasers. This radiation is ideal for laser cutting, hole drilling, and rapid prototyping. Narrowband, high-repetition-rate deep UV (DUV) light below 200 nm can also be obtained by using solid-state lasers and several sum-frequency mixing processes. This radiation is suitable for micro-lithographic applications and refractive eye surgery. The major challenge in fabricating a solid-state UV laser system lies in the ability and reliability of the NLO crystals. Borate crystals are often employed for high-power UV generation because of their relatively high tolerance to laser-induced damage, large optical nonlinear coefficients, and greater transparency in the UV region. Several crystals, such as β-BaB_2O_4 (BBO), LiB_3O_5 (LBO), and $CsLiB_6O_{10}$ (CLBO) [1-4], are commercially available for reliable all-solid-state UV laser systems. Other borate crystals, such as CsB_3O_5 (CBO), $KBe_2BO_3F_2$ (KBBF), $Sr_2Be_2BO_7$ (SBBO), $Gd_xY_{1-x}Ca_4O(BO_3)_3$ (GdYCOB) [5], and $K_2Al_2B_2O_7$ (KAB) [6], are still under development due to difficulties with crystal growth, optical damage, low

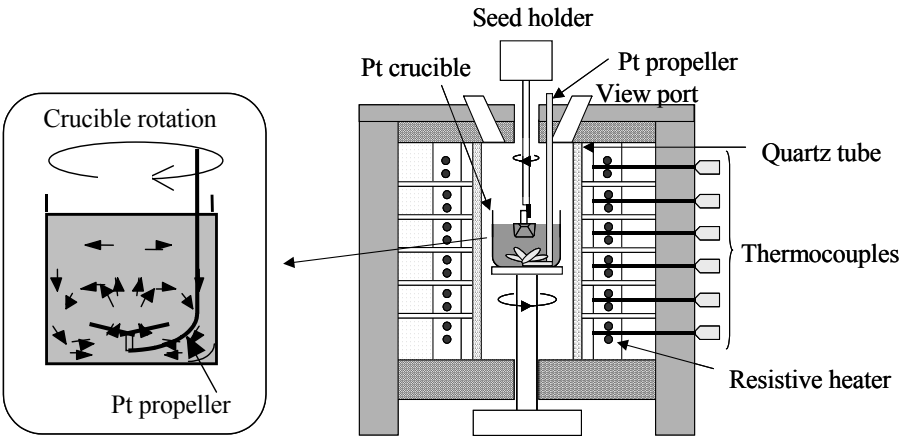

Fig. 1. Schematic of a newly developed, six-zone vertical furnace with a solution-stirring technique for top-seeded solution growth.

birefringence, or poor optical nonlinearity. Becker prepared a review of these borate crystals in 1998 [7]. Dmitriev *et al.* compiled comprehensive references for these materials in a handbook [8]. Here we focus on CLBO and discuss the crystal growth, and recent progress in UV light generation.

In general, thermal dephasing and laser-induced damage to NLO crystals are the primary limitations for development of high-power solid-state UV lasers. The bulk laser-induced damage threshold (LIDT) of conventional CLBO at a wavelength of 1064 nm is 29 GW/cm^2, greater than that of fused silica (25 GW/cm^2). However, the LIDT of CLBO at 266 nm is about 9 GW/cm^2, lower than that of fused silica (10.4 GW/cm^2) [9], despite the fact that both materials have insignificant photon absorption at 1064 nm and 266 nm. Some types of defects inside the optical materials are dominant factors for UV laser-induced damage, according to the general mechanism of laser-induced damages. Therefore, improving the crystallinity of CLBO crystals will presumably enhance the bulk LIDT.

CLBO crystals have been grown by the conventional TSSG method with a rotating seed crystal [4], as mentioned above. However, the high viscosity of the solution limits the mixing and mass transport in the solution, and makes it difficult to obtain uniform supersaturation and effective convection to the growth interfaces. These effects may cause crystal defects during growth and degrade laser-induced damage tolerance. Thus, we developed a new growth apparatus based on an effective solution-stirring technique that combines propeller and crucible rotation to thoroughly stir the solution, as shown in Fig. 1 [10]. CLBO crystals were grown under conditions of 30 sec spin-up time at 30

rpm and 30 sec spin-down time. The crucible inverted the rotation direction every 60 sec. Other conditions, such as the flux composition and cooling rate, were the same as the conventional method. CLBO with dimensions of 12 x 6 x 5 cm^3 was typically grown for 16 days.

We characterized the bulk LIDT, dislocation density, and self-heating by UV light absorption using CLBO samples cut from the center of a single crystal in the (001) direction with the (001) surfaces optically polished. The bulk LIDT was measured by using the fourth-harmonic of an Nd:YAG laser operating in a transverse and longitudinal single mode. The pulse widths of the 266 nm light were 0.75 ns. A lens with a focal length of 100 mm was used to focus the laser radiation inside the sample so that the focal point was located 5 mm below the (001) surface. The focal point was moved shot-by-shot (a 1-on-1 test). The formation of the bulk damage was identified by observation of a laser spark. Light scattering from a coaxial He-Ne laser beam was also employed as a real-time indication of laser-induced damage. The LIDT of conventional CLBO ranged from 8.8 to 10.4 GW/cm^2. In contrast, the LIDT of newly grown CLBO exceeded that of fused silica (10.4 GW/cm^2) and the conventional CLBO crystal. The average LIDT ranged from 15.0 to 20.0 GW/cm^2, and the highest in the sample was 25.4 GW/cm^2. This enhancement of the LIDT was reproducible for measurements conducted on several CLBO samples. Using these CLBO crystals we succeeded in generating a high-power UV beam of 42 W at 266 nm.

3. GROWTH OF HIGH QUALITY PROTEIN CRYSTALS

3.1. Forced nucleation of protein crystal by femto-second laser irradiation

The investigation of proteins has become increasingly important in biochemical and biomedical research. The structural information of proteins is useful for designing and developing novel drugs [11]. X-ray diffraction (XRD) provides important information regarding a three-dimensional molecular structure as well as for our understanding of the functions of particular compounds. Especially, over 60% of all commercial therapeutic drugs target membrane proteins. However, research on the structural characteristics of membrane proteins has been limited by difficulties in obtaining high-quality crystals. To date, there is no general method for obtaining high-quality membrane protein crystals. As a result, fewer than 50 integral membrane protein structures have been reported. In contrast, several thousand structures of soluble proteins have been determined using XRD analyses [12]. The solubility of membrane proteins is also an important consideration with respect to crystallization, and this feature is influenced to a large extent by the choice of detergent. In general, detergents are considered to be suitable for solubilization and crystallization, however, detergents are also known to dissolve membrane proteins during a certain period of time.

Protein crystals nucleate spontaneously in highly supersaturated solutions. To generate nucleation at an increased rate, extremely highly-supersaturated solutions can be used. In the supersaturated solutions, crystals grow at a very rapid rate, leading to poor crystallinity. Ideally, it would be useful if crystals could be grown in low supersaturated solutions to reduce the crystal growth rate. This is difficult to achieve using conventional methods. There is a clear need to develop a simple crystallization technique for membrane proteins that can be used to produce high-quality crystals. In a previous report, we described a novel technique for generating protein crystal nucleation using intense short-pulse laser irradiation. This method was called the laser irradiated growth technique (LIGHT) [13]. LIGHT enables us to shorten the crystallization period and results in the development of crystals that do not crystallize using conventional techniques. In our previous study, we confirmed the efficacy of LIGHT in the crystallization of soluble proteins. In this paper, we use LIGHT to facilitate nucleation and encourage the growth of high-quality membrane protein AcrB [14] crystals.

AcrB is a major multidrug efflux transporter in *Escherichia coli*. This protein is responsible for exporting various kinds of antibiotics, antiseptics, anti-cancerdrugs and cellular toxins from the cell. It is also a contributing factor to the multidrug resistance of *E. coli.* Multidrug resistance is an increasing problem in the treatment of bacterial infectious diseases and in cancer chemotherapy [15]. AcrB is composed of 1049 amino-acid residues that form twelve transmembrane α-helices and two large hydrophilic loops on the periplasmic surface. The crystaline structure of AcrB was determined at a resolution of 3.5 Å. Structural analyses have shown that three AcrB protomers are organized as a homo-trimer in the shape of a jellyfish [14]. This is the first crystal structure resolved at an atomic level for a multidrug efflux transporter, and also the first crystalline structure reported for a secondary transporter driven by proton motive force. The XRD analysis of AcrB crystals provides a structural basis for considering the molecular mechanism of multidrug export. Higher-resolution XRD data are, therefore, needed to gain a better understanding of molecular functions as well as to develop an antagonist. Trials have been carried out in order to optimize crystal growth conditions using conventional techniques.

The methods used to purify and prepare AcrB for crystallization are described in a previous report [14]. A protein solution [28 mg/ml histidine-tagged AcrB protein, 20mM sodium phosphate (pH6.2), 10% glycerol and 0.2% dodecylmaltoside] was mixed (1:1) with a reservoir solution [13-16% PEG 2000, 80mM sodium phosphate and 20mM sodium citrate-HCl (pH6.1)], and used for a 5 μl crystallization drop.

Trials using laser irradiation were conducted using a microscope at room temperature. A femtosecond laser was used to trigger nucleation. The

femtosecond laser system (Continuum, CPA 2002) was operated at a wavelength of 780 nm and a pulse width of 200 fs. The pulse repetition rate was set at 1 kHz. The laser beam was focused on the target for 1 s using the 10x objective lens in a protein drop at room temperature. The crystallization plates with and without laser irradiation were placed in an incubator at 298K.

AcrB crystals grew over a period of three to five days. The concentration of PEG 2000 was gradually increased from 13% to 16% in 1% increments to increase the supersaturation level of the protein solution. At a solution strength of more than 15% PEG 2000 (a highly supersaturated solution), extensive nucleation of AcrB crystals was observed [Fig. 2(a)]. These crystals grew rapidly, leading to the production of low-quality crystals and polycrystals unsuitable for XRD analysis. In contrast, nucleation occurred much less frequently at PEG 2000 solution strengths of less than 15%. AcrB crystals were obtained over the period of several days using LIGHT, even at much lower solution strengths (13% PEG 2000) [Fig. 2(b)]. In contrast, no AcrB crystallization was observed under the same conditions without laser irradiation. This technique was found to be useful for facilitating membrane protein crystallization.

High-quality XRD data were obtained from the AcrB crystals grown using LIGHT in a low-range supersaturated solution (13% PEG 2000). The data were collected on BL44XU at SPring-8 with an imaging-plate detector at cryogenic temperature (100 K). The crystal showed diffraction at a resolution of 2.3 Å. The crystal belongs to the space group R32 with cell dimensions of $a = b = 14.43$ nm and $c = 51.90$ nm in the hexagonal setting. The results reported here clearly demonstrate that LIGHT markedly improves crystallinity. The crystals of AcrB produced using conventional methods in a relatively low-range supersaturated solution (15% PEG 2000) showed a resolution of 3.5 Å, indicating a much lower quality. Crystal growth is clearly affected by modifying the growth conditions. However, there were no differences in crystal structural parameters such as the space group and lattice constants between cases with and without laser irradiation.

3.2. Growth of high quality protein crystal by solution stirring method

Triosephosphate isomerase (TIM) is an essential enzyme for glycolysis in both prokaryotes and eukaryotes and reversibly catalyses the isomerization of D-glyceraldehyde 3-phosphate to dihydroxyacetone phosphate. A number of TIM structures from various species are available and have been used for structural studies. For example, based upon parasitic structures, drug discovery has been developed [15]. In addition to effectiveness, selectivity against human TIM is necessary because TIM is also essential for human beings. High-resolution structures of human TIM as well as comprehensive understanding of the enzyme reaction should greatly help in the discovery of drugs with selectivity between the respective TIMs.

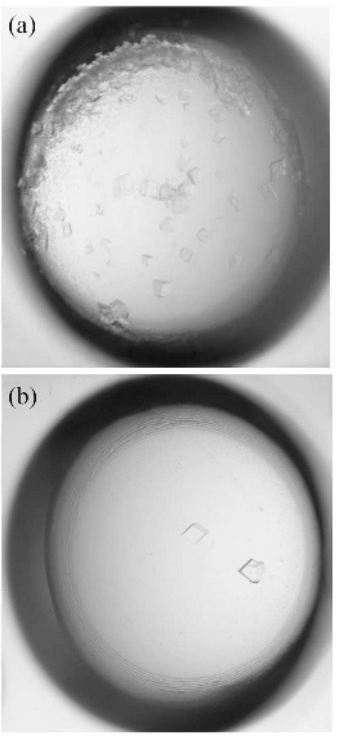

Fig. 2. Typical crystallization results obtained for AcrB crystals. (a) Conventional growth in a highly supersaturated solution (without laser irradiation) and (b) laser-irradiated growth in a low-range supersaturated solution, in which nucleation seldom occurs.

Crystals of human TIM (crystal form 1) were obtained using the normal vapour-diffusion technique as shown in Fig. 3a and diffracted to 2.8 Å resolution [16]. The crystals were suitable for structure analysis, but it was difficult to grow crystals suitable for high-resolution data collection. Gel-tube methods both on earth and under microgravity gave slightly larger crystals (crystal form 2) (Fig. 3b and 3c), and improved the crystal quality. The crystals from the gel-tube method under microgravity diffracted to 2.2 Å resolution [17]. However, it is difficult to get the opportunity and it costs too much for microgravity experiments.

In the previous studies, we have proved that the quality of bovine adenosine deaminase (ADA) crystals was improved using solution-stirring methods [18-20]. The solution-stirring method is simple and easy to try. In this work, in order to ascertain the utility of solution-stirring methods and get a high-resolution data of human TIM for further refinements, solution-stirring method was applied to TIM crystallization.

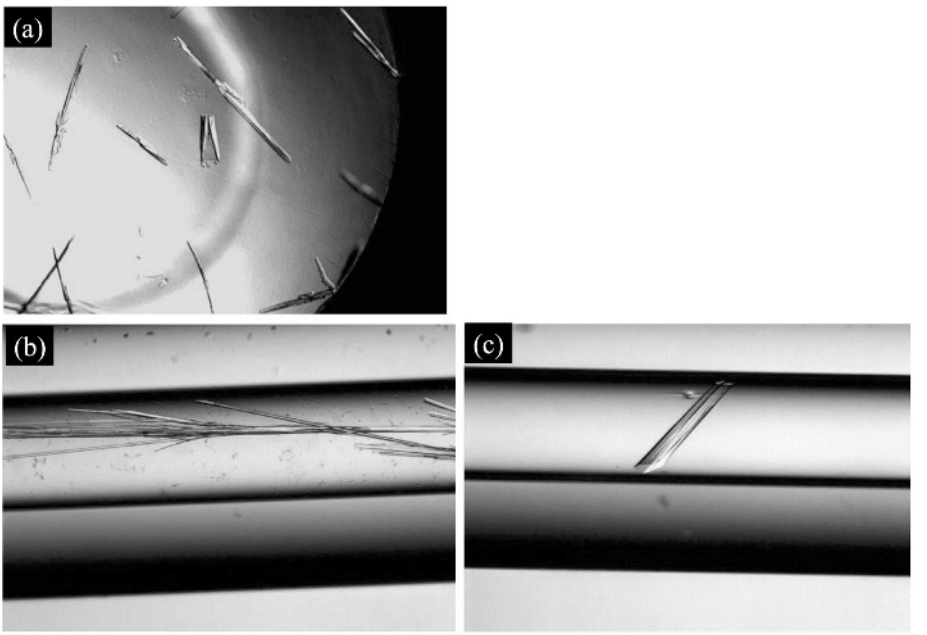

Fig. 3. Crystals of human triosephosphate isomerase from (a) the sitting-drop vapour-diffusion method, (b) the gel-tube method on earth and (c) the gel-tube method under microgravity.

Human TIM was purified as previously described [17]. Protein purity was determined by SDS-PAGE and dynamic light-scattering analysis. All other chemicals were reagent grade. The Micro-Stirring technique using sitting-drop vapor-diffusion technique [21, 22] was carried out. The crystallization plate and sealing tape were purchased from Emerald BioStructures. We used rotation speeds of 50 and 75 rpm to stir the protein solution for the Micro-Stirring

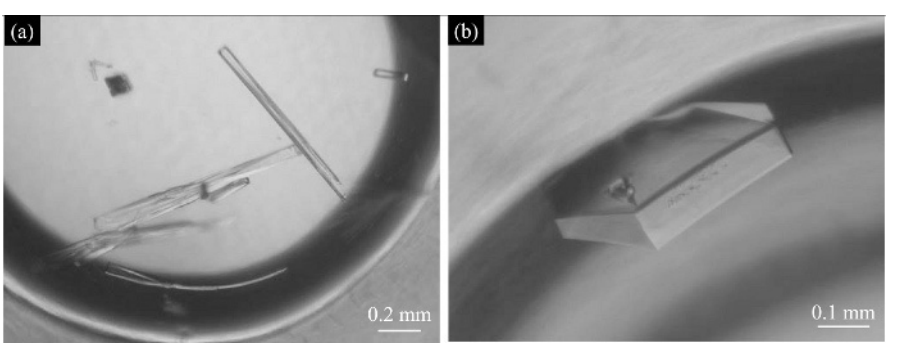

Fig. 4. Crystals of human triosephosphate isomerase from the Micro-Stirring technique at a rotation speed of (a) 50 and (b) 75 rpm.

technique. The TIM was crystallized at a protein concentration of 10 mg/ml by vapor diffusion in 30-35% PEG 4000, 0.1-0.5 M NaOAc, 5 mM DTT and 0.1 M Tris-HCl pH 8.5 at 293 K.

Human TIM crystals (crystal form 2) were obtained using the Micro-Stirring technique. The crystal shape and size at a rotation speed of 50 rpm (Fig. 4a) were similar to those in the gel-tube under microgravity (Fig. 3c). The results of this experiment demonstrate again that solution-stirring is a more effective method of producing high-quality protein crystals than conventional techniques. On the other hand, at higher rotation speeds of 75 rpm, larger crystals (crystal form 1) were obtained (Fig. 4b). The results suggest that the solution-stirring method is more valuable for human TIM crystallization than the gel-tube method under microgravity.

We acquired X-ray diffraction (XRD) data on human TIM crystals grown by the Micro-Stirring technique to evaluate crystallinity. Crystals were mounted in a nylon loop (Hampton Research) and cooled to 100 K in an N_2 gas stream (Rigaku). Diffraction data sets were collected at beamline 41XU at SPring-8 using an ADSC Quantum315 CCD detector. A wavelength of 0.93 Å and a crystal-to-detector distance of 155 mm were used. Data integration and scaling were performed with HKL2000 [23]. High-quality XRD data was obtained from the human TIM crystals grown using the Micro-Stirring technique (Fig. 5). The crystals showed diffraction maximally at a resolution of 1.2 Å and the data were processed at 1.41 Å resolution. Crystal and data-collection statistics are shown in Table 1. The results reported here clearly demonstrate that solution-stirring method dramatically improves crystallinity of human TIM. Furthermore, protein crystal growth and crystal morphologies in a stirred solution are strongly dependent on the stirring speed, or the solution flow [24, 25]. Therefore, optimized stirring conditions are essential for producing high-quality protein crystals. The structural details of the human TIM crystal at 1.41 Å resolution will be reported elsewhere.

Although the crystals of human TIM obtained using the normal vapour-diffusion technique diffracted to 2.8 Å resolution, the crystals produced using the gel-tube and solution-stirring methods showed resolution of 2.2 and 1.4 Å, respectively. Therefore, crystal growth of human TIM is strongly affected by modifying the growth conditions. In the case of ADA crystallization, the crystals are improved by not only a high magnetic field [26] but also solution-stirring [18]. These results represent that crystals will be improved by the solution-stirring method if they are improved by other methods modifying the growth conditions. We also propose that further refinements of crystallization conditions using the laser irradiated growth technique (LIGHT) [27, 28] and the combination of laser-irradiated growth and stirring which we have previously developed for obtaining high-quality protein crystals, could allow a supply of higher-resolution structures of human TIM.

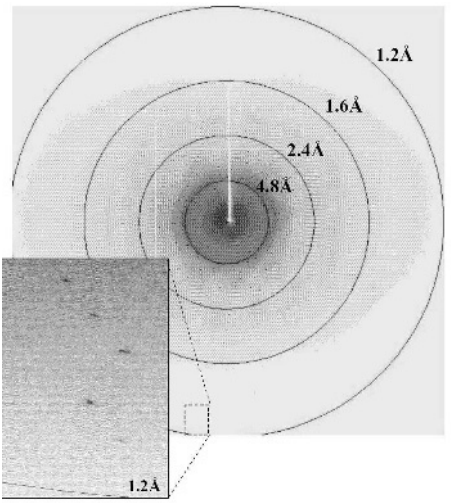

Fig. 5. XRD patterns of human TIM crystals grown by the Micro-Stirring technique.

4. NA FLUX LPE GROWTH OF BULK GAN CRYSTAL

GaN-based semiconductors are practically used as short-wavelength-emitting devices. To realize a high-intensity and high-efficiency laser diode (LD) and high-power devices, the number of dislocations in such devices should be reduced [29]. At present, the generation of high dislocation densities in devices is unavoidable because devices are fabricated on another substrate, such as sapphire or SiC, which has a large misfit with the GaN (0001) face. Thus, there is a strong demand for large GaN single crystals that can be used as substrates

Table 1
Crystallographic parameters and data collection and processing statistics of human TIM crystals grown by the Micro-Stirring technique. Values in parentheses are for the highest-resolution shell.

Crystallographic parameters	
Space group	$P2_12_12_1$
Unit-cell parameters (Å)	
a, b, c	64.95, 72.17, 92.48
Data collection and processing statistics	
Resolution (Å)	1.41 (1.44-1.41)
No. of observed reflections	478,965
No. of unique reflections	146,363
R_{merge} (%)	4.3 (41.2)
Completeness (%)	99.8 (91.5)

for the homoepitaxial growth of GaN-based semiconductors. Although the hydride vapor-phase epitaxy (HVPE) method [30-32], the high-pressure solution growth (HPSG) method [33-37], and the Na flux method [38-43] are candidate methods for growing large GaN single crystals, the high cost of crystal growth and crystal defects prevent full-scale practical applications. We previously demonstrated that a large GaN single crystal with a low dislocation density (on the order of 10^4 cm^{-2}) can be grown on MOCVD-GaN thin film, which has a high dislocation density on the order of 10^7 - 10^8 (cm^{-2}), by applying the liquid phase epitaxy (LPE) technique to the Na flux method [41, 42, 44]. Dislocation density was measured by cathodeluminescence (CL) measurement and chemical etching.

Some dislocation reduction techniques in a GaN crystal have already been reported. The most popular technique among them is the epitaxial lateral over (ELO) growth, in which SiO_2 masks formed on a GaN crystal inflect dislocations when an epitaxial layer develops on the mask [45, 46]. A low dislocation region can be grown using the ELO technique. Some dislocation reduction techniques that do not use masks have also been reported. M. Ishida et al. showed that a counter portion formed on a GaN surface can concentrate dislocations when the crystal grows on an uneven surface, resulting in the formation of a low dislocation region [47]. Yasuo Ohba et al. reported that the selective growth of islands having low dislocations enables the growth of low-dislocation GaN crystals [48]. In HVPE growth, the number of dislocations naturally decreases as thickness increases [49].

However, the mechanism underlying dislocation reduction in GaN crystal grown on MOCVD-GaN film by LPE has not yet been clarified. In this study, TEM observation around the interface between MOCVD-GaN and LPE-GaN revealed that the drastic decrease in the dislocation density occurs in the initial stage of LPE growth. On the basis of our TEM investigations of dislocations and our SEM observations, we propose a new dislocation reduction mechanism during LPE growth.

A GaN single crystal sample for TEM observation was prepared by applying the LPE technique to the Na flux method [44]. LPE-GaN was grown on MOCVD-GaN thin film fabricated on a sapphire (0001) substrate. (1) A 10-μm-thick MOCVD-GaN film with a sapphire (0001) substrate that has a dimensions of 10×5 (mm^2), metal-Na (0.88 g), and metal-Ga (1.0 g) were set in an alumina crucible. Then, the crucible was transferred into a pressure- and temperature-resistant stainless steel tube. (2) The tube was heated to 865 ^{o}C in an electric furnace and then subjected to a nitrogen pressure of 35 atm. LPE growth was achieved by nitrogen dissolution into a Ga-Na metal melt for 96 hrs. Temperature and pressure were kept constant throughout the experiment. (3) For TEM observations, a portion around the interface between LPE-GaN and MOCVD-GaN was quarried out, and then the sample was thinned to 200 nm

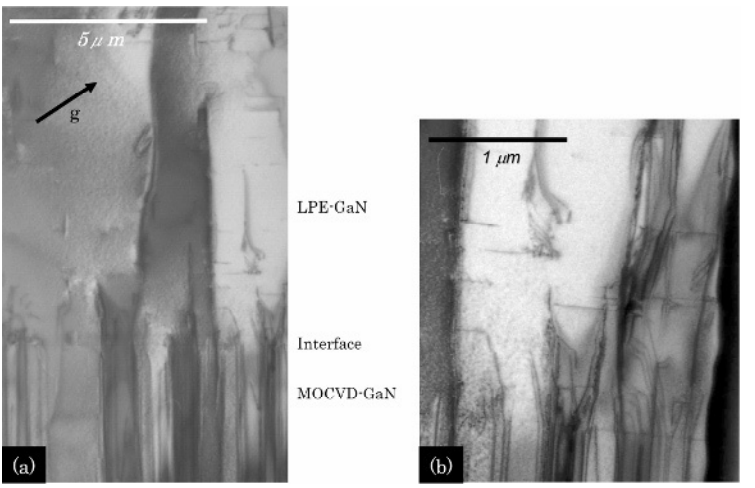

Fig. 6(a). TEM [1-100] photograph taken around the interface between MOCVD-GaN and LPE-GaN. And (b) Enlarged view of TEM [1-100] photograph around the interface between MOCVD-GaN and LPE-GaN.

using a focused ion beam (FIB) to investigate dislocation behavior by TEM (Hitachi H-800, accelerated voltage: 200 kV) as shown in Fig. 6. To observe all kinds of dislocations (Burgers vector b =<0001>, b=1/3<11-20>, and b=1/3<11-23>) in the crystal, a reflection vector of 11-22 was adopted, and then TEM images were captured by bright-field imaging under the Bragg condition. The direction of incident electron beam was approximately [1-100].

Figure 6(a) shows a TEM [1-100] image near the interface between LPE-GaN and MOCVD-GaN. After LPE growth started, almost all dislocations taking over from the MOCVD-GaN disappeared within 2 μm. It was confirmed that almost all dislocations were bent at the initial LPE growth stage and were then concentrated as shown in Fig. 6(b). Although some bent dislocations may move outside the sample, TEM observations suggest that a number of dislocations should be drastically reduced.

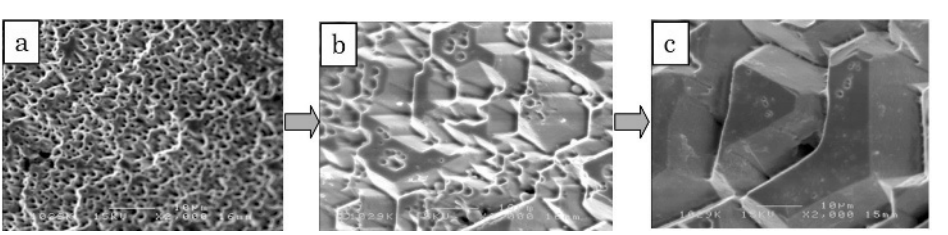

Fig. 7. Changes in surface morphology of LPE-GaN grown using Na flux method: a) “Initial stage of LPE (thickness: approximately 1～2μm)”; b) “Formation of (10-11) facets (thickness:

a fewμm)"; c) stable growth of large facets with coalescence (thickness: several tens of μm).

Figure 7 shows an Scanning Electron Microscope (SEM) image taken at each stage of LPE growth. At the stage of a few μm thickness, many small facets bounded by {10-11} formed across the whole surface of MOCVD-GaN (0001). Thereafter, the number of facets decreased as thickness increased and a (0001) face started to develop. Then, at the stable growth stage, GaN (0001) developed across the whole surface. In the Na flux method, a distinctive phenomenon in which the GaN {10-11} face forms easily at low supersaturation and then at higher supersaturation, and GaN (0001) preferentially develops has already been reported [50]. This phenomenon corresponds to our LPE growth regarding the preferentially developed change in the face index.

The observations made in this study can lead to a model of the drastic dislocation reduction in the LPE growth as shown in Fig. 8.

Although any artificial process such as coating of SiO_2 mask was not conducted, two dislocation reduction behaviors including 1) the concentration of dislocations at initial growth stage and 2) dislocation bending like an ELO at the later growth stage enabled us to grow GaN single crystals with an extremely low dislocation density (on the order of 10^4 cm^{-2}) in the LPE growth.

5. CONCLUSIONS

Controlling the processes of crystal core generation and crystal formation is essential for forming large superior crystals from flux. The primary challenge is overcoming the technical hurdles to control the flux state. This is a general principle that can be applied to oxides, proteins, and nitrides, i.e., regardless of the material. It is important to homogenize the state of flux as thoroughly as possible in the process of crystal formation, including the concentration and temperature, by stirring and maintaining supersaturation at the lowest level

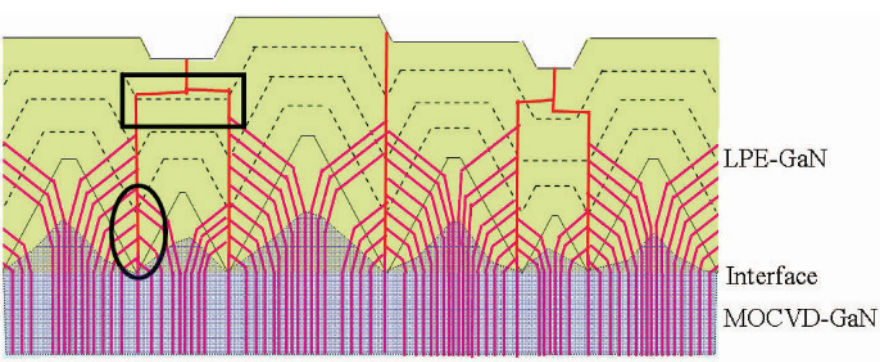

Fig. 8 Dislocation reduction model of LPE growth in Na flux method. Concentration and bending of bundled dislocations cause a drastic decrease in the dislocation density.

required to obtain the necessary growth speed. Stirring may enable us to control the size of clusters in the solution and to maintain them as spatially constant throughout the growth period. Improved crystallization of CLBO and proteins can be achieved under appropriate control of the flux state by thoroughly stirring the solutions. The supersaturation degree of solutions for materials for which crystal formation is difficult, such as proteins, should be increased to induce nucleation at the beginning of crystallization. However, flux is not in an ideal state for growing crystals once the core is formed. Therefore, the supersaturation degree must be increased in a limited micro area in the solution for a short duration to generate the crystal core and the solution must be subsequently returned to the ideal condition for crystal growth. We confirmed through the use of proteins that we can effectively achieve this by focusing femtosecond laser irradiation into the solutions.

ACKNOWLEDGMENTS

This work was partly supported by the Industrial Technology Research Grant Program from the NEDO, by the CREST from the JST, and by the Grant-in-Aid for National Project on Protein Structural and Functional Analyses from the MEXT.We also thank many collaborators and companies for their useful suggestions and help.

REFERENCES

[1] Y. Mori, I. Kuroda, S. Nakajima, T. Sasaki, and S. Nakai, Appl. Phys. Lett., 67, 1818 (1995).
[2] T. Sasaki, Y. Mori, I. Kuroda, S. Nakajima, K. Yamaguchi, and S. Watanabe, Acta Cryst., C51, 2222 (1995).
[3] Y. Mori, I. Kuroda, S. Nakajima, T. Sasaki, S. Nakai, Jpn. J. Appl. Phys., 34, L296 (1995).
[4] Y. Mori, I. Kuroda, S. Nakajima, T. Sasaki, and S. Nakai, J. Crystal Growth, 156, 307 (1995).
[5] M. Yoshimura, H. Furuya, T. Kobayashi, K. Murase, Y. Mori, and T. Sasaki, Opt. Lett., 24, 193 (1999).
[6] Z.G. Hu, T. Higashiyama, M. Yoshimura, Y.K. Yap, Y. Mori, and T. Sasaki, Jpn. J. Appl. Phys. 37, L1093 (1998).
[7] P. Becker, Adv. Mater., 10, 979 (1998).
[8] V.G. Dmitriev, G.G. Gurzadyan, D.N. Nikogosyan, in: A.L. Schawlow, A.E. Siegman, T. Tamir (Eds.), *Handbook of Nonlinear Optical Crystals*, 3rd Edition, Springer, Berlin, 1999.
[9] M. Yoshimura, Y. Kamimura, K. Murase, Y. Mori, H. Yoshida, M. Nakatsuka, and T. Sasaki, Jpn. J. Appl. Phys., 38, L129 (1999).
[10] K. Nakai, T. Kamimura, H. Sawada, M. Yoshimura, Y. Mori, and T. Sasaki, in: Proceedings of the Pacific Rim Conference on Lasers and Electro-Optics 1999, Vol.3, Paper P2.71, Technical digest IEEE catalog 99TH8464, Seoul, 1999, p.967.
[11] J. Drews: Science 287 (2000) 1960.

[12] C. Hunte, G. Jagow and H. Schägger: *Membrane Protein Purification and Crystallization* (Academic Press, California, 2003) 2nd ed.
[13] H. Adachi, K. Takano, Y. Hosokawa, T. Inoue, Y. Mori, H. Matsumura, M. Yoshimura, Y. Tsunaka, M. Morikawa, S. Kanaya, H. Masuhara, Y. Kai and T. Sasaki: Jpn. J. Appl. Phys. 42 (2003) L798.
[14] S. Murakami, R. Nakashima, E. Yamashita and A. Yamaguchi: Nature 419 (2002) 587.
[15] C. Walsh: Nature 406 (2000) 775.
[16] S. S. Velanker, S. S. Ray, R. S. Gokhale, S. Suma, H. Balaram, P. Balaram and M. Murthy: Structure 5 (1997) 751.
[17] S. C. Mande, V. Mainfroid, K. H. Lalk, K. Goraj, J. A. Martial and G. J. Hol: Protein Sci. 3 (1994) 810.
[18] T. Kinoshita, R. Maruki, M. Warizaya, H. Nakajima and S. Nishimura: Acta Crystallogr. F61 (2005) 346.
[19] H. Adachi, H. Matsumura, A. Niino, K. Takano, T. Kinoshita, M. Warizaya, T. Inoue, Y. Mori and T. Sasaki: Jpn. J. Appl. Phys. 43 (2004) L522.
[20] A. Niino, H. Adachi, K. Takano, H. Matsumura, T. Kinoshita, M. Warizaya, T. Inoue, Y. Mori and T. Sasaki: Jpn. J. Appl. Phys. 43 (2004) L1442.
[21] H. Adachi, K. Takano, A. Niino, H. Matsumura, T. Kinoshita, M. Warizaya, T. Inoue, Y. Mori and T. Sasaki: Acta Crystallogr. D61 (2005) 759.
[21] H. Adachi, K. Takano, M. Yoshimura, Y. Mori and T. Sasaki: Jpn. J. Appl. Phys. 42 (2003) L314.
[22] H. Adachi, K. Takano, H. Matsumura, M. T. Inoue, Mori and T. Sasaki: J. Synchrotron Rad. 11 (2004) 121.
[23] Z. Otwinowski and W. Minor: Methods Enzymol. 276 (1997) 307.
[24] M. Yaoi, H. Adachi, K. Takano, H. Matsumura, T. Inoue, Y. Mori and T. Sasaki: Jpn. J. Appl. Phys. 43 (2004) L686.
[25] M. Yaoi, H. Adachi, K. Takano, H. Matsumura, T. Inoue, Y. Mori and T. Sasaki: Jpn. J. Appl. Phys. 43 (2004) L1318.
[26] T. Kinoshita, M. Ataka, M. Warizaya, M. Neya and T. Fujii: Acta Crystallogr. D59 (2003) 1333.
[27] H. Adachi, K. Takano, Y. Hosokawa, T. Inoue, Y. Mori, H. Matsumura, M. Yoshimura, Y. Tsunaka, M. Morikawa, S. Kanaya, H. Masuhara, Y. Kai and T. Sasaki: Jpn. J. Appl. Phys. 42 (2003) L798.
[28] H. Adachi, S. Murakami, A. Niino, H. Matsumura, K. Takano, T. Inoue, Y. Mori, A. Yamaguchi and T. Sasaki: Jpn. J. Appl. Phys. 43 (2004) L1376.
[29] X. A. Cao and S. D. Arthur: Appl. Phys. Lett., 85, 18, 3971 (2004)
[30] K. Motoki, T. Okahisa, S. Nakahata, N. Matsumoto, H. Kimura, H. Kasai, K. Takemoto, K. Uematsu, M. Ueno, Y. Kumagai, A. Koukitu, H. Seki: J. Cryst. Growth, 237-239, (2002) 912
[31] E. Aujol, A. Trassoudaine, L. Siozade, A. Pimpinelli, R. Cadoret: J. Cryst. Growth, 230, (2001) 372
[32] C. E. C. Dam, A. P. Grzegorczyk, P. R. Hageman, R. Dorsman, C. R. Kleijn, P. K. Larsen: J. Cryst. Growth, 271, (2004) 192
[33] J. Karpinskin, J. Jun, S. Porowski: J. Cryst. Growth, 66, (1984) 1
[34] S. Porowski: J. Cryst. Growth, 166, (1996) 583
[35] S. Porowski, I. Grzegory: J. Cryst. Growth, 178, (1997) 174
[37] I. Grzegory, M. Bockowski, B. Lucznik, S. Krukowski, Z. Romanowski, M. Wroblewski and S. Porowski: J. Cryst. Growth, 246, (2002) 177
[38] H. Yamane, M. Shimada, S. J. Clarke, and F. J. DiSalvo: Chem. Mater., 9 (1997) 413

[39] F. Kawamura, M. Morishita, T. Iwahashi, M. Yoshimura, Y. Mori, and T. Sasaki: Jpn. J. Appl. Phys., 41 (2002) L1440
[40] M. Morishita, F. Kawamura, T. Iwahashi, M. Yoshimura, Y. Mori, and T. Sasaki: Jpn. J. Appl. Phys., 42 (2003) L565
[41] F. Kawamura, T. Iwahashi, K. Omae, M. Morishita, M. Yoshimura, Y. Mori, and T. Sasaki: Jpn. J. Appl. Phys., 42 (2003) L4
[42] F. Kawamura, T. Iwahashi, M. Morishita, K. Omae, M. Yoshimura, Y. Mori, and T. Sasaki: Jpn. J. Appl. Phys., 42 (2003) L729
[43] F. Kawamura, M. Morishita, K. Omae, M. Yoshimura, Y. Mori, and T. Sasaki: Jpn. J. Appl. Phys., 42 (2003) L879
[44] M. Morishita, F. Kawamura, M. Kawahara, M. Yoshimura, Y. Mori and T. Sasaki: J. Cryst. Growth, 270, (2004) 402
[45] M. Hao, S. Mahanty, Y. Morishima, H. Takenaka, J. Wang, S. Tottori, K. Nishino, Y. Naoi and S. Sakai: J. Appl. Phys., 85, 9, (1999) 6497
[46] Z. Yu, M. A. L. Johnson, J. D. Brown, N. A. El-Masry, J. W. Cook Jr. and J. F. Schetzina: J. Cryst. Growth, 195, (1998) 333
[47] M. Ishida, M. Ogawa, K. Orita, O. Imafuji, M. Yuri, T. Sugino and K. Itoh: J. Cryst. Growth, 221, (2000) 345
[48] Y. Ohba and S. Iida: Jpn. J. Appl. Phys., 41, (2002) L615
[49] K. Lee and K. Auh: MRS Internet J. Nitride Semicond. Res., 6. 9 (2001)
[50] M. Aoki, H. Yamane, M. Shimada, S. Sarayama and F. J. DiSalvo: Mater. Lett., 56, (2002) 660

Author Index